2011

QCD
and
High Energy Interactions

Sponsored by

. CNRS (Centre National de la Recherche Scientifique)
. CEA (Commissariat à l'Énergie Atomique)
. IN2P3 (Institut National de Physique Nucléaire et de Physique des Particules)
. NSF (National Science Foundation)
. FNRS (Fond National de la Recherche Scientifique)
. BSP (Belgian Science Policy)

XLVIth Rencontres de Moriond

La Thuile, Aosta Valley, Italy – March 20-27, 2011

2011 QCD and High Energy Interactions

Proceedings of the XLVIth RENCONTRES DE MORIOND

QCD and High Energy Interactions

La Thuile, Aosta Valley Italy *March 20-27, 2011*

2011

QCD and High Energy Interactions

edited by

Etienne Augé,

Jacques Dumarchez

and

Jean Trân Thanh Vân

The XLVIth Rencontres de Moriond

2011 QCD and High Energy Interactions

was organized by :

Etienne Augé (IN2P3, Paris)
Jacques Dumarchez (LPNHE, Paris)

with the active collaboration of :

E. Berger (A.N.L. Argonne)
S. Bethke (M.P.I. Munich)
A. Capella (L.P.T. Orsay)
A. Czarnecki (U. Alberta)
D. Denegri (C.E.A. Saclay)
N. Glover (Durham)
B. Klima (Fermilab)
M. Krawczyk (University of Warsaw)
L. McLerran (Brookhaven Nat. Lab.)
B. Pietrzyk (L.A.P.P. Annecy)
L. Schoeffel (CEA - IRFU/SPP - Saclay)
Chung-I Tan (Brown University)
J. Trân Thanh Vân (L.P.T. Orsay)
U. Wiedemann (CERN)

2011 RENCONTRES DE MORIOND

The XLVIth Rencontres de Moriond were held in La Thuile, Valle d'Aosta, Italy.

The first meeting took place at Moriond in the French Alps in 1966. There, experimental as well as theoretical physicists not only shared their scientific preoccupations, but also the household chores. The participants in the first meeting were mainly french physicists interested in electromagnetic interactions. In subsequent years, a session on high energy strong interactions was added.

The main purpose of these meetings is to discuss recent developments in contemporary physics and also to promote effective collaboration between experimentalists and theorists in the field of elementary particle physics. By bringing together a relatively small number of participants, the meeting helps develop better human relations as well as more thorough and detailed discussion of the contributions.

Our wish to develop and to experiment with new channels of communication and dialogue, which was the driving force behind the original Moriond meetings, led us to organize a parallel meeting of biologists on Cell Differentiation (1980) and to create the Moriond Astrophysics Meeting (1981). In the same spirit, we started a new series on Condensed Matter physics in January 1994. Meetings between biologists, astrophysicists, condensed matter physicists and high energy physicists are organized to study how the progress in one field can lead to new developments in the others. We trust that these conferences and lively discussions will lead to new analytical methods and new mathematical languages.

The XLVIth Rencontres de Moriond in 2011 comprised four physics sessions:

- March 13 - 20: "Electroweak Interactions and Unified Theories"
- March 13 - 20: "Quantum Mesoscopic Physics"
- March 20 - 27: "QCD and High Energy Hadronic Interactions"
- March 20 - 27: "Gravitational Waves and Experimental Gravity"

We thank the organizers of the XLVIth Rencontres de Moriond:

- A. Abada, J. Conrad, S. Davidson, P. Fayet, J.-M. Frère, P. Hernandez, L. Iconomidou-Fayard, P. Janot, M. Knecht, J. P. Lees, S. Loucatos, F. Montanet, L. Okun, J. Orloff, A. Pich, S. Pokorski, D. Wood for the "Electroweak Interactions and Unified Theories" session,

- D. Averin, C. Beenakker, Y. Blanter, K. Ennslin, Jie Gao, L. Glazman, C. Glattli, Y. Imry, Young Kuk, T. Martin, G. Montambaux, V. Pellegrini, M. Sanquer, S. Tarucha for the "Quantum Mesoscopic Physics" session,

- E. Augé, E. Berger, S. Bethke, A. Capella, A. Czarnecki, D. Denegri, N. Glover, B. Klima, M. Krawczyk, L. McLerran, B. Pietrzyk, L. Schoeffel, Chung-I Tan, J. Trân Thanh Vân, U. Wiedemann for the "QCD and High Energy Hadronic Interactions" session,

- M.-Ch. Angonin, R. Ansari, M.-A. Bizouard, L. Blanchet, M. Cruise, J. Dumarchez, Y. Giraud-Héraud, S. Hoedl, Ch. Magneville, E. Rasel, S. Reynaud, F. Ricci, R. Schnabel, J.-Y. Vinet, P. Wolf for the "Gravitational Waves and Experimental Gravity" session, joint with the GPhyS Colloquium

and the conference secretariat and technical staff:

V. de Sá-Varanda and C. Bareille, I. Cossin, G. Dreneau, D. Fligiel, S. Hurtado, N. Ribet, S. Vydelingum.

We are also grateful to Andrea Righetto, Gioacchino Romani, Erik Agostini, Patrizia Rago, Matteo Tuzzi and the Planibel Hotel staff who contributed through their hospitality and cooperation to the well-being of the participants, enabling them to work in a relaxed atmosphere.

The Rencontres were sponsored by the Centre National de la Recherche Scientifique, the Institut National de Physique Nucléaire et de Physique des Particules (IN2P3-CNRS), the Fondation NanoSciences, the Commissariat à l'Energie Atomique (DSM and IRFU), the Centre National d'Etudes Spatiales, the European Space Agency, the Fonds de la Recherche Scientifique (FRS-FNRS), the Belgium Science Policy and the National Science Foundation. We would like to express our thanks for their encouraging support.

It is our sincere hope that a fruitful exchange and an efficient collaboration between the physicists and the astrophysicists will arise from these Rencontres as from previous ones.

E. Augé, J. Dumarchez and J. Trân Thanh Vân

Contents

Foreword

1. Higgs

Searches for low-mass Standard Model Higgs at the Tevatron	M. Cooke	3
Searches for high-mass SM Higgs at the Tevatron	R. Lysák	7
Standard Model Higgs Searches at the Tevatron: Combinations	J. Hays	11
Searches for non-standard model Higgs at the Tevatron	R. St. Denis	15
LHC beam operations: past, present and future	M. Lamont	21
HERA precision measurements and impact for LHC predictions	V. Radescu	27
Higgs Boson Searches at CMS and ATLAS	W. Quayle	31
Theoretical uncertainties in Higgs searches	A. Djouadi	35

2. New Phenomena

SUSY Searches at the Tevatron	Ph. Gris	41
SUSY searches at ATLAS	N. Barlow	45
SUSY searches in CMS	M. Chiorboli	53
Non-SUSY searches at the TeVatron	J. Strologas	57
Non-SUSY searches at ATLAS	E.N. Thompson	61
The Quasi-Classical Model in SU(N) Gauge Field Theory	A.V. Koshelkin	67

3. Top

Top quark pair production cross section at the Tevatron	S. Amerio	73
Top Quark Mass Measurements at the Tevatron	Zhenyu Ye	79
Recent results on top physics at ATLAS	M. Cristinziani	83
Measurements of the properties of the top quark	O. Brandt	87
Heavy quark and quarkonia production with the LHCb detector	N. Mangiafave	91
Heavy flavour production at ATLAS	Z. Doležal	95
Heavy flavor production at CMS	K. A. Ulmer	99

4. Heavy Flavours

Heavy flavour in a nutshell	R. Lambert	105
Recent B physics results from the TeVatron	S. Behari	111
Search for $B_s^0 \to \mu^+\mu^-$ and $B_d^0 \to \mu^+\mu^-$ at LHCb	M.-O. Bettler	117
In pursuit of new physics with B decays	R. Fleischer	121
Charmless hadronic b-decays at *BABAR* AND BELLE	N. Arnaud	125
Estimating the Higher Order Hadronic Matrix Elements in the Heavy Quark Expansion	Th. Mannel	129
CP violation results and prospects with LHCb	C. Langenbruch	135
Direct CP asymmetry in $\bar{B} \to X_{s,d}\gamma$ decays	G. Paz	139
Charm spectroscopy at B factories	R. Cenci	143
Charm physics results and prospects with LHCb	P.M. Spradlin	147
Two body hadronic D decays	Cai-Dian Lü	151
Exotic/charmonium hadron spectroscopy at Belle and BaBar	D. Liventsev	157
Recent Results on Charmonium from BESIII	M. Maggiora	161
Unitarity of exclusive quark combination model: Exotic hadron production, entropy change and charmonium production for colour-singlet many-quark system	S.-Y. Li	165

5. QCD

Latest Jets Results from the Tevatron	C. Mesropian	171
Recent results on jets from CMS	F. Pandolfi	175
Recent results on jets with ATLAS	G. Pospelov	179
EPOS 2 and LHC Results	T. Pierog	183
About the helix structure of the Lund string	Š. Todorova-Novaá	187
Improving NLO-parton shower matched simulations with higher order matrix elements	K.M. Hamilton	191
New Results in Soft Gluon Physics	Ch. White	195

Central Exclusive Meson Pair Production in the Perturbative Regime	L.A. Harland-Lang	199
An average b-quark fragmentation function from e^+e experiments at the Z pole and recommendations for its use in other experimetnal environments	E. Ben-Haim	203
W^+W^+jj at NLO in QCD: an exotic Standard Model signature at the LHC	T. Melia	207
W/Z+Jets and W/Z+HF Production at the Tevatron	S. Camarda	211
W and Z physics with the ATLAS detector	N. Makovec	215
W/Z + Jets results from CMS	V. Ciulli	219
Tevatron results on multi-parton interactions	N.B. Skachkov	223
Investigations of double parton scattering example of $pp \to b\ \bar{b}$ jet jet X	E. L. Berger	227
Soft QCD results from ATLAS and CMS	C.-E. Wulz	233
Determination of $\boldsymbol{\alpha_S}$ using hadronic event shape distributions of data taken with the OPAL detector	J. Schieck	237
Reaching beyond NLO in processes with giant K-factors	S. Sapeta	241
Nonlocal Condensate Model for QCD Sum Rules	R.-C. Hsieh	245
An alternative subtraction scheme for NLO calculations	T. Robens	249
The NNPDF2.1 parton set	F. Cerutti	253
Holographic description of hadrons from string theory	S. Sugimoto	257
Nuclear matter and chiral phase transition at large-N_c	F. Giacosa	261
Recent Results on Light Hadron Spectroscopy at BESIII	Z. Wu	265
Measurement of the J/ψ inclusive production cross-section in pp collisions at $\sqrt{s}$=7 TeV with ALICE at the LHC	J. Wiechula	269
Study of K_{e4} decays in the NA48/2 experiment at CERN	B. Bloch-Devaux	273

6. Structure Functions, Diffraction

Hadronic final states and diffraction at HERA	I.A. Rubinskiy	279
Using HERA Data to Determine the Infrared Behaviour of the BFKL Amplitude	H. Kowalski	285
The AdS Graviton/Pomeron Description of Deep Inelastic Scattering at Small x	R. C. Brower	291
Diffraction, saturation and ***pp*** cross sections at the LHC	K. Goulianos	295
Transverse Energy Flow with Forward and Central Jets at the LHC	F. Hautmann	299

7. Heavy Ions

First measurements in Pb–Pb collisions at $\sqrt{s_{\rm NN}}$=2.76 TeV with ALICE at the LHC	M. Nicassio	305
Two-, three-, and jet-hadron correlations at STAR	K. Kauder	309
Forward Physics in d+Au Collisions: Cold Nuclear Matter Probed with J/ψ Production and Pion Correlations	R. Seto	313
Measurement of jet quenching with I_{CP} and $I_{AA,Pythia}$ in Pb-Pb collisions at $\sqrt{s_{NN}} = 2.76$ TeV with ALICE	J. F. Grosse-Oetringhaus	317
Jet Reconstruction and Jet Quenching in Heavy Ion Collisions at ATLAS	M. Spousta	321
Studies of Jet Quenching in HI Collisions at CMS	F. Ma	325
Jet quenching from RHIC to LHC	B. Zakharov	329
Electrical conductivity of quark matter in magnetic field	B. Kerbikov	333
The effect of triangular flow in jet-medium interaction	Chin-Hao Chen	337
The first Z boson measurement in the dimuon channel in PbPb collisions at $\sqrt{s} = 2.76$ TeV at CMS	L. Benhabib	341
Heavy-flavour production in pp and Pb–Pb collisions at ALICE	A. Mischke	347
Direct Photons and Photon-Hadron Correlations at PHENIX	B. Sahlmueller	351
Probing nuclear parton densities and parton energy loss processes through photon + heavy-quark jet production	F. Arleo	355
Measurements of $X_{\rm max}$ and tests of hadronic interactions with the Pierre Auger Observatory	C. Bleve	359

8. Conference Summary

Experimental summary: entering the LHC era	C. Vallée	365

List of participants 379

1.
Higgs

SEARCHES FOR LOW-MASS STANDARD MODEL HIGGS AT THE TEVATRON

M. COOKE
(on behalf of the CDF and D0 Collaborations)
Fermi National Accelerator Laboratory
Batavia, IL, United States of America

The key to reaching the sensitivity required for finding evidence for a standard model Higgs boson at the Fermilab Tevatron Collider is the improvement of analysis techniques that can lead to sensitivity gains beyond that from accumulating integrated luminosity. Recent results from the Tevatron experiments show that just such improvements are being made, and our projections indicate that with 10 fb^{-1} of integrated luminosity recorded by both CDF and D0 we may have the sensitivity to find evidence for a Higgs boson with a mass of 115 GeV.

The mechanism for spontaneous electroweak symmetry breaking in the standard model (SM) generates an additional particle, the Higgs boson, which has yet to be observed.[1,2,3] The search for this elusive particle has been a central aspect of the physics program at the Fermilab Tevatron Collider for many years. Although the SM does not predict the Higgs boson mass (m_H), the direct searches at the CERN e^+e^- Collider (LEP) and precision electroweak measurements constrain m_H to $114.4 < m_H < 185$ GeV at the 95% CL.[4,5] Direct searches at the Tevatron have further excluded the range $158 < m_H < 175$ GeV at the 95% CL, as shown in Figure 1.[6,7] As the Tevatron experiments accumulate integrated luminosity the expected search limits improve, but such improvements alone do not guarantee reaching 95% CL exclusion sensitivity for all m_H between 114.4 and 185 GeV. However, as shown in Figure 1, anticipated improvements to the Higgs search analyses should not only lead to 95% CL exclusion sensitivity in that mass range when using 10 fb^{-1} of data from each Tevatron experiment, but potentially 3σ evidence for a Higgs signal for $m_H \approx 115$ GeV and $150 < m_H < 180$ GeV.

The sensitivity of the Tevatron to a low-mass Higgs signal is of particular interest to the high-energy physics community because the lowest masses, near 115 GeV, will be the most difficult for the Large Hadron Collider experiments to exclude. In this region, with $m_H < 135$ GeV, the Higgs boson preferentially decays into to b quarks, which makes isolated Higgs production difficult to discern from the multijet production background. Instead, associated production with either a W or Z boson become the most sensitive search channels at the Tevatron while $H \to WW$, $H \to \tau\tau$ and $H \to \gamma\gamma$ play important roles in further improving the final combined limits.

The recent update to the CDF $ZH \to \mu\mu bb$ analysis includes two major changes that yield substantial sensitivity gains. By moving from a muon-based event trigger to a suite that includes jet triggers, the event selection efficiency is improved, as shown in Figure 2. This efficiency increase is largest for events with low muon p_T. Additional signal acceptance is obtained by moving from an event selection based on kinematic cuts to one based on a neural network. This

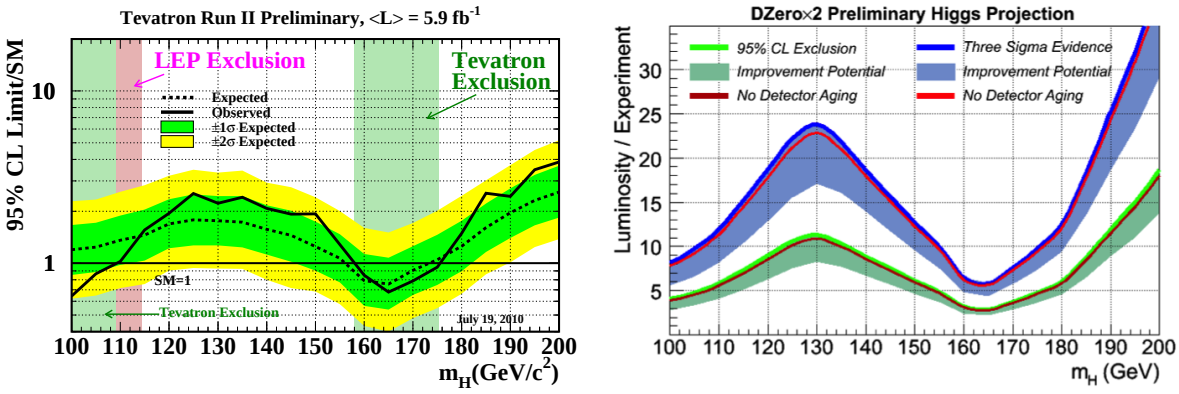

Figure 1: Left: Limits at the 95% CL on the cross section for a SM Higgs boson from the Tevatron as of July 2010. Right: The projected Tevatron 95% CL exclusion and 3σ evidence sensitivity to SM Higgs boson production as a function of Higgs boson mass (m_H) and delivered luminosity to each experiment. The shaded regions indicate the expected sensitivity gain through analysis improvements.

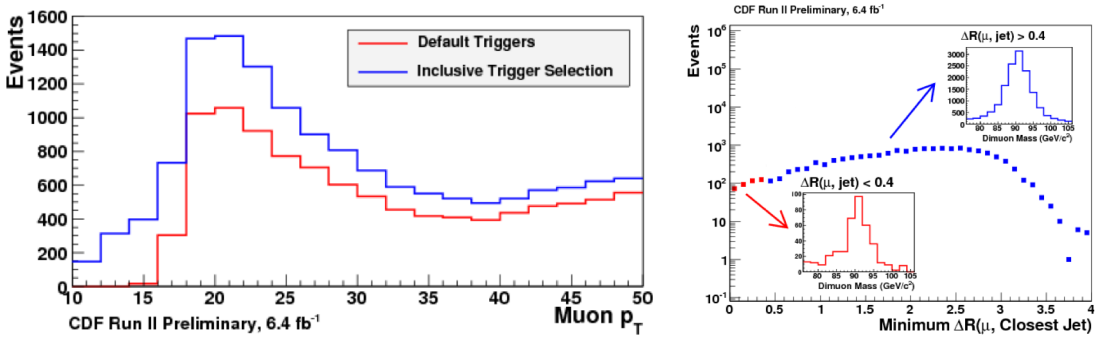

Figure 2: Left: Event selection efficiency in the CDF $ZH \to \mu\mu bb$ analysis increases substantially for low muon p_T events when moving to a more inclusive trigger suite. Right: Distribution of the minimum $\Delta\mathcal{R}$ between a muon and jet after using a neural network based event selection, with inset plots showing dimuon invariant mass for events that pass and fail the previous analysis cut of $\Delta\mathcal{R} > 0.4$.

allows for the recovery of signal-like events where $\Delta\mathcal{R}$ between a muon and a jet is below the previous cut threshold.[a] Together, these improvements help this analysis gain 25% improvement in the expected 95% CL limit at $m_H = 115$ GeV beyond the expected gain due to additional integrated luminosity when compared to its previous iteration.

Including more Higgs boson decay channels in the Tevatron combination helps improve our expected sensitivity by effectively adding extra signal acceptance to our overall search. Analyses at both CDF and D0 focus on Higgs decays that include both a hadronic tau decay (τ_h) and an electron or muon. This hadronic plus leptonic channel account for 46% of all $\tau\tau$ decays. It also includes contributions from both direct and associated production modes and many decay modes, leading to relatively consistent sensitivity at all m_H, as shown in Figure 3. The latest iteration of the D0 analysis added the $e\tau_h$ channel to the previous $\mu\tau_h$-only analysis and improved the expected sensitivity at $m_H = 115$ GeV by 15% beyond improvements due to the additional integrated luminosity.

For the low-mass associated production channels, discriminating the b-quark jet signature of a potential Higgs boson signal from the large background of light-quark multijet events is a key element of each analysis. Selecting events with one or two candidate b-jets substantially improves the signal to background ratio, as shown in Figure 4. At D0, recent improvements

[a] $\Delta\mathcal{R} = \sqrt{\Delta\phi^2 + \Delta\eta^2}$ between two objects, where pseudorapidity $\eta = -\ln[\tan(\frac{\theta}{2})]$ and θ is the angle between a particle and the beam axis.

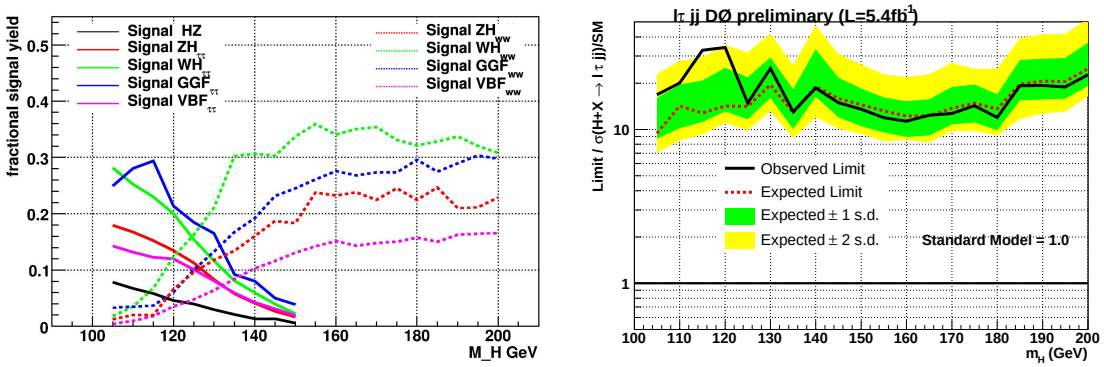

Figure 3: Left: Fraction of the total signal yield from various sources involving direct $H \to \tau\tau$ decays and tauonic or semitauonic $H \to WW$ decays in the $\tau^+\tau^- + 2$ jet channel at D0. Right: The expected and observed limits in this search channel as a function of m_H.

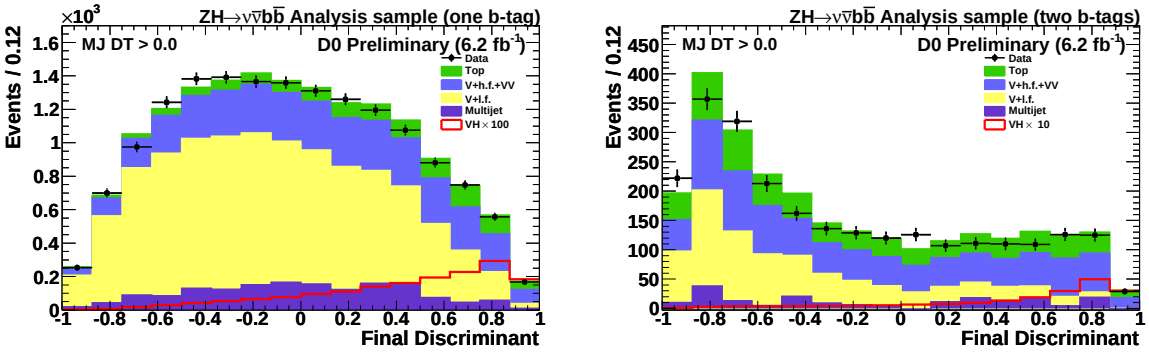

Figure 4: Left: Final multivariate discriminant output for $m_H = 115$ GeV in the one b-jet candidate channel for the $ZH \to \nu\nu bb$ search at D0. Right: Similar multivariate discriminant output in the two b-jet candidate channel.

in the algorithms used to identify b-quark jets and discriminate them from light-quark jets has directly lead to improvements in the sensitivity of the $ZH \to \nu\nu bb$ analysis. The new multivariate b-jet identifier has a substantially better light-quark jet fake rate vs. b-jet efficiency curve and also produces a continuous identification discriminant output that can be used as an input to the final signal discriminant. These advances have led to a 6% improvement over the previous result in the sensitivity at $m_H = 115$ GeV beyond the expectation due to the increased data sample alone and demonstrates the potential improvement for all D0 analyses that rely on b-jet identification.

Multivariate discriminants that separate potential signal events from the many sources of background are widely used as part of the Higgs boson search strategy at the Tevatron. Their output is used as the input for the limit setting procedure for many analyses. The recent D0 $H \to \gamma\gamma$ update switched from using the diphoton invariant mass distribution alone to set search limits to using the output from a boosted decision tree (BDT).[10,11] The BDT transforms the diphoton invariant mass, the transverse energy of the two photon candidates, the transverse momentum of the diphoton system and the azimuthal angle between the photon candidates into a single powerful discriminant, as shown in Figure 5. Compared to the previous iteration of this analysis, this improved technique helps gain a 17% improvement in sensitivity at $m_H = 115$ GeV beyond the improvement due to the increased data sample.

The Tevatron experiments expect to record over 10 fb^{-1} of integrated luminosity before beam collisions cease in the fall of 2011. Analysis techniques at both CDF and D0 continue to

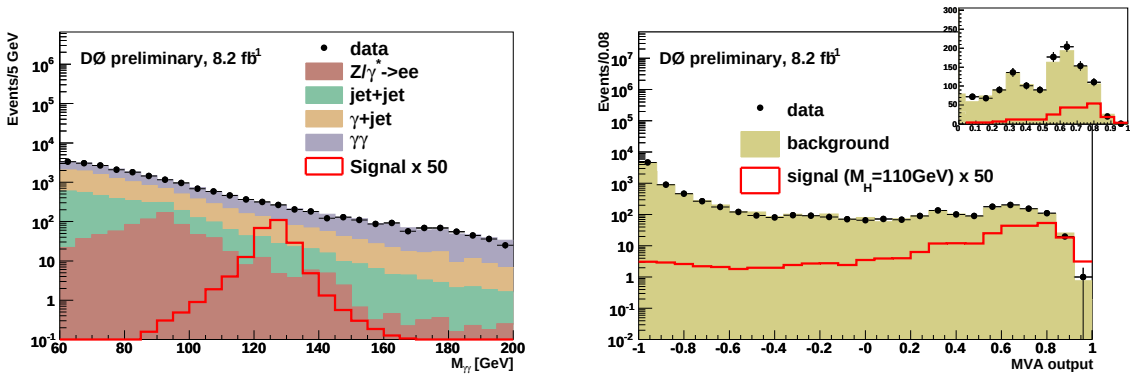

Figure 5: Left: Diphoton mass distribution for the $H \to \gamma\gamma$ search channel at D0. Right: Output of the final multivariate discriminant for $m_H = 110$ GeV.

improve our sensitivity to a Higgs boson signal beyond the expected gains from simply adding new events to our data set. With the full Tevatron data set analyzed, we expect to exceed 95% CL exclusion sensitivity for all allowed values of m_H and will be pushing for 3σ signal sensitivity at $m_H = 115$ GeV.

Acknowledgments

We thank the Fermilab staff and the technical staffs of the participating institutions for their vital contributions. This work was supported by DOE and NSF (USA), CONICET and UBACyT (Argentina), CNPq, FAPERJ, FAPESP and FUNDUNESP (Brazil), CRC Program, CFI, NSERC and WestGrid Project (Canada), CAS and CNSF (China), Colciencias (Colombia), MSMT and GACR (Czech Republic), Academy of Finland (Finland), CEA and CNRS/IN2P3 (France), BMBF and DFG (Germany), Ministry of Education, Culture, Sports, Science and Technology (Japan), World Class University Program, National Research Foundation (Korea), KRF and KOSEF (Korea), DAE and DST (India), SFI (Ireland), INFN (Italy), CONACyT (Mexico), NSC (Peoples Republic of China), FASI, Rosatom and RFBR (Russia), Slovak R&D Agency (Slovakia), Ministerio de Ciencia e Innovación, and Programa Consolider-Ingenio 2010 (Spain), The Swedish Research Council (Sweden), Swiss National Science Foundation (Switzerland), FOM (The Netherlands), STFC and the Royal Society (UK), and the A.P. Sloan Foundation (USA).

References

1. F. Englert and R. Brout, *Phys. Rev. Lett.* **13**, 321 (1964).
2. P. Higgs, *Phys. Rev. Lett.* **13**, 508 (1964).
3. G. Guralnik, C.R. Hagen and T.W.B. Kibble, *Phys. Rev. Lett.* **13**, 585 (1964).
4. LEP Electroweak Working Group, `http://lepewwg.web.cern.ch/LEPEWWG/`
5. ALEPH, DELPHI, L3, and OPAL Collaborations, The LEP Working Group for Higgs Boson Searches, *Phys. Lett.* B **565**, 61 (2003).
6. T. Aaltonen *et al.* (CDF and D0 Collaborations), *FERMILAB-CONF-10-257-E* (2010).
7. T. Aaltonen *et al.* (CDF and D0 Collaborations), *Phys. Rev. Lett.* **104**, 061802 (2010).
8. V.M. Abazov *et al.* (The D0 Collaboration), *D0 Note 6171-CONF* (2011).
9. V.M. Abazov *et al.* (The D0 Collaboration), *D0 Note 6170-CONF* (2011).
10. V.M. Abazov *et al.* (The D0 Collaboration), *D0 Note 6177-CONF* (2011).
11. A. Hoecker *et al.*, *arXiv:physics/0703039* (2007).

SEARCHES FOR HIGH-MASS SM HIGGS AT THE TEVATRON

R. LYSÁK
(ON BEHALF OF THE CDF AND D0 COLLABORATION)
Division of Elementary Particle Physics, Institute of Physics, Na Slovance 9, 182 21 Prague, Czech Republic

The Tevatron searches for a standard model (SM) high-mass Higgs boson in $p\bar{p}$ collisions at center-of-mass energy of $\sqrt{s} = 1.96$ GeV are presented. No significant excess over expected background is observed. Therefore 95% C.L. limits are set for SM Higgs production in mass range between 110 GeV/c^2 and 200 GeV/c^2. For the first time, both experiments now exclude individually a certain SM Higgs boson mass range. CDF excludes SM Higgs boson mass of $158 \leq m_H \leq 168$ GeV/c^2 using data corresponding up to 7.1 fb^{-1} of luminosity while D0 excludes the range of $163 \leq m_H \leq 168$ GeV/c^2 based on an integrated luminosity up to 8.2 fb^{-1}.

1 Introduction

In the standard model of particle physics the Higgs mechanism plays a central role in the unification of electromagnetic and weak interactions since it is responsible for electroweak symmetry breaking, thereby giving mass to the W and Z bosons. It predicts a scalar Higgs boson whose mass is not predicted. Its special property to couple strongly with heavy particles makes him particularly hard to produce. Before the Tevatron, the experiments performed at LEP put direct limit on the mass of the SM Higgs: $m_H > 114$ GeV/c^2 at 95% confidence level [1] [a]. The precise indirect measurements performed at LEP and by SLD and Tevatron experiments put the boundary from above: $m_H < 185$ GeV/c^2 when taking into account also LEP direct search limit [2]. Therefore we know where to concentrate when searching for the Higgs boson.

Tevatron CDF and D0 experiments have been searching for the Higgs bosons for many years now. The upper limits on SM Higgs production cross section were obtained by both collaborations during the last summer (2010). In high mass region, CDF experiment placed the

[a] All limits given in this paper are at 95% confidence level (C.L.).

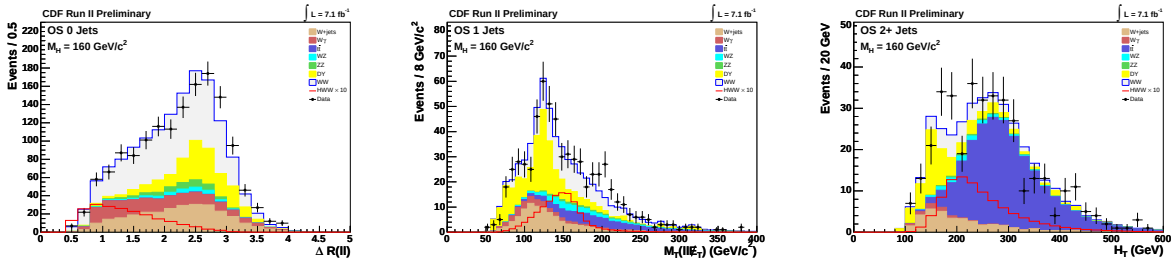

Figure 1: The discriminating variables used in CDF $H \to WW \to \ell\nu\ell'\nu'$ analysis. From left to right: ΔR in 0-jets channel, transverse mass of leptons and missing E_T in 1-jet channel and the total scalar transverse energy for $\geq$ 2-jet channel.

limit of $1.1 \cdot \sigma_{SM}$ (expected: $1.0 \cdot \sigma_{SM}$) at mass $M_H = 165$ GeV/c^2 while D0 obtained limit 1.0 (expected: $1.1 \cdot \sigma_{SM}$) thus excluding the Higgs boson at mass $M_H = 165$ GeV/c^2.

These proceedings present the latest update of searches for high-mass SM Higgs boson from both collaborations using data corresponding up to 8.2 fb^{-1} of integrated luminosity.

2 Overview of high-mass analyses

The Higgs boson is produced at Tevatron predominantly by gluon-gluon fusion ($gg \to H$) - 78% followed by associated Higgs production (WH/ZH) - 9%/6% and vector boson fusion ($qq \to qqH$) - 8% [b]. Depending on the Higgs mass, the cross section for $gg \to H$ varies from 1.4 pb (for $m_H = 110$ GeV/c^2) to 0.19 pb (for $m_H = 200$ GeV/c^2).

The Higgs boson decays predominantly to pair of b quarks for lower Higgs mass ($m_H \leq 135$ GeV/c^2) while for higher masses the W boson pair decay channel dominates – this is the decay channel CDF and D0 consider in their high-mass searches.

The general trend for Higgs analyses at Tevatron is determined by a small Higgs production rate. We first select as much inclusive sample as possible, separate the events into sub-channels for better signal to background separation and finally use multivariate discriminants to improve the sensitivity of the analysis.

2.1 $H \to WW \to \ell\nu\ell'\nu'$

The decay channel where both W bosons decay leptonically (e, μ) is the most sensitive high-mass channel since dilepton events provide clean signature.

At CDF, the events are separated according dilepton categories (high/low signal/background ratio), number of jets (0, 1, >= 2) and also dilepton mass (high/low $M_{\ell\ell}$). In low $M_{\ell\ell}$ region is the dominant $W\gamma$ background while in others regions its mostly WW and Drell-Yan production.

The plots showing the backgrounds and signal/background separating variables for different jet multiplicity channels can be seen in Fig. 1.

At D0, the events are separated according dilepton flavor (ee, $\mu\mu$, $e\mu$) and the number of jets (the same way as at CDF). Instead of applying basic simple cut on missing E_T to remove Drell-Yan events (as CDF does), D0 analysis uses boosted decision trees (BDT) discriminant to separate signal from at this stage dominant Drell-Yan background. After that, additional BDT is used to further separate remaining backgrounds from the signal. Different background are dominant according dilepton flavors: Drell-Yan for ee/$\mu\mu$ and WW/W+jets for $e\mu$ events.

The expected yield of number of signal and background events is 43.9 and 2655 at CDF while being 58.7 and 6707 at D0. The expected limits for dominant sub-channels are $1.52 \cdot \sigma_{SM}$

[b] here and whenever not explicitly mentioned in the following, numbers correspond to Higgs mass $m_H = 165$ GeV/c^2

for CDF 0-jet channel and $1.26 \cdot \sigma_{SM}$ for D0 $e\mu$ sub-channel.

2.2 Hadronic τ leptons

The inclusion of the channel where one lepton is hadronically decaying τ has an advantage of decent branching fraction while having still manageable background. The CDF experiment use production channel $H \to WW \to \ell\nu\tau_{HAD}\nu$ where it separates the events in two sub-channels according lepton type ($e - \tau$, $\mu - \tau$). D0 includes the hadronic τ events within two separate analysis. One includes $H \to \tau\tau_{HAD}jj$ channel [c] while the other one is $H \to WW \to \mu\tau_{HAD}$ which requires ≤ 1 jets in order to be orthogonal to the previous analysis. The dominant background is W + jets production where a jet is falsely reconstructed as a hadronic τ lepton. The expected yield of signal and background events is 1.7 and 829 at CDF while being 5.3 and 2428 at D0 ($H \to WW \to \mu\tau_{HAD}$). The expected limit for CDF analysis is $13.1 \cdot \sigma_{SM}$ while it is $12.3 \cdot \sigma_{SM}$ for D0 $H \to \tau\tau_{HAD}jj$ channel while $7.8 \cdot \sigma_{SM}$ for D0 $H \to WW \to \mu\tau_{HAD}+ \leq 1$ jet sub-channel.

2.3 $H \to WW \to \ell\nu jj$

The semileptonic decay channel has obvious advantage of large branching ratio (about factor of 6 larger comparing to dilepton channel) although the dominant background (W/Z + jets production) is huge. Only D0 includes this channel for now. The sample is separated according lepton flavor (e/μ). The expected yield of signal is 81 events (for $m_H = 160$ GeV/c^2) and about 121000 events for background. The expected limit on Higgs production is $5.1 \cdot \sigma_{SM}$.

2.4 Same sign

To further increase the sensitivity, we also search for Higgs boson in same-sign (SS) dilepton events. These occur naturally in $VH \to VWW$ production, when the associated vector boson (Z or W) and one of the W bosons from the Higgs decay leptonically. Since the decay of third boson most often results in the production of additional jets, CDF requires one or more jets in the final jets. D0 experiment separate the events into $ee, e\mu$ and $\mu\mu$ sub-channels.

The majority of background events in this channel originate from either a charge misidentification of a real lepton or a fake lepton from a jet or photon.

The expected yield of signal is 2.5 events and 90 background events at CDF while being 1.9 ($m_H = 160$ GeV/c^2) and 53 events at D0. The expected limit on Higgs production is $4.5 \cdot \sigma_{SM}$ at CDF while $7.0 \cdot \sigma_{SM}$ at D0.

2.5 Trileptons

Finally, CDF also includes the channel with three leptons in final state. These events occur in $WH \to WWW$ production, in the case all three W bosons decay leptonically and in $ZH \to ZWW$ production in case the associated Z boson decay leptonically and one of the W bosons from the Higgs decay leptonically.

The primary background in this search is WZ production which can also result in a signature of tree leptons and missing E_T. To allow better discrimination against the dominant WZ background, events are separated into tree channels depending on the number of reconstructed jets and whether or not there are two same-flavor opposite-sign leptons with the invariant mass that falls within 10 GeV/c^2 of the Z-boson mass.

[c] this includes $H \to \tau\tau$ and $H \to WW$ decays where the former is explored within dedicated CDF analysis and has very tiny contribution to high-mass results

For the most sensitive sub-channel which have dilepton mass outside the Z-boson mass window, the expected yield of signal is 0.9 events and 15 background events. The expected limit on Higgs production is $6.6 \cdot \sigma_{SM}$ for this sub-channel.

3 Limits on Higgs production

We combine all the above mentioned channels from each experiment. Since no excess of data above the background expectations is seen by CDF experiment nor the D0 experiment, we place the limits on SM Higgs boson production cross section. The limits are presented as a ratio of the 95% C.L. observed (and expected) limits to the SM Higgs boson production cross section and as a function of Higgs boson mass, see Fig. 2. When the ratio is lower than 1.0, we exclude the SM Higgs boson at 95% C.L. for a given mass. CDF collaboration excludes the SM Higgs boson in mass range 158 – 168 GeV/c^2 (with expected exclusion being 159 – 168 GeV/c^2) while D0 excludes the mass range of 163 – 168 GeV/c^2 (with expected exclusion being 160 – 168 GeV/c^2).

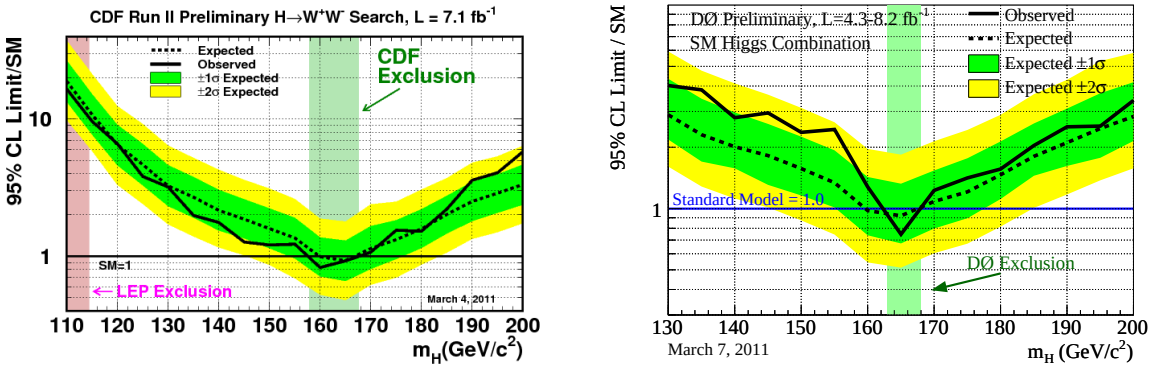

Figure 2: Ratio of the 95% C.L. observed (and expected) limits to the SM Higgs boson production cross section as a function of Higgs boson mass. Both, CDF (left plot) and D0 limits (right plot) are shown.

4 Conclusion

The CDF and D0 collaborations search for the high-mass standard model Higgs boson in many different channels. The CDF collaboration excludes the existence of Higgs boson at 95% C.L. with the mass in the range of 158 – 168 GeV/c^2 using integrated luminosity of up to 7.1 fb^{-1} while D0 collaboration excludes the mass range of 163 – 168 GeV/c^2 based on luminosity of up to 8.2 fb^{-1}.

The combination of CDF and D0 results leads to Higgs boson exclusion in the mass range of 158 – 173 GeV/c^2, see [3].

Acknowledgments

The author would like to thank the organizers for a wonderful conference.

References

1. R. Barate *et al.*, *Phys. Lett.* B **565**, 61 (2003).
2. Tevatron Electroweak Working Group, March 2011, http://tevewwg.fnal.gov
3. Jonathan Hays, "Combinations of Searches for SM Higgs at the Tevatron", these proceedings

Standard Model Higgs Searches at the Tevatron: Combinations

Jonathan Hays on behalf of the CDF and DØ Collaborations
Department of Physics, Imperial College London, Prince Consort Road, London SW7 2BW, United Kingdom

Combined limits are presented from CDF and D0 on direct searches for the standard model Higgs boson in $p\bar{p}$ collisions at the Fermilab Tevatron at $\sqrt{s}$= 1.96 TeV. The results presented here include updates with respect to previous combinations for those analyses targeted at Higgs bosons with masses in the range $130 < m_H < 200$ GeV, where the decay to W^+W^- provides the greatest sensitivity. In this update new data are included and existing analyses have been improved to enhance sensitivity. With up to 7.1fb^{-1} of data from CDF and up to 8.2fb^{-1} from D0, the 95% C.L. upper limit on Higgs boson production is a factor of 0.54 times the SM cross section for a mass of 165 GeV. The range $158 < m_H < 173$ GeV is excluded at the 95% C.L.

1 Introduction

The search for the origin of mass and the the mechanism behind electroweak symmetry breaking has been one of the major goals of particle physics for many years. Within the standard model (SM) this is achieved through the Higgs mechanism leading to the prediction of the existence of a relatively light massive scalar boson. Both CDF and D0 have performed new combinations [1,2] of multiple direct searches for the SM Higgs boson. These new combinations make use of a larger data sample and improved analysis techniques when compared with previous analyses.[3,4] In these proceedings the latest combination is presented. The general strategy has been to combine as many channels as possible and across both experiments to achieve the highest possible sensitivity. This update concentrates on the analysis in the higher mass region, $130 < m_H < 200$ GeV where the most important decay is W^+W^-, though acceptance for decays in tau pairs and di-photons are included from D0.

2 Combination

In this update the searches have been separated into 46 mutually exclusive final states (12 from CDF and 34 from D0). A summary of these are given in Table 1. Full details of the combination procedure and the contributing analyses can be found in [5] and references 1-14 therein.

These contributing analyses make use of many different observables, the distributions of which are used as input to the statistical combination. This makes it difficult to visualize in a single plot the comparison of the data with the predicted signal (s) and background (b) outcomes. Since events of similar signal-to-background ratio can be combined without substantial loss in sensitivity, one approach is to bin the data and the signal and background predictions in s/b and compare the results distributions. Since the analyses considered cover a large range of s/b they are histogrammed in Figure 1 in terms of $log_{10}(s/b)$ to enable the full range to be

Table 1: Table listing the various channels and sub-channels included in the latest update to the combined Higgs searches from the Tevatron, indicating the integrated luminosity used and the mass range.

Channel	Sub channels	Luminosity (fb^{-1}	m_H range (GeV)
Contributing channels from CDF			
$H \to W^+W^-$	$2\times$(0,1 jets) + (2+ jets) + (low-m_{ll}) + (e-τ_{had})+($\mu - \tau_{had}$)	7.1	130-200
$WH \to WW^+W^-$	(same-sign leptons 1+ jets) + (tri-leptons)	7.1	130-200
$ZH \to ZW^+W^-$	(tri-leptons 1 jet) + (tri-leptons 2+ jets)	7.1	130-200
Contributing channels from D0			
$H \to W^+W^- \to l^\pm\nu l^\mp\nu$	(0,1,2+ jets)	8.1	130-200
$H \to W^+W^- \to \mu\nu\tau_{had}\nu$		7.3	130-200
$H \to W^+W^- \to l\bar{\nu}jj$		5.4	130-200
$VH \to l^\pm l^\pm$ + X		5.3	130-200
$H+X \to l^\pm\tau^\mp_{had}jj$		4.3	130-200
$H \to \gamma\gamma$		8.2	130-150

shown in a single figure. In the left panel, the light (pale-blue) shaded histogram shows the background prediction, the dark (red) shaded region shows the signal prediction for the a SM Higgs boson of $m_H = 165$ GeV on top of the background prediction and the points show the observed data. Good agreement between data and background prediction is seen across several orders of magnitude in s/b. The right hand panel of Figure 1 shows a zoomed-in region of the left-hand plot looking at the high s/b region. Here, the points show the data with the expected background subtracted, the shaded histogram the predicted signal and the open histogram the approximate $\pm$ 1 standard deviation of the background prediction. Here it can clearly be seen that towards the right-hand edge of the plot the signal histogram rises above the uncertainties on the background model.

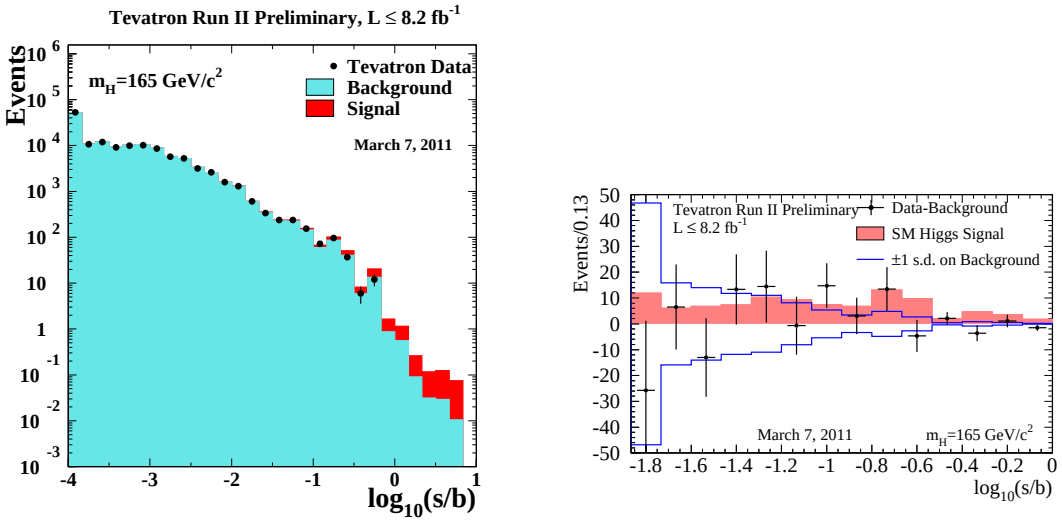

Figure 1: A comparison of the expected backgrounds (b) , signal (s) for a SM Higgs boson of $m_H = 165$ GeV, and data binned across all channels in $log_{10}(s/b)$. In the left panel the light shaded region represents the expected backgrounds, the dark shaded region the expected signal and the crosses are the data. In the right panel the expected background has been subtracted from the data. The solid histogram shows the expected signal, the points show the data and the open histogram shows the expected $\pm$1 standard deviation of the background prediction.

In order to ensure that the limits do not depend strongly on the choice of statistical analysis, two approaches are considered making use of both Bayesian and modified frequentist methods. In both cases the full distributions of the final discriminants are used, not just the overall rates. Systematic uncertainties are taken into consideration on both the signal and background

rates and the shapes of the discriminant distributions. Each independent source of systematic uncertainty is treated in a pseudo-Bayesian fashion by assigning a probability distribution and parameterising the impact on the signal and background distributions with a single nuisance parameter. Both methods allow for the data to constrain the nuisance parameters - one by integration the other by fitting. Where the data can provide a significant constraint this can mitigate the impact of the systematic uncertainties. Because of this possibility of constraint from the data it is important to carefully evaluate the systematic uncertainties and in particular their correlations. Incorrectly assigning a correlation between two uncertainties can lead to the fits over constraining the parameters and giving an incorrect result.

Experimental systematic uncertainties are in general correlated across analyses from the same experiment coming from things such as: lepton and jet identification efficiencies, trigger modeling, resolution and energy scale modeling. However, these are typically specific to a given detector and are not generally correlated between CDF and D0. Theoretical uncertainties are generally correlated across the two experiments where the same calculations are used. In general those backgrounds with large theoretical uncertainties are small and those backgrounds with larger contributions receive constraints from data - either in the statistical analysis itself or through control samples - which mitigates some of the larger theoretical uncertainties. Important contributions also come from the uncertainty on the dominant signal production cross section for this combination, $gg \to H + X$. A full description of the important sources of uncertainty and their correlations can be found in the Tevatron combination note [5] and the references to the contributing analyses therein. Additionally, references to the huge body of work that has gone into the theoretical predictions used in these searches can be found in the combination document.

3 Results and Conclusions

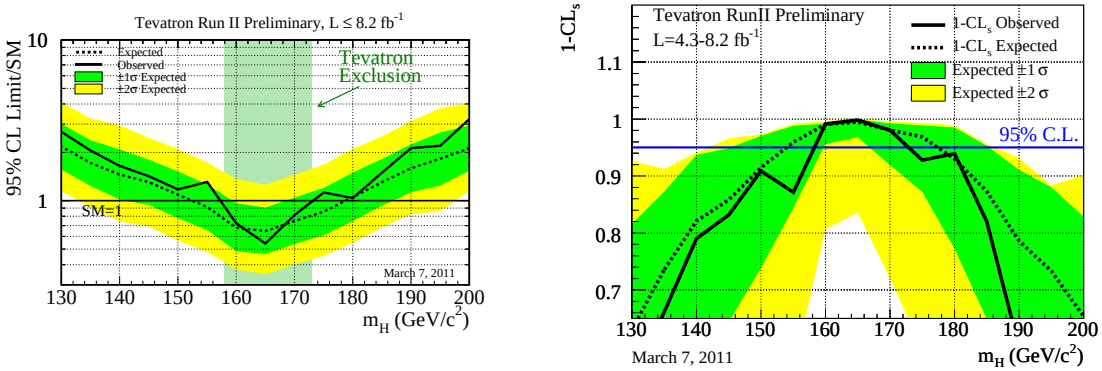

Figure 2: The 95% C.L. on the cross section $\sigma(p\bar{p} \to H + X$ relative to the SM Higgs expectation is shown for the Bayesian method in the left panel. In the right panel the exclusion strength 1-CLs is shown as a function of Higgs boson mass. In both cases the solid line shows the observed limit, the dashed line the expected limit and the yellow and green bands show the ± 1 and 2 standard deviation around the expectation.

Using the two statistical procedures mentioned in the previous section, 95% confidence limits on the cross section $\sigma(p\bar{p} \to H + X)$ for the mass range $130 < m_H < 200$ GeV are extracted. The largest disagreement between the two methods is 10% and on average they agree at the 1% level. The results from the Bayesian procedure (chosen *a priori* as the official result) are presented in terms of the ratio of the observed limits to the SM prediction in the left panel of Figure 2. Test masses for which the limit is below one are where the Higgs is excluded for that particular mass. The right hand plot shows the expected and observed 1-CLs values for the

various SM Higgs mass hypotheses. Those test masses for which the 1-CLs value is above 0.95 are excluded at least at the 95% confidence level. The relatively poor mass resolution of the dominant WW decay mode allows the use of a linear extrapolation of the limit between the test mass points - spaced on a 5 GeV grid. Thus, the region $158 < m_H < 173$ GeV is excluded at the 95% C.L. which is slightly less stringent than the expected sensitivity of $153 < m_H < 179$ GeV.

These results significantly extend the results from the individual experiments and previous combinations. The combined sensitivity is sufficient to exclude the SM Higgs boson at high mass and is expected to grow substantially in the future as more data are added and further improvements are made to the analysis techniques.

Acknowledgments

We thank the staffs at Fermilab and collaborating institutions, and acknowledge support from the DOE and NSF (USA); CEA and CNRS/IN2P3 (France); FASI, Rosatom and RFBR (Russia); CNPq, FAPERJ, FAPESP and FUNDUNESP (Brazil); DAE and DST (India); Colciencias (Colombia); CONACyT (Mexico); KRF and KOSEF (Korea); CONICET and UBACyT (Argentina); FOM (The Netherlands); STFC and the Royal Society (United Kingdom); MSMT and GACR (Czech Republic); CRC Program and NSERC (Canada); BMBF and DFG (Germany); SFI (Ireland); The Swedish Research Council (Sweden); and CAS and CNSF (China).

References

1. CDF Collaboration, "Search for $H \to WW^*$ Production Using 5.9fb^{-1}", CDF Conference Note 10432 (2011).
2. D0 Collaboration, "Combined Upper Limits on Standard Model Higgs Boson Production in the W^+W^-, $\tau\tau$ and $\gamma\gamma$ decay modes from the D0 Experiment in up to 8.2fb^{-1} of data", D0 Conference Note 6183 (2011).
3. The CDF and D0 Collaborations and the TEVNPHWG, "Combined CDF and D0 Upper limits on Standard Model Higgs Production with up to 6.7fb^{-1} of Data", FERMILAB-CONF-10-257-E, CDF Note 10241, D0 Note 6096, arXiv:1007.4587 [hep-ex] (2010);
   CDF Collaboration, "Combined Upper Limit on Standard Model Higgs Boson Production for HCP 2009", CDF Conference Note 9999 (2009);
   D0 Collaboration, "Combined Upper Limits on Standard Model Higgs Boson Production from the D0 Experiment in 2.1-5.4fb^{-1}", D0 Conference Note 6008 (2009);
   D0 Collaboration, "Combined Upper Limits on Standard Model Higgs Boson Production from the D0 Experiment in 0.9-5.0fb^{-1}, D0 Conference Note 5984 (2009);
   The CDF and D0 Collaborations and the TEVNPHWG, "Combined CDF and D0 Upper Limits on Standard Model Higgs Boson Production with 2.1 to 4.2 fb^{-1} of Data", FERMILAB-PUB-09-0557-E, CDF Note 9998, D0 Note 5983, arXiv:0911.3930 [hep-ex] (2009).
4. CDF Collaboration, "Inclusive Search for Standard Model Higgs Boson Production in the WW Decay channel using the CDF II Detector.", Phys. Rev. Lett. 104,061803 (2010);
   D0 Collaboration, "Search for Higgs Boson Production in Dilepton and Missing Energy Final States with 5.4fb^{-1} of $p\bar{p}$ collisions at $\sqrt{s} = 1.96$ TeV", Phys. Rev. Lett. 104,061804 (2010);
   The CDF and D0 Collaborations, "Combination of Tevatron Searches for the Standard Model Higgs Boson in the W^-W^+ Decay Mode", Phys. Rev. Lett. 104,061802 (2010).
5. The CDF and D0 Collaborations and the TEVNPHWG, "Combined CDF and D0 Upper Limits on Standard Model Higgs Boson Production with up to 8.2fb^{-1} of Data", FERMILAB-CONF-11-044-E, CDF Note 10441, D0 Note 6184, arXiv:1103.3233 [hep-ex].

SEARCHES FOR NON-STANDARD MODEL HIGGS AT THE TEVATRON

Richard St. Denis
University of Glasgow – Department of Physics and Astronomy
Glasgow G12 8QQ – United Kingdom

The latest results for the Tevatron search for non Standard Model Higgs bosons are presented. Searches for Higgs decays to W boson pairs are interpreted in an extension of the Standard Model to four generations and an observed (expected) exclusion is obtained from CDF for $123 \leq M_h \leq 202$ GeV/c^2 ($129 \leq M_h \leq 212$ GeV/c^2), comparable to the Tevatron combined limit. D0 searches for Higgs decays to photons in a fermiophobic Higgs model and finds no evidence for a signal, excluding $M_h \leq 112$ GeV/c^2, the most sensitive such search to date. MSSM SUSY production in association with a b quark and either with or without the requirement of the b jet tag in decays to tau pairs and with requirement of a b jet tag when decaying to b pairs is done by CDF and D0. No signficant excess is observed and limits with a sensitivity in MSSM to $\tan\beta$ of order 30 but with dependence on the Higgs mass, m_A, are set. A search for Higgs decays in a Hidden Valley model shows now signal and cross section limits as a function the proper decay length range from 15 pb at 0.25 cm to 100 pb at 5 cm.

1 Introduction

The Tevatron has celebrated a quarter century of physics that is culminating now in sensitivity to the Standard Model (SM) Higgs. These searches can be extended to other models beyond the Standard Model by either a reinterpretation of the SM searches or by dedicated new searches based on the unusual properties of these models. In the first category we will present two new analysis. The first is a search by CDF for a Higgs decay to W boson pairs which subsequently decay to charged leptons and neutrinos, the standard High mass search, but interpreted in terms of a model with four generations of quarks and leptons. The second is a search by D0 for Higgs decays to to photons but interpreted in a fermiophobic Higgs model where production is not via fermion loop but from associated production with a vector boson. Supersymmetry inspired searches are performed for a narrow resonance in Higgs decays to two taus either in association with an observed b quark or ignoring the presence of the b quark, or of a Higgs decay to two b quarks in the presence of a third b. Interpretation of the results within SUSY with specific

constraints on parameters are given. Finally a search for a Higgs boson decay to a pair of Hidden Valley particles from a new strong interaction which in turn decay with significant lifetime to two pairs of $b\ \bar{b}$ quarks follows similar experimental methods for the SUSY three b analysis.

2 Search for a Higgs in a Fourth Generation Model

A fourth generation of quarks and leptons is possible provided there is a neutrino with a mass greater than half the Z mass and that there are heavy t′ and b′ quarks [1]. In this model the electroweak constraints are altered and a Higgs boson having a mass of up to $M_h \leq 300$ GeV/c^2 is allowed. Since Higgs production is mainly through a quark loop, a fourth generation will enhance the standard model production rate by about a factor of nine, with little dependence on the details of the t′ and b′ masses. The analysis is the same as that for the Tevatron high mass SM Higgs search [2] except the associated production channels are removed and the branching ratios are recomputed in light of the fourth generation model. No signal is found and exclusion limits are computed using the same statistical methods as described in the SM Higgs search. An observed (expected) exclusion is obtained from CDF for $123 \leq M_h \leq 202$ GeV/c^2 ($129 \leq M_h \leq 212$ GeV/c^2). This is comparable to the Tevatron combined observed (expected) limits [3] $131 \leq M_h \leq 204$ GeV/c^2 ($125 \leq M_h \leq 218$ GeV/c^2) and the CMS observed (expected) limits [4], $144 \leq M_h \leq 207$ GeV/c^2 ($150 \leq M_h \leq 190$ GeV/c^2).

3 Search for a Higgs in a Fermiophobic Higgs Model

The D0 collaboration searches for Higgs decays to photons in a fermiophobic Higgs model in a data sample having an integrated luminosity of 8.2 fb^{-1}. In this model there is no fermion coupling; therefore, the only production channels available are WH, ZH and vector boson fusion. The branching ratio of $h_f \rightarrow \gamma\gamma$ is 6.2%, 33 times the SM cross section at a mass $m_{hf} = 110$ GeV/c^2. In this analysis two photons are searched for with a transverse energy, $E_T > 25$ GeV/c^2 within a pseudorapidity $|\eta| < 1.1$. A neural net is used to identify the photons and each photon candidate is tagged as either passing or failing a cut on the neural net score. Two candidates that both pass the cut are likely to be diphoton events whereas one that passes and one that fails is likely to be a photon plus jet combination. An unfolding of the pass/fail classification into a γ-γ, γ-jet, jet-γ or jet-jet combination is performed. The unfolding is uses Monte Carlo for the photon efficiency. The Monte Carlo is corrected with samples of radiative Z decays. The jet efficiencies are measured using di-jet Monte Carlo and cross checked against a data sample. The efficiencies for a photon to be identified as a photon or as a jet are the largest systematic uncertainty in the analysis.

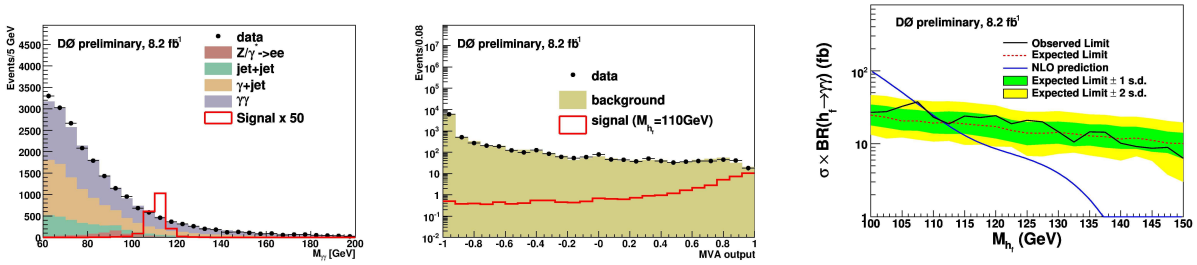

Figure 1: Invariant mass spectrum of diphoton candidates with background estimates and a hypothetical fermiophobic Higgs signal (left). Boosted decision tree output from a multivariate analysis (MVA) showing the background estimate with the data and a prediction of the contribution from a Higgs signal (center). Predicted cross section times branching ratio for a fermiophobic Higgs as a function of mass superimposed on the exclusion limits from this analysis. (right)

The background composition of the final sample is 3% $Z/\gamma \to l^+l^-$, 53% $\gamma\gamma$, 30% γ-jet and 14% jet-jet. The invariant mass spectrum of the diphoton candidates is shown in Figure 1. A boosted decision tree (BDT) is used with inputs including the diphoton invariant mass, the transverse energies of the two photons, the transverse momentum of the diphoton system and the angle between the photons. The last two variables take advantage of the associated production mechanism for fermiophobic Higgs and is not applicable to the SM Higgs decays to diphotons. The BDT output distribution shown in Figure 1 is fit for a signal as a function of candidate Higgs mass in the same manner as used for the SM and fourth generation Higgs searches. No signal is observed and a limit on a fermiophobic Higgs mass is set by observing the point where the predicted cross section time branching ratio crosses the observed limit on the production cross section as shown in Figure 1. Systematic uncertainties are treated as nuisance parameters and include the photon and jet efficiencies mentioned above, as well as luminosity, parton distribution functions, the photon identification, the veto for tracks and the cross sections for Drell–Yan production and prompt diphoton production. A fermiophobic Higgs is excluded at 95% CL for $m_{hf} < 112$ GeV/c^2. This is the best limit to date exceeding the CDF limit [5] of $m_{hf} < 106$ GeV/c^2 obtained with 2.7 fb^{-1} of integrated luminosity, the previous D0 limit [6] of $m_{hf} < 102.5$ GeV/c^2 obtained with 4.2 fb^{-1} of integrated luminosity, and the combined LEP result [7] of $m_{hf} < 109.7$ GeV/c^2.

4 Search for an MSSM SUSY Higgs

MSSM SUSY features two Higgs doublet fields, H_u, H_d which couple to u- and d-type fermions. The parameter $\tan\beta \equiv \langle H_d\rangle/\langle H_u\rangle$ enhances production by and decay to b quarks relative to the SM. There are five Higgs bosons in the theory, of which three are neutral: H^0, h^0, A^0 and two are charged: $H^\pm$. If the h^0 is light, it is SM-like, having a mass below 135 GeV/c^2 and the H^0 and A^0 are heavier and nearly degenerate. If however the H^0 is light then the h^0 and A^0 are nearly degenerate. This gives a further factor of two enhancement of the cross section and the degenerate object for either of the two mass hierarchies is denoted by ϕ^0. The cross sections are enhanced by a factor of $\tan\beta^2$. If $\tan\beta = 50$ then the total enhancement is 2500×2(for the degeneracy) which takes femtobarn cross sections to picobarn cross sections and are therefore observable at the Tevatron.

The production mechanism proceeds via gluon each from the proton and antiproton splitting to a $b\bar{b}$ pair. Two b quarks fuse to form the ϕ^0 and the other two form jets. It is also possible to produce the ϕ^0 through a b quark loop or through $bg \to \phi^0 b$ and finally via $q\bar{q} \to b\bar{b}\phi^0$ where the ϕ^0 is emitted as Higgstrallung from a b quark. Thus there are zero, one or two b quarks produced in association with the Higgs.

The ϕ^0 decays to tau pairs 10% of the time and to $b\bar{b}$ pairs 90% of the time. In the search for the b decay modes, a third b is required to suppress background from QCD production of $b\bar{b}$ pairs. The invariant mass of the two b quarks is measured and the properties of all three b jet candidates are examined to separate the quark flavors. For the tau decays, the CDF search ignores the associated b quarks while the D0 analysis also looks at events where a b jet is tagged. One tau is required to decay to an electron or muon while the other can decay hadronically. The CDF searches also includes decays of the second tau to an electron or muon. The visible mass of the tau candidate decay products is used as the discriminant variable in these searches.

4.1 $\phi \to \tau^+\tau^-$

For the tau analysis, the main background is Z decays to taus, with some contribution from W + jets and dibosons. Details vary for the analyses but generally the taus are required to have a transverse momentum greater than 10 or 20 GeV/c although CDF uses lower limits of 6

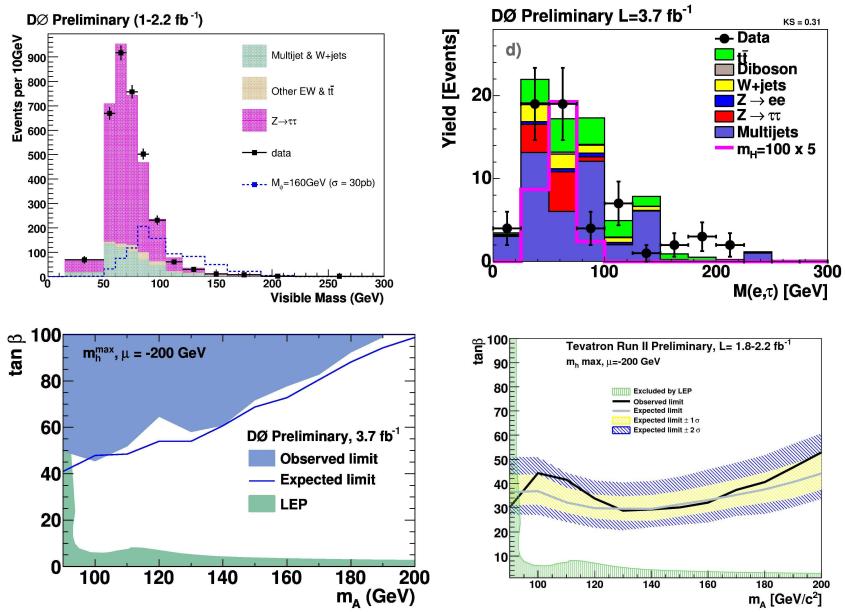

Figure 2: Invariant mass of the electron from the semileptonic tau decay and the hadronic tau, the visible mass (left). Same, but for events with a b tag in the SUSY $\phi \to \tau^+\tau^- + b$ search where one tau decays to an electron plus neutrinos and the other decays hadronically (left center) and the resulting exclusion limits in the $\tan\beta - m_A$ plane for SUSY (right center). Combined Tevatron results for exclusions based on a subsample of the data (right).

and 10 GeV/c for the decays that do not involve hadronic taus. The hadronic tau is identified using a narrow cone with a second isolation cone (CDF) or a neural net separated into samples corresponding to a π^+,$\pi^+\pi^0$ or three prong topologies. It is required that the lepton and missing energy be inconsistent with W production. In the CDF analysis a cut is applied to the scalar sum of the momentum of all visible objects (H_T) and in for the D0 analysis the cut is placed on the transverse mass, M_T, of the ϕ^0 candidate. The visible mass spectrum is compared to a model with a narrow resonance in order to search for a signal. This is shown for the D0 analysis in Figure 2.

In a separate analysis by the D0 collaboration, a b jet tagged using a neural net algorithm is required. The final result is obtained from a discriminant that includes the visible mass shown in Figure 2 for D0 in the case where one tau decays to an electron plus neutrinos and the other decays hadronically. The b tagging reduces the Drell–Yan background dramatically.

In both the b-tagged analysis and the analysis without b tagging, for both experiments, no significant signal is observed. When interpreted as a SUSY Higgs, limits on $\tan\beta$ of order 40 are obtained but with a mass dependence on the ϕ^0. An example result is shown in Figure 2 for the m_h^{max}, $\mu = -200$ GeV scenario. Combined Tevatron results [8] from the tau samples not having a b tag have a sensitivity to $\tan\beta$ values as low as 30 as shown in Figure 2.

4.2 $\phi \to b\bar{b} + b$

The data sample for this analysis consists of events with three or more tagged b jets with transverse momenta above 20 GeV/c. The D0 b tagger was described and the CDF tagger searches in a jet cone for tracks that form a secondary vertex. Both experiments achieve b tagging efficiencies of order 50% depending on the fake rate that is tolerated. The two leading b-tagged jets are used as the ϕ^0 candidate mass. The mass spectrum for the background is determined from a data sample with two b tags and imposing the b tagging probabilities calibrated with data on the third jet in order to obtain the proper kinematics. Monte Carlo is used to obtain the signal invariant mass spectra for various hypothesized masses.

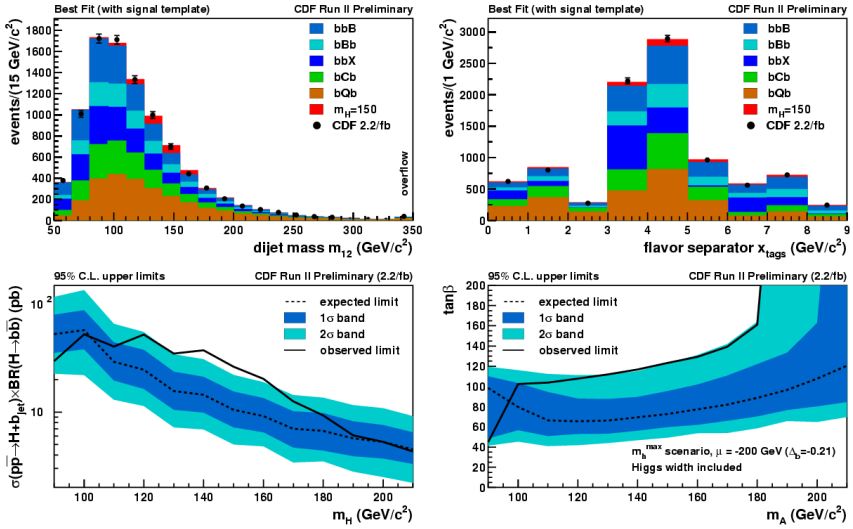

Figure 3: Invariant mass of the leading two jets in events with three b tags in the CDF SUSY $\phi \to b\bar{b} + b$ search (left). Flavor discriminant distribution,(left center) which, together go into a likelihood fit to give limits on cross section times branching ratio for a ϕ decay where the ϕ width is smaller than the detector resolution in the CDF SUSY $\phi \to b\bar{b} + b$ search (right center). Limits on $\tan\beta$ as a function of m_A in the $\mu = -200$ GeV scenario.

Additional discrimination is applied by both experiments. For CDF, the sum of the masses of the two b candidate vertices is plotted against the mass of the vertex of the third jet. This two dimension plot is divided into nine bins which are examined as 9 discrete values of a tagging variable, x_{tags}. The invariant mass and x_{tags} distributions are fit simultaneously for a signal. These distributions are shown for CDF analysis of a sample of data having an integrated luminosity of 2.2 fb^{-1} in Figure 3. A limit on cross section times branching ratio for a Higgs with a width that is negligible compared to the resolution is performed and the limits are shown in Figure 3. The most significant excess at M_{bb} around 140 GeV/c^2 is a 2.3σ deviation.

This can be interpreted in the MSSM; however, the increase in coupling strength for $\tan\beta >$ 100 also causes the resonance to get quite broad, reducing ability to detect a ϕ^0. The best sensitivity is obtained in scenarios with a negative SUSY mass parameter (μ). As shown in Figure 3 the channel is sensitive to $\tan\beta$ of order 60. Hence it can be seen that even though there is nine times more cross section than the tau channel, the background reduces the cross section advantage and slightly worse sensitivity is obtained.

D0 uses a six dimensional likelihood, D, composed of the following variables: the eta and phi separation of the of the pair of jets, the angle between the leading jet in the pair and the total momentum of the pair, the momentum imbalance of the pair, the combined rapidity of the pair and the event sphericity. The analysis is separated into searches in a high and low mass region bounded at $M_{bb} = 130$ GeV/c^2. The largest deviation from this analysis published [9] on a data sample having an integrated luminosity of 5.2 fb^{-1} is a 2σ effect at M_{bb} around 120 GeV/c^2. D0 obtains sensitivities as low as 45 in $\tan\beta$ for this analysis.

5 Hidden Valley Search

Hidden Valley theories [10] postulate a new strong force that can interact with heavy particles in the SM. Therefore a search for SM Higgs decays to pairs of Hidden Valley particles (HV) each of which decay to $b\bar{b}$ pairs is conducted. Methods similar to the SUSY search in b$\phi^0 \to b\bar{b}$ search are used; however, the b-tagging is calibrated to be able to observe much longer decay lengths for the HV particles. The backgrounds are again QCD heavy flavor production and discrimination

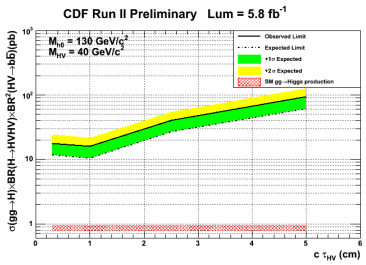

Figure 4: CDF Exclusion limits for cross section times products of branching ratios decay as a function of the decay length of a Hidden Valley particle coming from the interaction $h \to HVHV \to b\bar{b}b\bar{b}$.

against that background is provided by the HV decay length, ζ, and the b jet impact parameter, ψ, which have values near zero for the background but are of order centimeters for the signal. There is only one event observed with a large value of ζ and limits on the cross section time branching ratio as a function of decay length are shown in Figure 4 by CDF for a sample of data having an integrated luminosity of 5.8 fb^{-1}.

6 Summary

CDF and D0 are looking for Higgs bosons in a variety of models beyond the standard model and are using advanced analysis techniques in a harsh background environment to do this. Results were shown for data samples having an integrated luminosity between 2.4 and 8.2 fb^{-1}. The MSSM sensitivity to $\tan\beta$ of order 30 has been obtained. With the full dataset this sensitivity could be as low as 20. CDF now excludes a fourth generation model for $123 < m_h < 202$ GeV/c^2 comparable to the combined Tevatron limits and the CMS limits. When a fermiophobic Higgs is found, D0 claims that it must have a mass greater than 112 GeV/c^2. The Hidden Valley has been explored but nothing is seen just yet.

Acknowledgments

The author would like to thank the organizers for this invitation to speak and the wonderful atmosphere of the conference.

References

1. B. Holdom *et al.*, PMC Phys. A 3, 4 (2009).
2. R.Lysak, "Searches for High-Mass SM Higgs at the Tevatron", these proceedings.
3. T. Aaltonen *et al.*, The CDF and D0 Collaborations, Phys. Rev. D 82, 011102(R) (2010).
4. The CMS Collaboration, CERN-PH-EP/2011-015, arXiv:hep-ex/1025429v2. The expected limits quoted here have been read from the figure since numerical values are not quoted in the text.
5. T. Aaltonen *et al.*, The CDF Collaboration, Phys. Rev. Lett. 103, 061803 (2009).
6. V. M. Abazov *et al.*, The D0 Collaboration, Phys. Rev. Lett. 101, 051801 (2008).
7. A. Rosca, arXiv:hep-ph/0212038v1 (2002).
8. The TEVNPH Working Group for the CDF and D0 Collaborations, arXiv:hep-ex/1003.3363v2.
9. V. M. Abazov *et al.*, The D0 Collaboration, Phys. Lett. B 698, Issue 2, pp 97-174 (4 April 2011).
10. M. Strassler and K. Zurek, Phys. Lett. B **661**, 263 (2008). M. Strassler and K. Zurek, Phys. Lett. B **651**, 374 (2008).

LHC BEAM OPERATIONS: PAST, PRESENT AND FUTURE

M. Lamont
CERN, Geneva, Switzerland

LHC commissioning made good progress in 2009 and 2010 - a brief summary is presented. The present status of the machine is given and the short and medium term prospects discussed.

1 Introduction

2010 was the first full year of LHC commissioning and it saw a number of important operational milestones. These included: first collisions at 3.5 TeV; commissioning of the squeeze; the move to physics with nominal bunch intensity; the move to bunch trains followed by a phased increase in intensity. A peak luminosity of 2×10^{32} cm^{-2}s^{-1} was achieved with an integrated luminosity of 6 pb^{-1} per day delivered in the final week of proton operations. The year culminated in a successful ion run.

2011 has seen a rapid re-commissioning of the machine after the Christmas stop with the main milestones listed below.

- 19$^{\text{th}}$ February: circulating beams re-established.
- 3$^{\text{rd}}$ March: first collisions at 3.5 TeV, β^* =1.5 m with pilot beams.
- 5$^{\text{th}}$ March: nominal bunches at 3.5 TeV, start of collimator set-up program.
- 13$^{\text{th}}$ March: first stable beams, 3 bunches per beam, initial luminosity 1.6×10^{30} cm^{-2}s^{-1}

By 21$^{\text{st}}$ March 2011, the LHC was back up to a peak luminosity of 1×10^{32} cm^{-2}s^{-1} boding well for the push towards the year's target of 1 fb^{-1}.

2 Overview of 2010

The clear priority of 2010 was to lay the foundations for 2011 and the delivery of 1 fb^{-1}. The peak luminosity target was 1×10^{32} cm^{-2}s^{-1}. Solid operational experience of injecting, ramping, squeezing and establishing stable beams was gained and a large number issues were addressed along the way. A period of steady running at or around 1 MJ for an extended period was used to fully verify machine protection and operational procedures before performing a safe, phased increase in intensity with validation and a running period after each step-up in intensity.

The luminosity delivery in 2010 can be divided into three main periods: the initial luminosity run with low bunch currents; nominal bunch operation with up to 48 bunches; and the performance ramp up period after the commissioning of bunch trains. The main milestones of 2010 commissioning are outlined in Table 1. Some notable achievements of the year's commissioning are shown in Table 2.

Table 1: Main phases of 2010 commissioning.

Date	Commissioning phase
28th February	Injection of both beams, rough RF capture
30th March	First colliding beams at 3.5 TeV
March	Initial commissioning leading to first collisions
April	Squeeze commissioning
May	Physics 13 on 13 bunches with 2×10^{10} protons per bunch
June	Commissioning of nominal bunch intensity
July	Physics 25 on 25 bunches with 9×10^{10} protons per bunch
August	3 weeks running with stored beam energy of 1 to 2 MJ
September	Bunch train commissioning
Oct -Nov	Phased increase in total beam intensity

Table 2: 2010 commissioning: some notable records. Data courtesy of Atlas.

Peak stable luminosity	2.07×10^{32} cm^{-2}s^{-1}
Maximum luminosity delivered in one fill	6.3 pb^{-1}
Maximum luminosity delivered in one day	6.0 pb^{-1}
Maximum luminosity delivered in 7 days	24.6 pb^{-1}
Maximum colliding bunches	348
Maximum average events/bunch crossing	3.78
Longest time in Stable Beams – one fill	30.3 hours
Longest time in Stable Beams – one day	22.8 hours (94.9%)
Longest time in Stable Beams – 7 days	69.9 hours (41.6%)
Faster turnaround (protons)	3.66 hours
Maximum stored beam energy at 3.5 TeV	28 MJ
Maximum stored beam energy in physics	24 MJ

3 Machine status in 2010

2010 was a intense year of commissioning with many issues and problems addressed [1]. When the dust had settled the following key features related to beam based operation may be noted.

- The machine is magnetically and optically well understood with excellent agreement between the magnetic and optics models and measured beam parameters.
- The LHC is magnetically reproducible. This has proved important because set-up remains valid from fill to fill, and indeed from month to month.
- The aperture has been measure carefully and is as expected.
- The operational sequence, after a lot of hard work, allows the beams to be taken through the ramp, squeeze and into collision essentially without loss.
- Better than nominal beam intensity and beam emittance was delivered by the injectors resulting in excellent luminosity performance for a given beam current.
- It was possible to collide nominal bunch currents with smaller that nominal emittances with no serious problems from head-on beam-beam. This important result is another key reason behind the impressive luminosity performance.

- There was excellent cleaning by the collimator system and good control of beam losses at all stages of operation. There were no accidental beam induced quenches above injection energy.

The key machine parameters used in 2010 are shown in Table 3.

Table 3: Main machine parameter in use in 2010 compared with nominal 7 TeV values.

Parameter	2010	Nominal
Energy [TeV]	3.5	7.0
$\beta*$ [m]	3.5, 3.5, 3.5, 3.5	0.55, 10, 0.55, 10
Normalized emittance [μ m] (start of fill)	2.0 - 3.5	3.75
Bunch current	1.2e11	1.15e11
Maximum number of bunches	368 348 collisions/IP	2808
Maximum stored energy [MJ]	28	360
Peak luminosity [$cm^{-2}s^{-1}$]	2e32	1e34

The LHC has excellent single beam lifetime at 3.5 TeV before collisions of around over 200 hours. At the start of a fill the luminosity lifetime is initially in the range 15 to 20 hours lengthening to 25 to 30 hours later. The luminosity lifetime is reasonably well given by the observed emittance growth and the intensity decay. There is minimal drifts in beam overlap during physics and the beams are generally very stable.

The 2010 run was driven mainly by commissioning, and not operations for physics. In this regard, any analysis of operational efficiency should be regarded with some latitude. However for a first year the signs are very encouraging. Some very extensive equipment systems performed above expectations (considering mean time between failures etc.); the equipment groups are aware of the weak points and are working to improve them. Technical stops certainly caused problem initially but things got better during the course the year and overall there was impressive availability for a first full year of operations with the final number for machine availability being around 65% pf the scheduled time [2].

4 2010 - heavy ion run

The 2010 finished with a switch from protons to lead ions. The operations team successfully leveraged the experienced gained with protons to rapidly push through the ion commissioning program, relying on the fact that the magnetic machine for ions is near identical to that used for protons. The early ion parameters applicable to the 2010 run are shown in table 4 [5].

The first injection of Beam 1 took place on 4 November 2010. Stable Beams were declared for physics on 7 November. In the following days, the number of bunches per beam increase through 2, 5, 17, 69, 121 bunches, injecting single bunches or batches of 4 from the SPS in variants of the "Early" filling scheme (see Table 4). In the last few days of the run, injection of batches of 8 bunches allowed a total of 137 bunches to be established. The SPS supplied around 1.2 $\times 10^8$ ions per bunch which gave a peak luminosity of just over 3×10^{25} $cm^{-2}s^{-1}$. An integrated luminosity of 9.7 μb^{-1} was delivered to Alice, Atlas and CMS with some very interesting results.

Table 4: Parameter list for early (2010/2011) and nominal ion running.

Parameter	units	Early	Nominal
$\sqrt{s}$ per nucleon	TeV	2.76	5.5
Initial luminosity	$\mathrm{cm}^{-2}\mathrm{s}^{-1}$	1.25×10^{25}	1×10^{27}
Number of bunches		62	592
Bunch spacing	ns	1350	99.8
β^*	m	2	0.5
Pb ions per bunch		7×10^7	7×10^7
Transverse norm. emittance	μm	1.5	1.5
Luminosity half life (1,2,3 expts.)	hours	$3< \tau_{IBS} <70$	8, 4.5, 3

5 Outstanding problems

The splices in the interconnects remain a worry and still limit the beam energy to 3.5 TeV for the moment. Among a swathe of issues, two of the main concerns for 2011 are outlined below.

5.1 UFOs

Many sudden local beam losses have been recorded. There is no danger of a quench but preventive dumps are performed if the beam losses go above the threshold of the beam loss monitors implicated. The rise time of the losses is of the order 1 ms. A potential explanation is dust particles falling into beam with scattering creating losses and showers propagating downstream. This explanation has given rise to the moniker 'Unidentified Falling Object' or UFO. The UFOs are distributed around the ring and are seen in the arcs, inner triplets, and insertion regions. Most do not generate beam losses severe enough to dump the beam.

There are more events at higher beam intensities. UFOs are observed at 450 GeV with a lower beam loss amplitude. The losses are faster with intensity but it seems that the signal amplitude does not increase with total beam intensity, however statistics are limited for the moment and 2011 will show if this is the case or not. Additional quench tests will be used to benchmark the BLM thresholds, perhaps allowing more leeway in the setting of the thresholds. A revision of the BLM thresholds around the ring will also be made in an attempt to make the effect of UFOs on operational efficiency acceptable. Given that they occur at high energy, the straightforward cost of above threshold UFOs is machine efficiency and the 2 to 3 hour turnaround from high energy to high energy means that they can have a significant effect if they dump the beam on the order of once per day.

5.2 Electron cloud

Electron cloud effects in particle accelerators are well understood and have been very well studied over the years [3]. In the LHC electron cloud effects are predicted to occur both in the warm and cold regions. The most notable effects are: vacuum pressure rises (potentially causing background in experiments); single-bunch instabilities; multi-bunch instabilities; incoherent emittance growth; heat load in cold arcs (with quenches in the limit); and perturbation of beam diagnostics.

Experience of electron cloud in 2010 showed that it was very much dependent on bunch spacing: 150 ns saw local signs of electron cloud in the common beam pipe; 75 ns showed some first signs around the ring; and 50 ns induced enough vacuum activity to bring the vacuum valves in. Vacuum activity started off in regions with common beam pipe at 450 GeV as the number of bunches with 150 ns spacing was pushed up. Tests with solenoids wrapped around the beam pipe locally cured the problem, confirming the presence of electron cloud.

When the 50 ns bunch spacing was tried, the effects were very clearly seen. There was high vacuum activity in the warm regions (where the beams travel in separate beam pipes) and significant heat load in cold regions. Instabilities and beam size growth were observed. However, surface conditioning (scrubbing) was also observed with associated gas desorption rates and an implied drop in secondary emission yield (SEY). The time constant for the scrubbing processes was less than a day. The situation was a lot cleaner with 75 ns, however incoherent effects were seen and emittance blow-up was observed when 800 plus bunches in both beams were injected [4].

2010 observations are certainly due to a high SEY between 2 and 2.5, whereas 1.7 was usually the maximum value studied in the past. It is expected to be able to reach 200 to 300 bunches with 75 ns without scrubbing. Thereafter a 7 day scrubbing run with large emittance ($\geq$ 3.5 μm), high bunch intensity ($> 1.2 \times 10^{11}$) is planned. In addition solenoids have been installed at many locations during the 2010/11 Christmas technical stop.

6 Operation in 2011

The beam energy remains at 3.5 TeV in 2011; there are still some concerns about the interconnect splices. The β^*s for the run will be: 1.5 m in Atlas and CMS; 3 m in LHCb; and 10 m in Alice.

The modest official target for 2011 is 1 fb^{-1} delivered to each of Atlas, CMS and LHCb at 3.5 TeV. Projecting the performance in reached in 2010 it should be possible to do better for Atlas and CMS. 1 fb^{-1} will be a challenge for LHCb given their maximum acceptable luminosity of between 2 to 3×10^{32} cm^{-2}s^{-1} and associated pile-up limitations. Luminosity levelling via separation will be required to maximize the delivered luminosity. Alice's requirements for the proton run are modest with a demanded luminosity for the proton run of between 5 and 50×10^{29} cm^{-2}s^{-1} and a "pile-up" of around 0.05.

The baseline operational scenario for 2011 is itemized below.

- Re-commissioning with beam after the Christmas technical stop should take around 3 weeks. The exit conditions from this phase should be stable beams with low number of bunches.
- There will a ramp-up to around 200 bunches (75 ns) taking about 2 weeks. Multi-bunch injection commissioning will take place during this phase.
- Stable beams with 200 to 300 bunches will be delivered for around 2 weeks.
- There will then be a scrubbing run of 10 days which will include 50 ns injection commissioning.
- An intermediate energy run (beam energy 1.38 TeV) is planned with 5 days foreseen.
- 75 ns operation will be resumed and the number of bunches increased via a total of around 300, 400, 600, 800, 930 bunches. Machine protection and operations qualification will accompany each step. If 50 ns looks encouraging following the scrubbing run, this option may be used in place of 75 ns.
- Physics operation with 75 ns up to a maximum of 930 bunches, or operation with 50 ns up to a maximum of around 1380 bunches.

Given the parameters shown in Table 5 the estimated peak luminosity should be around 1.2×10^{33} cm^{-2}s^{-1} for 75 ns operation or up to 1.6×10^{33} cm^{-2}s^{-1} with 50 ns. There is the possibility to gently push up the bunch intensity and push down the emittances delivered by the injectors with the potential for correspondingly higher peak luminosities. Given the a peak

luminosity of 1.2×10^{33} cm^{-2}s^{-1}, around 130 days of delivery at or around this level, and reasonable operational efficiency reflected in the Hübner factor of around 0.2, the LHC should be able to deliver around 2 to 3 fb^{-1} in 2011.

Table 5: Anticipated performance related parameters for operation in 2011.

Parameter	Value
Energy	3.5 TeV
β^* in Atlas and CMS	1.5 m
Bunch spacing	75 ns (50 ns)
Bunch intensity	1.2×10^{11}
Stored beam energy	63 MJ (93 MJ)
Emittance [mm.mrad]	≈2.5
Days at peak luminosity	≈135
Hübner factor	0.2

So far in 2011 there has been impressive progress in re-commissioning with beam. Improvements and consolidation across the board has taken place during the Christmas technical stop. The machine operation is now reasonably well optimized, a faster ramp and squeeze is in place, and the essential mechanics for driving the machine through the nominal cycle well bedded in. It is with some measured confidence that the LHC team approaches the challenge of increasing the total beam intensity in the first half of the year.

7 Conclusions

The LHC performance in 2010 was very encouraging: the magnetic model and optics look excellent; the beam instrumentation is in good shape; beam cleaning and collimation works reliably with predicted efficiency; the machine protection system's performance has been excellent; the machine aperture looks good. The performance with beam (losses, lifetimes, luminosity, emittance growth) has also been surprisingly forgiving.

Given this positive situation, the outlook for 2011 sees an increase in number of bunches to between 930 and 1380 and a peak luminosity of between 1.2 and 1.6 $\times10^{33}$ cm^{-2}s^{-1}. This should allow the LHC to deliver around 2 to 3 fb^{-1}. Increasing intensity will bring a number of issues. The destructive power of the stored energy of the beam at high energy is an ever present concern and diligent attention to the machine protection system is mandatory. Of the other issues, UFOs and SEUs, perhaps, present the biggest threat to operational efficiency and they will both have to be carefully monitored and mitigation anticipated if their effects prove too serious.

References

1. Proceedings of the second 2010 Evian workshop on LHC beam operation, CERN-ATS-2011-017.
2. W. Venturini, LHC operational efficiency in 2010, Proceedings of the second 2010 Evian workshop on LHC beam operation, CERN-ATS-2011-017.
3. Proceedings ECLOUD'02, CERN, Geneva, 15-18 April 2003, CERN-2002-001.
4. G. Arduini, 50 and 75 ns operation, Proceedings of the second 2010 Evian workshop on LHC beam operation, CERN-ATS-2011-017.
5. J. Jowett, Ions in the LHC, Proceedings of Chamonix 2009 workshop on LHC Performance, CERN-ATS-2011-017.

HERA PRECISION MEASUREMENTS AND IMPACT FOR LHC PREDICTIONS

V. Radescu on behalf of the H1 and ZEUS Collaborations
Heidelberg Physikalisches Institut, Philosophenweg 12, D-69120 Heidelberg, Germany

A QCD fit analysis to the combined HERA inclusive deep inelastic cross sections measured by the H1 and ZEUS collaborations for $e^{\pm}p$ scattering to extract HERAPDF sets is presented. The results are used for predictions of $p\bar{p}$ processes at Tevatron and pp processes at the LHC. The QCD analysis has been extended to include the combined HERA II measurements at high Q^2 resulting in the HERAPDF1.5 sets, with full estimation of uncertainties. The precision of the new PDFs at high x is considerably improved, particularly in the valence sector. In addition, inclusion of the HERA jet data allows for a precise determination of the strong coupling. Moreover, inclusion of the preliminary combined HERA charm data provides constraints for the optimal value of the charm mass used in QCD theory models which may account for some of the differences among global PDF fits.

1 Combined H1 and ZEUS Cross Section Measurements

The main information on proton structure functions comes from the Deep Inelastic Scattering (DIS) collider experiments H1 and ZEUS at HERA. Measurements at HERA go well beyond the phase space accessible by fixed target experiments with an extended kinematic range of $0.045 < Q^2 < 30\,000$ GeV^2 and $6 \times 10^{-5} < x < 0.65$. To further benefit from the precision of the measurements the H1 and ZEUS cross sections are combined, resulting in the most consistent and precise DIS inclusive double differential cross-section measurement of neutral and charged current $e^{\pm}p$ scattering to date [1]. The data combination "procedure" has been repeated to include as well the preliminary high precision measurements at high Q^2 from the second run period of HERA. Therefore, these accurate measurements can be used as the sole input to the QCD analysis to determine the proton parton distribution functions (PDFs) as described in the following sections, which can be used then for precise predictions for LHC processes.

2 QCD Analysis settings

HERA PDFs are determined from QCD fits to HERA data alone. Only the region where perturbative QCD is valid, data above $Q^2_{\rm min} = 3.5$ GeV^2 are used in the central fit. The HERA data have a minimum invariant mass of the hadronic system, W, of 15 GeV, such that they are in a kinematic region where there is no sensitivity to non-perturbative effects common to fixed target data.

The fit procedure starts by parametrising PDFs at a starting scale $Q^2_0 = 1.9$ GeV^2, chosen to be below the charm mass threshold. The QCD settings are optimised for HERA measurements of proton structure functions which are dominated by gamma exchange, therefore the parametrised PDFs are the valence distributions xu_v and xd_v, the gluon distribution xg, and the u-type and d-type sea quark distributions $x\bar{U}$, $x\bar{D}$, where $x\bar{U} = x\bar{u}$, $x\bar{D} = x\bar{d} + x\bar{s}$. Using a simple parametrisation form with the normalisation parameters constrained by the QCD sum-rules and relying on additional assumptions [1] the number of free paramaters reduces to 10 for the fits to HERA I data. However, the more data become available, the more constraining assumptions can be released, therefore the number of free parameters once HERA II data are added is increased, allowing for more freedom to the gluon and valence distributions, HERAPDF1.5f. For example addition of the preliminary combined charm data, or jet data from H1 [2,3] and ZEUS [4,5] allows for more flexibility of the gluon distribution. The PDFs are then evolved using the DGLAP evolution equations [6] at NLO and NNLO in the $\overline{MS}$ scheme with the renormalisation and factorisation scales set to Q^2. The QCD predictions for the structure functions are obtained by convoluting the PDFs with the calculable coefficient functions taking into account mass effects for the heavy quarks based on the general mass variable flavour scheme [7]. The PDF uncertainties at HERA are classified in three categories: experimental, model, and parametrisation. The consistency of the input data set and its small systematic uncertainties enables us to calculate the experimental uncertainties on the PDFs using the χ^2 tolerance $\Delta\chi^2 = 1$. The model uncertainties are evaluated by varying the input assumptions, as performed in [1]. The parametrisation uncertainty is estimated as an envelope which is formed as a maximal deviation at each x value from the central fit.

3 Results and Comparisons

The inclusion of the precise high Q^2 preliminary HERA II data in the QCD fits results in HERAPDF1.5. Figure 1 shows the comparison between HERAPDF1.5 and HERAPDF1.0 which is based on HERA I data alone. The impact is noticeable especially in the high x region, where the valence contribution dominates. In addition, a meticulous study has been performed to estimate the uncertainties for the NNLO HERAPDF set, also shown in Figure 1, where the new NNLO set is compared to the HERAPDF1.0 NNLO. To answer the question about implications of the new PDF sets on the Higgs exclusion limits from Tevatron, Figure 2 shows a more explicit comparison of the gluon distribution at high x between HERAPDF and MSTW08 sets at NNLO. The HERAPDF1.5 NNLO set yields a harder gluon at high x compared to the HERAPDF1.0 NNLO set, which is prefered by the Tevatron jet data. The differences are mostly due to the use of a more flexible functional form made possible via the availability of a more precise data.

Another important result is related to the determination of the strong coupling. New results from HERA based solely on the inclusive DIS measurements can not yet pin down the value of α_S as shown in Figure 2 (right), where a scan in χ^2 as function of strong coupling is shown. However, as soon as the jet data are included in the QCD fit, resulting in HERAPDF1.6, it can be seen that the strong coupling is well constrainted. In fact, the addition of the HERA jet data into the fit allows the strong coupling and gluon to be simultaneously constrained. Figure 3 shows the impact of the inclusion of the jet data on the gluon distribution when the fit

is performed with the strong coupling as a free parameter. As a result, the HERA data prefer a rather larger value for $\alpha_S(M_Z) = 0.1202 \pm 0.0013(\text{exp}) \pm 0.0007(\text{mod}) \pm 0.0012(\text{had})^{+0.0045}_{-0.0036}(\text{th})$.

In addition, the inclusion of the preliminary HERA charm data provides constraints for the optimal value of the charm mass used in theory models. It has been observed that QCD fits without charm data have only a small sensitivity to the value of the charm mass. However, there is a strong preference for a particular m_c once charm data is included. This study has been performed for various schemes, such as those used in the global fit analyses of MSTW08 and CTEQ. The results conclude that each scheme describes the data well at the corresponding best value of the m_c. It is interesting to observe that differences in the PDF sets correspond to differences in the charm mass used in different schemes [8].

All HERAPDF sets derived solely from ep measurements are able to give a good prediction of the Z and W at Tevatron from the $p\bar{p}$ processes, and provide a competitive description to pp processes at the LHC as well.

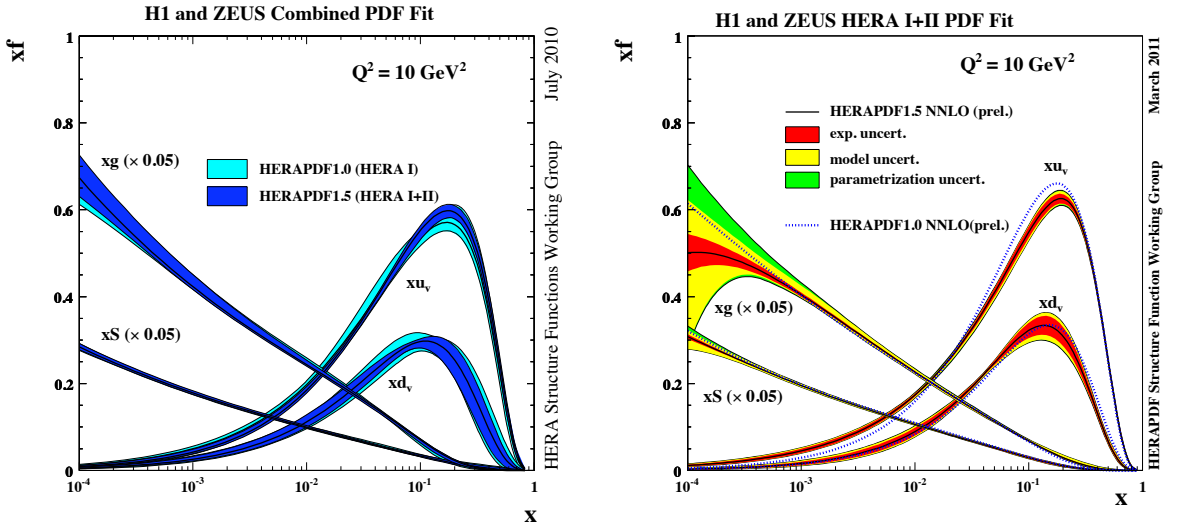

Figure 1: On the left hand side: the comparison between HERAPDF1.0 (light colour) based on the HERA I data and HERAPDF1.5 (dark colour) based on the HERA I and II data, using the total uncertainty band at $Q^2 = 10$ GeV^2 with gluon, sea (which are scaled by a factor of 0.05) and valence distributions. On the right hand side: the summary plot for HERAPDF1.5 at $Q^2 = 10$ GeV^2 at NNLO with the uncertainties including the experimental (red), model (yellow) and the PDF parametrisation (green), compared to the central fit for HERAPDF1.0 at NNLO.

4 Summary

HERA provides accurate determinations of the proton structure and can predict related Standard Model processes. Additional preliminary combined measurements from HERA II allow the high x region to be better constrained resulting in a more precise HERA PDF set, HERAPDF1.5 at NLO and NNLO in α_S with a detailed analysis of the uncertainties. The HERAPDF sets, which are based solely on ep data also describe the Tevatron data well and provide competitive predictions to the LHC processes. Inclusion of the HERA jet data allows for a precise determination of the strong coupling, for which HERA data prefers a rather larger value of α_S. In addition, inclusion of the preliminary combined HERA charm data provides constraints on the optimal value for the charm mass used in theory models and it may account for some of the differences among global PDF fits. Therefore, HERAPDF provides a large variety of meticulous studies based on new measurements from HERA for accurate predictions at the LHC [9].

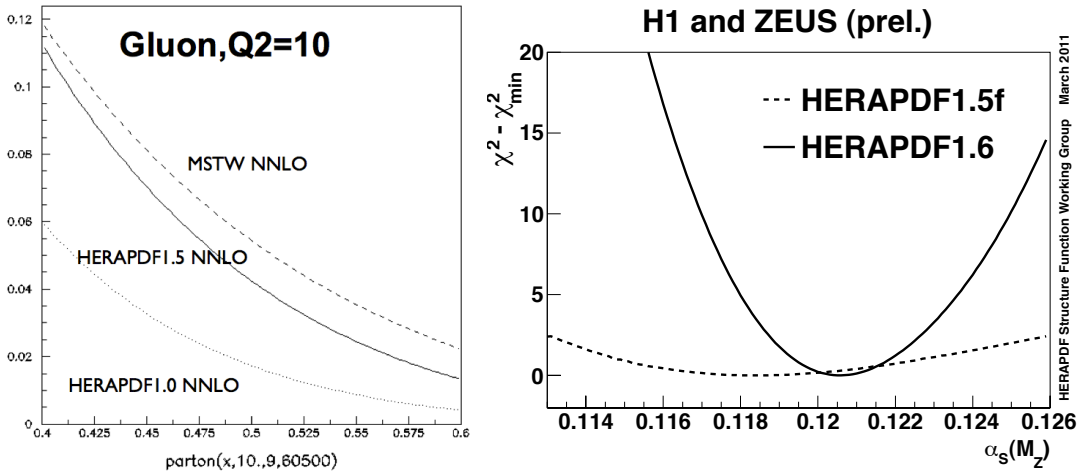

Figure 2: On the left hand side: the gluon distribution from the HERAPDF sets (based on HERA I only - HERAPDF1.0, and based on HERA I+II, HERAPDF1.5) to MSTW08 at NNLO in the high x region. On the right hand side: the $\Delta\chi^2$ distribution as a function of the value of $\alpha_S(M_Z)$ in the PDF fits for HERAPDF1.5f (dashed line) without jet data and HERAPDF1.6 (solid line) with jet data.

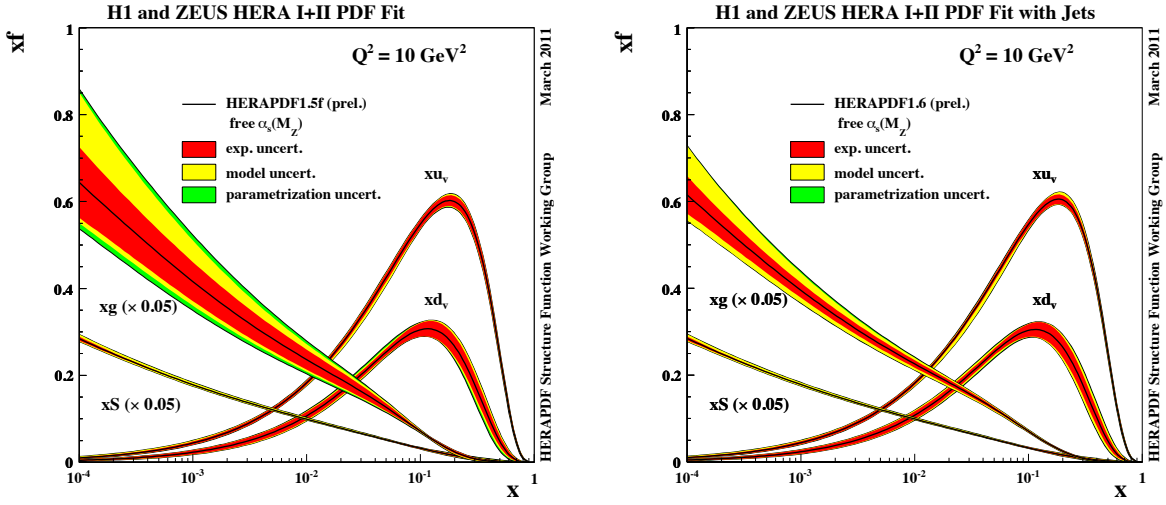

Figure 3: Summary plot for HERAPDF1.5f (left) and HERAPDF1.6 (right) as a function of x for $Q^2 = 10$ GeV^2. The strong coupling constant $\alpha_S(M_Z)$ is a free parameter in both fits. The central values of the PDFs (solid lines) are shown together with the experimental, model and parametrisation uncertainties represented by the red, yellow and green shaded bands, respectively.

References

1. H1 and ZEUS Collaborations, F. Aaron *et al.*, JHEP **1001**(2010) 109, arXiv:0911.0884.
2. H1 Collaboration, F. Aaron *et al.*, Eur. Phys. J. **C67** (2010) 1, arXiv:0911.5678.
3. H1 Collaboration, F. Aaron *et al.*, Eur. Phys. J.**C65**(2010) 363, arXiv:0904.3870.
4. ZEUS Collaboration, S.Chekanovetal *et al.*, Physics Letters **B547** (2002) 164.
5. ZEUS Collaboration, S.Chekanovetal *et al.*, Nuclear Physics **B765** (2007) 1.
6. QCDNUM package, M. Botje, (2010), arXiv:1005.1481.
7. R. S. Thorne code, revised in 2008.
8. V. Radescu slides, `http://moriond.in2p3.fr/QCD/2011/MondayMorning/Radescu.pdf`
9. The LHAPDF grid files are located at `https://www.desy.de/h1zeus/combined_results/index.php?do=proton_structure`

Higgs Boson Searches at CMS and ATLAS

W. Quayle on behalf of the ATLAS and CMS Collaborations
University of Wisconsin-Madison, 1150 University Ave., Madison, WI, 53706

Searches for Higgs bosons decaying to a variety of final states have been performed with the CMS and ATLAS detectors in 35-38 pb^{-1} of proton-proton collisions at the LHC. No evidence of a Higgs boson is found, and limits are set on the production rates as functions of mass and, for some channels, other model parameters. The strongest constraints come from the $H \to WW \to \ell\nu\ell\nu$ channel, where both ATLAS and CMS independently exclude Higgs boson production with a rate of 2.1 times the Standard Model prediction for a Higgs boson with $m_H = 160$ GeV. Projections of the expected sensitivity with higher luminosity show that both experiments expect to exclude a Standard Model Higgs boson in the mass range $130 < m_H < 460$ GeV with 1 fb^{-1} of integrated luminosity.

1 Introduction

The search for the Higgs boson [1,2,3] is one of the central goals of the LHC scientific programme. Direct searches at LEP [4] and Tevatron [5] have excluded the existence of a Standard Model Higgs boson below 114.4 GeV and in the range $158 < m_H < 173$ GeV, respectively. Searches for the Higgs boson have recently been performed by the ATLAS [6] and CMS [7] experiments in the $\sqrt{s} = 7$ TeV pp collision data recorded during the LHC run of 2010, and the limits set by these searches are summarized below.

2 $H \to WW^{(*)} \to \ell\nu\ell\nu$ and $H \to ZZ \to \ell\ell\nu\nu/\ell\ell qq$

For $m_H > 137$ GeV, the dominant decay mode of the Standard Model Higgs boson is $H \to WW$ [8]. The analysis performed by ATLAS [9] is based on straight cuts on kinematic variables and includes contributions from $H + 0j$, $H + 1j$, and $H + 2j$ events. The analysis performed by CMS [10] focuses on $H + 0j$ events, but makes use of a Boosted Decision Tree algorithm to enhance the discrimination between signal and background. Both searches make heavy use of control samples to extract estimates of the rate of backgrounds from WW, top, W+jets, and Z+jets. The W+jets background is normalized using events selected by loosening the lepton selection criteria. The top background control samples are based on altered cuts on jets and b-tagging. A pure Z+jets control sample is constructed by altering the cuts on $m_{\ell\ell}$ and E_T^{miss}, and the diboson control sample is defined by altered cuts on $m_{\ell\ell}$ and transverse opening angle $\Delta\phi_{\ell\ell}$. Figure 1 shows the limits set by ATLAS (left) and CMS (right). Both experiments set limits of around 2.1 times the Standard Model prediction at $m_H = 160$ GeV.

The second-dominant decay mode of the Standard Model Higgs boson in the high-mass region is $H \to ZZ$. The $H \to ZZ \to 4\ell$ channel is the cleanest signature, but its branching ratio is so small that in 35 pb^{-1} no 4ℓ candidates events were observed in ATLAS, and only one was observed in CMS. The branching ratios for $ZZ \to \ell\ell\nu\nu$ and $ZZ \to \ell\ell qq$ are large enough

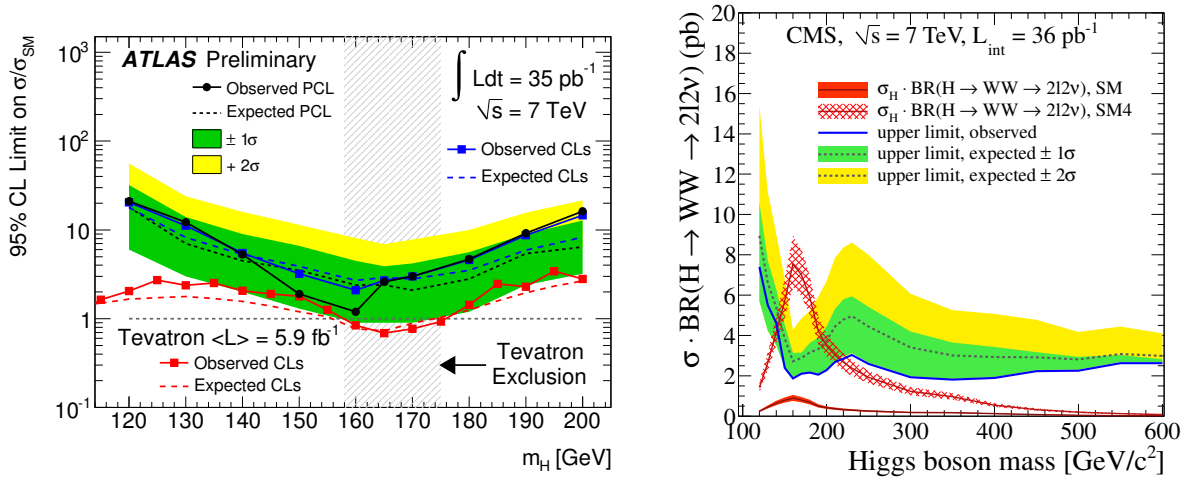

Figure 1: 95% CL limits on the Higgs boson production cross-section set by the ATLAS (left) and CMS (right) $H \to WW \to \ell\nu\ell\nu$ searches.

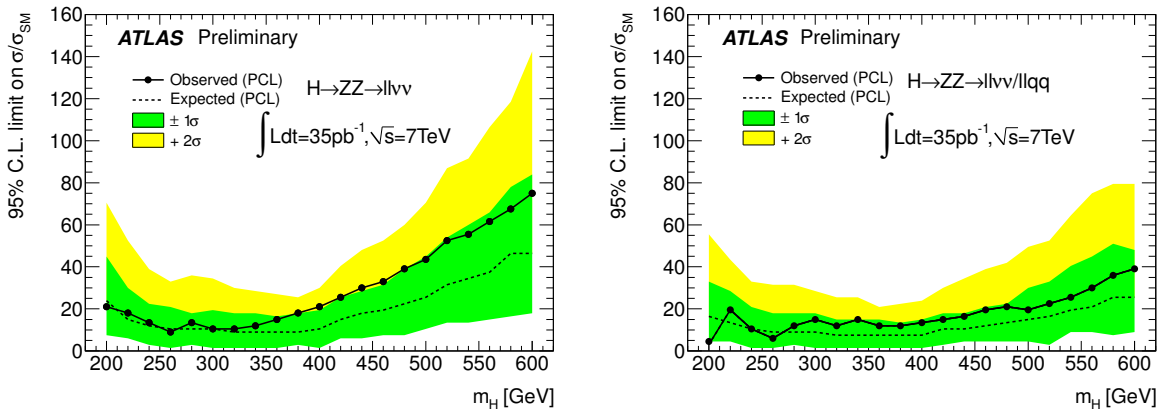

Figure 2: Left: 95% CL limits on the Higgs boson production cross-section set by the ATLAS $H \to ZZ \to \ell\nu\ell\nu$ search. Right: the limit obtained by combining the $H \to ZZ \to \ell\nu\ell\nu$ and $H \to ZZ \to \ell\nu qq$ searches.

to study even in 35 pb^{-1} of data [11], although the backgrounds in these channels are higher as well. A search for the former decay mode proceeds by selecting events with two leptons and large E_T^{miss} and reconstructing the transverse mass of the $\ell\ell\nu\nu$ system, while in a search for the $\ell\ell qq$ final state one can fully reconstruct the invariant mass of the ZZ system. Figure 2 shows the upper bounds on the Higgs boson production cross-section (in units of the Standard Model prediction) obtained from $H \to ZZ \to \ell\ell\nu\nu$ alone (left) and from the combination of the $\ell\ell\nu\nu$ and $\ell\ell qq$ channels (right). In the combined limit, the upper bound on the Higgs boson production cross-section ranges from 3.5 times the Standard Model prediction at low mass to about 30 times the Standard Model prediction at high mass.

3 $H \to \gamma\gamma$, $H/A \to \tau\tau$, and Charged Higgs

For Higgs bosons with a mass below about 140 GeV, the $H \to \gamma\gamma$ decay mode offers one of the most important discovery modes. A Higgs boson decaying to this final state would give rise to a narrow peak in the $\gamma\gamma$ invariant mass spectrum, with a FWHM of 4.4 GeV at ATLAS [12]. Figure 3 (left) shows the upper limit from ATLAS on the $H \to \gamma\gamma$ production cross-section in units of the Standard Model prediction. The upper limit varies between 8 and 38 times the

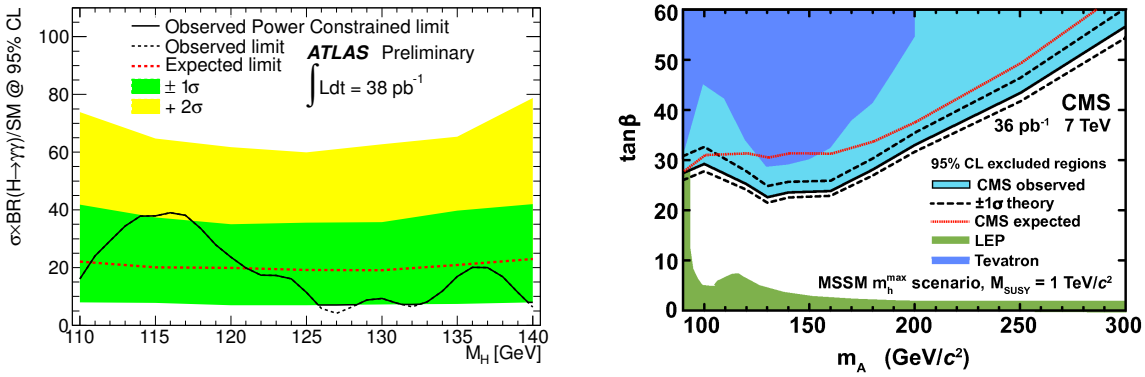

Figure 3: Left: the upper limit on the $H \to \gamma\gamma$ cross-section based on 38 pb^{-1} of ATLAS data. Right: The limits on $H/A \to \tau\tau$ production set by CMS in 36 pb^{-1} of data.

Standard Model prediction, depending on the Higgs boson mass.

In models with two Higgs doublets, the branching ratio for $H \to \tau\tau$ can recieve a substantial enhancement over the Standard Model value. Both ATLAS and CMS have therefore expressed the results of their $H \to \tau\tau$ searches in terms of the MSSM model parameters in the m_H^{max} scenario [13]. The ATLAS analysis of this final state [14] includes only the $\tau\tau \to lh$ channel and is based on the invariant mass of the visible τ decay products. The dominant background from $Z \to \tau\tau$ events is checked by replacing the muons from $Z \to \mu\mu$ in data with simulated τ leptons, and the W+jets background is estimated using a control sample where the charge of the lepton is the same as the charge of the hadronically decaying τ candidate. On the other hand, the CMS analysis [15] also includes the $\tau\tau \to ll$ channel, uses a Likelihood technique to reconstruct $M_{\tau\tau}$, and extracts the background with a fit to the $M_{\tau\tau}$ distribution. The results from the two searches are similar, and both exceed previous limits [16]. Figure 3 (right) shows the limits obtained from the search at CMS.

Models with additional Higgs doublets or triplets can contain singly charged Higgs bosons and, in the case of triplet models, doubly charged Higgs bosons. CMS has searched for doubly charged Higgs bosons ϕ^{++} decaying to several final states [17] and excluded masses ranging from 105 GeV in the case of $\phi^{++} \to e\tau/\mu\tau$ to 155 GeV in the case of $\phi^{++} \to \mu\mu$. A search for singly charged Higgs production at CMS in the channel $t \to bH^+ \to b\tau\nu$ has resulted in an upper limit on $BR(t \to bH^+)$ of about 25-30% for charged Higgs boson masses between 80 and 150 GeV [18].

4 Expected Sensitivity in Future Running

Figure 4 summarizes the limits that are expected to result from the analysis of the data that will be collected later this year and next year. The plot on the left shows the expected limits for several individual channels at ATLAS and their combination assuming Standard Model branching ratios after an integrated luminosity of 1 fb^{-1} [19,20]. The plot on the right shows the evolution of the combined limit from CMS as a function of integrated luminosity [21]. With 1 fb^{-1} of integrated luminosity, both experiments expect to exclude a Standard Model Higgs boson in the mass range $130 < m_H < 460$ GeV. At higher luminosities of 5-10 fb^{-1} and assuming an increase in the center-of-mass energy to $\sqrt{s} = 8$ TeV, it will be possible to exclude the full mass spectrum from the current lower bound at 114 GeV up to about 600 GeV with one experiment if there is no Higgs boson. If there is a Standard Model Higgs boson, then there is a better than 50% chance to discover it with 5σ significance at one experiment if its mass is in the range $130 < m_H < 500$ GeV.

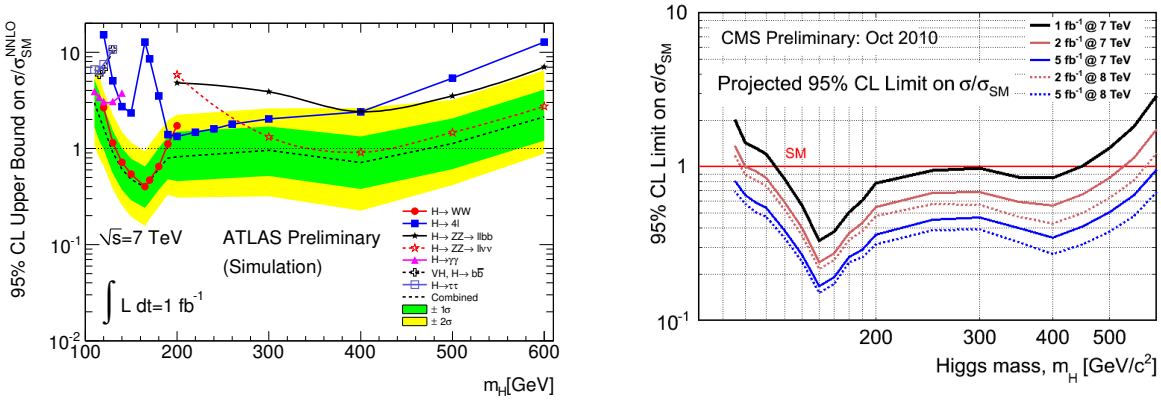

Figure 4: Left: the expected limits on several Higgs boson production channels and the combined limit assuming Standard Model branching ratios at ATLAS with 1 fb^{-1} of integrated luminosity. Right: the expected combined limits on Standard Model Higgs production at CMS, for several values of the integrated luminosity.

References

1. F. Englert and R. Brout, *Phys. Rev. Lett.* **13**, 321–323 (1964)
2. P. W. Higgs, *Phys. Lett.* **12**, 132-133 (1964)
3. P. W. Higgs, *Phys. Rev. Lett.* **13**, 508–509 (1964)
4. LEP Working Group for Higgs boson searches, *Phys. Lett.* **B565**, 61-75 (2003)
5. CDF and D0 Collaborations and the TEVNPHWG Working Group, arXiv:1103.3233v2 [hep-ex]
6. The ATLAS Collaboration, *Expected Performance of the ATLAS Experiment - Detector, Trigger, and Physics*, arXiv:0901.0512 [hep-ex]
7. The CMS Collaboration, CMS Technical Design Report, J. Phys. G: Nucl. Part. Phys. 34 (2006)
8. LHC Higgs Cross Section Working Group, S. Dittmaier, C. Mariotti, G. Passarino, and R. Tanaka (Eds.), *Handbook of LHC Higgs Cross Sections: 1. Inclusive Observables*, CERN-2011-002, arXiv:1101.0593 [hep-ph]
9. The ATLAS Collaboration, ATLAS Conference note ATLAS-CONF-2011-005
10. The CMS Collaboration, *Phys. Lett.* **B699** (2011) 25-47
11. The ATLAS Collaboration, ATLAS Conference note ATLAS-CONF-2011-026
12. The ATLAS Collaboration, ATLAS Conference note ATLAS-CONF-2011-025
13. M. Carena, S. Heinemeyer, C. E. M. Wagner, and G. Weiglein, Eur. Phys. J. **C26** (2003) 601-607
14. The ATLAS Collaboration, ATLAS Conference note ATLAS-CONF-2011-024
15. The CMS Collaboration, arXiv:1104.1619 [hep-ex]
16. The CDF Collaboration, the D0 Collaboration, and the Tevatron New Physics Higgs Working Group, arXiv:1003:3363 [hep-ex]
17. The CMS Collaboration, CMS Physics Analysis Summary CMS-PAS-HIG-11-001
18. The CMS Collaboration, CMS Physics Analysis Summary CMS-PAS-HIG-11-002
19. The ATLAS Collaboration, ATLAS Note ATL-PHYS-PUB-2010-015
20. The ATLAS Collaboration, ATLAS Note ATL-PHYS-PUB-2011-001
21. The CMS Collaboration, CMS Note 2010/008

THEORETICAL UNCERTAINTIES IN HIGGS SEARCHES

Abdelhak DJOUADI
Laboratoire de Physique Théorique, Université Paris-Sud XI et CNRS, F-91405 Orsay, France.
Theory Unit, CERN, 1211 Genève 23, Switzerland.

In this talk, we respond to the comments and criticisms made by the representatives of the CDF and D0 collaborations on our recent papers in which we point out that the theoretical uncertainties in the Higgs production cross section have been largely underestimated and, if properly taken into account, will significantly loosen the Tevatron Higgs exclusion bounds. We show that our approach to the theoretical uncertainties is fully justified and, furthermore, provide additional details on our statistical analysis of the CDF and D0 exclusion limit which show that it is conceptually correct.

1 Introduction

In two earlier papers[1,2], we updated the theoretical predictions for the production cross sections of the Standard Model Higgs boson at the Tevatron collider, focusing on the main search channel, the gluon–gluon fusion mechanism $gg \to H$, including the relevant higher order QCD and electroweak corrections[3]. We then estimated the various theoretical uncertainties affecting these predictions: the scale uncertainties which are viewed as a measure of the unknown higher order effects, the uncertainties from the parton distribution functions (PDFs) and the related errors on the strong coupling constant α_s, as well as the uncertainties due to the use of an effective field theory (EFT) approach in the determination of the radiative corrections in the process at next-to-next-to-leading order (NNLO). We found that contrary to the Higgs–strahlung processes[3], where the rates are well under control as the uncertainty is less than $\approx 10\%$, the theoretical uncertainties are rather large in the case of the gluon–gluon fusion channel, possibly shifting the central values of the NNLO cross sections by up to $\approx 40\%$. These uncertainties are thus significantly larger than the $\approx 10\%$–20% error assumed by the CDF and D0 experiments in their analysis that has excluded the Higgs mass range $M_H = 158$–175 GeV at 95% CL[4,5]. As $gg \to H$ is by far the dominant Higgs production channel in this mass range, we concluded that the above exclusion limit should be reconsidered in the light of these large theoretical uncertainties.

After our papers appeared, some criticisms have been made by the members of the CDF and D0 collaborations and of the Tevatron New Physics and Higgs working group (TevNPHWG)[6] concerning the theoretical modeling of the $gg \to H$ production cross section that we proposed. This criticism was made more explicit at this conference[7]. In this note, we respond to this criticism point by point and show that that our approach to the theoretical uncertainties is fully justified. In particular, we will make use of of a recent collective effort[8] made by theorists along with experimentalists of the ATLAS and CMS collaborations to evaluate the Higgs cross section at the LHC, with a special attention to the gluon fusion mechanism which is also the process of interest here. Several issues discussed in our papers[1,2] have been indeed addressed in

the report of this working group. It turns out that many of the proposals that we put forward for the $gg \to H$ process are in fact similar to those adopted in this comprehensive LHC study. We will thus also use the conclusions of this report (together with other studies that appeared meanwhile) to strengthen some arguments even more.

Another criticism made by the CDF and D0 collaborations is on the statistical analysis of the exclusion limit that we performed in Ref. [2], using the detailed information and the multivariate analysis given in a CDF paper [5]. Apparently, there was a misunderstanding on what we actually did in our "emulation" of the CDF/D0 limit: we did not increase the theoretical uncertainty (or add an extra uncertainty) but simply changed the normalisation as if the cross section was evaluated using another PDF set (such as HERA[9] or ABKM[10] rather than the adopted MSTW choice[11]). In this case, using the neural network output of the CDF analysis to re-estimate the sensitivity and the exclusion limit is fully justified and our analysis is conceptually correct.

Finally, we take this opportunity to correct an error made in Ref. [2] in the numerical evaluation of the $gg \to H$ cross section using the HERA PDF set [9]. This error will only slightly change part of the discussion in Ref. [2] and will not alter our general conclusions.

2 Summary of the answer to the criticisms

A detailed answer to these criticisms has recently appeared on the arXives [12]. Because of the lack of space, we will simply summarize here the main points that we put forward in our analysis of the $gg \to H$ cross section at the Tevatron and refer to Ref. [12] for the details.

2.1 Discussion of the theoretical uncertainties in the NNLO production rate

i) The scale uncertainty has not been overestimated in our analysis. We gave several arguments in favor of an extended domain for scale variation and in fact, it turns out that our uncertainty is comparable to that assumed by the CDF/D0 collaborations when the $gg \to H$ cross section is broken into jet cross sections and to the (even larger) uncertainty advocated in Ref. [13] when the impact of the jet veto is included in the Higgs+0 jet cross section alone.

ii) For the uncertainty from the EFT approach, many of its components have been discussed in other papers such as Ref. [8] and we simply made the effort to quantify the overall impact.

iii) We do not believe that we are overestimating the PDF uncertainties. In fact the result that we quote within the MSTW set is exactly the one that is obtained used the PDF4LHC recommendation[14]. We even believe that we are underestimating these PDF uncertainties, especially if the analysis of Ref. [15] turns out to be correct. In particular, the difference between the MSTW and ABKM predictions of 25–30% (which is the most significant one[a]) is still larger than our PDF uncertainty within the MSTW set, see the left–hand side of Fig. 1.

iv) We do not add linearly the PDF and scale+EFT uncertainties. Our procedure, which has been also advocated in other analyses like Ref. [16] for top–quark pair production, addressed also the theoretical part of the uncertainties. The result that we assume is indeed close to a linear sum (in fact slightly smaller), but a linear combination of scale+PDF uncertainties is exactly the one recommended in the LHC Higgs cross section working group report[8].

v) If the recommendations of the LHC Higgs cross section working group report [8] are adopted for the CDF uncertainties, one would obtain the same uncertainties as the ones that we are advocating in the paper (modulo the small EFT uncertainties); see the right–hand of Fig. 1 where the total uncertainties of various calculations are displayed.

vi) The various issues discussed here appear also in the case of Higgs production in supersymmetric extensions of the Standard Model. The theoretical uncertainties turn out to be also quite large in the main production channels [17], $gg + b\bar{b} \to$neutral Higgs$\to \tau^+\tau^-$.

[a] This is different from what we claimed previously as we had a numerical error in the cross section when evaluating it with HERAPDF which led to a 40% difference. We thank Graham Watt for pointing this to us.

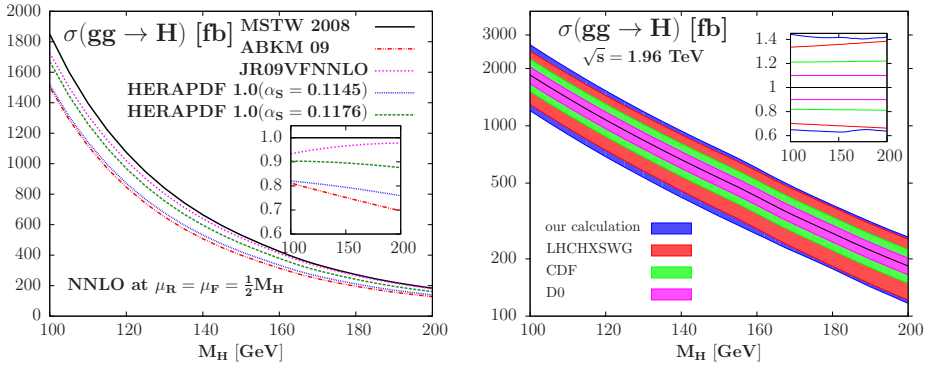

Figure 1: Left: The $gg \to H$ cross section as a function of M_H when the four NNLO PDF sets, MSTW, ABKM, JR and HERAPDF are used. Right: $\sigma^{\rm NNLO}_{gg\to H}$ at the Tevatron using the MSTW PDFs, with the uncertainty band when all theoretical uncertainties are added as in Ref. [1]; it is compared the uncertainties quoted by CDF and D0[4] as well as the one when the LHC procedure[8] is adopted. In the inserts show are the relative deviations.

2.2 Emulation of the CDF limit calculation

i) The PDF effect is not included as being a new source of systematic uncertainty but, rather, as a different choice for the PDF set from the CDF one[5], and which affects only the cross section normalisation. Thus, our goal was not to re-estimate the CDF sensitivity but the relative variation of the sensitivity when the cross section is changed by a different PDF choice.

ii) Our results are robust regarding the systematic uncertainties and their correlations, since we are using the multivariate outputs of the CDF analysis that include them.

iii) Our main results for the needed luminosity to recover the present sensitivity agree with estimates obtained in a simple and heuristic way; we believe that this agreement provides a nice check of our analysis. Note however, that we based our analysis on a 40% reduction of the $gg \to H$ cross section when using HERA PDFs. The correct figure with a reduction of only 30% as obtained with ABKM is shown in Fig. 2; this does not change our general conclusions[b].

iv) It is highly desirable that the CDF and D0 collaborations provide us with a fully cut-based analysis which will be easier to follow and reinterpret; we will be more than happy if they could simply redo our analysis in Ref. [2], assume a different normalisation of the production cross section and reinterpret the Higgs mass limit.

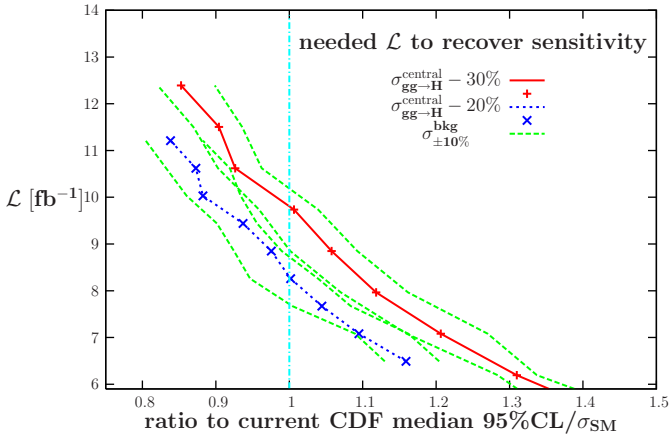

Figure 2: The luminosity needed by CDF to recover the current sensitivity (with 5.9 fb^{-1} data) when the $gg \to H \to \ell\ell\nu\nu$ signal rate is lowered by 20 and 30% and with a $\pm 10\%$ change in the $p\bar{p} \to WW$ background.

[b] This is particularly true as the updated results given by the CDF/D0 experiments at this conferences with 7.1 fb^{-1} data for CDF, lead to an exclusion limit that is slightly worse than the one quoted in Ref. [2] and only the range $M_H = 158$–173 GeV is excluded. Thus, even for a 30% reduction of the production cross section only instead of the 40% used earlier, one still needs ≈ 13 fb^{-1} data to recover the sensitivity obtained with 7.1 fb^{-1}.

2.3 The impact of different PDF parameterizations

Finally, concerning the discussions on the HERAPDF and ABKM parameterizations, let us stress again that they provide reasonable fits to the Tevatron jet data, contrary to an apparently common belief. There are issues about the PDF fits that need more investigation (in particular the point raised recently on the treatment of the NMC data which might lead to a significant impact) and until a better understanding of the large differences between the results of the various sets, one should use the ABKM and HERAPDF predictions as a reflection of the theoretical uncertainty in the game. This is very important since, except from MSTW, they are among the few other parameterizations which are available at NNLO, i.e. the order required to address Higgs production at hadron colliders. It is thus imperative that one assesses the impact of using these two sets for the Higgs production cross section. This is particularly important for a crucial issue such as the exclusion of the Higgs boson in a certain mass range.

3 Conclusion

In view of the above arguments (which have been detailed in Ref.[12]), we strongly believe that the analysis that we have developed in ours papers[1,2] is scientifically sound. It could appear at first sight that we have been a little bit conservative in the estimate of the theoretical uncertainties (although recent analyses tend to show that it is far from being the case), but when it comes to a such a crucial issue as excluding the Higgs boson (which we believe is the most important issue in today high–energy physics), it is more recommended than, to the opposite, being too aggressive. A too optimistic analysis that excludes a possibility that can be discovered somewhere else, would affect and alter the credibility of our field.

Acknowledgments: We thank the organisers of the Moriond–QCD conference in La Thuile this winter for their kind invitation to present our work and for making possible a critical debate with the experimentalists on the issues presented here. We acknowledge the project ANR CPV-LFV-LHC NT09-508531 (FR) for support.

References

1. J. Baglio and A. Djouadi, JHEP 1010 (2010) 064; arXiv:1003.4266 [hep-ph].
2. J. Baglio, A. Djouadi, S. Ferrag and R. Godbole, Phys. Lett. B699 (2011) 368; arXiv:1101.1832 [hep-ph] and erratum to appear.
3. For a review, see A. Djouadi, Phys. Rept. 257 (2008) 1.
4. The CDF and D0 Coll., Phys. Rev. Lett. 104 (2010) 061802; arXiv:1007.4587 [hep-ex].
5. The CDF collaboration, CDF note 10232, 16/08/2010.
6. http://tevnphwg.fnal.gov/results/SMHPubWinter2010/gghtheoryreplies_may2010.html ; http://tevnphwg.fnal.gov/results/SM_Higgs_Summer_10/addendumresponse_oct2010.html
7. J. Hayes on behalf of the CDF and D0 collaborations, these proceddings.
8. S. Dittmaier et al., "Handbook of LHC Higgs cross sections", arXiv:1101.0593 [hep-ph].
9. See `www.desy.de/h1zeus/combined_results`.
10. S. Alekhin et al., Phys. Rev. D81 (2010) 014032.
11. A. Martin et al., Eur. Phys. J. C63 (2009) 189; Eur. Phys. J. C64 (2009) 653.
12. J. Baglio, A. Djouadi and R. Godbole, Clarifications on the impact of theoretical uncertainties on the tevatron Higgs exclusion limits, arXiv:1107.0281 [hep-ph].
13. C.F. Berger et al., arXiv:1012:4480 [hep-ph].
14. M. Botje et al., e-Print: arXiv:1101.0538 [hep-ph].
15. S. Alekhin, J. Blumlein and S. Moch, arXiv:1102.5261.
16. M. Cacciari, S. Frixione, M. Mangano, P. Nason, G. Ridolfi, JHEP 0809 (2008) 127.
17. J. Baglio and A. Djouadi, Phys. Lett. B699 (2011) 372; arXiv:1103.6247 [hep-ph].

2.
New Phenomena

SUSY Searches at the Tevatron

Ph. Gris
(for the CDF and DØ collaborations)
Laboratoire de Physique Corpusculaire,
IN2P3/CNRS, 24 avenue des Landais , 63177 Aubière cedex, France

The results of search for Supersymmetry performed at the Tevatron Collider by the CDF and DØ collaborations are summarized in this paper. No significant deviations with respect to the Standard Model expectations were observed and constraints were set on supersymmetric parameters.

1 Introduction

Supersymmetry [1] (SUSY), a space-time symmetry that predicts for every Standard Model (SM) particle the existence of a superpartner that differs by half a unit of spin, may provide a solution to the hierarchy problem if SUSY particles have masses lower than 1 TeV, strongly motivating the search for such particles at the Fermilab Tevatron Collider. If there is supersymmetry in nature, it must be broken and the theorized breaking mechanisms lead to many models (supergravity, gauge mediated, anomaly mediated, ...) with possibly different phenomenologies. Searches performed by the CDF and DØ experiments aim at probing the extensive SUSY parameter space in terms of mass and final state.

2 Third generation squark searches

Because of the large Yukawa couplings of the third-generation quarks, the lightest stop $\tilde{t}_1$ and sbottom $\tilde{b}_1$, partners of the top and bottom quarks respectively, may be the lightest squarks and have masses reachable at the Tevatron.

2.1 Stop searches

$\tilde{t}_1 \rightarrow b l \tilde{\nu}$

A search for stop pairs has been performed by the DØ collaboration [2] in a dataset corresponding to an integrated luminosity of 5.4 fb^{-1}. The three-body decay chosen for the stop, $bl\tilde{\nu}$, lead to a final state containing two leptons (e and μ), two b-jets and missing transverse energy ($\not\!\!E_T$). The sneutrino $\tilde{\nu}$ is either the Lightest Supersymmetric Particle (LSP) or decays invisibly. The signal topology depends on the difference of the stop and sneutrino masses $\Delta m = m_{\tilde{t}_1} - m_{\tilde{\nu}}$: the transverse momentum (p_T) of the leptons and jets tend to decrease with Δm . The analysis was thus optimised for two mass domains (Δm above or below 60 GeV). The main background is composed of Drell-Yan events $Z/\gamma^* \rightarrow \tau^+\tau^-$. No significant deviation from SM predictions has been found. The results were translated into 95% C.L. limits in the ($m_{\tilde{t}_1}$,$m_{\tilde{\nu}}$) plane (Fig. 1, left).

$\tilde{t}_1 \rightarrow b\tilde{\chi}_1^+ \rightarrow b\ell\nu\tilde{\chi}_1^0$

A search for the two-body decay of the stop $\tilde{t}_1 \rightarrow b\tilde{\chi}_1^+$, has been performed by the CDF experiment [3]. In the scenario considered, the lightest neutralino $\tilde{\chi}_1^0$ is the LSP and the chargino decays to $b\ell\nu\tilde{\chi}_1^0$. The final state is composed of two leptons (ee,$e\mu$,$\mu\mu$), two b-jets and $\not\!\!E_T$. The

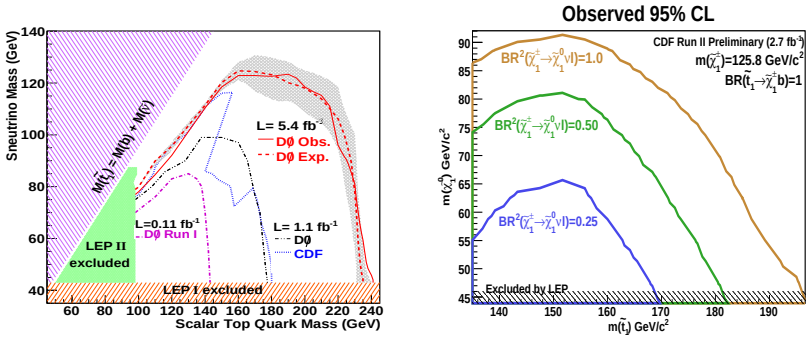

Figure 1: 95% C.L. limits extracted from stop searches. The three-body decay $bl\tilde{\nu}$ was considered by the DØ experiment (left) whereas the CDF collaboration has studied $\tilde{t}_1 \to b\tilde{\chi}_1^+$ (right).

selection criteria used in the analysis aim at removing the SM backgrounds (W/Z+jets, diboson, $t\bar{t}$, QCD) while keeping a high efficiency for the signal: the presence of at least two leptons and two jets is requested, as well as minimal $\not\!\!E_T$ (20 GeV). Classes of events were created depending on their heavy flavour content. The mass of the top squark candidate events were reconstructed and have provided discrimination between a $\tilde{t}_1\bar{\tilde{t}}_1$ signal and SM backgrounds. In a sample corresponding to an integrated luminosity of 2.7 fb^{-1}, data were found to be consistent with the expectations from SM processes and the results were used to extract the 95% C.L. exclusion limit in the $m_{\tilde{\chi}_1^0}$ vs $m_{\tilde{t}_1}$ plane for several values of the branching ratio $BR(\tilde{\chi}_1^\pm \to \ell\nu\tilde{\chi}_1^0)$ and $m_{\tilde{\chi}_1^\pm}$, assuming equal branching ratio into different lepton flavour and $BR(\tilde{t}_1 \to b\tilde{\chi}_1^+)$=100% (Fig. 1, right).

2.2 Sbottom searches

Assuming a SUSY spectrum mass hierarchy such that the sbottom decays exclusively as $\tilde{b}_1 \to b\tilde{\chi}_1^0$, the expected signal for direct sbottom pair production is composed of two b-jets and $\not\!\!E_T$ coming from the two $\tilde{\chi}_1^0$-LSP in the final state. The DØ collaboration [4] has searched for direct sbottom production in a data sample corresponding to an integrated luminosity of 5.2 fb^{-1}. Events were selected if they contained at least two jets, no lepton and a significant $\not\!\!E_T$ (at least 40 GeV). Events with b-jets in the final state were retained using a Neural Network (NN) b-tagging algorithm. The dominant source of background was composed of events with a light flavour jet mis-identified as a b-jet (mistag) and was estimated from data, whereas other backgrounds (except QCD) were evaluated using Monte Carlo (MC) simulations. No significant deviation from the SM background prediction has been observed and the results have been interpreted as a 95% C.L. exclusion limit in the $m_{\tilde{\chi}_1^0}$ vs $m_{\tilde{b}_1}$ plane.

3 Gaugino searches

If squarks and gluinos are too heavy to be produced at rates high enough to be currently detected at the Tevatron, a search for SUSY can be performed via the associated production of charginos and neutralinos $\tilde{\chi}_1^\pm$ $\tilde{\chi}_2^0$.

3.1 Search for trilepton events

In the scenario considered the gauginos decay via exchanges of vector bosons or sleptons into $\tilde{\chi}_1^0$(LSP) and SM fermions: $\tilde{\chi}_1^\pm \to \ell\nu\tilde{\chi}_1^0$, $\tilde{\chi}_2^0 \to \ell\ell\tilde{\chi}_1^0$. The CDF [5] and DØ [6] experiments have searched for final states containing three leptons and $\not\!\!E_T$ in data samples corresponding to integrated luminosities of 3.2 and 2.3 fb^{-1}, respectively. Classes of events were selected depending

on the quality (loose or tight) and the number of isolated leptons (e, μ, τ). Events with two identified leptons plus an isolated track were also retained. The background composed of real leptons (from diboson, $t\bar{t}$, Z+jets processes) was estimated from MC simulations whereas fake leptons(jets faking electrons, tracks faking muons) were extracted from data. After selection the observed data was found to be consistent with SM predictions and 95% C.L. exclusion limits on the production cross section and leptonic branching fraction have been estimated from data in the framework of the minimal SuperGRAvity (mSUGRA) model.

3.2 Search for diphoton + MET events

In Gauge Mediated Supersymmetry Mediated (GMSB) models, the superpartner of the graviton, the gravitino $\tilde{G}$, may be the LSP and have a very low mass (few keV). The lightest neutralino $\tilde{\chi}_1^0$ may be the Next-LSP (NLSP) and decays through: $\tilde{\chi}_1^0 \rightarrow \gamma\tilde{G}$. $\tilde{\chi}_1^0$ may be produced in cascade decay chains coming from the production of $\tilde{\chi}_1^\pm$ $\tilde{\chi}_1^\pm$ or $\tilde{\chi}_1^\pm$ $\tilde{\chi}_2^0$. The DØ experiment [7] has searched for events with at least two photons and large $\not\!\!E_T$(at least 35 GeV) in a data sample corresponding to an integrated luminosity of 6.3 fb^{-1}. No explicit requirement for additional presence of jets and leptons has been imposed. The dominant SM background arising from instrumental $\not\!\!E_T$ sources (SM $\gamma\gamma$, γ+jets, multijet) and from genuine $\not\!\!E_T$($W\gamma$,W+jets) was estimated from control data samples. No evidence for SUSY signal has been found and limits at the 95% C.L. were extracted for a specific set of the GMSB parameters that correspond to the Snowmass Slope constraints SPS8. A chargino (neutralino) mass lower than 330 GeV (175 GeV) has been excluded.

3.3 Search for leptonic jets+MET

Hidden valley models [8] introduce a new hidden sector weakly coupled to the SM. A large subset of hidden valley models also contain supersymmetry. In this scenario, the force carriers in the hidden sector are the dark photons γ_D. The lightest neutralino $\tilde{\chi}_1^0$ is not the LSP and can further decay into a hidden sector dark neutralino plus a photon or a dark photon. γ_D ultimately decays into a pair of spatially closed leptons (the leptonic jet) if m(γ_D)$\leq$ 2m(π), mass range of interest to explain astrophysical anomalies. The DØ experiment [9] has performed a search of the production $\tilde{\chi}_1^\pm$ $\tilde{\chi}_2^0$ in a 5.8 fb^{-1} data sample. Events were selected by requiring two leptonic jets (μ or e) in each event, the three classes $\mu\mu$, $e\mu$ and ee being treated separately. The main background arising from multijet production and photon conversion was estimated from data. 21 events survived the selections whereas 36.3$\pm$10.4 were expected. This result was translated as a 95% C.L. limit on the production cross section of the $\tilde{\chi}_1^\pm$ $\tilde{\chi}_2^0$ process.

4 R_{parity} violating searches

In SUSY theories, R_{parity}[10] is a quantum number equal to +1 for SM particles and -1 for superpartners. For searches presented above, R_{parity} was assumed to be conserved and LSP was stable. If it is not the case, LSP can decay into SM particles.

4.1 Search for tau sneutrino

If R_{parity} is violated the sneutrino $\tilde{\nu}$ may be produced in $d\bar{d}$ scattering and thus produced at the Tevatron. The DØ collaboration [11] has searched for the resonant production of the tau sneutrino $\tilde{\nu}_\tau$ (λ'_{311} coupling) decaying to $e\mu$ (λ_{321} coupling). Events were selected by requiring two isolated leptons ($E_T \geq$ 30 GeV) and no jet. 414 events survived the final cuts whereas 410$\pm$38 were expected from MC simulations. No evidence for tau sneutrino signal has been found in the 5.3

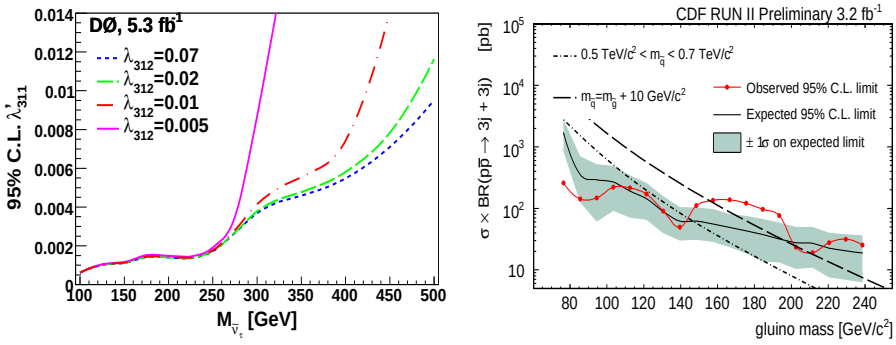

Figure 2: DØ cross section limit on the resonant sneutrino as a function of the sneutrino mass (left) and CDF cross section limit on the gluino pair production as a function of the gluino mass (right).

fb^{-1} data sample analysed. The resulting 95% C.L. limit on the cross section led to exclude sneutrino masses heavier than 300 GeV (Fig. 2, left).

4.2 Search for 3-jet resonances

The CDF experiment[12] has performed a model independent search for 3-jet hadronic resonances. Events with a high number of jets (at least six) and no $\not\!\!E_T$ were selected. The dominant multijet background was estimated from data using 5-jet events. To model new physics signatures that could hide in the analyzed data sample corresponding to an integrated luminosity of 3.2 fb^{-1}, gluino pairs decaying each into three partons (through λ'' couplings) were chosen. Kinematic quantities such as invariant mass and scalar p_T sum of jet triplets (and their correlations) were used to extract the signal. No significant excess of data has been observed and 95% C.L. limits on the production cross section of the process $\tilde{g}\tilde{g} \rightarrow$3 jets+3 jets have been set: gluino masses below 144 GeV have been excluded (Fig. 2, left).

5 Summary

This contribution reported the most recent results of searches for SUSY at the Tevatron. Analyses performed by the CDF and DØ collaboration using up to 6.3 fb^{-1} of data were summarized. No significant data excess has been observed and the results have been interpreted as 95% C.L. exclusion limits on the free parameters of several SUSY scenarios.

References

1. See, for instance: H.P. Nilles, *Phys. Rep.* **110**, 1 (1984).
2. V.M. Abazov *et al*, *Phys. Lett.* B **696**, 321 (2011).
3. T. Aaltonen *et al*, *Phys. Rev. Lett.* **104**, 251801 (2010).
4. V.M. Abazov *et al*, *Phys. Lett.* B **693**, 95 (2010).
5. CDF public note 9817.
6. V.M. Abazov *et al*, *Phys. Lett.* B **680**, 34 (2009).
7. V.M. Abazov *et al*, *Phys. Rev. Lett.* **105**, 221802 (2010).
8. M. Strassler and K. Zurek, *Phys. Lett.* B **651**, 374 (2007).
9. V.M. Abazov *et al*, *Phys. Rev. Lett.* **105**, 211802 (2010).
10. For a review see: R. Barbier *et al*, *Phys. Rep.* **420**, 1 (2005).
11. V.M. Abazov *et al*, *Phys. Rev. Lett.* **105**, 191802 (2010).
12. CDF public note 10256.

SUSY searches at ATLAS

N. Barlow, on behalf of the ATLAS collaboration.
Cavendish Laboratory, University of Cambridge,
Cambridge CB3 OHE, England

Results are presented on searches for supersymmetric particles in a dataset corresponding to an integrated luminosity of 35 pb^{-1} recorded by the ATLAS detector at the Large Hadron Collider (LHC) at CERN. The searches can be broadly classified into "Missing-E_T-based" searches, where it is expected that the Lightest Supersymmetric Particle (LSP) is stable and neutral, and is not directly detected, and other searches, which cover models where R-Parity is violated, or with meta-stable, charged supersymmetric particles. No signal was observed in any of these searches, and upper limits were placed on various regions of parameter space, which are in many cases more stringent than previous limits.

1 Introduction

Supersymmetry (SUSY) is one of the most widely investigated extensions to the Standard Model of particle physics, in which every fundamental Standard Model fermion has a supersymmetric boson partner, and vice versa. This naturally solves the hierarchy problem, and in the case where R-Parity is conserved, provides a candidate dark matter particle in the form of the Lightest Supersymmetric Particle (LSP), which would be stable.

Search strategies for R-Parity conserving supersymmetry using the ATLAS detector [1] are based on missing transverse energy (E_T^{miss}), and since production of coloured sparticles is expected to be favoured at the LHC, high p_T jets are also required. Searches are performed separately for final states with different numbers of high-p_T leptons, which can arise from model-dependent cascades of decays from the produced *sparticles* to the stable LSP.

In addition, searches are performed for various R-Parity violating SUSY scenarios, which can give rise to very different experimental signatures. Examples of these examined here are massive particles decaying to an electron-muon pair, and long-lived massive "R-hadrons".

2 Search for supersymmetry in final states with jets, missing transverse energy, and no leptons.

The ATLAS search for SUSY events with high-p_T jets and missing transverse energy [2] is designed to be as model-independent as possible. Four signal regions are defined, optimized for maximum exclusion reach on different regions of the squark mass versus gluino mass plane: $m_{\tilde{q}}, m_{\tilde{g}}$. These regions are defined in Table 1 in terms of several discriminating variables:

- E_T^{miss}: the missing transverse energy, measured using calorimeter cells over the full range of pseudorapidity $|\eta| < 4$, and corrected for the energy of reconstructed physics objects such as muons.

Table 1: Signal region definitions for the zero-lepton analysis.

	A	B	C	D
Njets	≥ 2	≥ 2	≥ 3	≥ 3
Leading jet p_T (GeV)	> 120	> 120	> 120	> 120
Other jet(s) p_T (GeV)	> 40	> 40	> 40	> 40
$E_T^{\rm miss}$ (GeV)	> 100	> 100	> 100	> 100
$\Delta\phi({\rm jet}, \vec{p_T}^{\rm miss}_{\rm min})$	> 0.4	> 0.4	> 0.4	> 0.4
$E_T^{\rm miss}/m_{\rm eff}$	> 0.3	-	> 0.25	> 0.25
$m_{\rm eff}$ (GeV)	> 500	-	> 500	> 1000
m_{T2} (GeV)	-	> 300	-	-

- $m_{\rm eff}$: the scalar sum of the p_T of the jets and $E_T^{\rm miss}$
- m_{T2}: defined in [3], a generalization of the *transverse mass* (m_T), designed for the situation where pair-produced particles decay into visible and invisible particles.

The principle background for this analysis is from QCD, but this is hugely reduced by imposing a cut on the angle $\Delta\phi$ between a jet and the missing transverse energy, which in background events can come from mismeasurement of a jet or the presence of neutrinos.

The remaining background sources (W+jets, Z+jets, $t\bar{t}$) are estimated using Monte Carlo (MC) simulation (ALPGEN [4] for W, Z, normalized to NLO cross-section, and MC@NLO [5] for $t\bar{t}$). Numerous cross-checks were performed on control regions in data to verify that the MC is accurately modeling the data.

No excess of events over the background expectation is seen in any of the four signal regions, and an 95% C.L. upper limit is placed on the "effective cross-section" (i.e. assuming 100% efficiency) for New Physics in any of the signal regions A, B, C, D, of: 1.3 pb, 0.35 pb, 1.1 pb, and 0.11 pb respectively.

Furthermore, these results can be interpreted in the context of "Minimal Supergravity" (mSUGRA) [6], a model with only four parameters plus a sign choice, as shown in Figure 1. In this framework, if the squark and gluino masses are similar, the exclusion limit is approximately $m_{\tilde{q},\tilde{g}} < 775$ GeV, and is relatively insensitive with respect to variations in the remaining mSUGRA parameters.

3 Search for supersymmetry in final states with jets, missing transverse energy, and one lepton.

For the one-lepton analysis [7], selected events are required to contain exactly one electron or muon, with $p_T > 20$ GeV, and at least three jets with energy greater than 30 GeV (60 GeV for the leading jet). The principal backgrounds are expected to be $t\bar{t}$ and W+jets events. These are estimated using a semi-data-driven approach, where the numbers of events in various control regions in the $E_T^{\rm miss}$ vs m_T plane, are fitted simultaneously with the number in the signal region. Monte Carlo simulation is used to estimate the shapes of the distributions of the different backgrounds, i.e. the relations between the numbers in the control regions and the numbers in the signal region. The background from QCD events is estimated in a purely data-driven way, solving linear equations to obtain the fake probability for a candidate passing "tight" particle identification requirements, via a "loose" lepton selection.

The expected numbers of background events in the signal regions for the electron and muon channels are (1.81 ± 0.75) and (2.25 ± 0.94) respectively. One event is observed for each channel, leading to upper limits on $\sigma \times A \times B.F.$ of 65 fb for the electron channel and 73 fb for the muon

channel. These results are combined and interpreted as an exclusion region in the mSUGRA m_0 vs $m_{1/2}$ plane as shown in Figure 1. If the squark and gluino masses are approximately equal, values less than about 700 GeV are excluded.

4 Searches for supersymmetry in final states with jets, missing transverse energy, and two leptons.

ATLAS SUSY searches for channels with missing transverse energy and two high-p_T leptons in the final state can be subdivided into three analyses: the *same sign* and *opposite sign* searches [8] look for pairs of leptons with same or opposite electrical charge but no requirement on flavour (electron or muon), while the *flavour subtraction* analysis [9] looks for any excess of opposite-sign-same-flavour lepton pairs over opposite-sign-different-flavour.

4.1 Same-sign and opposite-sign dilepton analyses

As very few Standard Model processes are expected to give rise to events with two leptons of the same sign, the signal region for this analysis has a comparatively loose cut of $E_T^{\rm miss} > 100$ GeV, while the opposite-sign analysis requires $E_T^{\rm miss} > 150$ GeV. The main background sources are $t\bar{t}$ events for the opposite-sign analysis, and events containing fake or misidentified leptons for the same-sign analysis. The top backgrounds are estimated using a data-driven method from control samples enriched in $t\bar{t}$ events, while as in the one-lepton analysis, the fake background is estimated from the "loose-tight" matrix method.

No excess over Standard Model expectations is observed in any of the signal regions for the different lepton flavour combinations (ee, $e\mu$, $\mu\mu$). The resulting limits on the mSUGRA plane are shown in Figure 1.

4.2 Flavour subtraction analysis

With the exception of Z or γ^* sources, opposite-sign-different-flavour lepton pairs are expected to occur as often in the Standard Model as opposite-sign-same-flavour pairs. However, due to lepton flavour conservation in SUSY decay chains, an excess of same-flavour pairs could prove a useful signal of new physics, and any features in the dilepton invariant mass spectrum could provide insight into SUSY mass splittings.

A quantity S is defined that incorporates reconstruction and trigger efficiencies into a measure of this excess, and the measured value of $S = 1.8 \pm 0.2$ is compatible with the Standard Model expectation of $S = 1.98 \pm 0.79 \pm 0.78$. Figure 2 shows the dilepton invariant mass spectra for same-flavour and opposite-flavour pairs.

5 Search for supersymmetry in final states with jets, missing transverse energy, and more than two leptons.

Channels with three or more leptons and missing transverse energy are expected to have very low Standard Model backgrounds, and were a "golden channel" for SUSY searches at the Tevatron. In this search [10], at least three leptons (electrons or muons) are required, in any charge and flavour combination, with minimum p_T of 20 GeV (unless the third lepton is a muon, in which case the requirement is $p_T > 10$ GeV). Pairs of leptons with the same flavour but opposite charge are vetoed if the invariant mass of their combination is close to the nominal Z mass, or very low (to suppress backgrounds from Drell-Yan production). At least two jets with $p_T > 50$ GeV are required, and the signal region is defined as $E_T^{\rm miss} > 50$ GeV.

The expected number of background events with three or more leptons passing the p_T requirements is 16.6 ± 1.3, and 19 are observed. Of these, 10 events pass the Z mass veto,

and none pass the jet p_T requirements. The resulting exclusion regions at 95% C.L. in the mSUGRA framework are shown in Figure 1, and are highly compatible with previous limits from the Tevatron.

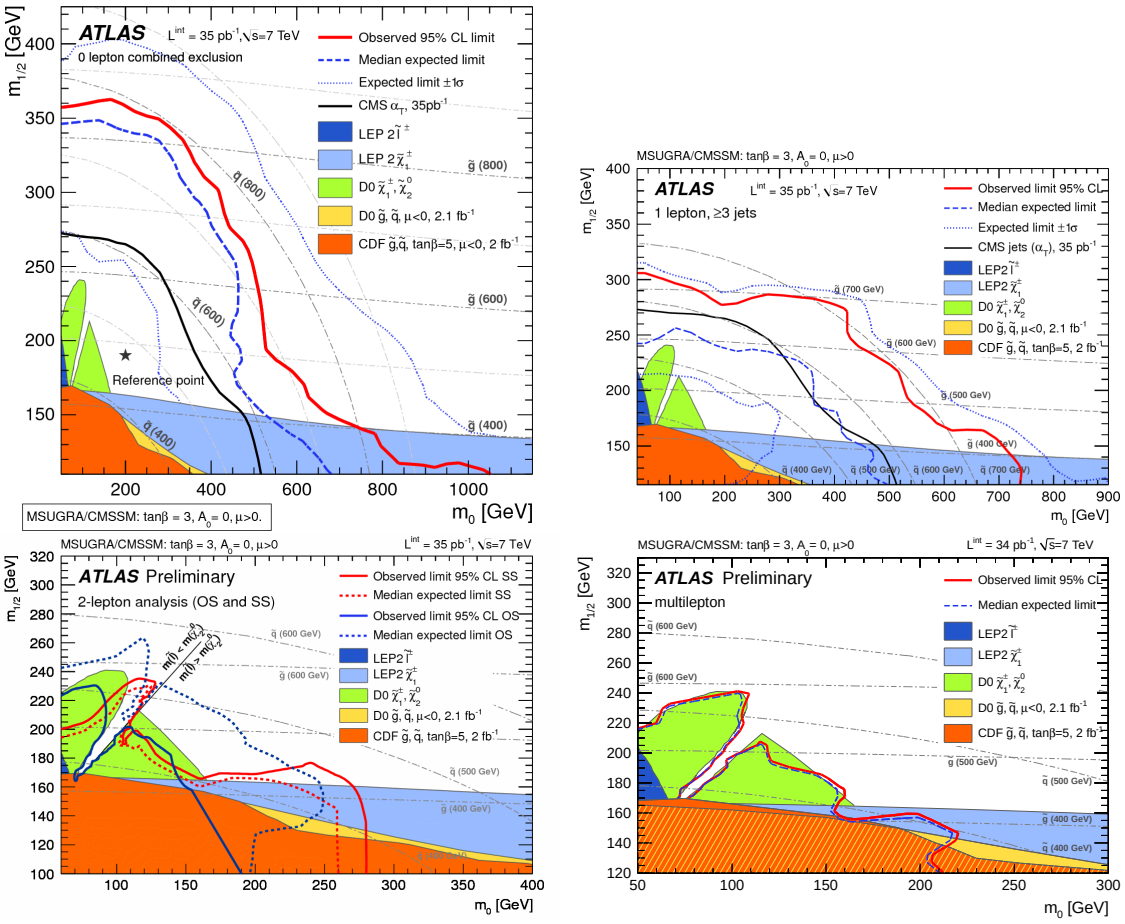

Figure 1: : Exclusion limits at the 95% C.L. on the $m_0.m_{1/2}$ plane in the mSUGRA framework, with $\tan\beta = 3$, $A_0 = 0$, and $\mu > 0$. The top left plot is from the 0-lepton analysis, the top right plot from the 1-lepton, the bottom left from the 2-lepton, and the bottom right for the multi-lepton analysis.

6 Searches for supersymmetry in final states with b-jets and missing transverse energy

Depending on the value of $\tan\beta$, the ratio of vacuum expectation values for the two Higgs doublets, the production of third generation squarks could be favoured at the LHC. It can therefore be advantageous to search for final states containg $b-$jets. Separate searches [11] are performed for final states with and without high-p_T leptons. In both cases, at least one jet is required to be b-tagged, using the SV0 algorithm [12], that selects tracks from a secondary vertex that are associated with the jet. The principal background is from $t\bar{t}$ events. Data-driven methods are used to estimate the QCD, W plus jets, and $t\bar{t}$ backgrounds. No excess of events is observed above the Standard Model expectation in the signal region. The zero-lepton (one-lepton) results can be interpreted in R-parity conserving models where sbottoms (stops) are the only squarks in the gluino decay cascade, gluino masses below 590 GeV (500 GeV) are excluded at the 95% C.L., as shown in Figure 2.

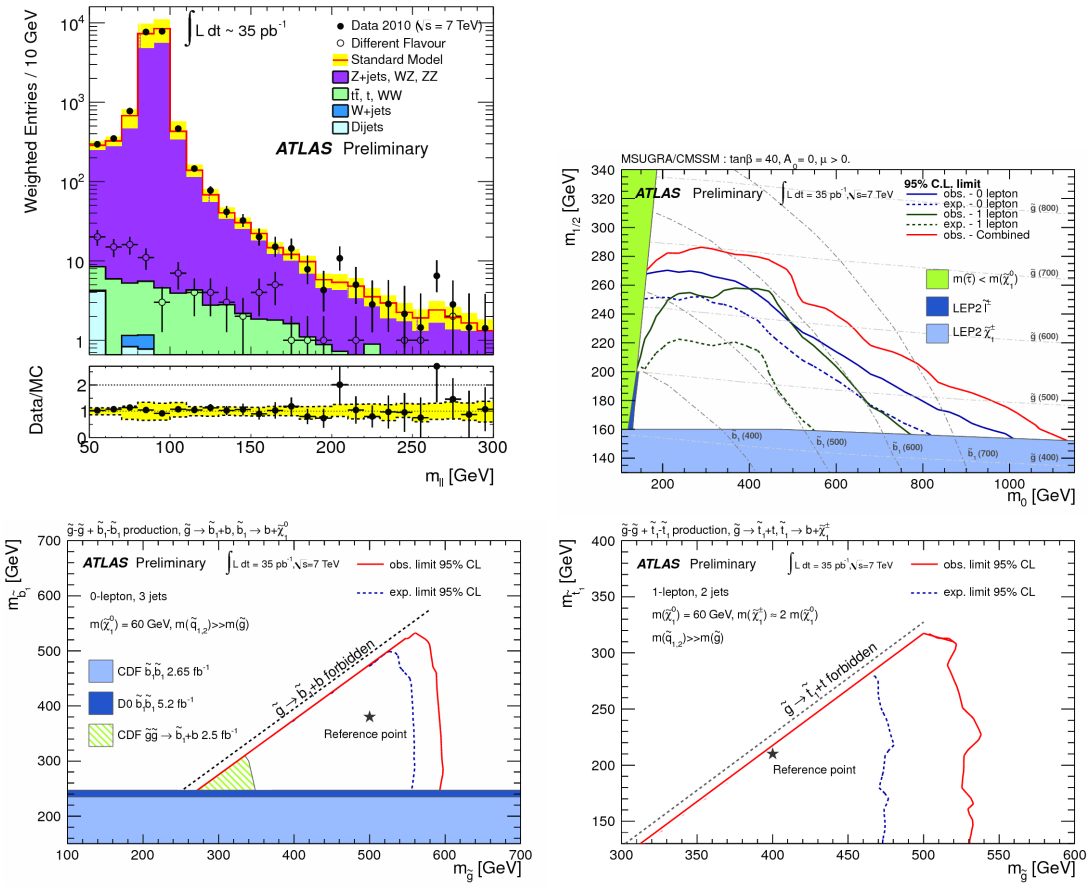

Figure 2: The top left plot shows the dilepton invariant mass spectra for oppositely signed same-flavour and opposite-flavour lepton pairs, weighted according to efficiency and acceptance correction factors, from the flavour subtraction analysis. The top right plot shows the exclusion limits on the mSUGRA $m_0.m_{1/2}$ plane, with high $\tan\beta$, from both b-jets analyses. The lower right plot shows the 95% C.L. exclusion region on the $m_{\tilde{b}}$ vs $m_{\tilde{g}}$ plane from the zero-lepton plus b-jets SUSY search, while the right plot shows the result of the one-lepton plus b-jets search on the $m_{\tilde{t}}$ vs $m_{\tilde{g}}$ plane.

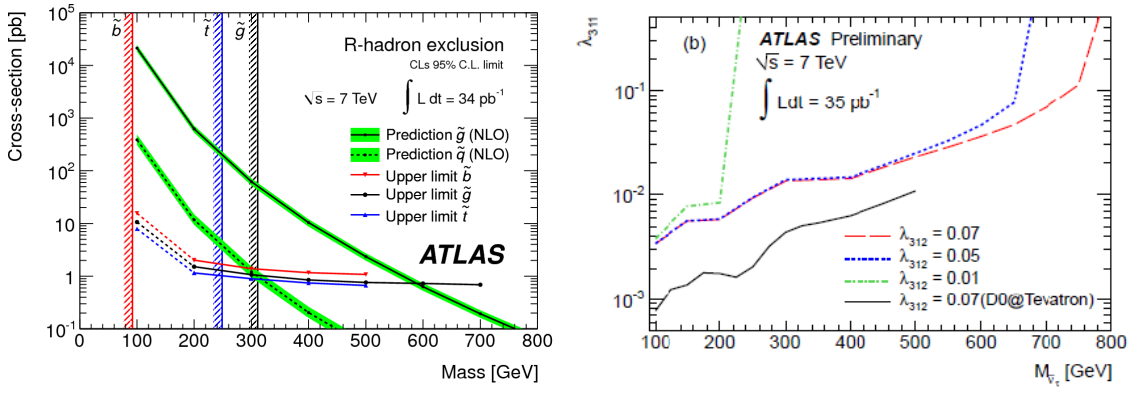

Figure 3: The left plot shows exclusion limits on the production cross-sections of stable squarks and gluinos as a function of mass. The right plot shows the exclusion limits from the $e\mu$ resonance search on the RPV coupling parameters λ'_{311} and λ_{312} as a function of $m_{\tilde{\nu_\tau}}$.

7 Stable massive particle search

Various R-Parity violating SUSY scenarios could give rise to meta-stable coloured sparticles, that could then hadronize to produce "R-hadrons". These could be electrically charged or neutral, or could even change charge due to interactions with detector material. As these particles can be slow ($\beta < 1$) and highly ionizing, the measurement of charge deposition dE/dx in the Pixel detector, and precise timing measurements from the Tile calorimeter, provide two independent methods for differentiating such Stable Massive Particles (SMPs) from SM background. In this analysis [13], masses of candidate particles are calculated by dividing its momentum (measured in the Inner Detector) by $\beta\gamma$ measured in the Pixel detector or Tile calorimeter. Backgrounds are determined from a data-driven method, where random momentum values are combined with random measurements of Pixel dE/dx and Tile β, as the outlying events in these distributions are found to be uncorrelated. No candidate SMPs are observed with mass > 100 GeV, and upper limits are set on the production cross-sections of squarks and gluinos, as shown in Figure 3.

8 $e\mu$ resonance search

In some R-Parity violating SUSY models which do not conserve flavour, a $\tilde{\nu_\tau}$ can decay into an electron and a muon. In this search [14], $e\mu$ candidates are required to have opposite charge, $p_T > 20$ GeV, and pass standard ATLAS particle identification criteria for electrons and muons respectively. Sources of background that can produce real oppositely charged pairs of electrons and muons include $Z \to \tau\tau$ events, $t\bar{t}$, and diboson events. These are estimated using MC, normalized to NLO cross-sections. Correction factors are applied to make the identification efficiency, energy scale and resolution in the simulation match those in the data. Other backgrounds can come from events containing one lepton and one jet, where the jet is misidentified as a lepton. These are estimated using a data-driven "loose-tight matrix" method, as described in Section 3. No excess of events above the expected Standard Model background is observed, and limits are placed on the mass of $\tilde{\nu_\tau}$ and on the R-Parity violating couplings λ'_{311} and λ_{312}, as shown in Figure 3.

9 Conclusions

The excellent performance of the LHC and the ATLAS detector enabled numerous searches for supersymmetry to exclude larger regions of parameter space than previous searches, using the

2010 data. Analysis techniques for estimating backgrounds and interpreting results in different theoretical frameworks have been developed, and shown to work well. With the potential for a data sample two orders of magnitude greater than that shown here to be collected and analysed in 2011, the near future will be an exciting time for SUSY.

References

1. ATLAS Collaboration, JINST 3 (2008) S08003.
2. ATLAS Collaboration, Phys. Lett. B 701 (2011) 186.
3. C. G. Lester et al., Phys. Lett. B463 (1999) 99-103.
4. M. L. Mangano et al., JHEP 07 (2003) 001.
5. S. Frixione et al., JHEP 06 (2002) 029
6. A. H. Chamseddine et al., Phys.Rev.Lett. 49 (1982) 970,
   R. Barbieri et al., Phys. Lett. B119 (1982) 343,
   L. E. Ibanez, Phys.Lett. B118 (1982) 73,
   L. J. Hall et al., Phys.Rev. D27 (1983) 2359-2378,
   N. Ohta, Prog.Theor.Phys. 70 (1983) 542,
   G. L. Kane et al., Phys.Rev. D49 (1994) 6173-6210.
7. ATLAS Collaboration, PRL 106 (2011), 131802.
8. ATLAS Collaboration, accepted by EPJCL, ArXiV:1103.6214 [hep-ex].
9. ATLAS Collaboration, accepted by EPJCL, ArXiV:1103.6208 [hep-ex].
10. ATLAS Collaboration, ATLAS-CONF-2011-039.
11. ATLAS Collaboration, accepted by PLB, ArXiV:1103.4344 [hep-ex].
12. ATLAS Collaboration, ATLAS-CONF-2010-099.
13. ATLAS Collaboration, Phys. Lett. B 701 (2011) 1.
14. ATLAS Collaboration, accepted by PRL, ArXiV:1103.5559 [hep-ex].

SUSY searches in CMS

M. Chiorboli
on behalf of the CMS Collaboration
CERN, 1211 Geneva 23, Switzerland
Istituto Nazionale di Fisica Nucleare, Via Enrico Fermi 40 - 00044 Frascati (Rome), Italy
Dipartimento di Fisica e Astronomia dell'Università di Catania, Via S. Sofia 64 - 95123 Catania, Italy

In the 2010 data taking period, the CMS experiment collected 36 pb^{-1} of integrated luminosity. An overview of the analyses performed on this dataset in the search for supersymmetric events is presented. No significant excess with respect to the backgrounds expected from the Standard Model has been observed in any final state. Exclusion regions beyond previous experiment searches are set, and a robust strategy is defined to make discoveries in the 2011-2012 LHC run

1 Analysis strategy

The strategy of the CMS Collaboration in the search for Supersymmetric events is based on one fundamental assumption: we don't know how Physics beyond the Standard Model will manifest itself. The guideline is hence not to follow the models, and to design instead a set of inclusive analyses based uniquely on the final states. This set of analyses has to be complete and robust. For a given final state, different approaches can be chosen to increase the robustness of the analysis.

2 Supersymmetry at CMS

The Supersymmetric analyses are performed using the physics objects reconstructed in the CMS detector [1]: electrons, muons, taus, photons, jets, missing transverse energy (MET), HT (the scalar sum of the jet transverse energies), MHT (the vectorial sum of the jet transverse energies). They have all been commissioned and understood during the initial stages of the 2010 run.

The analyses are essentially counting experiments: an excess of events is searched out of an estimated Standard Model background. Whenever possible, the backgrounds are estimated with data-driven methods. To make the analyses even more robust, the same background is often estimated with multiple data-driven methods. The cuts are not optimized to maximize the exclusion regions: the aim of the analyses is not to just define stringent exclusion limits, but to establish the methods needed to be ready for discoveries.

3 Fully Hadronic final states

Different approaches are used in the search for Supersymmetric events with jets and missing transverse energy in the final state. The first approach is based on the variable α_T [2], used

as main discriminator between events with real and fake missing transverse energy [3]. Three independent data-driven techniques have been used for the background estimate. 13 events are observed after all the selection, in agreement with the expectations from the Standard Model. A variation of the analysis based on the α_T variable is performed requiring a b-tagged jet in the final state, in order to reduce non-top backgrounds and to enhance the sensitivity to models with an increased third generation activity [4]. The other two approaches are based on the MHT variable [5] and on the Razor variable [6] respectively. These two approaches are complementary, since the former is based on the understanding of the detector response in detail, while the latter relies on the kinematics of the event. The two analyses use both data-driven techniques for the estimate of the backgrounds. The fact that they give similar limits gives further confidence of the capability of CMS to discover Supersymmetry when it will appear. The mSUGRA exclusion limits for all the hadronic analysis separately are shown in fig. 1. The combination of the exclusion limits from all the fully hadronic analyses is given in the framework of the simplified models [7], and is shown in fig. 2.

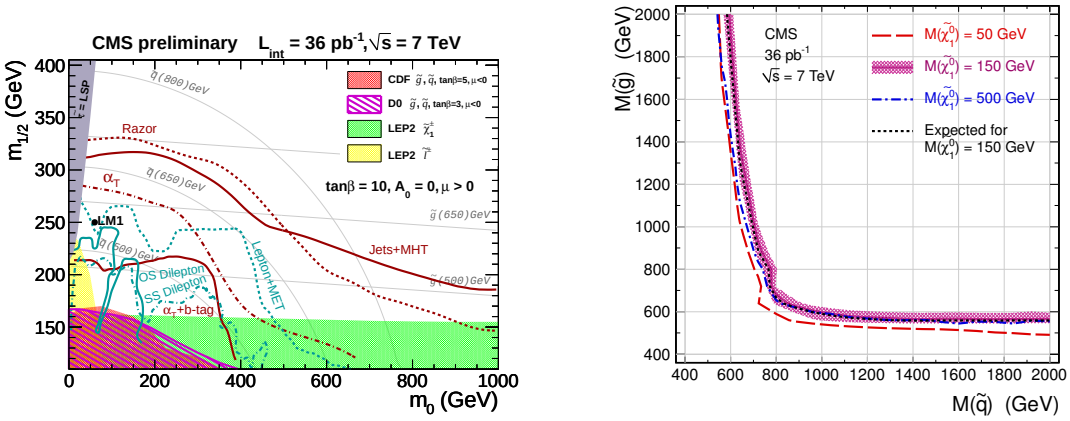

Figure 1: Left: Summary of the exclusion limits in the mSUGRA plane for the various CMS searches. Right: Exclusion limit in the squark-gluino plane for the search in the final state with two photons, jets and missing transverse energy.

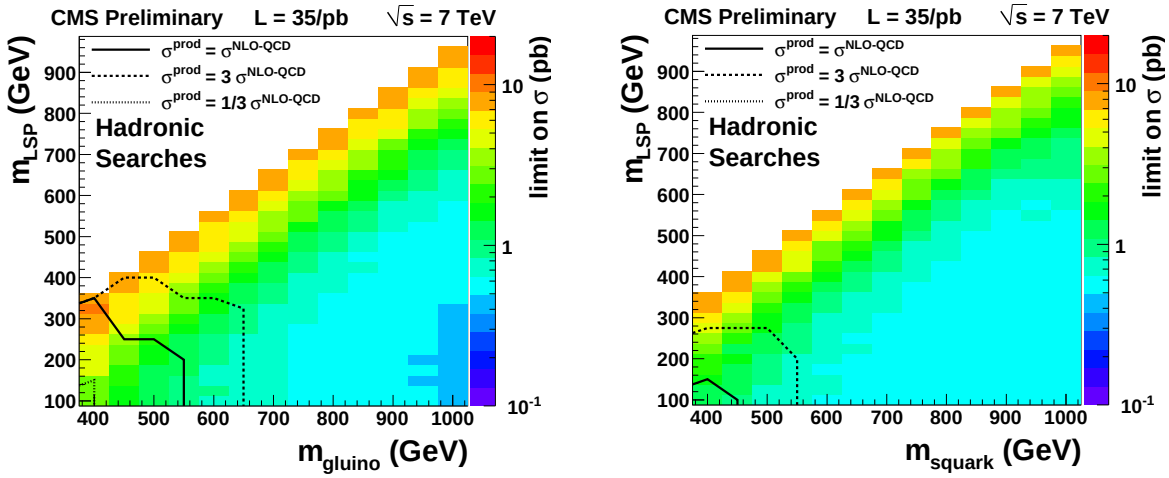

Figure 2: Limit on the production cross section in a simplified model in a LSP-gluino plane (left) and LSP-squark plane (right). The curves refer to an assumed interaction strength equal to the QCD interaction (solid), three times larger (dashed), one third of it (points). Theoretical uncertainties are not taken into account in the calculation of the limits.

4 Final states with photons, jets and missing transverse energy

The framework considered is the General Gauge Mediation (GGM), in which the Next-to-Lightest Supersymmetric Particle (NLSP) is the Neutralino, which decays into a Gravitino and a photon. The final state is hence characterized by two photons, jets and missing transverse energy given by the Gravitinos escaping the detector. As for the searches of the previous section, no assumption are made on the model, and the search is model independent, based exclusively on inclusive cuts on the objects of the final state [8]. The dominant background is given by QCD jets with misidentified photons and mismeasured missing transverse energy and is estimated with a data-driven technique. After the selection cuts one event is observed, in agreement with the background estimate. The result is interpreted as an exclusion curve in the squark-gluino mass plane, as shown in fig. 1. In GGM if Winos and Binos are mass degenerate NLSP's, the diphoton signature can be replaced by a photon-lepton signature. In this case the dominant background is given by Wγ events. The Monte Carlo for this process has been validated on the cross section measured by CMS [9], and is therefore used for the background estimate. In both the electron-γ and muon-γ final states one event is observed, in agreement with the estimated background [10].

5 Final States with two opposite sign leptons, jets and missing transverse energy

From Monte Carlo studies, the dominant background for this signature is $t\bar{t}$. For this reason, the same preselection as the one used in the CMS $t\bar{t}$ cross section measurement is used [11]. After the preselection cuts a good agreement is found between data and Monte Carlo in the distribution of many variables. Two independent data-driven estimates for the backgrounds are used. The first one is the so-called ABCD or matrix method: a plane is defined with two uncorrelated variables for $t\bar{t}$. The two variables are in this case HT and y = MET / $\sqrt{HT}$. After defining a signal region with tighter cuts than the ones used for the preselections, the plane is split in four sub-regions. If the assumption of the uniform distribution of the background in the plane is verified, the number of events in the fourth sub-region can be estimated from the other three sub-regions. The second data-driven technique is based on the assumption that in $t\bar{t}$ events the missing transverse energy is given by the neutrinos produced by the W's. Since the two leptons from the W's show a similar kinematic behaviour than the neutrinos, the missing transverse energy can be estimated from the dilepton spectrum. The method is validated in a control region defined by a low value of the y variable, and it is then applied to the signal region. One event is observed after all the selection cuts, in agreement with all the Monte Carlo and data-driven estimates of the background. In addition to the exclusion limit in the mSUGRA plane (fig. 1), a parametrization of efficiencies and acceptances is given. With this parametrization, generator level studies of every possible model are possible [12].

6 Final States with two same sign leptons, jets and missing transverse energy

The search in the same sign dilepton final state is performed in four different kinematic regions. After the selection of two electrons or muons, the first with $p_T > 20$ GeV/c and the second with $p_T > 10$ GeV/c, the first region is defined with HT>60 GeV/c and MET>80 GeV/c^2, the second with HT>200 GeV/c and MET>30 GeV/c^2. The third region is chosen in order to have lepton p_T's as low as possible: the cuts are 5 GeV/c for the muons and 10 GeV/c for the electrons, accompanied by HT>200 GeV/c and MET>30 GeV/c^2. The fourth region is defined with the same cuts on the electrons and muons as the third one. In this case tau's are also considered, with $p_T > 15$ GeV/c. Since the tau's are more affected by the QCD background the cuts on HT and MET are raised to HT>350 GeV/c and MET>50 GeV/c^2. The signature with two same

sign leptons is particularly interesting since this final state is absent in the Standard Model. The dominant background is therefore given by fake leptons: for instance $t\bar{t}$ events in which one lepton is a real isolated lepton from the W and the other one comes from the heavy flavour decay. The fake lepton contributions are estimated with several data-driven techniques, which are all based on the concept of the "tight-loose" method: the probability of a lepton passing a loose selection to pass also a tight selection is estimated in QCD multijet sample as a function of lepton p_T and η; the contribution in the signal region is estimated by multiplying this efficiency to the yield in a preselected loose sample. Different variations of the method are used for the different analyses and for the different backgrounds. The number of observed events in data is in agreement with all the Monte Carlo and data-driven estimates in all the four regions. The exclusion region in a mSUGRA plane is given (fig. 1), as well as a parametrization of efficiencies and acceptances to make possible generator level studies of different models. As a cross check, the same analysis has been repeated at generator level using this parametrization: an agreement with the actual exclusion region better than the theoretical error is achieved [13].

7 Conclusions

In this talk a review of the analyses performed by the CMS Collaboration with the first 35 pb^{-1} of data is presented. No evidence of Supersymmetry has been found, in any of the final states. The previous explored range of the model parameters has been significantly extended. The results are presented in the mSUGRA scenario in order to compare them with the results by previous experiments, but other interpretations are given in terms of simplified models. In addition, in some of the analyses, a parametrization of efficiencies and acceptances is given, in order to make possible generator level studies on other models. The most important achievement is that a road-map for discoveries has been established: the physics objects are commissioned; many different analyses are performed on many final states; the analyses are often complementary among them; the backgrounds are estimated with data-driven techniques whenever possible: multiple techniques are used for the various analyses, and for every analysis, different techniques are used for the different backgrounds. The CMS collaboration set up a robust and complete suite of analyses aimed at discoveries in the 2011-2012 run.

References

1. R. Adolphi *et al.* (CMS Collaboration), *J. Inst.* **3**, S08004 (2008).
2. L. Randall and D. Tucker-Smith, *Phys. Rev. Lett.* **101**, 221803 (2008).
3. V. Khachatryan *et al.* (CMS Collaboration), *Phys. Lett.* B **698**, 196-218 (2011).
4. CMS Collaboration, arXiv:1106.3272, CMS-SUS-10-011.
5. CMS Collaboration, arXiv:1106.4503, CMS-SUS-10-005.
6. CMS Collaboration, CMS-SUS-10-009.
7. J. Alwall, P. Schuster, and N. Toro, *Phys. Rev.* D **79**, 075020 (2009).
8. CMS Collaboration, arXiv:1103.0953, CMS-SUS-10-002.
9. CMS Collaboration, arXiv:1105.2758, CMS-EWK-10-008.
10. CMS Collaboration, arXiv:1105.3152, CMS-SUS-11-002.
11. V. Khachatryan *et al.* (CMS Collaboration), *Phys. Lett.* B **695**, 424-443 (2011).
12. CMS Collaboration, arXiv:1103.1348, CMS-SUS-10-007.
13. CMS Collaboration, arXiv:1104.3168, CMS-SUS-10-004.

NON-SUSY SEARCHES AT THE TEVATRON

John Strologas
Department of Physics and Astronomy, University of New Mexico, Albuquerque, New Mexico 87131, USA

We present recent results from searches for new physics beyond supersymmetry performed at the Tevatron accelerator at Fermilab. The CDF and DØ analyses presented here utilized data of integrated luminosity up to 6 fb^{-1}. We cover leptonic and bosonic resonances interpreted in the Randall-Sundrum graviton and new-boson models, rare final states, and the search for vector-like quarks.

1 Introduction

The search for new phenomena beyond the weak-scale supersymmetry is a vital part of the Fermilab program. Both CDF and DØ experiments at the Tevatron collider actively look for signals not expected by the standard model (SM) or minimal supersymmetric models. The searches can be sorted in three categories: a) searches for generic resonances that can be interpreted in several new-physics models b) searches for exotic combinations of final-state objects or abnormal kinematics (not necessarily predicted by current theories) and c) model-dependent searches that test a particular theory. We present here latest results from all these categories: searches for new dilepton and diboson resonances (interpreted as gravitons and new gauge bosons), searches for anomalous $\gamma + \not\!\!E_T$+X production, and searches for vector-like quarks.

2 Search for New Resonances

2.1 Search for RS-gravitons

The Randall-Sundrum (RS) model offers an explanation for the hierarchy problem with the introduction of an extra dimension accessible only to gravity-carrying gravitons. CDF completed a search for the RS-gravitons in the dielectron[1] and dimuon[2] channels using 5.7 fb^{-1} of integrated luminosity. Two electrons (muons) are selected, at least one with E_T (p_T) above 20 GeV (GeV/c). The leptons are isolated, i.e., the excess energy in a cone $\Delta R = \sqrt{\Delta\phi)^2 + (\Delta\eta)^2} = 0.4$ around each lepton is less than 10% of the energy (momentum) of the electron (muon). Cosmic-ray veto and $\gamma \rightarrow ee$ conversion removal are applied; no opposite charge is enforced. Main backgrounds come from the Drell-Yan (DY) process, and QCD background associated with one real lepton and one "fake" lepton (i.e., jet (track) faking an electron (muon)). Minor backgrounds come from diboson and $t\bar{t}$ processes. The QCD background is determined with CDF data, with the application of a probability that a jet (track) fakes an electron (muon) on events with one identified lepton. All other backgrounds are estimated with Monte Carlo simulations (MC) absolutely normalized to the next-to-leading order cross sections, the data luminosity, lepton-identification scale factors and trigger efficiencies. The dielectron and dimuon mass spectra are consistent with expectation. At the same time, the highest-dielectron-mass event ever observed is detected (M_{ee} = 960 GeV/c^2). The probability that at least one event is observed with a dielectron mass at least that high is 4%. The results are interpreted in the RS-graviton model, combined with a previous diphoton[3] graviton search. For the RS-model parameter $k/\overline{M}_{Pl} = 0.1$, RS-gravitons with mass less than 1111 GeV/c^2 are excluded at 95% confidence level (CL). Figure 1 shows the dielectron spectrum and Figure 2 shows the cross-section uper limit as a function of the graviton mass, along with theoretical cross sections for several values of $k/\overline{M}_{Pl}$.

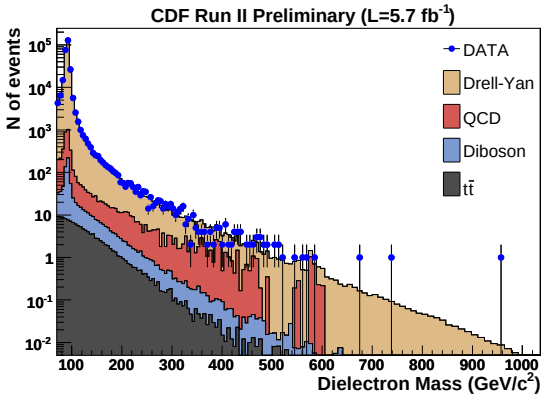

Figure 1: Dielectron mass spectrum from the CDF search for RS-gravitons.

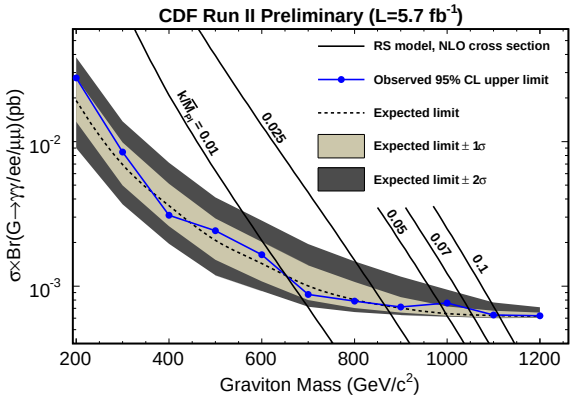

Figure 2: Exclusion plots from the CDF search for RS-gravitons decaying to $\gamma\gamma$ or ee or $\mu\mu$.

2.2 Search for Z'

New gauge-bosons are predicted by Grand Unifying Theories and would appear as resonances at hadron colliders. DØ recently searched for a new gauge boson $Z' \to ee$ using 5.4 fb^{-1} of integrated luminosity [4]. Two electrons with $p_T > 25$ GeV/c are selected and no opposite charge is required. The electrons are isolated: the excess energy in a cone $\Delta R = 0.4$ around the electron is less than 7% of its energy; additional track-based isolation is applied. The backgrounds are identical to the CDF dielectron search. The QCD background is estimated using a dielectron mass shape from DØ data that fail the electron identification selection and fitting in the Z resonance along with the DY background. The remaining minor SM backgrounds (diboson, $t\bar{t}$) are estimated using MC absolutely normalized. The dielectron spectrum is consistent with the one expected by the SM. For a Z' interacting with SM couplings, Z' masses below 1023 GeV/c^2 are excluded at 95% CL. Figure 3 shows the exclusion limits for several Z' models.

CDF recently published a $Z' \to \mu\mu$ search using 4.6 fb^{-1} of integrated luminosity [5]. The two muons are above 30 GeV/c, a cosmic-ray veto is applied and no opposite charge is required. The isolation requirements and the electroweak/QCD background estimations are the same as in the CDF RS-graviton search using dimuons. The mass spectrum is consistent with the SM; the SM-like Z' allowed masses are above 1071 GeV/c^2 at 95% CL. Figure 4 shows the exclusion limits for several Z' models.

2.3 Search for W'

The leptonic decay of the W' boson will lead to a lepton and missing transverse energy ($\not\!\!E_T$) coming from the undetected neutrino. CDF completed a 5.3 fb^{-1} search for W' decaying to electron and a neutrino [6]. One isolated electron with $E_T > 25$ GeV and $\not\!\!E_T > 25$ GeV are required. Given that the two objects have to have similar energy, $0.4 < E_T/\not\!\!E_T < 2.5$ is required. Events with two electrons are rejected. The main SM background is coming from the SM W decaying to the identical final state, W/Z decaying to taus with at least one leptonic decay and QCD multijets with fake leptons and fake or real $\not\!\!E_T$. The electron-neutrino transverse-mass spectrum is in good agreement with expectation. Assuming W' with SM left-right symmetric couplings, W' with a mass less than 1.12 TeV/c^2 are excluded at 95% CL. Figure 5 shows this exclusion limit.

In some models the new gauge boson couples stronger to the third generation. DØ performed a 2.3 fb^{-1} analysis looking for W' decaying to a top and a bottom quark with a final state of two bottom quarks, a lepton, and a neutrino [7]. The events selected include one $e(\mu)$ with p_T above

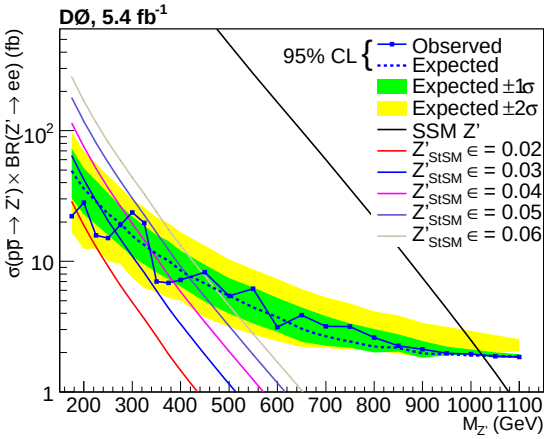

Figure 3: Exclusion plot from the DØ search for Z' decaying to two electrons.

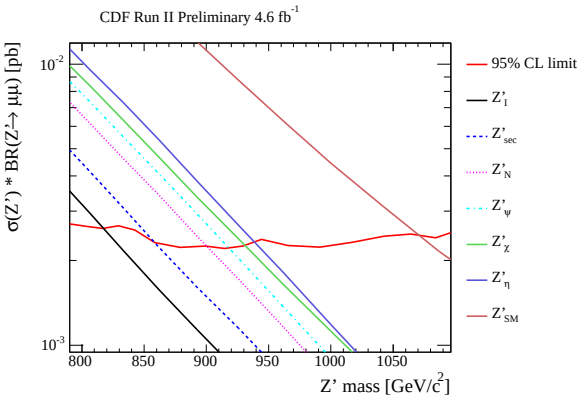

Figure 4: Exclusion plot from the CDF search for Z' decaying to two muons.

15/20 GeV/c. Events are segregated based on jet multiplicity (2, 3, or 4 jets) counting jets with $E_T > 15$ GeV (leading jet above 25 GeV) and based on b-tagging (1 or 2 tags). The total invariant mass is required to be above 400 GeV/c^2. Main SM backgrounds include W+jets and $t\bar{t}$ production. Minor backgrounds come from QCD multijet and Z+jets. Lower mass limits are presented for different combinations of left-handed and right-handed couplings and range from 863 to 916 GeV/c^2 at 95% CL. Figure 6 shows the exclusion limits for a W' with SM couplings.

2.4 Diboson Resonances

DØ searched for WW and WZ resonances using 4.1 fb^{-1} (trileptons) or 5.4 fb^{-1} (lepton(s)+jets) of data[8]. Three selections were used: either a W decays leptonically or the Z decays leptonically or both bosons decay leptonically, leading to 1-lepton+jets, 2-leptons+jets, or 3-lepton final signatures respectively. The leptons and jets are required to be above 20 GeV, where the $\not\!\!E_T$ for the three channels is required to be $\not\!\!E_T > 20$, $\not\!\!E_T < 50$, and $\not\!\!E_T > 30$ GeV respectively. In this analysis boosted W/Z decays to two jets could be reconstructed as one jet. Main backgrounds are W/Z+jets and diboson. The observations are consistent with the SM expectation. Due to higher backgrounds and under the assumption of lower branching fractions to leptons, the limits interpreted in the RS-graviton model or in W' are weaker than the respective direct dilepton ones ($M(W') > 690$ GeV/$c^2$and $M(G) > 754$ GeV/c^2 at 95% CL).

3 Search for Exotic Signatures

3.1 Search for exotic production of γ+jet

CDF performed a 4.8 fb^{-1} analysis[9] searching for abnormal generation of photon+jet, requiring the photon E_T to be above 30 GeV and the jet above 15 GeV. The photon and jet were separated so that $\Delta\phi(\text{photon}, \text{jet}) > 0.4$ rad. Four channels were investigated (>= 1 and >= 2 jets, with and without requiring $\not\!\!E_T > 20$ GeV). Main backgrounds are the SM production of γ, $\gamma\gamma$, charged-lepton, QCD multijets, cosmic rays and beam halo. Good agreement is observed in several kinematic distributions and no hint of new physics is seen.

3.2 Search for exotic production of lepton+γ+$\not\!\!E_T$+b-quark

CDF also performed a 6 fb^{-1} search [10] for abnormal production of lepton+γ+$\not\!\!E_T$+b-quark requiring lepton $E_T > 20$ GeV, $\not\!\!E_T > 20$ GeV, photon $E_T > 12$ GeV, and a b-tagged jet with

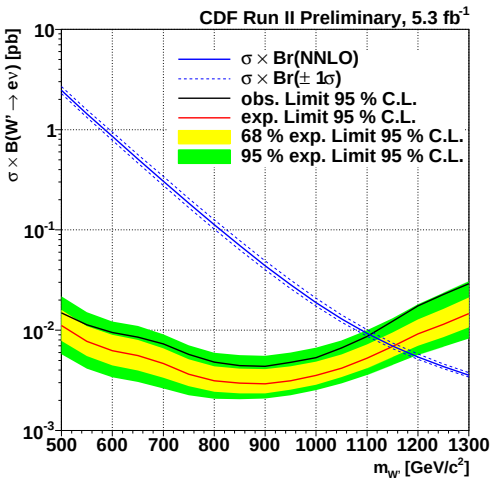

Figure 5: Exclusion plot from CDF search for W' decaying to an electron and a neutrino.

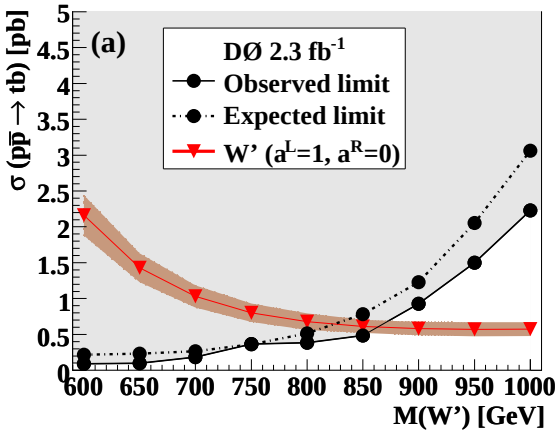

Figure 6: Exclusion plot from the DØ search for W' decaying to a top and bottom quarks.

$E_T > 20$ GeV. Main backgrounds are $t\bar{t} + \gamma$ and $W + \gamma$+jets. No new physics is seen, and this analysis yields an impressive measurement of SM $t\bar{t} + \gamma$ cross section of $\sigma = 0.18 \pm 0.07(\text{stat.}) \pm 0.04(\text{sys.}) \pm 0.01(\text{lum.})$ pb.

4 Search for Vector-like Quarks

DØ performed a 5.4 fb^{-1} search for vector-like quarks that would manifest themselves in W/Z + 2 jets [11]. For the Z+jets channel two electrons or muons above 20 GeV with p_T(dilepton) > 100 GeV/c, at least two jets above 20 GeV (leading > 100 GeV), $\not\!\!E_T < 50$ GeV and $70 < M_{\ell\ell} < 110$ GeV/c^2 are required. Main background comes from SM Z+jets. The mass of the vector-like quark must be above 430-551 GeV/c^2 (depending on the couplings) at 95% CL. For the W+jets channel one electron or muon is selected with $p_T > 50$ GeV/c, same jet requirement, $\not\!\!E_T > 50/40$ GeV and $(2M_T^W c^2 + \not\!\!E_T) > 80$ GeV. The main backgrounds come from SM W+jets, top quarks, QCD multijets, Z+jets, and diboson. The mass of the vector-like quark must be above 403-693 GeV/c^2 (depending on the couplings) at 95% CL.

References

1. T. Aaltonen *et al.* (CDF Collaboration), arXiv:1103.4650 [hep-ex] (2011).
2. T. Aaltonen *et al.* (CDF Collaboration), CDF public note 10479 (2011).
3. T. Aaltonen *et al.* (CDF Collaboration), Phys. Rev. D **83**, 011102(R) (2011).
4. V. Abazov *et al.* (D0 Collaboration), Phys. Lett. B **695**, 88 (2011).
5. T. Aaltonen *et al.* (CDF Collaboration), Phys. Rev. Lett. **106**, 121801 (2011).
6. T. Aaltonen *et al.* (CDF Collaboration), Phys. Rev. D **83**, 031102 (2011).
7. V. Abazov *et al.* (D0 Collaboration), Phys. Lett. B **699**, 145 (2011).
8. V. Abazov *et al.* (D0 Collaboration), Phys. Rev. Lett. **107**, 011801 (2011).
9. T. Aaltonen *et al.* (CDF Collaboration), CDF public note 10355 (2011).
10. T. Aaltonen *et al.* (CDF Collaboration), CDF public note 10270 (2011).
11. V. Abazov *et al.* (D0 Collaboration), Phys. Rev. Lett. **106**, 081801 (2011).

NON-SUSY SEARCHES AT ATLAS

E.N. Thompson
(on behalf of the ATLAS Collaboration)
Department of Physics
1126 Lederle Graduate Research Tower (LGRT)
University of Massachusetts
Amherst, MA 01003

The ATLAS detector has begun the search for new physics beyond the Standard Model (BSM) with an integrated luminosity of $\int Ldt \simeq 45$ pb^{-1} of data collected in 2010. After no significant evidence of new physics was found in the data, limits on possible signatures have been set, many of which are already more stringent than previous measurements. These proceedings review recent limits obtained on various BSM models, including excited quarks, axigluons, contact interactions, quantum black holes, heavy gauge bosons (W', Z'), gravitons, fourth-generation quarks and leptoquarks.

1 Introduction

Over the past few decades, experimental results have consistently agreed with the observable expectations of the Standard Model (SM); yet the cause of Electroweak Symmetry Breaking (EWSB), necessary to give mass to the $W^{\pm}$ and Z^0 bosons, remains unconfirmed. In addition, the SM contains 21 arbitrary parameters, and is unable to account for the number of quark/lepton families, matter-antimatter asymmetry, or gravity. Many theories beyond the Standard Model (BSM) have been developed to address limitations of the SM. The ATLAS detector [1], located on the Large Hadron Collider (LHC) ring at CERN near Geneva, Switzerland, was especially designed to measure high-momentum particles in anticipation of new physics discoveries at the electroweak scale ($\sim$1 TeV). Signatures in the detector span a large range of final-state objects, which include electrons, photons, jets, missing transverse energy ($\not\!\!E_T$) and muons.

In the early months of data-taking, understanding the performance of the detector was crucial while searching for new physics processes occurring at a much higher invariant mass than available at previous experiments. ATLAS collected a total of $\simeq 45$ pb^{-1} of integrated luminosity in 2010 at a center of mass energy $\sqrt{s} = 7$ TeV, and quickly 'rediscovered' many SM physics processes, setting the stage for new physics discovery. These proceedings discuss the new physics searches performed at ATLAS according to their final-state signatures, as well as their related detector performance issues at high momentum.

Slightly different datasets were used for each analysis due to varying trigger requirements and data quality conditions of the subdetectors used to measure the final-state objects. The uncertainty on the luminosity measurement for the analyses below was 11%.

2 Searches in the dijet final state

The 2→2 scattering processes as described by QCD in the Standard Model have been well studied, and any deviation from expected behavior of dijet processes would indicate new physics. Searches were performed in both the dijet invariant mass spectrum [2], given by

$$m_{jj} = \sqrt{(E_{j_1} + E_{j_2})^2 - (\vec{p}_{j_1} + \vec{p}_{j_2})^2},$$

as well as in the angular distribution $F_\chi(m_{jj})$ of dijets, where

$$F_\chi\left(\frac{[m_{jj}^{min} + m_{jj}^{max}]}{2}\right) \equiv \frac{N_{events}(|y^*| < 0.6,\ m_{jj}^{min},\ m_{jj}^{max})}{N_{events}(|y^*| < 1.7,\ m_{jj}^{min},\ m_{jj}^{max})}\ .$$

Here, N_{events} are the number of dijet events observed within the rest-frame rapidity y^* and invariant mass ranges specified. Models studied appearing as a resonance in the dijet mass spectrum include exited quarks [3] and axigluons [4]. Other signals could also appear as a non-resonant excess of events above the dijet invariant mass distribution, such as in $qqqq$ contact interactions [5] or quantum black hole (QBH) [6] models. More sensitivity to new physics may be gained by using the angular distribution, as QCD dijets are more central in the detector, while new physics signatures are more isotropic in nature. An analysis using the $F_\chi(m_{jj})$ distribution also benefits from less sensitivity to the absolute jet energy scale (JES) which is the largest systematic uncertainty for high-energy jets.

Using the calorimeter trigger and requiring high quality data in the Inner Detector (ID) and calorimeters, 36 pb^{-1} of integrated luminosity was used in the dijet analyses. Each of the two jets in the event were required to pass quality criteria ensuring that the energy deposition in the calorimeters was in-time. For the dijet resonance search, the two selected jets were additionally required to have a pseudorapidity $|\eta_j| < 2.5$, $|\Delta\eta_{jj}| < 1.3$ between them, and leading jet $p_T^{j1} > 150$ GeV, leaving 98,651 events with m_{jj} >500 GeV passing all selection. In the angular distribution analysis, the additional selection required dijets to satisfy tighter rapidity ranges, with 71,402 events in data after all selection. In both the resonance and angular distribution searches, the data were found to be consistent with SM expectations. Limits were set on the models mentioned above using a modified frequentist (CL$_{s+b}$) approach (for $F_\chi(m_{jj})$ searches) as well as a Bayesian credibility interval approach (for m_{jj} searches). The 95% C.L. lower limits are summarized in Table 1.

Table 1: 95% C.L. lower limits on various dijet physics signatures. Units are in TeV. The limit for QBH is given for number of dimensions > 6, and the Contact Interaction limit is set on the scale of the new interaction Λ.

	m_{jj}		$F_\chi(m_{jj})$	
Model	Expected	Observed	Expected	Observed
Excited Quark	2.07	2.15	2.12	2.64
QBH	3.64	3.67	3.49	3.78
Axigluon	2.01	2.10	-	-
Contact Interaction	-	-	5.72	9.51

3 Searches in the charged dilepton, lepton with $\not{E}_T$ and diphoton final states

Some extensions to the SM predict massive gauge bosons (W', Z') above 1 TeV. In the Sequential Standard Model (SSM) [7], the couplings of the fermions to the W' or Z' are the same as for the SM W and Z bosons. In another string-theory-inspired model [8], an E_6 gauge group symmetry-breaking leads to 6 different Z' states: Z'_ψ, Z'_N, Z'_I, Z'_S, Z'_η and Z'_χ. Additionally, models with

excited states W^* and Z^* [9] were also considered, as they have different kinematic distributions than those of the W' and Z'. Searches were performed in the dilepton channel [10] ($Z' \to e^+e^-$ and $Z' \to \mu^+\mu^-$) as well as the lepton plus $\not\!\!E_T$ channel [11] ($W' \to e\nu_e$ and $W' \to \mu\nu_\mu$). Similarly to the dijets searches, the invariant mass of the dileptons m_{ll} was used in order to search for Z' resonances. However, as the neutrino appears only as missing energy in the detector, only the transverse component of the mass $m_T = \sqrt{p_T^l \not\!\!E_T (1 - \cos\phi_{l\nu})}$ could be used in W' searches. The total integrated luminosity for the W' searches was 36 pb^{-1}, while the searches for $Z' \to e^+e^-$ and $Z' \to \mu^+\mu^-$ used 39 pb^{-1} and 42 pb^{-1}, respectively.

The underlying physics process is the same regardless of the participant leptons, however, the systematic uncertainties entering the analyses are different for the electron and muon channels and are handled separately. Higher-order QCD processes are less understood at high mass, and so the background to $W' \to e\nu_e$, $W' \to \mu\nu_\mu$ and $Z' \to e^+e^-$ signals arising from jets faking electrons or mis-measuring $\not\!\!E_T$ was estimated based on control regions in the data. In the muon channel, the largest uncertainty came from muon momentum resolution, mainly due to misaligned Muon Spectrometer (MS) chambers which were not modeled in simulation. This was reduced by requiring that muons use combined measurements in both the ID and MS, and also pass through regions of the MS with higher geometric acceptance and better-known alignment. In both channels of the Z' search, the total systematic uncertainty was reduced by normalizing the data to the simulation in the control region $70 < m_{ll} < 120$ GeV.

After all selection criteria, 31 (16) events were observed in the $e\nu$ ($\mu\nu$) channel having $m_T > 500$ GeV, and 66 (38) events observed in the ee ($\mu\mu$) channel in the signal region $m_{ll} > 150$ GeV. In both cases, the data agreed with SM expectations. Limits on the new physics cross sections were set using a modified frequentist approach for the W' searches and a Bayesian approach for the Z' searches. The 95% C.L. lower limits after combining the electron and muon channels are summarized in Table 2.

Table 2: 95% C.L. lower limits on various dilepton and lepton+$\not\!\!E_T$ physics signatures after electron and muon channels were combined. Units are in TeV.

Model	W'	W^*	Z'	Z^*	Z'_ψ	Z'_N	Z'_I	Z'_S	Z'_η	Z'_χ
Expected	1.450	1.320	1.088	1.185	0.837	0.860	0.922	0.945	0.866	0.965
Observed	1.490	1.350	1.048	1.152	0.738	0.763	0.842	0.871	0.771	0.900

Searches were also performed in the diphoton channel [12] where a Kaluza-Klein graviton resonance is predicted by the Randall-Sundrum model [13]. In this model an extra spacial dimension, characterized by its curvature k and compactification radius r_c, reduces the Plank scale $\bar{M}_{pl}$ down to the TeV scale. Because photons were reconstructed in the EM calorimeter, they had similar detector-related uncertainties as for the dielectron channel. No excess above the predicted diphoton invariant mass spectrum was found in 36 pb^{-1}, and limits on various combinations of the graviton mass ($m_{\gamma\gamma}$) and couplings ($k/\bar{M}_{pl}$) were set using a modified frequentist approach. This resulted in a 95% C.L. lower limit of 545 (920) GeV on the RS graviton mass with coupling $k/\bar{M}_{pl} = 0.02$ (0.1).

4 Searches with leptons and jets

Finally, other models predict multiple-object final-states, such as fourth generation quarks (Q_4) [14] and those involving new particles carrying both lepton and baryon number ("leptoquarks") [15]. In the decay of pairs of fourth generation quarks ($Q_4Q_4 \to W^+jW^-j \to l^+\nu jl^-\nu j$), boosted W bosons result in a final-state in which lepton-jet pairs are more collinear than in SM W pair production. A transverse "collinear mass" was constructed from lepton-jet pairs after assum-

ing that the neutrinos were the only contributors to $\not\!\!E_T$ and by choosing $|\Delta\eta(\nu,l)|$, $|\Delta\phi(\nu,l)|$ and jet assignments which minimized the difference between the two collinear masses in the event. Together, the scalar sum of the transverse energy in the event and the collinear mass was used as a discriminant to separate new physics from the dominant top quark pair production background. In 37 pb^{-1}, no evidence for fourth generation quarks was found, and a limit of $M_{Q_4} > 270$ GeV (95% C.L.) was set using a Feldman-Cousins approach. This was the first dilepton search for an up-type fourth generation quark, as well as the first search for fourth generation quarks performed at the LHC.

Searches for leptoquarks were performed using 35 pb^{-1} of data in both the first ($eejj$ and $e\nu jj$) and second ($\mu\mu jj$ and $\mu\nu jj$) generation channels. The sum of transverse energy in the event $S_T \equiv \sqrt{p_T^{l_1} + p_T^{l_2} + p_T^{j_1} + p_T^{j_2}}$ was used to look for the presence of a new physics signal in the $llqq$ channel. Here, in order to reject background events arising mainly Z with jets, M_{ll} was found by computing the invariant mass of pairs of leptons. In the $ll\nu j$ channel, however, because the neutrino could not be fully reconstructed, only the transverse mass was used to reject the dominant W plus jets background (defined similarly as for the lepton-neutrino pair in the W' search). Choosing lepton-jet and jet-neutrino pairs which minimize the difference between the invariant mass of the lepton-jet M_{LQ} and transverse mass of the jet-neutrino M_{LQ}^T, the average $\bar{M}_{LQ}$ between them was used as a discriminant in the $l\nu qq$ channel. The data were found to be consistent with SM expectations, and using a modified frequentist approach, 95% C.L limits on the leptoquark mass were set as a function of the branching fraction β for a single leptoquark to decay to a charged lepton + jet. For first generation leptoquarks, lower limits of $M > 376$ (319) GeV for β=1.0 (0.5) were found. In the second generation, the lower limits found were $M > 422$ (362) GeV for β=1.0 (0.5).

5 Summary

ATLAS has shown that it is able to push the energy frontier to the TeV scale and search for a variety of BSM signatures in the earliest stages of LHC data, in many cases setting the world's best limits. The knowledge gained from the first round of analyses presented at Rencontres de Moriond has paved the way for future work, and ATLAS eagerly awaits more data in the hopes of discovering new physics at the LHC.

References

1. The ATLAS Collaboration, G. Aad et al., *The ATLAS Experiment at the CERN Large Hadron Collider,* JINST **3**, S08003 (2008)
2. The ATLAS Collaboration, G. Aad et al., *Search for New Physics in Dijet Mass and Angular Distributions in pp Collisions at $\sqrt{s}$=7 TeV Measured with the ATLAS Detector,* New J. Phys. **13**, 053044 (2011)
3. U. Baur, I.Hinchliffe, and D. Zeppenfeld, *Excited Quark Production at Hadron Colliders,* Int. J. Mod. Phys **A2**, 1285 (1987)
   U. Baur, M. Spira, and P.M. Zerwas, *Excited-quark and -lepton production at hadron colliders,* Phys. Rev. **D42**, 815 (1990)
4. P. Frampton and S. Glashow, *Chiral Color: An Alternative to the Standard Model,* Phys. Lett. **B190**, 157 (1987)
   J. Bagger, C. Schmidt, and S. King, *Axigluon Production in Hadronic Collisions,* Phys. Rev. **D37**, 1188 (1988)
5. E. Eichten, I.Hinchliffe, K.D. Lane and C. Quigg *Supercollider Physics* Rev. Mod. Phys. **56**, 579 (1984)

P. Chiappetta and M. Perrottet, *Possible bounds on compositeness from inclusive one jet production in large hadron colliders,* Phys. Lett. **B253**, 489 (1991)
6. P. Meade and L. Randall, *Black Holes and Quantum Gravity at the LHC,* JHEP05 **2008**, 003 (2008)
7. P. Langacker, *The Physics of Heavy Z' Gauge Bosons,* Rev. Mod. Phys. **81**, 1199 (2009)
8. D. London and J. L. Rosner, *Extra Gauge Bosons in E_6,* Phys. Rev. **D34**, 1530 (1986)
9. M. Chizhov, V. Bednyakov, and J. Budagov, *Proposal for chiral-boson search at LHC via their unique new signature,* Physics of Atomic Nuclei **71**, 2096 (2008)
10. The ATLAS Collaboration, *Search for high mass dilepton resonances in pp collisions at $\sqrt{s}$=7 TeV with the ATLAS experiment,* arXiv:1103.6218, accepted by Phys. Lett. B (2011)
11. The ATLAS Collaboration, *Search for high-mass states with one lepton plus missing transverse momentum in proton-proton collisions at $\sqrt{s}$ = 7 TeV with the ATLAS detector,* accepted by Phys. Lett. B (2011)
12. The ATLAS Collaboration, *A Search for High Mass Diphoton Resonances in the Context of the Randall-Sundrum Model in $\sqrt{s}$ = 7 TeV pp Collisions,* ATLAS-CONF-2011-044 (http://cdsweb.cern.ch/record/1338573)
13. L. Randall and R. Sundrum, *Large Mass Hierarchy from a Small Extra Dimension,* Phys. Rev. Lett. **83**, 3370 (1999)
14. The ATLAS Collaboration, *Search for Fourth Generation Quarks Decaying to $WqWq \to ll\nu\nu qq$ in pp collisions at $\sqrt{s}$=7 TeV with the ATLAS Detector,* ATLAS-CONF-2011-022 (http://cdsweb.cern.ch/record/1336751)
15. The ATLAS Collaboration, *Search for pair production of first or second generation leptoquarks in pp collisions at $\sqrt{s}$=7 TeV using the ATLAS detector at the LHC,* arxiv:1104.4481, submitted to Phys Rev D (2011)

The Quasi-Classical Model in SU(N) Gauge Field Theory

A.V.Koshelkin.
General Physics Department, Moscow Institute for Physics and Engineering, Kashirskoye sh., 31, Moscow 115409, Russia

The quasi-classical model in a gauge theory with the Yang-Mills (YM) field is developed. On a basis of the exact solution of the Dirac equation in the $SU(N)$ gauge field which is in the eikonal approximation the Yang-Mills equations containing an external current are solved. The developed model proves to have the self-consistent solutions of the Dirac and Yang-Mills equations at $N \geq 3$. The obtained solutions take place provided that the fermion and gauge fields exist simultaneously, so that the fermion current completely compensates the current generated by the gauge field due to its self-interaction. The obtained solutions are considered in the context of QCD.

1 Introduction

The study of non-Abelian gauge fields plays an important role in the modern field theory[1]. The non-Abelian gauge field are a basis of QCD. The knowledge of solutions of the YM equations enable us to understand specifics of processes in the strong interacting matter generated in collisions of heavy ions of high energies.

The consistent consideration of strong interacting matter (generated, for example, in collisions of high energy ions) demands, generally, solving the Dirac and Yang-Mills equations simultaneously.

In the present paper the quasi-classical model in the $SU(N)$ gauge theory with the Yang Mills field is developed. The self-consistent solution of both the nonhomogeneous Yang-Mills equation and Dirac equations in an external field are derived when the gauge Yang-Mills field is in the eikonal form. It is shown that the self-consistent solutions of such equations take place when $N \geq 3$. They occur provided that the fermion and gauge fields exist simultaneously, so that the fermion current completely compensates the current generated by the gauge field due to its self-interaction. In this way, the interaction between the fermions and YM field, in the mean, leads to the re-normalization a fermion mass. The re-normalized mass depends strongly on the temperature of matter.

2 The YM equations in the presence of external current

We consider the $SU(N)$ gauge field A_a^ν generated by a fermion current. It satisfies following equations[2]:

$$\begin{aligned}
&\partial_\mu F_a^{\nu\mu}(x) - g \cdot f_{ab}{}^c A_\mu^b(x) F_c^{\nu\mu}(x) = -g J_a{}^\nu(x) \\
&F_a^{\nu\mu}(x) = \partial^\nu A_a^\mu(x) - \partial^\mu A_a^\nu(x) - g \cdot f_a{}^{bc} A_b^\nu(x) A_c^\mu(x), \\
&J_a{}^\nu(x) = \bar{\Psi}(x)\gamma^\nu T_a \Psi(x),
\end{aligned} \tag{1}$$

where the fermion fields $\Psi(x), \bar{\Psi}(x)$ are governed by the Dirac equation:

$$\left\{ i\gamma^{\mu} \left(\partial_{\mu} + ig \cdot A^{a}_{\mu}(x) T_{a} \right) - m \right\} \Psi(x) = 0$$
$$\bar{\Psi}(x) \left\{ i\gamma^{\mu} \left(\overleftarrow{\partial}_{\mu} - ig \cdot A^{*a}_{\ \mu}(x) T_{a} \right) + m \right\} = 0. \qquad (2)$$

Here, m is a fermion mass, g is the coupling constant; γ^{ν} are the Dirac matrixes[2], $x \equiv x^{\mu} = (x^{0}; \vec{x})$ is a vector in the Minkowski space-time; $\partial_{\mu} = (\partial/\partial t; \nabla)$; the Roman letters numerate a basis in the space of the associated representation of the $SU(N)$ group, so that $a, b, c = 1 \ldots N^{2} - 1$. We use the signature $diag\,(\mathcal{G}^{\mu\nu}) = (1; -1; -1; -1)$ for the metric tensor $\mathcal{G}^{\mu\nu}$. Summing over any pair of the repeated indexes is implied. The symbols T_{a} in Eqs.(1)-(2) are the generators of the $SU(N)$ group which satisfy the standard commutative relations and normalization condition[2]. The main goal is to derive the self-consistent solutions of of Eqs.(1)-(2) which will be localized in the confined region of space. We find the solution when the field $A^{a}_{\nu}(x)$ is in the form:

$$A^{\nu}_{a}(x) = A^{\nu}_{a}(\varphi(x)), \qquad (3)$$

where $\varphi(x)$ is some scalar function in the Minkowski space-time which is such that:

$$(\partial_{\mu}\varphi)(\partial^{\mu}\varphi) \equiv k_{\mu}k^{\mu} = 0; \qquad (4)$$

The last formula determines the well known eikonal approximation where $\varphi(x)$ can be interpretable as the function governing the wave surface of the field A^{ν}_{a}.

We take the axial gauge for the field $A^{a}_{\mu}(x)$:

$$\partial^{\mu} A^{a}_{\mu} = 0; \qquad k^{\mu} \dot{A}^{a}_{\mu} = 0, \qquad (5)$$

where the dot over the letter means differentiation with respect to the introduced variable φ.

Taking into account of both the dependence of $A^{a}_{\nu}(x)$ on the variable x via the function $\varphi(x)$ and formulae (4), (5), we derive from Eqs.(1), (2):

$$(\partial_{\mu}\partial^{\mu}\varphi(x))\, \dot{A}^{\nu}_{a} + gk^{\nu}\ f_{ab}{}^{c} A^{b}_{\mu}(\varphi)\dot{A}^{\mu}_{c}(\varphi) - g^{2} f_{ab}{}^{c}\ f_{c}{}^{sr} \left\{ A^{b}_{\mu}(\varphi) A^{\nu}_{s}(\varphi) A^{\mu}_{r}(\varphi) \right\} = g\ J^{\nu}_{a}(x). \qquad (6)$$

It follows from Eq.(6) that in order to derive the solution of the YM equation it is necessary to calculate the fermion current $J^{\nu}_{a}(x)$ (see Eqs.(1)). We assume that the field $A^{\nu}_{a}(\varphi)$ can expanded as follows in the local frame:

$$A^{\nu}_{a}(\varphi) = \mathcal{B}_{a}\partial^{\nu}\varphi(x) + A \left(e^{\nu}_{(1)}(\varphi) \cos\left(\varphi(x) + \varphi_{a}\right) + \ e^{\nu}_{(2)}(\varphi) \sin\left(\varphi(x) + \varphi_{a}\right) \right)$$
$$e^{\nu}_{(1)} k_{\nu} = e^{\nu}_{(2)} k_{\nu} = 0; \quad \dot{e}^{\nu}_{(1)} = e^{\nu}_{(2)}; \quad \dot{e}^{\nu}_{(2)} = -e^{\nu}_{(1)}\ ; \quad k^{\nu} \equiv \partial^{\nu}\varphi(x), \qquad (7)$$

where $e^{\nu}_{(1),(2)}(\varphi)$ are the space-like 4-vectors on the wave surface $\varphi(x)$ which are independent on the group variable a; the symbols A, $\mathcal{B}_{a}$ and φ_{a} are the constants in the Minkowski space-time. They are determined via the initial condition of the considered problem. It is obvious that the function $\varphi(x)$ can be taken so that the field $A^{a}_{\nu}(x)$ will be localized in the confined region of space.

3 Solution of Dirac equation

The solution of the Dirac equation (2) when the external field is given by the formula (7) has the following form[3]:

$$\Psi_{\sigma,\alpha}(x,p) = \ \cos\theta \cdot \exp\left(-ig^{2} \frac{(N^{2}-1)A^{2}}{2N(pk)} \varphi - ipx \right) \left\{ \left(1 - igT_{a} \frac{\tan\theta}{\theta(pk)} \int\limits_{0}^{\varphi} d\varphi' \left(A^{a}_{\mu} p^{\mu} \right) \right) + \right.$$

$$\frac{g\,(\gamma^\mu k_\mu)\left(\gamma^\mu A^a_\mu\right)}{2(pk)}\cdot\left[\frac{\tan\theta}{\theta}\;T_a+\frac{g}{(pk)}\;\frac{1}{2N}\;\int\limits_0^{\varphi}d\varphi'\left(A^a_\mu p^\mu\right)\Big(-i\frac{\tan\theta}{\theta}+\right.$$

$$\left.\frac{g}{(pk)}\frac{\theta-\tan\theta}{\theta^3}T_b\;\int\limits_0^{\varphi}d\varphi'\left(A^b_\mu p^\mu\right)\Big)\right]\Bigg\}\;u_\sigma(p)\cdot v_\alpha, \tag{8}$$

where $u_\sigma(p)$ and v_α are some spinors which are the elements of spaces of the corresponding representations.

Following the structure of the last formula it is naturally to determine the spinor $u_\sigma(p)$ as the standard Dirac spinors which satisfy the free Dirac equation and are normalized as follows:

$$\bar{u}_\sigma(p)u_\lambda(p')=\pm 2m\;\delta_{\sigma\lambda}\;\delta_{pp'};\quad p^2=m^2, \tag{9}$$

where the plus and minus signs correspond to the Dirac scalar production of the spinors $u_\sigma(p)$ and $u_\sigma(-p)$, respectively.

As for the spinors v_α we determine them by the relations:

$$v^\dagger_\alpha v_\beta=\delta_{\alpha\beta};\;Tr(T_a)=0;\;Tr(T_a\;T_b)=\frac{\delta_{ab}}{2}. \tag{10}$$

The function (8) can be normalized by the δ-function as follows:

$$\int d^3x\Psi^*_{\sigma,\alpha}(x,p')\Psi_{\sigma,\alpha}(x,p)=(2\pi)^3\delta^3(\vec{p}-\vec{p}\,'). \tag{11}$$

Then, the general solution of the Dirac equation (2) in the external field (7) is:

$$\Psi(x)=\sum_{\sigma,\alpha}\int\frac{d^3p}{\sqrt{2p^0}\,(2\pi)^3}\left\{\hat{a}_{\sigma,\alpha}(\vec{p})\Psi_{\sigma,\alpha}(x,p)+\hat{b}^\dagger_{\sigma,\alpha}(\vec{p})\Psi_{-\sigma,\alpha}(x,-p)\right\}, \tag{12}$$

where the symbols $\hat{a}^\dagger_{\sigma,\alpha}(\vec{p});\hat{b}^\dagger_{\sigma,\alpha}(\vec{p})$ and $\hat{a}_{\sigma,\alpha}(\vec{p});\hat{b}_{\sigma,\alpha}(\vec{p})$ are the operators of creation and cancellation of a fermion $(\hat{a}_{\sigma,\alpha}(\vec{p});\hat{a}^\dagger_{\sigma,\alpha}(\vec{p}))$ and anti-fermion $(\hat{b}_{\sigma,\alpha}(\vec{p});\hat{b}^\dagger_{\sigma,\alpha}(\vec{p}))$, respectively, which are governed by the standard commutative relations for fermion operators[2].

4 Self-consistent consistent solutions of Dirac and Yang-Mills equations

Substituting Eqs.(7), (12) into the formula (6) we derive:

$$2f_{ab}{}^c\sin(\varphi_b-\varphi_c)=f_{ab}{}^c\left\{\;f_c\;{}^{sr}\cos(\varphi_b-\varphi_r)+\{\cos(\varphi_b-\varphi_r)\;\cos(\varphi_s-\varphi_a)\}\;\frac{f_c\;{}^{bs}}{N}\right\}\mathcal{B}_s;$$

$$A^2\cdot C=-(N^2-1)\sum_{\sigma\alpha}\int\frac{d^3p}{p^{(0)}(2\pi)^3}\langle\hat{a}^\dagger_{\sigma,\alpha}(\vec{p})\hat{a}_{\sigma,\alpha}(\vec{p})+\hat{b}_{\sigma,\alpha}(\vec{p})\hat{b}^\dagger_{\sigma,\alpha}(\vec{p})\rangle,$$

$$C=\;f_{ab}{}^c\;f_c\;{}^{sr}\{\cos(\varphi_b-\varphi_r)\;\cos(\varphi_s-\varphi_a)\}<0. \tag{13}$$

The equations (13) are closed with respect to the unknown quantities A and $\mathcal{B}_a$. Having been solved they determine both the fermion and gauge field by means of Eqs.(7), (8), (12), (13) so that the wave surface $\varphi(x)$ is governed by relations (4), (5).

Note that in the case of the $N=2$ (when the $SU(2)$ gauge symmetry occurs) the convolution , C in Eq.(13) which contains cosines is always positive since the structure constants $f_{ab}{}^c$ are the completely antisymmetrical tensor of the third rang $(\varepsilon_{ab}{}^c)^{\,2}$:

$$C=\;f_{ab}{}^c\;f_c\;{}^{sr}\{\cos(\varphi_b-\varphi_r)\;\cos(\varphi_s-\varphi_a)\}=\sum_{a,b=0}^{N^2-1}\sin^2(\varphi_s-\varphi_a)\geq 0. \tag{14}$$

This means that in the framework of the developed model there is no self-consistent solution of the Dirac and Yang-Mills equations for the $SU(2)$ gauge symmetry. In the cases of the groups whose dimension is more then $N = 2$ the structure constants $f_{ab}{}^{c}$ can not be expressed in terms of the tensor $\varepsilon_{ab}{}^{c}$. As a result, it possible to fix the differences between phase in the convolution C so that $C \leq 0$.

As for the coefficients $\mathcal{B}_s$ they satisfy the set of linear algebraical equations which has the unique solution.

As a result, we have the following. The problem governed by Eqs.(1)-(2) has the unique solution when $N \geq 3$. The solutions are determined by (7), (8), (12), (13) and correspond to the eikonal consideration when the wave surface of the fields are determined by the equations:

$$(\partial_\mu \varphi(x)) \cdot (\partial^\mu \varphi(x)) = 0; \ (\partial_\mu \partial^\mu)\, \varphi(x) = 0 \tag{15}$$

It follows from (7), (8), (12), (13) that the Yang-Mills and Dirac equations has the self-consistent solution when the fermion current compensates the current of the gauge field which appears due to self-interaction of such field. In other words, in the the framework of the developed model there is no the YM field without fermions. In terms of QCD this means that quarks and gluons cannot separately exist in such approach.

5 Developed model in the context of QCD

In the RHIC and SPS experiments the characteristic temperature T of an equilibrium quark-gluon plasma is $T \sim 200 \div 400 MeV$. The estimations of the initial density of energy of the plasma give that the energy density $w \sim 10\ Gev \cdot F^{-3}$ while the volume of a fireball is not less than $V_0 \sim 10^2\ F^3$. Then the number of particles N_0 inside the fireball is of the order of

$$N_0 \sim \frac{w\ V_0}{T} \sim 2.5 \cdot 10^3, \tag{16}$$

that is in agreement with the quasi-classical approximation.

The gas parameter $n_0^{1/3} T^{-1}$ is of the order of $(n_0^{1/3} T^{-1}) \sim 1.46 \div 3.7$ at such density of the matter. On the other hand, the mean effective mass of a quark is of the order of

$$\begin{aligned} m_* &\sim \left(\frac{n_0}{g|C|T}\right)^{\frac{1}{2}} \ ; \qquad \frac{m}{T} \ll \left(\frac{n_0}{|C|T^3}\right) \ll 1; \\ m_* &\sim \ \sqrt[3]{n_0}\ ; \qquad \left(\frac{n_0}{|C|T^3}\right) \gg 1. \end{aligned} \tag{17}$$

It follows from the last formulae that in the intermediate range of the density of matter, $n_0 \sim (gT)^3$, the effective mass is proportional to the temperature of the matter that corresponds to the result of the calculations in the hard loop approximation[4]:

$$m_* \sim g\ T. \tag{18}$$

1. P.H.Frampton, Gauge Field Theories, Second Edition, Wiley, 2000.
2. A.I.Akhiezer, S.V.Peletminsky. The field and Fundanmetal Interactions. Kiev, Naukova Dumka, 1986.
3. A.V.Koshelkin. Phys. Lett. **B** 683 (2010) 205. 1974.
4. E.Braaten, R.D.Pisarski, Nucl. Phys. **B337** 596 (1990).

3.
Top

TOP QUARK PAIR PRODUCTION CROSS SECTION AT THE TEVATRON

SILVIA AMERIO
(on behalf of CDF and D0 Collaborations)
INFN Padova, via Marzolo, 8,
35131 Padova, Italy

This paper describes the most recent results of $t\bar{t}$ production cross section measurements performed by the CDF and D0 experiments, analyzing up to 5.7 fb^{-1} of data collected at a center-of-mass energy of 1.96 TeV at the Tevatron Fermilab collider. All possible $t\bar{t}$ final states are being investigated and the resulting measurements are currently limited by the systematic uncertainties. The best results are obtained in the lepton+jets final state, with relative precision ranging from 7 to 9 %, comparable to the theoretical one.

1 Introduction

The top quark was discovered at the Tevatron in 1995 [1]. Due to its large mass, it may play an important role in the mechanism of electroweak symmetry breaking. According to the standard model (SM), it decays with a branching ratio (BR) of almost 100% in a W boson and a b-quark without hadronizing, and as a consequence its properties can be measured directly from its decay products. At the Tevatron, where $p\bar{p}$ interactions occur at a center-of-mass energy $\sqrt{s} =$ 1.96 TeV, it is mainly produced in $t\bar{t}$ pairs via strong interaction through $q\bar{q}$ annihilation (BR $\sim$ 85%) or gg fusion (BR $\sim$ 15%). The most precise predictions of $t\bar{t}$ production cross section are currently given by approximate Next-to-Next-to-Leading-Order (NNLO) calculations, with precisions ranging from 6 to 9% [2]. For a top mass of 172.5 GeV/c^2, the $t\bar{t}$ production cross section is about 7.5 pb.

The measurement of $t\bar{t}$ production cross section is an important test of perturbative QCD (pQCD) calculations at high energy; it can also serve to indirectly extract the top quark mass, in a more precise defined theoretical framework with respect to the direct measurements [3]. A precise determination of the $t\bar{t}$ cross section is important to determine the $t\bar{t}$ background to many Higgs searches and it can also be a probe for new physics. As an example, the cross section value can be enhanced by new processes beyond the SM such as top pair production via new massive resonances [4], while the comparison of the top pair production cross section in different decay channels can be sensitive to the presence of top decays via a charged Higgs boson [5].

At CDF and D0 experiments $t\bar{t}$ pairs are observed and studied in all possible final states: *dileptonic*, when both Ws decay into leptons (electron e or muon μ), *lepton + jets*, where one W decays leptonically and the other into jets of particles, and *all hadronic*, where both Ws decay hadronically. Final states with τ leptons decaying leptonically are accounted for in the dilepton or lepton+jets channels, while channels with hadronic decays of τs are treated separately.

In all the analysis presented in this paper, the identification of jets originated by b quarks (b-jets) plays a fundamental role. Both collaborations identify b-jets exploiting the displacement

of their vertex with respect to the primary one: CDF selects displaced tracks within a jet and constrains them to a common vertex [6], while D0 uses a Neural Network (NN) [7] combining variables characterizing the properties of b-jets.

In the following sections we will describe in more detail the most recent results in the different $t\bar{t}$ decay channels.

2 The Dilepton Channel

The dilepton channel has a small branching ratio of about 5%, but the presence of two high-p_T leptons (e or μ) makes the signature of this final state very clean. The selection requires also missing tranverse energy ($\not\!\!E_T$) and one or at least two jets. The main physics background sources are Drell-Yan events and diboson production. W+jets and $W\gamma$ events can be source of instrumental background when a jet/γ is misidentified as a lepton.

The most recent and precise $t\bar{t}$ cross section measurement in the dilepton channel is from D0 and it is based on 5.4 fb^{-1} of integrated luminosity. Three different dilepton final states (ee, $\mu\mu$, $e\mu$) are selected, with lepton $p_T > 20$ GeV and at least two jets, except for the $e\mu$ channel where events with one jet are also considered. After the kinematic selection, a better separation between signal and background is achieved considering the distribution of the smallest of the two b-tagging NN discriminant outputs of the two leading jets (see fig. 1). The $t\bar{t}$ cross section is measured by simultaneously fitting the NN distributions in the four channels. In order to reduce the influence of systematic uncertainties on the cross section measurement, the nuisance parameters technique is used to constrain the overall uncertainty using the data NN output distribution itself: the impact of each uncertainty is parameterized in the likelihood function by a nuisance parameter that is constrained with a Gaussian probability with a mean of zero and a width corresponding to the size of the uncertainty. As the systematic uncertainties are the limiting factor in the precision of the $t\bar{t}$ cross section measurement, constraining them with data using this technique allows to improve the overall uncertainty of approximately 20% and to reach a relative precision of 11%. The final result is $\sigma_{t\bar{t}} = 7.4\ ^{+0.9}_{-0.8}$ (stat+syst) pb for $m_t = 172.5$ GeV/c^2 [8].

CDF best determination in the same final state, with a relative precision of about 13%, is obtained by means of a counting experiment on the samples without b-tagging requirement or with at least one b-tagged jet, considering all leptonic modes together. The resulting cross section value in the first sample, for $m_t = 172.5$ GeV/c^2 and using 5.1 fb^{-1} of integrated luminosity, is $\sigma_{t\bar{t}} = 7.40 \pm 0.58$ (stat) ± 0.63 (syst) ± 0.45 (lumi); the result in the b-tag sample (4.8 fb^{-1}) is $\sigma_{t\bar{t}} = 7.25 \pm 0.66$ (stat) ± 0.47 (syst) ± 0.44 (lumi)[9].

3 The Lepton + Jets Channel

With a branching ratio of about 30% and the presence of at least one high-p_T lepton in the final state, the lepton + jets is considered the golden channel in the top quark measurements. The main physics background source is W+jets production, while QCD production is a source of instrumental background when a jet is misidentified as a lepton.

As for the dilepton case, also in the lepton+jets channel the precision of $t\bar{t}$ cross section measurements is limited by the systematic uncertainties. One of the main sources is the estimate of the integrated luminosity, due to the uncertainty in the inclusive $p\bar{p}$ theoretical cross section and in the acceptance of the luminosity monitors. CDF removes this uncertainty measuring the $t\bar{t}$ cross section relative to the inclusive $Z/\gamma* \to ll$ cross section, and multiplying this ratio by the theoretical $Z/\gamma* \to ll$ value σ_Z^{th}. In this way the 6% experimental uncertainty on the integrated luminosity is substituted by the 2% uncertainty on σ_Z^{th}. This technique has been applied for the first time to two different $t\bar{t}$ cross section measurements by CDF, one based on b-tagging and

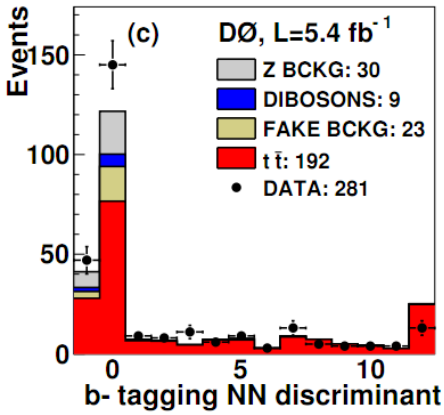

Figure 1: Expected and observed distributions for the smallest b-tagging NN discriminant outputs of the two leading jets for the $e\mu$ + 2 jets channel.

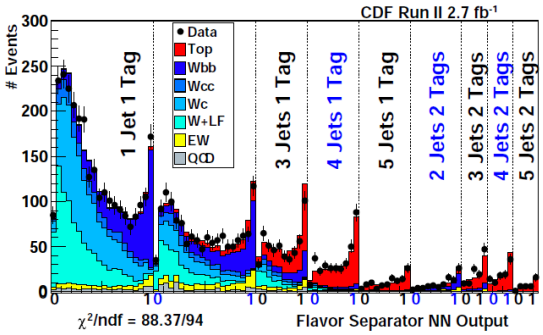

Figure 2: The data and best fit for the flavor separator distribution for samples defined by the number of jets and number of tags.

the other on a topological selection relying on a NN which exploits the kinematic properties of the event. The basic lepton+jets event selection is common to the two analyses and requires one central well identied high-p_T e or μ ($p_T > 20$ GeV), large amount of missing transverse energy ($\not\!\!E_T > 25$ GeV) and the presence of at least three central central jets with $E_T > 20$ GeV. In the b-tagging measurement, to further reduce background, an additional requirement is placed on the scalar sum H_T of the transverse energy of the lepton, $\not\!\!E_T$, and jets ($H_T > 230$ GeV). The b-tagging analysis, based on a data sample of 4.3 fb^{-1}, extracts the $t\bar{t}$ cross section from a likelihood fit; the other, based on 4.6 fb^{-1} of data, fits the NN output. The two measurements, combined using a best linear unbiased estimate method, give a $t\bar{t}$ cross section value $\sigma_{t\bar{t}} = 7.70 \pm 0.52$ (stat+syst+theory) pb for $m_t = 172.5$ GeV/c^2 [10]. The relative precision of about 7% makes this result the most precise $t\bar{t}$ cross section measurement up to date.

In the lepton+jets analysis, after requiring the events to have at least one b-tagged jet, the main source of background comes from W boson production with associated jets from heavy flavor (HF). This background is theoretically difficult and a source of systematic uncertainty. To reduce it, CDF constrains it with the data: a NN flavour separator, trained to discriminate $t\bar{t}$ signal from W + HF and W + light flavour (LF) backgrounds, is used to build templates for subsamples of data with different number of jets and b-tags (see fig. 2). A simultaneous fit for $\sigma_{t\bar{t}}$, W + HF and W + LF fractions and systematic uncertainties (included in the likelihood function as nuisance parameters), returns the cross section value of $\sigma_{t\bar{t}} = 7.64 \pm 0.57$ (stat+syst) ± 0.45 (lumi)[11], for $m_t = 175$ GeV/c^2 and on 2.7 fb^{-1} of data, with a relative precision of about 9%. This technique reduces the uncertainty of about 21% and the precision of the result could be further improved in the future measuring the ratio to the $Z/\gamma* \to ll$ cross section.

The same precision, but with a different technique, is obtained by D0 in the lepton+jets channel on 5.3 fb^{-1} of integrated luminosity. The data sample is splitted in sub-samples according to the number of jets and b-tags and a likelihood function is build multiplying discriminating distributions defined in the different samples. In the samples with high jet multiplicity and at least two b-tagged jets, which have high signal to background ratio (S/B), the distribution of the number of b-tagged jets is considered. In the low S/B samples, with none or only one b-tagged jet, a discriminant based on kinematic variables is used. The sample with exactly two jets, of which at least one b-tagged, is used to extract the W+HF fraction, as it is mainly composed by W+HF events. The systematic uncertainties are incorporated in the likelihood fit as nuisance parameters. The result, for $m_t = 172.5$ GeV/c^2, is $\sigma_{t\bar{t}} = 7.78\ ^{+0.77}_{-0.64}$ pb [12], with a relative precision

of about 9%.

3.1 Differential Cross Section Measurement

Thanks to the good S/B ratio and the high statistic samples, the lepton+jets final state is ideal to study the $t\bar{t}$ cross section as a function of selected top kinematic variables. Measurements of differential cross sections in the $t\bar{t}$ system test pQCD for heavy-quark production, and can constrain potential physics beyond the SM. CDF performs a measurement of the $t\bar{t}$ differential cross section with respect to the $t\bar{t}$ invariant mass, $\frac{\delta\sigma}{\delta M_{t\bar{t}}}$, on 2.7 fb^{-1} of integrated luminosity. After a standard lepton+jets selection, the $t\bar{t}$ invariant mass is reconstructed using the four-vectors of the b-tagged jet and the three remaining leading jets in the event, the lepton and the $\not\!\!E_T$. After subtracting the background processes, the distortions in the reconstructed distribution due to detector effects, object resolutions and geometric and kinematic acceptance are corrected for through a regularized unfolding technique. From the unfolded distribution, the $t\bar{t}$ differential cross section $\frac{\delta\sigma}{\delta M_{t\bar{t}}}$ is extracted and its shape is compared with the SM and found in good agreement [13].

D0 instead studies the dependence of the $t\bar{t}$ production cross section on the p_T of the top on 1 fb^{-1} of data. A constrained kinematic fit to the $t\bar{t}$ final state, which takes into account the unreconstructed neutrino and finite experimental resolution, is used to associate leptons and jets with individual top quarks. The reconstructed p_T spectrum is subsequently corrected for effects of finite experimental resolution, based on a regularized unfolding method using a migration matrix between the reconstructed and parton p_T derived from simulation. The resulting $\frac{\delta\sigma}{\delta p_T}$ distribution (see fig. 3) shows good agreement with results from NLO and NNLO pQCD calculations and from different MC event generators (MC@NLO, Pythia, Alpgen) [14].

These results, unlike the inclusive cross section results, are still limited by statistics and will benefit from the additional Tevatron data.

3.2 Final States with τ

The lepton+jets analysis described so far are also sensitive to the W decaying into τ lepton, if the τ decays into e or μ. Final states with a τ decaying into charged and neutral pions, which is difficult to distinguish from a generic jet, are treated separately. The measurement of the $t\bar{t}$ cross section in the τ + jets channel is important as, for example, a charged Higgs would preferably decay into a τ for large $\tan\beta$ value, thus enhancing the $t\bar{t}$ cross section in this final state.

D0 has a dedicated analysis to measure $t\bar{t}$ cross section in the τ+jets final state. Hadronically decaying τs are distinguished from fake ones by means of NNs. Another NN is trained to separate $t\bar{t}$ from QCD and W+jets background and its output is fitted to measure $\sigma_{t\bar{t}} \times BR(\tau + jets)$ $= 0.60^{+0.23}_{-0.22}(stat)^{+0.15}_{-0.14}(syst) \pm 0.04(lumi)$ pb. Using the theoretical cross section for $m_t = 170$ GeV/c^2, the measured BR is $0.074\ ^{+0.029}_{-0.027}$, in agreement with SM [15].

At CDF instead, two analysis measure the $t\bar{t}$ cross section in the final state with $\not\!\!E_T$ and high jet multiplicity: the idea is to focus on the $\not\!\!E_T$ from the neutrino associated to the W leptonic decay, instead of the lepton, thus being sensitive to leptonic W decays regardless of the lepton type. The first analysis selects events with more than four jets, of which at least one b-tagged. A NN is used to separate the $t\bar{t}$ signal from the background, mainly composed by QCD multijet events (see fig. 4). The cross section value is extracted from the sample of events with high NN output value. After the kinematic selection, about 40% of the sample is composed by τ+jets events. The resulting cross section value is $\sigma_{t\bar{t}} = 7.99 \pm 0.55$ (stat) $\pm$ 0.76 (syst) $\pm$ 0.46 (lumi) pb for $m_t = 172.5$ GeV/c^2 [16]. The second analysis, performed on 5.7 fb -1 of data, requires only 2 (3) jets, of which 1 (2) b-tagged, and extracts the $t\bar{t}$ cross section value by means of a

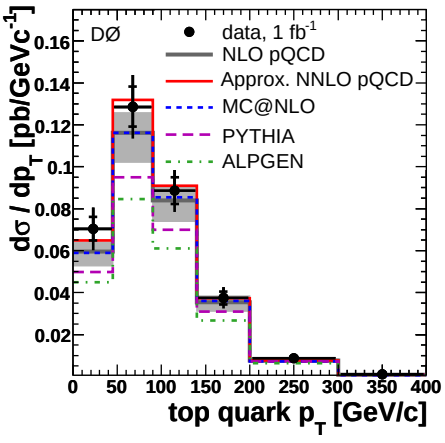

Figure 3: Inclusive $\frac{\delta\sigma}{\delta p_T}$ for $t\bar{t}$ production in data compared with expectations from NLO, approximate NNLO pQCD calculations and several event generators.

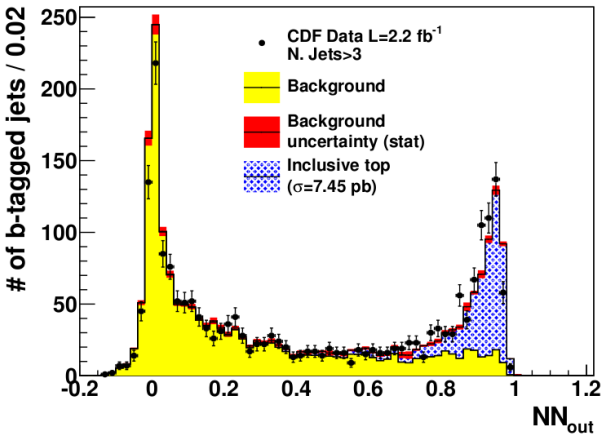

Figure 4: Neural network output distribution of observed and predicted number of b-tagged.

binned likelihood fit on the output of the NN trained to separate signal from background. The resulting cross section, for $m_t = 172.5$ GeV/c^2, is $\sigma_{t\bar{t}} = 7.12\ ^{+1.20}_{-1.12}$ pb [17]. This measurement is important as this final state is a background to SM Higgs searches in the low mass region.

4 The All-hadronic Channel

The all-hadronic channel has the highest branching ratio ($\sim 44\%$), but suffers from the largest background contribution due to QCD multijet events, which overwhelms the signal by three orders of magnitude. The experimental signature of this channel is characterized by the presence of six or more high E_T jets, two of which originate from b-quarks.

The most precise measurement in this channel is from CDF, made on a data sample corresponding to 2.9 fb^{-1} of integrated luminosity. After the application of a specific topological and kinematic NN based selection together with the b-tagging requirement, a constrained fitting technique is used to simultaneously measure the top quark mass and the jet energy scale reconstructing, event by event, the top and the W masses. The minimization returns also the number of $t\bar{t}$ events in the sample, from which the cross section is extracted. The result, $\sigma_{t\bar{t}} = 7.2 \pm 0.5$ (stat) $\pm$ 1.0 (syst) $\pm$ 0.4 (lumi) pb, is independent from the value of the top mass and has a relative precision of about 18% [18].

In the same channel, D0 separates $t\bar{t}$ signal from background building a likelihood discriminant. The observables input to the likelihood describe kinematic features of the event, such as the centrality C (scalar sum of jet p_T divided by the sum of jet energies) or the ratio of the dijet mass of the two leading b-tagged jets to the total mass of all the jets, and topological ones, such has the eigenvalues of the momentum tensor or the p_T-weighted average of the rapidities of the two leading b-tagged jets. The number of signal events is extracted by means of a fit of the likelihood output. For $m_t = 175$ GeV/c^2 and on 1 fb^{-1} of data, the measured cross section is $\sigma_{t\bar{t}} = 6.9 \pm 1.3$ (stat) $\pm$ 1.4 (syst) $\pm$ 0.4 (lumi), with a relative precision of 28% [19].

5 Conclusions

We have presented the most recent results of $t\bar{t}$ cross section measurements performed at the Tevatron. They are summarized in fig. 5 and 6 for CDF and D0 experiments respectively. $t\bar{t}$

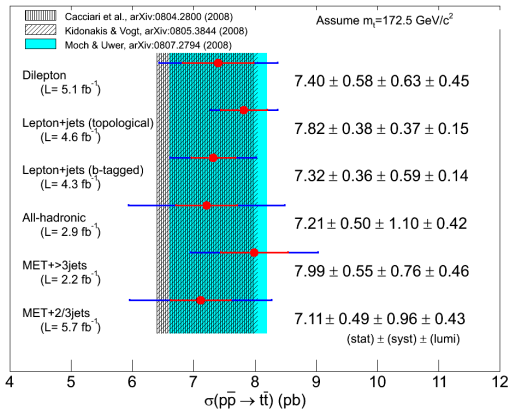

Figure 5: Summary of most recent CDF $t\bar{t}$ cross section measurements.

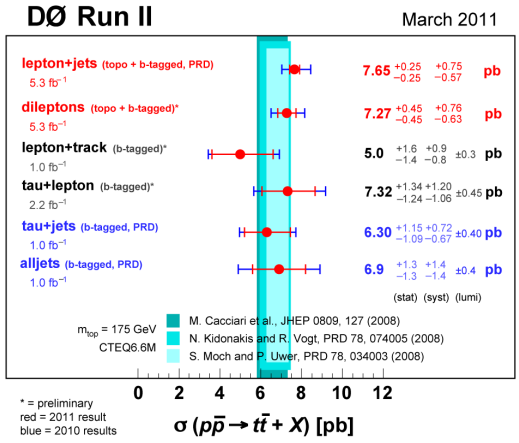

Figure 6: Summary of most recent D0 $t\bar{t}$ cross section measurements.

cross section has been measured in all possible decay channels, with precision comparable to the theoretical one. These measurements, which are all in good agreement with SM predictions, are important as tests of pQCD calculations and to precisely determine the background to new physics searches. Thanks to the high statistic samples and the use of very efficient multivariate analysis techniques, the precision of the results is currently limited by the systematic uncertainties: both collaborations are working to understand them better and reduce them by means of constraints to the data.

References

1. T. Aaltonen *et al.* (CDF Collab), Phys. Rev. Lett. **74**, 2626 (1995); V. M. Abazov *et al.* (D0 Collab), Phys. Rev. Lett. **74**, 2632 (1995).
2. N. Kidonakis, arXiv:1009.4935v2 [hep-ph] (2010); U. Lagenfeld, S. Moch, and P. Uwer, Phys. Rev. D **80**, 054009 (2009).
3. V. M. Abazov *et al.* (D0 Collab), arXiv:1104.2887 [hep-ex], Submitted to Phys. Lett. B.
4. C. T. Hill, Phys. Lett. B **266**, 419 (1991); T. Aaltonen *et al.* (CDF Collab), Phys. Rev. Lett. **100**, 231801 (2008).
5. R. Dermišek and J. F. Gunion, Phys. Rev. D **79**, 055014 (2009).
6. D. Acosta *et al.* (CDF Collab), Phys. Rev. D **71**, 052003 (2005).
7. V. M. Abazov *et al.* (D0 Collab), Nucl. Instrum. Meth. Phys. Res. A **620** , 490 (2010).
8. V. M. Abazov *et al.* (D0 Collab), arXiv:1105.5384 [hep-ex], submitted to Phys. Lett. B.
9. T. Aaltonen *et al.* (CDF Collab), CDF Conference Note 10163 (2010).
10. T. Aaltonen *et al.* (CDF Collab), Phys. Rev. Lett. **105**, 012001 (2010).
11. T. Aaltonen *et al.* (CDF Collab), CDF Public Note 10427 (Submitted to PRL).
12. V. M. Abazov *et al.* (D0 Collab), arXiv:1101.0124v1 [hep-ex].
13. T. Aaltonen *et al.* (CDF Collab), Phys. Rev. Lett. **102** 222003 (2009).
14. V. M. Abazov *et al.* (D0 Collab), Phys. Lett. B **693**, 515 (2010).
15. V. M. Abazov *et al.* (D0 Collab), Phys. Rev.D **82**, 071102 (2010).
16. T. Aaltonen *et al.* (CDF Collab), arXiv:1105.1806v1 [hep-ex], submitted to Phys. Rev. D.
17. T. Aaltonen *et al.* (CDF Collab), Conference Note 10237.
18. T. Aaltonen *et al.* (CDF Collab), Phys. Rev. D **81**, 052011 (2010).
19. V. M. Abazov *et al.* (D0 Collab), Phys. Rev. D **82**, 032002 (2010).

Top Quark Mass Measurements at the Tevatron

Zhenyu Ye (for CDF and DØ collaborations)
Fermilab, Batavia 60510, U.S.A.

We report the latest results on the top-quark mass and on the top-antitop mass difference from the CDF and DØ collaborations using data collected at the Fermilab Tevatron $p\bar{p}$ collider at $\sqrt{s} = 1.96$ TeV. We discuss general issues in top-quark mass measurements and present new results from direct measurements and from top-pair production cross-section. We also report new results on the top-antitop mass difference.

1 Introduction

The observation of the top quark in 1995 [1] confirmed the existence of the six quarks in three generations of fermions expected in the standard model (SM) of particle interactions. The large mass of the top quark (m_t), corresponding to a Yukawa coupling to the Higgs boson equal to 1 within the current uncertainties, suggests a special role for the top quark in the breaking of electroweak symmetry. It is therefore not surprising that the precise determination of the mass of the top quark has received great attention. The interest in the top-quark mass also arises from the constraint imposed on the mass of the Higgs boson (m_H) from the relationship among the values of m_t, m_H, and the SM radiative corrections to the mass of the W boson (m_W) [2]. We report the latest Tevatron results on the top-quark mass from direct measurements in section 2, and those from top-pair production cross-section in section 3.

The SM is a local gauge-invariant quantum field theory conserving CPT invariance. In the above measurements we assume the top and antitop quarks have the same mass since a difference in the mass of a particle and its antiparticle would constitute a violation of CPT invariance. Because of its mass, the lifetime of the top quark is much shorter than the time-scale of hadronization. The top quark can decay before interacting, making it the only quark whose characteristics can be studied in isolation. Thus the top quark provides a unique opportunity to measure directly the mass difference between a quark and its antiquark. We present results on the top-antitop mass difference ($\Delta M = M_t - M_{\bar{t}}$) in section 4.

2 Direct Measurements of Top-Quark Mass

Direct measurements of the top-quark mass have been performed in the dilepton ($t\bar{t} \to l^+\nu_l l^-\bar{\nu}_l b\bar{b}$), lepton+jets ($t\bar{t} \to l\nu_l q\bar{q}'b\bar{b}$) and all hadronic ($t\bar{t} \to q\bar{q}'q''\bar{q}'''b\bar{b}$) channels [a]. Events are selected after requiring there are 2, 1 or 0 high transverse momentum (p_T) leptons and at least 2, 4 or 6 high p_T jets in the dilepton, lepton+jets or all hadronic channel, respectively, and requiring large missing transverse momentum ($\not\!\!p_T$) in the dilepton and lepton+jets channels. A requirement on

[a] Here $l = e$, μ.

the minimum number of jets identified as b-quark jets is often applied in the lepton+jets and all hadronic channels. After putting additional kinematic cuts to further suppress background contribution, the remaining background is dominated by the contribution from Z/γ^*+jets, W+jets, or multijet production [4].

Two approaches are most often used in direct measurements of the top-quark mass. One approach is the so-called matrix element (ME) method. It is based on the likelihood to observe a sample of selected events in the detector. The likelihood is calculated as a function of m_t using theoretically predicted differential cross-sections and experimentally determined detector resolutions. An integration is performed over all possible momentum configurations of the final state particles with transfer functions that relates an assumed final-state momentum configuration to the measured quantities in the detector. The other approach is the template method, which is based on a comparison of Monte Carlo (MC) templates for different assumed values of m_t with distributions of kinematic quantities measured in data. In both approaches m_t and its uncertainty extracted from data are corrected by calibration curves obtained from MC pseudo-experiments. The ME measurement requires significantly much more computation time than a template measurement, but has a superior performance in terms of the measurement statistical uncertainty, and has consistently provided the single best result for the m_t measurements.

In direct top-quark mass measurements, the dominant contribution to the total uncertainty comes from the uncertainty of the jet energy scale (JES). Typical JES uncertainties at CDF and DØ are about 2%, which could lead to an uncertainty of about 2 GeV in the measured m_t. One way to get around this is to use kinematic variables that are insensitive to the JES, such as lepton p_T. Unfortunately in these cases the sensitivity of the measurements to m_t is also reduced, leading to a much larger statistical uncertainty in the measured m_t [5]. A different approach, the so-called *in situ* JES calibration, has been developed for the lepton+jets and all hadronic channels. Here a global factor on the JES is constrained by using the two jets produced from hadronic W decay and the well-measured m_W value. The uncertainty on m_t due to the JES uncertainty can be reduced by a factor of 2 or more by using the *in situ* JES calibration, as reported in recent measurements.

Another challenge in direct top-quark mass measurements comes from the jet-parton assignment. For example, most measurements with the template method use the reconstructed top-quark and W masses to build the MC templates and compare with data. In order to be able to reconstruct the top-quark and W one has to know which jet comes from which parton. In the lepton+jets channel with 4 quarks in the final state, the number of jet-parton permutations that need to be considered is 12. This number can be as high as 180 in the all hadronic channel. By requiring one or more jets that are identified as b-quark jets, not only the background contribution is reduced, the number of jet-parton permutations is also greatly reduced. Another approach to reduce the number of possible jet-parton permutations is based on kinematic fitters, which compare the difference between the measured kinematic variables and expected ones with the measurement uncertainties. Only the best jet-parton permutation(s) determined by the kinematic fitter is considered. Finally one can also combine the results from all the jet-parton permutations using the likelihood of each permutation being the correct jet-parton assignment.

The two most recent DØ results are both based on the ME method. The first one is obtained in the lepton+jets channel using 3.6 fb^{-1} of data [6]. Exactly 4 jets in one event is required, with at least one of the jets being identified as a b-quark jet. The dominate background contribution is W+jets production, which is modeled using ALPGEN MC generator interfered with PYTHIA for parton showering and hadronization. The measurement combines an *in situ* JES calibration with the standard JES derived in studies of γ+jet and dijet event. Compared to previous measurements at DØ, a major improvement in this new measurement is the significant reduction of the uncertainty associated with the modeling of differences in the calorimeter response to b-quark and light-quark jets originating from the introduction of a new flavor-dependent jet energy

response correction. The measurement gives $m_t = 174.9 \pm 0.8(stat) \pm 0.8(JES) \pm 1.0(syst)$ GeV. This is the best top-quark mass measurement at DØ. The second result comes from the dilepton channel using 5.4 fb^{-1} of data [7]. Exactly 2 jets in one event is required without explicit b-quark jet identification. The dominant background contribution comes from Z/γ^*+jets production. An *in situ* JES calibration is not applied since there is no hadronically decayed W. Thus the dominant uncertainty is coming from JES systematic uncertainties. The measurement gives $m_t = 174.0 \pm 1.8(stat) \pm 2.4(syst)$ GeV. This is the best top-quark mass measurement in the dilepton channel in the world.

The two most recent CDF results both use the template method with *in situ* JES calibrations. The first one is obtained in the all hadronic channel using 5.8 fb^{-1} of data [8]. The event selection uses a Neural Network (NN) trained on $t\bar{t}$ signal MC. Exactly 6 to 8 jets in an event are required with at least one of them being identified as b-quark jet. The background is dominated by multijet production, and is modeled using data and b-quark jet tag rate obtained from events with exactly 5 jets. A kinematic fitter is used to reconstruct the top-quark and W masses, which are then used to build the MC templates to compare with data. The measurement gives m_t $= 172.5 \pm 1.4(stat) \pm 1.0(JES) \pm 1.1(syst)$ GeV. This is the second best measurement at CDF. The second new CDF result comes from the MET+jets channel using 5.7 fb^{-1} of data [9]. Events are collected by a multijet trigger, and are required to have 4 to 6 jets, 0 lepton, and large $\not\!\!p_T$. NN and b-quark jet identification are used to suppress background contribution. It is found in MC studies that most of the signal events come from the $t\bar{t}$ lepton+jets decay channel, in which the lepton escapes the detection or is a τ lepton which decays hadronically. The measurement gives $m_t = 172.3 \pm 1.8(stat) \pm 1.5(JES) \pm 1.0(syst)$ GeV. It provides sensitivity complementary to the other top-quark mass measurements.

The latest combination of the direct top-quark mass measurements from the Tevatron gives the result $m_t = 173.3 \pm 0.6(stat) \pm 0.9(syst)$ GeV [3], corresponding to a relative uncertainty of 0.6%. As the uncertainty is dominated by the systematic uncertainty, programs are on-going to understand better the sources of the systematic uncertainties in order to achieve an better accuracy. This Tevatron combination was performed in July 2010, and did not include any of the above mentioned results nor the updated best CDF result in the lepton+jets channel using the ME method [10]. It is expected that with the full Tevatron RunII data of about 10 fb^{-1}, the total uncertainty in the measured m_t will be below 1.0 GeV. More direct top-quark mass results from CDF and DØ can be found at public web pages [11].

3 Determination of Top-Quark Mass from Top Pair Production Cross Section

Beyond Leading Order (LO) Quantum Chromodynamics (QCD), the mass of the top quark is a parameter depending on the renormalization scheme. The definition of mass in field theory can be divided into two categories: (i) driven by long-distance behavior, which corresponds to the pole-mass scheme, and (ii) driven by short-distance behavior, which for example is represented by the $\overline{\rm MS}$ scheme. In the direct measurements of the top-quark mass, the quantity measured in data is calibrated w.r.t. assumed top-quark mass values in MC, thus corresponds to the scheme in the MC simulation. The top quark mass scheme in MC has not been directly connected with the pole or $\overline{\rm MS}$ scheme, although it has been argued that the top quark mass in MC scheme should be close to the pole mass [12].

DØ has updated the study on determining the top-quark pole mass and $\overline{\rm MS}$ mass through top pair production cross section ($\sigma_{t\bar{t}}$) [13]. In this study, a likelihood $L(m_t)$ is calculated by comparing the measured $\sigma_{t\bar{t}}$ in the lepton+jets channel using 5.3 fb^{-1} of data with next-to-leading-order (NLO) or next-next-to-leading-order (NNLO) calculations:

$$L(m_t) = \int f_{\rm exp}(\sigma|m_t)[f_{\rm scale}(\sigma|m_t) \otimes f_{\rm PDF}(\sigma|m_t)], \quad (1)$$

where f's are probability functions of $\sigma_{t\bar{t}}$ and m_t, determined from DØ measured $\sigma_{t\bar{t}}$ with weak dependence on m_t in MC through acceptance and detection efficiency effects ($f_{\rm exp}$), or from theoretical calculations using top quark pole mass or $\overline{\rm MS}$ mass with renormalization and PDF uncertainties ($f_{\rm scale} \otimes f_{\rm PDF}$). The m_t extracted from $L(m_t)$, under the assumption m_t in MC equal to the top quark pole mass, is found to agree with the average value of m_t from the Tevatron combination [3], while the m_t extracted assuming m_t in MC equal to the top quark $\overline{\rm MS}$ mass is found to be different from the average Tevatron value. The uncertainty in such extracted m_t, which is dominated by systematic uncertainties in the measured $\sigma_{t\bar{t}}$, is quite large to make a more quantitative statement.

4 Measurements of Top-Antitop Quark Mass Difference

DØ published the first measurement of the top-antitop mass difference using a ME method on 1 fb^{-1} of data, and found $\Delta M = 3.8 \pm 3.4(stat) \pm 1.2(syst)$ GeV [14]. The top and antitop quark masses (M_t and $M_{\bar{t}}$) are measured independently. Recently, CDF has also contributed a measurement using a template method on 5.6 fb^{-1} of data, and found $\Delta M = -3.3 \pm 1.4(stat) \pm 1.0(syst)$ GeV [15]. The result deviates from the expectation of CPT invariance, $\Delta M = 0$ GeV, at about 2σ level. In the CDF measurement, $M = (M_t + M_{\bar{t}})/2$ is constrained to be 172.5 GeV. DØ has updated the measurement using 3.6 fb^{-1} of data, and found $\Delta M = 0.9 \pm 1.8(stat) \pm 0.9(syst)$ GeV [16]. The result is consistent with the expectation of CPT invariance. The top-antitop quark mass difference measurements are dominated by statistical uncertainty. The uncertainty is expected to be improved with the full Tevatron RunII data.

References

1. S. Abachi *et al.* (D0 Collaboration), *Phys. Rev. Lett.* **74**, 2632 (1995); F. Abe *et al.* (CDF Collaboration), *Phys. Rev. Lett.* **74**, 2626 (1995).
2. The ALEPH, CDF, D0, DELPHI, L3, OPAL, SLC Collaborations, the LEP Electroweak Working Group, the Tevatron Electroweak Working Group, and the SLD electroweak and heavy flavour groups, arXiv:hep-ex/1012.2367v2, (2011); LEP Electroweak Working Group, `http://lepewwg.web.cern.ch/LEPEWWG/`.
3. The Tevatron Electroweak Working Group, arXiv:hep-ex/1007.3178v1, (2010); Tevatron Electroweak Working Group, `http://tevewwg.fnal.gov`.
4. See Silvia Amerio's contribution in the same conference for details.
5. CDF Collaboration, CDF public note 9881 (2009).
6. D0 Collaboration, accepted by *Phys. Rev.* D, arxiv:1105.6287 (2011).
7. D0 Collaboration, accepted by *Phys. Rev. Lett.*, arxiv:1105.0320 (2011).
8. CDF Collaboration, CDF public note 10456 (2011).
9. CDF Collaboration, CDF public note 10433 (2011).
10. CDF Collaboration, *Phys. Rev. Lett.* **105**, 252001 (2010).
11. D0 Collaboration, `http://www-d0.fnal.gov/Run2Physics/top/top_public_web_pages/top_public.html#mass`; CDF Collaboration, `http://www-cdf.fnal.gov/physics/new/top/public_mass.html`.
12. S. Fleming, A. H. Hoang, S. Mantry and I. W. Stewart, *Phys. Rev.* D **77**, 074010 (2008).
13. D0 Collaboration, accepted by *Phys. Lett.* B, arXiv:1104.2887 (2011).
14. D0 Collaboration, *Phys. Rev. Lett.* **103**, 132001 (2009).
15. CDF Collaboration, *Phys. Rev. Lett.* **106**, 152001 (2011).
16. D0 Collaboration, submitted to *Phys. Rev.* D, arxiv:1106.2063 (2011).

RECENT RESULTS ON TOP PHYSICS AT ATLAS

M. CRISTINZIANI
on behalf of the ATLAS Collaboration
Physikalisches Institut, Universität Bonn, Nussallee 12, 53127 Bonn, Germany

During the 2010 pp run of the Large Hadron Collider at $\sqrt{s} = 7$ TeV, a substantial data sample of high p_{T} triggers, 35 pb^{-1}, has been collected by the ATLAS detector, corresponding to about 2,500 produced top-quark pair events containing at least one lepton (e or μ) in the final state. Measurements of the top-quark pair production cross-section, the top mass, the W helicity fractions in top-quark decays and studies of single-top quark production and top-quark pair production with anomalous missing transverse energy are presented.

1 Introduction

Top-quark measurements are of central importance to the LHC physics programme. The production of top-quark pairs in pp collisions is a process which is situated at the boundary between the Standard Model (SM) and what might lie beyond it. Within the SM, top quarks are predicted to almost always decay to a W-boson and a b-quark. The decay topologies are determined by the decays of the W-boson. In pair-produced top-quarks the single-lepton and dilepton modes, with branching ratios of 37.9% and 6.5% respectively, give rise to final states with one or two leptons (electrons or muons), missing transverse energy ($E_{\mathrm{T}}^{\mathrm{miss}}$) and jets, some with b-flavour.

2 Top quark pair production cross-section $\sigma_{t\bar{t}}$

The measurement of $\sigma_{t\bar{t}}$ is a milestone for early LHC physics. Within the SM the $t\bar{t}$ production cross-section at $\sqrt{s} = 7$ TeV is calculated to be 165^{+11}_{-16} pb at approximate NNLO[1] for a top-quark mass of 172.5 GeV. A precise determination of $\sigma_{t\bar{t}}$ tests these perturbative QCD predictions. First measurements of $\sigma_{t\bar{t}}$ at the LHC have been reported by ATLAS[2] and CMS[3] with 3 pb^{-1}. Here, approximately ten times more data have been analysed.

2.1 Dilepton channel

The cross-section in the dilepton channel is extracted with a cut-and-count method[4]. Candidate events are selected by requiring two opposite-signed high-p_{T} leptons in the ee, $\mu\mu$ and $e\mu$ topologies, and at least two jets. The background contribution from Drell-Yan production is suppressed by requiring for same-flavour events large $E_{\mathrm{T}}^{\mathrm{miss}}$ and for $e\mu$ events large H_T, the scalar sum of jet and lepton transverse energies. Remaining Drell-Yan events and background from fake leptons are estimated with data-driven methods. Across the three channels 105 events are selected with an expected S/B ratio of 3.6. The cross-section is extracted with a profile likeli-

hood technique, with a simultaneous fit to the three channels and taking into account systematic uncertainties. This results in $\sigma_{t\bar{t}} = 174 \pm 23$ (stat.)$^{+19}_{-17}$ (syst.) ± 7 (lumi.) pb.

Additional studies are performed to corroborate this measurement: a technique that normalizes the $t\bar{t}$ signal yield to the measured rate of Z-boson decays; a two-dimensional template shape fit using the $E_{\mathrm{T}}^{\mathrm{miss}}$ vs N_{jets} variables to simultaneously measure the production cross-sections of the $t\bar{t}$, WW and $Z \to \tau\tau$ final states; and a cross-section measurement that requires at least one b-tagged jet and a looser kinematic selection to optimize the S/B ratio. All measurements are in good agreement with each other.

2.2 Single-lepton channel

Two complementary measurements have been performed in the single-lepton channel. In the first measurement no explicit identification of secondary vertices inside jets (b-tagging) is performed [5]. The main background consists of W+jet events and QCD multi-jet events, where one jet mimics a reconstructed lepton. The latter are particularly difficult to simulate correctly and are thus estimated using data-driven techniques. Selected events are classified according to lepton flavour (2009 candidate events observed in μ+jets and 1181 in e+jets) and according to jet multiplicity: exactly 3 jets or ≥ 4 jets. Three variables that exploit the different kinematic behaviour of $t\bar{t}$ and the W+jets background events are identified and used in a multivariate likelihood fit to extract $\sigma_{t\bar{t}} = 171 \pm 17$ (stat.)$^{+20}_{-17}$ (syst.) ± 6 (lumi.) pb. The main systematic uncertainties are due to the limited knowledge of the jet energy scale and reconstruction efficiency as well as the amount of initial and final state radiation.

A second method exploits the b-tagging capabilities, albeit making use of a simple and robust tagging algorithm with a modest rejection factor [6]. A multivariate likelihood discriminant is constructed using template distributions of four variables, among which the average of the weights of the most significant b-tags. Here, data are further split with an additional jet-bin (3, 4 or ≥ 5 jets). A profile likelihood technique is used to extract $\sigma_{t\bar{t}}$ and constrain the systematic effects from data. The result is $\sigma_{t\bar{t}} = 186 \pm 10$ (stat.)$^{+21}_{-20}$ (syst.) ± 6 (lumi.)pb, where the systematic uncertainties are dominated by the uncertainties in the b-tagging algorithm calibration from data and the heavy flavour fraction in W+jets events. Cross-check measurements are performed with kinematic fits of the reconstructed top mass and cut-and-count methods and are found to be in good agreement with this result.

2.3 Combination

The most precise cross-section measurements in the dilepton and single-lepton channels are combined, taking into account correlated systematic uncertainties [7]. The result has a total uncertainty of 10%, $\sigma_{t\bar{t}} = 180 \pm 9$ (stat.) ± 15 (syst.) ± 6 (lumi.) pb, and is in excellent agreement with the SM prediction as shown in Figure 1 (right).

3 Single-top production

The observation of electroweak production of single-top quarks has been reported by the CDF and D0 collaborations in 2009. This final state provides a direct probe of the W-t-b coupling and is sensitive to many models of new physics. The measurement of the production cross-section determines the magnitude of the quark mixing matrix element V_{tb} without assumptions on the number of quark generations. With the available data sample searches for single-top quark production in the t- and Wt-channels are performed [8].

The t-channel search is based on the selection of events with exactly one identified lepton, jets and $E_{\mathrm{T}}^{\mathrm{miss}}$. In a cut-based analysis a reconstructed three-jet invariant mass compatible with m_{top} is required, as well as the leading jet to be in the forward direction. This selects 32

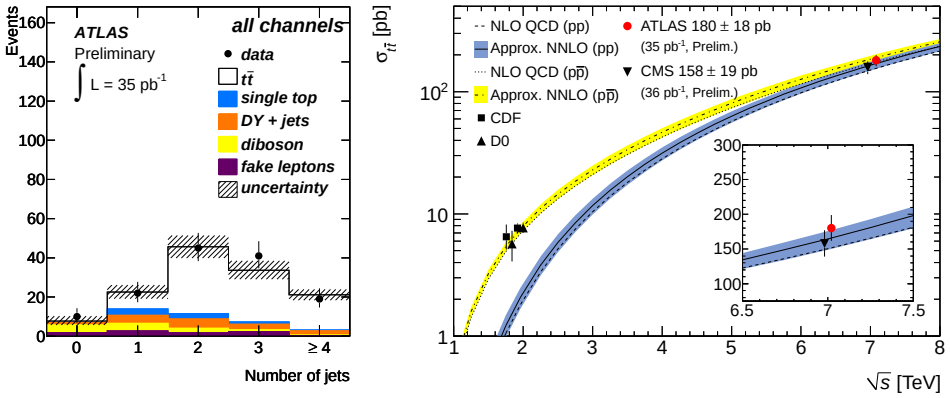

Figure 1: Selected dilepton events superimposed on expectations from simulation and data-driven estimations (left). Cross-section measurements at Tevatron and LHC compared to approximate NNLO predictions (right).

candidate events. Using data-driven methods to estimate the QCD and W+jets backgrounds, a production cross-section of $\sigma_t = 53^{+46}_{-36}$ pb is measured, which translates to an upper limit of 162 pb at 95% confidence level. A likelihood function approach is also used to cross-check the result. Both results are consistent with the SM expectation of 66 pb.

The Wt-channel analysis is based on the selection of events with either one or two leptons, jets and $E_{\mathrm{T}}^{\mathrm{miss}}$. The expected SM cross-section for this single-top process is 15 pb. A 95% confidence level limit is set on the Wt-channel production cross section of $\sigma_{Wt} < 158$ pb. In the dilepton channel, the $t\bar{t}$ background is estimated from data, by considering the one-jet bin as a control region.

4 Top quark properties

4.1 Mass

The top-quark mass, a fundamental parameter of the SM, is a source of large contributions to electroweak radiative corrections and, in conjunction with precision electroweak measurements, can be used to derive constraints on the Higgs boson mass or heavy particles predicted in SM extensions. The current world average is $m_{\mathrm{top}} = 173.3 \pm 1.1$ GeV.

The main systematic on the determination of the top-quark mass is the uncertainty in the jet energy scale (JES). Three complementary template analyses have been developed [9] that address the uncertainty due to the JES in different ways: a 2D analysis that simultaneously determines m_{top} and a global jet energy scale factor between data and predictions; a 1D analysis exploiting a kinematical likelihood fit to all decay products of the $t\bar{t}$ system; a 1D analysis which is based on the ratio between the per-event reconstructed invariant mass of the top-quark and the mass of the W-boson associated to the hadronically decaying top-quark candidate. The latter method yields a top-quark mass measurement of $m_{\mathrm{top}} = 169.3 \pm 4.0 \pm 4.9$ GeV.

4.2 W-boson polarisation in top-quark decays

The polarisation states of the W-bosons that emerge from top-quark decays are well defined in the SM, due to the $V - A$ structure of the charged current weak interactions. These can be extracted from the angular distributions of the decay products in $t \to bW \to b\ell\nu_\ell$.

In a first measurement [10], templates of the $\cos\theta^\star$ distribution are built from simulation and fitted to selected events with a single charged lepton, $E_{\mathrm{T}}^{\mathrm{miss}}$ and at least four jets, where at least one of them is b-tagged. Here $\theta^\star$ is the angle between the direction of the lepton and the reversed

momentum direction of the b quark from the top-quark decay, both boosted into the W-boson rest frame. Events are reconstructed in the single-lepton channel with a kinematic fit method. Assuming $F_R = 0$ helicity fractions $F_0 = 0.59 \pm 0.12$ and $F_L = 0.41 \pm 0.12$ are extracted. A second measurement is based on angular asymmetries constructed from the $\cos\theta^\star$ variable, the events are reconstructed with a χ^2 fitting technique and an iterative procedure is applied to correct for detector and reconstruction effects in order to recover the undistorted distribution on parton level. The helicity fractions are measured to be $F_0 = 0.65 \pm 0.15$, $F_L = 0.36 \pm 0.10$ and $F_R = -0.01 \pm 0.07$. Both results are in good agreement with the SM prediction and are used to place limits on anomalous couplings V_R, g_L and g_R that arise in new physics models.

4.3 Search for anomalous $E_{\mathrm{T}}^{\mathrm{miss}}$ in $t\bar{t}$ events

A search for anomalous $E_{\mathrm{T}}^{\mathrm{miss}}$ in the single-lepton $t\bar{t}$ final state has been performed [11]. Such a phenomenon can arise from a number of extensions of the SM, but the focus here is on a search for a pair-produced exotic top partner T with mass $m(T)$, that decays to a top-quark and a long lived neutral scalar particle A_0. The final state for such a model is identical to $t\bar{t}$, but with a large amount of $E_{\mathrm{T}}^{\mathrm{miss}}$ from the undetected A_0's. First limits from the LHC on the mass of such a particle are established, excluding $m(T) < 300$ GeV for $m(A_0) = 10$ GeV and $m(T) < 275$ GeV for $m(A_0) = 50$ GeV with 95% confidence.

5 Conclusion and Outlook

With the first 35 pb^{-1} of pp collision data collected at $\sqrt{s} = 7$ TeV in 2010, a suite of top-quark measurements has been presented by ATLAS. Some of these measurements have uncertainties that are already competitive with uncertainties of theoretical predictions. For instance, $\sigma_{t\bar{t}}$ is now measured with an accuracy at the level of 10%. With the increase of the dataset by two orders of magnitude the whole spectrum of top physics can be explored at LHC.

Acknowledgments

I wish to thank the LHC crew and the ATLAS Collaboration for the excellent data quality, the many authors and contributors of the top physics analyses shown here, Stan Bentvelsen and Wouter Verkerke for reading the manuscript and the organizers of these *Recontres* for keeping the *spirit of Moriond* alive. I also gratefully acknowledge the support of the Deutsche Forschungsgemeinschaft (DFG) through the Emmy-Noether grant CR-312/1-1.

References

1. S. Moch, P. Uwer, *Phys. Rev.* D78 (2008) 34003; U. Langenfeld, S. Moch, P. Uwer arXiv:0907.2527 [hep-ph]
2. ATLAS Collaboration, *Eur. Phys. J.* C 71 (2011) 1577
3. CMS Collaboration, *Phys. Lett.* B695 (2011) 424
4. ATLAS Collaboration, ATLAS-CONF-2011-034, http://cdsweb.cern.ch/record/1337784
5. ATLAS Collaboration, ATLAS-CONF-2011-023, http://cdsweb.cern.ch/record/1336753
6. ATLAS Collaboration, ATLAS-CONF-2011-035, http://cdsweb.cern.ch/record/1337785
7. ATLAS Collaboration, ATLAS-CONF-2011-040, http://cdsweb.cern.ch/record/1338569
8. ATLAS Collaboration, ATLAS-CONF-2011-027, http://cdsweb.cern.ch/record/1336762
9. ATLAS Collaboration, ATLAS-CONF-2011-033, http://cdsweb.cern.ch/record/1337783
10. ATLAS Collaboration, ATLAS-CONF-2011-037, http://cdsweb.cern.ch/record/1337787
11. ATLAS Collaboration, ATLAS-CONF-2011-036, http://cdsweb.cern.ch/record/1337786

MEASUREMENTS OF THE PROPERTIES OF THE TOP QUARK

O. Brandt on behalf of the CDF and D0 Collaborations
II. Physikalisches Institut, Friedrich-Hund-Platz 1,
Göttingen, Germany

We review recent measurements of the properties of the top quark: the decay width of the top quark, of spin correlations between the top and the antitop quarks in $t\bar{t}$ production, the W boson helicity in top decays, the strong colour flow in $t\bar{t}$ events, and the asymmetry of $t\bar{t}$ production due to the strong colour charge. The measurements are performed on data samples of up to 5.4 fb^{-1} of integrated luminosity acquired by the CDF and D0 collaborations in Run II of the Fermilab Tevatron $p\bar{p}$ collider at a centre-of-mass energy of $\sqrt{s} = 1.96$ TeV.

PACS 14.65.Ha – Top quarks.

1 Introduction

The pair-production of the top quark was discovered in 1995 by the CDF and D0 experiments [1] at the Fermilab Tevatron proton-antiproton collider. Observation of the electroweak production of single top quarks was presented only two years ago [2]. The large top quark mass [3] and the resulting Yukawa coupling of about 0.996 ± 0.006 indicates that the top quark could play a crucial role in electroweak symmetry breaking. Precise measurements of the properties of the top quark provide a crucial test of the consistency of the standard model (SM) and could hint at physics beyond the SM. Only a small fraction of those measurements will be presented in the following, while their full listing can be found in Refs. [4,5].

At the Tevatron, top quarks are mostly produced in pairs via the strong interaction. At the time of the conference, about 9.5 fb^{-1} of integrated luminosity per experiment were recorded by CDF and DØ, which corresponds to about 70k produced $t\bar{t}$ pairs. In the framework of the SM, the top quark decays to a W boson and a b quark nearly 100% of the time, resulting in a $W^+W^-b\bar{b}$ final state from top quark pair production. Thus, $t\bar{t}$ events are classified according to the W boson decay channels as "dileptonic", "all–jets", or "lepton+jets". More details on the channels and their experimental challenges can be found in Ref. [6], while the electroweak production of single top quarks is reviewed in Ref. [7].

2 Measurement of the decay width of the top quark

The D0 collaboration extracted the total decay width of the top quark [8], $\Gamma_t = \Gamma_{t\to Wb}/\mathcal{B}_{t\to Wb}$, from the partial decay width $\Gamma_{t\to Wb}$ measured using the t-channel cross section for single top quark production, and from the branching fraction $\mathcal{B}_{t\to Wb}$ measured in $t\bar{t}$ events using up to 2.3 fb^{-1} of integrated luminosity. This extraction is made under the assumption that the electroweak coupling in top quark production is identical to that in the decay. In this spirit, only the t-channel single top-quark production cross-section was used, since contributions from physics

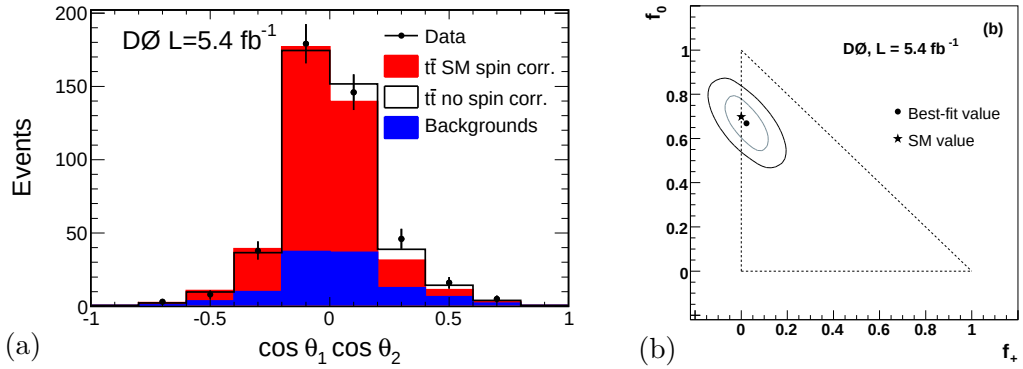

Figure 1: **(a)** The distribution in $\cos\theta_1 \cos\theta_2$ for the entire dilepton sample with a dataset of 5.4 fb^{-1} at D0. The summed $t\bar{t}$ signal with (without) NLO QCD spin correlations is shown as a red (open) histogram. **(b)** The result of the model-independent W boson helicity fit with a dataset of 5.4 fb^{-1} at D0. The ellipses indicate the 68% and 95% CL contours.

beyond the SM are expected to have different effects on t- and s-channels. Another theoretical input is the validity of next-to-leading order (NLO) calculations of $\Gamma^{\rm SM}_{t\to Wb}$ and $\sigma^{\rm SM}_{t-{\rm channel}}$, which enter the calculation as follows: $\Gamma_t = \frac{\sigma_{t-{\rm channel}}}{\mathcal{B}_{t\to Wb}} \times \frac{\Gamma^{\rm SM}_{t\to Wb}}{\sigma^{\rm SM}_{t-{\rm channel}}}$. Properly taking into account all systematic uncertainties and their correlations among the measurements of $\Gamma_{t\to Wb}$ and $\sigma_{t-{\rm channel}}$, D0 finds $\Gamma_t = 1.99^{+0.69}_{-0.55}$ GeV, which translates into a top-quark lifetime of $\tau_t = (3.3^{+1.3}_{-0.9})\times 10^{-25}$ s, in agreement with the SM expectation. This constitutes the world's most precise indirect determination of Γ_t to date. CDF has performed a direct measurement of Γ_t, and set a limit $\Gamma_t < 7.6$ GeV at 95% confidence level (CL) [9].

3 Measurement of spin correlations between top and antitop quarks

While the top quarks are unpolarised in $t\bar{t}$ production at hadron colliders, the orientation of their spins is correlated. In contrast to other quarks, this correlation is not affected by fragmentation due to the short life time of the top quark, and is thus reflected in its decay products. The spin correlation is defined as $C \equiv \frac{N_{\uparrow\uparrow}+N_{\downarrow\downarrow}-N_{\uparrow\downarrow}-N_{\downarrow\uparrow}}{N_{\uparrow\uparrow}+N_{\downarrow\downarrow}+N_{\uparrow\downarrow}+N_{\downarrow\uparrow}}$ with $-1 < C < +1$, and depends on the choice of the spin quantisation axis, which, for the measurements presented here, is defined by the direction of the incoming proton beam ("beamline axis"). D0 performed a measurement of C in the dilepton channel using 5.4 fb^{-1} of data [10] by analysing the distribution $1/\sigma_{t\bar{t}} \times {\rm d}^2\sigma_{t\bar{t}}/{\rm d}\cos\theta_1 {\rm d}\cos\theta_2 = 0.25\cdot(1 - C\cos\theta_1\cos\theta_2)$, shown in Fig. 1 (a), and found $C = 0.10 \pm 0.45$. Here, $\theta_{1,2}$ are the angles between the three-momenta of ℓ^+ (resp. ℓ^-) in the t (resp. $\bar{t}$) rest frames and the quantisation axis. CDF performed a similar measurement in the lepton+jets final states using 5.3 fb^{-1} of data [11], and found $C = 0.72 \pm 0.69$. Both measurements are in agreement with the NLO QCD prediction of $C = 0.78^{+0.03}_{-0.04}$. The above analyses are complementary to the LHC, where the gg production mechanism dominates, and a much smaller C is expected.

4 Measurement of W boson helicity in $t\bar{t}$ events

In the SM, the top quark decays into a W boson and a b quark with a probability of $> 99.8\%$, where the on-shell W boson can be in a left-handed, longitudinal, and right-handed helicity state. A NLO calculation within the SM of the corresponding helicity fractions predicts $f_- = 0.301$, $f_0 = 0.698$, and $f_+ = 4.1 \times 10^{-4}$, respectively. A significant deviation from the SM expectation would indicate a contribution from new physics. D0 has measured the f_0 and f_+ helicity fractions in dilepton and lepton+jets final states using up 5.4 fb^{-1} of data [12]. A model-independent fit to the distribution in $\cos\theta^*$, where θ^* is the angle between the three-momentum

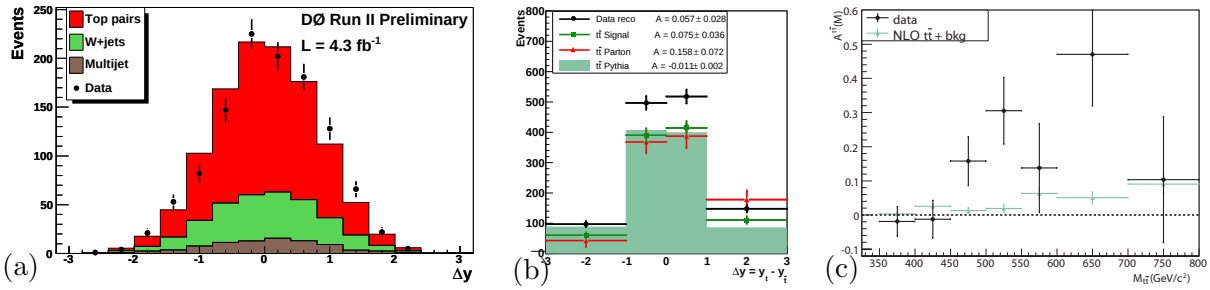

Figure 2: **(a)** The distribution in Δy for data and signal plus background fit to the discriminant with a dataset of 4.3 fb^{-1} at D0. **(b)** The distribution in Δy for all correction levels with a dataset of 5.3 fb^{-1} at CDF. The corresponding $A_{\rm fb}$ values are summarised in the legend. **(c)** The distribution in $A_{\rm fb}$ in the $t\bar{t}$ rest frame versus $M_{t\bar{t}}$ is shown for 5.3 fb^{-1} of CDF data and MCNLO $t\bar{t}$ signal plus background.

of the top quark and the down-type fermion, yields $f_0 = 0.669 \pm 0.102$ and $f_+ = 0.023 \pm 0.053$ as shown in Fig. 1 (b), in agreement with the SM expectation. CDF performed a similar model-independent measurement in dilepton events using 4.8 fb^{-1} of data, and found $f_0 = 0.78 \pm 0.21$ and $f_+ = -0.12 \pm 0.12$ [13].

5 Measurement of the strong colour flow in $t\bar{t}$ events

At leading order in α_s, the strong colour charge can be traced from final to initial state partons, i.e. final state partons originating from the same initial state parton are "colour-connected". The potential energy of this colour-connection string is released in form of hadroproduction, and can be detected in the calorimeter. This can serve to separate processes which otherwise appear similar, like e.g. the decay of the Higgs boson and $g \to b\bar{b}$ production, which correspond to a colour singlet and octet, respectively. D0 performed the first measurement of the colour representation of the hadronically decaying W bosons in $t\bar{t}$ events in the lepton+jets channel [14]. Using calorimeter-based topological observables and a dataset corresponding to 5.3 fb^{-1}, D0 finds a fraction of W bosons in colour-singlet configuration of 0.56 ± 0.42, in agreement with the SM.

6 Measurement of the strong colour charge production asymmetry in $t\bar{t}$ events

In the SM, the pair production of top quarks in $p\bar{p}$ collisions at LO is symmetric under charge conjugation. NLO calculations predict a small forward-backward asymmetry $A_{\rm fb}$ of the order of 5% in the $t\bar{t}$ rest frame, which is due to a negative contribution from the interference of diagrams for initial and final state radiation, and a (larger) positive contribution from the interference of box and tree-level diagrams. A common definition for such an asymmetry is $A_{\rm fb} \equiv \frac{N^{\Delta y>0} - N^{\Delta y<0}}{N^{\Delta y>0} + N^{\Delta y>0}}$, where $\Delta y \equiv y_t - y_{\bar{t}}$, y_t ($y_{\bar{t}}$) is the rapidity of the t ($\bar{t}$) quark, and $y = \frac{1}{2} \ln \frac{E+p_z}{E-p_z}$.

D0 measured $A_{\rm fb}$ in the $t\bar{t}$ rest frame in lepton+jets final states on a dataset corresponding to 4.3 fb^{-1} using $t\bar{t}$ event candidates fully reconstructed with a kinematic fitter, and found $A_{\rm fb} = 8\% \pm 4\%$ [15]. D0's result, shown in Fig. 2 (a), is about 2 standard deviations (SD) away from the MC@NLO [16] prediction of $1 \pm 2\%$. A similar measurement was performed by CDF in lepton+jets final states [17], where additional tests for invariance under charge and parity conjugation are carried out, and the distribution in $A_{\rm fb}$, shown in Fig. 2 (b), is corrected back to parton level. After all corrections, CDF finds $A_{\rm fb} = 16\% \pm 7\%$, which is about 1.5 SD away from the MC@NLO prediction of $6\% \pm 1\%$. CDF also investigated the dependence of $A_{\rm fb}$ on the invariant mass of the $t\bar{t}$ system, $M_{t\bar{t}}$, which is compared to the prediction of MC@NLO plus backgrounds in Fig. 2 (c). Motivated by the resolution in $M_{t\bar{t}}$, CDF measures $A_{\rm fb}$ in two bins of $M_{t\bar{t}} < 450$ GeV and $M_{t\bar{t}} > 450$ GeV. CDF finds that $A_{\rm fb} = 48\% \pm 11\%$ at parton level and

after all corrections in the $M_{t\bar{t}} > 450$ GeV bin is > 3 SD away from the NLO SM prediction of $A_{\rm fb} = 9\% \pm 1\%$. Another measurement, carried out by CDF in the dilepton channel using 5.1 fb^{-1} of data, yields $A_{\rm fb} = 42\% \pm 16\%$ parton level after all corrections [18], which is about 2.5 SD away from the SM NLO prediction. The above results indicate tension between the measurement and the NLO SM prediction. Several mechanisms originating from new physics contributions have been suggested to explain this discrepancy, however, it has been pointed out that non-vanishing and acceptance-dependent contributions at higher orders in α_s within the SM could play an important role in understanding these findings.

7 Conclusions

Several measurements of key properties of the top quark were presented, most of which are in good agreement with the SM expectations. The forward-backward asymmetry $A_{\rm fb}$ of $t\bar{t}$ production displays notable tension between the measuremnets and the SM NLO calculations. Both CDF and D0 expect to acquire about 12 fb^{-1} of data by the end of Run II of the Tevatron in September 2011, and we are looking forward to updates of the exciting measurements presented here with the full dataset.

Acknowledgments

I would like to thank my collaborators from the CDF and D0 experiments for their help in preparing this article. I also thank the staffs at Fermilab and collaborating institutions, as well as the CDF and D0 funding agencies.

References

1. F. Abe *et. al.* (CDF Coll.), Phys. Rev. Lett. **74**, 2626 (1995), S. Abachi *et. al.* (D0 Coll.), Phys. Rev. Lett. **74**, 2632 (1995).
2. T. Aaltonen *et. al.* (CDF Coll.), Phys. Rev. Lett. **103**, 092001 (2009), V. M. Abazov *et. al.* (D0 Coll.), Phys. Rev. Lett. **103**, 092002 (2009).
3. Z. Ye, these proceedings.
4. `http://www-cdf.fnal.gov/physics/new/top/public_mass.html`
5. `http://www-d0.fnal.gov/Run2Physics/WWW/results/top.htm`, `http://www-d0.fnal.gov/Run2Physics/WWW/documents/Run2Results.htm`.
6. S. Amerio, these proceedings.
7. V. Bazterra, these proceedings.
8. V. M. Abazov *et. al.* (D0 Coll.), Phys. Rev. Lett. **106**, 022001 (2011).
9. T. Aaltonen *et. al.* (CDF Coll.), Phys. Rev. Lett. **105**, 232003 (2010).
10. V. M. Abazov *et. al.* (D0 Coll.), Fermilab-Pub-11/052-E, submitted to Phys. Rev. Lett. B, arXiv:1103.1871 [hep-ex] (2011).
11. T. Aaltonen *et. al.* (CDF Coll.), CDF Conf. Note 10211 (2010).
12. V. M. Abazov *et. al.* (D0 Coll.), Phys. Rev. D **83**, 032009 (2011).
13. T. Aaltonen *et. al.* (CDF Coll.), CDF Conf. Note 10333 (2010).
14. V. M. Abazov *et. al.* (D0 Coll.), Phys. Rev. D **83**, 092002 (2011).
15. V. M. Abazov *et. al.* (D0 Coll.), D0 Conf. Note 6062 (2010).
16. S. Frixione and B.R. Webber, JHEP **0206**, 029 (2002), S. Frixione, P. Nason and B.R. Webber, JHEP **0308** 007 (2003).
17. T. Aaltonen *et. al.* (CDF Coll.), Fermilab-Pub-10-525-E, submitted to PRD, arXiv:1101.0034 [hep-ex] (2010).
18. T. Aaltonen *et. al.* (CDF Coll.), CDF Conf. Note 10436 (2011).

HEAVY QUARK AND QUARKONIA PRODUCTION WITH THE LHCb DETECTOR

N. MANGIAFAVE (for the LHCb collaboration)
High Energy Physics Group, Cavendish Laboratory, University of Cambridge, JJ Thomson Avenue, Cambridge CB3 0HE, United Kingdom

The measurements of the J/ψ, double J/ψ, $\Upsilon(1S)$ and B_c^+ production cross-sections performed at LHCb and based on ~ 37 pb^{-1} data collected by the LHCb experiment in the 2010 run at the LHC are reported.

1 Introduction

The heavy quark production mechanism at high energy hadronic machines is still an unsolved issue in QCD. Measurements of prompt J/ψ and Υ production cross-sections as a function of the transverse momentum (p_T) are crucial for understanding the relative contributions of the colour-singlet (CS) and colour-octet (CO) mechanisms. Further hints can be given by the measurement of the double J/ψ production cross-section, where higher order corrections are greatly suppressed. Since the B_c^+ is the lightest state composed of a heavy quark and a heavy anti-quark of different flavours ($\bar{b}c$), other powerful tests of QCD predictions are the measurements of the B_c^+ mass, lifetime and production cross-section . These proceedings report the measurements of J/ψ, double J/ψ, $\Upsilon(1S)$ and B_c^+ production cross-sections at pp collisions at the centre of mass energy $\sqrt{s} = 7$ TeV performed by the LHCb experiment [1] with the dataset collected in the 2010 run at the Large Hadron Collider (LHC) machine.

2 J/ψ production cross-section

The J/ψ differential production cross-section as a function of J/ψ rapidity (y) and p_T has been measured [2] at LHCb in the fiducial region $y \in [2.0; 4.5]$ and $p_T \in [0; 14]$ GeV/c with an integrated luminosity of about 5.2 pb^{-1}. The J/ψ candidates, reconstructed from their decay $J/\psi \to \mu^+\mu^-$, have been divided into two categories: J/ψ prompt (directly produced from the pp collision and also feed down from χ_c and $\psi(2S)$) and non-prompt J/ψ from b-hadrons. The fiducial region has been divided into bins of width 1 GeV/c in p_T and 1 unit of rapidity in y. In each bin the number of selected J/ψ candidates has been estimated by fitting the invariant mass of the dimuon pairs. In order to distinguish between prompt and non-prompt production, fits to the J/ψ pseudo-proper time (t_z) have been performed in each bin: t_z is defined as $t_z = (z_{J/\psi} - z_{PV})M_{J/\psi}/p_z$ where z is the cartesian axis parallel to the beam, $z_{J/\psi}$ is the z coordinate of the J/ψ decay vertex, z_{PV} is the z coordinate of the associated production vertex, $M_{J/\psi}$ is the J/ψ invariant mass and p_z is the z component of the J/ψ momentum. The largest source of systematic uncertainty on the prompt J/ψ production cross-section measurement is due to the unknown J/ψ polarization and the results are therefore quoted

for prompt J/ψ under the fully transverse, fully longitudinal and no polarization hypotheses. The measured prompt production cross-section as a function of p_T ($\mathrm{d}\sigma/\mathrm{d}p_T$) has been compared to different theoretical predictions based on CS, non-relativistic QCD (NRQCD), and colour evaporation (CEM) models both at leading order (LO) and at next to leading order (NLO) (also NNLO for CS). There is good agreement between the theory predictions and the data. The agreement between the measured non-prompt production cross-section in bins of J/ψ p_T and fixed-order next-to-leading log computations is also excellent. The measured prompt J/ψ production cross-section integrated over the fiducial region, assuming unpolarized J/ψ, is $\sigma_{J/\psi} = 10.52 \pm 0.04 \pm 1.40^{+1.64}_{-2.20}$ μb where the first uncertainty is statistical, the second is systematic and the third is the uncertainty related to the assumption of unpolarized J/ψ. The integrated non-prompt production cross-section is $\sigma_{J/\psi} = 1.14 \pm 0.01 \pm 0.16$ μb. Extrapolating this to the full polar angle range, the $b\bar{b}$ production cross-section is $\sigma(pp \to b\bar{b}X) = 288 \pm 4 \pm 48$ μb, in excellent agreement with a previous independent LHCb measurement [3].

3 Double J/ψ production cross-section

The production of two J/ψ's in the same pp interaction is expected to be rare and can be affected by the existence of charm tetraquark states. At LHCb, the double J/ψ production cross-section has been measured [4] in the fiducial region J/ψ $p_T \in [0; 10]$ GeV/c and $y \in [2.0; 4.5]$. A dataset corresponding to an integrated luminosity of 35.2 pb^{-1} has been used. In selecting the J/ψ candidates, reconstructed from their decays into two muons, particular care has been used to minimize the effect of clone tracks (i.e. two almost identical tracks reconstructed from the same true particle) in order to avoid double counting the same J/ψ. The pile-up effect, which would lead to assigning the same production vertex to J/ψ's producted in different pp interactions, has been found to be negligible. The number of double J/ψ events has been extracted using a double background subtraction procedure. For every selected $(\mu^+\mu^-)_1$, $(\mu^+\mu^-)_2$ pair the invariant mass distribution of 1 is obtained in bins of the invariant mass of 2. The fitted yield of 1 in bins of 2 is efficiency corrected event by event and then fitted (see Figure 1 (left)). In order to make the measurement model independent, the per-event efficiency is evaluated in bins of J/ψ p_T, y and the angle between the μ^+ momentum in the J/ψ centre-of-mass frame and the direction of the Lorentz boost from the laboratory frame to the J/ψ centre-of-mass frame. The number of observed double J/ψ candidates before the efficiency correction is 139.6 ± 17.8, corresponding to a statistical significance $> 6\sigma$. The measured double J/ψ cross-section in the fiducial region is $\sigma_{J/\psi J/\psi} = 5.6 \pm 1.1 \pm 1.2$ nb where the first uncertainty is statistical and the second is systematic. This result is in good agreement with a LO QCD calculation [5] which predicts 4.34 nb (4.15 nb) with (without) initial state gluon radiations included. A comparison between the measured and predicted double J/ψ invariant mass distributions is shown in Figure 1 (right), where the discrepancy at low invariant mass may be due to non-direct double J/ψ production which is not accounted for by the theoretical model [5].

4 $\Upsilon(1S)$ production cross-section

The $\Upsilon(1S)$, $\Upsilon(2S)$ and $\Upsilon(3S)$ states have been observed from their decays into two muons with sufficient resolution to separate fully the $\Upsilon(2S)$ and $\Upsilon(3S)$ invariant mass peaks (see Figure 2 (left)). The $\Upsilon(1S)$ differential production cross-section as a function of $\Upsilon(1S)$ y and p_T has been measured [6] in the fiducial region $p_T \in [0; 15]$ GeV/c and $y \in [2.0; 4.5]$. The fiducial region has been divided into bins of width 1 GeV/c in p_T and 1 unit of rapidity in y and a dataset corresponding to an integrated luminosity of 32.4 pb^{-1} has been used. The $\Upsilon(1S)$ yield has been extracted from a fit to the di-muon invariant mass distribution using a Crystal Ball to model the signal shape and an exponential to model the background shape (see

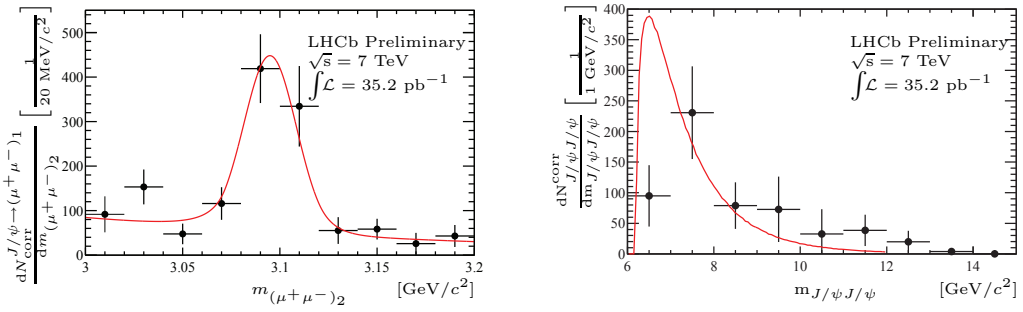

Figure 1: Left: The efficiency corrected fitted yields of $J/\psi \to (\mu^+\mu^-)_1$ in bins of $(\mu^+\mu^-)_2$ invariant mass. The line represents the fit from a double Crystal Ball function for the signal and an exponential function for the background. Right: The efficiency corrected yields of double J/ψ events as a function of the invariant mass of the double J/ψ system (points with error bars). The overlaid curve corresponds to the theory prediction [5].

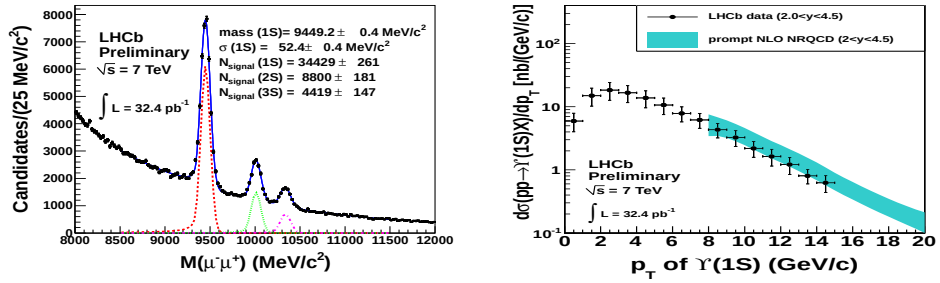

Figure 2: Left: The invariant mass distribution of the selected $\Upsilon \to \mu^+\mu^-$ candidates. The three peaks correspond to the $\Upsilon(1S)$, $\Upsilon(2S)$ and $\Upsilon(3S)$ signals (from left to right). The superimposed curves and the signal yields are the result of the fit. Right: The measured differential $\Upsilon(1S)$ production cross-section as a function of p_T integrated over y (black dots) compared to the prediction calculated from NRQCD at NLO, including contributions from χ_b and $\Upsilon(2S)$ decays, summing the colour-singlet and colour-octet contributions [7] (coloured band).

Figure 2 (left)). The results have been reported under the assumption of unpolarized $\Upsilon(1S)$ and the biggest systematic uncertainty comes from this assumption. The measured $\Upsilon(1S)$ production cross-section, integrated over the fiducial region, assuming unpolarized $\Upsilon(1S)$ is $\sigma_{\Upsilon(1S)} = 108.3 \pm 0.7^{+30.9}_{-25.8}$ nb where the first uncertainty is statistical and the second is systematic. The measured $\Upsilon(1S)$ differential production cross-section as a function of $\Upsilon(1S)$ p_T ($\mathrm{d}\sigma/\mathrm{d}p_T$) has been compared with LO and NLO NRQCD, and with NLO and NNLO CS theoretical predictions. The predictions take into account the $\Upsilon(1S)$ feed down from χ_b and $\Upsilon(2S)$ and are in good agreement with data (see, for example, Figure 2 (right)). The LHCb results have been compared with the CMS experimental results [8]. Although CMS covers a different rapidity range ($y \in [0.0; 2.0]$) the results are consistent between the two experiments.

5 B_c^+ to B^+ relative production cross-section

The B_c^+ at LHCb has been observed in its decay $B_c^+ \to J/\psi(\mu^+\mu^-)\,\pi^+$. Since the B_c^+ absolute branching fraction is unknown, we measure the B_c^+ production cross-section ($\sigma(B_c^+)$) times the $B_c^+ \to J/\psi\ \pi^+$ branching ratio (BR). This measurement has been performed relative to $B^+ \to J/\psi\ K^+$ in order to cancel out most of the systematic uncertainties. Hence the quantity measured at LHCb is [9]:

$$R_{c^+} = \frac{\sigma(B_c^+) \times \mathrm{BR}(B_c^+ \to J/\psi\ \pi^+)}{\sigma(B^+) \times \mathrm{BR}(B^+ \to J/\psi\ K^+)}. \quad (1)$$

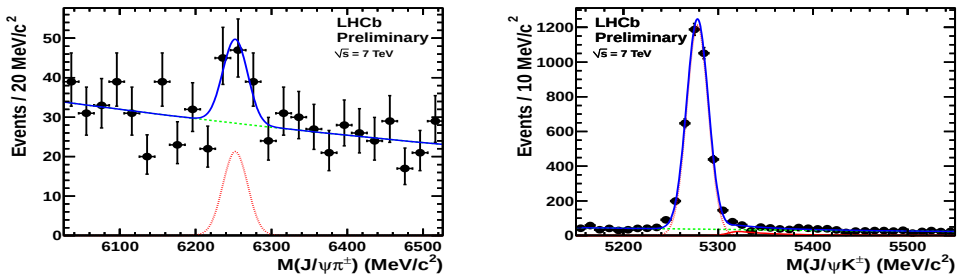

Figure 3: The invariant mass distribution for $B_c^+ \to J/\psi(\mu^+\mu^-)\,\pi^+$ (left) and $B^+ \to J/\psi\,K^+$ (right) candidates, with the fit results superimposed. The blue solid line represents the total fit function, the red dashed line the signal contribution, the green dashed line the combinatorial background contribution. For the $B^+ \to J/\psi\,K^+$ mass distribution, the red solid line represents the background from Cabibbo-suppressed $B^+ \to J/\psi\,\pi^+$ decays.

The analysis has been performed in the fiducial region B $p_T > 4$ GeV/c and B pseudo-rapidity $\eta \in [2.5; 4.5]$ using 32.5 pb^{-1} of integrated luminosity. The B_c^+ and B^+ selection criteria have been chosen to be as similar as possible to reduce the systematic uncertainties on R_{c^+}. The number of B_c^+ and B^+ have been extracted from a fit to the $J/\psi\,\pi$ and $J/\psi\,K$ invariant mass distributions (see Figure 3). In both cases a Gaussian shape has been used for the signal and an exponential shape has been used for the combinatorial background. The non-combinatorial background from the Cabibbo suppressed decay $B^+ \to J/\psi\,\pi^+$ has also been taken into account. Since the B_c^+ production spectrum and lifetime are poorly known, the efficiency has been evaluated from Monte Carlo simulation in bins of B p_T and η to reduce the dependence on theoretical models. The measured R_{c^+} in the fiducial region is $R_{c^+} = (2.2 \pm 0.8 \pm 0.2)\%$ where the first uncertainty is statistical and the second is systematic. A model dependant approach obtained with the B_c^+ generator BCVEGPY [10] (i.e. a complete LO α_s^4 calculation) and the CTEQ6LL [11] PDF gives $R_{c^+}^{\text{model-dependant}} = (1.4 \pm 0.4 \pm 0.1)\%$.

6 Conclusions

With the 2010 data the differential production cross-sections of J/ψ and $\Upsilon(1S)$ and the production cross-section of double J/ψ and B_c^+ (relative to B^+) have been measured with the LHCb detector. The results are in good agreement with the theoretical calculations and the observation of the B_c^+ looks very promising for future measurements.

References

1. The LHCb Collaboration, A.A. Alves *et al*, JINST **3**, S08005 (2008).
2. The LHCb Collaboration, R. Aaij *et al*, arXiv:1103.0423v1 [hep-ex].
3. The LHCb Collaboration, R. Aaij *et al*, *Phys. Lett.* B **694**, 209 (2010).
4. The LHCb Collaboration, R. Aaij *et al*, CERN-LHCb-CONF-2011-009.
5. A.V. Berezhnoy *et al*, arXiv:1101.5881v1 [hep-ph].
6. The LHCb Collaboration, R. Aaij *et al*, CERN-LHCb-CONF-2011-016.
7. K. Wang, Y.Q. Ma, K.T. Chao, private communication.
8. The CMS Collaboration, arXiv:1012.5545v1.
9. The LHCb Collaboration, R. Aaij *et al*, CERN-LHCb-CONF-2011-017.
10. Chao-Hsi Chang, Jian-Xiong Wang, Xing-Gang Wu, Comput.Phys.Commun. **175**, 624 (2006).
11. J. Pumplin *et al*, JHEP **0207**, 012 (2002).

HEAVY FLAVOUR PRODUCTION AT ATLAS

Z. DOLEŽAL
on behalf of the ATLAS Collaboration
Institute of Particle and Nuclear Physics, Faculty of Mathematics and Physics, Charles University in Prague, V Holešovičkách 2, CZ 18000 Prague, The Czech Republic

ATLAS is a general purpose detector built at the Large Hadron Collider at CERN, Geneva. In addition to the high p_{T} program it has a rich flavour physics program. Latest results of heavy flavour production in ATLAS are presented, focusing on D and B meson production and J/ψ prompt and indirect cross-section measurements.

1 Introduction

ATLAS is a general purpose detector built at the Large Hadron Collider at CERN, Geneva. Its main objective is to search for physics beyond the Standard Model. In addition to this program it has a rich flavour physics program as well. Flavour-related processes serve also as a very useful tool to understand detector performance using well known particles with c and b quarks and measurements of production cross-sections for D hadrons, B hadrons, J/ψ and Υ to test QCD predictions for proton-proton (pp) collisions at $\sqrt{s} = 7$ TeV. With higher statistics (several fb^{-1} expected in 2011 and 2012) properties of B hadrons and other interesting observables will be measured.

2 ATLAS Detector and Triggers

A detailed description of the ATLAS detector can be found here[1]. Only the most important parts of the nominal detector relevant for flavour physics studies are described in this paper. The Inner Detector uses its magnetic field of 2 T to measure charged particle tracks in a pseudo-rapidity range of $|\eta| < 2.5$. In the barrel region it consists of 3 pixel layers followed by 4 silicon strip detector layers and the Transition Radiation Tracker allowing to reach design momentum precision of $\sigma_{p_{\mathrm{T}}}/p_{\mathrm{T}} = 0.05\%\, p_{\mathrm{T}} \oplus 1\%$. Muon detector system (MS) - the outermost detector of

ATLAS - consists of four parts (monitored drift tubes, cathode strip chambers, thin-gap chambers and resistive plate chambers). It covers $|\eta| < 2.7$ and due to its toroidal magnetic field it can measure transverse momenta with $\sigma_{p_T}/p_T = 10\%$ at $p_T = 1$ TeV. This system also provides important muon triggers.

Two levels of muon reconstruction are used. Muons that have an ID track matched to an MS track are fully reconstructed (*combined* muons) and their momentum is measured by refitting their track through the detector to give the best precision. Some muons have a clear ID track, but only track segments in the MS so they can be reconstructed only partially (*tagged* muons).

The ATLAS trigger consists of three levels, Level 1 (L1), Level 2 (L2) and Event Filter (EF). L1 trigger is a hardware trigger based on MS, Calorimeters and Minimum Bias Trigger Scintillator (MBTS). L2 and EF triggers are software triggers and are together called High Level Trigger (HLT). Due to a constant increase of data rate throughout 2010, varying trigger conditions and thresholds were used to take data for measurements presented in this paper.

3 Quarkonia

Reconstructed invariant mass distributions of $c\bar{c}$ and $b\bar{b}$ mesons decaying into muon pairs are used to study Inner Detector performance and alignment algorithms. The resulting spectra obtained from the analysis of 41 pb^{-1} (full 2010 ATLAS dataset) are shown at Fig. 1. The fitted mass values are in a good agreement with the world averages.

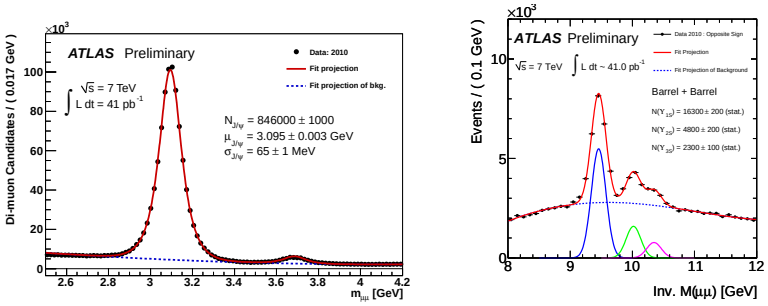

Figure 1: Di-muon invariant mass spectrum at the J/ψ and ψ(2S) mass range (right) and at the Υ(1S,2S,3S) mass range

4 J/$\psi \to \mu^+\mu^-$ Differential Cross-sections

The study of charmonium production is not interesting for detector performance evaluation only. Processes leading to this production are not well understood. Therefore attention has been paid in ATLAS to measure the J/ψ production cross-section. The analysis was based on an integrated luminosity of 2.3 pb^{-1} and results of inclusive differential cross-section, its prompt and non-prompt fraction in four rapidity bins covering $|y| < 2.4$ and J/ψ p_T range between 1 and 70 GeV have been obtained. A detailed description can be found here[2].

4.1 Inclusive J/$\psi \to \mu^+\mu^-$ Differential Cross-section

In order to recover true number of J/ψ decays several corrections for detector efficiency, bin migration and acceptance effects have to be taken into account. Therefore a weight w is applied to each observed J/ψ candidate defined as

$$1/w = P = \mathcal{A} \cdot \mathcal{M} \cdot \varepsilon^2_{\text{trk}} \cdot \varepsilon^+_\mu(p^+_T, \eta^+) \cdot \varepsilon^-_\mu(p^-_T, \eta^-) \cdot \varepsilon_{\text{trig}} \quad (1)$$

Here $\mathcal{M}$ is a correction factor for bin migrations, $\varepsilon_{\rm trk}$, ε_{μ} and $\varepsilon_{\rm trig}$ are the ID tracking, single muon reconstruction and trigger efficiencies, respectively. The kinematic acceptance $\mathcal{A}$ depends strongly on the spin alignment (polarisation) of J/ψ. This has not been measured yet at LHC. Large number of spin alignments have been studied, and 5 extreme cases were identified. Acceptance maps for these points were generated and an envelope of the most extreme values is shown in the cross-section plots. The offline single muon reconstruction efficiencies are obtained from data using tag-and-probe method, described here[3,4]. The resulting inclusive differential cross-sections for the central rapidity bin are shown in Fig. 2 (left).

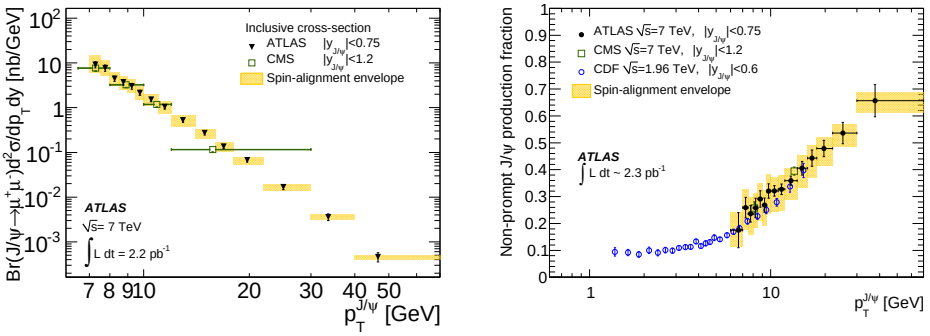

Figure 2: Inclusive J/ψ production cross-section (left) and non-prompt to inclusive fraction (right) as a function of J/ψ transverse momentum, for the central rapidity bin. Yellow overlay shows a band representing the variation of the result under various spin-alignment scenarios.

4.2 Non-prompt Fraction

The J/ψ mesons studied in this process can be created via two mechanisms: (i) prompt production in the pp collisions and decays of heavier charmonium states, and (ii) J/ψ production from the decay of b-hadrons created in the collision. The prompt decays occur very close to the primary vertex, while b-hadrons, having long lifetime will decay further away. b-hadrons are not fully reconstructed, so the flight distance of the J/ψ is used to calculate the variable called the *pseudo-proper time* for each event – this then serves as a discriminant between prompt and non-prompt decays. An unbinned maximum likelihood fit in bins of rapidity and $p_{\rm T}$ is used to extract this fraction from the data. Fig. 2 (right) shows non-prompt fraction as a function of $p_{\rm T}$ for the central rapidity bin, while both prompt and non-prompt cross-sections compared with theory predictions are shown in Fig. 3.

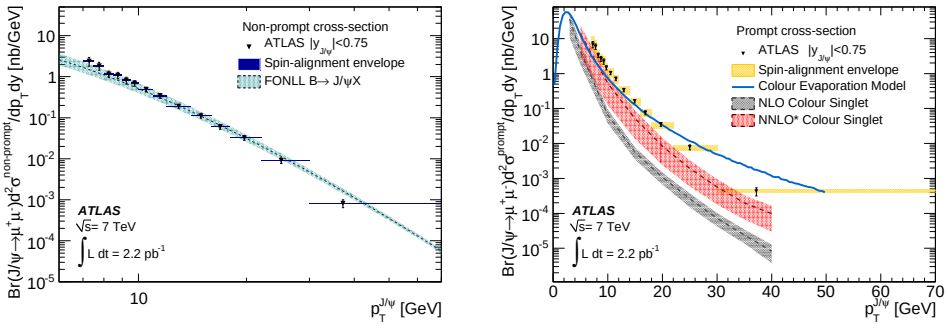

Figure 3: Non-prompt J/ψ production cross-section (left) and prompt J/ψ production cross-section as a function of J/ψ transverse momentum, both for the central rapidity bin. Blue (left) and yellow overlay (right) shows the variation of the result under various spin-alignment scenarios. Overlaid in other colours are theory predictions.

5 D mesons

High cross-sections of D mesons production together with clean signatures help studying one of the first hard-QCD processes at the LHC. ATLAS has measured [5] differential cross-sections as a function of transverse momentum and pseudorapidity for $D^{*\pm}$ and $D^{\pm}$ production (see Fig. 4).

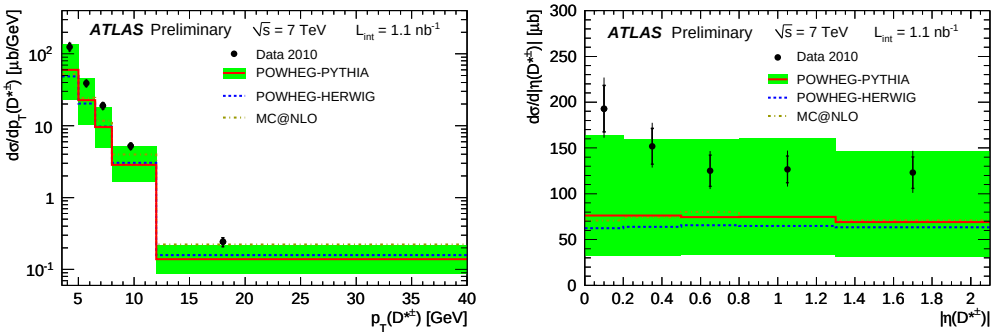

Figure 4: Differential cross-section for $D^{*\pm}$ mesons as a function of p_T (left) and η (right) compared to the NLO QCD calculations of POWHEG-PYTHIA, POWHEG-HERWIG and MC@NLO

6 B Meson Studies

Studying open b production provides another useful tool for understanding reconstruction and flavour tagging algorithms, but serves also as a prerequisite for further studies of CP violation and rare b hadron decays. There are many new results of ATLAS namely concerning B_d and B_s meson observation and lifetime measurement [6], but their description goes beyond the extent of this paper.

7 Summary and Future Plans

The first year of ATLAS data-taking has brought many exciting results also in the flavour sector. Future plans include precise B meson characterisation in several decay channels ($B_d \to J/\psi K^{*0}$, $B_s \to J/\psi\phi$, $B_c \to J/\psi\pi$) and searches for the New Physics in the $B_s \to \mu^+\mu^-$ rare decays.

References

1. ATLAS Collaboration, The ATLAS Experiment at the CERN Large Hadron Collider, JINST 3 S08003 (2008)
2. ATLAS Collaboration, Measurement of the differential cross-sections of inclusive, prompt and non-prompt J/ψ production in proton-proton collisions at $\sqrt{s} = 7$ TeV, arXiv:1104.3038v1 [hep-ex], accepted by Nuclear Physics B
3. ATLAS Collaboration, Determination of the muon reconstruction efficiency in ATLAS at the Z resonance in proton-proton collisions at $\sqrt{s} = 7$ TeV, ATLAS-CONF-2011-008, Feb 2011, CERN, Geneva.
4. ATLAS Collaboration, A measurement of the ATLAS muon reconstruction and trigger efficiency using J/ψ decays, ATLAS-CONF-2011-021, Mar 2011, CERN, Geneva.
5. ATLAS Collaboration, Measurement of $D^{(*)}$ meson production cross-sections in pp collisions at $\sqrt{s} = 7$ TeV with the ATLAS detector, ATLAS-CONF-2011-017, Mar 2011, CERN, Geneva.
6. ATLAS Collaboration, Observation of the B_d^0 and B_s^0 mesons in the decays ($B_d^0 \to J/\psi K^0$ and $B_s^0 \to J/\psi\Phi$ in ATLAS, ATLAS-CONF-2011-050, Apr 2011, CERN, Geneva.

HEAVY FLAVOR PRODUCTION AT CMS

K. A. ULMER, on behalf of the CMS collaboration
Department of Physics, University of Colorado,
390 UCB, Boulder, CO, USA

Measurements of heavy flavor production in pp collisions at $\sqrt{s} = 7.0$ TeV recorded at the CMS experiment are presented. Double differential cross sections with respect to transverse momentum and rapidity are shown for J/ψ and $\Upsilon(1S)$, $\Upsilon(2S)$, and $\Upsilon(3S)$. The inclusive open beauty rate is measured with two different techniques, including a study of the angular correlations between b jets in events with two identified b jets. Lastly, the B^+, B^0, and B_s^0 production rates are measured from the reconstruction of exclusive final states.

1 Introduction

Cross sections for heavy quark production in hard scattering interactions provide an interesting testing ground for QCD calculations. Theoretically, large uncertainties remain due to the dependence on the renormalization and factorization scales. Measurements from the LHC at the center of mass energy of $\sqrt{s} = 7.0$ TeV provide new opportunities to test and further our understanding of the heavy quark production mechanisms.

CMS is a general purpose experiment at the Large Hadron Collider[1]. The main detector components used in these analyses are the silicon tracker and the muon systems. The silicon tracker measures charged particles in the pseudorapidity range $|\eta| < 2.5$ within a 3.8 T field of the superconducting solenoid. It provides an impact parameter resolution of ~ 15 μm and a p_{T} resolution of about 1.5% for particles with transverse momenta up to 100 GeV. Muons are measured in the pseudorapidity range $|\eta| < 2.4$ with detection planes made using three technologies: drift tubes, cathode strip chambers, and resistive plate chambers.

2 Onia production

The first heavy flavor production measurements at CMS were made by reconstructing J/ψ [2] and Υ [3] mesons in their decays to two muon final states. Candidates are formed by fitting pairs of oppositely-signed muons to a common vertex and event yields are obtained by fitting invariant mass distributions. The observed yields are corrected for detector acceptance, reconstruction inefficiencies, and trigger inefficiencies in bins of candidate transverse momentum p_{T} and rapidity y to measure double differential cross sections. The fraction of J/ψ mesons produced from long-lived B decays is also measured by fitting the lifetime distribution of the reconstructed J/ψ mesons. The three lowest Υ states are all visible due to the excellent mass resolution of the CMS detector. The yields of the $\Upsilon(2S)$ and $\Upsilon(3S)$ states are measured with respect to the $\Upsilon(1S)$ state as functions of the Υ p_{T} and y.

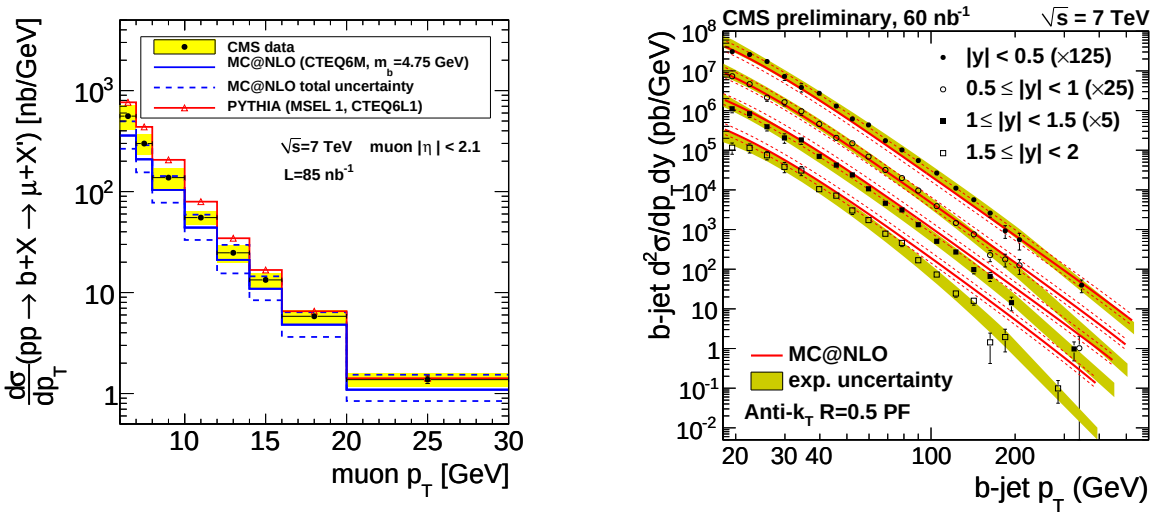

Figure 1: Inclusive b-jet production cross section measured as a function of muon p_{T} from semi-muonic decays (left) and as a function of b-jet p_{T} from tagged jets (right) compared to simulation.

3 Inclusive open beauty production

Two independent techniques are used to measure inclusive beauty production. The first technique makes use of semi-muonic decays of B hadrons [4]. Reconstructed charged tracks with $p_{\mathrm{T}} > 300$ MeV are clustered into jets with the anti-k_{T} algorithm with $R = 0.5$. Events are then selected where the jet contains a reconstructed muon with $p_{\mathrm{T}} > 6$ GeV and $|\eta| < 2.1$. For jets originating from b quarks, the decay kinematics demand that, on average, the muon direction will be further displaced from the jet direction than for muons from lighter jets ($udscg$). The observed distribution of the quantity $p_{\mathrm{T}}^{rel} = |\vec{p}_{\mu} \times \vec{p}_{j}|/|\vec{p}_{\mu}|$ is fit to separate signal b jets from background. Templates for the signal and background p_{T}^{rel} shapes are obtained from simulation (for signal and c quark backgrounds) or data (uds quark and gluon backgrounds) and are crosschecked in data for those obtained from simulation.

The inclusive b-quark production cross section is obtained by correcting the measured b-quark yield by the selection efficiency in bins of muon p_{T} as shown in Figure 1. The total visible cross section is measured to be $(1.32 \pm 0.01(\mathrm{stat.}) \pm 0.30(\mathrm{syst.}) \pm 0.15(\mathrm{lumi.}))$ μb for b-jet decays with a muon with $p_{\mathrm{T}} > 6$ GeV and $|\eta| < 2.1$. The measured cross section is larger than that predicted by MC@NLO ($0.95^{+0.42}_{-0.21}$ μb) and smaller than that predicted by Pythia (1.9 μb).

The second technique used to measure the inclusive beauty production rate relies on the identification of displaced secondary vertices within reconstructed jets to tag them as b jets [5]. An inclusive jet sample is used to search for jets containing a secondary vertex. The secondary vertex is required to contain at least three charged tracks and the vertex must be well separated from the primary event vertex since long-lived B hadrons give rise to a larger separation than lighter jets. A separation cut is chosen such that $\approx 60\%$ efficiency is obtained with $\approx 0.1\%$ rate for mistagging light jets as b jets.

The production of b jets is calculated as a double differential cross section versus jet p_{T} and y, where the reconstructed values have been corrected to the particle p_{T} and y. The measured results are shown in Figure 1. The leading systematic uncertainties arise from the b-jet energy scale corrections, the data-driven uncertainties on the b-tagging efficiency and from the mistag rates for light jets. The overall agreement with MC@NLO is reasonable, though the modeling of the rapidity dependence shows discrepancies between the data and simulation.

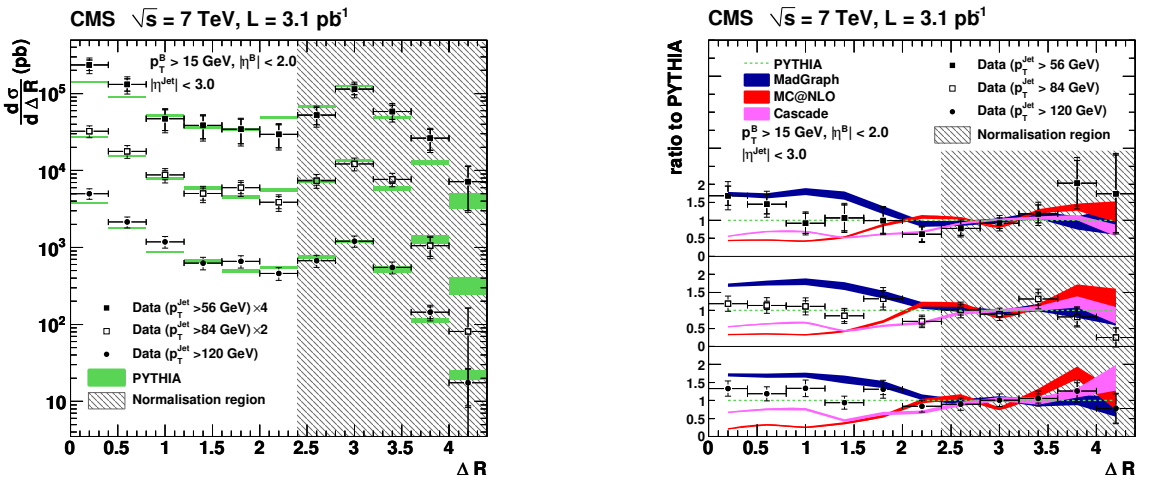

Figure 2: Correlation results between reconstructed pairs of b-tagged jets compared to Pythia simulation (left) and other theoretical predictions normalized to the Pythia result (right).

4 $b\bar{b}$ correlations

The secondary vertex finding technique also allows for the study of correlations between $b\bar{b}$ pairs [6]. The correlations between two B candidates can provide useful information about the $b\bar{b}$ pair production mechanism, where pairs produced from gluon splitting are expected to have small separations, while those from flavor creation are expected to dominate at large separation. Secondary vertices are reconstructed with at least three charged tracks and a 3D flight length from the primary vertex greater than five times its uncertainty. The flight length of the B candidate is computed as the direction from the primary vertex to the secondary vertex. For events with exactly two such identified secondary vertices, the quantity $\Delta R = \sqrt{\Delta\phi^2 + \Delta\eta^2}$ is computed, where $\Delta\phi$ is the difference in polar angle and $\Delta\eta$ is the difference in pseudorapidity between the two B candidate directions.

Results are shown in Figure 2 for events where both B candidates have $p_{\mathrm{T}} > 15$ GeV and $|\eta| < 2.0$. The reconstructed jet momentum is corrected back to the true value, and the results are reported for three different regions of leading jet p_{T}. The results are normalized to the region with $\Delta R > 2.4$, which is expected to be better understood theoretically. The data show an excess at low ΔR values compared to the prediction from Pythia suggesting that the contribution from gluon splitting is larger than expected.

5 Exclusive B production

A fully exclusive reconstruction technique is used to measure the cross sections for B^+ [7], B^0 [8], and B_s^0 mesons. The three species are reconstructed by fitting to a common vertex a J/ψ plus a K^+, K_S^0, or a ϕ, respectively. The J/ψ mesons are reconstructed in their decays to $\mu^+\mu^-$, while the K_S^0 and ϕ mesons are reconstructed in their decays to $\pi^+\pi^-$ and K^+K^-, respectively. The dominant backgrounds in each analysis arise from events with a prompt J/ψ. To distinguish the signals from these backgrounds, a two-dimensional fit to the B mass and B lifetime is used for each B species to extract the signal yield in bins of B p_{T} and y. The fitted lifetimes in all three cases are consistent with the known values.

For B^+, 912 signal events are observed in 6 pb^{-1} of data, while 809 and 549 events are observed for B^0 and B_s^0 in 40 pb^{-1}. The fitted signal yields are corrected for the detector acceptance and reconstruction and trigger inefficiencies to calculate the cross section. For the B^+ and B^0 measurements, candidates with B $p_{\mathrm{T}} > 5$ GeV are used, while for B_s^0 $p_{\mathrm{T}} > 8$ GeV

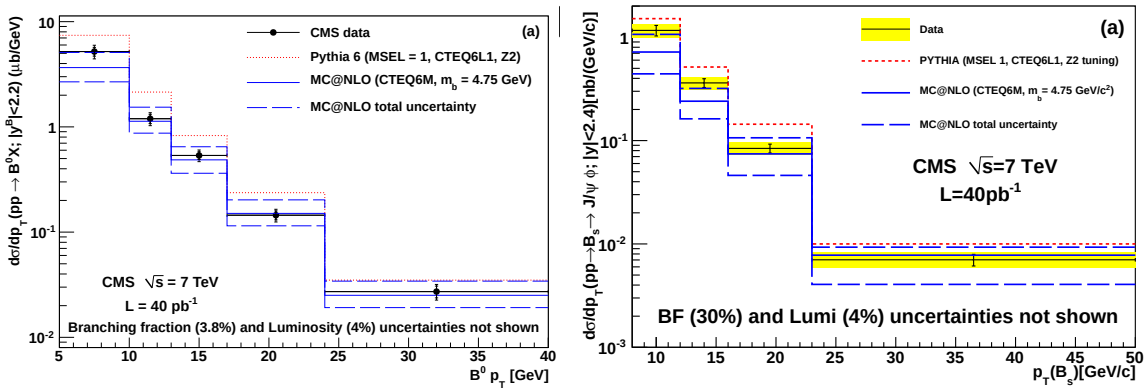

Figure 3: Measured differential production cross sections versus p_{T} for B^0 (left) and B_s^0 (right) mesons compared to theoretical predictions.

are considered. For B^+ and B_s^0 (B^0) B candidates are required to have $|y| < 2.4$ (2.2). The total visible cross sections are measured to be $(28.1 \pm 2.4 \pm 2.0 \pm 3.1)$ μb for B^+ and $(33.2 \pm 2.5 \pm 3.5)$ μb for B^0, where the first error is statistical, the second is systematic, and the third for B^+ is the uncertainty in the luminosity, while the luminosity uncertainty is included in the systematic for B^0. The total visible cross section times the branching fraction for $B_s^0 \to J/\psi\phi$ is measured to be $(6.9 \pm 0.6 \pm 0.5 \pm 0.3)$ nb for B_s^0. In all cases, the observed cross sections are found to be lower than those predicted by Pythia and higher than those predicted by MC@NLO, though compatible within uncertainties. The results for B^0 and B_s^0 versus p_{T} are shown in Figure 3.

6 Conclusions

A variety of measurements of heavy flavor production have been made by CMS in pp collisions at $\sqrt{s} = 7$ TeV. These include J/ψ and Υ double-differential production cross sections, measurements of inclusive beauty production from multiple complementary methods, including $b\bar{b}$ correlation measurements, and three exclusive B production cross section measurements. While the agreement with MC models is generally good, none of the theoretical models considered yet describe all of the features observed in the data.

References

1. The CMS Collaboration, *JINST* **3**, S08004 (2008).
2. V. Khachatryan *et al.* [CMS Collaboration], Eur. Phys. J. C **71**, 1575 (2011) [arXiv:1011.4193 [hep-ex]].
3. V. Khachatryan *et al.* [CMS Collaboration], arXiv:1012.5545 [hep-ex].
4. V. Khachatryan *et al.* [CMS Collaboration], JHEP **1103**, 090 (2011) [arXiv:1101.3512 [hep-ex]].
5. V. Khachatryan *et al.* [CMS Collaboration], CMS-PAS-BPH-10-009, http://cdsweb.cern.ch/record/1280454, (2010).
6. V. Khachatryan *et al.* [CMS Collaboration], JHEP **1103**, 136 (2011) [arXiv:1102.3194 [hep-ex]].
7. V. Khachatryan *et al.* [CMS Collaboration], Phys. Rev. Lett. **106**, 112001 (2011) [arXiv:1101.0131 [hep-ex]].
8. S. Chatrchyan *et al.* [CMS Collaboration], arXiv:1104.2892 [hep-ex].

4.
Heavy Flavours

HEAVY FLAVOUR IN A NUTSHELL

Robert W. Lambert
CERN, Geneva, Switzerland

Moriond QCD brings together particle physicists of varied interests. This review and introduction to heavy flavour physics is aimed at those not in the heavy-flavour field to describe the motivation and methodology of precision flavour physics, and introduce the most tantalising searches for new physics. The LHC experiments are expected to make great inroads into constraining the new physics parameter space and discover the new physics which I will argue *must* be present to describe our observed universe.

1 Introduction

Heavy flavour is a broad subject both experimentally and theoretically, stretching back two hundred years to the proposal of the first flavoured object, the proton, in 1815 [1]. In this paper the general topics and basic theory aspects are discussed as needed to develop an understanding of the field today, such that the Reader may be equipped to understand the remaining proceedings from this section of the conference and participate in discussions with their colleagues over the key results.

This paper is a summary of existing works, particularly three very interesting and important papers of the last twelve months: the measurement by the DØ collaboration of a 3.2σ deviation from the Standard Model in the flavour-specific asymmetry of neutral B-meson mixing [2], an update of B-mixing both theoretically and experimentally by Lenz and Nierste [3], plus the recently updated results of the WMAP seven-year sky survey [4].

For more complete, more advanced, theoretical and experimental summaries, the Reader is directed to the similar introduction in the previous conference in this series [5], the summary paper mentioned earlier [3], and the other excellent proceedings from this same conference.

1.1 Welcome to Our Universe

The Wilkinson Microwave Anisotropy Probe, WMAP, makes precision measurements of the properties of the cosmic microwave background radiation. It is amazing that such a simple experiment can produce some of the most profound results in physics. In combination with some other simple cosmological observations, we are able to measure the cosmological density of the universe and divide the total density into constituents from different sources. Shockingly we discover only 5 % of the mass of the universe can be attributed to baryonic matter [4]. However, even 5 % is much higher than could be expected from our existing theories which stipulate all matter and antimatter should have been annihilated just after the big bang.

The fact there is any matter left over at all requires there to be a difference between the behaviour of matter and antimatter, which violates CP-symmetry (CPV) [6]. We can quantify the

amount of CPV required by taking the ratio of the remaining matter to the number of photons from the annihilation, and we find this number is approximately one part in a billion. In our Standard Model of particle physics (SM), even with maximal CPV, the equivalent predicted asymmetry is lower than the observed asymmetry by more than ten orders of magnitude. We know then that there must be new physics waiting to be discovered and that it must contain new sources of CPV.

There are indeed many other problems with what we call the Standard Model; but the puzzles of dark matter and dark energy, the matter-antimatter asymmetry, and the lack of a good quantum theory of gravity, are the most obvious shortfalls.

1.2 Heavy Flavour as a Tool for New Physics

Heavy flavour physics is a precision tool to discover new physics. The reach of heavy flavour is very broad since the production and decay of any heavy meson inevitably involve aspects from every portion of the Standard Model. Even a simple decay such as $B_s^0 \to D_s^{(*)(*)\pm} l^{\mp} \nu_l$, probes: all three generations of quarks and leptons, QCD, QED, and weak interactions. Arguably also the Higgs mechanism and even the top quark (mediating the observed B_s^0-mixing) play a role. Heavy flavour is a microcosm of the entire Standard Model so it should exhibit the same flaws as the Standard Model and probe all avenues of new physics.

Precision measurements are completely complementary to direct searches for new physics. Direct searches for new heavy particles at the energy frontier are limited in their reach by the energy of the collider at hand. Precision measurements, however, are sensitive to the quantum-mechanical effects of new physics in loops and virtual processes, to scales well beyond the energy of the collider. Typically we say up to 1000-times the energy of the collider.

Having identified that heavy flavour is a powerful tool to search for new physics, we would like to use it to answer the following two questions.

1. Where is the CP-violation we need to explain the observed universe?

2. Given that there must be new physics, what is its flavour structure?

To answer those questions we must identify how and where to look for new physics, and for that we need a recipe or a map.

1.3 A Map of the Search for New Physics

When looking for new physics we can follow the following prescription. Identify channels and observables where new physics is not expected and make precision measurements of well-predicted observables. Then identify a similar or related area where new physics can enter and perform precision measurements of related observables to detect any new physics.

Tree-level Standard-Model-like decays are a good example of where new physics is not expected. Consequently to look for new physics we are especially interested in channels with loops and penguins (radiative loops), where any new physics charges, currents, and virtual heavy particles, can enter into the loop and change the result dramatically.

We are also interested in looking for new sources of CP-violation. In the SM there is only one source of CP-violation, which is a phase in the weak mixing matrix, the CKM matrix. To observe this phase, or any new physics phase, we construct observables with two competing phases, and measure phase differences through interference. In the Standard Model the CKM phase manifests most obviously in the b-quark system [7], which again emphasises that heavy flavour physics is crucial. We can construct many different observables to measure this single known phase, and search closely for inconsistencies, the signs of new CP-violating physics.

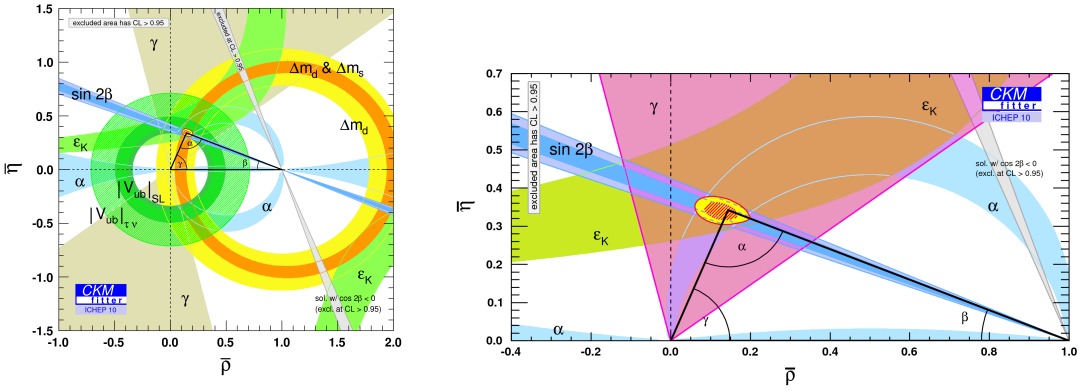

Figure 1: Overlapping constraints on the phase in the CKM matrix, reproduced [8]. $\bar{\rho}$ and $\bar{\eta}$ are effectively the real and imaginary parts of the CKM phase. The red hashed region of the global combination corresponds to 68 % CL. On the left all current experimental constraints are used. On the right only observables which explicitly violate CP are used. The CKM-angle γ is highlighted in pink to demonstrate it is a weak constraint.

1.4 Status of the CKM-mechanism

Combining measurements of CKM-parameters from many different sources we then usually plot all the phase constraints on a single 2D complex plane to constrain the real part ($\bar{\rho}$) and imaginary part ($\bar{\eta}$) of the phase in the CKM [8]. This popular image is reproduced here as Fig. 1. In the wide range of experimental observables across many different channels, all of the results agree very well and are very consistent with the CKM-model for weak mixing and CP-violation. This confirms that the Standard Model is very self-consistent, and that the CKM-mechanism is an excellent description, but it does not leave much breathing room for new physics.

Fortunately we do have several unexplored and promising places to search for new physics [9].

2 Hottest New Physics Searches

There are many searches for new physics in precision flavour physics, but this paper only briefly covers five areas which are typical of certain classes of precision search.

1. Precision CKM-measurements, such as the determination of the CKM-angle γ.
2. Decays with penguins and loops, such as the rare decay $B^0_d \to K^* \mu^+ \mu^-$.
3. Very rare decays with possible new physics enhancements, such as the rare decays $B^0_{s/d} \to \mu^+ \mu^-$.
4. Generic CP-asymmetry searches, such as $B \to K\pi$, where we have a so-called "$K\pi$-puzzle."
5. Mixing of heavy neutral mesons, for example $B^0_{s/d}$-mixing.

2.1 Determination of the CKM-angle γ

In Fig. 1, right, is replotted the constraints on the CPV phase, with only the explicit CP-violating observables. Any disagreement in such a plot could point immediately to new CP-violating physics. Here the CKM-angle γ is not well known and could hide moderate new physics. More precise measurements of γ are planned at the LHC, specifically at LHCb [9].

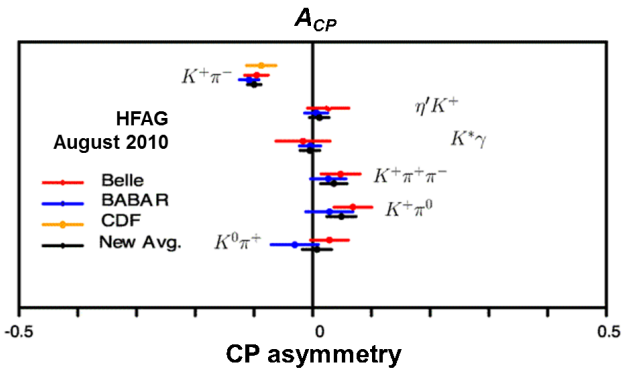

Figure 2: Selected measurements of direct CP-asymmetry in decays of the form $B \to K\pi$, reproduced [10] with modification. The CP-asymmetry in the $B^0 \to K^+\pi^-$ mode disagrees with all other measurements, this unexpected feature is known as the "$K\pi$-puzzle."

2.2 $B^0_d \to K^*\mu^+\mu^-$

The flavour structure of new physics may be exposed in departures from the SM in penguin and loop processes. $B^0_d \to K^*\mu^-\mu^+$ is a rare-decay channel with both penguin *and* other competing loop contributions [9]. In this channel there are several observables with high sensitivity to new physics, particularly to the angular structure of new physics models such as supersymmetry. One key observable is the forward-backward-asymmetry, A_{fb} where there are many current results available, but where none as yet show a deviation from the Standard Model.

2.3 $B^0_{s/d} \to \mu^+\mu^-$

Extremely rare decays are often very sensitive to new physics contributions. $B^0_{s/d} \to \mu^+\mu^-$ are two channels with a very clear experimental signature, very precise theoretical prediction, and very large sensitivity to new physics [9]. In certain supersymmetric models the SM branching fraction may be increased by a very large factor. Very recent results from the Tevatron and LHCb show no departure so far, but the prospect is good for the coming months [11].

2.4 The $K\pi$-puzzle

Generic searches for observable CP-violation in decays could reveal unexpected new sources of CP-violation. In channels of the form $B \to K\pi$ we already have a hint of departure from the expectations. Naively we would expect all decays of this form to exhibit similar levels of direct CP-violation, however, as shown in Fig. 2 the CP-asymmetry in the $B^0 \to K^+\pi^-$ mode disagrees with all other measurements. This is known as the "$K\pi$-puzzle," and is an interesting hint for new physics [10]. Precision studies at the LHC will confirm or deny this disagreement [9].

2.5 New Physics in Mixing

Recently it has been reported that physics in neutral B-meson mixing is already divergent from the Standard Model [12] by more than 3σ. Mixing is a very curious, unintuitive, pure quantum-mechanical phenomenon, where particle and antiparticle partners both contribute to the same observed state. The observed state is an oscillating time-dependent mixture of particle and antiparticle, and the oscillation is mediated by a box diagram in the SM, most simply described by a mixing matrix. Since mixing is a loop-level process, generic new physics can change both the magnitude and the phase of the mixing, and so it is usual to define a complex number parameter to characterise the new physics contribution. In the selected analysis [12] the authors

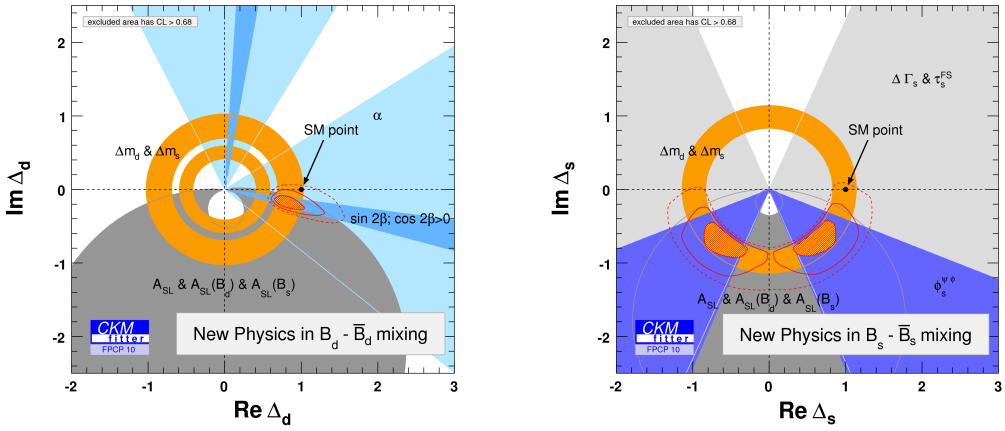

Figure 3: Constraints on new physics in neutral B-meson mixing, for the matrix element M_{12}, reproduced [12]. $\Delta_q = (M_{12}^{NP}/M_{12}^{SM})$, $q = s, d$. A combined fit finds that the Standard Model point at (1,0) is disfavoured by 3.6σ, which rests mostly on the recent measurement of flavour-specific asymmetry by the DØ collaboration [2].

choose to allow for new physics only in the most sensitive element of the mixing matrix, M_{12}, and so define $\Delta_q = (M_{12}^{NP}/M_{12}^{SM})$, the complex ratio of the new physics and Standard Model values. This parameter is constrained by several current measurements as reproduced here in Fig. 3. The measurements currently agree, but with a central value which is 3.6σ from the SM.

The majority of this departure can be attributed to the recent measurement by the DØ collaboration [2], the first independent evidence for new CPV physics.

3 Flavour-Specific Asymmetry

The DØ collaboration recently produced an exciting and surprizing result in the measurement of flavour-specific asymmetry in the semileptonic decays of b-quarks [2]. They determine the total dimuon charge asymmetry, which is interpreted as the direct result of the flavour-specific asymmetries in the B_s^0 and B_d^0 system (a_{fs}^s and a_{fs}^d, respectively). They measure a quantity

$$A^b \approx (a_{fs}^s + a_{fs}^d)/2 = [-9.57 \pm 2.51(stat) \pm 1.46(syst)] \times 10^{-3}$$

which is 3.2 standard deviations from the Standard Model prediction [2].

Fig. 4 is reproduced [2] and slightly modified to also include the expected LHCb sensitivity taken from simulation (Monte Carlo or MC), applying the real-data yields and estimates of systematic uncertainties. In the environment of the LHC, such a measurement is made more challenging by the expected production asymmetry [13], however, using a novel time-dependent [14] technique LHCb can make an accurate measurement of $\Delta A_{fs} = (a_{fs}^s - a_{fs}^d)/2$, with a statistical sensitivity (as predicted from the MC) of $\approx 2 \times 10^{-3}$ in $1\,\text{fb}^{-1}$. This measurement is complementary to the DØ measurement, and almost orthogonal in the $(a_{fs}^s : a_{fs}^d)$-plane.

4 Conclusion

I have argued that there must be new physics waiting to be discovered such that our particle physics theory can describe the observed universe. The LHC is a machine purpose-built to discover this new physics. At the LHC the complementarity of direct searches and precision measurements is crucial to identify and classify the new physics. LHCb is *the* precision heavy-flavour experiment at the LHC and will measure many different observables which all place

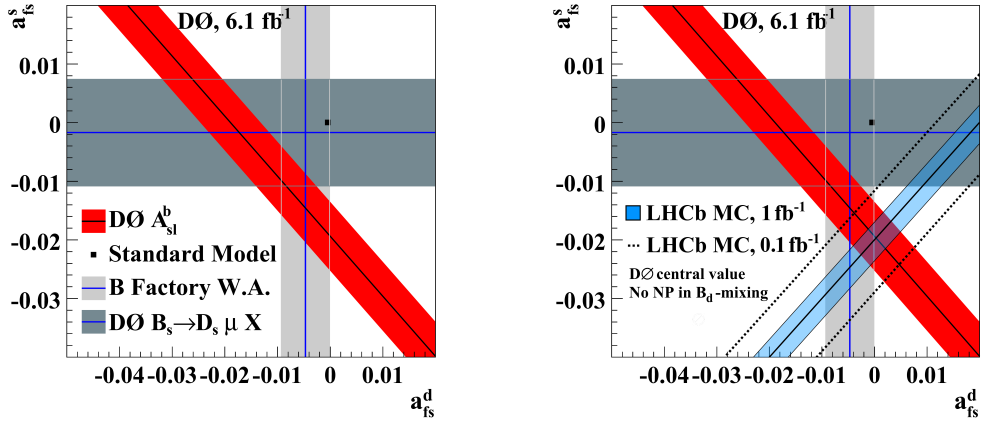

Figure 4: Measurements and prospects for new physics in flavour-specific asymmetry. The asymmetry in neutral B^0 mixing, a^d_{fs} is plotted against the asymmetry in neutral B^0_s-mixing, a^s_{fs}. The left figure is reproduced [2] (slightly modified), the recent DØ measurement in red is the first measurement inconsistent with the Standard Model point of $\sim (0, 0)$. The right figure also has superimposed the LHCb expected result from simulation (Monte Carlo), should the DØ central value hold and should there be no new physics in a^d_{fs}. There we scale the Monte Carlo (MC) prediction [14] to the yields in real data and add also the expected systematic uncertainties.

good constraints on this new physics. Finally we have already seen evidence for a departure of observation from the Standard Model in the mixing of neutral mesons, thanks to the recent measurement from DØ. In this interesting area LHCb will endeavour to make an early complementary measurement. We stand at the very beginning of the LHC era, which is already proving to be one of the most exciting times in the history of particle physics.

5 Acknowledgements

Many thanks to the conference organisers for the invitation. Thanks to J. Albrecht, U. Kerzel, T. Ruf and G. Wilkinson, for their invaluable support. Thanks also to the CKM fitter group for updating the fit results in the so-called "B_s-triangle," pointing out to me a long-standing goof in the LHCb TDR and other publications, including my own Thesis, also for putting up with my crazy questions about their fitting methods.

References

1. W. Prout, Annals of Philosophy **6** (1815) pp. 321-330.
2. DØ Collaboration, Phys. Rev. Lett. **105** (2010) pp. 081801, hep-ex arxiv:1005.2757.
3. A. Lenz and U. Nierste, hep-ph arXiv:1102.4274 (2010).
4. N. Jarosik *et al.*, ApJS **192** 14 (2011).
5. G. Wilkinson, proceedings of this conference, 2010.
6. A. D. Sakharov, JETP **5** (1967) pp. 24-27. Republished in Soviet Physics Uspekhi.
7. A. B. Carter and A. I. Sanda, Phys. Rev. D **23** (1981) pp. 1567-1579.
8. CKMfitter Group, Eur. Phys. J. C41, 1-131 (2005), http://ckmfitter.in2p3.fr.
9. LHCb collaboration, CERN-LHCb-PUB-2009-029, hep-ex arXiv:0912.4179.
10. HFAG, http://www.slac.stanford.edu/xorg/hfag/rare/ichep10/acp/index.html
11. LHCb collaboration, CERN-LHCb-PH-EP-2011-029, hep-ex arXiv:1103.2465.
12. A. Lenz *et al.*, Phys. Rev. D **83** (2011) pp. 036004, hep-ph arXiv:1102.4274.
13. U. Nierste, hep-ph 0406300 (2006).
14. R. W. Lambert, CERN-THESIS-2009-001 (2008).

RECENT B PHYSICS RESULTS FROM THE TEVATRON

SATYAJIT BEHARI
(for the CDF and DØ Collaborations)

Department of Physics, The Johns Hopkins University,
3400 N. Charles Street, Baltimore, MD 21218, USA

We review recent B physics results from the CDF and DØ experiments in $p\bar{p}$ collisions at $\sqrt{s}$ = 1.96 TeV. Using a data sample of 1.4-6.0 fb^{-1} collected by the CDF II detector we present searches for New Physics in B_s sector and some competitive results with B-factories in the B /charm sector. In the first category we report the BR in $B_s \to J/\psi f_0(980)$ decays and the time-integrated mixing probability ($\bar{\chi}$) of B mesons. In the second category BR and A_{CP} in doubly Cabibbo-suppressed $B^{\pm} \to D^0 h^{\pm}$ decays and time-integrated CP violation in $D^0 \to h^+h^-$ are presented.

1 Search for New Physics in B_s decays

Our current understanding of B_s physics, within the Standard Model (SM) and its sensitivity to New Physics (NP), is derived exclusively from the large Tevatron Run II data samples. One of the most interesting topics in this area is the measurement of B_s mixing phase, β_s. This phase is expected to be tiny in the Standard Model (SM):

$$\beta_s^{SM} = arg(-V_{ts}V_{tb}^*/V_{cs}V_{cb}^*) \approx 0.02, \tag{1}$$

and it is unconstrained by the 2006 measurements of the B_s mixing frequency. Presence of NP can lead to large values of this phase which is not excluded experimentally yet.

The β_s^{SM} phase can be accessed through measuring the time evolution of flavor-tagged $B_s \to J/\psi\phi$ decays, or inclusively by measuring the anomalous mixing rate difference, A_{sl}^b, between B_s and $\bar{B_s}$. Both these methods are pursued at CDF and DØ .

Using 5.2 fb^{-1} and 6.1 fb^{-1} data samples, respectively, CDF and DØ have performed detailed angular analyses of the $B_s \to J/\psi\phi$ decays to disentangle their CP-even and CP-odd components. Their initial results indicate departure from SM by 0.8σ [1] and 1.1σ [2], calling for more scrutiny through independent measurements.

1.1 Measurement of $BR(B_s \to J/\psi f_0(980))$

A simpler way to measure β_s is through the study of $B_s \to J/\psi f_0(980), f_0(980) \to \pi^+\pi^-$ decays. This is a pure CP-odd decay which can provide a clean measurement of β_s without a need for angular analysis. As a first step towards this CDF searched for this suppressed decay mode using 3.8 fb^{-1} data [3], collected using a di-muon trigger.

The search for $B_s \to J/\psi f_0(980)$ decays proceeds through an initial loose selection of $\mu\mu\pi\pi$ candidates, followed by a Neural Network discrimination, based on kinematic variables,

track and vertex displacement and isolation, for efficient background suppression. An identical selection is used for the $B_s \to J/\psi\phi$ reference mode. A simultanous log-likelihood fit to the signal and normalization modes yields 502±37(stat.)±18(syst.) $B_s \to J/\psi f_0(980)$ and 2302±499(stat.)±49(syst.) $B_s \to J/\psi\phi$ candidates.

Fig. 1 shows the invariant mass distribution of the $J/\psi\pi\pi$ candidate events. In addition

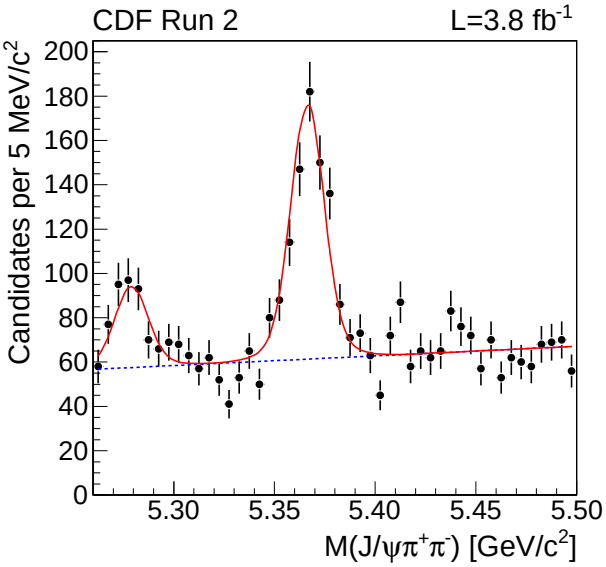

Figure 1: The invariant mass of $J\psi\pi\pi$ candidate events, measured by CDF with 3.8 fb^{-1} of data.

to the B_s peak with a significance of observation of 17.9σ, also seen is the $B^0 \to J/\psi\rho^0$ peak. The ratio between $BR(B_s \to J/\psi f_0(980), f_0(980) \to \pi\pi)$ and $BR(B_s \to J/\psi\phi, \phi \to KK)$ candidates, $R_{f_0/\phi}$, is 0.257 ± 0.020 (stat.) ± 0.014(syst.), resulting in a measurement of the branching ratio

$$BR(B_s \to J/\psi f_0(980), f_0(980) \to \pi\pi) = 1.63 \pm 0.12(stat.) \pm 0.09(syst.) \pm 0.50(PDG) \times 10^{-4}. \quad (2)$$

This is the most precise result obtained to date and confirms earlier resuts from Belle [4] and LHC-b [5].

1.2 Time-integrated mixing probability ($\bar{\chi}$) of B mesons

One of the most exciting results from Tevatron in recent times is the dimuon charge asymmetry measurement by the DØ Collaboration using muon pairs produced in semileptonic decays of b hadrons [6]. The asymmetry A^b_{sl} is defined as

$$A^b_{sl} = \frac{N_b^{++} - N_b^{--}}{N_b^{++} + N_b^{--}}, \quad (3)$$

where N_b^{++} and N_b^{--} are the numbers of same sign dimuon events produced due to the b hadrons decaying semileptonically, one before and the other after mixing. The quantity A^b_{sl} is expected to be approximately zero within the SM ($\approx$ a few 10^{-4}), if mixing rates $(B \to \bar{B})$ and $(\bar{B} \to B)$ are equal. Using a 6.1 fb^{-1} Run II data sample DØ measured $A^b_{sl} = (-0.957 \pm 0.251(stat.) \pm 0.146(syst.))\%$, which differs from the SM prediction [7] of $A^b_{sl}(SM) = (-0.023^{+0.005}_{-0.006})\%$ at about 3.2σ, indicating an anomalously large B_s mixing phase.

The CDF Collaboration is pursuing an alternate path for independent verification of the interesting DØ result. The same sign (SS) and opposite sign (OS) muon impact parameter

(IP) distributions are fitted separately to disentangle the long-lived di-muon component that originates from B decays. The IP fitting method is a robust technique demonstrated well in the correlated $B\bar{B}$ cross-section measurement [8].

As a first step towards an A_{sl}^b measurement, CDF further puts to test the IP fitting method and measures the time-integrated mixing probability, $\bar{\chi}$ [9], defined as

$$\bar{\chi} = \frac{\Gamma(B^0_{d,s} \to \bar{B}^0_{d,s} \to l^+ X)}{\Gamma(B_{all} \to l^{\pm} X)} = f_d \cdot \chi_d + f_s \cdot \chi_s \tag{4}$$

where $f_{d,s}$ are production fractions and $\chi_{d,s}$ are mixing probabilities of B_d and B_s mesons. The number of OS and SS muon pairs is measured and $\bar{\chi}$ is extracted from the ratio $R = [N(\mu^+\mu^+) + N(\mu^-\mu^-)]/N(\mu^+\mu^-)$. Fig. 2 shows the muon IP distributions for same sign dimuon pairs, with IP fit results for b, c, prompt and other sources. Using a 1.4 fb^{-1} data sample

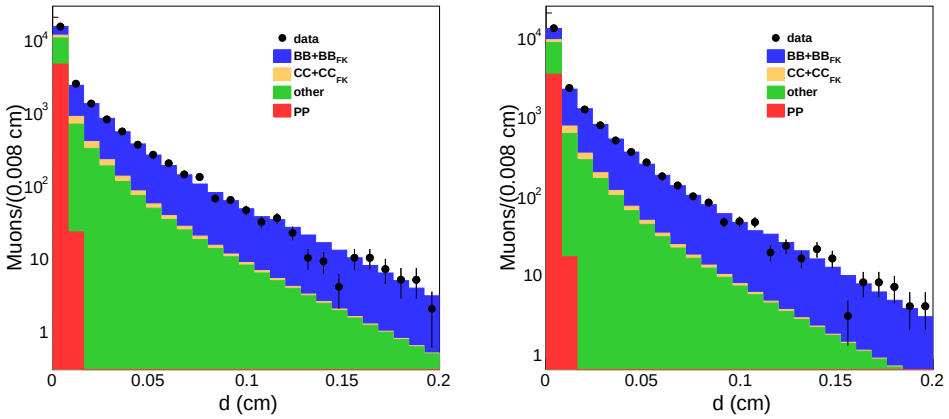

Figure 2: The muon impact parameter (IP) distributions are shown for same sign (a) $\mu^+\mu^+$ and (b) $\mu^-\mu^-$ pairs with IP fit results for b, c, prompt and other sources.

CDF measures an SS to OS ratio of R = 0.467±0.011, leading to $\bar{\chi}$=0.126±0.008, in very good agreement with the LEP result of $\bar{\chi}$=0.126±0.004. This validates the IP fitting method and presents an encouraging prospect towards CDF's future A_{sl} measurement.

2 New Tevatron results in the B /charm sector

Over the past decade, the Belle and BaBar B-factories have shaped up our knowledge of the $B_{u,d}$ and charm physics. With accumulation of large volume of Tevatron Run II data, the CDF and DØ experiments have caught up with, and in some cases surpassed, them in precision. In this section we present two new measurements from the CDF collaboration, competitive with the B-factories.

2.1 BR and A_{CP} in $B^{\pm} \to D^0 h^{\pm}$ decays

The branching fractions and searches for CP asymmetries in $B^{\pm} \to D^0 h^{\pm}$ decays allow for a theoretically clean measurement of γ, the least well constrained angle of the CKM matrix (known to 10-20° level). The proposed ADS method [10] relies on interference between $B^{\pm}$ decay modes proceeding through color allowed and suppressed modes followed by D^0 decay via doubly Cabibbo-suppressed (DCS) and Cabbibo-favoured modes, respectively, which can lead to large A_{CP}.

The DCS fraction and asymmetry in $B \to DK$ decays are defined as:

$$R_{ADS}(K) = \frac{BR(B^- \to [K^+\pi^-]_D K^-) + BR(B^+ \to [K^-\pi^+]_D K^+)}{BR(B^- \to [K^-\pi^+]_D K^-) + BR(B^+ \to [K^+\pi^-]_D K^+)} \tag{5}$$

$$A_{ADS}(K) = \frac{BR(B^- \to [K^+\pi^-]_D K^-) - BR(B^+ \to [K^-\pi^+]_D K^+)}{BR(B^- \to [K^-\pi^+]_D K^-) + BR(B^+ \to [K^+\pi^-]_D K^+)} \tag{6}$$

$$\tag{7}$$

Similar quantities for pions, $R_{ADS}(\pi)$ and $A_{ADS}(\pi)$, can be defined. The experimental challenge is to suppress the combinatorial and physics backgrounds when extracting the highly suppressed DCS signal. Using 5 fb^{-1} of CDF Run II data, a likelihood fit combining mass and particle ID information is used to distinguish the signal ($D^0\pi$ and D^0K) modes from the background [11]. Fig. 3 shows the invariant $K\pi\pi$ mass distributions for DCS signal modes separately for B^+ and B^- decays. The yields for π and K modes are 73±16 and 34±14, respectively. The

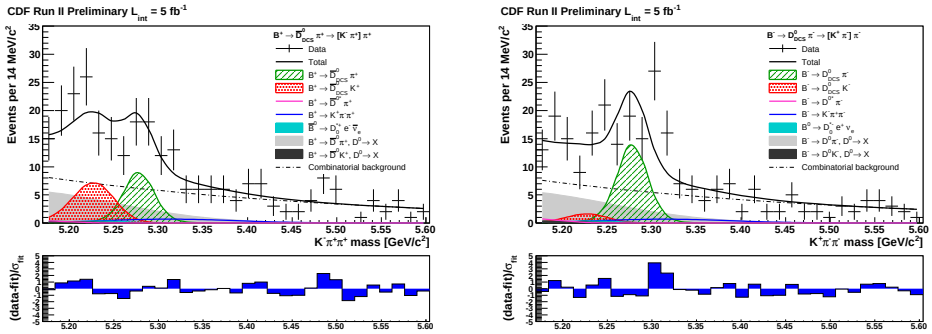

Figure 3: Invariant $K\pi\pi$ mass distributions for data and various background and signal contributions, separately for B^+ and B^- decays.

DCS fraction and asymmetry results for the Kaon mode are shown in Fig. 4, demonstrating good agreement with those from BaBar and Belle. This is the first application of the ADS method at

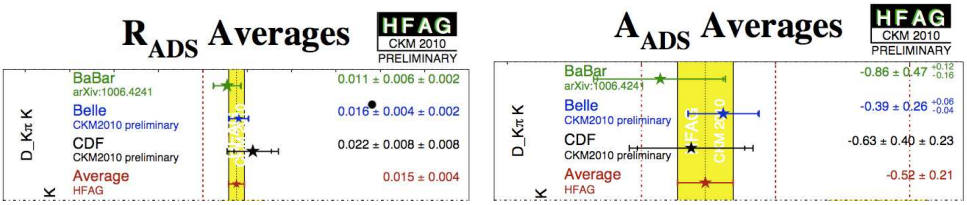

Figure 4: The DCS fraction and asymmetry results for the Kaon mode.

a hadron machine. CDF's new measurement of direct CP asymmetry for the DCS modes will be used in the future to extract γ.

2.2 Time-integrated A_{CP} in $D^0 \to h^+h^-$ decays

CP violation in the charm sector has been an area of great interest. Recent studies [12] have pointed out that, similar to D^0 oscillations, NP contributions could play a role in enhancing the size of CP violation in the charm sector. Since in SM there is negligible penguin contribution to the charm decays, an A_{CP} larger than ∼0.1% would be a clear indication of NP. The relevant asymmetry is defined as

$$A_{CP}(h^+h^-) = \frac{\Gamma(D^0 \to h^+h^-) - \Gamma(\bar{D^0} \to h^+h^-)}{\Gamma(D^0 \to h^+h^-) + \Gamma(\bar{D^0} \to h^+h^-)}. \tag{8}$$

Using a 5.94 fb^{-1} data sample of self-tagged $D^{*\pm} \to D^0\pi_s^\pm \to [h^+h^-]\pi_s^\pm$ decays CDF extracts clean $D^0 \to h^+h^-$ samples [13]. The asymmetry in $\pi\pi$ and KK samples is measured and corrected for the instrumental asymmetry using $K\pi$ samples, with and without the D^* tag. Fig. 5 shows the CP asymmetries for $D^0 \to \pi\pi$ and $D^0 \to KK$ decay modes and 68%-95% C.L. for their combination with the B-factory results. The resulting asymmetries are world's best:

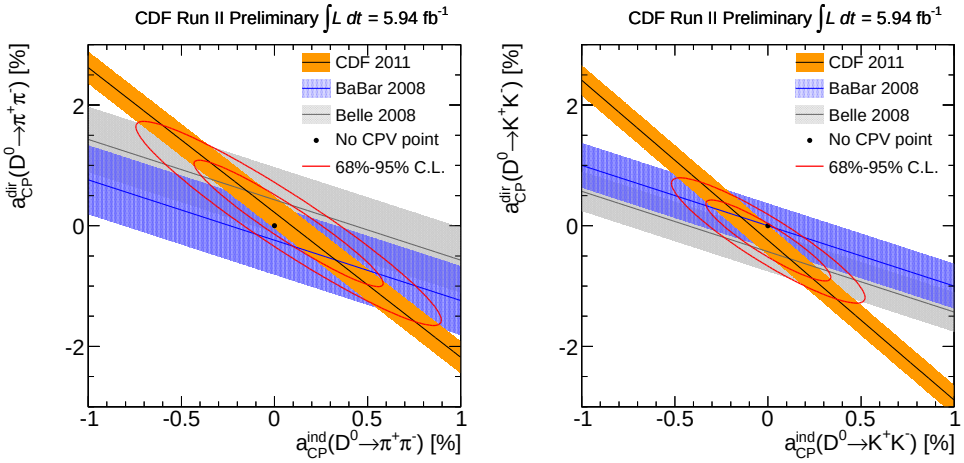

Figure 5: CP asymmetries in $D^0 \to \pi\pi$ and $D^0 \to KK$ decay modes and combination (contour) with the B-factory results.

$$A_{CP}(D^0 \to \pi^+\pi^-) = [+0.22 \pm 0.24(stat.) \pm 0.11(syst.)]\% \quad (9)$$

$$A_{CP}(D^0 \to K^+K^-) = [-0.24 \pm 0.22(stat.) \pm 0.10(syst.)]\% \quad (10)$$

and are compatible with Belle/BaBar 2008 results.

3 Conclusion

The Tevatron will continue to produce a steady flow of high luminosity data until Oct. 2011 when it is scheduled to shutdown permanently. Since mid-2000's the Tevatron experiments have emerged as leaders in the field of Heavy Flavor physics and would leave behind a rich legacy for current/future experiments through many landmark measurements. This article reviews a few of the interesting spring 2011 Heavy Flavor results from the Tevatron, which use a fraction of the accumulated data. With many more analyses in the pipeline and more data to be analyzed we look forward to challenging the SM predictions and constraining NP model parameters in the months and years to come.

Acknowledgments

The author would like to thank his CDF and DØ collaborators for their help in preparing this contribution and the conference organizers/secretariate for making the event an unique and thoroughly enjoyable experience.

References

1. The CDF Collaboration, CDF Public Note 10206 (2010).
2. The DØ Collaboration, DØ Conf. Note 6093 (2010).
3. T. Aaltonen *et al.* (The CDF Collaboration), arXiv:1106.3682v1 [hep-ex].

4. J. Li *et al.* (Belle Collaboration), *Phys. Rev. Lett.* **106**, 121802 (2011).
5. R. Aaij *et al.* (LHCb Collaboration), *Phys. Lett.* B **698**, 115 (2011).
6. V. Abazov et al, *Phys. Rev. Lett.* **105**, 081801 (2010).
7. Lenz, Nierste, arXiv:0612167 [hep-ph].
8. T. Aaltonen *et al.* (CDF collaboration), *Phys. Rev.* D **77**, 072004 (2008).
9. The CDF Collaboration, CDF Public Note 10335 (2011).
10. Atwood, Dunietz, Soni, *Phys. Rev. Lett.* **78**, 3257 (1997) and *Phys. Rev.* D **63**, 036005 (2001).
11. The CDF Collaboration, CDF Public Note 10309 (2010).
12. Grossman, Kagan, Nir, *Phys. Rev.* D **75**, 036008 (2006).
13. The CDF Collaboration, CDF Public Note 10296 (2010).

Search for $B_s^0 \to \mu^+\mu^-$ and $B_d^0 \to \mu^+\mu^-$ at LHCb

M.-O. Bettler
Istituto Nazionale di Fisica Nucleare (INFN), Sezione Firenze, Italy
and
European Organization for Nuclear Research (CERN), Geneva, Switzerland

A search for the decays $B_s^0 \to \mu^+\mu^-$ and $B_d^0 \to \mu^+\mu^-$ is performed with about $37\,\text{pb}^{-1}$ of pp collisions at $\sqrt{s} = 7\,\text{TeV}$ collected by the LHCb experiment at the Large Hadron Collider at CERN. The observed numbers of events are consistent with the background expectations. The resulting upper limits on the branching fractions are $\mathcal{B}(B_s^0 \to \mu^+\mu^-) < 5.6 \times 10^{-8}$ and $\mathcal{B}(B^0 \to \mu^+\mu^-) < 1.5 \times 10^{-8}$ at 95% confidence level.

1 Introduction

Within the Standard Model (SM) the $B_d^0 \to \mu^+\mu^-$ and $B_s^0 \to \mu^+\mu^-$ flavour changing neutral current transitions are rare as they occur only via loop diagrams and are helicity suppressed [a]. Their branching fractions (BF) predicted by the SM [1] are $\mathcal{B}(B_s^0 \to \mu^+\mu^-) = (0.32 \pm 0.02) \times 10^{-8}$ and $\mathcal{B}(B^0 \to \mu^+\mu^-) = (0.010 \pm 0.001) \times 10^{-8}$.

In New Physics models, their BF can be significantly enhanced, although in some models they are lowered. For instance, within the Minimal Supersymmetric SM [2], the BF can get contributions $\propto \tan^6\beta/M_A^4$, where M_A denotes the pseudoscalar Higgs mass and $\tan\beta$ the ratio of Higgs vacuum expectation values.

The best published 95% C.L. limits come from the D0 collaboration [3] ($6.1\ \text{fb}^{-1}$), $\mathcal{B}(B_s^0 \to \mu^+\mu^-) < 5.1 \times 10^{-8}$, and from the CDF collaboration [4] ($2\ \text{fb}^{-1}$), $\mathcal{B}(B_s^0 \to \mu^+\mu^-) < 5.8 \times 10^{-8}$ and $\mathcal{B}(B^0 \to \mu^+\mu^-) < 1.8 \times 10^{-8}$. CDF has also presented preliminary results [5] with $3.7\ \text{fb}^{-1}$, that lower the limits to $\mathcal{B}(B_s^0 \to \mu^+\mu^-) < 4.3 \times 10^{-8}$ and $\mathcal{B}(B^0 \to \mu^+\mu^-) < 0.76 \times 10^{-8}$.

The measurements presented in these proceedings use about $37\,\text{pb}^{-1}$ of integrated luminosity collected by LHCb between July and October 2010 at $\sqrt{s} = 7\,\text{TeV}$.

2 The LHCb detector

The LHCb detector [6] is a single-arm forward spectrometer with an angular coverage from about 10 mrad to 300 mrad in the bending plane. It consists of a vertex locator, a warm dipole magnet, a tracking system, two RICH detectors, a calorimeter system and a muon system.

Track momenta are measured to a precision of $\delta p/p = 0.35\ (0.5)\,\%$ at 5 (100) GeV/c. The RICH system provides charged hadron identification in a momentum range 2–100 GeV/c. Typically, kaon identification efficiencies of over 90% can be attained for a $\pi \to K$ fake rate below 10%. The calorimeter system identifies high transverse energy (E_T) hadron, electron and photon

[a] In this proceedings the inclusion of charge-conjugate states is implicit.

candidates and provides information for the trigger. The muon system provides information for the trigger and muon identification with an efficiency of $\sim 95\,\%$ for a misidentification rate of about 1–2 % for momenta above $10\,\mathrm{GeV}/c$.

LHCb has a two-level flexible and efficient trigger system exploiting the finite lifetime and large mass of heavy flavour hadrons to distinguish them from the dominant light quark processes. The first trigger level is implemented in hardware while the second trigger level is software implemented. The forward geometry allows the LHCb first level trigger to collect events with one or two muons with P_{T} values as low as $1.4\,\mathrm{GeV}/c$ for single muon and $P_{\mathrm{T}}(\mu_1) > 0.48\,\mathrm{GeV}/c$ and $P_{\mathrm{T}}(\mu_2) > 0.56\,\mathrm{GeV}/c$ for dimuon triggers. The E_{T} threshold for the hadron trigger varied in the range 2.6 to 3.6 GeV.

3 Analysis Strategy

The search for $B^0_{(s)} \to \mu^+\mu^-$ at LHCb is described in detail in Ref. [7]. Most of the background is removed by selection cuts, keeping $\sim 60\,\%$ of the reconstructed signal decays. Then each event is given a probability to be signal or background in a two-dimensional probability space defined by the dimuon invariant mass and a multivariate discriminant likelihood, the Geometrical Likelihood (GL) [10,11]. The compatibility of the observed distribution of events with a given BF hypothesis is computed using the $\mathrm{CL_S}$ method [8]. The number of expected signal events is evaluated by normalizing with channels of known BF to ensure that knowledge of the absolute luminosity and $b\bar{b}$ production cross-section is not required.

3.1 Event selection

The selection consists of loose requirements on track separation from the interaction point, decay vertex quality and compatibility of the reconstructed origin of the B meson with the interaction point. The selection cuts were defined in simulation before starting data analysis. Events passing the selection are considered $B^0_{(s)} \to \mu^+\mu^-$ candidates if their invariant mass lies within $60\,\mathrm{MeV}/c^2$ of the nominal $B^0_{(s)}$ mass. A similar selection is applied to the normalization channels, in order to minimize systematic errors in the ratio of efficiencies. Assuming the BF predicted by the SM, 0.04 (0.3) $B^0_{(s)} \to \mu^+\mu^-$ events are expected after all selection requirements. There are 343 (342) $B^0_{(s)} \to \mu^+\mu^-$ candidates selected from data in the B^0_s (B^0) mass window.

The dominant background after the $B^0_{(s)} \to \mu^+\mu^-$ selection is expected to be $b\bar{b} \to \mu\mu X$ [9]. This is confirmed by comparing the expected yield and the kinematic distributions of the side-band data with a $b\bar{b} \to \mu\mu X$ MC sample. The muon misidentification probability as a function of momentum obtained from data using $K^0_S \to \pi^+\pi^-$, $\Lambda \to p\pi^-$ and $\phi \to K^+K^-$ decays is in good agreement with MC expectations. It was found that the background from misidentified $B^0_{s,d} \to h^+h'^-$ is negligible for the amount of data used in this analysis.

3.2 Signal and background likelihoods

The discrimination of the signal from the background is achieved through the combination of two independent variables: the GL and the invariant mass. The invariant mass in the search regions ($\pm 60\,\mathrm{MeV}/c^2$ around the $B^0_{(s)}$ masses) is divided into six equal-width bins, and the GL into four equal-width bins distributed between zero and one.

The GL combines information related with the topology and kinematics of the event as the $B^0_{(s)}$ lifetime, the minimum impact parameter of the two muons, the distance of closest approach of the two tracks, the $B^0_{(s)}$ impact parameter and p_T and the isolation of the muons with respect to the other tracks of the event. These variables are combined using the method described in

Ref. [10,11]. The expected GL distribution for signal events is flat, while for background events it falls exponentially.

The GL variable is defined using MC simulations but calibrated with data using $B^0_{(s)} \to h^+h'^-$ selected as the signal events and triggered independently on the signal in order to avoid trigger bias. The number of $B^0_{(s)} \to h^+h'^-$ events in each GL bin is obtained from a fit to the inclusive mass distribution.

The $B^0_{(s)} \to \mu^+\mu^-$ mass resolution is estimated from data via two methods. The first uses an interpolation to $M_{B^0_s}$ between the measured resolutions for $c\bar{c}$ resonances (J/ψ, ψ(2S)) and $b\bar{b}$ resonances ($\Upsilon(1S)$, $\Upsilon(2S)$, $\Upsilon(3S)$) decaying into two muons. Both methods yield consistent results and their weighted average, $\sigma = 26.7 \pm 0.9\,\mathrm{MeV}/c^2$, is taken as the invariant mass resolution for both B^0 and B^0_s decays.

The prediction of the number of background events in the signal regions is obtained by fitting an exponential function to the $\mu\mu$ mass sidebands independently in each GL bin. The mass sidebands are defined in the range between $M_{B^0_{(s)}} \pm 600\ (1200)\,\mathrm{MeV}/c^2$ for the lower (upper) two GL bins, excluding the two search regions ($M_{B^0_{(s)}} \pm 60\,\mathrm{MeV}/c^2$).

3.3 Normalization

The number of expected signal events is evaluated by normalizing with three channels of known BF, $B^+ \to J/\psi K^+$, $B^0_s \to J/\psi\phi$ and $B^0 \to K^+\pi^-$. The first two decays have similar trigger and muon identification efficiency to the signal but a different number of final-state particles, while the third channel has the same two-body topology but cannot be efficiently selected with the muon triggers.

For a given normalization channel, $\mathcal{B}(B^0_{(s)} \to \mu^+\mu^-)$ can be calculated as:

$$\begin{aligned}\mathcal{B}(B^0_{(s)} \to \mu^+\mu^-) &= \mathcal{B}_{\rm norm} \times \frac{\epsilon^{\rm REC}_{\rm norm}\epsilon^{\rm SEL|REC}_{\rm norm}\epsilon^{\rm TRIG|SEL}_{\rm norm}}{\epsilon^{\rm REC}_{\rm sig}\epsilon^{\rm SEL|REC}_{\rm sig}\epsilon^{\rm TRIG|SEL}_{\rm sig}} \times \frac{f_{\rm norm}}{f_{B^0_{(s)}}} \times \frac{N_{B^0_{(s)}\to\mu\mu}}{N_{\rm norm}} \\ &= \alpha_{B^0_{(s)}\to\mu\mu} \times N_{B^0_{(s)}\to\mu\mu}\,,\end{aligned}$$

where $\alpha_{B^0_{(s)}\to\mu\mu}$ denotes the normalization factor, $f_{B^0_{(s)}}$ the probability that a b-quark fragments into a $B^0_{(s)}$ and $f_{\rm norm}$ the probability that a b-quark fragments into the b-hadron relevant for the chosen normalization channel with BF $\mathcal{B}_{\rm norm}$. The reconstruction efficiency ($\epsilon^{\rm REC}$) includes the acceptance and particle identification, $\epsilon^{\rm SEL|REC}$ denotes the selection efficiency on reconstructed events and $\epsilon^{\rm TRIG|SEL}$ is the trigger efficiency on selected events. The ratios of reconstruction and selection efficiencies are estimated from simulations and checked with data, while the ratios of trigger efficiencies on selected events are determined from data [15].

The normalization factors calculated using the three channels give compatible results; the final normalization factors are weighted averages and read $\alpha_{B^0_{(s)}\to\mu\mu} = (8.6 \pm 1.1) \times 10^{-9}$ and $\alpha_{B^0\to\mu\mu} = (2.24 \pm 0.16) \times 10^{-9}$.

4 Results

For each of the 24 bins, the expected number of background events is computed from the fits to the invariant mass sidebands. For a given BF hypothesis, the expected number of signal events is computed using the normalization factors and the signal likelihoods. For each BF hypothesis, the compatibility of the expected distributions with the observed distribution is evaluated using the $\mathrm{CL_S}$ method [8].

The observed distribution of $\mathrm{CL_S}$ as a function of BF hypothesis can be seen in Fig. 1. The expected distributions of possible values of $\mathrm{CL_S}$ assuming the background-only hypothesis are

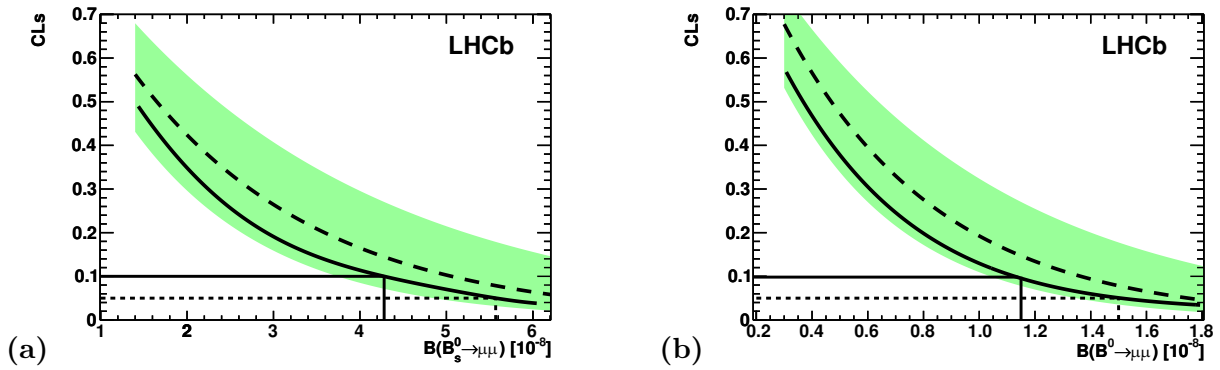

Figure 1: (a) Observed (solid curve) and expected (dashed curve) CL_s values as a function of $\mathcal{B}(B_s^0 \to \mu^+\mu^-)$. The green shaded area contains the $\pm 1\sigma$ interval of possible results compatible with the expected value when only background is observed. The 90 % (95 %) C.L. observed value is identified by the solid (dashed) line. (b) the same for $\mathcal{B}(B^0 \to \mu^+\mu^-)$.

also shown in the same figure as a green area covering the region of $\pm 1\sigma$ of background-only compatible observations. The uncertainties in the signal and background likelihoods and normalization factors are used to compute the uncertainties in the background and signal predictions. The upper limits read:

$$\begin{aligned} \mathcal{B}(B_s^0 \to \mu^+\mu^-) &< 4.3\ (5.6) \times 10^{-8} \text{ at } 90\,\%\ (95\,\%) \text{ C.L.}, \\ \mathcal{B}(B^0 \to \mu^+\mu^-) &< 1.2\ (1.5) \times 10^{-8} \text{ at } 90\,\%\ (95\,\%) \text{ C.L.}, \end{aligned}$$

while the expected values of the limits are $\mathcal{B}(B_s^0 \to \mu^+\mu^-) < 5.1\ (6.5) \times 10^{-8}$ and $\mathcal{B}(B^0 \to \mu^+\mu^-) < 1.4\ (1.8) \times 10^{-8}$ at 90 % (95 %) C.L. The limits observed are similar to the best published limits for the $B_s^0 \to \mu^+\mu^-$ decay and more restrictive for the $B^0 \to \mu^+\mu^-$ decay.

References

1. A.J. Buras, arXiv:1012.1447;
   E. Gamiz *et al*, *Phys. Rev.* D**80** (2009) 014503;
   A.J. Buras, *Phys. Lett.* B**566** (2003) 115.
2. C. Hamzaoui, M. Pospelov and M. Toharia, "Higgs-mediated FCNC in supersymmetric models with large tan β", *Phys. Rev.* D**59** (1999) 095005; S.Rai Choudhury and N. Gaur, *Phys. Lett.* B**451** (1999) 86; K.S. Babu and C.F. Kolda, *Phys. Rev. Lett.***84** (2000) 228.
3. V. Abazov *et al.* [D0 Collaboration], *Phys. Lett.* B**693** (2010) 539.
4. T. Aaltonen *et al.* [CDF Collaboration], *Phys. Rev. Lett.***100** (2008) 101802.
5. T. Aaltonen *et al.* [CDF Collaboration], CDF Public Note 9892.
6. A.A. Alves *et al.* [LHCb Collaboration], *JINST***3** (2008) S08005.
7. R. Aaij *et al.* [LHCb Collaboration], *Phys. Lett.* B**699** (2011), 330.
8. A.L. Read, *J. Phys.* G**28** (2002) 2693;
   T. Junk, *Nucl. Instrum. Methods* A**434** (1999) 435.
9. B. Adeva *et al.* [LHCb Collaboration], arXiv:0912.4179.
10. D. Karlen, *Comp. Phys.* **12** (1998) 380.
11. D. Martinez Santos, CERN-THESIS-2010-068.
12. K. Nakamura *et al.* [Particle Data Group], *J. Phys.* G**37** (2010) 075021.
13. D. Asner *et al.* [Heavy Flavour Averaging Group], arXiv:1010.1589. Updated values for f_d/f_s available at http://www.slac.stanford.edu/xorg/hfag/osc/end_2009/ have been used.
14. R. Louvot, arXiv:0905.4345.
15. E. Lopez Asamar et al., LHCb-PUB-2007-073.

IN PURSUIT OF NEW PHYSICS WITH B DECAYS

ROBERT FLEISCHER
Nikhef, Theory Group, Science Park 105
NL-1098 XG Amsterdam, The Netherlands

Decays of B mesons offer interesting probes to search for physics beyond the Standard Model. Thanks to the data taking at the LHC, we are at the beginning of a new era of precision B physics. I will discuss recent developments concerning the analyses of promising channels to search for signals of New Physics at the LHC, $B_s^0 \to J/\psi\phi$, $B_s^0 \to K^+K^-$ and $B_s^0 \to \mu^+\mu^-$.

1 Setting the Stage

The lessons from the data on weak decays of B, D and K mesons collected so far is that the Cabibbo–Kobayashi–Maskawa (CKM) matrix is the dominant source of flavour and CP violation. New effects have not yet been established although there are potential signals in the flavour sector. The implications for the structure of New Physics (NP) is that we may actually have to deal with a large characteristic NP scale $\Lambda_{\rm NP}$, i.e. one that is not just in the TeV regime, or (and?) that symmetries prevent large NP effects in the flavour sector.

The best known example of the latter feature is "Minimal Flavour Violation" (MFV), where – sloppily speaking – CP and flavour violation is essentially the same as in the Standard Model (SM). However, it should be emphasized that MFV is still far from being experimentally established and that there are various non-MFV scenarios with room for sizeable effects.[1]

Nevertheless, we have to be prepared to deal with smallish NP signals. But the excellent news is that we are at the beginning of a new era in particle physics, the LHC era, which will also bring us to new frontiers in high-precision B physics.

2 Promising B-Physics Probes to Search for New Physics

2.1 $B_s^0 \to J/\psi\phi$

A particularly interesting decay is $B_s^0 \to J/\psi\phi$, offering a sensitive probe for CP-violating NP contributions to B_s^0–$\bar{B}_s^0$ mixing. In the SM, the corresponding CP-violating phase ϕ_s is tiny, taking a value of about -2°. However, NP effects may well generate a sizable phase, which actually happens in various specific extensions of the SM.[1] This phase enters the mixing-induced CP violation $\mathcal{A}_{\rm CP}^{\rm mix}$ in $B_s^0 \to J/\psi\phi$, which arises from the interference between B_s^0–$\bar{B}_s^0$ mixing and decay processes. As the final state is a mixture of CP-odd and CP-even eigenstates, a time-dependent angular analysis of the $J/\psi[\to \mu^+\mu^-]\phi[\to\ K^+K^-]$ decay products is needed in order to disentangle them.[2] Neglecting doubly Cabibbo-suppressed terms of the decay amplitude (see below), hadronic parameters cancel and $\mathcal{A}_{\rm CP}^{\rm mix} = \sin\phi_s$. Since the tiny SM value of ϕ_s implies smallish CP violation in $B_s^0 \to J/\psi\phi$, this channel plays a key role in the search for NP.[3]

Since a couple of years, measurements of CP violation in $B_s^0 \to J/\psi\phi$ at the Tevatron indicate possible NP effects in B_s^0–$\bar{B}_s^0$ mixing, which are also complemented by the measurement of the anomalous like-sign dimuon charge asymmetry at DØ. LHCb has also joined the arena, with a first untagged analysis reported at Moriond 2011,[4] and a first tagged analysis reported a couple of weeks later. Interestingly, this measurement points to a picture similar to that obtained at the Tevatron, with a sign of a sizable, negative value of ϕ_s. However, the large uncertainties preclude definite conclusions. Fortunately, the prospects for analyses of CP violation in $B_s^0 \to J/\psi\phi$ are excellent: the 2011 LHCb data (1 fb^{-1}) should allow the world's best measurement of ϕ_s.

SM penguin effects, which are described by a CP-conserving hadronic parameter $ae^{i\theta}$, are usually neglected in these analyses. They enter the decay amplitude in the following form:

$$A(B_s^0 \to J/\psi\phi) \propto \mathcal{A}\left[1 + \epsilon(ae^{i\theta})e^{i\gamma}\right], \tag{1}$$

where $\epsilon \equiv \lambda^2/(1-\lambda^2) = 0.05$ with $\lambda \equiv |V_{us}|$, and modify the mixing-induced CP asymmetry as $\mathcal{A}_{\rm CP}^{\rm mix} \propto \sin(\phi_s + \Delta\phi_s)$.[5] The hadronic shift $\Delta\phi_s$ can be controlled through $B_s^0 \to J/\psi\bar{K}^{*0}$, which has recently been observed by the CDF and LHCb collaborations. Two scenarios emerge:

- *Optimistic:* large $\mathcal{A}_{\rm CP}^{\rm mix} \sim -40\%$ would be an unambiguous signal of NP.
- *Pessimistic:* smallish $\mathcal{A}_{\rm CP}^{\rm mix} \sim -(5...10)\%$ would require more work to clarify the picture.

The hadronic shift $\Delta\phi_s$ must in any case be controlled in order to match the future LHCb experimental precision, in particular for an LHCb upgrade.

An interesting probe for similar penguin topologies is also provided by the $B_s^0 \to J/\psi K_{\rm S}$ channel,[6] which is related to $B_d^0 \to J/\psi K_{\rm S}$ by the U-spin symmetry of strong interactions, allowing a determination of the angle γ of the unitarity triangle and the control of the penguin uncertainties in the extraction of the B_d^0–$\bar{B}_d^0$ mixing phase ϕ_d from $B_d^0 \to J/\psi K_{\rm S}$. CDF has recently observed the $B_s^0 \to J/\psi K_{\rm S}$ mode. A detailed phenomenological analysis has recently been performed,[7] with a first (toy) feasibility study for LHCb. This study has shown that the determination of γ is feasible, while the main application will be the control of the penguin effects. The $B_s^0 \to J/\psi K_{\rm S}$ decay looks particularly interesting for the LHCb upgrade.

2.2 $B_s^0 \to K^+K^-$

The decay $B_s^0 \to K^+K^-$ can be related to $B_d^0 \to \pi^+\pi^-$ by means of the U-spin symmetry of strong interactions.[8] In the SM, the decay amplitudes can be written as follows:

$$A(B_s^0 \to K^+K^-) \propto \mathcal{C}'\left[e^{i\gamma} + d'e^{i\theta'}/\epsilon\right], \quad A(B_d^0 \to \pi^+\pi^-) \propto \mathcal{C}\left[e^{i\gamma} - d\,e^{i\theta}\right], \tag{2}$$

where $\mathcal{C}$, $\mathcal{C}'$ and $d\,e^{i\theta}$, $d'\,e^{i\theta'}$ are CP-conserving "hadronic" parameters. The U-spin symmetry implies $d' = d$, $\theta' = \theta$, allowing the determination both of γ and of the hadronic parameters $d(= d')$, θ and θ' from the observables of the $B_s^0 \to K^+K^-$, $B_d^0 \to \pi^+\pi^-$ system.[8] At LHCb, thanks to precise measurements of the corresponding CP-violating asymmetries, this strategy is expected to give an experimental accuracy for γ of only a few degrees.[9]

In order to get ready for the LHCb data (and improved Tevatron measurements), an analysis of $B_s^0 \to K^+K^-$ was recently performed.[10] As input, it uses B-factory data in combination with ${\rm BR}(B_s \to K^+K^-)$ measurements by CDF and Belle at the $\Upsilon(5S)$ resonance as well as updated information on U-spin-breaking form-factor ratios. The following result for γ is obtained:

$$\gamma = (68.3^{+4.9}_{-5.7}|_{\rm input}{}^{+5.0}_{-3.7}|_{\xi}{}^{+0.1}_{-0.2}|_{\Delta\theta})^\circ, \tag{3}$$

where $\xi \equiv d'/d = 1 \pm 0.15$ and $\Delta\theta \equiv \theta' - \theta = \pm 20^\circ$ was assumed to explore the sensitivity to U-spin-breaking effects. This result is in excellent and remarkable agreement with the fits of the unitarity triangle, $\gamma = (67.2 \pm 3.9)^\circ$ [CKMfitter] and $(69.6 \pm 3.1)^\circ$ [UTfit].

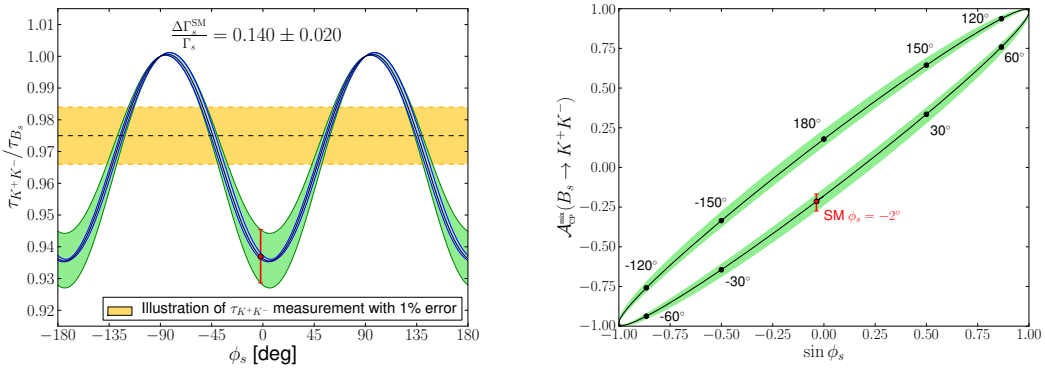

Figure 1: Dependence of $\tau_{K^+K^-}$ and $\mathcal{A}_{\rm CP}^{\rm mix}(B_s \to K^+K^-)$ on ϕ_s, as obtained and discussed in Ref. [10].

Consequently, large CP-violating NP contributions to the decay amplitudes in Eq. (2) are already excluded. However, NP may well enter through B_s^0–$\bar{B}_s^0$ mixing. A particularly nice and simple observable is the effective $B_s^0 \to K^+K^-$ lifetime $\tau_{K^+K^-}$.[10] In the left panel of Fig. 1, the SM prediction for $\tau_{K^+K^-}$ and its dependence on ϕ_s is shown. The major source of the theoretical uncertainty is the SM value of the width difference of the B_s system whereas the uncertainties of the input parameters and U-spin-breaking corrections have a much smaller impact, as illustrated by the narrow band. LHCb has recently reported the first measurement of $\tau_{K^+K^-}$,[11] and the uncertainty should soon be reduced significantly, where an error as illustrated in the figure appears to be achievable. The next observable to enter the stage is the mixing-induced CP asymmetry $\mathcal{A}_{\rm CP}^{\rm mix}(B_s \to K^+K^-)$. In the right panel of Fig. 1, its correlation with $\sin\phi_s$ is shown. The analysis of this observable turns out to be again very robust with respect to the uncertainties of the input quantities.

It becomes obvious that $\tau_{K^+K^-}$ and $\mathcal{A}_{\rm CP}^{\rm mix}(B_s \to K^+K^-)$ offer interesting probes for CP-violating NP in B_s^0–$\bar{B}_s^0$ mixing,[10] thereby complementing the analyses of $B_s^0 \to J/\psi\phi$. Once the CP asymmetries of the $B_s^0 \to K^+K^-$, $B_d^0 \to \pi^+\pi^-$ system have been measured by LHCb, γ can be extracted in an optimal way.[8] Based on the picture emerging from the current data, a stable situation with respect to U-spin-breaking corrections is expected.[10]

2.3 $B_s^0 \to \mu^+\mu^-$

The $B_s^0 \to \mu^+\mu^-$ channel originates from penguin and box topologies in the SM and is a well-known probe for NP. The upper bounds from the Tevatron and the first LHCb constraint, which was reported at Moriond 2011,[12] are about one order of magnitude above the SM expectation of $\mathrm{BR}(B_s \to \mu^+\mu^-) = (3.6 \pm 0.4) \times 10^{-9}$, where the error is dominated by a lattice QCD input.[1]

Concerning the measurement of $B_s^0 \to \mu^+\mu^-$ at LHCb, the major source of uncertainty for the normalization of the branching ratio is f_d/f_s, where f_q is the fragmentation function describing the probability that a b quark hadronizes as a B_q meson.[9]

In view of this challenge, a new strategy was proposed,[13] allowing the measurement of f_d/f_s at LHCb. The starting point is

$$\frac{N_s}{N_d} = \frac{f_s}{f_d} \times \frac{\epsilon(B_s \to X_1)}{\epsilon(B_d \to X_2)} \times \frac{\mathrm{BR}(B_s \to X_1)}{\mathrm{BR}(B_d \to X_2)}, \tag{4}$$

where the N factors denote the observed number of events and the ϵ factors are total detector efficiencies. Knowing the ratio of the branching ratios, f_d/f_s could be extracted. In order to implement this feature in practice, the $B_s \to X_1$ and $B_d \to X_2$ decays have to satisfy the following requirements: the ratio of their branching ratios must be "easy" to measure at

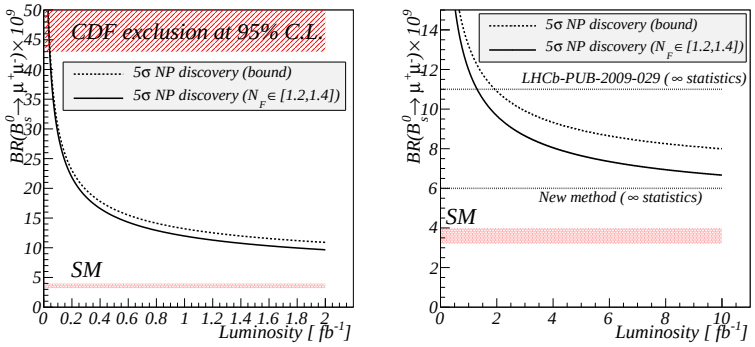

Figure 2: Illustration of the LHCb NP reach in $B_s^0 \to \mu^+\mu^-$ resulting from the strategy proposed in Ref. [13].

LHCb, the decays must be robust with respect to the impact of NP, and the ratio of their BRs must be theoretically well understood. These requirements are satisfied by the U-spin-related $\bar{B}_s^0 \to D_s^+\pi^-$ and $\bar{B}_d^0 \to D^+K^-$ decays. In these channels, "factorization" of hadronic matrix elements is expected to work very well, and the theoretical precision is limited by non-factorizable U-spin-breaking effects, leading to an uncertainty at the few-percent level. These features can also be tested through experimental data, supporting this picture.[14] The NP discovery potential in $B_s^0 \to \mu^+\mu^-$ at LHCb resulting from this method is illustrated in Fig. 2, which shows the smallest value of $\mathrm{BR}(B_s^0 \to \mu^+\mu^-)$ allowing the detection of a 5σ deviation from the SM as a function of the luminosity at LHCb (at the nominal beam energy of 14 TeV).[13]

LHCb has reported the first results for f_s/f_d from this strategy at this conference,[15] yielding $f_s/f_d = 0.245 \pm 0.017|_{\mathrm{stat}} \pm 0.018|_{\mathrm{sys}} \pm 0.018|_{\mathrm{theo}}$. This is an average over the data for the $\bar{B}_s^0 \to D_s^+\pi^-$, $\bar{B}_d^0 \to D^+K^-$ and $\bar{B}_s^0 \to D_s^+\pi^-$, $\bar{B}_d^0 \to D^+\pi^-$ systems, where the latter offers a variant of the method for extracting f_s/f_d.[14]

3 Concluding Remarks

We are moving towards new frontiers in B physics. There are good chances that these studies will reveal first footprints of NP at the LHC. Exciting years are ahead of us!

References

1. A. J. Buras, PoS E **PS-HEP2009** (2009) 024 [arXiv:0910.1032 [hep-ph]].
2. A. S. Dighe, I. Dunietz and R. Fleischer, Eur. Phys. J. C **6** (1999) 647.
3. I. Dunietz, R. Fleischer and U. Nierste, Phys. Rev. D **63** (2001) 114015.
4. LHCb Collaboration, LHCb-CONF-2011-002.
5. S. Faller, R. Fleischer and T. Mannel, *Phys. Rev.* D **79** (2009) 014005.
6. R. Fleischer, *Eur. Phys. J.* C **10** (1999) 299.
7. K. De Bruyn, R. Fleischer and P. Koppenburg, *Eur. Phys. J.* C **70** (2010) 1025.
8. R. Fleischer, *Phys. Lett.* B **459** (1999) 306; *Eur. Phys. J.* C **52** (2007) 267.
9. B. Adeva *et al.* [LHCb Collaboration], LHCb-PUB-2009-029 [arXiv:0912.4179 [hep-ex]].
10. R. Fleischer and R. Knegjens, *Eur. Phys. J.* C **71** (2011) 1532.
11. LHCb Collaboration, LHCb-CONF-2011-018.
12. R. Aaij *et al.* [LHCb Collaboration], *Phys. Lett.* B **699** (2011) 330.
13. R. Fleischer, N. Serra and N. Tuning, *Phys. Rev.* D **82** (2010) 034038.
14. R. Fleischer, N. Serra and N. Tuning, *Phys. Rev.* D **83** (2011) 014017.
15. LHCb Collaboration, LHCb-CONF-2011-013.

CHARMLESS HADRONIC B-DECAYS AT *BABAR* AND Belle

N. ARNAUD, representing the *BABAR* and Belle collaborations
Laboratoire de L'Accélérateur Linéaire, IN2P3/CNRS et Université Paris Sud XI, F-91898 Orsay Cedex, France

We report recent results for charmless hadronic B decays from the B-factories. Three *BABAR* analyses are presented: $B \to \phi\phi K$; $B^+ \to \rho^0 K^{*+}$ and $B^+ \to f_0(980)K^{*+}$; inclusive $B \to XK^+$, XK^0 and $X\pi^+$ beyond the charm threshold. Two Belle results are described: search for the $X(214)$ through charmless rare B decays; first measurement of inclusive $B \to X_s\eta$.

1 Introduction

Charmless hadronic B decays are rare processes which branching fractions (BFs) are mostly in the $10^{-6} - 10^{-5}$ range. Yet, about 100 decay modes have been measured [1] with a significance $\geq 4\sigma$, mostly by the B-factories. Indeed these modes allow one to probe the Standard Model of particle physics (SM). The processes are dominated by $b \to u$ trees and $b \to s, d$ gluonic penguins. As the trees are suppressed by the Cabibbo-Kobayashi-Maskawa mechanism [2], the penguins amplitudes are often significant or even dominant. Such loops are ideal places to look for New Physics (NP) as yet-unknown heavy particles could contribute to these decays and yield amplitudes that are significantly different from the SM ones. Moreover, interferences between amplitudes accommodate searches for CP violation and allow relative phase measurements through Dalitz Plot (DP) analysis. Finally, studying such decays helps testing predictions from factorization, perturbative QCD, SU(3) flavour symmetry, etc.

These proceedings review recent results[3,4,5,6,7] from the *BABAR* [8] and Belle [9] experiments which took data during the past decade at the high luminosity$B$-factories PEP-II [10] and KEK-B [11]. Unless otherwise noted, the first uncertainty quoted for a result is statistical and the second systematic. Charge-conjugate states are assumed throughout this document.

2 Analysis techniques

When studying charmless hadronic B decays, the signal is usually small relatively to a large background coming from the production of light quark pairs ($e^+e^- \to q\overline{q}$ with $q = u, d, s, c$: the 'continuum') and other B decays. Correctly reconstructed B decays are selected using two kinematical variables computed in the center-of-mass (CM) frame: the energy-substituted mass $m_{\rm ES} = \sqrt{\left(E^{\rm CM}_{\rm beam}\right)^2 - \left(p^{\rm CM}_B\right)^2}$ (Belle: M_{bc}) which peaks at the B mass, and the energy difference $\Delta E = E_B - \sqrt{s}/2$ that peaks at 0 ($\sqrt{s}$ is the total CM energy). Multivariate analyses combining event-shape variables computed in the CM frame are used to separate B decays ('spherical' as the $B\overline{B}$ pairs are almost produced at rest) from continuum events ('jet-like' as more kinetic energy is available for these decays). Several exclusive or inclusive B background decays are studied

and then grouped in classes with similar kinematics and topological properties. These event categories are used in an unbinned extended likelihood fit which combines several discriminating variables and is usually conducted to compute the contributions of the different event categories included in the analysis. The '$B_{\rm reco}$' technique is another way to fight against background. In this case, one of the two B mesons produced in the event is fully reconstructed through exclusive hadronic ($B \to D^{(*)}Y^{\pm}$ where $Y^{\pm}$ is a combination of hadrons) or semi-leptonic ($B \to D^{(*)}l\nu_l$) decays. For each of these channels, Monte-Carlo simulations allow one to compute their purity and efficiency. Depending on the analysis needs, samples favouring either of these criteria can be selected by choosing a subset of the numerous '$B_{\rm reco}$' modes reconstructed in data.

3 Results

3.1 $B \to \phi\phi K$ (BABAR)

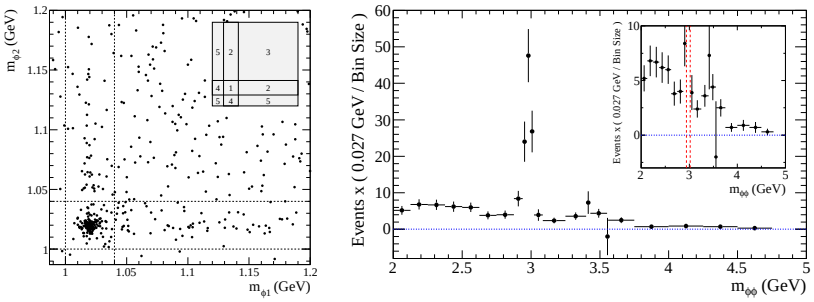

Figure 1: Left plot: signal-enhanced distribution of the selected data in the $m_{\phi 2}$ vs. $m_{\phi 1}$ plane. 5 zones have been defined in this plane (see inset) to measure the signal yield and the contributions of the 4 peaking B background categories. Right plot: fitted $B \to \phi\phi K^+$ yield as a function of the $\phi\phi$ invariant mass. The η_c resonance is clearly visible whereas there is no sign of the χ_c resonances in the two narrow bins around 3.5 GeV/c^2.

The final state $\phi\phi K$ occurs through either a one-loop 'penguin' $b \to s\bar{s}s$ transition or the $b \to c\bar{c}s$ tree-level decay $B \to \eta_c K$ with $\eta_c \to \phi\phi$. Therefore, these two amplitudes can interfere if the $\phi\phi$ invariant mass $m_{\phi\phi}$ is close to the η_c resonance. In the SM, no CP violation is expected from this effect as the relative weak phase difference between the two amplitudes is approximately 0. Conversely, measuring a significant direct CP asymmetry in this channel [12] would clearly trigger NP contributions to the penguin loop. This analysis uses 464×10^6 $B\overline{B}$ events. The branching fractions measured in the invariant mass range below the η_c resonance ($m_{\phi\phi} < 2.85$ GeV) are $\mathcal{B}(B^+ \to \phi\phi K^+) = (5.6 \pm 0.5 \pm 0.3) \times 10^{-6}$ and $\mathcal{B}(B^0 \to \phi\phi K^0) = (4.5 \pm 0.8 \pm 0.3) \times 10^{-6}$ – the neutral mode had not been previously observed with a significance greater than 5σ. They are consistent with the previous *BABAR* measurement [13] (now superseded) and larger than (although statistically compatible with) the Belle results [14]. They are also higher than the theoretical predictions [15]. The direct CP asymmetries for the $B^{\pm}$ modes are $A_{CP} = -0.10 \pm 0.08 \pm 0.02$ below the η_c threshold ($m_{\phi\phi} < 2.85\,{\rm GeV/c^2}$) and $A_{CP} = 0.09 \pm 0.10 \pm 0.02$ in the η_c resonance region ($2.94 \leq m_{\phi\phi} \leq 3.02\,{\rm GeV/c^2}$). These are consistent with zero, in agreement with the SM. Finally, angular distributions of the $B^+ \to \phi\phi K^+$ decays have been studied. They are consistent with $J^P = 0^-$ in the η_c resonance region and favor $J^P = 0^+$ below.

3.2 $B^+ \to \rho^0 K^{*+}$ and $B^+ \to f_0(980)K^{*+}$ (BABAR)

Several B decays to vector-vector (VV) modes like $B^+ \to \rho^0 K^{*+}$ (not observed prior to this analysis) have been studied. For most of them, there is a discrepancy regarding the longitudinal polarization f_L between the predictions from QCD factorization models ($f_L \sim 1$) and the mea-

surements ($f_L \sim 0.5$). Several attempts to understand this 'polarization puzzle' [16] have been made, either within or beyond the SM. This analysis uses a sample of $(467 \pm 5) \times 10^6$ $B\overline{B}$ pairs and supersedes the previous *BABAR* results. It reports measurements of the branching fraction $\mathcal{B}(B^+ \to \rho^0 K^{*+}) = (4.6 \pm 1.0 \pm 0.4) \times 10^{-6}$ (first observation with a 5.3σ significance, compatible with theoretical predictions), longitudinal polarization $f_L = 0.78 \pm 0.12 \pm 0.03$ (both consistent with the theoretical predictions and with the measured values for the two other $K^*\rho$ modes) and direct CP-violation asymmetry $A_{CP} = 0.31 \pm 0.13 \pm 0.03$ for the decay $B^+ \to \rho^0 K^{*+}$ such as measurement of the branching fraction $\mathcal{B}(B^+ \to f_0(980) K^{*+}) = (4.2 \pm 0.6 \pm 0.3) \times 10^{-6}$ and direct CP-violation asymmetry $A_{CP} = -0.15 \pm 0.12 \pm 0.03$ for the mode $B^+ \to f_0(980) K^{*+}$ which shares the same final states (assuming a branching fraction of 100% for $f_0(980) \to \pi^+\pi^-$).

3.3 Inclusive $B \to XK^+$, XK^0 and $X\pi^+$ beyond the charm threshold (BABAR)

For these decays, theoretical models [18] predict enhancements up to one order of magnitude of the branching fractions with respect to the SM if NP enters in the loop diagrams. This analysis uses 383 $\times$ 10^6 $B\overline{B}$ pairs out of which 2 $\times$ 10^6 events are reconstructed using the hadronic $B_{\rm reco}$ selection technique. Partial branching fractions above the end point for decays to charmed mesons – the momentum p^* of the candidate hadron greater than 2.34 (2.36) GeV/c for kaons (pions) in the $B_{\rm sig}$ rest frame – are reported: $\mathcal{B}(B \to XK^+,\ p* > 2.34\ \text{GeV/c}) = (1.2 \pm 0.3 \pm 0.4) \times 10^{-4} < 1.9 \times 10^{-4}$ at 90% C.L.; $\mathcal{B}(B \to XK^0,\ p* > 2.34\ \text{GeV/c}) = (1.9 \pm 0.5 \pm 0.5) \times 10^{-4} < 2.9 \times 10^{-4}$ at 90% C.L.; $\mathcal{B}(B \to X\pi^+,\ p* > 2.34\ \text{GeV/c}) = (3.7 \pm 0.5 \pm 0.6) \times 10^{-4}$, a decay observed inclusively independently of known exclusive modes. These results are in agreement with the SM and exclude large enhancement due to NP. In addition, no direct CP-asymmetry is observed in the charged modes: $A_{CP}(B \to XK^+) = 0.57 \pm 0.24 \pm 0.05$ and $A_{CP}(B \to X\pi^+) = 0.10 \pm 0.16 \pm 0.05$.

3.4 Search for the $X(214)$ through charmless rare B decays (Belle)

The goal of this analysis is to search for a light scalar or vector particle decaying into a pair of muons. Such X particle could help understanding recent astrophysical observations[19]. Moreover, the HyperCP collaboration has reported the observation of 3 events $\Sigma^+ \to pX(\to \mu^+\mu^-)$ with a mass of 214.3 MeV/c^2 and a lifetime around 10^{-14} s. Two rare decay modes ($B^0 \to K^{*0}X$ and $B^0 \to \rho^0 X$ are searched in a dataset of 657×10^6 $B\overline{B}$ events; branching fractions in the range $10^{-9} - 10^{-6}$ are expected[20] for a sgoldstino of mass 214 MeV/c^2. Two techniques have been used to evaluate the background yield in the signal box defined using the variables M_{bc} and ΔE. The first one consists in counting the number of selected events using MC samples about 3 times larger than the dataset; in the second approach, the number of events is fitted using parameterizations based on sidebands. As a cross-check, various MC distributions are compared to those computed using a small fraction of the data. Finally, no signal is observed and frequentist upper limits are derived: $\mathcal{B}(B^0 \to K^{*0}X) < 2.26\,(2.27) \times 10^{-8}$ and $\mathcal{B}(B^0 \to \rho^0 X) < 1.73\,(1.73) \times 10^{-8}$ for a scalar (vector) X particle decaying into two muons with a lifetime smaller than 10^{-12} s. This rules out some models for a sgoldstino interpretation of the HyperCP observation.

3.5 First measurement of inclusive $B \to X_s\eta$ (Belle)

This study is motivated by the results of inclusive $B \to X_s\eta'$ analysis which show an unexpectedly large branching fraction and a spectrum which peaks at high mass[21]. It uses as well 657×10^6 $B\overline{B}$ events and is based on a pseudo-inclusive method: the X_s is reconstructed in 18 exclusive channels containing a K^+ or a $K^0_s(\to \pi^+\pi^-)$ and up to 4 pions of which at most 1 is a $\pi^0(\to \gamma\gamma)$. For $m_{X_s} < 2.6$ GeV/c^2, the $B \to X_s\eta$ measured branching fraction is $[26.1 \pm 3.0\,^{+1.9}_{-2.1}\,^{+4.0}_{-7.1}] \times 10^{-5}$, where the last error comes from the modeling of the X_s system with PYTHIA. This result is

consistent with the known decays $B \to K\eta$ and $B \to K^*(892)\eta$. Over half of the events (7σ significance) are located in the high-mass region ($m_{X_s} > 1.8$ GeV/c^2), which was not covered by previous exclusive measurements. Using the 13 modes for which the B flavor is given by the final state, the direct CP-asymmetry can be computed: $A_{CP} = -0.13 \pm 0.04\,^{+0.02}_{-0.03}$ which is consistent with predictions. The m_{X_s} spectrum shapes and branching fractions are comparable for the η and the η', which rules out the hypothesis of specific η' mechanisms.

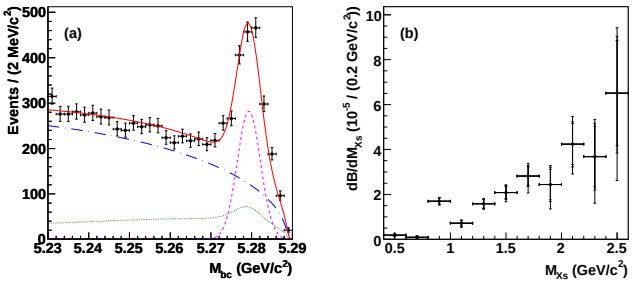

Figure 2: Left: M_{bc} distribution for the full mass range; the points are the data, the solid red line the overall fit function, the magenta dashed line the signal, the green dotted line the $b \to c$ background and the blue dash-dotted the continuum. Right: differential branching fraction as a function of m_{X_s}.

Acknowledgments

I'd like to thank E. Ben-Haim and A. Gaz for their comments on my talk and the proceedings.

References

1. D. Asner *et al*, arXiv:1010.1589 [hep-ex]; http://www.slac.stanford.edu/xorg/hfag
2. M. Kobayashi and T. Maskawa, *Prog. Theor. Phys.* **49**, 652 (1973).
3. J.P. Lees *et al*, *Phys. Rev.* D **84**, 012001 (2011).
4. P. del Amo Sanchez *et al.*, *Phys. Rev.* D **83**, 051101 (2011).
5. P. del Amo Sanchez *et al.*, *Phys. Rev.* D **83**, 031103 (2011).
6. H. J. Hyun *et al*, *Phys. Rev. Lett.* **105**, 091801 (2010).
7. K. Nishimura *et al*, *Phys. Rev. Lett.* **105**, 191803 (2010).
8. B. Aubert *et al.*, *Nucl. Instrum. Methods* A **479**, 1 (2002).
9. A. Abashian *et al.*, *Nucl. Instrum. Methods* A **479**, 117 (2002).
10. PEP-II Conceptual Design Report, SLAC-0418 (1993).
11. S. Kurokawa and E. Kikutani, *Nucl. Instrum. Methods* A **499**, 1 (2003).
12. M. Hazumi, *Phys. Lett.* B **583**, 285 (2004).
13. B. Aubert *et al.*, *Phys. Rev. Lett.* **97**, 261803 (2006).
14. H. C. Huang *et al.*, *Phys. Rev. Lett.* **91**, 241802 (2003); Y. T. Shen *et al.*, arXiv:0802.1547
15. S. Fajfer, T. N. Pham, and A. Prapotnik, *Phys. Rev.* D **69**, 114020 (2004); C.-H. Chen and H.-n. Li, *Phys. Rev.* D **70**, 054006 (2004).
16. See discussion in the *BABAR* article [4] and references therein.
17. B. Aubert *et al.*, *Phys. Rev. Lett.* **97**, 201801 (2006).
18. See discussion in the *BABAR* article [5] and references therein.
19. J. Chang *et al.*, *Nature* **456**, 362 (2008)); O. Adriani *et al.*, *Nature* **458**, 607 (2009).
20. S.V. Demidov and D. S. Gorbunov, *JETP Lett.* **84**, 479 (2007).
21. T. E. Browder *et al.*, *Phys. Rev. Lett.* **81**, 1786 (1998); G. Bonvicini *et al.*, *Phys. Rev.* D **68**, 011101 (2003); B. Aubert *et al.*, *Phys. Rev. Lett.* **93**, 061801 (2004).

Estimating the Higher Order Hadronic Matrix Elements in the Heavy Quark Expansion

THOMAS MANNEL

Theoretische Elementarteilchenphysik, Naturwiss. Techn. Fakultät, Universität Siegen, 57068 Siegen, Germany

The non-perturbative input in the heavy quark expansion relevant for precision determinations of CKM matrix elements from heavy hadron decays consists of certain forward matrix elements of local operators. While at low orders these matrix elements may be determined from experiment, the number of independent matrix elements at higher orders is way too large to extract them from data. Hence an estimate for these matrix elements from the theoretical side is necessary. In this contribution I present a way to estimate these matrix elements in a simple way.

1 Introduction

The theoretical description of semi-leptonic decays of heavy hadrons is in a very mature state. The major tool for reliable calculations is the Heavy Quark Expansion (HQE) and Heavy Quark Effective Theory (HQET) together with the Heavy Quark Symmetries (HQS) appearing in the heavy mass limit.

The determination of V_{cb} can be performed from exclusive as well as from inclusive decays. While the inclusive determination makes use of the HQE, the exclusive determination uses HQS, which constrain the form factors at the non-recoil point, where the four-velocities of the initial and final state hadrons are the same.

The theory for the inclusive determination based on HQE has reached the status of a precision calculation. It is based on the computation of the total rate, which in HQE is given as a combined series in $\alpha_s(m_b)^n$, $(\Lambda_{\rm QCD}/m_b)^m$, and $(\Lambda_{\rm QCD}/m_c)^k(\Lambda_{\rm QCD}/m_b)^{l+3}$ [1]. Currently the leading term $m = k = 0$ is known to order α_s^2 [2,3], the first sub-leading corrections are partially known to order $\alpha_s^2 \times (\Lambda_{\rm QCD}/m_b)^2$ [4], while the tree level terms are known to order $(\Lambda_{\rm QCD}/m_b)^m$ [5], and the term involving inverse powers of m_c $(\Lambda_{\rm QCD}/m_c)^2(\Lambda_{\rm QCD}/m_b)^3$ [6]. Overall, this calculation has reached a theoretical uncertainty at the level of one percent.

In order to explore the higher orders of the HQE quantitatively, it is mandatory to have a way to estimate the hadronic matrix elements appearing as the nonperturbative input. In the following I shall present a method for such an estimate.

2 Estimating the hadronic matrix elements of the HQE

Within HQE, the total semileptonic rate as well as the differential distributions are represented in terms of an expansion of the form

$$\begin{aligned} d\Gamma &= d\Gamma_0 + \left(\frac{\Lambda_{\rm QCD}}{m_b}\right)^2 d\Gamma_2 + \left(\frac{\Lambda_{\rm QCD}}{m_b}\right)^3 d\Gamma_3 + \left(\frac{\Lambda_{\rm QCD}}{m_b}\right)^4 d\Gamma_4 \\ &+ d\Gamma_5 \left(a_0 \left(\frac{\Lambda_{\rm QCD}}{m_b}\right)^5 + a_2 \left(\frac{\Lambda_{\rm QCD}}{m_b}\right)^3 \left(\frac{\Lambda_{\rm QCD}}{m_c}\right)^2 \right) + ... + d\Gamma_7 \left(\frac{\Lambda_{\rm QCD}}{m_b}\right)^3 \left(\frac{\Lambda_{\rm QCD}}{m_c}\right)^4 \end{aligned} \tag{1}$$

The coefficients $d\Gamma_i$ are themselves functions of m_c/m_b which are – up to logarithms of m_c – regular in the limit $m_c \to 0$, and which have an expansion in $\alpha_s(m_b)$. Furthermore, the $d\Gamma_i$ depend on non-perturbative parameters corresponding to matrix elements of increasing dimension.

The relevant hadronic matrix elements are

$$2M_H \mu_\pi^2 = -\langle H(v)|\bar{Q}_v (iD)^2 Q_v|H(v)\rangle : \quad \text{Kinetic Energy} \tag{2}$$

$$2M_H \mu_G^2 = \langle H(v)|\bar{Q}_v \sigma_{\mu\nu} (iD^\mu)(iD^\nu) Q_v|H(v)\rangle : \quad \text{Chromomagnetic Moment} \tag{3}$$

for $d\Gamma_2$ and

$$2M_H \rho_D^3 = -\langle H(v)|\bar{Q}_v (iD_\mu)(ivD)(iD^\mu) Q_v|H(v)\rangle : \quad \text{Darwin Term} \tag{4}$$

$$2M_H \rho_{LS}^3 = \langle H(v)|\bar{Q}_v \sigma_{\mu\nu} (iD^\mu)(ivD)(iD^\nu) Q_v|H(v)\rangle : \quad \text{Spin-Orbit Term} \tag{5}$$

for $d\Gamma_3$.

Going to higher orders one faces a proliferation of the number of independent matrix elements. At order $1/m_b^4$ we have already nine matrix elements, at order $1/m_b^5$ this increases to 18, and at $1/m_b^6$ there will be already 72 independent non-perturbative parameters.

Obviously these parameters cannot be determined from experiment any more, and hence we have to find a way to estimate them theoretically. To this end, we define a way for such an estimate based on a simple asumption which, however, can be systematically refined.

The higher order matrix elements can all be expressed in the form

$$\langle B|\bar{b}\, iD_{\mu_1} iD_{\mu_2} \cdots iD_{\mu_n}\, \Gamma\, b(0)|B\rangle, \tag{6}$$

where Γ denotes an arbitrary Dirac matrix. The representation is obtained by splitting the full chain $iD_{\mu_1} iD_{\mu_2} \cdots iD_{\mu_n}$ into $A = iD_{\mu_1} iD_{\mu_2} \cdots iD_{\mu_k}$ and $C = iD_{\mu_{k+1}} iD_{\mu_{k+2}} \cdots iD_{\mu_n}$.

In order to discuss the idea of the method we shall first assume that the derivatives in A and C are all spatial derivatives. In the following we show the intermediate state represenation

$$\langle B|\bar{b}\, A\, C\, \Gamma\, b(0)|B\rangle = \frac{1}{2M_B} \sum_n \langle B|\bar{b}\, A\, b(0)|n\rangle \cdot \langle n|\bar{b}\, C\, \Gamma\, b(0)|B\rangle, \tag{7}$$

where we have assumed the B mesons to be static and at rest, $|B\rangle = |B(p=(M_B, \vec{0}))\rangle$, and $|n\rangle$ are the single-b hadronic states with vanishing spatial momentum.

Eq. (7) can be proven based on the operator product expansion. We introduce a ficticious heavy quark Q which will be treated as static, and consider a correlator at vanishing spatial momentum transfer $\vec{q}$

$$T_{AC}(q_0) = \int \mathrm{d}^4x\, e^{iq_0x_0} \langle B|iT\left\{\bar{b}AQ(x)\, \bar{Q}C\Gamma b(0)\right\}|B\rangle. \tag{8}$$

We shall use the static limit for both b and Q, and hence introduce the 'rephased' fields $\tilde{Q}(x) = e^{im_Q q_0 x_0} Q(x)$ and likewise for b, and omit tilde in them in what follows. The form of

the resulting exponent suggests to define $\omega = q_0 - m_b + m_Q$ as the natural variable for T_{AC}, and $\frac{1}{2M_B} T_{AC}(\omega)$ is assumed to have a heavy mass limit.

With large m_Q we can perform the OPE for $T_{AC}(\omega)$ at $|\omega| \gg \Lambda_{\rm QCD}$ still assuming that $|\omega| \ll m_Q$ and neglecting thereby all powers of $1/m_Q$. In this case the propagator of Q becomes static,

$$iT\{Q(x)\bar{Q}(0)\} = \frac{1+\gamma_0}{2}\delta^3(\vec{x})\,\theta(x_0)\,P\,\exp\left(i\int_0^{x_0} A_0\,{\rm d}x_0\right), \tag{9}$$

and yields

$$T_{AC}(\omega) = \langle B|\bar{b}\,A\frac{1}{-\omega-\pi_0-i0}C\,\tfrac{1+\gamma_0}{2}\Gamma\,b|B\rangle\,, \tag{10}$$

where $\pi_0 = iD_0$ is the time component of the covariant derivative. This representation allows immediate expansion of $T_{AC}(\omega)$ in a series in $1/\omega$ at large $|\omega|$:

$$T_{AC}(\omega) = -\sum_{k=0}^{\infty}\langle B|\bar{b}\,A\frac{(-\pi_0)^k}{\omega^{k+1}}C\,\tfrac{1+\gamma_0}{2}\Gamma\,b|B\rangle\,. \tag{11}$$

Alternatively, the scattering amplitude can be written through its dispersion relation

$$T_{AC}(\omega) = \frac{1}{2\pi i}\int_0^{\infty}{\rm d}\epsilon\,\frac{1}{\epsilon-\omega+i0}\,{\rm disc}\,T_{AC}(\epsilon)\,, \tag{12}$$

where we have used the fact that in the static theory the scattering amplitude has only one, 'physical' cut corresponding to positive ω. The discontinuity is given by

$$i\int {\rm d}^4x\;e^{i\epsilon x_0}\langle B|\bar{b}AQ(x)\,\bar{Q}C\Gamma b(0)|B\rangle \tag{13}$$

and amounts to

$${\rm disc}\,T_{AC}(\epsilon) = \sum_{n_Q} i\int {\rm d}^4x\;e^{-i\vec{p}_n\vec{x}}\;e^{i(\epsilon-E_n)x_0}\langle B|\bar{b}AQ(0)|n_Q\rangle\,\langle n_Q|\bar{Q}C\Gamma b(0)|B\rangle, \tag{14}$$

where the sum runs over the complete set of the intermediate states $|n_Q\rangle$; their overall spatial momentum is denoted by $\vec{p}_n$ and energy by E_n.

The spatial integration over ${\rm d}^3x$ and integration over time ${\rm d}x_0$ in Eq. (14) yield $(2\pi)^3\delta^3(\vec{p}_n)$ and $2\pi\,\delta(E_n-\epsilon)$, respectively. Therefore only the states with vanishing spatial momentum are projected out, and we denote them as $|n\rangle$:

$${\rm disc}\,T_{AC}(\epsilon) = \sum_n 2\pi i\,\delta(\epsilon-E_n)\;\langle B|\bar{b}AQ(0)|n\rangle\,\langle n|\bar{Q}C\Gamma b(0)|B\rangle. \tag{15}$$

Inserting the optical theorem relation (15) into the dispersion integral (12) we get

$$T_{AC}(\omega) = \sum_n \frac{\langle B|\bar{b}AQ(0)|n\rangle\,\langle n|\bar{Q}C\Gamma b(0)|B\rangle}{E_n-\omega+i0}\,, \tag{16}$$

and the large-ω expansion takes the form

$$T_{AC}(\omega) = -\sum_{k=0}^{\infty}\frac{1}{\omega^{k+1}}\;\sum_n\;E_n^k\,\langle B|\bar{b}AQ(0)|n\rangle\,\langle n|\bar{Q}C\Gamma b(0)|B\rangle\,. \tag{17}$$

Equating the leading terms in $1/\omega$ of $T_{AC}(\omega)$ in Eq. (11) and in Eq. (17) we arrive at the relation

$$\langle B|\bar{b}\;A\,C\,\tfrac{1+\gamma_0}{2}\,\Gamma\,b(0)|B\rangle = \sum_n\,\langle B|\bar{b}\,A\,Q(0)|n\rangle\cdot\langle n|\bar{Q}\;C\,\Gamma\,b(0)|B\rangle \tag{18}$$

which is the intermediate state representation (7). Note that the projector $(1+\gamma_0)/2$ in the left hand side can be omitted since the $\bar b$ field satisfies $\bar b = \bar b(1+\gamma_0)/2$ in the static limit.

Operators involving time derivatives can be obtained by considering higher values of k in Eqs. (11) and (17) which describe the subleading in $1/\omega$ terms in the asymptotics of $T_{AC}(\omega)$. We readily generalize the saturation relation (7):

$$\langle B|\bar b\, A\, \pi_0^k\; C\, \tfrac{1+\gamma_0}{2}\Gamma\tfrac{1+\gamma_0}{2}\, b(0)|B\rangle = \sum_n\, (E_B - E_n)^k\, \langle B|\bar b\, A\, Q(0)|n\rangle \cdot \langle n|\bar Q\; C\, \tfrac{1+\gamma_0}{2}\Gamma\tfrac{1+\gamma_0}{2}\, b(0)|B\rangle\,. \quad (19)$$

Thus, each insertion of operator $(-\pi_0)$ inside a composite operator acts as a factor of the intermediate state excitation energy. This is expected, for equation of motion of the static quark field Q allows to equate

$$i\partial_0\, \bar Q C b(x) = \bar Q \pi_0 C b(x)$$

for any color-singlet operator $\bar Q C b(x)$. At the same time we have

$$i\partial_0\, \langle n|\bar Q C b(x)|B\rangle = -(E_n - M_B)\, \langle n|\bar Q C b(x)|B\rangle.$$

The intermediate state representation (7) still does not assume any approximation aside from the static limit for the b quark, yet it may be used to apply a dynamic QCD approximation. The one we employ here uses as an input the B-meson heavy quark expectation values (6) of dimension 5 and 6, which are expressed through μ_π^2, μ_G^2, ρ_D^3 and ρ_{LS}^3.

All operators with four and more derivatives must have an even number of spatial derivatives due to rotational invariance. Thus the operators with four derivatives have either four spatial derivatives, or two time and two spatial derivatives.

We shall discuss the $D=7$ operators with four spatial derivatives, and apply (18):

$$\langle B|\bar b\, iD_j iD_k iD_l iD_m \Gamma\, b|B\rangle = \sum_n \langle B|\bar b iD_j iD_k b|n\rangle\, \langle n|\bar b\, iD_l iD_m \Gamma\, b|B\rangle. \quad (20)$$

The intermediate states $|n\rangle$ in the sum are either the ground-state multiplet B, B^*, or excited states with the suitable parity of light degrees of freedom. The ground-state factorization approximation assumes that the sum in (20) is to a large extent saturated by the ground state spin-symmetry doublet. Hence we retain only the contribution of the ground state and discard the contribution of higher excitations. In the case of dimension seven operators the result is expressed in terms of the expectation values with two derivatives, i.e. μ_π^2 and μ_G^2; matrix elements involving B^* are related to them by spin symmetry.

Applying this we obtain for spin-singlet and spin-triplet B expectation values of $D=7$ involving spatial derivatives only:

$$\frac{1}{2M_B}\langle B|\bar b\, iD_j iD_k iD_l iD_m\, b|B\rangle \;=\; \frac{(\mu_\pi^2)^2}{9}\delta_{jk}\delta_{lm} + \frac{(\mu_G^2)^2}{36}\,(\delta_{jm}\delta_{kl} - \delta_{jl}\delta_{km}) \quad (21)$$

$$\begin{aligned}\frac{1}{2M_B}\langle B|\bar b\, iD_j iD_k iD_l iD_m\, \sigma_{ab}\, b|B\rangle \;=\; & -\frac{\mu_\pi^2\mu_G^2}{18}\,(\delta_{jk}\delta_{la}\delta_{mb} - \delta_{jk}\delta_{lb}\delta_{ma} + \delta_{lm}\delta_{ja}\delta_{kb} - \delta_{lm}\delta_{jb}\delta_{ka}) + \\ & \frac{(\mu_G^2)^2}{36}\,[\delta_{jm}(\delta_{lb}\delta_{ka} - \delta_{la}\delta_{kb}) - \delta_{jl}(\delta_{ka}\delta_{mb} - \delta_{kb}\delta_{ma}) + \\ & \delta_{kl}(\delta_{ja}\delta_{mb} - \delta_{jb}\delta_{ma}) - \delta_{km}(\delta_{ja}\delta_{lb} - \delta_{jb}\delta_{la})]\,. \end{aligned} \quad (22)$$

Finally, we need to consider the expectation values of the form $\langle B|\bar b\, iD_j iD_0^k iD_l\,[\sigma]\; b|B\rangle$ for $k=2,3$ which evidently belong to the tower of $\mu_{\pi,G}^2$ and $\rho_{D,LS}^3$. Likewise, their values could be considered as the input describing strong dynamics, along with the latter; yet they have not been constrained experimentally. The intermediate states saturating such expectation values have opposite parity to the ground state (P-wave states) regardless of number of time derivatives.

The counterpart of the ground-state saturation approximation here is retaining the contribution of the lowest P-wave resonance in the sum; then each power of time derivative amounts to the extra power of $-\bar{\epsilon}$, where $\bar{\epsilon}=M_P-M_B\approx 0.4\,\mathrm{GeV}$.

In fact, there are two families of the P-wave excitations of B mesons corresponding to spin of light degrees of freedom $\frac{3}{2}$ or $\frac{1}{2}$. The combinations $\mu_\pi^2-\mu_G^2$, $\rho_D^3+\rho_{LS}^3$, ... receive contributions only from the $\frac{1}{2}$-family, whereas the $\frac{3}{2}$-family gives rise to $\frac{\mu_\pi^2+2\mu_G^2}{3}$, $\frac{\rho_D^3-2\rho_{LS}^3}{3}$, etc.[7] (the transition amplitude into the lowest $\frac{1}{2}$ P-state appears to be suppressed). Therefore, it makes sense to consider these two structures separately and approximate

$$\langle B|\bar{b}\,iD_j(-iD_0)^{k+1}iD_l\,b|B\rangle \;=\; \left(\bar{\epsilon}_{3/2}^k\frac{2\rho_D^3-\rho_{LS}^3}{9}+\bar{\epsilon}_{1/2}^k\frac{\rho_D^3+\rho_{LS}^3}{9}\right)\delta_{jl} \tag{23}$$

$$\langle B|\bar{b}\,iD_j(-iD_0)^{k+1}iD_l\sigma_{jl}\,b|B\rangle \;=\; -\bar{\epsilon}_{3/2}^k\frac{2\rho_D^3-\rho_{LS}^3}{3}+\bar{\epsilon}_{1/2}^k\frac{2\rho_D^3+2\rho_{LS}^3}{3}\,. \tag{24}$$

Note that assuming $\bar{\epsilon}_{1/2}=\bar{\epsilon}_{3/2}=\bar{\epsilon}$ implies $\rho_D^3\simeq\bar{\epsilon}\mu_\pi^2$ and $-\rho_{LS}^3\simeq\bar{\epsilon}\mu_G^2$; the first relation seems to be satisfied by the preliminary values of μ_π^2 and ρ_D^3 extracted from experiment.

This ground state saturation method can be extended also to higher dimensional operators in an obvious way. Furthermore, there is also the possibility for a refinement of the method by including more states aside from the ground state. In this way a systematic approach can be constructed to obtain reliable estimates for the higher order matrix elements.

3 Conclusion

Evaluating the contributions appearing at order $1/m_b^4$ quantitatively the impact on the determination of V_{cb} is small and of the expected size. The determination of V_{cb} makes use of the total rate which receives only small corrections. Inserting the numerics we get for

$$\delta\Gamma|_{1/m_b^i}=(\Gamma|_{1/m_i}-\Gamma|_{1/m_{i-1}})/\Gamma_{\mathrm{parton}}$$

the results

$$\delta\Gamma\Big|_{1/m_b^4}\approx+0.29\%\quad\delta\Gamma\Big|_{1/m_b^3}\approx-2.84\%\quad\delta\Gamma\Big|_{1/m_b^2}\approx-4.29\%$$

Hence the impact on V_{cb} is only a small improvement due to the reduction of the uncertainty due to the higher-order terms of the HQE. However, once moments of differential distributions are considered, the impact of the higher-order terms becomes more pronounced, in particular for higher moments.

References

1. D. Benson, I. I. Bigi, T. Mannel and N. Uraltsev, Nucl. Phys. B **665** (2003) 367 [arXiv:hep-ph/0302262].
2. K. Melnikov, Phys. Lett. B **666** (2008) 336 [arXiv:0803.0951 [hep-ph]].
3. M. Dowling, A. Pak and A. Czarnecki, Phys. Rev. D **78** (2008) 074029 [arXiv:0809.0491 [hep-ph]].
4. T. Becher, H. Boos, E. Lunghi, JHEP **0712**, 062 (2007). [arXiv:0708.0855 [hep-ph]].
5. T. Mannel, S. Turczyk, N. Uraltsev, JHEP **1011**, 109 (2010). [arXiv:1009.4622 [hep-ph]].
6. I. Bigi, T. Mannel, S. Turczyk and N. Uraltsev, JHEP **1004** (2010) 073 [arXiv:0911.3322 [hep-ph]].
7. I.I. Bigi, M. Shifman and N. Uraltsev, Ann. Rev. Nucl. Part. Sci. **47** (1997) 591.

CP VIOLATION RESULTS AND PROSPECTS WITH LHCB

C. LANGENBRUCH on behalf of the LHCb collaboration
Heidelberg University, Physikalisches Insitut, Philosophenweg 12, 69120 Heidelberg, Germany

The LHCb experiment at the Large Hadron Collider searches for New Physics by performing precision measurements of CP-violating processes in the B sector. A key measurement of the LHCb physics program is the extraction of the CP-violating phase ϕ_s via a time dependent angular analysis of the decay $B_s^0 \to J/\psi\,\phi$. In the Standard Model the phase ϕ_s which arises in the interference between B_s^0 mixing and decay is predicted to be small, $\phi_s = -0.0363 \pm 0.0017$. [1] Possible deviations from this prediction can be attributed to New Physics. Key results on the way to a measurement of ϕ_s are presented. The decay amplitudes in the $P \to VV$ decays $B \to J\psi\,K^*$ and $B_s^0 \to J\psi\,\phi$ are extracted via an angular analysis. The decay $B_s^0 \to J\psi\,\phi$ additionally gives access to $\Delta\Gamma_s$ which is determined to be $\Delta\Gamma_s = (0.077 \pm 0.119_{\text{stat.}} \pm 0.021_{\text{syst.}})\,\text{ps}^{-1}$ assuming $\phi_s = 0$. [2] A crucial ingredient for the extraction of ϕ_s is the determination of the B_s^0 production flavor (flavor tagging). The flavor tagging procedure is verified by the determination of the mixing frequency in the B_d^0 and B_s^0 systems giving $\Delta m_d = (0.499 \pm 0.032_{\text{stat.}} \pm 0.003_{\text{syst.}})\,\text{ps}^{-1}$ and $\Delta m_s = (17.63 \pm 0.11_{\text{stat.}} \pm 0.04_{\text{syst.}})\,\text{ps}^{-1}$ respectively. [3,4] The data used were taken with the LHCb detector in 2010 and correspond to an integrated luminosity of $36\,\text{pb}^{-1}$.

1 Introduction

B_s^0 mixing as shown in Figure 1b gives rise to transitions between the flavor eigenstates B_s^0 and $\bar{B}_s^0$. As a result the flavor eigenstates differ from the mass eigenstates B_L and B_H with masses m_L and m_H. Their mass difference determines the B_s^0 mixing frequency $\Delta m_s = m_H - m_L$. The mass eigenstates also exhibit different total decay widths Γ_L and Γ_H respectively. The Standard Model predicts the decay width difference $\Delta\Gamma_s = \Gamma_L - \Gamma_H$ to be sizeable, $\Delta\Gamma_s = (0.087 \pm 0.021)\,\text{ps}^{-1}$. [5]

The CP-violating phase ϕ_s arises due to interference between the tree level decay shown in Figure 1a and mixing via box diagrams as given in Figure 1b followed by decay. Neglecting penguin contributions the phase ϕ_s is in the Standard Model given by $\phi_s = -2\beta_s$ where $\beta_s = \arg\left(-V_{\text{ts}}V_{\text{tb}}^*/V_{\text{cs}}V_{\text{cb}}^*\right)$ is the smallest angle of the $b-s$ unitarity triangle. Contributions from New Physics can lead to a deviation from this prediction $\phi_s = \phi_s^{\text{SM}} \to \phi_s = \phi_s^{\text{SM}} + \phi_s^{\text{NP}}$.

The Tevatron has measured the B_s^0 mixing frequency $\Delta m_s = (17.77 \pm 0.10_{\text{stat.}} \pm 0.07_{\text{syst.}})\,\text{ps}^{-1}$ with high precision, [6] however the limits on $\Delta\Gamma_s$ and ϕ_s are much less stringent. [7] LHCb aims to improve these measurements using the large number of B-mesons produced at the Large Hadron Collider. The LHCb experiment, as a dedicated B physics experiment, is particularly well suited for this task. LHCb exhibits an efficient low p_T trigger system, excellent mass and proper time resolution as well as good particle identification over the full relevant momentum range. In the following the main steps towards a measurement of ϕ_s at LHCb will be discussed.

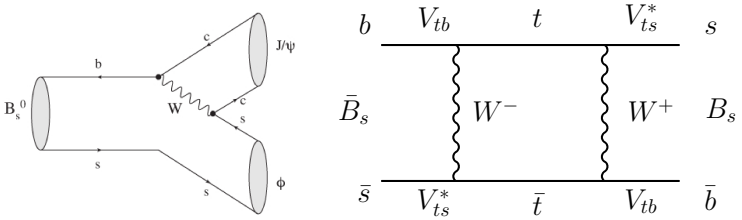

(a) Tree level signal decay (b) B_s^0 mixing diagram

Figure 1: The signal decay $B_s^0 \to J/\psi\,\phi$ can occur via direct decay (1a) or via mixing (1b) followed by decay.

Table 1: Lifetimes determined from b-hadron $\to J/\psi\,X$ decays.

Decay channel	Yield	LHCb result τ[ps]	PDG τ[ps]
$B^+ \to J/\psi\,K^+$	6741 ± 85	$1.689 \pm 0.022_{\text{stat.}} \pm 0.047_{\text{syst.}}$	1.638 ± 0.011
$B_d^0 \to J/\psi\,K^*$	2668 ± 58	$1.512 \pm 0.032_{\text{stat.}} \pm 0.042_{\text{syst.}}$	1.5252 ± 0.009
$B_d^0 \to J/\psi\,K_S^0$	838 ± 31	$1.558 \pm 0.056_{\text{stat.}} \pm 0.022_{\text{syst.}}$	1.525 ± 0.009
$B_s^0 \to J/\psi\,\phi$	570 ± 24	$1.447 \pm 0.064_{\text{stat.}} \pm 0.056_{\text{syst.}}$	1.477 ± 0.046
$\Lambda_b \to J/\psi\,\Lambda$	187 ± 16	$1.353 \pm 0.108_{\text{stat.}} \pm 0.035_{\text{syst.}}$	$1.391^{+0.038}_{-0.037}$

2 Determination of lifetimes in b-hadron $\to J/\psi\,X$ decays

B-hadron lifetimes are studied using the decays $B_d^0 \to J/\psi\,K^*$, $B_d^0 \to J/\psi\,K_S^0$, $B^+ \to J/\psi\,K^+$, $B_s^0 \to J/\psi\,\phi$ and $\Lambda_b \to J/\psi\,\Lambda$. Signal yields and lifetimes resulting from the fit of a single exponential to the reconstructed proper time distributions are given in Table 1. While the results are compatible with the current world average the measurements have not yet reached a competitive error. The study however gives valuable input to the analysis of $B_s^0 \to J/\psi\,\phi$ by providing proper time resolutions and acceptances. [8]

3 Angular analysis of the $P \to VV$ decay $B_d^0 \to J\psi\,K^*$

The decay $B_d^0 \to J\psi\,K^*$ is a decay of a pseudo-scalar meson to two vector mesons. Since the vector mesons in the final state can have different relative angular momenta an angular analysis is required to statistically separate the decay amplitudes. The three decay amplitudes A_0, $A_\perp$ and $A_\parallel$ correspond to the three possible relative angular momenta $L = 0, 1$ and 2. $\delta_\perp$ and $\delta_\parallel$ denote the strong phases of $A_\perp$ and $A_\parallel$ relative to A_0. The extracted amplitudes and phases are given in Table 2a and agree with previous measurements within their errors. [2] This result constitutes a valuable cross-check for the correct implementation of angular dependent acceptance effects caused by detector geometry and selection. The possible presence of a non-resonant S-wave component was accounted for in the fit. Other systematic uncertainties that have been evaluated include the background shape, acceptance effects and the signal mass model.

4 Extraction of $\Delta\Gamma_s$ from an untagged angular analysis

The decay $B_s^0 \to J/\psi\,\phi$ has a structure which is very similar to the decay $B \to J/\psi\,K^*$ discussed in the previous section since both decays are $P \to VV$ transitions. The decay width difference $\Delta\Gamma_s$ can be extracted by performing an untagged (i.e. without using information on the initial B_s^0 flavor) angular analysis of $B_s^0 \to J/\psi\,\phi$ decays. For this study $\phi_s = 0$ is assumed which is close to the Standard Model prediction. The results are given in Table 2b. The extracted

Table 2: Results from untagged angular fits of the two $P \to VV$ decays $B_d^0 \to J/\psi\, K^*$ (Table 2a) and $B_s^0 \to J/\psi\, \phi$ (Table 2b). $\phi_s = 0$, which is close to the Standard Model prediction, is assumed for the untagged fit of the signal channel $B_s^0 \to J/\psi\, \phi$.

(a) Untagged fit of $B_d^0 \to J/\psi\, K^*$ events

Parameter	LHCb result $\pm$ stat. $\pm$ syst.
$\lvert A_\parallel \rvert^2$	$0.252 \pm 0.020 \pm 0.016$
$\lvert A_\perp \rvert^2$	$0.178 \pm 0.022 \pm 0.017$
$\delta_\parallel$[rad]	$-2.87 \pm 0.11 \pm 0.10$
$\delta_\perp$[rad]	$3.02 \pm 0.10 \pm 0.07$

(b) Untagged fit of $B_s^0 \to J/\psi\, \phi$ events

Parameter	LHCb result $\pm$ stat. $\pm$ syst.
Γ_s [ps^{-1}]	$0.679 \pm 0.036 \pm 0.027$
$\Delta\Gamma_s$ [ps^{-1}]	$0.077 \pm 0.119 \pm 0.021$
$\lvert A_0(0) \rvert^2$	$0.528 \pm 0.040 \pm 0.028$
$\lvert A_\perp(0) \rvert^2$	$0.263 \pm 0.056 \pm 0.014$

value, $\Delta\Gamma_s = (0.077 \pm 0.119_{\text{stat.}} \pm 0.021_{\text{syst.}})\,\text{ps}^{-1}$, [2] is well in agreement with the current best measurement $\Delta\Gamma_s = (0.075 \pm 0.035_{\text{stat.}} \pm 0.01_{\text{syst.}})\,\text{ps}^{-1}$. [7] However the measurement is limited by the small statistics of the 2010 data sample and therefore not competitive yet. The signal yield amounts to only 571 ± 24 events. Systematic uncertainties that have been studied include the background shape, the angular acceptance description and a possible S-wave contribution. To estimate the sensitivity of the untagged fit to ϕ_s a Feldman-Cousins study [9] is performed in the two-dimensional ϕ_s-$\Delta\Gamma_s$ plane. The resulting confidence-contours are given in Figure 2. They show that with the current statistics ϕ_s can not be constrained when performing the untagged analysis. For the extraction of ϕ_s information about the initial B_s^0 flavor is needed.

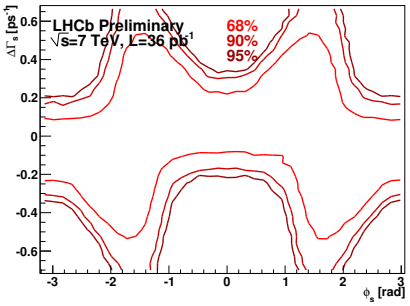

Figure 2: $\phi_s - \Delta\Gamma_s$ confidence contours of the untagged analysis of $B_s^0 \to J/\psi\, \phi$ events. The contours are determined by performing a Feldman-Cousins study with 1000 toys for each grid point. The untagged analysis provides no constraints on ϕ_s.

5 Determination of the $B_{d,s}^0$ mixing frequency

The mixing frequency in the B_d^0 system is determined from the time dependent mixing asymmetry in the decay $B_d^0 \to D\pi$, defined as $A(t) = (N_{\text{unmixed}}(t) - N_{\text{mixed}}(t))/(N_{\text{unmixed}}(t) + N_{\text{mixed}}(t))$. Figure 3a shows the mixing asymmetry extracted from 5999 ± 82 signal events. The mixing frequency in the B_d^0 system is determined to be $\Delta m_d = (0.499 \pm 0.032_{\text{stat.}} \pm 0.003_{\text{syst.}})\,\text{ps}^{-1}$ which is in agreement with the world average $\Delta m_d = (0.507 \pm 0.005)\,\text{ps}^{-1}$. [3]

The mixing frequency in the B_s^0 system is determined using $B_s^0 \to D_s\pi, D_s\pi\pi\pi$ decays. Figure 3b shows the likelihood scan over the mixing frequency Δm_s. Mixing is observed with a statistical significance of 4.6σ and the mixing frequency Δm_s is determined to be $\Delta m_s = (17.63 \pm 0.11_{\text{stat.}} \pm 0.04_{\text{syst.}})\,\text{ps}^{-1}$. [4] This measurement, performed with the 2010 data, is competitive with the measurement published previously by the CDF collaboration, $\Delta m_s = (17.77 \pm 0.10_{\text{stat.}} \pm 0.07_{\text{syst.}})\,\text{ps}^{-1}$. [6] Since the B_s^0 oscillation is much faster than the oscillation in

the B_d^0 system LHCb profits from its excellent proper time resolution and is able to overcome the statistical limitation.

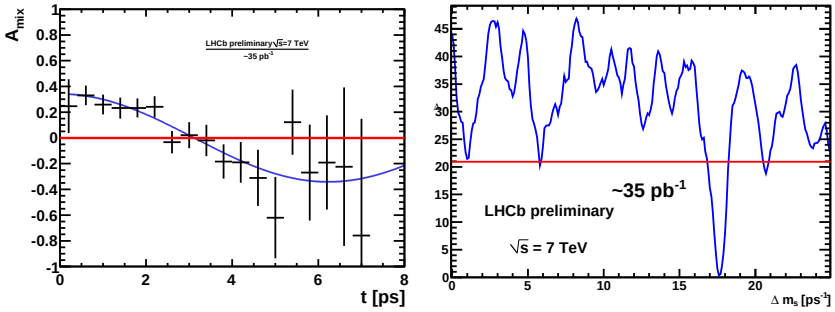

(a) B_d^0 mixing asymmetry (b) Likelihod scan over Δm_s

Figure 3: (a) The mixing frequency in the B_d^0 system is determined via the time dependent mixing asymmetry. (b) The results of the likelihood scan over the mixing frequency Δm_s in the B_s^0 system. A minimum is observed for $\Delta m_s = (17.63 \pm 0.11_{\text{stat.}})\,\text{ps}^{-1}$.

6 Summary

The main steps on the way to a measurement of ϕ_s at LHCb have been presented. Using the data taken by the LHCb detector in 2010 the polarization amplitudes and strong phases for the $P \to VV$ decay $B_d^0 \to J/\psi\, K^*$ have been extracted. An untagged analysis was performed to determine the decay width difference in the B_s^0 system giving $\Delta\Gamma_s = (0.077 \pm 0.119_{\text{stat.}} \pm 0.021_{\text{syst.}})\,\text{ps}^{-1}$. Additionally the mixing frequencies in both the B_d^0 and B_s^0 systems have been extracted. The measurement of $\Delta m_s = (17.63 \pm 0.11_{\text{stat.}} \pm 0.04_{\text{syst.}})\,\text{ps}^{-1}$ is competitive with the world average.

References

1. CKMfitter Group (J. Charles et al.), Eur. Phys. J. C41, 1-131 (2005) [hep-ph/0406184], updated results and plots available at: http://ckmfitter.in2p3.fr
2. The LHCb Collaboration, "Untagged angular analysis of $B_s^0 \to J/\psi\,\phi$ and $B^0 \to J/\psi\, K^*$ with the 2010 data", LHCb-CONF-2011-002.
3. The LHCb Collaboration, "Measurement of Δm_d in $B^0 \to D\pi$", LHCb-CONF-2011-010.
4. The LHCb Collaboration, "Measurement of Δm_s and calibration and tuning of the Same-Side Tagging algorithm with $B_s^0 \to D_s\pi$ decays using the 2010 data sample", LHCb-CONF-2011-005.
5. Alexander Lenz, Ulrich Nierste, Numerical updates of lifetimes and mixing parameters of B mesons, Proceedings of the CKM workshop 2010 in Warwick, hep-ph/1102.4274v1
6. CDF Collaboration (A. Abulencia et al.), "Observation of B0(s) - anti-B0(s) Oscillations", Phys.Rev.Lett.97:242003,2006., hep-ex/0609040
7. CDF Collaboration (A. Abulencia et al.), "An Updated Measurement of the CP Violating Phase β_s with $L = 5.2\,\text{fb}^{-1}$", Public Note 10206
8. The LHCb Collaboration, "b-hadron lifetime measurements with exclusive $B \to J/\psi\, X$ decays reconstructed in the 2010 data", LHCb-CONF-2011-001.
9. G. J. Feldman and R. D. Cousins, "A Unified Approach to the Classical Statistical Analysis of Small Signals," Phys. Rev. D **57**, 3873 (1998) [arXiv:physics/9711021].

DIRECT CP ASYMMETRY IN $\bar{B} \to X_{s,d}\,\gamma$ DECAYS

GIL PAZ
Enrico Fermi Institute
The University of Chicago, Chicago, Illinois, 60637, USA

The CP asymmetry in inclusive $\bar{B} \to X_{s,d}\,\gamma$ decays is an important probe of new physics. The theoretical prediction was thought to be of a perturbative origin, and in the standard model, to be about 0.5 percent. In a recent work with M. Benzke, S.J. Lee and M. Neubert, we have shown that the asymmetry is in fact dominated by non-perturbative effects. Since these are hard to estimate, it reduces the sensitivity to new physics effects. On the other hand, these new non-perturbative effects suggest a new test of new physics by looking at the difference of the CP asymmetries in charged versus neutral B-meson decays.

1 Introduction

Inclusive radiative B decay modes such as $\bar{B} \to X_s\,\gamma$ do not occur in the Standard Model (SM) at tree-level. They can only take place via loop suppressed processes. At low energies, one can describe the decay $\bar{B} \to X_s\,\gamma$ via the operator $Q_{7\gamma} = (-e/8\pi^2) m_b \bar{s}\sigma_{\mu\nu}F^{\mu\nu}(1+\gamma_5)b$, which appears in the effective Hamiltonian as $\mathcal{H}_{\rm eff} \ni -(G_F/\sqrt{2})\lambda_t C_{7\gamma} Q_{7\gamma}$. The decay $\bar{B} \to X_s\,\gamma$ can also receive contributions from loops that contain particles which appear in extensions of the SM, making it an important probe of new physics effects. Such effects would only modify the Wilson coefficient $C_{7\gamma}$ in the effective Hamiltonian.

But $Q_{7\gamma}$ is not the only operator that contributes to $\bar{B} \to X_s\,\gamma$. Instead of producing the photon directly, we can produce a gluon or a quark pair and convert them to a photon. In other words, the contribution of operators such as $Q_{8g} = (-g/8\pi^2) m_b \bar{s}\sigma_{\mu\nu}G^{\mu\nu}(1+\gamma_5)b$ and $Q_1^c = (\bar{c}b)_{V-A}(\bar{s}c)_{V-A}$ is also important. Such a conversion usually "costs us" either a factor of α_s from a loop that contains a "hard" gluon, or a factor of $\Lambda_{\rm QCD}/m_b$ from a production of extra "soft" particles in the conversion process. In summary, in order to describe inclusive radiative B decays we need the full effective Hamiltonian

$$\mathcal{H}_{\rm eff} = \frac{G_F}{\sqrt{2}} \sum_{p=u,c} \lambda_p \left(C_1 Q_1^p + C_2 Q_2^p + \sum_i C_i Q_i + C_{7\gamma} Q_{7\gamma} + C_{8g} Q_{8g} \right) + \text{h.c.}\,, \tag{1}$$

where $\lambda_p = V_{pb}^* V_{ps}$ ($\lambda_p = V_{pb}^* V_{pd}$) for $\bar{B} \to X_s\,\gamma$ ($\bar{B} \to X_d\,\gamma$) decays. The most important operators, due to their larger Wilson coefficients, are $Q_{7\gamma}, Q_{8g}$, and Q_1. From the effective Hamiltonian one can calculate various observables, in particular the CP asymmetry which is the topic of this talk.

The measured CP asymmetry in $\bar{B} \to X_s\,\gamma$, as given by the Heavy Flavor Averaging Group, is [1]

$$\mathcal{A}_{X_s\gamma} = \frac{\Gamma(\bar{B} \to X_s\gamma) - \Gamma(B \to X_{\bar{s}}\gamma)}{\Gamma(\bar{B} \to X_s\gamma) + \Gamma(B \to X_{\bar{s}}\gamma)} = -(1.2 \pm 2.8)\%\,. \tag{2}$$

This result is based on averaging of BaBar, Belle, and CLEO measurements, which actually measure $\mathcal{A}_{X_s\gamma}(E_\gamma \geq E_0)$ with $1.9 \leq E_0 \leq 2.1\,\mathrm{GeV}$.

What about the theoretical prediction? It is well known that in order to observe CP violation we should have an interference of two amplitudes that differ both in their "weak" (CP odd) and "strong" (CP even) phases. The weak phases can appear from the CKM matrix elements in (1), or from complex Wilson coefficients in (1). The latter source cannot contribute in the SM, where the Wilson coefficients are real. The strong phases can arise, for example, from loops, and as such are α_s suppressed. Indeed, the theoretical prediction for the CP asymmetry was thought to be of a perturbative origin. The perturbative theoretical prediction is given by [2,3]

$$\begin{aligned}\mathcal{A}^{\rm dir}_{X_s\gamma}(E_0) = \alpha_s \Bigg\{ & \frac{40}{81}\,\mathrm{Im}\,\frac{C_1}{C_{7\gamma}} - \frac{8z}{9}\Big[v(z)+b(z,\delta)\Big]\,\mathrm{Im}\Big[(1+\epsilon_s)\,\frac{C_1}{C_{7\gamma}}\Big] \\ & - \frac{4}{9}\,\mathrm{Im}\,\frac{C_{8g}}{C_{7\gamma}} + \frac{8z}{27}\,b(z,\delta)\,\frac{\mathrm{Im}[(1+\epsilon_s)\,C_1 C_{8g}^*]}{|C_{7\gamma}|^2} + \frac{16z}{27}\,\tilde{b}(z,\delta)\,\Big|\frac{C_1}{C_{7\gamma}}\Big|^2\,\mathrm{Im}\,\epsilon_s \Bigg\},\end{aligned} \tag{3}$$

where $\delta = (m_b - 2E_0)/m_b$, $z = (m_c/m_b)^2$ and $\epsilon_s = (V_{ub}V_{us}^*)/(V_{tb}V_{ts}^*) \approx \lambda^2(i\bar\eta - \bar\rho)$. One can simplify this expression by taking $m_c^2 = \mathcal{O}(m_b\Lambda_{\rm QCD})$, and expanding in $z, \delta = \mathcal{O}(\Lambda_{\rm QCD}/m_b)$. In this limit [4]

$$\mathcal{A}^{\rm dir}_{X_s\gamma} = \alpha_s \left\{ \frac{40}{81}\,\mathrm{Im}\frac{C_1}{C_{7\gamma}} - \frac{4}{9}\,\mathrm{Im}\frac{C_{8g}}{C_{7\gamma}} - \frac{40\Lambda_c}{9m_b}\,\mathrm{Im}\Big[(1+\epsilon_s)\,\frac{C_1}{C_{7\gamma}}\Big] + \mathcal{O}\Big(\frac{\Lambda^2_{\rm QCD}}{m_b^2}\Big)\right\}, \tag{4}$$

where $\Lambda_c(m_c, m_b) \approx 0.38\,\mathrm{GeV}$. In the SM, where C_i are real, we find a triple suppression: from α_s, from $\mathrm{Im}(\epsilon_s) \sim \lambda^2 \approx 0.05$, and from $(m_c/m_b)^2 \sim \Lambda_{\rm QCD}/m_b$. All together, the theoretical prediction for the SM is an asymmetry of about 0.5% [5,2,6]. A dedicated analysis [7] finds $\mathcal{A}^{\rm SM}_{X_s\gamma} = (0.44^{+0.15}_{-0.10} \pm 0.03^{+0.19}_{-0.09})\%$, where the errors are from m_c/m_b, CKM parameters, and scale variation, respectively.

Comparing the theoretical prediction to the measured value, $\mathcal{A}_{X_s\gamma} = -(1.2 \pm 2.8)\%$, there is room for new physics effects. There are many studies of such effects on the CP asymmetry, see for example the references within [4]. From the experimental side, reducing the experimental error below the 1% level is one of the goals of the future B factories [8,9]. There is a problem, though, since the theoretical prediction is not complete...

2 Resolved Photon Contributions

The theoretical prediction of (3) is missing the resolved photon contributions [10,11]. Unlike the direct photon contribution in which the photon couples to a local operator mediating the weak decay, the resolved photon contribution arise from indirect production of the photon, accompanied by other soft particles. The resolved photon contributions give rise to non-perturbative $\mathcal{O}(\Lambda_{\rm QCD}/m_b)$ corrections to $\Gamma(\bar B \to X_s\,\gamma)$. This is very different from other inclusive B decays, such as $\bar B \to X_{c,u}\,l\,\bar\nu$, where the non-perturbative corrections to the total rate are $\mathcal{O}(\Lambda^2_{\rm QCD}/m_b^2)$. The resolved photon contributions give the largest error of about 5% on the total $\bar B \to X_s\,\gamma$ rate.

How important are they for the CP asymmetry? For the total rate the direct photon contributions are an $\mathcal{O}(1)$ effect, while the resolved photon contributions are $\mathcal{O}(\Lambda_{\rm QCD}/m_b)$ suppressed. For the CP asymmetry the direct photon contribution discussed above are α_s suppressed, so the resolved photon contributions can give a potentially large effect.

Before giving explicit expressions for the resolved photon contributions to the CP asymmetry, let us comment on their structure. Schematically, the resolved photon contributions appear in the form of $\mathcal{A}^{\rm res}_{X_s\gamma} \sim \bar J \otimes h$. The functions $\bar J$ can be calculated in perturbation theory. The soft

functions h are matrix elements of non-local operators. They cannot be extracted from data, and must be modeled. How do the strong phases arise for the resolved photon contributions? It can be shown [11] that the functions h are real by using parity, time reversal, and heavy quark symmetry. The functions J, on the other hand, are complex since they arise from uncut propagators and loops.

At the lowest order in α_s and $\Lambda_{\rm QCD}/m_b$, the resolved photon contribution to the CP asymmetry is

$$\mathcal{A}_{X_s\gamma}^{\rm res} = \frac{\pi}{m_b}\left\{ {\rm Im}\left[(1+\epsilon_s)\,\frac{C_1}{C_{7\gamma}}\right]\tilde\Lambda_{17}^c - {\rm Im}\left[\epsilon_s\,\frac{C_1}{C_{7\gamma}}\right]\tilde\Lambda_{17}^u + {\rm Im}\,\frac{C_{8g}}{C_{7\gamma}}\,4\pi\alpha_s\,\tilde\Lambda_{78}^{\bar B}\right\}, \tag{5}$$

with

$$\begin{aligned}
\tilde\Lambda_{17}^u &= \frac{2}{3}\;h_{17}(0)\\
\tilde\Lambda_{17}^c &= \frac{2}{3}\int_{4m_c^2/m_b}^\infty \frac{d\omega_1}{\omega_1}\,f\!\left(\frac{m_c^2}{m_b\,\omega_1}\right)\;h_{17}(\omega_1)\\
\tilde\Lambda_{78}^{\bar B} &= 2\int_{-\infty}^\infty \frac{d\omega_1}{\omega_1}\left[\;h_{78}^{(1)}(\omega_1,\omega_1) - h_{78}^{(1)}(\omega_1,0)\right],
\end{aligned} \tag{6}$$

where $f(x) = 2x\ln[(1+\sqrt{1-4x})/(1-\sqrt{1-4x})]$. The soft functions h_{ij} are in light-cone gauge $\bar n\cdot A = 0$,

$$\begin{aligned}
h_{17}(\omega_1,\mu) &= \int\frac{dr}{2\pi}\,e^{-i\omega_1 r}\,\frac{\langle\bar B|\bar h(0)\,\bar{\not n}\,i\gamma_\alpha^\perp\bar n_\beta\,gG_s^{\alpha\beta}(r\bar n)\,h(0)|\bar B\rangle}{2M_B}\\
h_{78}^{(1)}(\omega_1,\omega_2,\mu) &= \int\frac{dr}{2\pi}\,e^{-i\omega_1 r}\int\frac{du}{2\pi}\,e^{i\omega_2 u}\,\frac{\langle\bar B|\bar h(0)\,T^A\,\bar{\not n}\,h(0)\;\sum_q e_q\,\bar q(r\bar n)\,\bar{\not n}\,T^A q(u\bar n)|\bar B\rangle}{2M_B}\,.
\end{aligned} \tag{7}$$

Using the modeling of the soft function as in [11] allows us to estimate the size of resolved photon contributions. We need to estimate each of the $\tilde\Lambda_{ij}$ in (5).

In order to estimate $\tilde\Lambda_{78}^{\bar B}$, one can use Fierz transformation and the Vacuum Insertion Approximation (VIA) to express $h_{78}^{(1)}$ as a the square of B meson light-cone amplitudes ϕ_+^B. This allows us to write

$$\tilde\Lambda_{78}^{\bar B}\Big|_{\rm VIA} = e_{\rm spec}\,\frac{2f_B^2\,M_B}{9}\int_0^\infty d\omega_1\,\frac{\left[\phi_+^B(\omega_1,\mu)\right]^2}{\omega_1}\,,$$

where $e_{\rm spec}$ denotes the electric charge of the spectator quark in units of e ($e_{\rm spec} = 2/3$ for B^- and $-1/3$ for $\bar B^0$). Using [12] to constrain the integral, one finds that in the VIA, $\tilde\Lambda_{78}^{\bar B} \in e_{\rm spec}[17\,{\rm MeV},\,190\,{\rm MeV}]$.

Both $\tilde\Lambda_{17}^u$ and $\tilde\Lambda_{17}^c$ depend on h_{17}. Being a soft function, h_{17} has support over a hadronic range. Since in the expression for $\tilde\Lambda_{17}^c$, the integral starts at at $4m_c^2/m_b \approx 1$ GeV, we can expect a small overlap. Indeed one finds that [13], $-9\,{\rm MeV} < \tilde\Lambda_{17}^c < +11\,{\rm MeV}$. For $\tilde\Lambda_{17}^u$ there is no such suppression and we have $-330\,{\rm MeV} < \tilde\Lambda_{17}^u < +525\,{\rm MeV}$. The range is not symmetric since the normalization of h_{17} is $2\lambda_2 \approx 0.24\,{\rm GeV}^2$. This is the same result as one would obtain from estimating $\tilde\Lambda_{17}^u$ using naive dimensional analysis.

Including both the direct and resolved contributions and using $\mu = 2\,{\rm GeV}$ for the factorization scale, we find that the total CP asymmetry in the SM is

$$\mathcal{A}_{X_s\gamma}^{\rm SM} \approx \pi\left|\frac{C_1}{C_{7\gamma}}\right|{\rm Im}\,\epsilon_s\left(\frac{\tilde\Lambda_{17}^u-\tilde\Lambda_{17}^c}{m_b} + \frac{40\alpha_s}{9\pi}\,\frac{\Lambda_c}{m_b}\right) = \left(1.15\times\frac{\tilde\Lambda_{17}^u-\tilde\Lambda_{17}^c}{300\,{\rm MeV}} + 0.71\right)\%\,.$$

The direct contribution is slightly higher then the 0.5% mention before, since we are using a slightly lower factorization scale. The conclusion is that the asymmetry is actually dominated

by non-perturbative effects. Using the above estimates for $\tilde{\Lambda}^u_{17}$ and $\tilde{\Lambda}^c_{17}$, we find that the CP asymmetry in the SM can be in the range $-0.6\% < \mathcal{A}^{\rm SM}_{X_s\gamma} < 2.8\%$.

Beyond the SM, where the Wilson coefficients can be complex, we find that the asymmetry should be

$$\begin{aligned}\frac{\mathcal{A}_{X_s\gamma}}{\pi} \;\approx\; & \left[\left(\frac{40}{81}-\frac{40}{9}\,\frac{\Lambda_c}{m_b}\right)\frac{\alpha_s}{\pi}+\frac{\tilde{\Lambda}^c_{17}}{m_b}\right]\mathrm{Im}\,\frac{C_1}{C_{7\gamma}}-\left(\frac{4\alpha_s}{9\pi}-4\pi\alpha_s\,e_{\rm spec}\,\frac{\tilde{\Lambda}_{78}}{m_b}\right)\mathrm{Im}\,\frac{C_{8g}}{C_{7\gamma}} \\ & -\left(\frac{\tilde{\Lambda}^u_{17}-\tilde{\Lambda}^c_{17}}{m_b}+\frac{40}{9}\,\frac{\Lambda_c}{m_b}\,\frac{\alpha_s}{\pi}\right)\mathrm{Im}\left(\epsilon_s\,\frac{C_1}{C_{7\gamma}}\right). \qquad (8)\end{aligned}$$

Notice that the second term in this equation depends on the flavor of the spectator quark. In other words, the CP asymmetry can be different for charged and neutral B's. This effect arises already at order $\Lambda_{\rm QCD}/m_b$ for the resolved photon contribution. For the direct photon contribution such effects are more power suppressed. This allows us to suggest a new test of physics beyond the SM by measuring the CP asymmetry difference

$$\mathcal{A}_{X_s^-\gamma}-\mathcal{A}_{X_s^0\gamma}\approx 4\pi^2\alpha_s\,\frac{\tilde{\Lambda}_{78}}{m_b}\,\mathrm{Im}\,\frac{C_{8g}}{C_{7\gamma}}\approx 12\%\times\frac{\tilde{\Lambda}_{78}}{100\,\mathrm{MeV}}\,\mathrm{Im}\,\frac{C_{8g}}{C_{7\gamma}}\,. \qquad (9)$$

We conclude with several comments about $\bar{B}\to X_d\,\gamma$. All the above expressions apply also to this decay mode. All that we need to do is replace ϵ_s by $\epsilon_d=(V_{ub}V^*_{ud})/(V_{tb}V^*_{td})=(\bar{\rho}-i\bar{\eta})/(1-\bar{\rho}+i\bar{\eta})$. As a result the CP asymmetry is enhanced by a factor of $\mathrm{Im}(\epsilon_d)/\mathrm{Im}(\epsilon_s)\approx -22$. Including resolved photon contributions we find an asymmetry in the range $-62\% < \mathcal{A}^{\rm SM}_{X_d\gamma} < 14\%$. Another quantity of interest is the untagged CP asymmetry for $\bar{B}\to X_{s+d}\,\gamma$. Up to tiny U-spin breaking corrections, the direct photon contribution to the untagged asymmetry vanishes in SM [5,2,14]. This result does not change even after including resolved photon effects.

Acknowledgments

I would like to thank organizers for the invitation to give a talk at Moriond QCD 2011. This work is supported by DOE grant DE-FG02-90ER40560.

References

1. Heavy Flavor Averaging Group, [arXiv:1010.1589].
2. A. L. Kagan, M. Neubert, Phys. Rev. D **58**, 094012 (1998).
3. H. H. Asatryan, H. M. Asatrian, G. K. Yeghiyan, G. K. Savvidy, Int. J. Mod. Phys. A **16**, 3805 (2001).
4. M. Benzke, S. J. Lee, M. Neubert, G. Paz, Phys. Rev. Lett. **106**, 141801 (2011).
5. J. M. Soares, Nucl. Phys. B **367**, 575 (1991).
6. A. Ali, H. Asatrian, C. Greub, Phys. Lett. B **429**, 87 (1998).
7. T. Hurth, E. Lunghi, W. Porod, Nucl. Phys. B **704**, 56 (2005).
8. M. Bona *et al.* [SuperB Collaboration], [arXiv:0709.0451].
9. T. Aushev *et al.*, [arXiv:1002.5012].
10. S. J. Lee, M. Neubert, G. Paz, Phys. Rev. D **75**, 114005 (2007).
11. M. Benzke, S. J. Lee, M. Neubert, G. Paz, JHEP **1008**, 099 (2010);
12. S. J. Lee and M. Neubert, Phys. Rev. D **72**, 094028 (2005)
13. M. Benzke, S. J. Lee, M. Neubert, G. Paz, in preparation.
14. T. Hurth, T. Mannel, Phys. Lett. B **511**, 196 (2001).

CHARM SPECTROSCOPY AT B FACTORIES

RICCARDO CENCI
(on the behalf of the *BABAR* and BELLE collaborations)
4315 Department of Physics (Bldg 82), University of Maryland,
College Park, MD 20742-4111, U.S.A.

We report on the most recent measurements of charm spectroscopy obtained using the *BABAR* and BELLE datasets.

1 Introduction

The spectrum of quark-antiquark systems was initially predicted in 1985 using a relativistic chromodynamic potential model [1] and those predictions were updated in 2001 using recent lattice results [2]. While predictions for lower states are in agreement with the most recent experimental observations, some discrepanciencies are still present for higher ones.

Charm meson studies can be performed at the B factories experiments, like *BABAR* and BELLE, because their datasets include approximately the same number of $b\bar{b}$ and $c\bar{c}$ events, being the cross sections of the two processes comparable at their center-of-mass (CM) energy. Charm mesons can be selected using two methods: as products of B decays, when the B candidate is fully reconstruct (*exclusive* mode), or directly in $c\bar{c}$ events, where $b\bar{b}$ events are rejected requiring a momentum larger than 2.6 GeV/c for the meson candidates (*inclusive* mode).

In this proceeding, we will describe the most recent charm spectroscopy results obtained by the *BABAR* and BELLE experiments [3].

2 Inclusive study of $D^+\pi^-$, $D^0\pi^+$ and $D^{*+}\pi^-$ systems using *BABAR* dataset

In this analysis we study $D^+\pi^-$, $D^0\pi^+$ and $D^{*+}\pi^-$ final states with the inclusive mode using a dataset of 454 fb^{-1} collected by the *BABAR* detector [4]. To extract the resonance parameters we define the variable $M(D^+\pi^-) = m(K^-\pi^+\pi^+\pi^-) - m(K^-\pi^+\pi^+) + m_D^+$ and $M(D^0\pi^+) = m(K^-\pi^+\pi^-) - m(K^-\pi^+) + m_{D^0}$, where m_D^+ and m_D^0 are the nominal values of the D^+ and D^0 mass [5]. We remove the contribution due to fake D^+ and D^0 candidates by subtracting the $M(D\pi)$ distribution obtained by selecting events in the D^+ and D^0 candidate mass sidebands. The $M(D^+\pi^-)$ and $M(D^0\pi^+)$ distributions are presented, respectively, in Figs. 1(a) and 1(b).

The two distributions show similar features: prominent peaks for $D_2^*(2460)$, peaking backgrounds at about 2.3 GeV/c^2, and new structures around 2.6 and 2.75 GeV/c^2. The peaking backgrounds are due to decays from the $D_1(2420)$ and $D_2^*(2460)$ where a slow π^0 is missing in the reconstruction. The two distributions are fit to a smooth combinatoric background plus the appropriate relativistic Breit-Wigner (BW) function for each resonance. Due to broad resonances, some of their parameters need to be constrained to be around the nominal values [5] or fixed to the values obtained in the $D^{*+}\pi^-$ analysis described below. Because the peaking

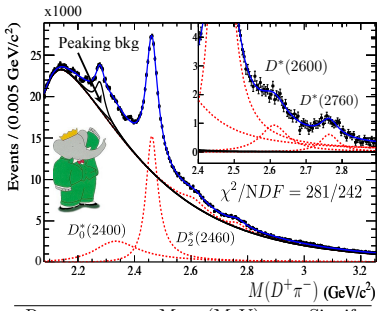

Resonance	Mass (MeV)	Signif.
$D^*(2600)^0$	$2608.7 \pm 2.4 \pm 2.5$	3.9σ
$D^*(2760)^0$	$2763.3 \pm 2.3 \pm 2.3$	8.9σ

(a) $D^+\pi^-$ system

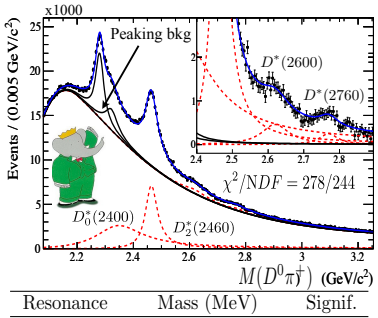

Resonance	Mass (MeV)	Signif.
$D^*(2600)^+$	$2621.3 \pm 3.7 \pm 4.2$	2.8σ
$D^*(2760)^+$	$2769.7 \pm 3.8 \pm 1.5$	3.5σ

(b) $D^0\pi^+$ system

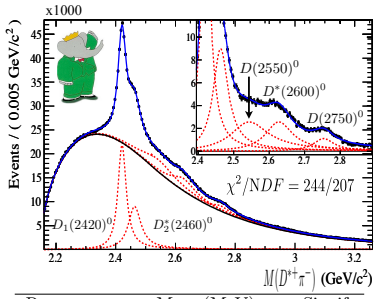

Resonance	Mass (MeV)	Signif.
$D(2550)^0$	$2539.4 \pm 4.5 \pm 6.8$	3.0σ
$D(2750)^0$	$2752.4 \pm 1.7 \pm 2.7$	4.2σ

(c) $D^{*+}\pi^-$ system

Figure 1: Mass distribution of the reconstructed candidates. Points correspond to data, with the total fit overlaid as a solid blue curve. The red dashed curves are the signal components. The black solid curve correspond to the smooth combinatoric background and to the peaking backgrounds at 2.3 GeV/c^2. The inset plots show the distributions after subtraction of the combinatoric background. In the table, the first error for the mass is statistic, while the second is the systematic one.

backgrounds are larger in the $M(D^0\pi^+)$ distribution, when fitting that distribution additional parameters need to be fixed to the values fitted to $M(D^+\pi^-)$ distribution, assuming isospin symmetry. The parameters and the significances for the new structures are shown in the tables in Fig. 1. The new resonances found in the $D^0\pi^+$ system are consistent with being the isospin partners of the $D^+\pi^-$ system resonances.

To search for new states in the $D^{*+}\pi^-$ system we define the variable $M(D^{*+}\pi^-) = m(K^-\pi^+(\pi^+\pi^-)\pi_s^+\pi^-) - m(K^-\pi^+(\pi^+\pi^-)\pi_s^+) + m_D^{*+}$, where m_D^{*+} is the value of the D^{*+} mass [5]. The $M(D^{*+}\pi^-)$ distribution is shown in Fig. 1(c) and shows the following features: prominent $D_1(2410)^0$ and $D_2^*(2460)^0$ peaks, and two structures at $\sim 2.60\,\text{GeV}/c^2$ and $\sim 2.75\,\text{GeV}/c^2$. The fit to this distribution is really similar to the previous ones, but here the final state contains additional information about the spin-parity quantum number of the resonances. In the rest frame of the D^{*+}, we define the helicity angle θ_H as the angle between the pion π^- and the slow pion π^+ from the D^{*+} decay. Fitting the $M(D^{*+}\pi^-)$ distribution in a limited range of θ_H, we find that another resonance around 2.55 GeV/c^2 need to be introduced, in addition to the two mentioned above. Again some parameters need to be fixed to the values obtained from the fit to $M(D^+\pi^-)$ distribution. The parameters and the significances for the new structures are shown in Fig. 1(c). The final model is then used to extract the signal yields as a function of $\cos\theta_H$ for 10 sub-samples. The $\cos\theta_H$ distribution parameter for the $D_1(2420)$ are consistent with previous measurements [6]. The $D(2550)^0$ and $D^*(2600)^0$ have mass values and $\cos\theta_H$ distributions consistent with the predicted radial excitations, respectively, $D_0^1(2S)$ and $D_1^3(2S)$.

3 $D_1(2420)^0 \to D^0\gamma$ radiative transistion using BELLE dataset

In this analysis we search for the radiative transition $D_1(2420)^0 \to D^0\gamma$ using a dataset of 656 fb^{-1} collected at CM energies near 10.58 GeV by the BELLE detector [7]. The standard ΔE and $m_{\rm bc}$ variables are used to select the B mesons in the $B^- \to \pi^- D_1(2420)^0$ mode. The corresponding pionic decays $B^- \to \pi^- D_{(0,2)}^0 \to \pi^0 D^0 \to K^-\pi^+$ form an important background to the radiative transition analysis, with the D_2 peaking close to the signal region, and have never previously been measured. This background is included in the final fit performed on the $m(D^0\gamma)$ distribution. In the rest frame of the D^0, we define the decay angle θ_J as the angle between the γ and the pion π^+ from the D^0 decay. The final fit is performed simultaneously over 4 separate ranges of $\cos\theta_J$, as shown in Fig. 2.

The preliminary result we obtain for the branching fraction is: $\mathcal{B}(B^- \to \pi^- D_1(2420)^0) \times \mathcal{B}(D_1(2420)^0 \to D^0\gamma) = 5.0 \pm 0.5(\text{stat}) \pm 1.5(\text{syst})$. Candidates in the $\cos\theta_J$ range $[-1.0, 0.7]$

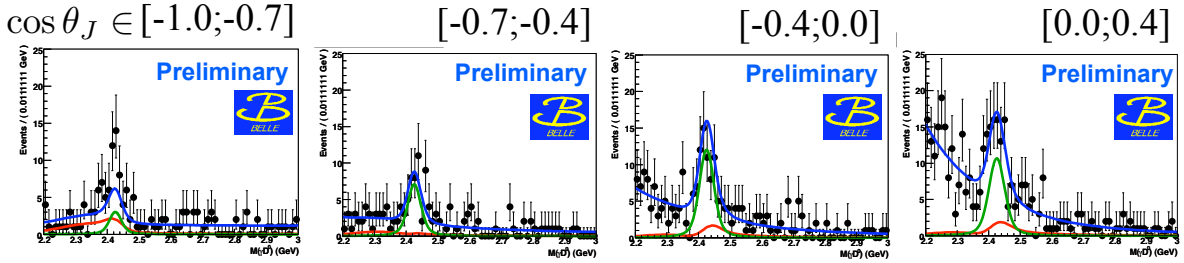

Figure 2: $m(D^0\gamma)$ distribution of the reconstructed candidates. Points with errors correspond to data, with the total fit overlaid as a solid blue curve. The green curve is the signal component, while the red curve is the peaking background one.

have a small contribution in the final result, but the disagreement between the fit and the data in that range generate an underestimation of the peaking background component. Therefore, work is still in progress to better understand the contribution from this background process.

4 Study of the decays $B \to D_{s1}(2536)^+\overline{D}^{(*)}$ using BELLE dataset

The $D_{s1}(2536)^+$ is a narrow P-wave resonance observed some years ago, but its properties are still not well measured. In this analysis we study the production of $D_{s1}(2536)^+$ in doubly charmed B meson decays, $B \to D_{s1}(2536)^+D^{(*)}$, where $D^{(*)}$ is either a D^0, D^- or D^{*-}, using a dataset of 605 fb^{-1} collected at CM energies near 10.58 GeV by the BELLE detector [8].

The $D_{s1}(2536)^+$ are reconstructed in three modes: $D^{*0}(D^0\gamma)K^+$, $D^{*0}(D^0\pi^0)K^+$, and $D^{*+}(D^0\pi^+)K^0_S$. The B candidates are also reconstructed in three modes: $B^+ \to D_{s1}(2536)^+\overline{D}^0$, $B^0 \to D_{s1}(2536)^+D^-$, and $B^0 \to D_{s1}(2536)^+D^{*-}$. The signal region is defined as a box in the ΔE-$m_{\rm bc}$ plane. The signal yields for each combination of B and $D_{s1}(2536)^+$ decay modes are obtained with a simultaneous fit to the data and the fit results are shown in Fig. 3.

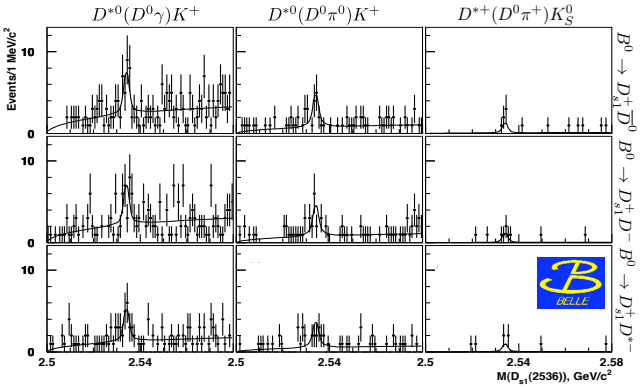

(a)

B decay mode	$\mathcal{B}(\times 10^{-4})$	Signif.
$D_{s1}(2536)^+(D^*K)\overline{D}^0$	$3.97 \pm 0.85 \pm 0.56$	7.0σ
$D_{s1}(2536)^+(D^*K)D^-$	$2.75 \pm 0.62 \pm 0.36$	6.9σ
$D_{s1}(2536)^+(D^*K)D^{*-}$	$5.01 \pm 1.21 \pm 0.70$	6.3σ
$D^*K = D^{*0}K^+ + D^{*+}K^0_S$	$\pm(\text{stat}) \pm (\text{syst})$	

(b)

Figure 3: (a) $D_{s1}(2536)^+$ mass distribution: the points with errors are the data, while the curves show the fit result. (b) Values for the measured branching fractions and corresponding significances.

Results are consistent with previous measurements. We also compute the following branching ratios: $\mathcal{B}(D_{s1}(2536)^+ \to D^{*0}K^+)/\mathcal{B}(D_{s1} \to D^{*+}K^0_S) = 0.88 \pm 0.24(\text{stat}) \pm 0.08(\text{syst})$, $\mathcal{B}(B \to DD_{s1}(2536))/\mathcal{B}(B \to DD^*_s) = 0.049 \pm 0.010$, and $\mathcal{B}(B \to D^*D_{s1}(2536))/\mathcal{B}(B \to D^*D^*_s) = 0.044 \pm 0.010$, and we find that they follow the theoretical expectations [9].

5 Measurements of $D_{s1}(2536)^+$ parameter values using *BABAR* dataset

In this analysis a precise measurement of the $D_{s1}(2536)^+$ mass and decay width is performed based on a dataset of 385 fb^{-1} collected at CM energies near 10.58 GeV by the *BABAR* detector [10]. The $D_{s1}(2536)^+$ candidates are reconstructed using the inclusive mode with the following decay chain: $D_{s1}(2536)^+ \to K^0_S D^{*+}(\to \pi^+ D^0)$, and $D^0 \to K^-\pi^+(\pi^+\pi^-)$. To improve the mass

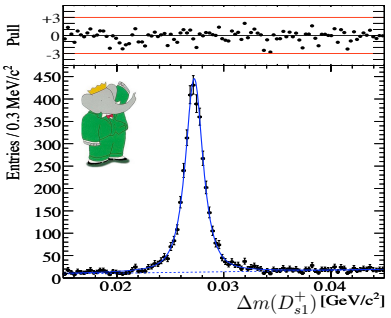

(a)

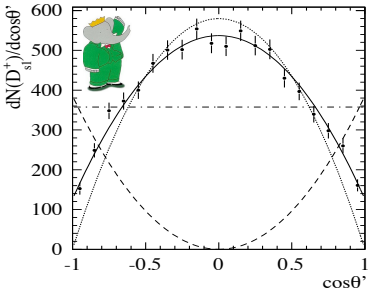

(b)

J^P	$dN(D_{s1}^+)/d\cos\theta'$	χ^2/NDF	Line
0^-	$a\cos^2\theta'$	4578.0/19	dashed
$1^-,2^+,3^-$	$a\sin^2\theta'$	190.9/19	dotted
$1^+,2^-,3^+,...$	$a(\sin^2\theta'+\beta\cos^2\theta')$ $\beta=1$ (fixed)	802.5/19	dash-dotted
$1^+,2^-,3^+,...$	$a(\sin^2\theta'+\beta\cos^2\theta')$ $\beta=0.23\pm0.02$	14.7/18	solid

(c)

Figure 4: (a) $\Delta m(D_{s1}(2536)^+)$ distribution: the points with errors are the data, while the solid curve show the fit result. The dotted line indicates the background lineshape. (b) Efficiency-corrected signal yield as function of $\cos\theta'$ in data. The various lines represent the fit to the models detailed in (c).

resolution, we examined the mass difference $\Delta m(D_{s1}(2536)^+) = m(D_{s1}(2536)^+) - m(D^{*+}) - m(K_S^0)$. We fit the $\Delta m(D_{s1}(2536)^+)$ distribution to a linear background plus a relativistic Breit-Wigner convolved with a resolution function, the width of which depends on the CM momentum of the $D_{s1}(2536)^+$ candidate. The fit of $\Delta m(D_{s1}(2536)^+)$ distribution for the candidates where D^0 is reconstructed in $K^-\pi^+$ is shown in Fig. 4(a). We find the mass of $D_{s1}(2536)^+$ to be $(2535.08 \pm 0.01(\text{stat}) \pm 0.15(\text{syst}))\,\text{MeV}/c^2$, the mass difference $m(D_{s1}(2536)^+) - m(D^{*+}) = (524.83 \pm 0.01(\text{stat}) \pm 0.04(\text{syst}))\,\text{MeV}/c^2$, and, for the first time, we measured the total decay width of $D_{s1}(2536)^+$: $\Gamma(D_{s1}(2536)^+) = (0.92(\text{stat}) \pm 0.03 \pm 0.04(\text{syst}))\,\text{MeV}/c^2$.

We performed also an angular analysis for the D^{*+} decay and we define as decay angle θ' the angle between the D^0 momentum vector in the D^{*+} CM system and the D^{*+} momentum vector in the $D_{s1}(2536)^+$ CM system. Data are corrected for the efficiency and divided in 20 bins of $\cos\theta'$. We fit the $\cos\theta'$ distribution to different theoretical models, as shown in Figs. 4(b) and 4(c). The unnatural $J^P = 1^+$ parity for D^{*+} is confirmed.

6 Conclusions

We presented here a summary of the last results in charm spectroscopy using the B factories datasets. We reported about the observation of new excited states of D meson and $D_1(2420)^0 \to D^0\gamma$ radiative decay. Last measurements of B decays that include a $D_{s1}(2536)^+$ meson follow the theoretical expectations. We obtained also the most precise measurement of $D_{s1}(2536)^+$ parameters, including the first measurement of its width. In the end, the large datasets collected at B factories have already been used to perform many interesting measurements of charm spectroscopy, while more analyses are still in progress. A clearer picture can be obtained only with much larger dataset from a super-flavour factory.

References

1. S. Godfrey and N. Isgur, *Phys. Rev.* D **32**, 189 (1985).
2. M. Di Pierro, N. Eitchen, *Phys. Rev.* D **64**, 114004 (2001).
3. Charge conjugates are implied throughout this proceeding.
4. P. Del Amo Sanchez *et al.* [The BABAR Collaboration], *Phys. Rev.* D **82**, 111101 (2010).
5. C. Amsler *et al.* [Particle Data Group], *Phys. Lett.* B **667**, 1 (2008).
6. S. Chekanov *et al.* [ZEUS Collaboration], Eur. Phys. J. C **60**, 25 (2009).
7. http://belle.kek.jp/belle/talks/ICHEP10/watson.pdf
8. T. Aushev *et al.* [Belle Collaboration], *Phys. Rev.* D **83**, 051102 (2011).
9. A. Le Yaouanc, L. Oliver, O. Pene and J. C. Raynal, *Phys. Lett.* B **387**, 582 (1996).
10. J. P. Lees *et al.* [The BABAR Collaboration], *Phys. Rev.* D **83**, 072003 (2011).

CHARM PHYSICS RESULTS AND PROSPECTS WITH LHCb

P.M. SPRADLIN
Department of Physics and Astronomy, University of Glasgow, Kelvin Building, University Avenue, Glasgow G12 8QQ, United Kingdom

Precision measurements in charm physics offer a window into a unique sector of potential New Physics interactions. LHCb is poised to become a world leading experiment for charm physics, recording enormous samples with a detector tailored for flavor physics. This article presents recent charm production, *CPV*, and mixing studies from LHCb, including LHCb's first charm *CP* asymmetry measurement with 37 pb^{-1} of data collected in 2010. Significant updates to the material presented at the 2011 Rencontres de Moriond QCD and High Energy Interactions are included.

1 Charm production at the LHCb experiment

LHCb [1], the dedicated flavor experiment at CERN's Large Hadron Collider (LHC), is the only LHC experiment with a broad charm physics program including measurements of charm *CP* violation (*CPV*) and D^0-$\overline{\text{D}}^0$ mixing. The cross-section to produce charm hadrons into the LHCb acceptance in the LHC's $\sqrt{s} = 7$ TeV proton-proton collisions is 1.23 ± 0.19 mb, creating a huge potential data set.[2] The LHCb trigger system has a flexible design that includes charm triggers so that this prolific production can be exploited.

LHCb recorded a total integrated luminosity of 37.7 pb^{-1} in 2010. The charm samples collected in 2010 are already large enough for LHCb to be competitive in several measurements. With an expectation of more than 1 fb^{-1}, the 2011-12 run will yield even larger samples.

Because the LHC collides protons, there may be asymmetries in the production of charm and anti-charm hadrons. LHCb has measured the production asymmetry of $\text{D}^0/\overline{\text{D}}^0$ using 37 pb^{-1} of 2010 data.[3] The analysis uses both untagged samples of reconstructed D^0 decays and tagged samples that are reconstructed as the product of a $\text{D}^{*+} \to \text{D}^0\pi^+_{\text{slow}}$ decay. In the tagged sample, the initial flavor of the D is identified (tagged) as D^0 or $\overline{\text{D}}^0$ by the charge of the tagging slow pion, $\pi^{\pm}_{\text{slow}}$. In both samples, D^0 is reconstructed in the final states $\text{K}^-\pi^+$, K^-K^+, and $\pi^-\pi^+$. For a final state f, the raw observed untagged asymmetry, $\mathcal{A}_{\text{Raw}}(f)$, and the raw observed D^*-tagged asymmetry, $\mathcal{A}^*_{\text{Raw}}(f)$, can be factored into components:

$$\mathcal{A}_{\text{Raw}}(f) \equiv \frac{N(\text{D}^0 \to f) - N(\overline{\text{D}}^0 \to \bar{f})}{N(\text{D}^0 \to f) + N(\overline{\text{D}}^0 \to \bar{f})} = \mathcal{A}_{CP}(f) + \mathcal{A}_{\text{D}}(f) + \mathcal{A}_{\text{P}}(\text{D}^0), \quad (1)$$

$$\begin{aligned} \mathcal{A}^*_{\text{Raw}}(f) &\equiv \frac{N(\text{D}^{*+} \to \text{D}^0(f)\pi^+_{\text{slow}}) - N(\text{D}^{*-} \to \overline{\text{D}}^0(\bar{f})\pi^-_{\text{slow}})}{N(\text{D}^{*+} \to \text{D}^0(f)\pi^+_{\text{slow}}) + N(\text{D}^{*-} \to \overline{\text{D}}^0(\bar{f})\pi^-_{\text{slow}})} \\ &= \mathcal{A}_{CP}(f) + \mathcal{A}_{\text{D}}(f) + \mathcal{A}_{\text{D}}(\pi_{\text{slow}}) + \mathcal{A}_{\text{P}}(\text{D}^{*+}), \end{aligned} \quad (2)$$

where the $N(\text{decay})$ are the numbers of reconstructed decays, $\mathcal{A}_{CP}(f)$ is the *CP* asymmetry of the D^0 decay (further studied in Section 2), $\mathcal{A}_{\text{D}}(f)$ and $\mathcal{A}_{\text{D}}(\pi_{\text{slow}})$ are the detection asymmetries

of f and $\pi^{\pm}_{\rm slow}$, and $\mathcal{A}_{\rm P}(\rm D^0)$ and $\mathcal{A}_{\rm P}(\rm D^{*+})$ are the production asymmetries. For the self-conjugate final states $\rm K^-K^+$ and $\pi^-\pi^+$, $\mathcal{A}_{\rm D}(\rm K^-K^+) = \mathcal{A}_{\rm D}(\pi^-\pi^+) = 0$. Therefore, the remaining detection asymmetries can be canceled by considering combinations of raw asymmetries,

$$\mathcal{A}_{\rm Raw}(\rm K^-\pi^+) - \mathcal{A}^*_{\rm Raw}(\rm K^-\pi^+) + \mathcal{A}^*_{\rm Raw}(\rm K^-K^+) = \mathcal{A}_{\rm P}(\rm D^0) + \mathcal{A}_{CP}(\rm K^-K^+), \quad (3)$$

$$\mathcal{A}_{\rm Raw}(\rm K^-\pi^+) - \mathcal{A}^*_{\rm Raw}(\rm K^-\pi^+) + \mathcal{A}^*_{\rm Raw}(\pi^-\pi^+) = \mathcal{A}_{\rm P}(\rm D^0) + \mathcal{A}_{CP}(\pi^-\pi^+). \quad (4)$$

Using the HFAG world averages of $\mathcal{A}_{CP}(\rm K^-K^+)$ and $\mathcal{A}_{CP}(\pi^-\pi^+)$[4] and a Bayesian minimizer to optimally solve this over-constrained system for $\mathcal{A}_{\rm P}(\rm D^0)$, we measure a mean value of $\mathcal{A}_{\rm P}(\rm D^0) = [-1.08 \pm 0.32\,(\rm stat) \pm 0.12\,(\rm syst)]\,\%$ in LHCb's acceptance.

2 Time-integrated *CPV* in D mesons

LHCb is searching for evidence of new sources of *CP* asymmetry in the time-integrated decay rates of D mesons. The time-integrated *CP* asymmetry, $\mathcal{A}_{CP}(f)$, is conventionally defined as

$$\mathcal{A}_{CP}(f) = \frac{\Gamma(\rm D \to \it f) - \Gamma(\overline{\rm D} \to \bar{f})}{\Gamma(\rm D \to \it f) + \Gamma(\overline{\rm D} \to \bar{f})} \quad (5)$$

for a given final state f. For $\rm D^0$ decays, $\mathcal{A}_{CP}$ may have contributions from both indirect and direct *CPV* . In the Standard Model, *CPV* in the charm system is highly suppressed. Indirect *CPV* is negligibly small and should be common for all decay modes. Direct *CPV* is expected to be $\mathcal{O}(10^{-3})$ or less and to vary among decay modes.[5] In *CPV* searches in singly Cabibbo suppressed decays, such as $\rm D^0 \to K^-K^+$, participation of well-motivated new physics (NP) particles in the interfering penguin amplitude could enhance direct *CPV* up to $\mathcal{O}(10^{-2})$.[6]

LHCb recently presented its first time-integrated *CPV* measurement with decays $\rm D^0 \to K^-K^+$ and $\rm D^0 \to \pi^-\pi^+$.[3] The analysis uses the tagged samples of $\rm D^{*+} \to D^0\pi^+_{slow}$ decays also used in the measurement of $\mathcal{A}_{\rm P}(\rm D^0)$ (Section 1). Using Equation 2, the difference in $\mathcal{A}_{CP}(f)$ for $f = \rm K^-K^+$ and $\pi^-\pi^+$ can be measured precisely with the production and detection asymmetries canceling exactly:

$$\Delta\mathcal{A}_{CP} \equiv \mathcal{A}_{CP}(\rm K^-K^+) - \mathcal{A}_{CP}(\pi^-\pi^+), \quad (6)$$

$$= \mathcal{A}^*_{\rm Raw}(\rm K^-K^+) - \mathcal{A}^*_{\rm Raw}(\pi^-\pi^+). \quad (7)$$

In 37 $\rm pb^{-1}$ of LHCb 2010 data, we measure $\Delta\mathcal{A}_{CP} = [-0.28 \pm 0.70\,(\rm stat) \pm 0.25\,(\rm syst)]\,\%$, consistent with zero. This result is approaching the sensitivity of *CPV* measurements performed by the B-factories in these decay modes,[7,8] but not yet at the level of CDF's recent measurement.[9] Due to differential proper-time acceptance between the $\rm K^-K^+$ and $\pi^-\pi^+$ samples, the measured value of $\Delta\mathcal{A}_{CP}$ includes a residual 10% of the mode-independent indirect *CP* asymmetry. No limiting systematic bias has been identified in the method, so future iterations of the measurement with the much larger data set anticipated for 2011-2012 will be significantly more precise.

3 Time-dependent *CPV* and mixing measurements in $\rm D^0$

The conventional parameterization of charm mixing is fully explained elsewhere.[10] Briefly, the mass eigenstates of the neutral D system $\rm D_1$ and $\rm D_2$ are expressed as normalized superpositions of the flavor eigenstates $\rm D^0$ and $\overline{\rm D}^0$, $\rm D_{1,2} = \it p\rm D^0 \pm \it q\overline{\rm D}^0$, where p and q are complex scalars, $|p|^2 + |q|^2 = 1$. The relative argument of q and p is conventionally chosen equal to the phase that parameterizes *CPV* in the interference between mixing and direct decays, $\arg\frac{q}{p} = \phi$. *CP* is violated in the mixing if $|\frac{q}{p}| \neq 1$ and in the interference between mixing and decay if $\phi \neq 0$. Letting $m_{1,2}$ and $\Gamma_{1,2}$ represent respectively the masses and widths of $\rm D_{1,2}$, mixing is parameterized by the mass difference $x \equiv \frac{m_1 - m_2}{\Gamma}$ and the width difference $y \equiv \frac{\Gamma_1 - \Gamma_2}{2\Gamma}$ where $\Gamma \equiv \frac{1}{2}(\Gamma_1 + \Gamma_2)$.

LHCb is working towards its first measurements of *CPV* and mixing in D^0-$\overline{D}^0$ with lifetime ratios of $D^0 \to K^-\pi^+$ and $D^0 \to K^-K^+$ decays. The lifetime of decays to the *CP*-even eigenstate K^-K^+, $\tau(K^-K^+)$, is related to the lifetime of the flavor-specific final state $K^-\pi^+$, $\tau(K^-\pi^+)$, by the mixing parameters:

$$y_{CP} \equiv \frac{\tau(K^-\pi^+)}{\tau(K^-K^+)} - 1 = y\cos\phi - \frac{1}{2}\left(\left|\frac{q}{p}\right| - \left|\frac{p}{q}\right|\right) x\sin\phi. \tag{8}$$

If *CP* is conserved, $y_{CP} = y$. The asymmetry in the lifetimes of D^0 and $\overline{D}^0$ decays to the *CP* eigenstate K^-K^+ is related to the *CPV* and mixing parameters by

$$A_\Gamma \equiv \frac{\tau(\overline{D}^0 \to K^-K^+) - \tau(D^0 \to K^-K^+)}{\tau(\overline{D}^0 \to K^-K^+) + \tau(D^0 \to K^-K^+)} = \frac{1}{2}\left(\left|\frac{q}{p}\right| - \left|\frac{p}{q}\right|\right) y\cos\phi - x\sin\phi. \tag{9}$$

D^*-tagged candidates are used in the measurement of A_Γ, while y_{CP} can be measured with the larger untagged sample.

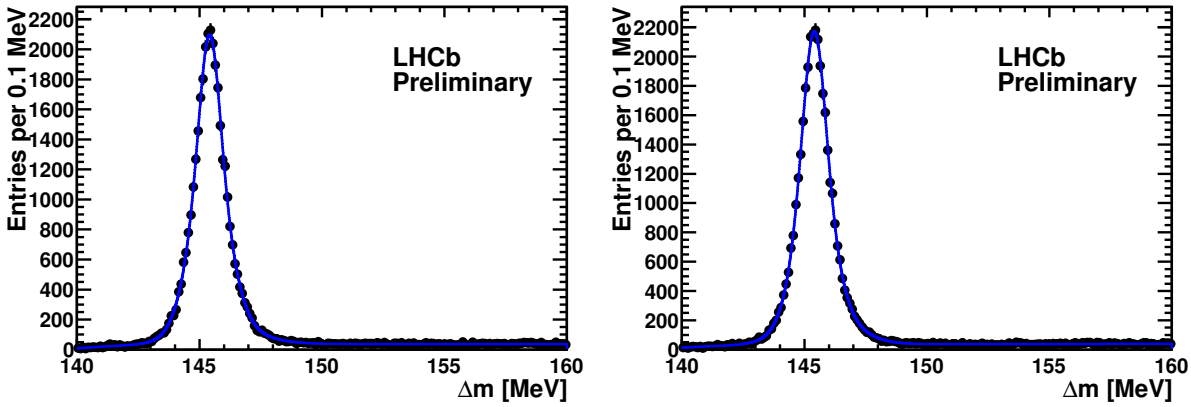

(a) $D^{*+} \to D^0\pi^+$ (b) $D^{*-} \to \overline{D}^0\pi^-$

Figure 1: Distributions of the mass difference, Δm, between D^0 ($\overline{D}^0$) candidates and their parent D^{*+} (D^{*-}) candidates for decays $D^{*+} \to D^0\pi^+$, $D^0 \to K^-\pi^+$ (c.c.).

In the 2010 run, we collected a sample of untagged $D^0 \to K^-K^+$ decays comparable in size to those of recent Belle and BaBar measurements.[11,12] In 2011-2012, LHCb expects to have the world's largest charm sample in this mode. The measurements of y_{CP} and A_Γ are currently blinded. As a test, the A_Γ analysis was applied to a subset of the 2010 data in the right-sign (RS) control channel $D^0 \to K^-\pi^+$. Figure 1 shows the distributions of the differences Δm between the masses of the reconstructed D^0 candidates and their parent D^{*+} candidates for the RS validation sample. The purity of the sample is better than 90%.

Since the most powerful signal/background discriminants in hadronic collisions exploit the relatively long lifetime of D mesons, the trigger and selection criteria introduce a proper-time acceptance for the reconstructed D^0 decays. Unbiased time-dependent measurements require careful treatment of the acceptance effects of these discriminants. LHCb can precisely evaluate the proper-time acceptance on an event-by-event basis with the swimming method.[13,14] Statistical separation of D^0 mesons produced at the primary interaction vertex from those produced in the decays of *b*-hadrons is accomplished using the impact parameter (IP) χ^2 of the D^0. The event-by-event acceptance and the IP χ^2 are incorporated into an unbinned multi-dimensional likelihood fit to measure the lifetimes. Figure 2 shows the proper-time distributions for the tagged RS validation sample. The lines on the plots are the fitted distributions from the unbinned multi-dimensional likelihood fit.

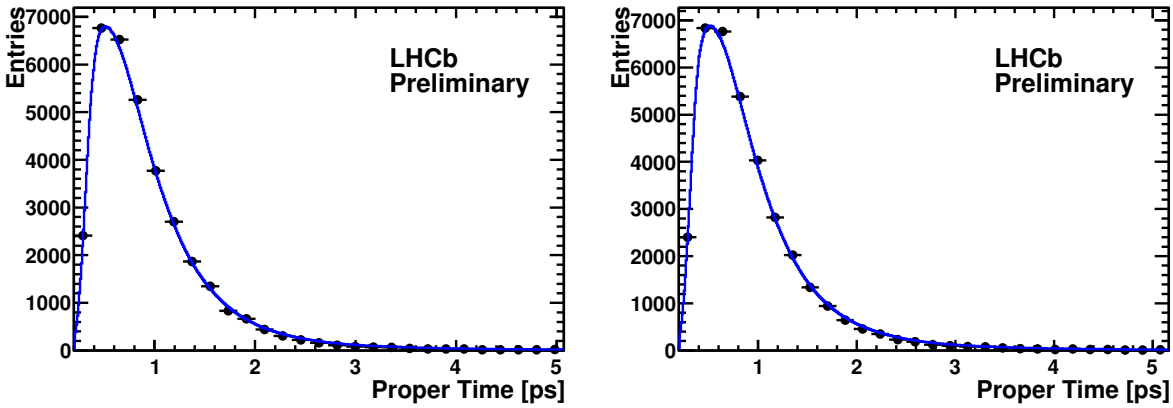

(a) D^0 (b) $\overline{D}^0$

Figure 2: Distributions of the reconstructed proper time of D^0 ($\overline{D}^0$) candidates for decays $D^{*+} \to D^0\pi^+$, $D^0 \to K^-\pi^+$ (c.c.). The line on each plot is the result of a likelihood fit incorporating per-event acceptance distributions computed with the swimming method.

4 Summary

LHCb had a successful year of data taking in 2010, collecting 37.7 pb^{-1} of pp collisions at $\sqrt{s} = 7$ TeV. We observe an asymmetry in D^0 production of $\mathcal{A}_P(D^0) = [-1.08 \pm 0.32\,(\text{stat}) \pm 0.12\,(\text{syst})]\%$, which is the first evidence for an asymmetry in heavy flavor production at the LHC. In our first precision charm *CPV* measurement with this data, the difference between the time-integrated *CP* asymmetries of $D^0 \to K^-K^+$ and $D^0 \to \pi^-\pi^+$ decays is measured to be $\Delta\mathcal{A}_{CP} = [-0.28 \pm 0.70\,(\text{stat}) \pm 0.25\,(\text{syst})]\%$. A broad program of charm physics is underway and further results in more channels are soon to follow. With the large data set expected in 2011-2012, LHCb is poised to become a leader in charm physics.

References

1. **LHCb** Collaboration, A. A. Alves *et al. JINST* **3** (2008) S08005.
2. **LHCb** Collaboration, Conference Report LHCb-CONF-2010-013, Dec, 2010.
3. **LHCb** Collaboration, Conference Report LHCb-CONF-2011-023, May, 2011.
4. **Heavy Flavor Averaging Group** Collaboration, D. Asner *et al.* and online update at `http://www.slac.stanford.edu/xorg/hfag`.
5. S. Bianco, F. L. Fabbri, D. Benson, and I. Bigi *Riv. Nuovo Cim.* **26N7** (2003) 1–200.
6. Y. Grossman, A. L. Kagan, and Y. Nir *Phys. Rev.* **D75** (2007) 036008.
7. **BaBar** Collaboration, B. Aubert *et al. Phys. Rev. Lett.* **100** (2008) 061803.
8. **Belle** Collaboration, M. Staric *et al. Phys. Lett.* **B670** (2008) 190–195.
9. **CDF** Collaboration, CDF note 10296, Feb, 2011.
10. **Particle Data Group** Collaboration, K. Nakamura *et al.*, "D^0-$\overline{D}^0$ Mixing," in *Review of particle physics*, vol. G37, p. 075021. 2010.
11. **Belle** Collaboration, M. Staric *et al. Phys. Rev. Lett.* **98** (2007) 211803.
12. **BaBar** Collaboration, B. Aubert *et al. Phys. Rev.* **D80** (2009) 071103.
13. M. Gersabeck, V. V. Gligorov, J. Imong, and J. Rademacker LHCb Public note LHCb-PUB-2009-022, Nov, 2009.
14. **CDF** Collaboration, T. Aaltonen *et al. Phys. Rev.* **D83** (2011) 032008.

Two body hadronic D decays

Yu Fusheng, Cai-Dian Lü, Xiao-Xia Wang
Institute of High Energy Physics and Theoretical Physics Center for Science Facilities, Chinese Academy of Sciences, Beijing 100049, People's Republic of China

We analyze the decay modes of $D/D_s \to PP, PV$ on the basis of a hybrid method with the generalized factorization approach for emission diagrams and the pole dominance model for the annihilation type contributions. Our results of PV final states are better than the previous method, while the results of PP final states are comparable with previous diagrammatic approach.

1 Introduction

The CLEO-c and the two B factories already give more measurements of charmed meson decays than ever. The BESIII and super B factories are going to give even much more data soon. Therefore, it is a good chance to further study the nonleptonic two-body D decays. However, it is theoretically unsatisfied since some model calculations, such as QCD sum rules or Lattice QCD, are ultimate tools but formidable tasks. In B physics, there are QCD-inspired approaches for hadronic decays, such as the perturbative QCD approach (pQCD),[1] the QCD factorization approach (QCDF),[2] and the soft-collinear effective theory (SCET).[3] But it doesn't make much sense to apply these approaches to charm decays, since the mass of charm quark, of order 1.5 GeV, is neither heavy enough for a sensible $1/m_c$ expansion, nor light enough for the application of chiral perturbation theory.

After decades of studies, the factorization approach is still an effective way to investigate the hadronic D decays [4]. However, the naive factorization encounters well-known problems: the Wilson coefficients are renormalization scale and γ_5-scheme dependent, and the color-suppressed processes are not well predicted due to the smallness of a_2. The generalized factorization approaches were proposed to solve these problems, considering the significant nonfactorizable contributions in the effective Wilson coefficients [5]. Besides, in the naive or generalized factorization approaches, there are no strong phases between different amplitudes, which are demonstrated to be existing by experiments.

On the other hand, the hadronic picture description of non-leptonic weak decays has a longer history, because of their non-perturbative feature. Based on the idea of the vector dominance, which is discussed on strange particle decays,[6] the pole-dominance model of two-body hadronic decays was proposed.[7] This model has already been applied to the two-body nonleptonic decays of charmed and bottom mesons [7,8].

In this work, the two-body hadronic charm decays are analyzed based on a hybrid method with the generalized factorization approach for emission diagrams and the pole dominance model for the annihilation type contributions [9].

2 The hybrid method

In charm decays, we start with the weak effective Hamiltonian for the $\Delta C = 1$ transition

$$\mathcal{H}_{eff} = \frac{G_F}{\sqrt{2}} V_{CKM}(C_1 O_1 + C_2 O_2) + h.c., \tag{1}$$

with the current-current operators

$$\begin{aligned} O_1 &= \bar{u}_\alpha \gamma_\mu (1-\gamma_5) q_{2\beta} \cdot \bar{q}_{3\beta} \gamma^\mu (1-\gamma_5) c_\alpha, \\ O_2 &= \bar{u}_\alpha \gamma_\mu (1-\gamma_5) q_{2\alpha} \cdot \bar{q}_{3\beta} \gamma^\mu (1-\gamma_5) c_\beta. \end{aligned} \tag{2}$$

In the generalized factorization method, the amplitudes are separated into two parts

$$\langle M_1 M_2 | \mathcal{H}_{eff} | D \rangle = \frac{G_F}{\sqrt{2}} V_{CKM} a_{1,2} \langle M_1 | \bar{q}_1 \gamma_\mu (1-\gamma_5) q_2 | 0 \rangle \langle M_2 | \bar{q}_3 \gamma^\mu (1-\gamma_5) c | D \rangle, \tag{3}$$

where a_1 and a_2 correspond to the color-favored tree diagram ($\mathcal{T}$) and the color-suppressed diagram ($\mathcal{C}$) respectively. To include the significant non-factorizable contributions, we take $a_{1,2}$ as scale- and process-independent parameters fitted from experimental data. Besides, a large relative strong phase between a_1 and a_2 is demonstrated by experiments. Theoretically, the existence of large phase is reasonable for the importance of inelastic final state interactions in the charmed meson decays, with on-shell intermediate states. Therefore, we take

$$a_1 = |a_1|, \quad a_2 = |a_2| e^{i\delta}, \tag{4}$$

where a_1 is set to be real for convenience.

On the other hand, annihilation type contributions are neglected in the factorization approach. However, the weak annihilation (W-exchange and W-annihilation) contributions are sizable, of order $1/m_c$, and have to be considered. It is also demonstrated to be important by the difference of life time between D^0 and D^+. The pole-dominance model is a useful tool to calculate the considerable resonant effects of annihilation diagrams. For simplicity, only the lowest-lying pole is considered in the single-pole model. Taking $D^0 \to PP, PV$ as example, the annihilation type diagram in the pole model is shown in Fig.1(a). D^0 goes into the intermediate state M via the effective weak Hamiltonian in Eq.(1), shown by the quark line in the Fig.1(b), and then decays into $PP(PV)$ through strong interactions. Angular momentum should be conserved at the weak vertex, and all conservation laws be preserved at the strong vertex. Therefore, the intermediate particles are scalar mesons for PP modes and pseudoscalar mesons for PV modes. In D^0 decays, they are W-exchange diagrams, but W-annihilation amplitudes in the $D^+_{(s)}$ decay modes.

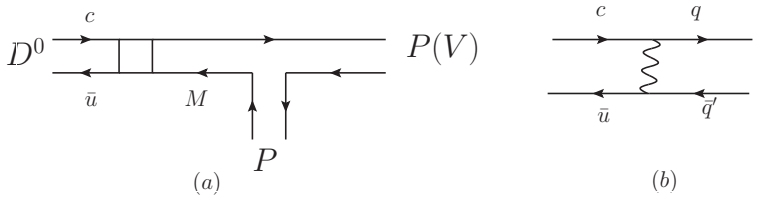

Figure 1: Annihilation diagram in the pole-dominance model

The weak matrix elements are evaluated in the vacuum insertion approximation[8],

$$\begin{aligned} \langle M | \mathcal{H} | D \rangle &= \frac{G_F}{\sqrt{2}} V_{CKM} a_{A,E} \langle M | \bar{q}_1 \gamma_\mu (1-\gamma_5) q_2 | 0 \rangle \langle 0 | \bar{q}_3 \gamma^\mu (1-\gamma_5) c | D \rangle \\ &= \frac{G_F}{\sqrt{2}} V_{CKM} a_{A,E} f_M f_D m_D^2, \end{aligned} \tag{5}$$

where the effective coefficients a_A and a_E correspond to W-annihilation and W-exchange amplitudes respectively. Strong phases relative to the emission diagrams are also considered in these coefficients.

For the PV modes, the effective strong coupling constants are defined through the Lagrangian

$$\mathcal{L}_{VPP} = ig_{VPP}V^{\mu}(P_1\partial_{\mu}P_2 - P_2\partial_{\mu}P_1), \tag{6}$$

where g_{VPP} is dimensionless and obtained from experiments. By inserting the propagator of the intermediate state M, the annihilation amplitudes are

$$\langle PV|\mathcal{H}_{eff}|D\rangle = \frac{G_F}{\sqrt{2}}V_{CKM}a_{A,E}f_M f_D m_D^2 \frac{1}{m_D^2 - m_M^2} g_{VPM} 2(\varepsilon^* \cdot p_D). \tag{7}$$

As for the PP modes, the intermediate mesons are scalar particles. The effective strong coupling constants are described by

$$\mathcal{L}_{SPP} = -g_{SPP}m_S SPP. \tag{8}$$

However, the decay constants of scalar mesons are very small, which is shown in the following relation

$$\frac{f_S}{\bar{f}_S} = \frac{m_2(\mu) - m_1(\mu)}{m_S}, \tag{9}$$

where f_S is the vector decay constant used in the pole model, $\bar{f}_S$ is the scale-independent scalar decay constant, $m_{1,2}$ are the running current quark mass, and m_S is the mass of scalar meson. Therefore, the scalar pole contribution is very small, resulting in little resonant effect of annihilation type contributions in the PP modes. On the contrary, large annihilation contributions are given in the PV modes by relative large decay constants of intermediate pseudoscalar mesons.

3 Numerical results and discussions

In this method, only the effective Wilson coefficients with relative strong phases are free parameters, which are chosen to obtain the suitable results consistent with experimental data. For PP modes,

$$\begin{aligned} a_1 &= 0.94 \pm 0.10, & a_2 &= (0.65 \pm 0.10)e^{i(142\pm10)^\circ}, \\ a_A &= (0.20 \pm 0.10)e^{i(300\pm10)^\circ}, & a_E &= (1.7 \pm 0.1)e^{i(90\pm10)^\circ}. \end{aligned} \tag{10}$$

For PV modes,

$$\begin{aligned} a_1^{PV} &= 1.32 \pm 0.10, & a_2^{PV} &= (0.75 \pm 0.10)e^{i(160\pm10)^\circ}, \\ a_A^{PV} &= (0.12 \pm 0.10)e^{i(345\pm10)^\circ}, & a_E^{PV} &= (0.62 \pm 0.10)e^{i(238\pm10)^\circ}. \end{aligned} \tag{11}$$

All the predictions of the 100 channels are shown in the tables of ref.[9]. The prediction of branching ratio of the pure annihilation process $D_s^+ \to \pi^+\pi^0$ vanishes in the pole model within the isospin symmetry. It is also zero in the diagrammatic approach in the flavor SU(3) symmetry. Simply, two pions can form an isospin 0,1,2 state, but 0 is ruled out because of charged final states, and isospin-2 is forbidden for the leading order $\Delta C = 1$ weak decay. The only left s-wave isospin-1 sate is forbidden by Bose-Einstein statics. In the pole model language, G parity is violated in the isospin-1 case. Therefore, no annihilation amplitude contributes to this mode.

The theoretical analysis in the $\eta - \eta'$ sector is kind of complicated. The predictions with η' in the final state are always smaller in this hybrid method than those case of η due to the smaller phase space. However, it is opposite by experiments in some modes, such as $D_s^+ \to \pi^+\eta(\eta')$,

$D^0 \to \bar{K}^0\eta(\eta')$. This may be the effects of SU(3) flavor symmetry breaking for η_q and η_s, the error mixing angle between η and η' [a], inelastic final state interaction, or the two gluon anomaly mostly associated to the η', etc.. The mode of $D_s^+ \to \rho^+\eta(\eta')$ is similar with the above two cases, the opposite ratio of η over η' between theoretical prediction and the data. But this is a puzzle by experiment measurement, which is taken more than ten years ago [11]. As is questioned by PDG [12], this branching ratio of $(12.5 \pm 2.2)\%$ considerably exceeds the recent inclusive η' fraction of $(11.7 \pm 1.8)\%$.

Recently, model independent diagrammatic approach is used to analyze the charm decays [13]. All two-body hadronic decays of D mesons can be expressed in terms of some distinct topological diagrams within the SU(3) flavor symmetry, by extracting the topological amplitudes from the data [14]. Since the recent measurements of $D_s^+ \to \pi^+\rho^0$ [15] and $D_s^+ \to \pi^+\omega$ [16] give a strong constraint on the $W-$annihilation amplitudes, one cannot find a nice fit for A_P and A_V in the diagrammatic approach to the data with $D_s^+ \to \bar{K}^{*0}K^+, \bar{K}^0K^{*+}$ simultaneously. Compared to the calculations in the model-independent diagrammatic approach [14], our hybrid method gives more predictions for the PV modes in which the predictions are consistent with the experimental data. It is questioned that the measurement of $Br(D_s^+ \to \bar{K}^0K^{*+}) = (5.4 \pm 1.2)\%$,[17] which was taken two decades ago, was overestimated. Since $|C_V| < |C_P|$ and $A_V \approx A_P$ as a consequence of very small rate of $D_s^+ \to \pi^+\rho^0$, it is expected that $Br(D_s^+ \to \bar{K}^0K^{*+}) < Br(D_s^+ \to \bar{K}^{*0}K^+) = (3.90 \pm 0.23)\%$. Our result in the hybrid method also agrees with this argument.

As an application of the diagrammatic approach, the mixing parameters $x = (m_1 - m_2)/\Gamma$ and $y = (\Gamma_1 - \Gamma_2)/\Gamma$ in the $D^0 - \bar{D}^0$ mixing are evaluated from the long distance contributions of the PP and VP modes [18]. The global fit and predictions in the diagrammatic approach are done in the SU(3) symmetry limit. However, as we know, the nonzero values of x and y come from the SU(3) breaking effect. Part of the flavor SU(3) breaking effects are considered in the factorization method and in the pole model. Therefore, our hybrid method takes its advantage in the analysis of $D^0 - \bar{D}^0$ mixing.

Acknowledgments

This work is partially supported by National Science Foundation of China under the Grant No. 10735080, 11075168; and National Basic Research Program of China (973) No. 2010CB833000.

References

1. Y. -Y. Keum, H. -n. Li, A. I. Sanda, Phys. Lett. **B504**, 6-14 (2001) [hep-ph/0004004];
   Y. Y. Keum, H. -N. Li, A. I. Sanda, Phys. Rev. **D63**, 054008 (2001) [hep-ph/0004173];
   C. -D. Lu, K. Ukai, M. -Z. Yang, Phys. Rev. **D63**, 074009 (2001) [hep-ph/0004213];
   C. -D. Lu, M. -Z. Yang, Eur. Phys. J. **C23**, 275-287 (2002) [hep-ph/0011238].
2. M. Beneke, G. Buchalla, M. Neubert, C. T. Sachrajda, Phys. Rev. Lett. **83**, 1914-1917 (1999) [hep-ph/9905312];
   M. Beneke, G. Buchalla, M. Neubert, C. T. Sachrajda, Nucl. Phys. **B591**, 313-418 (2000) [hep-ph/0006124].
3. C. W. Bauer, D. Pirjol, I. W. Stewart, Phys. Rev. Lett. **87**, 201806 (2001) [hep-ph/0107002];
   C. W. Bauer, D. Pirjol, I. W. Stewart, Phys. Rev. **D65**, 054022 (2002) [hep-ph/0109045].
4. M. Wirbel, B. Stech, M. Bauer, Z. Phys. **C29**, 637 (1985);
   M. Bauer, B. Stech, M. Wirbel, Z. Phys. **C34**, 103 (1987).
5. H. -Y. Cheng, Phys. Lett. **B335**, 428-435 (1994) [hep-ph/9406262];
   H. -Y. Cheng, Z. Phys. **C69**, 647-654 (1996) [hep-ph/9503219].

[a] The theoretical and phenomenological estimates for the mixing angle ϕ is 42.2° and $(39.3 \pm 1.0)^\circ$, respectively.[10]

6. J. J. Sakurai, Phys. Rev. 156, 1508 (1967).
7. A. K. Das, V. S. Mathur, Mod. Phys. Lett. **A8**, 2079-2086 (1993) [hep-ph/9301279]; P. F. Bedaque, A. K. Das, V. S. Mathur, Phys. Rev. **D49**, 269-274 (1994) [hep-ph/9307296];
8. G. Kramer, C. -D. Lu, Int. J. Mod. Phys. **A13**, 3361-3384 (1998) [hep-ph/9707304].
9. Y. Fusheng, X. -X. Wang, C. -D. Lu, [arXiv:1101.4714].
10. T. Feldmann, P. Kroll, B. Stech, Phys. Rev. **D58**, 114006 (1998). [hep-ph/9802409].
11. C. P. Jessop *et al.* [CLEO Collaboration], Phys. Rev. **D58**, 052002 (1998) [hep-ex/9801010].
12. K. Nakamura *et al.* [Particle Data Group Collaboration], J. Phys. G **G37**, 075021 (2010).
13. J. L. Rosner, Phys. Rev. **D60**, 114026 (1999) [hep-ph/9905366].
14. H. -Y. Cheng, C. -W. Chiang, Phys. Rev. **D81**, 074021 (2010) [arXiv:1001.0987 [hep-ph]].
15. B. Aubert *et al.* [BABAR Collaboration], Phys. Rev. **D79**, 032003 (2009), arXiv:0808.0971 [hep-ex].
16. J. Y. Ge *et al.* [CLEO Collaboration], Phys. Rev. **D80**, 051102 (2009). [arXiv:0906.2138 [hep-ex]].
17. W. Y. Chen *et al.* [CLEO Collaboration], Phys. Lett. **B226**, 192 (1989).
18. H. Y. Cheng and C. W. Chiang, Phys. Rev. D **81** (2010) 114020 arXiv:1005.1106 [hep-ph].

EXOTIC/CHARMONIUM HADRON SPECTROSCOPY AT BELLE AND BABAR

DMITRI LIVENTSEV
Institute for Theoretical and Experimental Physics,
B. Cheremushkinskaya 25, 117218 Moscow, Russia

A brief review of experimental results on charmonium and charmonium-like hadron spectroscopy at B-factories is presented. A special focus is put on recent results of η_c and $\eta_c(2S)$ study, $X(3872)$ radiative decays, $\omega J/\psi$ final state study and search for charmonium production in radiative Υ decays.

1 Conventional and "exotic" charmonium states

The first charmonium state J/ψ was discovered in 1974 [1]. Then in six years nine more $(c\bar{c})$ states were observed. No new states were found during next 22 years, until in 2002 Belle reported the detection of $\eta_c(2S)$ [2]. In 2003 Belle discovered $X(3872)$ [3], which marked the beginning of "exotic", or unconventional charmonium-like states era. Such states decay in ways, peculiar to usual charmonium, but have masses, widths, quantum numbers and decay ratios, which can hardly be explained by the classical quark-parton model. Since then two conventional and more than dozen "exotic" charmonium states were reported. Comprehensive review of their characteristics, possible explanations etc can be found in [4]. In this paper we report some recent experimental results on this topic from B-factories.

2 η_c and $\eta_c(2S)$

Although η_c and $\eta_c(2S)$ have been around for some time and studied by different experiments, there is still large spread in their mass and width measurements [5]. Moreover, our knowledge of hadronic decays of these charmonia is rather poor. Both Belle and BaBar performed recently new measurements of η_c and $\eta_c(2S)$ characteristics.

BaBar claimed that $\gamma\gamma \to \eta_c \to K_S K^{\pm}\pi^{\mp}$ is the "right place" for such study since Breit-Wigner line shape is appropriate approximation here [6]. With data set of $469\,\mathrm{fb}^{-1}$ mass and width of η_c were measured relative to J/ψ. In the same paper transition form factor in $\gamma\gamma \to \eta_c$ decay was measured and nice agreement with pQCD was observed. BaBar also reported mass and width measurement of $\eta_c(2S)$ in the same production process [7].

Belle took another approach. They studied $B^{\pm} \to K^{\pm}\eta_c(\eta_c(2S))$, $\eta_c(\eta_c(2S)) \to (K_S K\pi)^0$ decay chain and consistently took into account interference between decay under study and nonresonant decay into the same final state [8]. Results, obtained with and without interference are quite different, which means that taking it into account is important.

Until recently only one decay mode of $\eta_c(2S)$ was known, $\eta_c(2S) \to (K_S K\pi)^0$. Decays to 4-prong final state have not been observed [9]. Belle with $923\,\mathrm{fb}^{-1}$studied decays to 6-prong final

states: 6π, $2K4\pi$, $4K2\pi$, $K_SK3\pi$ [10]. $\eta_c(2S)$, as well as χ_{c0} and χ_{c2}, were clearly seen in 6π, $2K4\pi$, and $K_SK3\pi$ distributions. BaBar looked at $K^+K^-\pi^+\pi^-\pi^0$ invariant mass spectrum from $\gamma\gamma$ process and found $\eta_c(2S)$ signal, as well as η_c, χ_{c0} and χ_{c2} [7].

3 $X(3872)$ radiative decays

The $X(3872)$ was discovered by Belle as a narrow peak in $J/\psi\pi^+\pi^-$ invariant mass from $B^\pm \to J/\psi\pi^+\pi^-K^\pm$ decays [3]. It was confirmed by CDF [11], D0 [12] and BaBar [13]. Among newly observed "exotic" charmonium-like states $X(3872)$ is the most studied one. It has very small width $\Gamma < 2.3\,\text{GeV}$ at 90% CL for a state above open charm threshold. Its mass is very close to D^0D^{*0} threshold, $M(X(3872)) - (m_{D^0} + m_{D^{*0}}) = -0.32 \pm 0.35\,\text{GeV}$. In decays to $J/\psi\pi^+\pi^-$ invariant mass of $\pi\pi$ pair is consistent with originating from $\rho \to \pi^+\pi^-$, indicating $C = +1$ parity of $X(3872)$. Since all charmonia are isospin singlets, decays to $J/\psi\rho$ violate isospin and should be strongly suppressed. CDF studied angular distributions in $X(3872) \to J/\psi\pi^+\pi^-$ decay and concluded that possible J^{PC} assignments for $X(3872)$ are 1^{++} and 2^{-+} [14].

There are several unoccupied charmonium levels with appropriate quantum numbers but their predicted masses are either too high (χ'_{c1}, $J^{PC} = 1^{++}$) or too low (η_{c2}, $J^{PC} = 2^{-+}$). The whole set of $X(3872)$ characteristics also makes it hard to describe $X(3872)$ as a conventional charmonium. Proximity of $X(3872)$ mass to D^0D^{*0} threshold led to a suggestion, that it may be a molecule-like D^0D^{*0} bound state [15].

Weighty argument in distinguishing between different possibilities are radiative decays $X(3872) \to \gamma\psi'$ and $X(3872) \to \gamma J/\psi$. If $X(3872)$ is a charmonium state χ'_{c1}, partial with of $X(3872) \to \gamma\psi'$ decay should be larger than that of $X(3872) \to \gamma J/\psi$ by more than factor of ten [16]. In case of molecular state or η_{c2} the situation is reversed and $\gamma J/\psi$ mode is favoured [17,18].

The first evidence for $X(3872) \to \gamma J/\psi$ by Belle was based on $256\,\text{fb}^{-1}$ with 13.6 ± 4.4 events [19] and was confirmed by BaBar on $424\,\text{fb}^{-1}$ with 23.0 ± 6.4 events [20]. Observation of this channel confirmed even parity of $X(3872)$. In 2009 BaBar reported evidence of $X(3872) \to \gamma\psi'$ based on $424\,\text{fb}^{-1}$ with 25.4 ± 7.4 signal events ($3.6\,\sigma$) [21] (see Fig. 1, (a)). The signal yield implied $\mathcal{B}(X(3872) \to \gamma\psi')/\mathcal{B}(X(3872) \to \gamma J/\psi) = 3.4 \pm 1.4$. However in 2010 Belle based on a larger sample $711\,\text{fb}^{-1}$ found no evidence for $X(3872) \to \gamma\psi'$ (see Fig. 1, (b), (c)), while $\gamma J/\psi$ mode was observed at a rate that agrees with BaBar [22]. Belle set a 90% CL upper limit on the $\gamma\psi'/\gamma J/\psi$ ratio of < 2.0.

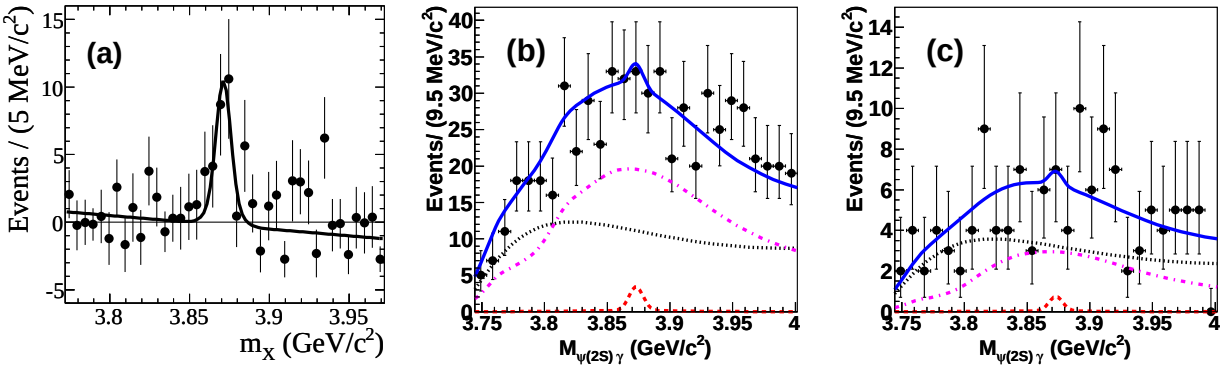

Figure 1: The $\gamma\psi'$ invariant mass distribution for (a) $B^+ \to \gamma\psi'K^+$ from BaBar, obtained by fit in bins, (b) $B^+ \to \gamma\psi'K^+$ and (c) $B^0 \to \gamma\psi'K^0$ from Belle.

4 Study of $\omega J/\psi$ final state

Three states with masses close to 3940 MeV were found: $X(3940)$ [23], $Y(3940)$ [24] and $Z(3930)$ [25], the latter usually identified with χ'_{c2}. These three states are considered to be distinct particles, though there is no decisive evidence for this. $Y(3940)$ mass is well above DD and DD^* thresholds, but the partial width of decay to hidden charm is unexpectedly large: $\mathcal{B}(Y \to \omega J/\psi)/\mathcal{B}(Y \to D^0 D^{*0}) > 0.71$ [26].

Belle studied untagged two-photon process $\gamma\gamma \to \omega J/\psi$ with 694 fb^{-1} of data, collected at $\Upsilon(4S)$, $\Upsilon(3S)$ and $\Upsilon(5S)$ resonances. A state with $M = 3915 \pm 4$ MeV and $\Gamma = 17 \pm 11$ MeV was found [27], compatible with $Y(3940)$. If it is so, it narrows its quantum numbers J^{PC} to $0^{\pm+}$ or $2^{\pm+}$. Measured partial width $\Gamma_{\gamma\gamma}\mathcal{B}(Y \to \omega J/\psi) = 61 \pm 19$ eV (for 0^{++}). If $\Gamma_{\gamma\gamma} \sim \mathcal{O}(1\,\text{keV})$, a typical value for charmonium, then $\Gamma(Y \to \omega J/\psi) \sim \mathcal{O}(1\,\text{MeV})$, which is very large for a hadronic inter-charmonium transition.

Though mass of $X(3872)$ is too small for decay to $\omega J/\psi$, in some models it may decay to low-mass tail of the ω and J/ψ with a rate, comparable to decay $X(3872) \to \pi\pi J/\psi$ [18]. In 2005 Belle reported an evidence for subthreshold decay $X(3872) \to \omega J/\psi$, consistent with the prediction [19]. In 2008 BaBar studied B-decay $B^+ \to \pi\pi\pi^0 J/\psi K^+$ and in mass distribution of $\pi\pi\pi^0 J/\psi$ observed $Y(3940)$, but did not find $X(3872)$ [28]. In 2010 BaBar remade this analysis with 433 fb^{-1} and lower requirement on $\pi\pi\pi^0$ invariant mass loosened from 0.7695 GeV to 0.7400 GeV. Both $Y(3940)$ and $X(3872)$ were observed with masses and widths, consistent with previous measurements. BaBar also investigated the shape of $\pi\pi\pi^0$ invariant mass distribution for selected $X(3872) \to \omega J/\psi$ events. They found that it favours P-wave description by $1.5\,\sigma$ ($\chi^2/\text{NDF} = 10.17/5$ for S-wave, $\chi^2/\text{NDF} = 3.53/5$ for P-wave), which indicates $J^P = 2^-$ for $X(3872)$, which thus may be interpreted as η'_{c2} charmonium state. However, possible interference between different decays, contributing to $\pi\pi\pi^0 J/\psi$ final state, was not taken into account, and explanation of significant rate of $X(3872) \to D\bar{D}\pi$ would be a challenge for η'_{c2} [29].

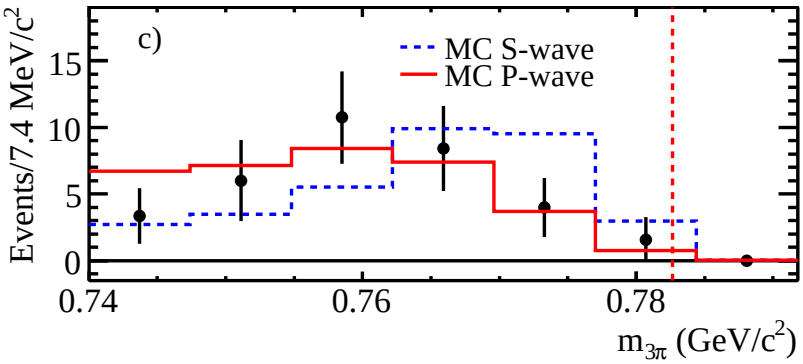

Figure 2: The $\pi^+\pi^-\pi^0$ invariant mass distribution for $X(3872) \to \pi^+\pi^-\pi^0 J/\psi$ decays from BaBar.

5 Search for charmonium production in radiative Υ decays

Belle used its extensive data set, collected at $\Upsilon(1S)$ resonance, to investigate $b\bar{b} \to c\bar{c}\gamma$ transitions [30]. Calculation predicts $\sim 10^{-6}$ decay rates for lowest lying P-wave spin-triplet (χ_{cJ}, $J = 0, 1, 2$) and $\sim 5 \times 10^{-5}$ for S-wave spin-singlet state η_c [31]. No prediction exists for allowed excited or "exotic" states, like $X(3872)$. The photon detection required $E_\gamma^{lab} > 3.5$ GeV, which corresponded to 4.8 GeV mass of a particle, produced in $\Upsilon(1S)$ radiative decay. Initial state radiation (ISR) was removed by requirement on photon polar angle. ISR production of ψ' in $\pi^+\pi^- J/\psi$ channel was used as a cross-check, and the cross section for this process was determined as 20.2 ± 1.1 pb, in agreement with theoretical calculation. One event was observed in the signal

region of $X(3872)$, which corresponds to upper limit $\mathcal{B}(\Upsilon(1S) \to \gamma X(3872)) \times \mathcal{B}(X(3872) \to \pi^+\pi^- J/\psi) < 2.2 \times 10^{-6}$ at 90% CL. Furthemore, no evidence for excited charmonium states below 4.8 GeV was found.

Acknowledgments

We thank the KEKB group for excellent operation of the accelerator, the KEK cryogenics group for efficient solenoid operations, and the KEK computer group and the NII for valuable computing and SINET4 network support. We acknowledge support from MEXT, JSPS and Nagoya's TLPRC (Japan); ARC and DIISR (Australia); NSFC (China); MSMT (Czechia); DST (India); MEST, NRF, NSDC of KISTI, and WCU (Korea); MNiSW (Poland); MES and RFAAE (Russia); ARRS (Slovenia); SNSF (Switzerland); NSC and MOE (Taiwan); and DOE (USA).

This work was done with partial support of Russian Federation President grant MK-450.2010.2.

References

1. J. Aubert *et al.*, Phys. Rev. Lett. **33**, 1402 (1974); J.E. Augustin *et al.*, Phys. Rev. Lett. **33**, 1406 (1974).
2. S.-K. Choi *et al.* (Belle collaboration), Phys. Rev. Lett. **89**, 102001 (2002).
3. S.-K. Choi *et al.* (Belle collaboration), Phys. Rev. Lett. **91**, 262001 (2003).
4. N. Brambilla *et al.*, Eur. Phys. J. C**71**, 1534 (2011).
5. K. Nakamura *et al.* (Particle Data Group), J. Phys. G**37**, 1 (2010).
6. P. Lees *et al.* (BaBar collaboration), Phys. Rev. D**81**, 052010 (2010).
7. V. Druzhinin, talk at ICHEP 2010.
8. A. Vinokurova *et al.* (Belle collaboration), arXiv: 1105.0978 [hep-ex].
9. S. Uehara *et al.* (Belle collaboration), Eur. Phys. J. C**53**, 1 (2008).
10. H. Nakazawa, talk at ICHEP 2010.
11. D. Acosta *et al.* (CDF collaboration), Phys. Rev. Lett. **93**, 072001 (2004).
12. V.M. Abazov *et al.* (D0 collaboration), Phys. Rev. Lett. **93**, 162002 (2004).
13. B. Aubert *et al.* (BaBar collaboration), Phys. Rev. D**71**, 071103 (2005).
14. A. Abulencia *et al.* (CDF collaboration), Phys. Rev. Lett. **98**, 132002 (2007).
15. E.S. Swanson, Phys. Lett. B**588**, 189 (2004).
16. T. Barnes, S. Godfrey and E.S. Swanson, Phys. Rev. D**72**, 054026 (2005).
17. Y.Jia, W.-L. Sang and J.Xu, arXiv: 1007.4541 [hep-ph].
18. E.S. Swanson, Phys. Lett. B**598**, 197 (2004).
19. K. Abe *et al.* (Belle Collaboration), hep-ex/0505037.
20. B. Aubert *et al.* (BaBar collaboration), Phys. Rev. D**74**, 071101 (2006).
21. B. Aubert *et al.* (BaBar collaboration), Phys. Rev. Lett. **102**, 132001 (2009).
22. V. Bhardwaj *et al.* (Belle Collaboration), arXiv:1105.0177 [hep-ex].
23. K. Abe *et al.* (Belle Collaboration), Phys. Rev. Lett. **98**, 082001 (2007).
24. S.-K. Choi *et al.* (Belle Collaboration), Phys. Rev. Lett. **94**, 182002 (2005).
25. S. Uehara *et al.* (Belle Collaboration), Phys. Rev. Lett. **96**, 082003 (2006).
26. T. Aushev *et al.* (Belle collaboration), Phys. Rev. D**81**, 031103 (2010).
27. S. Uehara *et al.* (Belle Collaboration), Phys. Rev. Lett. **104**, 092001 (2010).
28. B. Aubert *et al.* (BaBar collaboration), Phys. Rev. Lett. **101**, 082001 (2008).
29. Yu.S. Kalashnikova, A.V. Nefediev, Phys. Rev. D**82** 097502 (2010).
30. C.P. Shen *et al.* (Belle collaboration), Phys. Rev. D**82**, 051504 (2010).
31. Y.-J. Gao, Y.-J. Zhang, K.-T. Chao, hep-ph/0701009.

Recent Results on Charmonium from BESIII

M. MAGGIORA (on behalf of the BESIII collaboration)
Department of General Physics "A. Avogadro", University of Turin,
Via Pietro Giuria 1, 10136 Torin, Italy

We report the latest outcomes for the Charmonium system investigation on 226×10^6 J/ψ and 106×10^6 ψ' events collected with the BESIII detector at the BEPCII e^+e^- collider.

1 Introduction

Both BESIII and BEPCII represent a significant upgrade with respect to the BESII/BEPC experimental scenario. The spectrometer and the physics program, primarily aimed to investigate hadron spectroscopy and τ-charm physics, are described elsewhere [1,2]. The unprecedented BEPCII luminosities and the high BESIII performance allowed to collect data samples at J/ψ and ψ' energies already significantly larger w.r.t those available in the literature; the analyses reported herewith have been performed on 226×10^6 J/ψ and 106×10^6 ψ' events.

2 $\psi' \to \pi^0 h_c$

Clear signals have been observed (Fig. 1) for $\psi' \to \pi^0 h_c$ with and without the subsequent radiative decay $h_c \to \gamma\eta_c$. The determination [3] in the same experimental scenario of both $\mathcal{B}(\psi' \to \pi^0 h_c) = (8.4 \pm 1.3 \pm 1.0) \times 10^{-4}$ and $\mathcal{B}(\psi' \to \pi^0 h_c) \times \mathcal{B}(h_c \to \gamma\eta_c) = (4.58 \pm 0.40 \pm 0.50) \times 10^{-4}$ allows to access $\mathcal{B}(h_c \to \gamma\eta_c) = (54.3 \pm 6.7 \pm 5.2)\%$. $M(h_c) = 3525.40 \pm 0.13 \pm 0.18$ MeV/c^2 and $\Gamma(h_c) = 0.73 \pm 0.45 \pm 0.28$ MeV (< 1.44 MeV at 90% C.L.) have been determined as well.

Our measurements for $\mathcal{B}(\psi' \to \pi^0 h_c)$, $\mathcal{B}(h_c \to \gamma\eta_c)$ and $\Gamma(h_c)$ are the first experimental results for these quantities; the values obtained for $M(h_c)$ and $\mathcal{B}(\psi' \to \pi^0 h_c) \times \mathcal{B}(h_c \to \gamma\eta_c)$ are consistent with previous CLEO results [4] and of comparable precision. The measured $1P$ hyperfine mass splitting $\Delta\ M_{hf} \equiv \langle M(^3P) \rangle - M(^1P_1) = -0.10 \pm 0.13 \pm 0.18$ MeV/c^2 is consistent with no strong spin-spin interaction. For a detailed discussion of such results in the framework of the existing experimental evidences and theoretical predictions see [3].

3 $\psi' \to \gamma\chi_{cJ}$; $\chi_{c0,2} \to \pi^0\pi^0, \eta\eta$ $\quad (\eta, \pi^0 \to \gamma\gamma)$

We have investigated the decays of the χ_{c0} and χ_{c2} states into the pseudo-scalar pairs $\pi^0\pi^0$ and $\eta\eta$, the corresponding χ_{c1} decays being forbidden by parity conservation. Significantly clear signals (Fig. 2.a-b) lead to the branching fractions: $\mathcal{B}(\chi_{c0} \to \pi^0\pi^0) = (3.23 \pm 0.03 \pm 0.23 \pm 0.14) \times 10^{-3}$, $\mathcal{B}(\chi_{c2} \to \pi^0\pi^0) = (8.8 \pm 0.2 \pm 0.6 \pm 0.4) \times 10^{-4}$, $\mathcal{B}(\chi_{c0} \to \eta\eta) = (3.44 \pm 0.10 \pm 0.24 \pm 0.2) \times 10^{-3}$ and $\mathcal{B}(\chi_{c2} \to \eta\eta) = (6.5 \pm 0.4 \pm 0.5 \pm 0.3) \times 10^{-4}$, where the uncertainties are statistical,

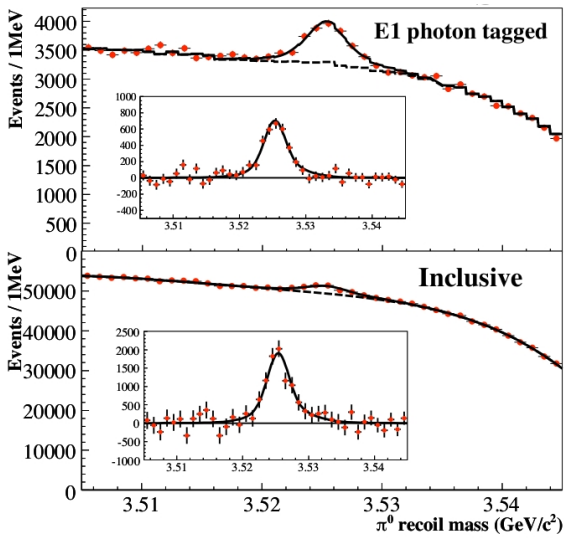

Figure 1: The π^0 recoil mass spectra and fits for: (top) the $E1$-tagged analysis: $\psi' \to \pi^0 h_c, h_c \to \gamma\eta_c$; (bottom) the inclusive analysis: $\psi' \to \pi^0 h_c$. Fits are shown as solid lines, background as dashed lines; insets show the background-subtracted spectra.

systematic due to this measurement, and systematic due to the branching fractions of $\psi' \to \gamma\chi_{cJ}$, respectively. For a full description of this analysis see [5].

4 $\psi' \to \gamma\chi_{cJ}$; $\chi_{cJ} \to \pi^0\pi^0\pi^0\pi^0$ $(\pi^0 \to \gamma\gamma)$

The branching fractions of the P-wave spin-triplet Charmonium χ_{cJ} decays into $\pi^0\pi^0\pi^0\pi^0$ have been determined for the first time: $B(\chi_{c0} \to \pi^0\pi^0\pi^0\pi^0) = (3.34 \pm 0.06 \pm 0.44) \times 10^{-3}$, $B(\chi_{c1} \to \pi^0\pi^0\pi^0\pi^0) = (0.57 \pm 0.03 \pm 0.08) \times 10^{-3}$ and $B(\chi_{c2} \to \pi^0\pi^0\pi^0\pi^0) = (1.21 \pm 0.05 \pm 0.16) \times 10^{-3}$, where the uncertainties are statistical and systematic, respectively; these fractions include decay modes with intermediate resonances except $\chi_{c0} \to K^0_S K^0_S$ and $\chi_{c2} \to K^0_S K^0_S$, which have been removed from this measurement. The contributions from the different states ($J = 0, 1, 2$) are clearly visible in Fig. 2.c; a complete description of the this analysis can be found in [6].

5 $\chi_{cJ} \to \gamma V,\ V = \phi, \rho^0, \omega$; $\phi \to K^+K^-,\ \rho^0 \to \pi^+\pi^-,\ \omega \to \pi^+\pi^-\pi^0$ $(\pi^0 \to \gamma\gamma)$

The sample of radiative $\psi' \to \gamma\chi_{cJ}$ events (top frames in Fig. 3) allowed to determine $\mathcal{B}(\chi_{c1} \to \gamma\rho^0) = (228 \pm 13 \pm 22) \times 10^{-6}$ and $\mathcal{B}(\chi_{c1} \to \gamma\omega) = (69.7 \pm 7.2 \pm 6.6) \times 10^{-6}$, in good agreement

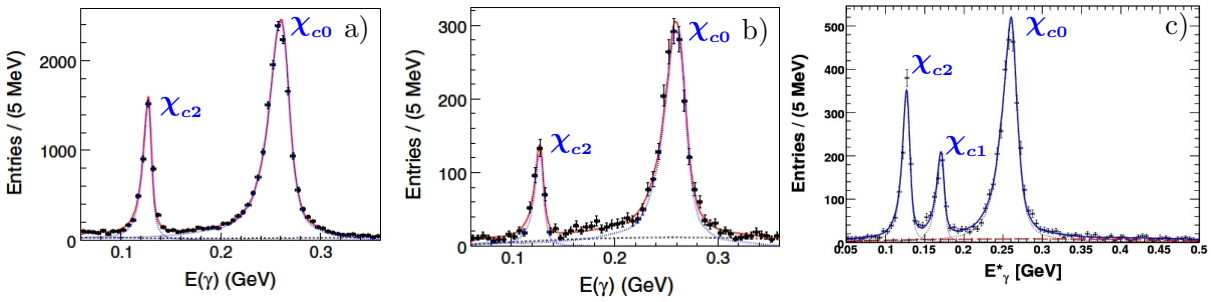

Figure 2: The radiative photon energy spectrum of: a) selected $\chi_{c0,2} \to \pi^0\pi^0$ events; b) selected $\chi_{c0,2} \to \eta\eta$ events; c) those $\chi_{cJ} \to \pi^0\pi^0\pi^0\pi^0$ events surviving the selection performed with the fit described in [6] . Fits (solid curves) include χ_{cJ} signals (dotted curves) and background polynomials (dashed curves).

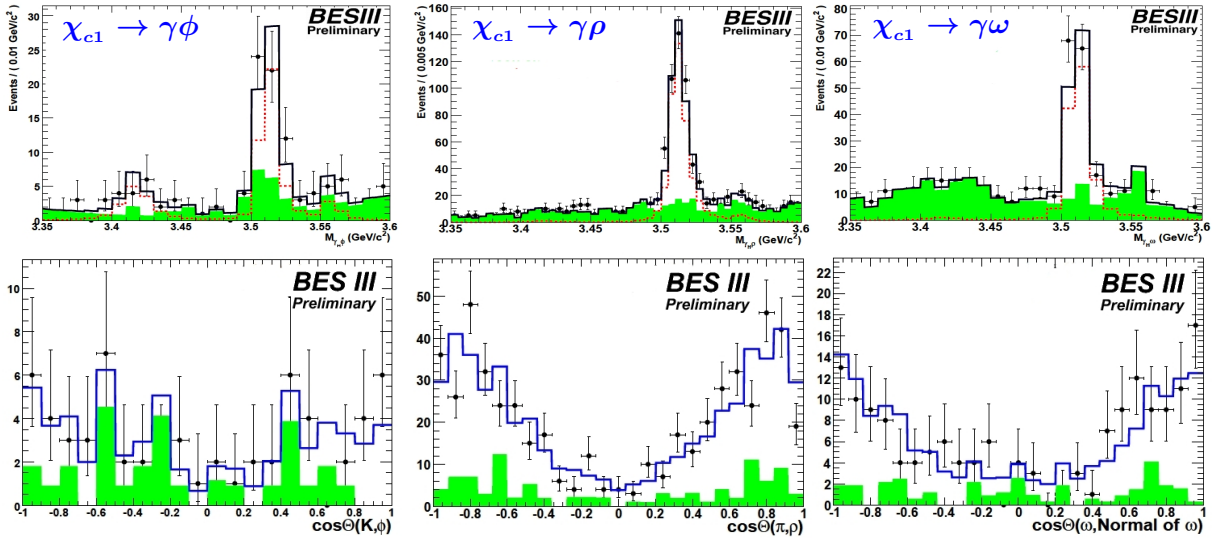

Figure 3: $\chi_{c1} \to \gamma V$. Top: invariant mass distributions of (left) K^+K^-, (center) $\pi^+\pi^-$, and (right) $\pi^+\pi^-\pi^0$; bottom: corresponding $\cos\Theta$ distributions (see text). Histograms: best fits; dashed histograms: signal shapes; grey-shaded histograms: sum of the sideband background and the background polynomial (see [8]).

with earlier CLEO measurements[7], and $\mathcal{B}(\chi_{c1} \to \gamma\phi) = (25.8 \pm 5.2 \pm 2.3) \times 10^{-6}$, observed for the first time; errors are statistical and systematic respectively. Upper limits at the 90% confidence level on the branching fractions for χ_{c0} and χ_{c2} decays into these final states are determined as well. The angular dependences (bottom frames of Fig. 3) on $\cos\Theta$, Θ being the angle between the vector meson flight direction in the χ_{c1} rest frame and either the π^+/K^+ direction in the ρ^0/ϕ rest frame or the normal to the ω decay plane in the ω rest frame, allow to determine the fractions of the transverse polarization component of the vector meson in $\chi_{c1} \to \gamma V$ decays: $0.29^{+0.13+0.10}_{-0.12-0.09}$ for $\chi_{c1} \to \gamma\phi$, $0.158 \pm 0.034^{+0.015}_{-0.014}$ for $\chi_{c1} \to \gamma\rho^0$, and $0.247^{+0.090+0.044}_{-0.087-0.026}$ for $\chi_{c1} \to \gamma\omega$.

The present picture suggests that the longitudinal component is dominant in $\chi_{c1} \to \gamma V$ decays; for a complete description of this analysis see [8].

6 $\chi_{cJ} \to VV,\ V = \phi, \omega\ ;\ \phi \to K^+K^-,\ \omega \to \pi^+\pi^-\pi^0\ \ (\pi^0 \to \gamma\gamma)$

The clear signals of Fig. 4 allow to investigate the χ_{cJ} decays into vector meson pairs ($\phi\phi$, $\phi\omega$, $\omega\omega$). The first observations of the χ_{c1} branching fractions $\mathcal{B}(\chi_{c1} \to \phi\phi) = (4.4 \pm 0.3 \pm 0.5) \times 10^{-4}$ and $\mathcal{B}(\chi_{c1} \to \omega\omega) = (6.0 \pm 0.3 \pm 0.7) \times 10^{-4}$ indicate that the helicity selection rule is significantly violated in these modes. The measured branching fractions $\mathcal{B}(\chi_{c0} \to \phi\phi) = (8.0 \pm 0.3 \pm 0.8) \times 10^{-4}$, $\mathcal{B}(\chi_{c0} \to \omega\omega) = (9.5 \pm 0.3 \pm 1.1) \times 10^{-4}$, $\mathcal{B}(\chi_{c2} \to \phi\phi) = (10.7 \pm 0.3 \pm 1.2) \times 10^{-4}$ and $\mathcal{B}(\chi_{c2} \to \omega\omega) = (8.9 \pm 0.3 \pm 1.1) \times 10^{-4}$ are consistent with and more precise than the previously published values [9]. The doubly OZI suppressed decays $\mathcal{B}(\chi_{c0} \to \phi\omega) = (1.2 \pm 0.1 \pm 0.2) \times 10^{-4}$

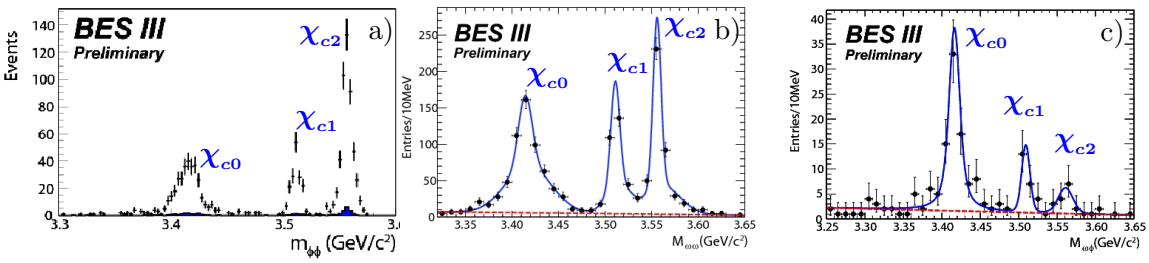

Figure 4: Invariant mass of a) $\phi\phi$, b) $\omega\omega$ and c) $\phi\omega$. Curves: best fit results; long dash lines: fitted sideband.

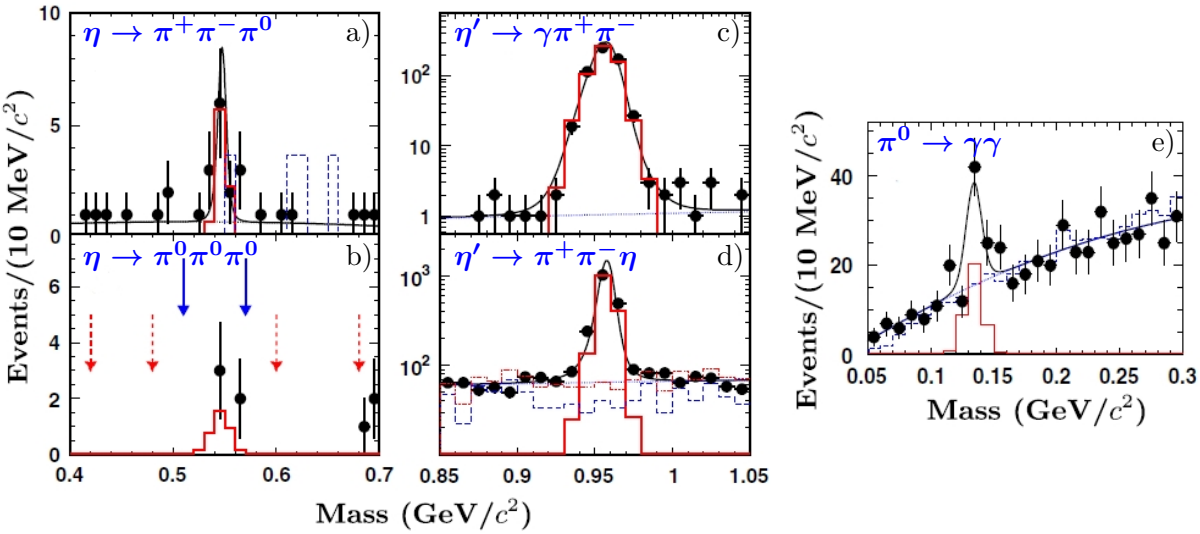

Figure 5: Mass distributions of the pseudo-scalar meson candidates for $\psi' \to \gamma P$: $\gamma\eta$ [a): $\eta \to \pi^+\pi^-\pi^0$; b): $\eta \to \pi^0\pi^0\pi^0$], $\gamma\eta'$ [c): $\eta' \to \gamma\pi^+\pi^-$; d): $\eta' \to \pi^+\pi^-\eta$, $\eta \to \gamma\gamma$], $\gamma\pi^0$ [e): $\pi^0 \to \gamma\gamma$]. For more details see [12].

and $\mathcal{B}(\chi_{c1} \to \phi\omega) = (2.2 \pm 0.6 \pm 0.2) \times 10^{-5}$ are also observed for the first time. This analysis is described in details in [10].

7 $\psi' \to \gamma P$, $P = \pi^0, \eta, \eta'$; $\eta \to \pi^+\pi^-\pi^0$, $\eta \to 3\pi^0$, $\eta' \to \gamma\pi^+\pi^-$, $\eta' \to \pi^+\pi^-\eta$ $(\eta, \pi^0 \to \gamma\gamma)$

The processes $\psi' \to \gamma\pi^0$ and $\psi' \to \gamma\eta$ are observed for the first time with signal significances of 4.6σ and 4.3σ (Fig. 5), and branching fractions $\mathcal{B}(\psi' \to \gamma\pi^0) = (1.58 \pm 0.40 \pm 0.13) \times 10^{-6}$ and $\mathcal{B}(\psi' \to \gamma\eta) = (1.38 \pm 0.48 \pm 0.09) \times 10^{-6}$, respectively; the first errors are statistical and the second ones systematic. The branching fraction $\mathcal{B}(\psi' \to \gamma\eta') = (126 \pm 3 \pm 8) \times 10^{-6}$ is measured as well, leading for the first time to the determination of the ratio of the η and η' production rates from ψ' decays, $R_{\psi'} = \mathcal{B}(\psi' \to \gamma\eta)/\mathcal{B}(\psi' \to \gamma\eta') = (1.10 \pm 0.38 \pm 0.07)\%$; such ratio is below the 90% C.L. upper bound determined by the CLEO Collaboration [11] and one order of magnitude smaller w.r.t the corresponding $\eta - \eta'$ production ratio for the J/ψ decays, $R_{J/\psi} = (21.1 \pm 0.9)\%$ [11]. For a detailed description of this analysis see [12].

References

1. D. M. Asner *et al.* arXiv:0809.1869 [hep-ex].
2. M. Ablikim *et al.* Nucl. Instrum. Meth. A **614** (2010) 345 [arXiv:0911.4960 [phys.ins-det]].
3. M. Ablikim *et al.* Phys. Rev. Lett. **104** (2010) 132002 [arXiv:1002.0501 [hep-ex]].
4. S. Dobbs *et al.* Phys. Rev. Lett. **101** (2008) 182003 [arXiv:0805.4599 [hep-ex]].
5. M. Ablikim *et al.* Phys. Rev. D **81** (2010) 052005 [arXiv:1001.5360 [hep-ex]].
6. M. Ablikim *et al.* Phys. Rev. D **83** (2011) 012006 [arXiv:1011.6556 [hep-ex]].
7. J. V. Bennett *et al.* Phys. Rev. Lett. **101** (2008) 151801 [arXiv:0807.3718 [hep-ex]].
8. M. Ablikim *et al.* arXiv:1103.5564 [hep-ex].
9. K. Nakamura *et al.* J. Phys. G **37** (2010) 075021.
10. M. Ablikim *et al.* arXiv:1104.5068 [hep-ex].
11. T. K. Pedlar *et al.* Phys. Rev. D **79**, 111101 (2009) [arXiv:0904.1394 [hep-ex]].
12. M. Ablikim *et al.* Phys. Rev. Lett. **105** (2010) 261801 [arXiv:1011.0885 [hep-ex]].

Unitarity of exclusive quark combination model: Exotic hadron production, entropy change and charmonium production for colour-singlet many-quark system

LI Shi-Yuan
School of Physics, Shandong University, Jinan, 250100, P. R. China

Confinement indicates an asymptotic quark state not observable except its energy is zero. Unitarity indicates that the total probability of a definite state of quark system to transit to any final state is exactly one. This talk reviews some important conclusions/predictions from the basic properties like unitarity of the combination model, as addressed by the title.

I. Introduction: Unitarity of exclusive quark combination model

Quark Combination Model (QCM) was proposed in early seventies of 20th century (Anisovich, Bjorken) to describe the multi-production process in high energy collisions, based on the constituent quark model of hadrons. Various versions of QCM have succeeded in explaining many data. Recently in central gold-gold collisions at the Relativistic Heavy Ion Collider (RHIC), several 'unexpected' phenomena which lay difficulties for other hadronization mechanisms can be easily understood in quark combination mechanism. Common of all the hadronization models, QCM responds to describe the non-perturbative QCD phase. It includes two steps: 1) the 'partons' in various collisions turn into constituent quarks; 2) these quarks combined into hadrons according to certain rules. One can regard the combination model as a 'reverse employment' of the constituent quark model. In the following of this paper we concentrate on step 2, the combination process, which is the 'realization' of confinement for the constituent quarks. We will investigate the most general principles which a QCM has to respect, so that to see what can be reliablly *predicted* by such a model, rather than seek how to employ a certain version of QCM to make a good postdiction and parameterization of the data. For this purpose, we deal with a colour-singlet (CS) system of many quarks prepared from step 1, but without addressing how the hard partons turned into constituent quarks, especially, 'where is the gluon'? (Prof. Dixon asked after this presentation) in step 1. Charm and bottom quarks are produced form hard interactions. They in step 1 are 'dressed' to be a constituent but their momentum spectra are not largely modified. This special advantage will be discussed in the following.

Without digging into details of any special kind of QCM, one easily figures out two principles which it must respect: First of all, energy-momentum conservation is the principle law of physics, reflecting the basic symmetry space-time displacement invariance. The models must precisely (as precisely as possible, in practice) transfer the energy and momentum of the parton system into the constituent quark system and then the hadron system. Second, when applying the combination rules on a CS separated system of constituent quarks, it is necessary that all the quarks are combined into hadrons, or else there are free quarks with non-zero mass and energy, which obviously contradicts to any observations that suggest confinement. Moreover, these free quarks take away energy and momentum, hence make danger of the energy-momentum

conservation. This second principle is referred as Unitarity of the relevant model. These two principles are closely connected, with the first one the natural result of the second one.

For a QCM which respects and can reflect unitarity, the combination process can be described by a unitary time-evolution operator U , with

$$\sum_h | < h|U|q > |^2 =< q|U^+U|q >= 1. \tag{1}$$

The quark state $|q >$, describes a CS quark system, and the corresponding hadron state $|h >$ describes the hadron system. The matrix element $U_{hq} =< h|U|q >$ gives the transition amplitude. For a separated system, the energy-momentum conservation is inherent, by the natural commutation condition $[U, H] = [U, \mathbf{P}] = \mathbf{0}$, with $H, \mathbf{P}$ the energy and momentum operator of the systems. This is just the confinement which says that the total probability for the CS quark system to transit to all kinds of hadron is exactly 1, and agrees with the fact that all the constituent quark states and the hadron states are respectively two complete sets of bases of the same Hilbert space [a], i.e., $\sum |q >< q| = \sum |h >< h| = 1$ for the colour-singlet system. So combination process *never* changes the degree of freedom of the system.

Since lack of space, the Refs. are to be found from Ref. [1].

II. Unitarity of the combination model naturally suppresses the production of exotic hadrons (multi-quark states)

Two important points should be considered:

1. As a matter of fact from experiments,

$$\sum_{h=B,\bar{B},M} | < h|U|q > |^2 \sim 1 - \varepsilon,\ \varepsilon \to 0^+, \tag{2}$$

here $B, \bar{B}, M$ denote baryon, antibaryon and meson respectively. Naïvely from the group theory, *colour confinement* seems not so restrict as Eq. (2). The CS state, i.e., the invariant, totally antisymmetric representation of the $SU_C(3)$ group, requires at least one quark and one antiquark, or three (anti)quarks, but more (anti)quarks can also construct this representation, hence possibly to form a CS "hadron". They are to be called exotic hadrons (here not including glueball or hybrid). Until now, no experiment can definitely show ε in Eq. (2) is exactly 0 or a small but *non*-vanishing number. If definitely $\varepsilon = 0$, there must be underlying properties of QCD which we still not very familiar. Even ε is not vanishing, its smallness, definitely confirmed by experiments and shown in Eq. (2), also provides interesting challenges, especially on hadronization models. The small production rate of a special kind of exotic hadron seems easy to be adopted. However, taking into account so many possibilities to construct the CS representations by *various* numbers of (anti)quarks, that the total sum of them is still quite small, is very nontrivial as a property of QCD and even nontrivial for a hadronization model to reproduce.

2. Colour recombination destroys the distinction between multiquark state and molecule state. All kinds of Exotic hadrons have one common property: The (anti)quarks can be grouped into several clusters, with each cluster *possibly* in CS. However, the ways of grouping them into

[a] This is very natural, if one adopts that QCD is really the uniquely correct theory for the hadron physics, with its effective Hamiltonian H_{QCD}. Then all the hadron states with definite energy-momentum should be its eigenstates and expand the Hilbert space of states (though we do not know how to solve H_{QCD} mathematically). While a model is proposed in language of constituent quarks which composite the hadrons, all of the quark states with definite energy-momentum should be eigenstates of the same H_{QCD} (Here we consider constituent quark model, and ignore the rare probability of exotic hadrons like glueball, hybrid, hence need not consider gluon states). So these two sets of bases are of different *representations*, as is more easy to be recognized if one imagines that all the wave functions of hadrons are written in terms of quark states in some special framework of quark models and notices that the planer wave function as well as other special functions (bound state wave functions) are all possible to be complete bases for a definite functional space, mathematically.

clusters are not unique, as it is simply known from group theory that the reduction ways for a direct product of several representations are not unique. Furthermore, these clusters need not necessarily be in CS respectively, since the only requirement is the whole set of these clusters in CS. For example, the system $q_1\bar{q}_2q_3\bar{q}_4$ (the constituents of a "tetraquark") can be decomposed/clustered in the following ways: $(q_1q_3)_{\bar{3}}\otimes(\bar{q}_2\bar{q}_4)_3 \to 1, \quad (q_1\bar{q}_2)_{1\ or\ 8}\otimes(q_3\bar{q}_4)_{1\ or\ 8} \to 1, \quad \cdots$ In the above example, only the second case, when these two $q\bar{q}$ pairs are in CS respectively, it seems possible to be considered as a hadron molecule. But dynamically, the colour interactions in the system via exchanging gluons can change the colour state of each separate cluster, so each kind of grouping/reduction way seems no special physical meaning. Such an ambiguity, which has been considered in many hadronization and decay processes as "colour recombination/rearrangement" obstacles the possibility to consider the exotic hadron in a unique and uniform way, while leads to the possibility of introducing some phenomenological duality. Namely, even we consider the production of exotic hadron as "hadron molecule" formation, the subsequent colour interactions in the system can eventually transit this "molecule" into a "real" exotic hadron, at least by some probability.

From the above discussion, and in the calculation by Shandong QCM (SDQCM), one can introduce a model dependent definition of multiquark state, i.e., the number of quarks to be combined into the hadron is definite though quark pair could be created in the bound state. The fact $\epsilon \to 0^+$ is employed by introducing the parameter x. It is clear that to an extreme if we have infinite kinds of exotic hadrons, x should be vanishing, expecting infinite number of vanishing variables (production rates corresponding to each certain exotic hadron) summing up to get a finite small result (the total production rate of all exotic hadrons). So it is predicted that if the Gell-mann Zweig quark model can be extrapolated to multiquark states, production of each of the species could be vanishing and not observable.

III. Unitarity in exclusive QCM guarantees the non-decreasing of entropy in the combination process for a CS separated system

1. By the formula of entropy $S = -tr(\rho \ln \rho)$ for a separated system, we can conclude a unitary transition will not change the entropy.

$$\rho(t) = |t, i > P_i < i, t| = U(t,0)|0, i > P_i < i, 0|U^\dagger(t,0) = U(t,0)\rho(0)U^\dagger(t,0). \tag{3}$$

Here $U(t,0)$ is the time evolution operator. P_i is the probability of the state with index i. Taking $\rho(0)$ as the distribution of the constituent quark system *just before combination*, while $\rho(t)$ *just after*, of the hadron system, then $U(t,0)$ is exactly the operator U introduced in Eq. (1). This is a uniform unitary transformation on the Hermitian operator ρ, which does not change the trace of $\rho \ln \rho$. So the entropy holds as a constant in the combination process, same as energy and momentum.

2. Energy conservation is kept for each combination step for the many quark CS separated system, by tuning the constituent quark masses in the programme. Then an ideal quasistatic process can be employed to calculate the entropy change. The result is again zero. The details are described in arXiv:1005.4664.

IV. Charmonium production, Unitarity does not introduce any new rules

In several combination models, including the SDQCM mentioned above, one has considered the open charm hadron production by introducing the charm quark into the bulk of the light quarks with its specific spectrum, to let all these four kinds of quarks to combine on equal footing. In this consideration, one has to deal with the case when a charm quark antiquark pair can be combined together under the combination rule to keep consistency. On the other hand, one can raise the question whether charmonium (or bottomium) can be produced under exactly the same mechanism as light $q\bar{q}$ hadron, i.e., via the common combination rules.

Charm/bottom is the kind of 'constituent quarks' which is more easy to be tracked than the light ones, and the 'dressing process' will not change the spectrum much. The light quark sector,

many of them come from gluon nonperturbative QCD transition, which is yet quite unclear, as described above. So it is more reliable talking about the charm distribution before combination. The above investigation of charmonium as well as the open charm in QCM can help the study of its energy loss in medium.

When according to the combination rules, a $c\bar{c}$ pair can be combined, we further restrict their invariant mass to lower than some definite value (say, that of $\Psi(3S)$) to be a charmonium. This will not change the unitarity mentioned above. This has a good analogy: the charmonium and open charm corresponding to the positronium and free electron (discrete and continuous spectrum), respectively. Such a restriction does not affect comparing with data, either, since charmonium resonances more massive than $\Psi(3S)$ almost all decay into open charms.

Our results indicate that at RHIC, the charmonium can be described exactly in the same way of the open charm particle by SDQCM without introducing any new rule. This check is to be done for LHC soon.

More details in the long write up will come soon. A preliminary figure can be seen from the presentation slides, P9; A table and formulae show the relative ratio of different kind of charmonium, see P8.

V. Postscript

In the above section, when comparing our result on J/Ψ spectrum and concluding consistent with RHIC data, we neglect the contribution of bottom. In higher energies and larger transverse momentum P_T, e.g., in LHC, the contribution of B decay will increase and could be dominant for enough large P_T. In this case one need a separation of prompt in experiments, as done by CDF in Tevatron. To coincide with inclusive data, the theoretical calculation must include the bottom production. On the other hand, J/Ψ is a good measure of B for large P_T (Two body decay to $J/\Psi + h$ is an important way to measure B). Such a fact can be seen from the talks in this Rencontre (Z. Dolezal, K. Ulmer). Combined with the celebrating J/Ψ suppression data in Pb-Pb of large p_T reported by ATLAS in this Rencontre (B. Wosiek), it is easy to conclude that the bottom energy loss is almost the same as the light quark for large P_T, as expected by the author in discussions around the dinner table in La Thuile. The 'non-photonic' electron and forward muon data measured by ALICE presented on QM2011 (Annecy, May) is not contradicted with such a expectation, though the R_{AA} a little larger comparing to e.g., pion. However, one sees R_{AA} increasing with P_T and the P_T of electron/moun represents the behaviour of B around $2P_T$. Such a energy loss behaviour is well understood by considering the spacetime picture of the jet (heavy or light) medium interaction, as explained in the talk by the author in last year's Rencontre. This kind of interaction has an analogy of hadron hadron interaction. The production process (pionization) is the main mechanism to lose energy. The produced particles composite the rapidity plateau, so that can be of large angle w.r.t the jet. Since the width and height of the plateau increase with the interaction energy, the energy loss also increases with jet energy. These have been confirmed by CMS measurements reported in La Thuile (F. Ma). $\frac{\Delta E}{E}$ is a constant for a large range of jet energy.

Acknowledgments

My collaborators (HAN W., JIN Y., SHANG Y., SHAO F., SI Z., YAO T., YIN F.) in doing the works presented here are first of all thanked. The works are partially supported by NSFC with grant Nos. 10775090, 10935012, NSFSC with grant Nos. ZR2009AM001, ZR2010AM023, JQ200902, and Independent Innovation Foundation of SDU.

1. The Refs. are to be found from arXiv:1005.4664, P.R.C80:035202,2009, SDU thesis of Shang and Yin ('09,'10), and Li S.-Y., Yao, T. and Yin F., in preparation.

5.
QCD

Latest Jets Results from the Tevatron

Christina Mesropian
on behalf of the CDF and D0 Collaborations
The Rockefeller University,1230 York Avenue,
New York, NY, 10065, USA

A comprehensive overview of the latest aspects of jet physics in proton-antiproton collisions at $\sqrt{s}$ =1.96 TeV is presented. In particular, measurements of the inclusive jet production, dijet and multi-jet production, and jet substructure studies are discussed.

1 Inclusive Jet Production

The experimental measurements of jet cross section at the Tevatron provide stringent test of QCD predictions, information on the strong coupling constant, α_S, and constraints on proton parton distribution functions, PDFs. The inclusive jet cross section measurements were performed by the CDF collaboration [1, 2] using midpoint cone [3] and k_T [4] algorithms and by D0 collaboration using the midpoint algorithm [5]. Both experiments extended measurements to the forward rapidity regions. The systematic uncertainties in these measurements are dominated by the uncertainty in the jet energy scale. The extensive efforts to determine jet energy scale, using single particle response technique in the case of CDF, and $\gamma + jet$ event calibration method at D0, allowed to achieve the jet energy scale uncertainties of 2-3% and 1-2%, respectively. The understanding gained by these measurements is important for any analyses which have jets as an object of interest.

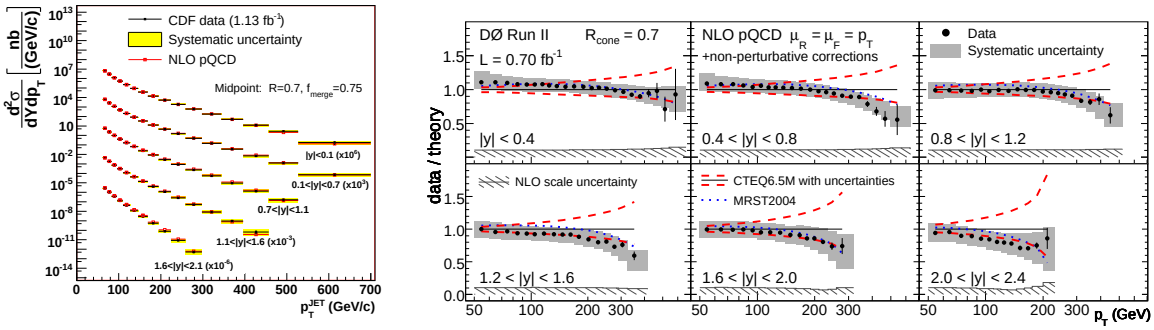

Figure 1: Measured inclusive jet differential cross sections in five rapidity regions by CDF compared to NLO QCD predictions (left); Ratios of the measured cross sections over NLO QCD predictions by D0 (right).

Fig. 2 shows a comparison of the measured cross sections to the theoretical predictions. The measurements are found to be in agreement with NLO QCD predictions for both experiments

and for different clustering algorithms. The experimental uncertainties are lower than the uncertainties associated with the theoretical predictions. Since inclusive jet measurements allow to constrain PDFs of the proton, especially gluon densities at high x, ($x \geq 0.25$), two groups performing global QCD analyses to determine PDFs included these Tevatron measurements in their compilation, with resulting PDFs referred as MSTW2008 and CT09. Inclusion of the Tevatron measurements lead to somewhat softer high-x gluons than the ones previously available.

The inclusive jet cross section is directly related to the measurement of the strong coupling constant. The CDF collaboration performed this analysis using the 1994-95 data, and D0 recently published a new α_S determination [6] based on the inclusive jet cross section measurement discussed above. The value of the strong coupling constant is determined from sets of inclusive jet cross section data points by minimizing the χ^2 function between data and the theoretical results. In order to avoid the complications arising from the α_S dependence on PDF determinations, only 22 data points out of 110 were kept for α_S determination. This measurement provides the most precise result for the strong coupling constant from the hadron colliders $\alpha_S(M_Z) = 0.1161 \pm^{0.0048}_{0.0041}$.

The CDF [7] and D0 [8] experiments used the dijet invariant mass distribution to search for resonances decaying into jets. In the case of D0, measurements of the dijet angular distributions are performed in different regions of the dijet invariant mass. A good agreement between data and theory, which translates into improved limits in different models, is observed for both experiments.

2 Multi-Jet Production

We present a measurement by the D0 collaboration of the differential inclusive three-jet cross section as a function of the invariant three-jet mass (M_{3jet}). The data set corresponds to an integrated luminosity of 0.7 fb^{-1}. The measurement is performed in three rapidity regions ($|\ y\ |$<0.8, $|\ y\ |$<1.6, and $|\ y\ |$<2.4) and in three regions of the third jet transverse momenta. The events are required to have p_T of the leading jet larger than 150 GeV and for any pair of jets to be well separated in $y - \phi$ space. The comparison of the experimental data with the NLO theoretical predictions shows a reasonable agreement, see Fig. 2.

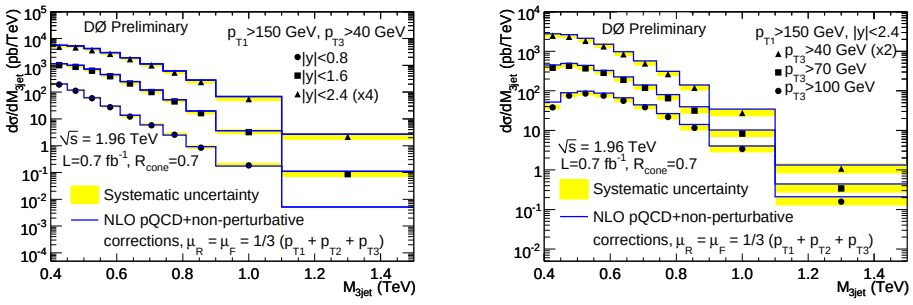

Figure 2: Three-jet mass cross section in regions of jet rapidities (left), and third jet p_T (right). Full lines correspond to the NLO calculations with NLOJET++ and MSTW2008 PDF set.

Using the same data sample the D0 collaboration also performed a measurement of the ratios of the multi-jet cross sections. The inclusive n-jet event sample (for n = 2,3) is defined by all events with n or more jets with $p_T > p_{Tmin}$ and $|\ y\ |$<2.4. The rapidity requirement restricts the jet phase space to the region where jets are well-reconstructed in the D0 detector and the energy calibration is known to 1.2 - 2.5%. The ratio of cross sections is less sensitive to experimental and theoretical uncertainties than the individual cross sections, due to cancellations of correlated uncertainties. $R_{3/2}$ is measured as a function of the leading jet p_T in an event, $p_{T_{max}}$. Since the variable $p_{T_{max}}$ is independent of the jet multiplicity, all events which belong to a given $p_{T_{max}}$

bin for the inclusive trijet event sample also belong to the same $p_{T_{max}}$ bin for the inclusive dijet event sample. Given the definitions above for inclusive n-jet event samples, $R_{3/2(p_{Tmax})}$ equals the conditional probability for an inclusive dijet event (at p_{Tmax}) to contain a third jet with $p_T > p_{Tmin}$. The data is well described by the SHERPA event generator (using default settings) with tree-level matrix elements for 2-, 3-, and 4-jet production. For the PYTHIA event generator, the results depend strongly on the chosen parameter tune. Commonly used tunes (for both the angular-ordered and the p_T -ordered parton shower), see Fig. 3, overshoot the measured ratios significantly over the whole p_{Tmax} range for all p_{Tmin} requirements.

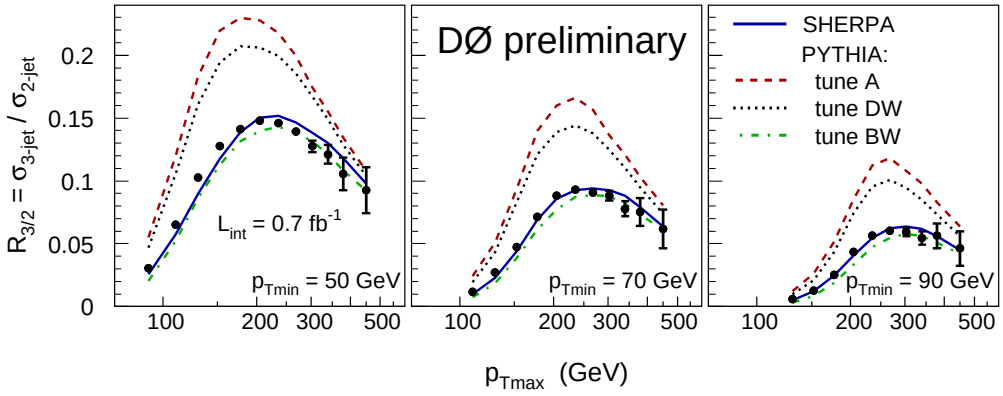

Figure 3: $R_{3/2}$ ratio measured as a function of the leading jet p_{Tmax} for different p_{Tmin} requirements for the other jets. Predictions from SHERPA and PYTHIA (three tunes using the virtuality-ordered parton shower) are compared to the data.

3 Study of Substructure of High p_T Jets

The study of high transverse momentum (p_T) massive jets provides an important test of pQCD and gives insight into the parton showering mechanism. In addition, massive boosted jets compose an important background in searches for various new physics models, the Higgs boson, and highly boosted top quark pair production. Particularly relevant is the case where the decay

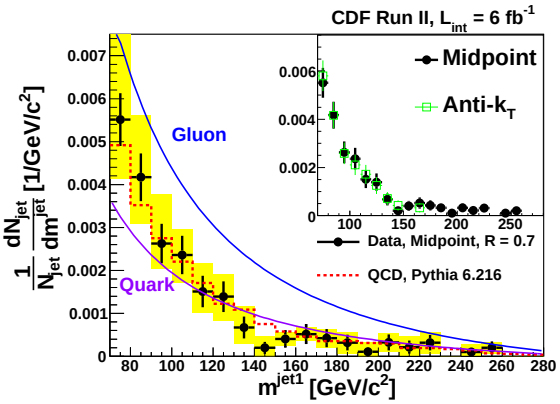

Figure 4: The normalized jet mass distribution for midpoint jets with $p_T > 400$ GeV/c. The theory predictions for the jet functions for quarks and gluons are shown as solid curves and have an estimated uncertainty of 30%. The inset compares midpoint and $anti-k_t$ jets.

of a heavy resonance produces high-p_T top quarks that decay hadronically. In all these cases, the hadronic decay products can be detected as a single jet with substructure that differs from

pQCD jets once the jet p_T is greater than 400-500 GeV/c. The CDF collaboration performed measurement of substructure of jets with p_T >400 GeV/c by studing distributions of the jet mass and measuring angularity, the variable describing the energy distribution inside the jet, and planar flow, the variable differentiating between two-prong and three-prong decays. At small cone sizes and large jet mass, these variables are expected to be quite robust against soft radiation and allow, in principle, a comparison with theoretical predictions in addition to comparison with MC results. Jets are reconstructed with the midpoint cone algorithm (cone radii R=0.4, 0.7, and 1.0) and with the $anti-k_t$ algorithm [9] (with distance parameter R=0.7). Events are selected in a sample with 6 fb^{-1} based on the inclusive jet trigger. There is a good agreement between the measured m^{jet_1} distribution with the analytic predictions for the jet function and with PYTHIA MC predictions. The midpoint and $anti-k_t$ algorithms have very similar jet substructure distributions for high mass jets, see Fig. 4. The angularity distribution shown on Fig. 5(left) in addition to reasonable agreement data and PYTHIA MC also demonstrates that the high mass jets coming from light quark and gluon production are consistent with two-body final states and that further rejection against high mass QCD jets can be obtained by using the planar flow variable, Fig. 5(right).

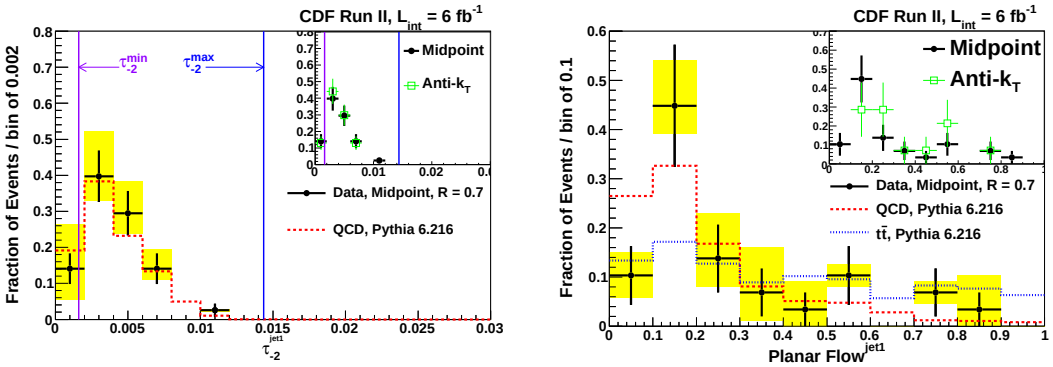

Figure 5: The angularity distribution for midpoint jets with p_T >400 GeVc. The $t\bar{t}$ rejection cuts and requirement for 90 GeV/c^2 < m^{jet1} <120 GeV/c^2 are applied. The PYTHIA calculation (red dashed line) and the pQCD kinematic endpoints are shown (left); The planar flow distributions after applying the top rejection cuts and requiring 130 GeV/c^2 < m^{jet1} <210 GeV/c^2. PYTHIA QCD (red dashed line) and $t\bar{t}$ (blue dotted line) jets are shown (right).

Acknowledgments

I would like to thank organizers for their kind invitation to the conference.

References

1. T. Aaltonen *et al.*, *Phys. Rev.* D **78**, 052006 (2008).
2. A. Abulencia *et al.*, *Phys. Rev.* D **75**, 092006 (2007).
3. G.C. Blazey *et al.*, (2000), arXiv:hep-ex/0005012.
4. S. Catani *et al.*, *Nucl. Phys.* B **406**, 187 (1993);
   S.D. Ellis *et al.*, *Phys. Rev.* D **48**, 3160 (1993).
5. V.M. Abazov *et al.*, *Phys. Rev. Lett.* **101**, 062001 (2008).
6. V.M. Abazov *et al.*, *Phys. Rev.* D **80**, 111107R (2009).
7. T. Aaltonen *et al.*, *Phys. Rev.* D **79**, 112002 (2009).
8. V.M. Abazov *et al.*, *Phys. Lett.* B **693**, 531 (2010).
9. S.G.P Cacciari and G. Soyez, *JHEP* **04**, 063 (2008).

RECENT RESULTS ON JETS FROM CMS

F. PANDOLFI for the CMS Collaboration
Università di Roma 'Sapienza' and INFN Sezione di Roma,
Piazzale Aldo Moro 5, 00185 Rome Italy

We present an overview of the results on jets from proton-proton collisions at a center-of-mass energy of $\sqrt{s} = 7$ TeV using data collected by the CMS experiment in 2010. It includes the *in situ* jet calibration and resolution measurements, the inclusive jet cross section measurement and a search for quark contact interactions with a dijet angular analysis.

1 Introduction

The Large Hadron Collider offers the possibility of confronting QCD at the energy frontier. The data it delivers gives us new insight on the precision of perturbative QCD (pQCD) predictions and the modeling of non-perturbative effects in the current Monte Carlo (MC) generators. Jets can also be employed, as will be shown, in the search for physics beyond the Standard Model.

At a hadron collider most final states have jets. Hence jets as a physics objects must be understood, whether they are part of the signal being analysed, or of the background. In order to do so both their energy scale and resolution have to be measured to a good degree of precision.

In this brief article an overview of the results on jets at the CMS [1] detector based on the 2010 data taking is given. Section 2 shows the results of the jet *in situ* calibration and resolution measurements. Section 3 describes physics results obtained with jets.

2 Jet Calibration and Resolution Measurement

Three main methods are employed in CMS to reconstruct jets [2]: calorimeter jets are constructed by the clustering of projective calorimeter towers; jet-plus-track jets improve the measurement of calorimeter jets by exploiting the associated tracks; Particle-Flow jets cluster particle candidates created by the Particle-Flow full-event reconstruction technique, which attempts to measure every stable particle produced in a collision through the combination of all CMS subdetectors. Jets are clustered using the anti-k_{T} [3] algorithm, with a radius parameter of $R = 0.5$.

Jets have to undergo a series of energy corrections before they can be used in an analysis. CMS has developed a factorized approach, in which the corrections are defined in order to be be independent of each other, and can be applied sequentially. The corrections are:

- an offset correction, which takes into account multiple proton-proton interactions in the given bunch crossing (*pile-up*);
- a relative correction, which uniforms the detector response as a function of pseudorapidity;

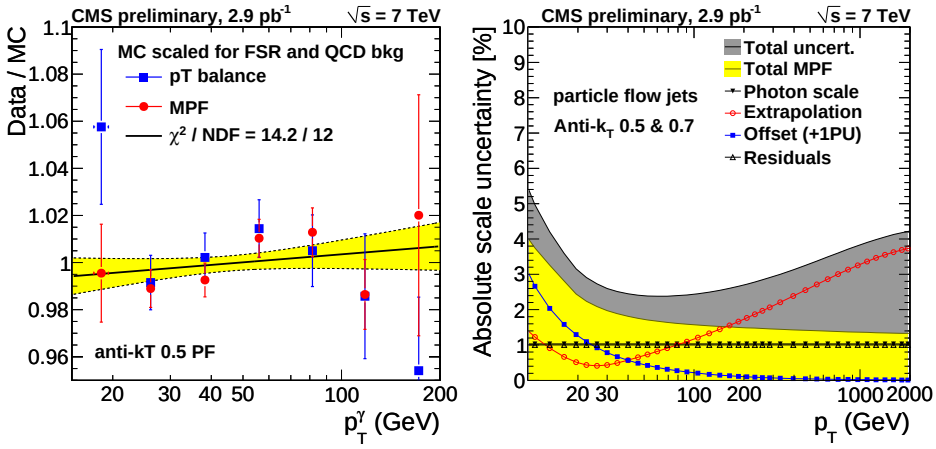

Figure 1: Left: Ratio between measured jet absolute energy scale with photon+jet events and the one predicted by the MC simulation, as a function of photon p_{T}. Results obtained with the Missing-E_{T} Projection Fraction (MPF) method (red) are compared to a traditional photon/jet balancing technique (blue). Right: Uncertainty on the absolute scale measurement with the MPF method. Different sources of error are shown.

- an absolute correction, which addresses the non-compensating nature of the CMS calorimeters, and uniforms the response as a function of jet transverse momentum.

The measurement of the relative and absolute corrections has been performed on the first 3 pb^{-1} of data recorder in 2010. The jet absolute correction is measured on photon+jet events, in which the precision with which the photon is reconstructed in the crystal electromagnetic calorimeter is exploited in order to infer the recoiling jet's true momentum. The absolute response is extracted making use of the knowledge of the full event missing transverse energy, with a method know as the Missing-E_{T} Projection Fraction (MPF)[2]. This method is particularly suited for the Particle-Flow event reconstruction, which, through the use of the tracker, ensures a relatively high response also in the case of soft radiation. It is therefore expected to be the most insensitive to biases related to additional event activity.

Results obtained with the photon+jet pt balancing technique are shown in Fig. 1 (left), where the MPF data/MC ratio (blue) is shown as a function of the photon transverse momentum. Results obtained with a more traditional photon/jet balancing technique are shown as comparison (red). The points are compatible with the Monte Carlo prediction. The estimated systematic uncertainty on this measurement is shown in Fig. 1 (right). Various possible sources

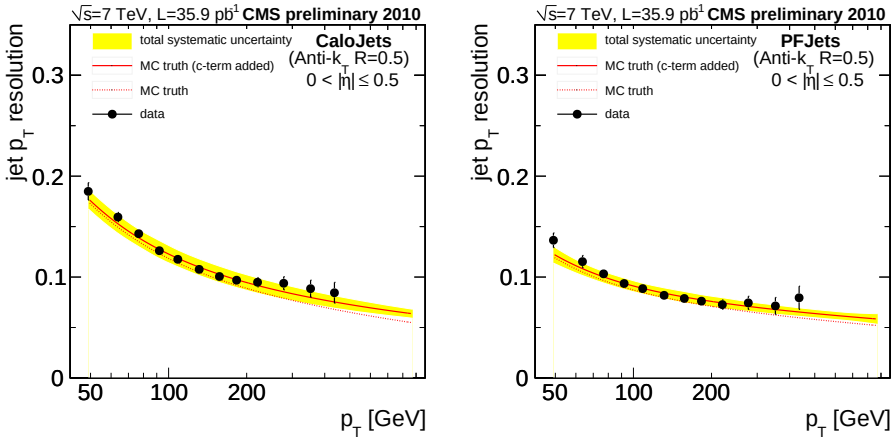

Figure 2: Jet transverse momentum resolution measurement with the dijet asymmetry method in the central part of the detector ($|\eta| < 0.5$). Calorimeter jet results are shown on the left, Particle-Flow jets on the right.

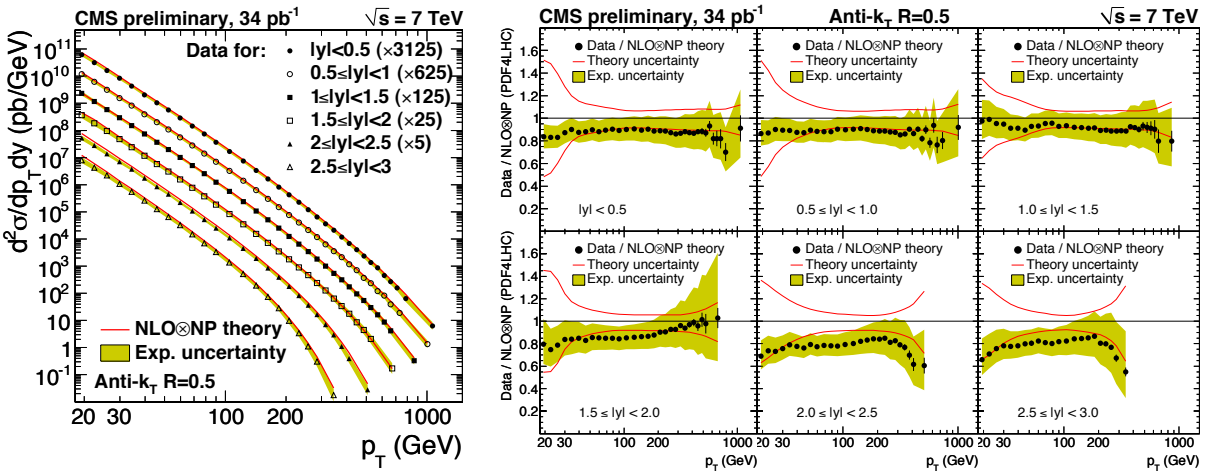

Figure 3: Top: Unsmeared inclusive jet transverse momentum spectrum in the six rapidity bins with next-to-leading-order (NLO) theoretical prediction, corrected for non-perturbative effects (NP) superimposed. Bottom: Ratio between data and theoretical prediction. The solid line represents the total theoretical uncertainty, the shaded band the experimental systematic uncertainty.

of bias have been investigated: uncertainty relative to the MPF method, on the photon energy scale, on the extrapolation to the high transverse momentum region with different hadronization models, effects of pile-up and of non-closure of the MC-truth energy corrections. The total uncertainty is taken as the quadrature sum of all components and is found to be less than 4% in most of the transverse momentum range, and less than 3% in the 20-300 GeV interval.

The jet p_{T} resolution is measured with the dijet asymmetry method [2]. Dijet events are selected and the asymmetry variable $\mathcal{A}$ is defined as the relative difference of the jet transverse momenta $\mathcal{A} = (p_{\mathrm{T},1} - p_{\mathrm{T},2})/(p_{\mathrm{T},1} + p_{\mathrm{T},2})$. The jet resolution is extracted from the width of the asymmetry distribution. Results for the resolution measurement are shown in Fig. 2 for central jets ($|\eta| < 0.5$) on the left for calorimeter jets, on the right for Particle-Flow jets, and it is found to be compatible with the simulation.

3 Measurements with Jets

The inclusive jet production cross section is a benchmark test of pQCD. The measurement [4] has been carried out by CMS on the full 2010 dataset, and its results are shown in Fig. 3 (left). Compared to previous colliders, the CMS measurement extends both at higher transverse momenta (benefiting from the high center of mass energy), and at lower ones, reaching down to 18 GeV. The measurement is performed in 6 rapidity bins, up to $|y| = 3$.

The data is unfolded to take into account the finite detector resolution and is compared to the NLO pQCD prediction, corrected for non perturbative (NP) effects. The NLO corrections are derived using `NLOJet++` [5] within the fastNLO [6] framework with CT10 [7] parton distribution function sets. The theory is found to be in agreement with the data over more than 10 orders of magnitude. This is further emphasized in Fig. 3 (right), where the ratios between the observed and predicted trends are shown, for the six rapidity bins. The data points are shown with an experimental uncertainty band (yellow) which is dominated by the uncertainty on the jet energy scale, whereas the uncertainty on the theoretical prediction is marked with a red line, and is dominated by the NP correction uncertainties at low transverse momenta and by the parton density function uncertainties at high transverse momenta. The data is found to be compatible with the theoretical prediction within uncertainties.

We also present a dijet angular analysis [8] which provides both a stringent test of pQCD predictions, and sensitivity for the presence of physics beyond the Standard Model. This analysis selects dijet events, and studies the exponential of the absolute rapidity gap between the two jets $\chi_{\rm dijet} = \exp(|y_1 - y_2|)$ in increasing dijet invariant mass bins, as shown in Fig. 4. At low invariant masses, this measurement proves to be a precision test of the pQCD predictions (grey shade). The observed good agreement between the data and the theoretical prediction can be considered a success for the latter.

At high invariant mass, $\chi_{\rm dijet}$ is sensitive to the presence of quark contact interactions, arising in a quark compositeness scenario, which would enhance centrally produced dijet events ($\chi_{\rm dijet} \sim 1$). The effect on the $\chi_{\rm dijet}$ distribution is shown for a compositeness scale of $\Lambda = 5$ TeV, for destructive (Λ^+) and constructive (Λ^-) interference with the QCD Lagrangian. This measurement has excluded the presence of quark contact interactions up to a scale of $\Lambda^+ = 5.6$ TeV ($\Lambda^- = 6.7$ TeV).

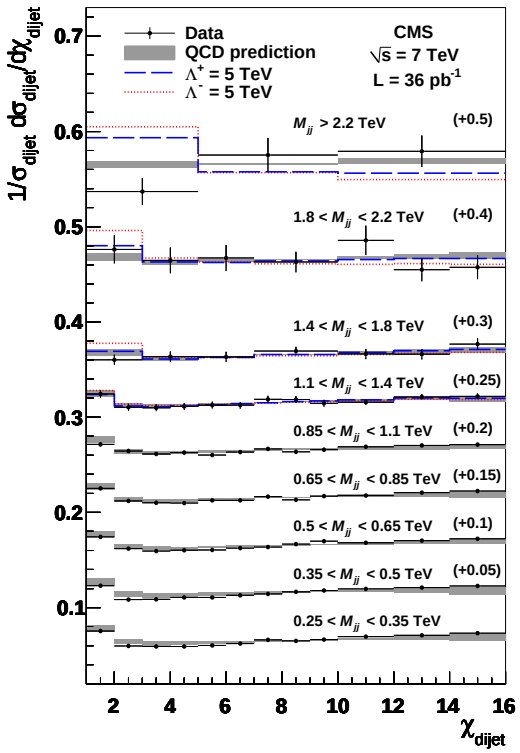

Figure 4: Normalized $\chi_{\rm dijet}$ distributions in several dijet invariant mass (M_{jj}) ranges. Results are compared with the predictions of pQCD at NLO (grey) and with the predictions including a contact interaction term of compositeness scale $\Lambda^+ = 5$ TeV (dashed) and $\Lambda^- = 5$ TeV (dotted). Data uncertainties include statistical and systematic contributions. The shaded band shows the magnitude of theoretical uncertainties.

4 Conclusions

An overview of the results on jets from proton-proton collisions at $\sqrt{s} = 7$ TeV using data collected by the CMS experiment in 2010 has been presented. The jet energy scale has been determined with photon+jet balancing with a precision better than 3% for $30 < p_{\rm T} < 200$ GeV. The jet $p_{\rm T}$ resolution has been measured with the dijet asymmetry technique, and found to be in agreement with the simulation. An inclusive jet cross section measurement has been performed, showing a remarkable level of agreement with the NLO pQCD prediction. Finally, a dijet angular analysis has been employed in the search for quark contact interactions, setting a limit of 5.6 TeV (6.7 TeV) for destructive (constructive) interference with the QCD Lagrangian.

References

1. CMS Collaboration, JINST 3:S08004 (2008)
2. CMS Collaboration, CMS PAS **JME-10-010** (2010).
3. M. Cacciari, G. P. Salam, and G. Soyez, JHEP 0804:063 (2008).
4. CMS Collaboration, CMS PAS **QCD-10-011**
5. Z. Nagy, *Phys. Rev. Lett.* **88**, 1222003 (2002) and *Phys. Rev.* D **68**, 094002 (2003)
6. T. Kluge, K. Rabbertz, M. Wobisch, `arXiv:hep-ph/060985`
7. H.-L. Lai *et al*, *Phys. Rev.* D **82**, 074024 (2010)
8. CMS Collaboration, *Phys. Rev. Lett.* **106**, 201804 (2011)

RECENT RESULTS ON JETS WITH ATLAS

GENNADY POSPELOV
on behalf of the ATLAS collaboration
Max-Planck-Institut für Physik (Werner-Heisenberg-Institut)
Föhringer Ring 6, 80805, München, Germany

Recent results on jets from proton-proton collisions at $\sqrt{s} = 7\,\text{TeV}$ measured with the ATLAS detector at the Large Hadron Collider are presented. In particular, the determination of jet energy scale uncertainty, the measurements of the inclusive jet production cross section and the ratio of the three-to-two jet cross sections are discussed. These measurements rely on the data set collected by ATLAS in 2010 corresponding to an integrated luminosity of $45\,\text{pb}^{-1}$.

1 Introduction

In March 2010 the Large Hadron Collider (LHC) at CERN started to collide protons on protons at $\sqrt{s} = 7\,\text{TeV}$ center-of-mass energy. Up to the end of the year the ATLAS detector [1] collected a data sample corresponding to the integrated luminosity of $45\,\text{pb}^{-1}$. Jet production, being the dominant high transverse-momentum process, provides a wide variety of observables for the most fundamental and direct tests of the theory of strong interactions. First results on jet production cross sections using an integrated luminosity of $17\,\text{nb}^{-1}$ were reported in Summer 2010 [2]. Those measurements considered jets with transverse momentum $60\,\text{GeV} < p_\text{T} < 700\,\text{GeV}$ and rapidity [a] $|y| < 2.8$.

Since then, significant efforts have been made to obtain a deeper understanding of the calorimeter and trigger response to jets, and to further minimize experimental uncertainties. The result of these studies was the extension of inclusive jet measurements in the region $20\,\text{GeV} < p_\text{T} < 1.4\,\text{TeV}$ and $|y| < 4.4$, with the experimental uncertainties of the order of the theoretical ones [3]. Other encouraging results, concerning the measurement of the di-jet azimuthal decorrelations [4], the measurement of the di-jet production with a jet veto [5] and measurement of multi-jet cross sections [6] have been obtained and presented at conferences in Spring 2011.

These proceedings discuss the recent ATLAS jet results based on the full 2010 data sample, with highlights on the jet energy scale determination and on the jet cross section measurements.

2 Jet reconstruction and energy scale determination

2.1 Jet reconstruction and calibration in the ATLAS detector

The starting point of the jet reconstruction in ATLAS is the topological clustering [7] of the calorimeter cells calibrated at electromagnetic (EM) scale. Clusters are initiated by seeds,

[a] the rapidity for massive jets is defined as $y = \frac{1}{2}\, ln\, \frac{E+p_z}{E-p_z}$

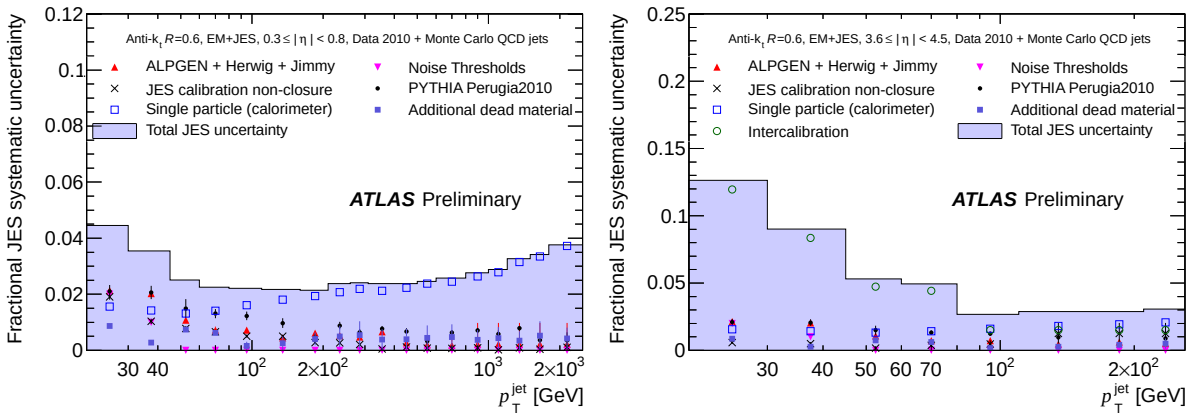

Figure 1: Fractional jet energy scale systematic uncertainty as a function of p_{T} for jets in the pseudorapidity region $0.3 < |\eta| < 0.8$ in the barrel calorimeter (left) and in the pseudorapidity region $3.6 < |\eta| < 4.5$ in the forward calorimeter (right).

which are cells with large signal to noise ratio. Neighbouring cells in 3D space are collected to form the cluster in an iterative procedure based on cell energy significances and neighbouring relations. Resulting clusters are used then as input objects for an anti-k_{T} algorithm [8] with distance parameters R=0.6 and R=0.4 to form jets.

The ATLAS calorimeter system is non-compensating, i.e. it generates smaller signal per unit of incoming energy for hadrons than for electrons. Additional imperfections in the reconstruction can arise from energy deposits outside active regions of the calorimeters, shower leakage, and threshold effects from clustering and jet algorithms.

The present calibration scheme [9] applies jet-by-jet Monte Carlo based corrections as a function of the jet energy and pseudorapidity [b] to jets reconstructed at EM scale. To derive the correction factors, truth jets are formed by running the same anti-k_{T} algorithm on stable particles from Monte Carlo simulation. Each correction factor is then calculated by dividing the truth particle jet energy by the energy of the matching calorimeter jet at EM scale. This calibration scheme restores jet energy scale (JES) within 2% for the full kinematic range and allows a direct evaluation of the systematic uncertainty.

2.2 Jet energy scale uncertainty

The jet energy scale uncertainty is the dominant experimental uncertainty for numerous physics results with jets in final states. The systematic uncertainty of the present calibration scheme is determined from a combination of test-beam data, in-situ measurements in proton-proton collisions and from systematic variations of parameters of the Monte Carlo simulations.

As a first step, the uncertainty of the response of the ATLAS calorimeter system to single isolated hadrons is determined from the E/p ratio measured in-situ by the calorimeter and the tracker. This data is supplemented by the uncertainty known from single pion testbeam measurements in the well-understood barrel region $|\eta| < 0.8$. Finally the uncertainty of the calorimeter responce to hadrons is propagated to the uncertainty of the calorimeter response to jets using Monte Carlo and known jet composition. Additional uncertainties on the description of the material of the ATLAS detector, of the electronic noise and uncertainties from the modeling of the fragmentation and underlying event are estimated using Monte Carlo test samples generated with different conditions.

Figure 1 (left) shows the final fractional jet energy scale uncertainty and its individual

[b] the pseudorapidity is defined in terms of the polar angle θ as $\eta = -ln\, tan(\theta/2)$

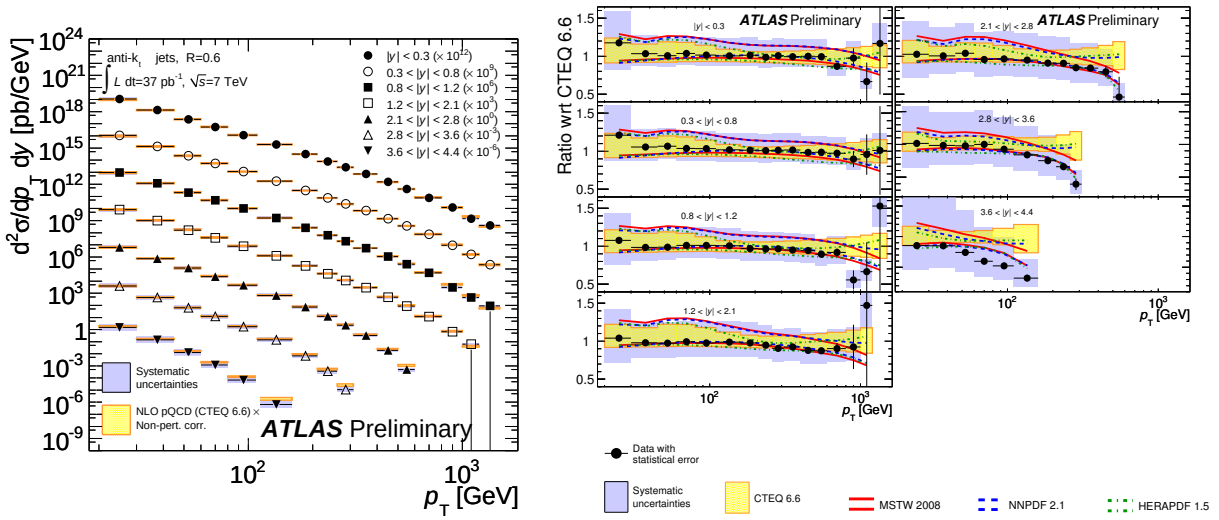

Figure 2: Inclusive jet double-differential cross section as a function of jet p_T in different regions of $|y|$ for jets identified using the anti-k_T algorithm with R = 0.6.

contributions as a function of the jet p_T for the central region. The total uncertainty is lower than 4.5% for all jets with $p_T > 20$ GeV with the dominant contribution coming from the calorimeter uncertainty.

The uncertainty for other pseudorapidity regions is assessed using in-situ di-jet intercalibration [10]. Figure 1 (right) shows the fractional JES uncertainty in the forward region as a function of jet p_T. The total JES uncertainty amounts to about 14% with the intercalibration uncertainty as a dominant source.

3 Cross section measurements

ATLAS measurements of inclusive jet cross sections [3] are performed as a function of jet p_T in 7 bins of jet rapidity up to $|y| < 4.4$. The measured cross section is corrected for experimental effects, like detector inefficiencies, resolution and trigger effects back to the hadronic final state using bin-by-bin unfolding calculated from Monte Carlo (PYTHIA, MC10 tune). The corrected spectrum is compared to NLO QCD theoretical predictions, calculated with the NLOJET++ program and CTEQ 6.6 NLO parton density functions (PDF) as a baseline. NLO calculations are corrected for non-perturbative effects to account for hadronization and underlying events. The corrections are evaluated from the ratio of the cross section with and without hadronisation and underlying event obtained from leading-logarithmic parton shower generators (PYTHIA, AMBT1 tune).

Figure 2 (left) shows both measured and predicted (using CTEQ 6.6 PDF set) double-differential inclusive jet cross section as a function of jet p_T in seven rapidity regions for anti-k_T jets with R = 0.6. The experimental uncertainty (blue band) stays within 10-40 % over the full kinematic range studied, with the dominant contribution from the JES uncertainty. The theoretical uncertainty (yellow band), largely coming from uncertainty of PDFs, is on the level of the experimental one. A comparison of the measured cross section with predictions obtained using the CTEQ 6.6, MTSW 2008, NNPDF 2.1, and HERAPDF 1.5 PDF sets is shown in Figure 2 (right). The data points and the error bands are normalized to the theoretical predictions obtained by using the CTEQ 6.6 PDF set. Predictions using HERAPDF 1.5 appeared to follow the data most closely, though consistency within experimental and theoretical uncertainties with most other PDF sets is observed.

A first dedicated study of multi-jet final states [6] for events containing two or more jets with

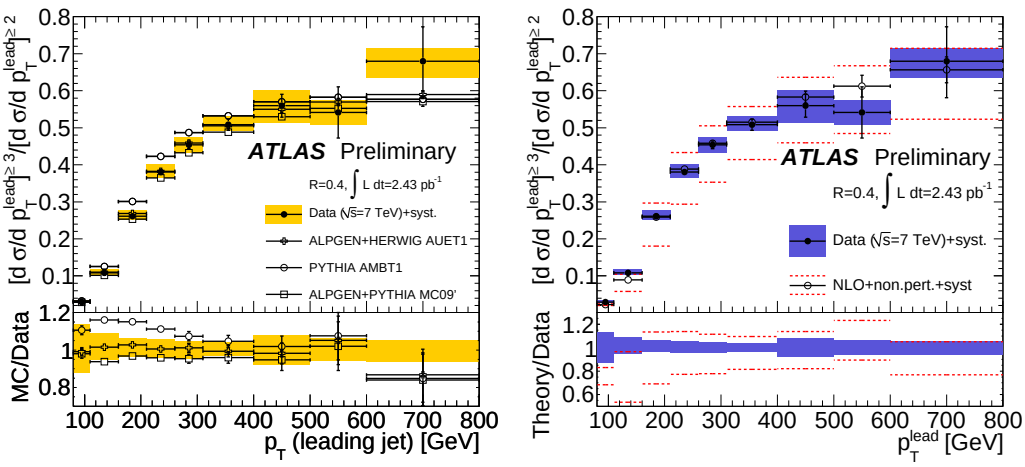

Figure 3: Ratio of three-to-two jet differential cross section as a function of the leading jet p_T. The results are compared to leading order parton shower Monte Carlo simulations (left) and to next-to-leading order pQCD calculations with the MSTW 2008 NLO PDF (right).

$p_{\mathrm{T}} > 60\,\mathrm{GeV}$, of which at least one has $p_{\mathrm{T}} > 80\,\mathrm{GeV}$, is performed by ATLAS with an integrated luminosity of $2.43\,\mathrm{pb}^{-1}$. Figure 3 (left) presents results for the measurement of the three-to-two jet inclusive cross section as a function of the p_{T} of the leading jet after unfolding of detector effects. The systematic uncertainty of this ratio is small ($\sim 5\%$) due to the reduced impact of the JES uncertainty and the cancellation of the uncertainty of the luminosity measurements. Experimental data are compared with predictions from leading order Monte Carlo simulations with parton showers from PYTHIA, ALPGEN+PYTHIA and ALPGEN+HERWIG. ALPGEN generally describes the data well, whether HERWIG or PYTHIA parton showers are used, while PYTHIA predicts a larger three jet cross section than what is measured. Figure 3 (right) shows a comparison of the same experimental results with next-to-leading order calculations (MSTW 2008 NLO PDF) corrected for non-perturbative effects. The systematic uncertainties on the theoretical prediction are shown as dotted red lines above and below the theoretical prediction. Good agreement is found between the data and the theory prediction within systematic uncertainties for both studies except in the lowest transverse momentum bin.

1. ATLAS Collaboration, JINST 3 (2008) S08003.
2. ATLAS collaboration, ATLAS-CONF-2010-050 (http://cdsweb.cern.ch/record/1273169), CERN, Geneva, July, 2010.
3. ATLAS Collaboration, ATLAS-CONF-2011-047 (http://cdsweb.cern.ch/record/1333967), CERN, Geneva, March, 2011.
4. ATLAS Collaboration, Phys. Rev. Lett. 106 172002 (2011).
5. ATLAS Collaboration, ATLAS-CONF-2011-038 (http://cdsweb.cern.ch/record/1332225), CERN, Geneva, March, 2011.
6. ATLAS Collaboration, ATLAS-CONF-2011-043 (http://cdsweb.cern.ch/record/1331131), CERN, Geneva, March, 2011.
7. W. Lampl et al., ATL-LARG-PUB-2008-002 (http://cdsweb.cern.ch/record/1099735), CERN, Geneva, April, 2008.
8. M. Cacciari, G. Salam, and G. Soyez, JHEP 0804 (2008) 063.
9. ATLAS Collaboration, ATLAS-CONF-2011-032 (http://cdsweb.cern.ch/record/1333972), CERN, Geneva, March, 2011.
10. ATLAS Collaboration, ATLAS-CONF-2011-014 (http://cdsweb.cern.ch/record/1329854), CERN,Geneva, March, 2011.

EPOS 2 and LHC Results

Tanguy Pierog[(1)], Iu. Karpenko[(2,3)], and K. Werner[(3)]
[(1)] *Karlsruhe Institut of Technology, Institut für Kernphysik, Postfach 3640, 76021 Karlsruhe Germany*
[(2)] *Bogolyubov Institute for Theoretical Physics, Kiev 143, 03680, Ukraine*
[(3)] *SUBATECH, University of Nantes – IN2P3/CNRS– EMN, Nantes, France*

To study the effects related to the formation of a Quark-Gluon-Plasma in heavy ion collisions, the proton-proton collisions are usually used as a reference. If this approach seems to be valid at RHIC or for very high transverse momentum at LHC, it might be different at intermediate p_t for LHC energies, where some collective effects might be visible already in *pp* data (ridge,...). Within a global model such as EPOS 2, where light and heavy systems are treated using the same physics, we can test the collective effects both in *pp* and lead-lead collisions at LHC. In this paper, it will be shown that the collective effect are not negligible already for *pp* at LHC.

1 Introduction

The CMS collaboration published recently results [1] on two particle correlations in $\Delta\eta$ and $\Delta\phi$, in *pp* scattering at 7 TeV. Most remarkable is the discovery of a ridge-like structure around $\Delta\eta = 0$, extended over many units in $\Delta\eta$, referred to as "the ridge", in high multiplicity *pp* events. A similar structure has been observed in heavy ion collisions at RHIC, and there is little doubt that the phenomenon is related to the hydrodynamical evolution of matter. This "fluid dynamical behavior" is actually considered to be the major discovery at RHIC [2].

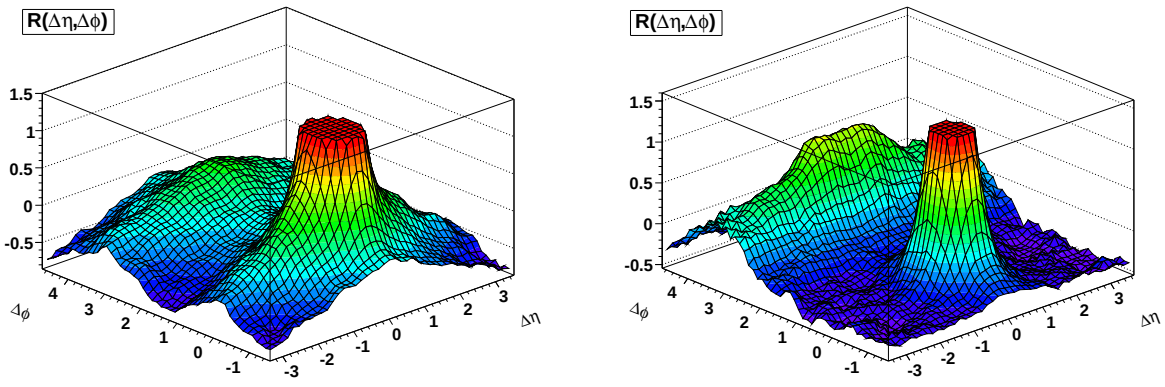

Figure 1: (Color online) Two particle correlation function R versus $\Delta\eta$ and $\Delta\phi$ for high multiplicity events in *pp* collisions at 7 TeV, as obtained from a hydrodynamical evolution based on flux tube initial conditions (lefthand-side). On the righthand-side the calculation is done without hydro evolution .i.e. particle production directly from string (flux tube) decay.We consider particles with p_t between 1 and 3 GeV/c.

So does *pp* scattering provide as well a liquid, just ten times smaller than a heavy ion

collision? It seems so! We showed recently [3] that if we take exactly the same hydrodynamic approach which has been so successful for heavy ion collisions at RHIC [4], and apply it to *pp* scattering, we obtain already very encouraging results compared to *pp* data at 0.9 TeV and now 7 TeV [5]. In this paper based on [6], we apply this fluid approach, always the same procedure, to understand the 7 TeV results at LHC.

2 Ridge in *pp*

Before the discussion on the details of the approach, we present the most important result of this work, namely the correlation function. In fig. 1 left panel, we show that our hydrodynamic picture indeed leads to a near-side ridge, around $\Delta\eta = 0$, extended over many units in $\Delta\eta$. In fig. 1 right panel, we show in the corresponding result for the pure basic string model, without hydro evolution. There is no ridge any more! This shows that the hydrodynamical evolution "makes" the effect. One should note that the correlation functions are defined and normalized as in the CMS publication, so we can say that our "ridge" is quite close in shape and in magnitude compared the experimental result. The experimental high multiplicity bin corresponds to about 7 times average, whereas in our calculation (extremely demanding concerning CPU power) "high multiplicity" refers to 5.3 times average (we actually trigger on events with 10 elementary scatterings). We cannot go beyond at the moment.

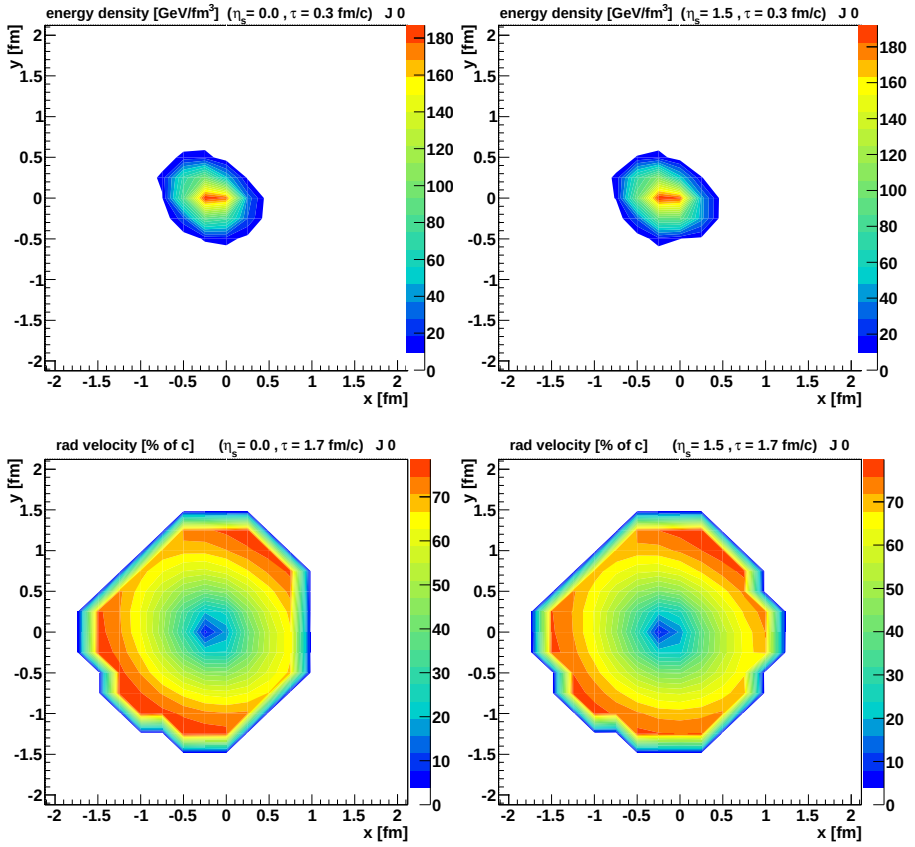

Figure 2: (Color online) Initial energy density (upper panel) and radial flow velocity at a later time (lower panel) for a high multiplicity *pp* collision at 7 TeV at a space-time rapidity $\eta_s = 0$ (left) and $\eta_s = 1.5$ (right).

It is easy to understand the origin of the ridge, in a hydrodynamical approach based on flux tube initial conditions. Imagine many (say 20) flux tubes of small transverse size (radius ≈ 0.2 fm), but very long (many units of space-time rapidity η_s). For a given event, their transverse

positions are randomly distributed within the overlap area of the two protons. Even for zero impact parameter (which dominated for high multiplicity events), this randomness produces azimuthal asymmetries, as shown in fig. 2, upper panel. The energy density obtained from the overlapping flux tubes (details will be discussed later) shows an elliptical shape. And since the flux tubes are long, and only the transverse positions are random, we observe the same asymmetry at different longitudinal positions ($\eta = 0$ and $\eta = 1.5$ in the figure). So we observe a translational invariant azimuthal asymmetry! If one takes this asymmetric but translational invariant energy density as initial condition for a hydrodynamical evolution, the translational invariance is conserved, and in particular translated into other quantities, like the flow. In fig. 2, lower panel, we show the radial flow velocity at a later time again at the two space-time rapidities $\eta_s = 0$ (left) and $\eta_s = 1.5$ (right). In both cases, the flow is more developed along the direction perpendicular to the principal axis of the initial energy density ellipse. This is a very typical fluid dynamical phenomenon, referred to as elliptical flow. Important for this discussion: the asymmetry of the flow is again translational invariant, the same for different values of η_s.

Finally, particles are produced from the flowing liquid, with a preference in the direction of large flow. This preferred direction is therefore the same at different values of η_s. And since η_s and pseudorapidity η are highly correlated, one observes a $\Delta\eta\Delta\phi$ correlation, around $\Delta\eta = 0$, extended over many units in $\Delta\eta$: a particle emitted a some pseudorapidity η has a large chance to see a second particle at any pseudorapidity to be emitted in the same azimuthal direction.

Our "flux tube + hydro" approach has been extensively discussed in [3,4]; the main features being a crucial event-by-event treatment of the hydrodynamic evolution (3D treatment, realistic equation of state), where the initial condition for each event is obtained from an EPOS 2 calculation. This is a multiple scattering approach, formulated in Gribov-Regge fashion using cutting rule techniques in order to obtain partial cross sections of string distributions[7]. In case of very high energy proton-proton scattering, the density of strings will be so high that they cannot possibly decay independently. For technical reasons, we split each string into a sequence of string segments, at a given proper-time τ_0. One distinguishes between string segments in dense areas (more than some critical density ρ_0 of segments per unit volume), from those in low density areas. The high density areas are referred to as core, the low density areas as corona. String segments with transverse momentum larger than some $p_t^{\rm cut}$ (close to a kink) are excluded from the core. Based on the four-momenta of infinitesimal string segments, one computes the energy density $\varepsilon(\tau_0, \vec{x})$ and the flow velocity $\vec{v}(\tau_0, \vec{x})$, which serve as initial conditions for the subsequent hydrodynamic evolution, which lets the system expand and cool down till freeze out at some T_H according to the Cooper-Frye prescription.

3 Minimum Bias Results

In the following we will compare two different scenarios: the full calculations, including hydro evolution (full), and a calculation without hydrodynamical evolution (base). In fig. 3, we show pseudorapidity distributions of charged particles, compared to data from ALICE [8] . The two scenarios do not differ very much, and agree roughly with the data. We then investigate transverse momentum distributions. Here the base calculation (without hydro) underestimates the data at intermediate p_t by a large factor, whereas the full calculation gets close to the data. This is a very typical behavior of collective flow: the distributions get harder at intermediate values of p_t (around 1-5 GeV/c). As a consequence this type of distributions showing some collective effect already in pp should not be used as reference spectra for the heavy ion collisions. In order not to underestimate the collective effects in PbPb scattering at LHC, only the low multiplicity pp events should be used as reference.

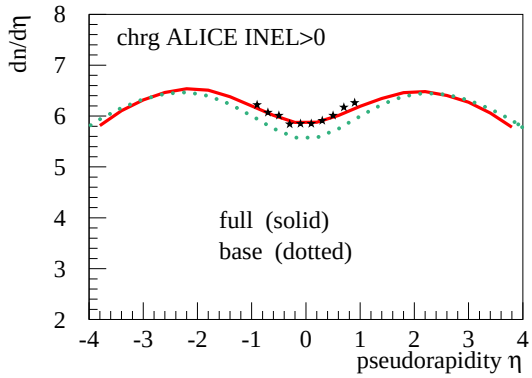

Figure 3: Pseudorapidity distribution in *pp* scattering at 7 TeV (INEL¿0 trigger) for the full calculation (solid line) or without hydrodynamic evolution (dotted), compared to data (points).

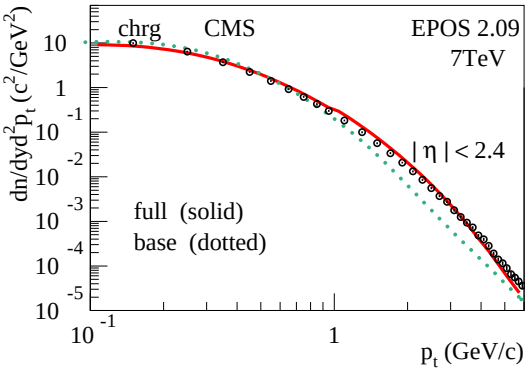

Figure 4: Transverse momentum distributions in *pp* scattering at 7 TeV, for the full calculation (solid line) or without hydrodynamic evolution (dotted) compared to data (points).

4 Summary

Our hydrodynamic approach based on flux tube initial conditions, which has already been applied to explain very sucessfully hundreds of of spectra in AuAu collisions at RHIC, and which excellently describes the so-far published LHC spectra and Bose-Einstein correlation functions, provides in a natural fashion a so-called near-side ridge correlation in $\Delta\eta$ and $\Delta\phi$. This structure appears as a consequence of a longitunial invariant asymmetry of the energy density from overlapping flux tubes, which translates into longitudinal invariant elliptical flow. The presence of collective effect in *pp* scattering being established, we showed that the effect on transverse momentum distributions is not negligible and should be taken into account when using *pp* distributions as reference for the PbPb spectra.

Acknowledgments

This research has been carried out within the scope of the ERG (GDRE) "Heavy ions at ultra-relativistic energies", a European Research Group comprising IN2P3/CNRS, Ecole des Mines de Nantes, Université de Nantes, Warsaw University of Technology, JINR Dubna, ITEP Moscow, and Bogolyubov Institute for Theoretical Physics NAS of Ukraine. Iu. K. acknowledges partial support by the MESU of Ukraine, and Fundamental Research State Fund of Ukraine, agreement No F33/461-2009. Iu.K. and K.W. acknowledge partial support by the Ukrainian-French grant "DNIPRO", an agreement with MESU of Ukraine No M/4-2009. T.P. and K.W. acknowledge partial support by a PICS (CNRS) with KIT (Karlsruhe).

References

1. CMS Collaboration, CERN-PH-EP/2010-031
2. P. Huovinen, in Quark-Gluon Plasma 3, eds. R. C. Hwa and X. N. Wang (World Scientific, Singapore, 2004)
3. K. Werner *et al.*, Phys. Rev. **C83** (2011) 044915.
4. K. Werner *et al.*, Phys. Rev. **C82** (2010) 044904.
5. K. Werner *et al.*, [arXiv:1104.2405 [hep-ph]].
6. K. Werner, I. .Karpenko, T. Pierog, Phys. Rev. Lett. **106** (2011) 122004.
7. H. J. Drescher *et al.*, Phys. Rept. 350, 93, 2001
8. ALICE collaboration, Aamodt *et al.*, [arXiv:1004.3514]
9. CMS Collaboration, V. Khachatryan *et al.*, [arXiv:1005.3299]

ABOUT THE HELIX STRUCTURE OF THE LUND STRING

Šárka Todorova-Novaá
Tufts University, Department of Physics and Astronomy, 4 Colby St, Medford, MA-02155, U.S.A.

An alternative fragmentation scenario based on the assumption of existence of a helix-like ordered gluon field at the end of parton cascade provides a significantly better description of hadronic Z^0 data. The model predicts azimuthal ordering of direct hadrons which should be visible also at Tevatron and LHC.

1 Introduction

The idea of the formation of a helix-like ordered gluon field at the end of the parton cascade has been proposed by Andersson et al. [1], on the basis of the study of the optimal packing of soft gluons in the phase space under the helicity conservation rules. The replacement of the 1-dimensional string with a 3-dimensional object has direct impact on the modelling of the intrinsic transverse momenta of direct hadrons. In the standard Lund fragmentation algorithm, the transverse momentum is created in the tunneling process, assuming local momentum conservation and no correlation between size and direction of the transverse momentum between breaking points. In the model with helix-like structure of the QCD field, the string tension operates in the transverse plane and there is no need to assign an additional transverse momentum to partons emerging in the tunneling process. Without the additional component of the transverse momentum from the tunneling process, the transverse momentum (p_T) of the emerging hadron is entirely defined by the transverse structure of the QCD field in between the adjacent string break-up points. Observable effects can be expected both in the inclusive p_T spectrum (especially in the low p_T region dominated by the fragmentation effects), and in the azimuthal ordering of hadrons.

It is important to note that the form of the helix field is not entirely predicted and that it is possible to find several parametrization of the helix field which are conform to the assumptions made in [1].

2 Helix string model(s)

The original proposal linked the difference in the helix phase to the rapidity difference along the string

$$\Delta\Phi = \Delta y/\tau \tag{1}$$

where τ is a parameter and $\Delta\Phi$ stands for difference in the helix phase corresponding to the rapidity difference Δy along the string (for details consult [1]). The model predicted a visible effect in the azimuthal ordering of hadrons, but the dedicated analysis of LEP data failed to produce a significant signal [2].

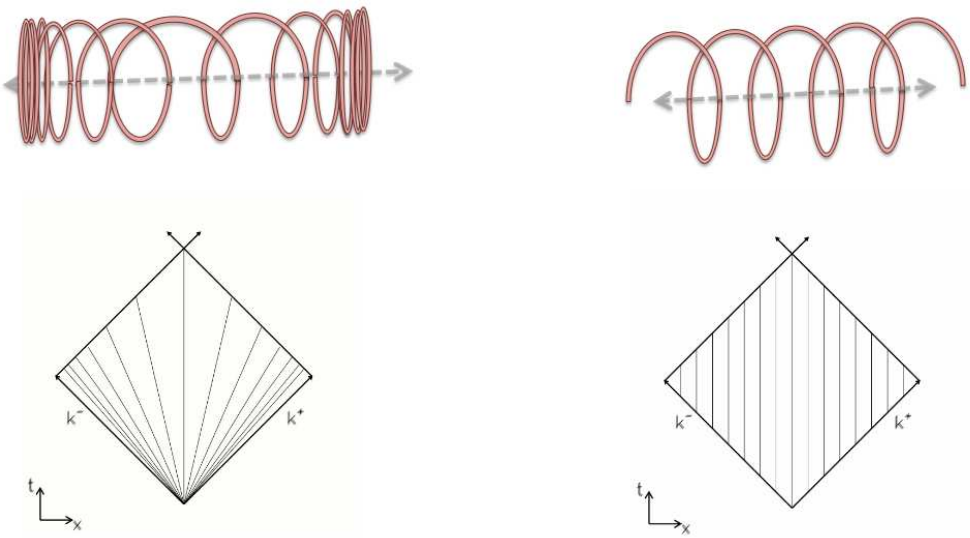

Figure 1: Helix string parametrizations. Left: original proposal (Eq.1). Right: modified helix scenario (Eq.2). The lines in the string area diagram connect points with identical helix phase.

A modified version of the helix string scenario has been proposed in [3], with helix phase difference proportional to the amount of energy stored in the QCD string (in the string rest frame)

$$\Delta\Phi = S\ \kappa\ \Delta l \tag{2}$$

where S is a parameter, κ is string energy density, and Δl is distance (along the string) separating points with helix phase difference $\Delta\Phi$.

The difference between models is illustrated by Fig. 1. In the original helix string scenario, the helix winding becomes faster towards string endpoints, while the modified scenario defines a regular, static helix structure.

3 Experimental signature

The modified helix string fragmentation scenario (Eq.2) predicts a number of features which can be observed experimentally. The size of transverse momentum p_T of a direct hadron is correlated with its energy E (in the rest frame of the string) via relation

$$|\vec{p_T}| = 2\ r|sin(0.5\ S\ E)| \tag{3}$$

where r stands for radius of the helix structure. The correlations are shown in Fig. 2 (left) for a toy case of simple hadronic system without hard gluon kinks. Fig. 2 (right) shows the difference between the standard p_T modelling (via tunneling) and the helix driven p_T modelling in the inclusive p_T spectrum. Direct observation of $E-p_T$ correlations is difficult due to the smearing by parton shower, but the qualitative difference in the shape of the inclusive spectrum is preserved. Interestingly enough, such type of discrepancy is readily observed in hadronic data [4,5].

The parameters of the helix string model have been adjusted using LEP data with help of Rivet/Professor tools [6]. A simultaneous tuning of 6 parameters (including helix radius r, pitch S, Lund parameters (a, b), parton shower cut-off and effective coupling constant Λ_{QCD}) has been performed for two parton shower algorithms (Pythia p_T ordered parton shower [7] and Ariadne parton shower [8]) interfaced to private implementation of the helix string fragmentation algorithm

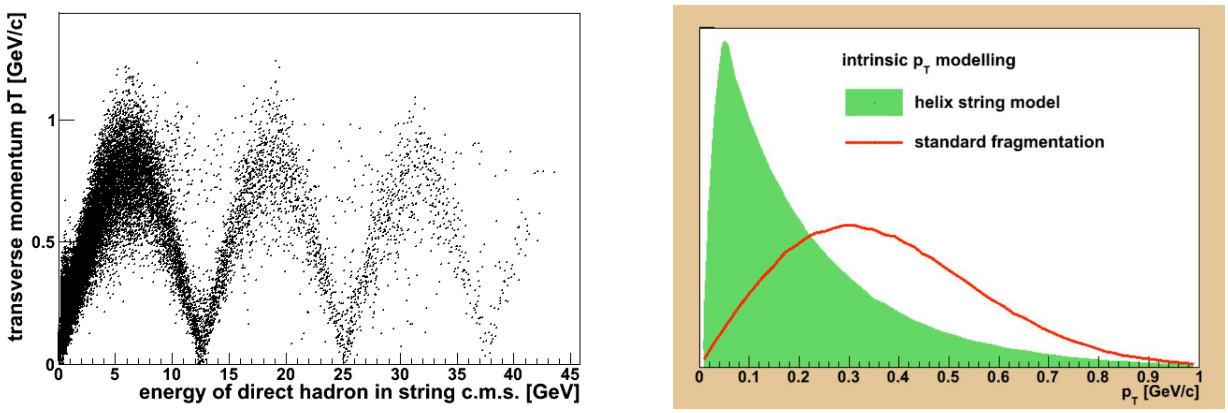

Figure 2: Left: Correlations between the energy and the size of the transverse momentum for direct hadrons produced in the fragmentation of a simple $q\bar{q}$ helix string with structure given by (Eq.2). Right: The impact of the helix string fragmentation on the inclusive p_T spectrum of final charged hadrons. Pythia modelling of hadronic Z^0 decays with suppressed parton shower (generator level study) .

[9]. The global results of the tune - the χ^2 difference with respect to the data - are shown in Table 1. Fragmentation of the helix-like structured string describes the data significantly better than the standard Lund string fragmentation, despite the limited scope of the tuning (identified particle spectra and heavy quark distributions have not been included in the tune). The tuned helix string parameters and further details can be found in [10]. The results can be attributed to the interplay between intrinsic p_T modelling and the effect of the parton shower, and the study is an excellent illustration of the fact that a better description of the soft region (here with helix string fragmentation) has a significant impact on the overall description of the data.

The helix-like ordering of gluons should also translate into *ordering of hadrons in the azimuthal angle*, experimentally observable via spectral analysis of characteristic correlations between azimuthal opening angle of a pair of hadrons and the energy-distance between them (measured along the string). Though it is impossible to reconstruct the history of the string fragmentation from the knowledge of the momenta of final hadrons only, the generator level studies suggest an approximate ordering of final hadrons in rapidity (or pseudorapidity), retains enough sensitivity to detect the presence of azimuthal ordering. The measurement can be performed using LEP data, or so called minimum bias sample collected by hadron colliders (Tevatron,LHC).

At hadron colliders, the measurement of the azimuthal ordering can be performed in 'soft' event selection, with a cut on maximal hadron $p_T \sim 1$ GeV/c, which should select events where fragmentation effects dominate over contribution from the parton shower.

Data set	Pythia [11]	helix + Pythia	Ariadne	helix + Ariadne
inclusive spectra + event shapes $N_{bin} = 619$	4075	2453	2453	1489
ident.part.rates + b-fragmentation $N_{bin} = 47$	444	669(*)	614(*)	586(*)

Table 1: Sum (over all bins) of χ^2 difference between data and models. The 'Pythia/Ariadne' labels distinguish between Pythia 6.421 pT-ordered parton shower, and Ariadne 4.12 parton shower. (*) distributions not included in the tune.

The azimuthal ordering should be visible as a peak in a suitably defined power spectrum (in order to obtain a clear signal, the definition of the power spectrum has to reflect the parametrization of the helix string structure, see discussion in [3]). A typical size and position of the expected signal is shown in Fig. 3, based on the prediction of the helix string model tuned at LEP data.

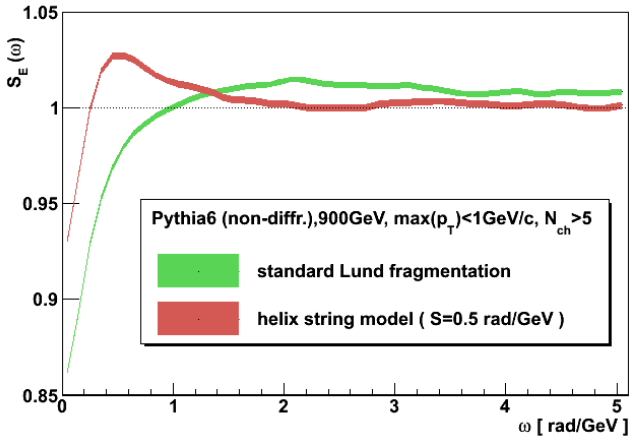

Figure 3: Azimuthal ordering of hadrons can be detected as a peak in the power spectrum defined according to the expected helix structure. Pythia modelling of non-diffractive events at $\sqrt{s}$=900 GeV. Generator level study.

4 Conclusions

The hypothesis of the existence of a helix-like ordered gluon field explains some characteristic discrepancies between modelling of hadronic processes and the data. The interplay between soft non-perturbative region and the parton shower activity is better described using the helix string hypothesis (the comparison is done using a representative set of inclusive charged spectra and event shape variables). The helix string scenario predicts azimuthal ordering of direct hadrons, experimentally observable at LHC. If confirmed, such an effect may be considered a first direct evidence in favour of the helix-like QCD string.

References

1. B. Andersson, G. Gustafson, J. Hakkinen, M. Ringner and P. Sutton, JHEP **9809** (1998) 014 [arXiv:hep-ph/9807541].
2. DELPHI Coll., DELPHI 98-156 PHYS 799.
3. Š. Todorova,[arXiv:1101.2407]
4. DELPHI Coll., Z. Phys. C73 (1996) 11., CERN-PPE/96-120.
5. New J.Phys.13 (2011) 053033.
6. A. Buckley, H. Hoeth, H. Lacker, H. Schulz and J. E. von Seggern, doi:10.1140/epjc/s10052-009-1196-7.
7. T. Sjöstrand, S. Mrenna and P. Z. Skands, JHEP **0605** (2006) 026 [arXiv:hep-ph/0603175].
8. L.Lönnblad, Comput.Phys.Commun. 71 (1992) 15.
9. Š. Todorova, https://nova.www.cern.ch/nova/helix.html
10. Š. Todorova,[arXiv:1012.5778]
11. H. Schulz, private communication.

Improving NLO-parton shower matched simulations with higher order matrix elements

K.M. HAMILTON and P.NASON
INFN, Sezione di Milano Bicocca,
Piazza della Scienza 3, 20126 Milan, Italy.

We examine the criteria to be met in unifying matrix element-parton shower (MEPS) merging and next-to-leading order-parton shower (NLOPS) matching methods, in such a way as to preserve their best features and negate their deficiencies. We are naturally led to consider the extent to which these requirements can be met today, using existing simulations, without modification. Based on this analysis we tender a pragmatic proposal for merging MEPS and NLOPS events to yield much improved MENLOPS event samples. We present a small sample of results obtained by applying the method to the simulation of W boson production, where it yields marked improvements over the pure NLOPS approach for observables sensitive to multi-jet radiation, while leaving the NLO accuracy of inclusive quantities fully intact.

1 Introduction

Currently there are two proven methods, MC@NLO and POWHEG [1,2,3], for including NLO corrections within parton shower algorithms. Simulations based on these approaches provide predictions for infrared safe observables with full NLO accuracy, reverting to the conventional parton shower approximation to generate features of events associated with further higher order corrections, beyond NLO, e.g. multiple emissions. Despite the obvious advantages associated with promoting parton shower event generators to NLO accuracy (NLOPS), such simulations are not sufficiently versatile to model all features of the data in detail. In particular, since the parton shower approximation is typically used to describe all but the hardest emission, these event generators do not offer a satisfactory description of particle production in association with multiple hard jets.

The other leading advancement in this area of research aims to improve the simulation of precisely this class of events. These matrix element-parton shower (MEPS) merging procedures take parton level events, of assorted multiplicity, from tree level event generators, and dress them with parton showers, yielding event samples smoothly populating all of phase space, without overcounting any regions. The distribution of the hard emissions, and hence jets, is then governed by the exact real matrix elements, while only the jet substructure is determined by the parton shower; previously the former was only simulated according to the multiple soft and collinear limits of those same matrix elements. Like the NLOPS case, MEPS methods are also not without their shortcomings. Since MEPS simulations are fundamentally constructed from tree level matrix elements and leading-log resummation, predictions for inclusive observables based on these calculations exhibit acute sensitivity to the renormalization and factorization scales.

Clearly the NLOPS and MEPS approaches are complementary. Futhermore, for both classes of simulation there now exists a substantial and rapidly growing number of phenomenologically

important event generator packages. It is therefore natural to look for a means to unify them, ideally, with little or no interference to the existing mature body of computer code.

We compare the MEPS and NLOPS approaches, quantifying their best features, with a view to defining what is required to obtain an exact theoretical solution of the merging problem. Motivated by the presence of the large number of validated MEPS and NLOPS simulations available today, we then seek to address the question of how close one may get to achieving a theoretically exact merging, simply by manipulating the event samples which they produce.

Although the method that we ultimately advocate proves very much adequate for practical applications, theoretically, it is not an exact solution to the merging problem. In this work we have, however, accomplished two important goals: firstly, we have clarified what is needed in order to achieve a full theoretical solution of the merging problem; second, we have found a practical method to merge MEPS and NLOPS simulations that can be immediately applied to processes for which such simulations already exist.

2 Theoretical considerations for NLOPS and MEPS combination: MENLOPS

In the following we shall discuss the problem of MEPS-NLOPS merging with reference to the POWHEG formalism and conventions used therein. The NLO accuracy of this approach is encoded in the so-called hardest emission cross section, the cross section for the hardest radiated particle in the inclusive process. For a simple process, one for which the NLO kinematics can be seen to comprise of just one singular region, e.g. the beam axis in W production, this can be written [2]

$$\mathrm{d}\sigma_{\mathrm{PW}} = \overline{B}\left(\Phi_B\right)\,\mathrm{d}\Phi_B\,\left[\Delta_R\left(p_T^{\min}\right) + \frac{R\left(\Phi_R\right)}{B\left(\Phi_B\right)}\,\Delta_R\left(k_T\left(\Phi_R\right)\right)\,\mathrm{d}\Phi_{\mathrm{rad}}\right], \tag{1}$$

where the function $\overline{B}\left(\Phi_B\right)$ is the NLO cross section differential in the Born kinematic variables Φ_B — for vector boson production Φ_B may be taken to be the mass and rapidity of the produced boson, for example. The function $R(\Phi_R)$ is the real emission cross section with $\Phi_R = (\Phi_B, \Phi_{\mathrm{rad}})$, Φ_{rad} being the *radiative variables*, specifying the kinematics of the hardest emitted parton with respect to the configuration Φ_B. Lastly, the POWHEG Sudakov form factor is defined as

$$\Delta_R\left(p_T\right) = \exp\left[-\int \mathrm{d}\Phi_{\mathrm{rad}}\,\frac{R\left(\Phi_R\right)}{B\left(\Phi_B\right)}\,\theta\left(k_T\left(\Phi_R\right) - p_T\right)\right], \tag{2}$$

where k_T is equal to the transverse momentum of the radiated parton in the collinear limit.

The key feature of the hardest emission cross section through which NLO accuracy is attained, is its *unitarity* with respect to the Born kinematics, Φ_B, specifically, the fact that integral over Φ_{rad} at fixed Φ_B yields one. This unitarity arises by virtue of the fact that the Sudakov form factor and the coefficient which multiplies it, form an exact differential $\mathrm{d}\Delta_R$. Noting this one can see immediately, for example, that observables depending only on Φ_B are determined with NLO accuracy, since $\overline{B}\left(\Phi_B\right)$ is the NLO cross section differential in those variables. This unitarity is also central in the proof that other more general observables are also accurate at NLO, for which we invite the reader to see Frixione *et al* for a proof.[3]

On general grounds we may express the cross section for the hardest emission in a MEPS simulation in a similar form:

$$\mathrm{d}\sigma_{\mathrm{ME}} = B\left(\Phi_B\right)\,\mathrm{d}\Phi_B\,\left[\Delta_{\widehat{R}}\left(p_T^{\min}\right) + \frac{\widehat{R}\left(\Phi_R\right)}{B\left(\Phi_B\right)}\,\Delta_{\widehat{R}}\left(k_T\left(\Phi_R\right)\right)\,\mathrm{d}\Phi_{\mathrm{rad}}\right]. \tag{3}$$

By contrast to the POWHEG case, the prefactor here, $B(\Phi_B)$, is the leading order cross section differential in Φ_B, as opposed to the NLO one. Also, the $\widehat{R}\left(\Phi_R\right)$ function differs by an amount of relative order α_{S} with respect to the exact NLO real emission cross section, $R\left(\Phi_R\right)$, in Eq. 1,

due to the inclusion of higher order multi-leg matrix elements in the MEPS simulation. Lastly, the Sudakov form factor $\Delta_{\widehat{R}}(k_T(\Phi_R))$ is not the same as that in Eq. 2 but rather it is something one cannot generally claim to have full analytic control over; qualitiatively speaking, it is some convolution of the parton shower Sudakov form factor, in the regions of phase space where the shower generates radiation, and the external Sudakov suppression weights applied to the bare matrix element configurations, populating the remaining wide angle emission phase space.

Naively, considering Eq. 1, it is tempting to think that by reweighting MEPS events by the ratio $\overline{B}(\Phi_B)/B(\Phi_B)$ one may imbue it with NLO accuracy. While this is indeed a step toward promoting the MEPS simulation to NLO accuracy, it is only part of the story. Crucially, the fact that the exponent of the Sudakov form factor in the MEPS simulation is not the same as its coefficient, $\widehat{R}(\Phi_R)/B(\Phi_B)$, (beyond the collinear limit) means that the second term in Eq. 3 is not an exact differential and so the MEPS hardest emission cross section is not unitary. In general the integral over the radiative phase space for a given Φ_B in the MEPS case does not identically equal one but rather a function $N(\Phi_B) \sim 1 + \mathcal{O}(\alpha_S)$. Thus, to promote a MEPS simulation to NLOPS accuracy, while retaining the benefits of the real emission matrix elements beyond the NLO ones, one must determine precisely, numerically, the function $N(\Phi_B)$ and reweight the events instead by the ratio $\overline{B}(\Phi_B)/(B(\Phi_B)N(\Phi_B))$.

Clearly there are a number of other theoretical details to be addressed before one can claim this as a general solution to the MEPS-NLOPS merging problem, however, we consider what we have presented to be sufficient for implementing MENLOPS matching in simple processes e.g. vector boson / Higgs boson production.

3 A practical proposal for producing MENLOPS samples

Even for simple processes it is clear that the reweighting procedure we advocate, despite its apparent simplicity, is nevertheless *technically* somewhat challenging to implement. The determination of the $\overline{B}(\Phi_B)$ and unitarity violating $N(\Phi_B)$ functions is inevitably computationally intensive, as is the usual generation of the MEPS sample itself (many of whose events will be discarded in the NLO reweighting procedure).

Prior to embarking on protracted and computationally demanding exercises, such as that implied here, having understood the key criteria to be adhered to, it is prudent to consider whether one may arrive at a working solution by some more economical route. In particular, given the large volume of publicly available MEPS and NLOPS code, it is worth considering how far one can get towards producing MENLOPS samples by judiciously combining their outputs, rather than interfering with the code itself.

Having taken time to appreciate the connection between unitarity and NLO accuracy in POWHEG simulations, we make the following simple observation: if it is the case that the $\geq$2-jet fraction of the NLOPS sample is less than a fraction α_S of the total, one can effectively replace it by the same number of MEPS $\geq$2-jet events — equivalent in their distribution up to *relative* terms $\mathcal{O}(\alpha_S)$ — while impacting on inclusive observables at the NNLO level only. Of course, the fact that the $\geq$2-jet component of the sample is formed by the MEPS generator means, by construction, that multi-jet events are now described according to the relevant multi-leg matrix elements. In this way, adhering to the condition that the $\geq$2-jet fraction be less than α_S, we may always improve on pure NLOPS event samples by taking the $\geq$ 2-jet component from the MEPS simulation, at no cost to its NLO accuracy.

We are then led to construct approximate MENLOPS event samples combining MEPS and POWHEG events according to their jet multiplicities in the following proportions[4]

$$\mathrm{d}\sigma = \mathrm{d}\sigma_{\mathrm{PW}}(0) + \frac{\sigma_{\mathrm{PW}}(\geq 1)}{\sigma_{\mathrm{ME}}(\geq 1)} \frac{\sigma_{\mathrm{ME}}(1)}{\sigma_{\mathrm{PW}}(1)} \mathrm{d}\sigma_{\mathrm{PW}}(1) + \frac{\sigma_{\mathrm{PW}}(\geq 1)}{\sigma_{\mathrm{ME}}(\geq 1)} \mathrm{d}\sigma_{\mathrm{ME}}(\geq 2), \tag{4}$$

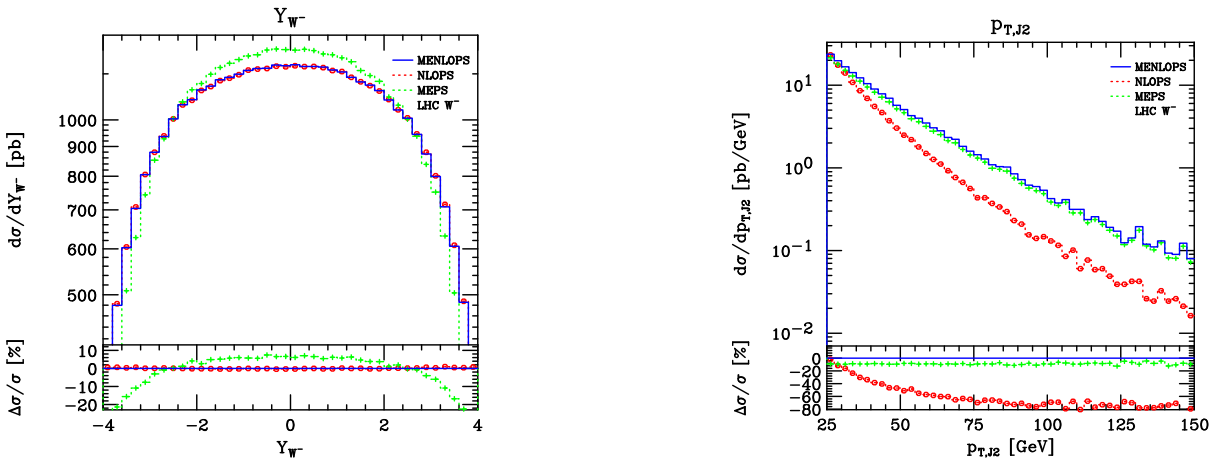

Figure 1: Rapidity of the vector boson (left) and p_T spectrum of the second jet (right) in W boson production at the LHC. Blue histograms show the MENLOPS predictions, while NLOPS and MEPS predictions are depicted as red circles and green crosses, respectively.

$\sigma_{\mathrm{PW/ME}}(j)$ denoting the cross section for producing j jets in the POWHEG / MEPS methods.

The limit on the $\geq$2-jet component of the merged MENLOPS sample directly translates into a lower bound on the jet radius parameter used to divide the NLOPS and MEPS samples prior to combination (the MENLOPS merging scale). The MEPS simulation also involves a jet merging scale beneath which the distribution of radiation is determined by the parton shower approximation applied to the hard matrix element configurations generated above it. The difference in the two merging scales defines a region in phase space, in the $\geq$2-jet part of the sample, where the MEPS simulation benefits from the use of higher order matrix elements where, in the same window of jet radii, the MENLOPS sample distributes jets according to a parton shower approximation applied to a hard single emission configuration. The key question concerning the quality of the approximation in Eq. 4 then is: how close can one take the MENLOPS merging scale to that used in the MEPS simulation while keeping $\sigma(\geq 2) < \alpha_S$? If the condition on the $\geq$ 2-jet fraction can be met and the window between the jet merging scales is small, or zero, then the exact reweighting method becomes academic with respect to the simple one in Eq. 4.

4 Results: *W* boson production

We applied the simple prescription in Eq. 4 to the simulation of W boson production in 14 TeV pp collisions. We were able to merge a POWHEG sample with a MEPS sample with the MENLOPS merging scale taken down at the minimal MEPS one (20 GeV in the exclusive k_T clustering algorithm). The NLO and multi-jet accuracy of the results are clear in Fig. 1; for inclusive observables the MENLOPS and pure NLOPS predictions are indistinguishable, while for exclusive jet observables they assume the form of the superior MEPS simulation.

References

1. S. Frixione and B. R. Webber, *JHEP* **0206** (2002) 029
2. P. Nason, *JHEP* **0411** (2004) 040
3. S. Frixione, P. Nason, and C. Oleari, *JHEP* **0711** (2007) 070
4. K. Hamilton, P. Nason, *JHEP* **1006** (2010) 039

New Results in Soft Gluon Physics

C.D. WHITE
School of Physics and Astronomy, University of Glasgow, Glasgow G12 8QQ, Scotland, UK

We examine soft gluon physics, focusing on recently developed path integral methods. Two example applications of this technique are presented, namely the classification of soft gluon amplitudes beyond the eikonal approximation, and the structure of multiparton webs. The latter reveal new mathematical structures in the exponents of scattering amplitudes.

1 Introduction

It is well-known that QCD radiation leads to unstable results in perturbation theory when the momentum of the emitted radiation becomes low ("soft"). Typically, if ξ is some dimensionless energy variable representing the total energy carried by soft gluons, then one finds differential cross-sections of the form

$$\frac{d\sigma}{d\xi} = \sum_{n,m} \alpha_S^n \left[c_{nm}^0 \frac{\log^m(\xi)}{\xi} + c_{nm}^1 \log^m(\xi) + \dots \right] \tag{1}$$

involving large logarithms (of soft origin) to all orders in perturbation theory. Here the first set of terms can be obtained from the so-called *eikonal approximation*, in which the momentum of the emitted gluons formally goes to zero. Much is known already about these logarithms. The second set of terms arises from the *next-to-eikonal (NE) limit*, corresponding to a first order expansion in the momentum of the emitted gluons. These logarithms, although suppressed by a power of the energy scale ξ, can be numerically significant in many scattering processes.

In the soft phase-space region in which $\xi \to 0$, the above perturbation expansion breaks down in that all terms become large. The solution to this problem is to work out the logarithms to all orders in the coupling constant and sum them up ("resummation"). This is by now a highly developed subject, and many different approaches already exist for summing eikonal logarithms (e.g. Feynman diagram approaches, SCET). Here I will explain the basic idea using the *web* approach [1,2,3], and using the schematic scattering process shown in figure 1. This consists of a

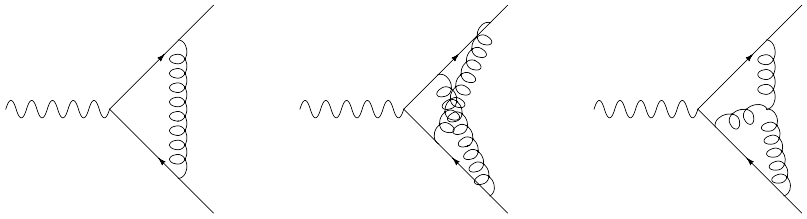

Figure 1: Schematic hard scattering process dressed by soft gluons.

hard interaction (in this case a virtual photon and quark pair of nonzero momentum), which is dressed by gluons (we do not distinguish real and virtual emissions in the figure). When these gluons become soft, this generates the large logs in eq. (1). However, one may show that the soft gluon diagrams *exponentiate*. That is, if $\mathcal{A}$ is the amplitude for the Born interaction $\mathcal{A}_0$ dressed by any number of soft gluons, one has [1,2,3]

$$\mathcal{A} = \mathcal{A}_0 \exp\left[\sum \tilde{C}_W W\right], \tag{2}$$

where the sum in the exponent is over soft-gluon diagrams W. This is a powerful result for two reasons. Firstly, large logs coming from the soft gluon diagrams sit in an exponent, thus get summed up to all orders in perturbation theory. Secondly, not all soft gluon diagrams have to be calculated. It turns out that only those which are irreducible ("webs") need to be considered, and the first few examples are shown in figure 1. The webs have modified colour factors $\tilde{C}(W)$, which are not the usual colour factors of perturbation theory, and these are zero for non-webs. We see that crucial to resummation is the notion of exponentiation, and indeed this is common to all other approaches.

Having very briefly reviewed soft gluon physics, let us now focus on the following open problems:

1. *Can we systematically classify next-to-eikonal logarithms?* As remarked above, much less is known about the second set of logs in eq. (1) than the first set. A number of groups have looked at this in recent years [4,5,6,7,8,9].

2. *What is the equivalent of webs for multiparton processes?* The webs of [1,2,3] are only set up for cases in which two coloured particles interact e.g. Drell-Yan production, deep inelastic scattering, $e^+e^- \to q\bar{q}$ etc. Recent work has tried to generalise the web concept to processes with many coloured particles [10,11], which are ubiquitous at hadron colliders.

Both of these questions are conveniently addressed using the path integral technique for soft gluon resummation. The essential idea of this approach is that QCD scattering processes are rewritten in terms of (first-quantised) path integrals over the trajectories of the hard emitting particles. To see what this means in more detail, consider the cartoon shown in figure 2, which shows Drell-Yan production, in which incoming quarks fuse to make a final state vector boson. If we think about this process in position space, the incoming particles can emit gluons at various places along their spacetime trajectories. We have already seen that the eikonal approximation (which gives the first set of logs in eq. (1)) corresponds to the emitted gluons having zero momentum. Then the incoming particles do not recoil, and so follow classical straight line trajectories. Beyond the eikonal approximation, each trajectory will get a small kick or wobble upon emission of a gluon. The sum over all possible wobbles that each trajectory can have is equivalent, in a well-defined sense, to a sum over possible gluon emissions of nonzero momentum. The sum over wobbles of a trajectory is nothing other than a Feynman path integral, as used in Feynman's original formulation of quantum mechanics. Thus, it follows that there should be a

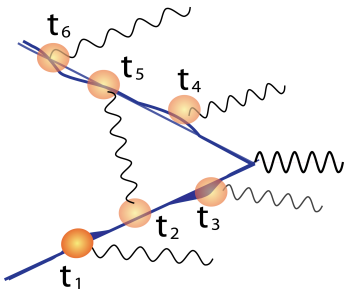

Figure 2: Spacetime depiction of Drell-Yan production, showing the trajectories of the incoming quarks.

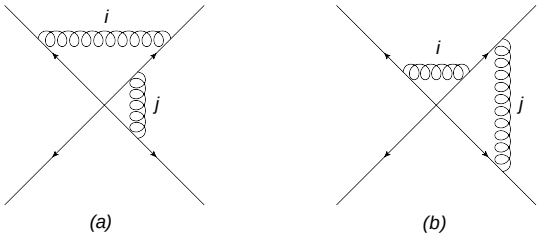

Figure 3: Example web at two loop order, for a four parton process.

description of soft gluon physics in terms of path integrals for the hard external particles, where the leading term of each path integral (the classical trajectory) gives the eikonal approximation. If one can then somehow systematically expand about the classical trajectory and keep the "first-order set of wobbles", this gives the next-to-eikonal corrections [8]. With this approach, we have proved that the structure of NE corrections to scattering amplitudes has the generic form

$$\mathcal{A} = \mathcal{A}_0 \exp\left[\mathcal{M}^E + \mathcal{M}^{NE}\right] \times [1 + \mathcal{M}_{rem.}] + \mathcal{O}(NNE). \tag{3}$$

Here the left-hand side denotes the amplitude for a given Born interaction $\mathcal{A}_0$ dressed by soft and next-to-soft gluons. The first term in the exponent denotes eikonal webs [1,2,3], and the second term constitutes next-to-eikonal webs. Finally there is a remainder term whose interpretation is also understood [8]. The above formula has been confirmed using an explicit diagrammatic proof, and preliminary calculations in Drell-Yan production have been carried out which pave the way for resummation of next-to-eikonal effects [9]. Interestingly, the same schematic structure of next-to-eikonal corrections also holds in perturbative quantum gravity [12].

We now turn to the second open problem above, that of generalising webs (diagrams which sit in the exponent of the soft gluon amplitude) from two parton to multiparton scattering. In the two parton case of eq. (2), we saw that webs were single (irreducible) diagrams. This becomes more complicated in multiparton processes: webs are no longer irreducible, but become compound sets of diagrams, related in a particular way. Consider, for example, the two diagrams shown in figure 3, which are a two-loop soft gluon correction to a hard interaction involving four partons. Taking diagram (a), we can make a second diagram by permuting the gluons on the upper right-hand line. This gives diagram (b), and by performing the permutation again we get back the original diagram. The graphs thus form a closed set under permutations of gluon emissions. Such closed sets are argued to be the appropriate generalisation of webs to multiparton scattering [10]. The derivation of these results uses the *replica trick*, an elegant technique for proving exponentiation properties which is borrowed from statistical physics.

Each diagram D in a given closed set (web) has a kinematic part $\mathcal{F}(D)$ and a colour factor $C(D)$. In the normal amplitude, these are simply multiplied together. However, in the exponent of the amplitude, the colour and kinematic parts of web diagrams mix with each other. That

is, a single web contributes a term

$$\sum_{D,D'} \mathcal{F}_D R_{DD'} C_{D'} \tag{4}$$

to the soft gluon exponent, where the sum is over diagrams in the web, and $R_{DD'}$ is a *web mixing matrix* which describes how the vectors of kinematic and colour factors are entangled. The study of multiparton webs is thus entirely equivalent to the study of web mixing matrices. They are matrices of constant numbers (e.g. independent of the number of colours) that encode a huge amount of physics! An ongoing goal is to classify general properties of these matrices, and to translate these into physical results.

We already know about some interesting properties. Firstly, any row of any web mixing matrix has elements which sum to zero. Secondly, any web mixing matrix is idempotent, that is $R^2 = R$. The matrices are thus projection operators, having eigenvalues of 0 and 1 (with an appropriate degeneracy). These properties have been interpreted physically [10], and the proofs use both the replica trick and known properties of combinatorics [13]. This latter point is itself interesting, as a pure mathematician could have proved these results without in fact knowing any of the underlying physics. This suggests that there are two ways of finding out more about web mixing matrices - either one may apply known physics constraints and see what this implies in web mixing matrix language, or one may study the matrices from a pure combinatorics point of view, and learn in the process about the entanglement of colour and kinematics [a]!

To summarise, path integral methods prove highly powerful in analysing soft gluon physics, allowing new results to be obtained. Specifically, we have outlined the classification of next-to-eikonal corrections, and also the structure of multiparton webs. The results have application to the resummation of logarithms in cross-sections, but may also have more formal applications in elucidating the structure of scattering amplitudes in a variety of field theory contexts. Investigation of these possibilities is ongoing.

Acknowledgments

I wish to thank the organisers of the Moriond QCD session for a very enjoyable conference, and am also grateful to my collaborators Einan Gardi, Eric Laenen, Lorenzo Magnea and Gerben Stavenga. This research was supported by the STFC Postdoctoral Fellowship "Collider Physics at the LHC".

References

1. J.G.M. Gatheral, *Phys. Lett.* B **B133**, 90 (1983)
2. J. Frenkel and J.C. Taylor, *Nucl. Phys.* B **B246**, 231 (1984)
3. G. Sterman in *AIP Conf. Proc.*, **74**, 22 (1981)
4. E. Laenen, L. Magnea and G. Stavenga, *Phys. Lett.* B **B669**, , (173)2008
5. S. Moch and A. Vogt, JHEP **11**, 099 (2009)
6. G. Soar, S. Moch, J.A.M. Vermaseren and A. Vogt,*Nucl. Phys.* B **B832**, 152 (2010)
7. G. Grunberg and V. Ravindran, JHEP **10**, 055 (2009)
8. E. Laenen, G. Stavenga and C. D. White, JHEP **0903**, 054 (2009)
9. E. Laenen, L. Magnea, G. Stavenga and C. D. White, JHEP **1101**, 141 (2011)
10. E. Gardi, E. Laenen, G. Stavenga and C. D. White, JHEP **1011**, 155 (2010)
11. A. Mitov, G. Sterman and I. Sung, *Phys. Rev.* D **82**, 096010 (2010)
12. C. D. White, JHEP **1105**, 060 (2011)
13. E. Gardi and C. D. White, JHEP **1103**, 079 (2011)

[a] Note that extra complications arise when the renormalisation of webs is considered [11].

Central Exclusive Meson Pair Production in the Perturbative Regime

[a] L.A. Harland-Lang [b]
Cavendish Laboratory, University of Cambridge, J.J. Thomson Avenue, Cambridge, CB3 0HE, UK

V.A. Khoze
Department of Physics and Institute for Particle Physics Phenomenology, University of Durham, DH1 3LE, UK

M.G. Ryskin
Petersburg Nuclear Physics Institute, Gatchina, St. Petersburg, 188300, Russia

W.J. Stirling
Cavendish Laboratory, University of Cambridge, J.J. Thomson Avenue, Cambridge, CB3 0HE, UK

We present a study of the central exclusive production (CEP) of meson pairs [1], $M\overline{M}$, at sufficiently high invariant mass that a perturbative QCD formalism is applicable. Within this framework, $M\overline{M}$ production proceeds via the $gg \to M\overline{M}$ hard scattering sub-process, which can be calculated within the hard exclusive formalism. We present explicit calculations for the $gg \to M\overline{M}$ helicity amplitudes for different meson states and, using these, show results for meson pair CEP in the perturbative regime.

Central exclusive production processes of the type

$$pp(\bar{p}) \to p + X + p(\bar{p}) \,, \tag{1}$$

can significantly extend the physics programme at high energy hadron colliders [2,3,4]. Here X represents a system of invariant mass M_X, and the '+' signs denote the presence of large rapidity gaps. Such reactions provide a very promising way to investigate both QCD dynamics and new physics in hadron collisions [5,6,7,8,9,10,11,12], providing an especially clean environment in which to measure the nature and quantum numbers (in particular, the spin and parity) of new states.

These processes have been measured at the Tevatron by the CDF collaboration, who have published a search for $\gamma\gamma$ CEP [13] with $E_T(\gamma) > 5$ GeV, and many more candidate events have been observed [4] by lowering the $E_T(\gamma)$ threshold to $\sim$2.5 GeV. This process (together with charmonium CEP, the observation of which was reported in [14]), can serve as a 'standard candle' reaction with which we can check the predictions for new physics CEP at the LHC [7,15]. A good quantitative theoretical understanding of the $\pi^0\pi^0$ CEP background is therefore crucial, as one or both of the photons from $\pi^0 \to \gamma\gamma$ decay can mimic the 'prompt' photons from $gg \to \gamma\gamma$ CEP.

As discussed in [5,6,7], the observation of χ_{c0} CEP via two-body decay channels to light mesons is of special interest for both studying the dynamics of heavy quarkonia and for testing the

[a] KRYSTHAL collaboration
[b] speaker

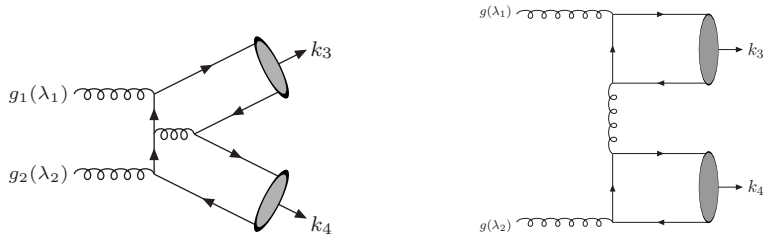

Figure 1: (a) A typical diagram for the $gg \to M\overline{M}$ process. (b) Representative 'ladder' diagram, which contributes to the production of flavour-singlet mesons.

QCD framework of CEP. However, in this case we may expect a sizeable background resulting from direct QCD meson pair production; such a non-resonant contribution should therefore be carefully evaluated.

Studies of meson pair CEP would also present a new test of the perturbative formalism, with all its non-trivial ingredients, from the structure of the hard sub-processes to the incorporation of rescattering effects of the participating particles. Recall [16] that in exclusive processes, the incoming gg state satisfies special selection rules in the limit of forward outgoing protons, namely it has $J_z = 0$, where J_z is the projection of the total gg angular momentum on the beam axis, and positive C and P parity. Hence only a subset of the helicity amplitudes for the $gg \to X$ sub-process contributes. The CEP mechanism therefore provides a unique possibility to test the polarization structure of the $gg \to X$ reaction.

We will consider the $gg \to M\overline{M}$ process relevant to CEP within the 'hard exclusive' formalism, which was used previously [17,18] to calculate the related $\gamma\gamma \to M\overline{M}$ amplitudes. The leading order contributions to $gg \to M\overline{M}$ can be written in the form

$$\mathcal{M}_{\lambda\lambda'}(\hat{s},\theta) = \int_0^1 \mathrm{d}x\,\mathrm{d}y\,\phi_M(x)\phi_{\overline{M}}(y)\,T_{\lambda\lambda'}(x,y;\hat{s},\theta)\;. \tag{2}$$

where $\hat{s}$ is the $M\overline{M}$ invariant mass, λ, λ' are the gluon helicities and θ is the scattering angle in the gg cms frame. $T_{\lambda\lambda'}$ is the hard scattering amplitude for the parton level process $gg \to q\overline{q}\,q\overline{q}$, where each (massless) $q\overline{q}$ pair is collinear and has the appropriate colour, spin, and flavour content projected out to form the parent meson. $\phi(x)$ is the meson wavefunction, representing the probability amplitude of finding a valence parton in the meson carrying a longitudinal momentum fraction x of the meson's momentum. We can then calculate the relevant parton-level helicity amplitudes for the $gg \to M\overline{M}$ process, for the production of scalar flavour-nonsinglet meson states ($\pi\pi$, K^+K^-, $K^0\overline{K}^0$). There are seven independent Feynman diagrams to compute– a representative diagram is given in Fig. 1 (a). An explicit calculation gives

$$T_{gg}^{++} = T_{gg}^{--} = 0\;, \tag{3}$$

$$T_{gg}^{+-} = T_{gg}^{-+} = \frac{\delta^{\mathrm{AB}}}{N_C}\,\frac{64\pi^2\alpha_S^2}{\hat{s}xy(1-x)(1-y)}\,\frac{(x(1-x)+y(1-y))}{a^2-b^2\cos^2\theta}\,\frac{N_C}{2}\left(\cos^2\theta - \frac{2C_F}{N_C}a\right)\;, \tag{4}$$

where A, B are colour indices and

$$a = (1-x)(1-y)+xy \qquad\qquad b = (1-x)(1-y)-xy\;. \tag{5}$$

We can see that the $gg \to M\overline{M}$ amplitude for $J_z = 0$ gluons (3) vanishes at LO for scalar flavour-nonsinglet mesons, which, recalling the $J_z = 0$ selection rule that strongly suppresses the CEP of non-$J_z = 0$ states, will lead to a strong suppression (by $\sim$ two orders of magnitude)

in the CEP cross section. However it should be noted that any NNLO corrections or higher twist effects which allow a $J_z = 0$ contribution may cause the precise value of the cross section to be somewhat larger than the leading-order, leading-twist $|J_z| = 2$ estimate, although qualitatively the strong suppression will remain. An important consequence of this is that the $\pi^0\pi^0$ QCD background to the $\gamma\gamma$ CEP process described above is predicted to be small. Some sample cross section plots for $\pi\pi$ CEP and the production of other meson states are shown in Fig. 2.

We can also see that the $|J_z| = 2$ amplitude (4) vanishes for a particular value of $\cos^2\theta$. This vanishing of a Born amplitude for the radiation of massless gauge bosons, for a certain configuration of the final state particles is a known effect, usually labelled a 'radiation zero' [19]. The position of the zero is determined by an interplay of both the internal (in the present case, colour) and space-time (the particle 4-momenta) variables, as can be seen in (4), where the position of the zero depends on the choice of meson wavefunction, $\phi(x)$, through the variables a and b, as well as on the QCD colour factors. However, it should again be noted that, as the $|J_z| = 2$ amplitude is strongly suppressed by the $J_z = 0$ selection rule, any NNLO or higher twist effects which allow a $J_z = 0$ component to the cross section may give comparable contributions; it is therefore not clear that such a zero would in this case be seen clearly in the data. On the other hand, the destructive interference effects which lead to the zero in the $|J_z| = 2$ amplitude (4) will tend to suppress the CEP rate.

It is also possible for the $q\overline{q}$ forming the mesons to be connected by a quark line, via the process shown in Fig. 1 (b). These amplitudes will only give a non-zero contribution for the production of $\mathrm{SU}(3)_F$ flavour-singlet states, i.e. $\eta'\eta'$ and, through η–η' mixing, $\eta\eta$ and $\eta\eta'$ production. The relevant amplitudes are given by

$$T^{\mathrm{lad.}}_{++} = T^{\mathrm{lad.}}_{--} = \frac{\delta^{AB}}{N_C}\frac{64\pi^2\alpha_S^2}{\hat{s}xy(1-x)(1-y)}\frac{(1+\cos^2\theta)}{(1-\cos^2\theta)^2}\,, \tag{6}$$

$$T^{\mathrm{lad.}}_{+-} = T^{\mathrm{lad.}}_{-+} = \frac{\delta^{AB}}{N_C}\frac{64\pi^2\alpha_S^2}{\hat{s}xy(1-x)(1-y)}\frac{(1+3\cos^2\theta)}{2(1-\cos^2\theta)^2} \tag{7}$$

for the production of scalar mesons. As the $J_z = 0$ amplitudes do not vanish, we will expect $\eta'\eta'$ CEP to be strongly enhanced relative to, for example, $\pi\pi$ production, due to the $J_z = 0$ selection rule which operates for CEP. In the case of $\eta\eta$ production, the flavour singlet contribution will be suppressed by a factor $\sin^4\theta_P \sim 1/200$, where θ_P is the octet-singlet mixing angle [20], which may therefore be comparable to the $|J_z| = 2$ flavour-octet contribution. In fact, after an explicit calculation we find that the $\eta\eta$ CEP cross section is expected, in the regions of phase space where the perturbative formalism is applicable, to be dominant over $\pi\pi$ CEP.

A further interesting possibility we should in general consider is a two-gluon Fock component $|gg\rangle$ to the $\eta(\eta')$ mesons, which can readily be included using the formalism outlined above. In particular, the relevant perturbative $gg \to 4g$ amplitude can be calculated in the usual way and, as this does not vanish for $J_z = 0$ initial-state gluons, we may expect it to enhance the $\eta\eta$ and $\eta'\eta'$ CEP rates. This will depend sensitively on the size of the two-gluon wavefunction: therefore, by considering the CEP of $\eta(\eta')$ pairs at sufficiently high invariant mass, it may be possible to extract some information about the relative importance of the leading-twist quark and gluon wavefunctions.

Finally we have also calculated in the same way the amplitudes $T^{gg}_{\lambda_1\lambda_2,\lambda_3\lambda_4}$ for the $g(\lambda_1)g(\lambda_2) \to V(\lambda_3)\overline{V}(\lambda_4)$ process, where $V(\overline{V})$ are spin-1 mesons; for the sake of brevity, these are given explicitly elsewhere [1]. We should also in general consider a 'non-perturbative' double-Pomeron-exchange picture for low values of the meson pair invariant mass, where we may not expect the perturbative framework described above to be applicable, see [1] for some discussion of this, as well as of a secondary perturbative mechanism, where both the t-channel gluons exchanged in the standard CEP picture couple to quark lines. We find that this process, which represents the

perturbative tail of the non-perturbative production mechanism, is a power correction to the standard CEP process, and will therefore be strongly suppressed at high values of the meson pair $k_\perp$. We also note that the above $gg \to M\overline{M}$ helicity amplitudes can be considered within the MHV formalism [21], which in some cases greatly simplifies the calculation – see [1] for details.

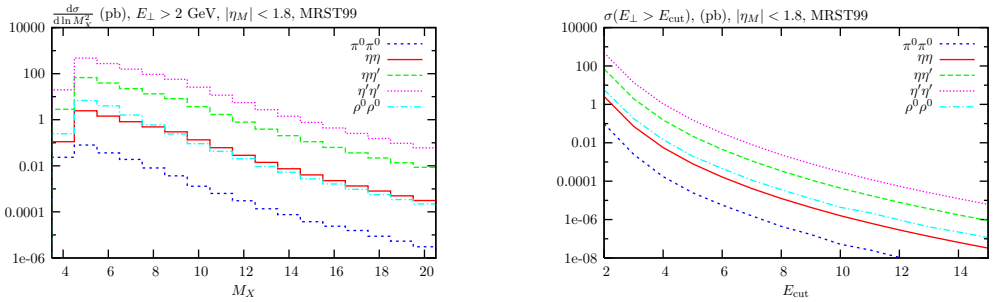

Figure 2: $\mathrm{d}\sigma/\mathrm{d}\ln M_X^2$ for meson transverse energy $E_\perp > 2$ GeV, and cross section as a function of the cut $E_{\rm cut}$ on the meson $E_\perp$ at $\sqrt{s} = 1.96$ TeV for the CEP of meson pairs, calculated within the perturbative framework.

To conclude, we have presented a study of the CEP of meson pairs in the perturbative regime, with the $gg \to M\overline{M}$ subprocess helicity amplitudes calculated within the hard exclusive formalism. This is of relevance as a background to $\gamma\gamma$ CEP in the case of $\pi^0\pi^0$ production, and to the CEP of heavy resonant states which decay to light meson pairs. Moreover, it is also a process which is important in its own right, allowing novel tests of the overall perturbative formalism as well as displaying various interesting theoretical properties.

LHL thanks the Organisers for providing an excellent scientific environment at the Workshop.

References

1. L. A. Harland-Lang, V. A. Khoze, M. G. Ryskin, W. J. Stirling, arXiv:1105.1626 [hep-ph]
2. V. A. Khoze, A. D. Martin, M. G. Ryskin, Eur. Phys. J. C **23**, 311 (2002)
3. M.G.Albrow *et al.*, J. Inst. **4** T10001 (2009)
4. M. Albrow, arXiv:1010.0625 [hep-ex]
5. V. A. Khoze, A. D. Martin, M. G. Ryskin, W. J. Stirling, Eur. Phys. J. C **35**, 211 (2004)
6. L. A. Harland-Lang, V. A. Khoze, M. G. Ryskin, W. J. Stirling, Eur. Phys. J. C **65**, 433 (2010)
7. L. A. Harland-Lang, V. A. Khoze, M. G. Ryskin, W. J. Stirling, Eur. Phys. J. **C69** , 179 (2010)
8. L. A. Harland-Lang, V. A. Khoze, M. G. Ryskin, W. J. Stirling, Eur. Phys. J. **C71** , 1545 (2011)
9. S. Heinemeyer *et al.* Eur. Phys. J. C **53**, 231 (2008)
10. S. Heinemeyer et al. arXiv:1012.5007 [hep-ph]
11. V. A. Khoze, A. D. Martin, M. G. Ryskin, A. G. Shuvaev, Eur. Phys. J. C **68**, 125 (2010)
12. M. G. Albrow, T. D. Coughlin, J. R. Forshaw, Prog. Part. Nucl. Phys. **65** (2010) 149-184
13. T. Aaltonen *et al.* [CDF Collaboration], Phys. Rev. Lett. **99**, 242002 (2007)
14. T. Aaltonen *et al.* [CDF Collaboration], Phys. Rev. Lett. **102**, 242001 (2009)
15. V. A. Khoze, A. D. Martin, M. G. Ryskin, W. J. Stirling, Eur. Phys. J. C **38**, 475 (2005)
16. V. A. Khoze, A. D. Martin and M. G. Ryskin, Eur. Phys. J. C **19**, 477 (2001)
17. S. J. Brodsky, G. P. Lepage, Phys. Rev. **D24** (1981) 1808
18. M. Benayoun, V. L. Chernyak, Nucl. Phys. **B329** (1990) 285
19. S. J. Brodsky, R. W. Brown, Phys. Rev. Lett. **49** (1982) 966
20. F. J. Gilman, R. Kauffman, Phys. Rev. **D36** (1987) 2761
21. M. L. Mangano, S. J. Parke, Phys. Rept. **200** (1991) 301-367

AN AVERAGE b-QUARK FRAGMENTATION FUNCTION FROM e^+e^- EXPERIMENTS AT THE Z POLE AND RECOMMENDATIONS FOR ITS USE IN OTHER EXPERIMENTNAL ENVIRONMENTS

E. BEN-HAIM
LPNHE, IN2P3/CNRS, Université Pierre et Marie Curie-Paris VI

The nature of b-quark jet hadronisation has been investigated using data taken at the Z peak by the ALEPH, DELPHI, OPAL and SLD experiments, who measured the $x_{\rm B}^{weak} = E_{\rm B}^{weak}/E_{beam}$ distribution. Combining all these measurements, the average value of $x_{\rm B}^{weak}$ is found to be 0.7092 ± 0.0025. The resulting average $x_{\rm B}^{weak}$ distribution is also analyzed in the framework of two choices for the perturbative contribution (parton shower and Next to Leading Log QCD calculation) in order to extract the non-perturbative component to be used in studies of b-hadron production in other experimental environments than e^+e^- collisions at the Z peak. In the parton shower framework, data favour the Lund model ansatz and corresponding values of its parameters have been determined within PYTHIA 6.156:

$$a = 1.48^{+0.11}_{-0.10} \text{ and } b = 0.509^{+0.024}_{-0.023} \text{ GeV}^{-2} \ ,$$

with a correlation factor $\rho = 92.6\%$.

1 Introduction

The fragmentation of a $\rm b\bar{b}$ quark pair from Z decay, into jets of particles including the parent b-quarks bound inside b-hadrons, is a process that can be viewed in two stages. The first stage involves the b-quarks radiating hard gluons at scales of $Q^2 \gg \Lambda^2_{\rm QCD}$ for which the strong coupling is small $\alpha_s \ll 1$. These gluons can themselves split into further gluons or quark pairs in a kind of 'parton shower'. By virtue of the small coupling, this stage can be described by perturbative QCD implemented either as exact QCD matrix elements or leading-log parton shower cascade models in event generators. As the partons separate, the energy scale drops to $\sim \Lambda^2_{\rm QCD}$ and the strong coupling becomes large, corresponding to a regime where perturbation theory no longer applies. Through the self interaction of radiated gluons, the colour field energy density between partons builds up to the point where there is sufficient energy to create new quark pairs from the vacuum. This process continues with the result that colourless clusters of quarks and gluons with low internal momentum become bound up together to form hadrons. This 'hadronisation' process represents the second stage of the b-quark fragmentation which cannot be calculated in perturbation theory. In simulation programs this is made via a 'hadronisation model' which, in the case of b-hadron production, parameterises how energy/momentum is shared between the parent b-quark and its final state b-hadron.

The purpose of this study is to measure the non-perturbative contribution to b-quark fragmentation in a way that is independent of any non-perturbative hadronisation model. Up to the choice of either QCD matrix element or leading-log parton shower to represent the perturbative phase, results are obtained that are applicable to any b-hadron production environment

in addition to the $e^+e^- \rightarrow \mathrm{Z} \rightarrow \mathrm{b\overline{b}}$ data on which the measurements were made. A detailed description of this work is given elsewhere. [1]

Generally, the study of the fragmentation process is done through the *fragmentation function*: the probability density function of some variable relating the kinematical properties of the b-hadron to those of the b-quark. A common choice of this variable is x_{B}^{weak}, defined as

$$x_{\mathrm{B}}^{weak} \;=\; \frac{E_{\mathrm{B}}^{weak}}{E_{\mathrm{b}}} \;. \tag{1}$$

It corresponds to the fraction of the energy taken by the b-hadron with respect to the energy of the b-quark directly after its production i.e. before any gluons have been radiated. This definition is particularly suited to e^+e^- annihilation as both the numerator and denominator are directly observable ($E_{\mathrm{b}} = E_{\mathrm{beam}}$). Another example is the variable

$$z \;=\; \frac{(E+p_{||})_{\mathrm{B}}}{(E+p)_{\mathrm{b}}} \;. \tag{2}$$

Here, $p_{||}$ represents the hadron momentum in the direction of the b-quark and $(E+p)_{\mathrm{b}}$ is the sum of the energy and momentum of the b-quark just before hadronisation begins. From a phenomenological point of view, z is the relevant choice of variable for a parameterisation implemented in an event generator algorithm. However, because z depends explicitly on the properties of the parent b-quark, it is not a quantity that can be directly measured by experiments.

2 The DELPHI measurement and the averaged distribution at the Z pole

The DELPHI experiment used two different and complementary approaches to reconstruct the energy of weakly decaying b-hadrons, E_{B}^{weak}: Regularised Unfolding and Weighted Fitting. [1] These measurements, presented in terms of x_{B}^{weak}, are then combined to an average energy distribution. The resulting distribution is shown in Fig 1, and the average value $\left\langle x_{\mathrm{B}}^{weak} \right\rangle$ is measured to be 0.699 ± 0.011.

Other measurements of the x_{B}^{weak} distribution have been made at the Z peak by ALEPH, [2] OPAL [3] and SLD. [4] They are also shown in Fig. 1. In order to obtain a combined distribution of all these measurements with the one from DELPHI, a global fit has been done using the smooth parameterisation:

$$f(x) = p_0 \times \left[p_1 x^{p_2}(1-x)^{p_3} + (1-p_1)x^{p_4}(1-x)^{p_5}\right] \;. \tag{3}$$

This procedure has been used since each of the four measurements is given with a different choice of binning and has a different number of effective degrees of freedom. The fitted parameters $p_1, .., p_5$ are:

$$p_1 = 12.97^{+0.77}_{-0.71}\,,\; p_2 = 2.67^{+0.15}_{-0.14}\,,\; p_3 = 2.29^{+0.19}_{-0.17}\,,\; p_4 = 1.45^{+0.28}_{-0.22}\,,\; p_5 = 0.663^{+0.035}_{-0.036}\;. \tag{4}$$

The quoted uncertainties have been rescaled by a factor 1.24 to account for the dispersion of the results, mainly between ALEPH and SLD measurements, which are respectively peaked on the high and low sides of the distribution. The average value of the combined "world average" distribution is found to be $\left\langle x_{\mathrm{B}}^{weak} \right\rangle = 0.7092 \pm 0.0025$. The averaging procedure is explained in detail elsewhere. [1]

3 Analytic extraction of the non-perturbative QCD component

The measured x_{B}^{weak} distribution is interpreted as the combined result of a perturbative and a non-perturbative part. In order to separate out the non-perturbative contribution, a choice for the perturbative part must be made. The following cases are considered:

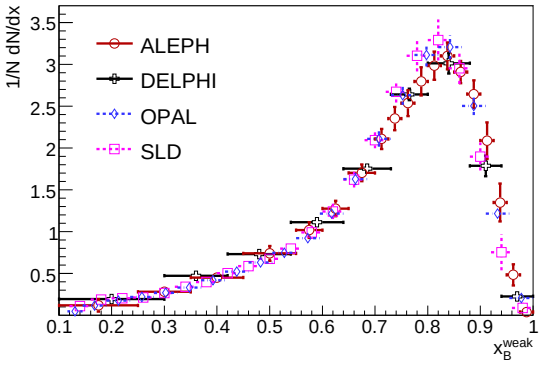

Figure 1: Comparison between the various measurements of the b-quark fragmentation distribution versus x_B^{weak}.

- the perturbative contribution is taken from a parton shower Monte-Carlo generator;

- the perturbative contribution is taken to be a NLL QCD calculation. [5]

For each case, the non-perturbative component $f_{\mathrm{non-pert.}}(x)$ is extracted using a method based on the inverse Mellin transformation. The corresponding results, obtained from the world average x_B^{weak} distribution, are shown in Fig 2. A non-perturbative component extracted in this way does not depend on any hadronisation model, but on the other hand it depends on the choice of the perturbative component and has to be used jointly with the adequate one. This dependence is clearly seen from comparison of the two parts of Fig. 2. Notice that the non-perturbative QCD component corresponding to the NLL QCD computation has to be extended in the region $x > 1$. This "non-physical" behaviour is directly related to the break-down of the theory when x_B^{weak} gets close to 1. The non-perturbative contribution extracted in this way may be used in studies of b-hadron production in other experimental environments than e^+e^- collisions at the Z pole. For a detailed explanation of the method see Refs. [1,6]

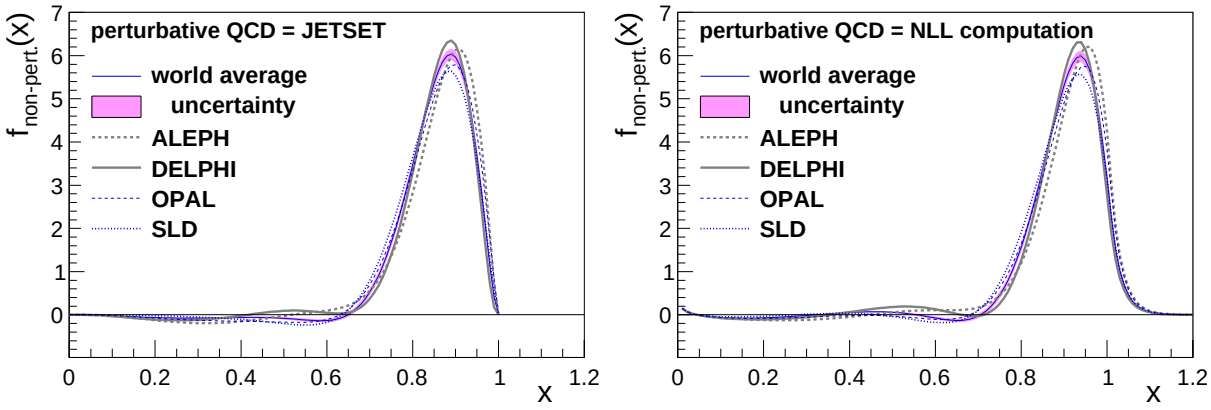

Figure 2: Comparison of the extracted non-perturbative QCD component of the b-quark fragmentation function for the results from ALEPH, DELPHI, OPAL, SLD and the combined world average distribution. Left: The perturbative QCD component has been taken from JETSET 7.3. Right: The perturbative QCD component has been taken from NLL QCD. The shaded error bands represent the experimental uncertainty of the combined distributions.

4 Fits to hadronisation models

The measured x_{B}^{weak} distribution has been compared to functional forms that are in common use inside event generators, e.g. Lund, [7] Lund-Bowler [8] and Peterson. [9] Since the models are functions of z and, in the case of Lund and Lund-Bowler, of a transverse mass variable $m_{\mathrm{b}\perp}^2$ (defined within the Lund generator and varies event-to-event), these functions cannot simply be fitted to the unfolded distributions. Instead, parameters of these models have been fitted to data using a high statistics Monte-Carlo sample at the generator level by applying event-by-event weights. The detailed procedure is described elsewhere. [1] Only the Lund and Lund-Bowler models give reasonable description of the data, the Lund ansatz being clearly favoured. The corresponding values of its parameters within PYTHIA 6.156, [a] are obtained by minimising the sum of χ^2 for the x_{B}^{weak} distributions from the four experiments:

$$a = 1.48^{+0.11}_{-0.10} \text{ and } b = 0.509^{+0.024}_{-0.023} \text{ GeV}^{-2} \ , \tag{5}$$

with a correlation factor $\rho = 92.6\%$. These parameters are expected to be valid in studies of b-hadron production in other experimental environments than e^+e^- collisions at the Z pole. The result is shown in Fig. 3.

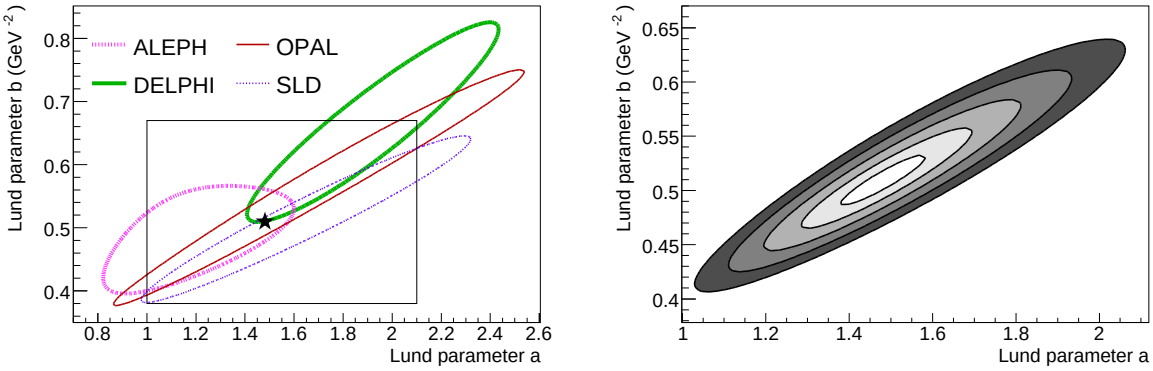

Figure 3: Left: Contours of 68.3% coverage probability for the a and b Lund parameters corresponding to a separate fit to each experiment and the result obtained in the combined fit marked by $\star$. Right: Contours varying from 1 standard deviation (lightest grey) to 5 standard deviations (darkest grey) for the a and b Lund parameters obtained in the combined fit. These contours correspond to coverage probabilities of 39.3%, 63.2%, 77.7%, 86.5% and 91.8%. The box drawn in the figure on the left corresponds to the area presented in the figure on the right.

References

1. J. Abdallah *et al.*, DELPHI Collaboration, *Eur. Phys. J.* C **71**, 1557 (2011).
2. A. Heister *et al.*, ALEPH Collaboration, *Phys. Lett.* B **512**, 30 (2001).
3. G. Abbiendi *et al.*, OPAL Collaboration, *Eur. Phys. J.* C **29**, 463 (2003).
4. K. Abe *et al.*, SLD Collaboration, *Phys. Rev.* D **65**, 092006 (2002), Erratum-ibid. D **66**, 079905 (2002).
5. M. Cacciari and S. Catani, *Nucl. Phys.* B **617**, 253 (2001).
6. E. Ben-Haim *et al.*, *Phys. Lett.* B **580**, 108 (2004).
7. B. Andersson, G. Gustafson, B. Soderberg, Z. Phys. C **20**, 317 (1983).
8. M.G. Bowler, Z. Phys. C **11**, 169 (1981).
9. C. Peterson, D. Schlatter, I. Schmitt, P.M. Zerwas, *Phys. Rev.* D **27**, 105 (1983).

[a] Parameters obtained for the non-perturbative component depend on the choice for the perturbative evaluation (e.g. PYTHIA 6.156, JETSET 7.3).

W^+W^+jj at NLO in QCD: an exotic Standard Model signature at the LHC

Tom Melia
Department of Physics, Theoretical Physics, 1 Keble Road, Oxford OX1 3NP, England

The process $pp \to W^+W^+jj$ gives rise to an exotic Standard Model signature at the LHC, involving high-$p_\perp$ like-sign leptons, missing energy and jets. In this brief article the motivation for study, along with selected results from the computation of NLO QCD corrections to the QCD-mediated part of this process[1] are presented. It is shown that the corrections reduce the dependence of the cross-section on renormalisation and factorisation scales, and produce a relatively hard third jet in a significant fraction of events.

1 Introduction

The process $pp \to W^+W^+jj$ is a quirky one, both theoretically and experimentally [1]. At a particle collider, the signature involves like-sign leptons, jets and missing energy – an exotic signal from the Standard Model! The mechanisms by which two positively charged W bosons can be created are rather restricted and this leads to the theoretical quirkiness. Figure 1 shows a typical Feynman diagram for this process (even though in our calculation we do not compute a single one). Charge conservation requires that the W bosons be emitted from separate quark lines. Because a massive particle is always produced on each fermion line, the cross-section for the process $pp \to W^+W^+jj$ remains finite *even if the requirement that two jets are observed is lifted*. This rather unusual feature is seldom present in NLO QCD calculations.

At $\sqrt{s} = 14$ TeV, the cross-section for this process is about 1 pb (40% of this for W^-W^-jj) and therefore accessible. When the W bosons decay leptonically, the two positively charged isolated leptons and missing energy give rise to a nearly background-free signature. The observation of this process is interesting in its own right, but there are other reasons to study it. Of particular importance are various physics cases for which $pp \to W^+W^+jj$ is a background process. Interestingly, such cases can be found both within and beyond the Standard Model. For example, it is possible to use same-sign lepton pairs to study double parton scattering at the LHC [2] in which case the single scattering process $pp \to W^+W^+jj$ is the background. Events with same-sign leptons, missing energy and two jets can also appear due to resonant slepton production which may occur in R-parity violating SUSY models [3] or in the case of diquark production [4] with subsequent decay of the diquark to e.g. pairs of top quarks. Similarly, one of the possible production mechanisms of the double-charged Higgs boson at the LHC has a signature of two same-sign leptons, missing energy and two jets [5]. A final reason is that the diagrams which contribute are a subset of the diagrams for $pp \to W^+W^-jj$, an important background to Higgs boson production in weak boson fusion. This calculation can be seen as a theoretical stepping stone leading to the recently computed NLO corrections to $pp \to W^+W^-jj$ [6].

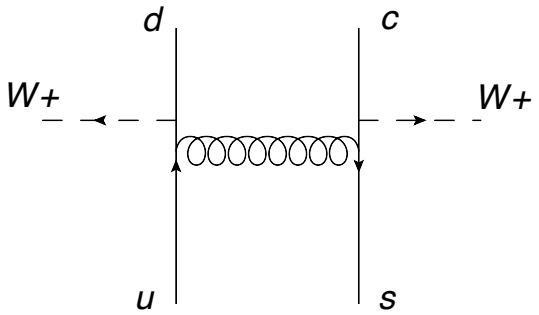

Figure 1: A typical Feynman diagram which contributes to the process $pp \to W^+W^+jj$.

Full details of the calculation can be found in Ref. [1], but it is worth pointing out that because $pp \to W^+W^+jj$ is a $2 \to 4$ process, one-loop six-point tensor integrals of relatively high rank need to be dealt with. It is only very recently that theoretical methods for one-loop calculations have become adequate to handle computations of such a complexity. We use the framework of generalized D-dimensional unitarity [7,8], closely following and extending the implementation described in Ref. [9],and demonstrating the ability of this method to deal with complicated final states involving two colourless particles. This process has since been implemented in the `POWHEG BOX` [10], and is the first $2 \to 4$ NLO process to be matched with a parton shower.

2 Results

We consider proton-proton collisions at a center-of-mass energy $\sqrt{s} = 14$ TeV. We require leptonic decays of the W-bosons and consider the final state $e^+\mu^+\nu_e\nu_\mu$. The W-bosons are on the mass-shell and we neglect quark flavour mixing. We impose standard cuts on lepton transverse momenta $p_{\perp,l} > 20$ GeV, missing transverse momentum $p_{\perp,\mathrm{miss}} > 30$ GeV and charged lepton rapidity $|\eta_l| < 2.4$. We define jets using anti-$k_\perp$ algorithm [11], with $\Delta R_{j_1 j_2} = 0.4$ and, unless otherwise specified, with a transverse momentum cut $p_{\perp,j} = 30$ GeV on the two jets. The mass of the W-boson is taken to be $m_W = 80.419$ GeV, the width $\Gamma_W = 2.140$ GeV. W couplings to fermions are obtained from $\alpha_{\mathrm{QED}}(m_Z) = 1/128.802$ and $\sin^2\theta_W = 0.2222$. We use MSTW08LO parton distribution functions for leading order and MSTW08NLO for next-to-leading order computations, corresponding to $\alpha_s(M_Z) = 0.13939$ and $\alpha_s(M_Z) = 0.12018$ respectively [12]. We do not impose lepton isolation cuts. All results discussed below apply to the QCD production $pp \to W^+W^+jj$; the electroweak contribution to this process is ignored.

Since the cross section remains finite even if the requirement that two jets are observed is lifted, we can consider the production of same-sign gauge bosons in association with n jets $pp \to W^+W^+ + n$ jets, where $n = 0, 1, 2$ or $n \geq 2$. Fig. 2 shows the dependence of the production cross-sections for $pp \to e^+\mu^+\nu_e\nu_\mu + n$ jets on the renormalisation and factorisation scales, which we set equal to each other.

Considering the range of scales 50 GeV $\leq \mu \leq$ 400 GeV, we find the two-jet inclusive cross-section to be $\sigma^{\mathrm{LO}} = 2.7 \pm 1.0$ fb at leading order and $\sigma^{\mathrm{NLO}} = 2.44 \pm 0.18$ fb at next-to-leading order. The forty percent scale uncertainty at leading order is reduced to less than ten percent at NLO. We observe similar stabilization of the scale dependence for the 0- and 1-jet exclusive multiplicities. Combining these cross-sections we obtain a total NLO cross-section of about 2.90 fb for $pp \to e^+\mu^+\nu_e\nu_\mu$ inclusive production. This implies about 60 $e^+\mu^+ + e^+e^+ + \mu^+\mu^+$ events per year at the LHC with 10 fb^{-1} annual luminosity. While this is not a gigantic number, such events will have a very distinct signature, so they will definitely be seen and it will be possible to study them.

The dramatic change in the two-jet exclusive cross-section apparent from Fig. 2 is discussed

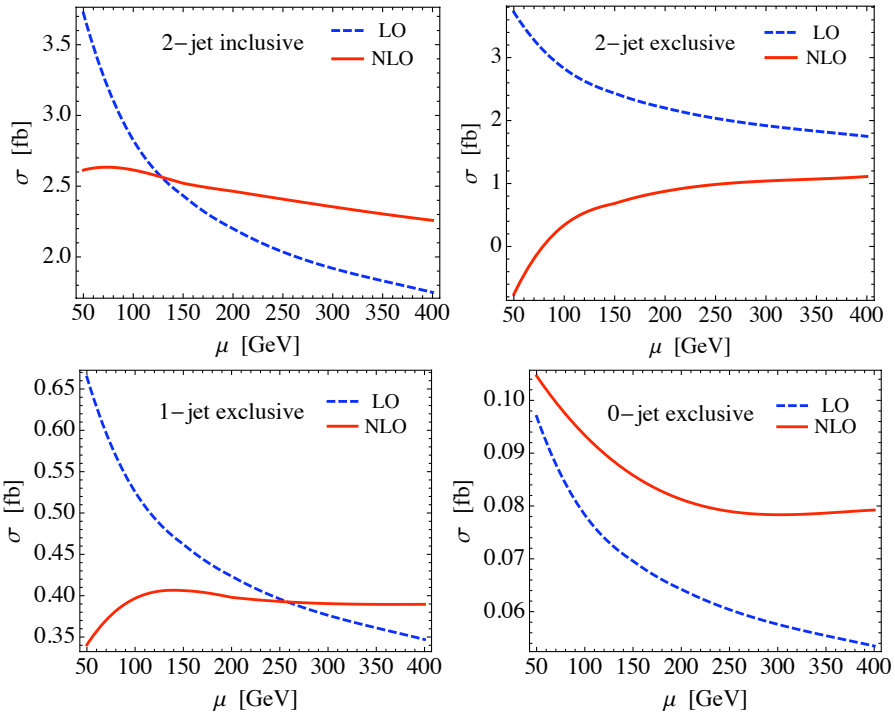

Figure 2: The dependence on factorisation and renormalisation scales of cross-sections for $pp \to e^+ \mu^+ \nu_e \nu_\mu + n$ jets, $n = 0, 1, 2$ at leading and next-to-leading order in perturbative QCD. Here $\mu_F = \mu_R = \mu$.

and investigated in Ref.[1]. We find that the feature observed here, that the two-jet exclusive is significantly smaller than the two-jet inclusive, remains present when we increase the jet cut and so allow for greater perturbative convergence of the exclusive cross section. This smallness implies that quite a large fraction of events in $pp \to e^+\mu^+\nu_e\nu_\mu + \geq 2$ jets have a relatively hard third jet. This feature may be useful for rejecting contributions of $pp \to W^+W^+jj$ when looking for multiple parton scattering.

Selected kinematic distributions are shown in Fig. 3. It is clear that jets in $pp \to W^+W^+jj$ are hard; a typical transverse momentum of the hardest jet is close to 100 GeV and the transverse momentum of the next-to-hardest jet is close to 40 GeV. The NLO distributions show a characteristic depletion at large values of $p_{\perp,j}$. One reason this change occurs is because a constant, rather than a dynamical, renormalisation scale is used in our leading order calculation. Scale dependencies of the distributions are reduced dramatically. The angular distance ΔR_{lj} between a charged lepton of fixed flavor (e^+ or μ^+) and the next-to-hardest jet is displayed, as well as the distribution of the relative azimuthal angle of the two charged leptons. Although the distribution of angular distance between leptons and the next-to-hardest jet is broad, it peaks at $\Delta R_{lj} \approx 3$. NLO QCD effects do not change this conclusion but, interestingly, they make the angular distance between next-to-hardest jet and the charged lepton somewhat larger. The distribution of the relative azimuthal angle of the two charged leptons becomes less peaked at $\Delta\phi_{l^+l^+} = \pi$, although the two leptons still prefer to be back to back. It is interesting to remark that, if the two same sign leptons are produced through a double-parton scattering mechanism, their directions are not correlated. Hence, yet another possibility to reduce the single-scattering-background is to cut on the relative azimuthal angle between the two leptons.

To conclude, selected results from the calculation of NLO QCD corrections to the QCD-mediated process $pp \to W^+W^+jj$ have been presented. Methods developed very recently for computing one-loop amplitudes allowed for relatively straightforward calculation of this $2 \to 4$ process. The detector signature is an exotic one, and is exciting to study at the LHC.

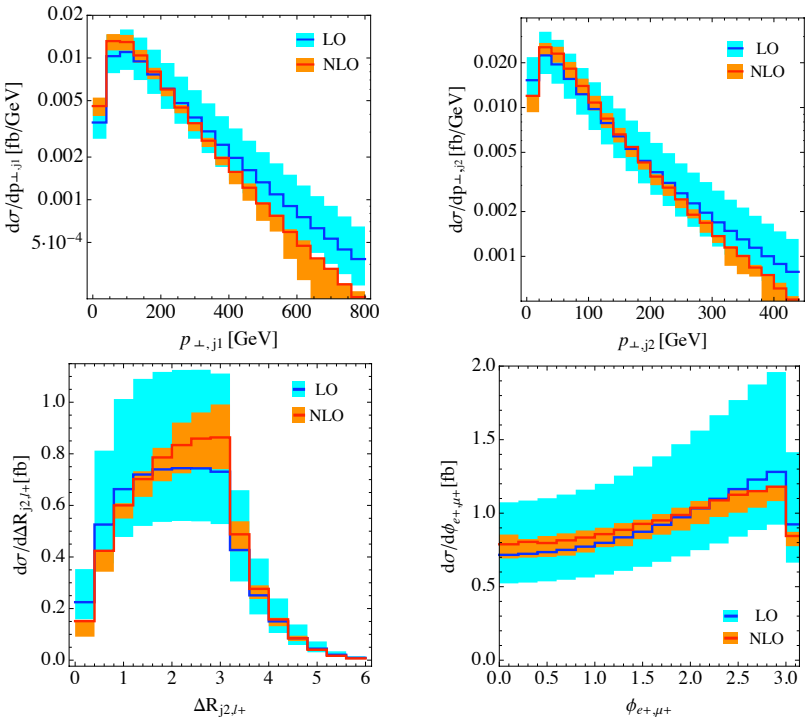

Figure 3: Distributions of the transverse momentum of the two hardest jets and angular distributions in the process $pp \to e^+ \mu^+ \nu_e \nu_\mu + 2$ jets at leading and next-to-leading order in perturbative QCD for inclusive two-jet events. The bands show renormalisation and factorisation scale uncertainty, for 50 GeV $\leq \mu \leq$ 400 GeV. Solid lines show leading and next-to-leading order predictions for $\mu = 150$ GeV.

Acknowledgments

I wish to thank the organisers of the Moriond QCD session for providing both financial support and a fantastic conference. This write-up is based on work done in collaboratoration with Kirill Melnikov, Raoul Röntsch and Giulia Zanderighi and closely follows Ref.[1], and the research is supported by the British Science and Technology Facilities Council.

References

1. T. Melia, K. Melnikov, R. Rontsch, and G. Zanderighi, JHEP **12**, 053 (2010).
2. A. Kulesza and W. J. Stirling, Phys. Lett. B**475**, 168 (2000);
   E. Maina, JHEP **0909**, 081 (2009);
   J. R. Gaunt, C. H. Kom, A. Kulesza and W. J. Stirling, hep-ph/1003.3953.
3. H. K. Dreiner, S. Grab, M. Krämer and M. K. Trenkel, Phys. Rev. D**75**, 035003 (2007).
4. H. Zhang, E. Berger, Q. Cao, C. Chen, and G. Shaughnessy, Phys. Lett. B **696**, 68 (2011);
   T. Han, I. Lewis and T. McElmurry, JHEP **1001**, 123 (2010).
5. See e.g. J. Maalampi and N. Romanenko, Phys. Lett. B **532**, 202 (2002).
6. T. Melia, K. Melnikov, R. Rontsch, and G. Zanderighi, arxiv:1104.2327.
7. R. K. Ellis, W. T. Giele and Z. Kunszt, JHEP **0803**, 003 (2008).
8. W. T. Giele, Z. Kunszt and K. Melnikov, JHEP **0804**, 049 (2008).
9. R. K. Ellis, W. T. Giele, Z. Kunszt, K. Melnikov and G. Zanderighi, JHEP **0901**, 012 (2009).
10. T. Melia, P. Nason, R. Rontsch, and G. Zanderighi, arxiv:1102.4846.
11. M. Cacciari, G. P. Salam and G. Soyez, JHEP **0804**, 063 (2008).
12. A. D. Martin, W. J. Stirling, R. S. Thorne and G. Watt, Eur. Phys. J. C **63**, 189 (2009).

W/Z+Jets and W/Z+HF Production at the Tevatron

Stefano Camarda
Institut de Física d'Altes Energies. Barcelona, 01893-E, Spain
On behalf of the CDF and DO Colaborations.

The CDF and D0 Collaborations have a comprehensive program of studying the production of vector bosons, W and Z, in association with energetic jets. Understanding the standard model W/Z+jets and W/Z+c, b-jets processes is of paramount importance for the top quark physics, for the Higgs boson and for many new physics searches. In this contribution recent measurements of the associated production of jets and vector bosons in Run II at the Tevatron are presented. The measurements are compared to predictions from various theoretical models.

1 Introduction

The study of the production of electroweak bosons in asociation with jets of hadrons constitutes a fundamental item in the high-p_T physics program at Tevatron. Vector bosons plus jets final states are a major background to many interesting physics processes like single and pair top quarks production, SM Higgs, and supersymmetry. Precise measurements of W/Z + jets production provide a stringent test of pQCD predictions [1] at high Q^2, and offer the possibility to validate Monte Carlo simulation tools [2]. The latest vector boson plus jets results at Tevatron are reviewed and discussed.

2 W/Z + Jets measurements

The CDF experiment recently measured the Z + jets production cross sections in the $Z/\gamma^* \rightarrow \mu^+\mu^-$ decay channel with $\sim 6fb^{-1}$ of integrated luminosity [3]. Differential cross sections as a function of p_T^{jet}, $|y|^{jet}$, and jet multiplicity, have been measured. Events are required to have two opposite signed muons with a reconstructed invariant mass in the range $66 \leqslant M_Z \leqslant 116\ GeV/c^2$ around the Z boson mass. Jets are clustered with the Midpoint algorithm [5] in a cone radius of 0.7, and are required to have $p_T \geqslant 30\ GeV/c$ and $|y| \leqslant 2.1$. The background estimation is performed both with data-driven and MC techniques, the QCD and W+jet backgrounds are estimated from data using a same charge dimuon sample, other backgrounds contributions like $Z+\gamma$, $t\bar{t}$ and diboson are estimated from MC. The cross sections are unfolded back to the particle level accounting for acceptance and smearing effects employing Alpgen + Pythia MC. The data is compared to NLO pQCD predictions obtained with the MCFM program. The theoretical predictions include parton-to-particle correction factors that account for the non-perturbative underlying event and fragmentation effects, estimated with pythia Monte Carlo simulations. Figure 1 (left) shows the measured inclusive differential cross section in Z + 1 jet events. The corrected NLO predictions agree with the data within experimental and systematic uncertainties over the full p_T^{jet} range. An update on the Z + jets production cross section in the $Z/\gamma^* \rightarrow e^+e^-$

decay channel has been performed at CDF with $\sim 6.2 fb^{-1}$ of integrated luminosity. A previous measurement was already published with 1.7 fb^{-1} [6]. The measurement is defined in the same kinematic region and with the same jet reconstruction employed in the muon channel, with the exception that in the $Z/\gamma^* \to e^+e^-$ channel one of the lepton can be reconstructed in the forward region of the detector $1.1 \leqslant |\eta_e| \leqslant 2.8$. Figure 1 (right) shows the measured cross section as a function of jet multiplicity compared to LO and NLO pQCD predictions obtained with MCFM.

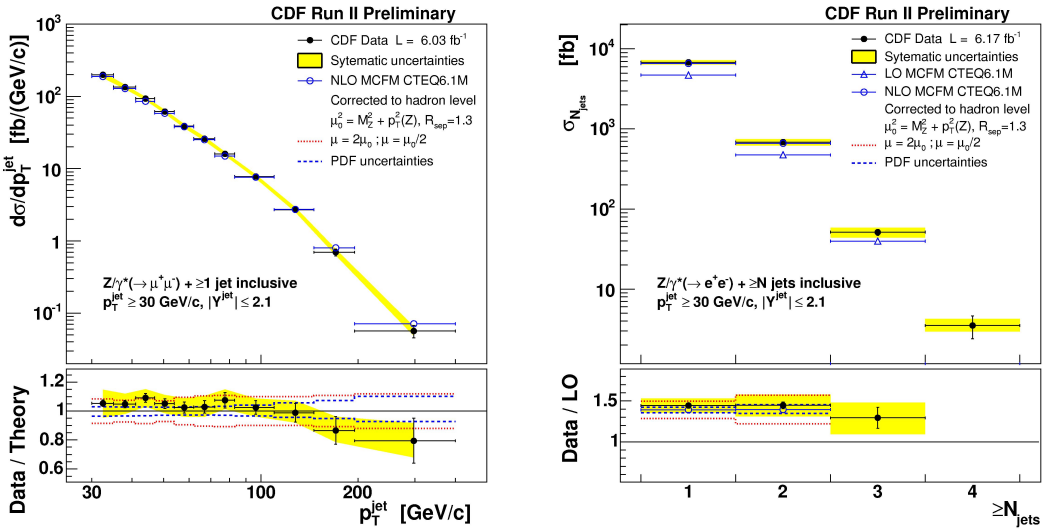

Figure 1: Measured inclusive jet differential cross sections as a function of p_T^{jet} in $Z/\gamma^* \to \mu^+\mu^- + \geqslant 1$ jet events and as a function of jet multiplicity in $Z/\gamma^* \to e^+e^-$ + jets events. Data (black dots) are compared to NLO pQCD predictions (open circles). The shaded bands show the total systematic uncertainty, except for the 5.8% luminosity uncertainty. The dashed and dotted lines indicate the PDF uncertainty and the variation with μ_0 of the NLO pQCD predictions, respectively.

The D0 experiment has performed several measurements of the angular correlations between the Z and the leading jet in $Z/\gamma^* \to \mu^+\mu^-$ + jets events [7] with data corresponding to an integrated luminosity of ~ 1 fb^{-1}. Jets are clustered with the midpoint algorithm in a cone radius of 0.5, and selected in the kinematic region of $p_T \geqslant 20 GeV/c$ and $|y| \leqslant 2.8$. The differential cross sections are normalized to the inclusive Z cross section, in order to reduce the systematic uncertainties. The data is compared to NLO pQCD predictions from MCFM, Pythia with tunes QW and Perugia, Alpgen interfaced to Pythia with the same tunes, Herwig (with Jimmy for multiple interactions) and Sherpa. The Sherpa generator is providing a good description of the shape, but a normalization factor is missing. The NLO MCFM prediction is on good agreement with data.

A new measurements of W + jets production cross section has been done at the CDF experiment with 2.8 fb^{-1} of integrated luminosity [4]. Both the $W \to e\nu$ and $W \to \mu\nu$ channels have been measured, and several kinematics variables have been explored. Events are selected with a reconstructed electron or muon of $p_T \geqslant 20 GeV/c$ and $|\eta| \leqslant 1.1$. The transverse mass of the W, reconstructed with the lepton and $\not\!\!E_T$, is required to be $M_T^W \geqslant 40(30)$ GeV/c^2 for the electron (muon) channel. Data are compared to Alpgen + Pythia MC prediction, which is normalized in a control region with the same requirements except that $M_T^W \geqslant 20$ GeV/c^2. Figure 2 shows the cross section as a function of the p_T of the leading jet in $W \to \mu\nu + \geqslant 1$ jet and as a function of M_{jj} in $W \to e\nu + \geqslant 2$ jets events.

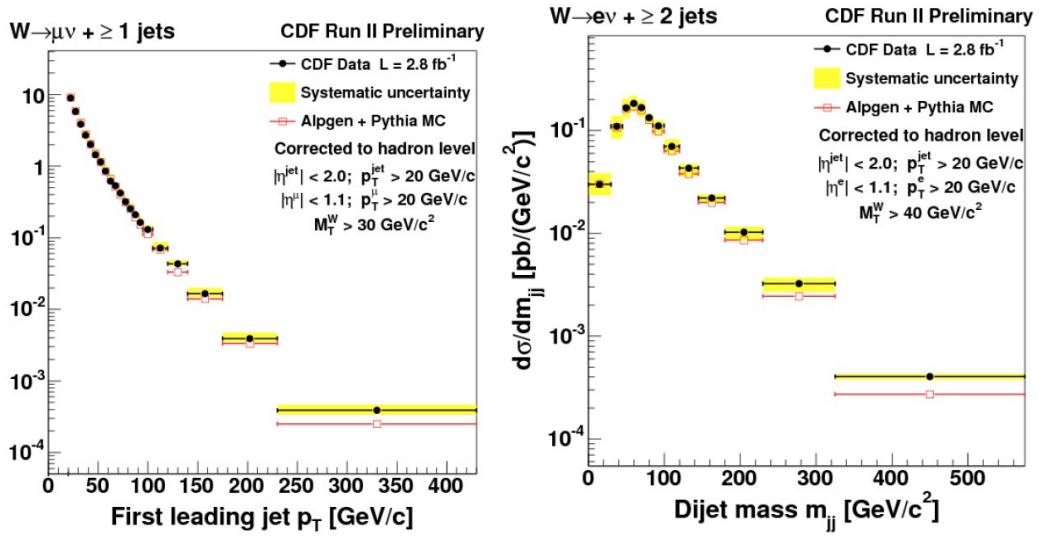

Figure 2: Measured inclusive jet differential cross sections as a function of leading p_T^{jet} in $W \rightarrow \mu\nu + \geqslant 1$ jet events and as a function of M_{jj} in $W \rightarrow e\nu + \geqslant 2$ jets events. Data (black dots) are compared to Alpgen + Pythia predictions (open squares). The shaded bands show the total systematic uncertainty.

3 W/Z + Heavy Flavor Jet Production

The measurement of vector boson production with associated heavy flavor jets provides an important test of pQCD predictions. Understanding these processes is also critical in many searches for new particles, like low-mass Higgs boson and super-symmetric particles.

The Z + b-jet production cross section has been measured at CDF with 2 fb^{-1} of integrated luminosity [8]. Jets are clustered with the standard cone algorithm in a cone radius of 0.7 and are required to have $E_T \geqslant 20GeV$ and $|\eta| \leqslant 1.5$. The $Z/\gamma^* \rightarrow \mu^+\mu^-$ and $Z/\gamma^* \rightarrow e^+e^-$ channels are combined, and the b-quark composition is extracted from a fit to the mass of a displaced secondary vertex reconstructed within the jet. The Z + b-jet cross section is normalized to the inclusive Z cross section in order to reduce the systematic uncertainties, the measured value is $\frac{\sigma(Z+b)}{\sigma(Z)} = 3.32 \pm 0.53 \pm 0.42 \times 10^{-3}$. The NLO prediction is evaluated using MCFM with two different choice of the renormalization and factorization scale: $Q^2 = M^2 + P_T^2$ which gives a prediction of 2.3×10^{-3} and $Q^2 =< P_{T,jet}^2 >$ which gives a prediction of 2.8×10^{-3}. The choice of the renormalization and factorization scale introduces a large uncertainty in the theoretical prediction, within this uncertainty the measured cross section is in good agreement with the predicted value.

In the same Z + b-jet final state the D0 Collaboration recently published a result with 4.2 fb^{-1} of integrated luminosity [9]. Jets are clustered with the Midpoint algorithm in a cone of 0.5. Figure 3 shows the p_T of the leading jet in the $Z/\gamma^* \rightarrow \mu^+\mu^-$ channel on the left and in the $Z/\gamma^* \rightarrow e^+e^-$ channel on the right plot. In this measurement the b-fraction is extracted using Artificial Neural Network techniques. The cross section is normalized to the Z+jets productions, and the NLO prediction is evaluated with a renormalization and factorization scale set to the invariant mass of the Z boson $Q^2 = M_Z^2$. The measured cross section $\frac{\sigma(Z+b)}{\sigma(Z+jet)} = 0.0193 \pm 0.0022 \pm 0.0015$ is in good agreement with the theoretical prediction of 0.0192 ± 0.0022.

The CDF experiment performed a measurement of the cross section for jets from b-quarks produced with a W boson using data corresponding to an integrated luminosity of 1.9 fb^{-1} .

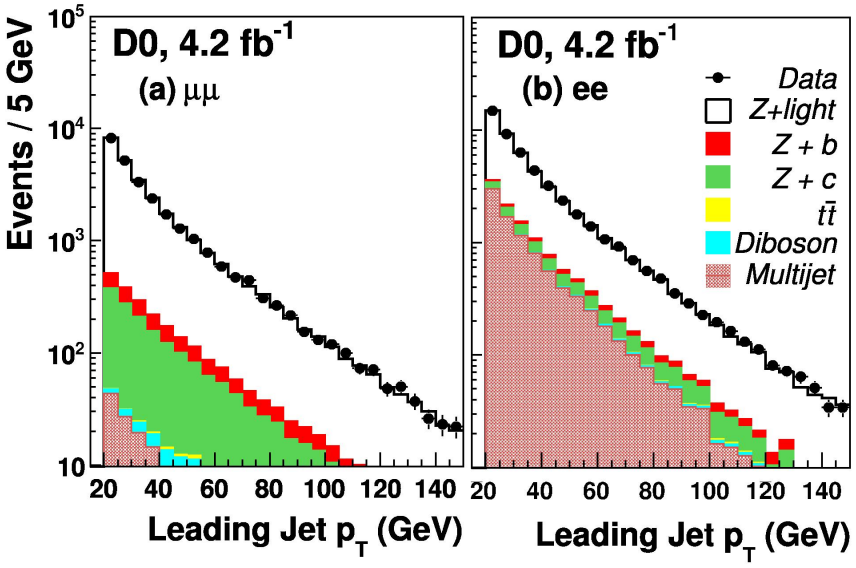

Figure 3: Leading jet p_T in $Z/\gamma^* \rightarrow \mu^+\mu^-$ (left) and $Z/\gamma^* \rightarrow e^+e^-$ (right) + jets events. The Z + b-jet contribution used to measure the $\frac{\sigma(Z+b)}{\sigma(Z+jet)}$ cross section ratio is shown in red color.

Events that are consistent with the electronic and muonic W boson decay and contain one or two jets with $E_T \geqslant 20GeV$ and $|\eta| \leqslant 2.0$ are selected. The b-jet flavor composition is determined through a fit to the distribution of the secondary vertex mass in the data. The measured cross section is $\sigma(W + \text{b-jets}) \times BR(W \rightarrow l\nu) = 2.74 \pm 0.27 \pm 0.42\ pb$. This result cannot be accommodated by different available theoretical predictions. The Pythia prediction is 1.10 pb, while Alpgen predicts 0.78 pb, and a recent MCFM NLO calculation of $1.22 \pm 0.14\ pb$ is also signicantly lower than the measurement.

Summary

New results at the Tevatron of Z/W + jets and Z/W + heavy flavor production are in general good agreement with the NLO predictions, even if with large uncertainties in some cases. There are prospects for more precise measurements of W/Z + HF production, and for the combination of the electron and muon channels in the Z+jets production.

References

1. D.J. Gross and F. Wilczek, *Phys. Rev.* D **8**, 3633 (1973).
2. J.Campbell and R.K. Ellis, *Phys. Rev.* D **65**, 113007 (2002).
3. CDF Collaboration, *CDF Conference Note 10216* http://www-cdf.fnal.gov/physics/new/qcd/abstracts/zjets_10.html
4. CDF Collaboration, *CDF Conference Note 10423* http://www-cdf.fnal.gov/physics/new/qcd/abstracts/zjets_10.html
5. A. Abulencia et al. (CDF Collaboration), *Phys. Rev.* D **74**, 071103(R) (2006).
6. T. Aaltonen et al. (CDF Collaboration), *Phys. Rev. Lett.* **100**, 102001 (2008).
7. D0 Collaboration *Phys. Lett.* B **682**, 370 (2010)
8. CDF Collaboration *Phys. Rev.* D **79**, 052008 (2009)
9. D0 Collaboration *Phys. Rev.* D **83**, 031105 (2011)
10. CDF Collaboration *Phys. Rev. Lett.* **104**, 131801 (2010)

W and Z physics with the ATLAS detector

N. Makovec
Laboratoire de l'Accélérateur Linéaire d'Orsay

We present measurements involving W and Z boson production in pp collisions at $\sqrt{s}$=7 TeV with an integrated luminosity of $\sim$35 pb^{-1} recorded by the ATLAS detector at the Large Hadron Collider. Several analysis are presented: Drell-Yan $W \to \ell\nu$ and $Z/\gamma^* \to \ell\ell$ ($\ell = e, \mu$) production cross sections, muon charge asymmetry from W boson decays, production of jets in association with a Z/γ^*boson in the final state and diboson production ($W\gamma$,$Z\gamma$,W^+W^-). The measurements are compared to perturbative QCD predictions with various parton distribution functions.

1 Introduction

The leptonic decays of W and Z bosons provide a very clean experimental signature with which to measure their production cross sections and test the predictions from perturbative Quantum ChromoDynamics (pQCD) at the Large Hadron Collider (LHC) and the accuracy of Parton Distribution Functions (PDF) which parameterize the parton's momentum distribution in the proton. Measurements of such processes, in particular in association with jets, are also important to control backgrounds to other Standard Model measurements like the top cross-section measurement [1] or to searches for physics beyond the Standard Model like the search for squark and gluino production [2]. Here we report measurements involving W and Z boson production in pp collisions at $\sqrt{s}$=7 TeV with an integrated luminosity of $\sim$35 pb^{-1}.

2 Measurement of the total $W^{\pm}$ and Z/γ^* cross sections and muon charge asymmetry

The total W and Z cross section is measured using the following formula:

$$\sigma_{tot} = \sigma_{W/Z} \times BR(W/Z \to \ell\nu/\ell\ell) = \frac{N - B}{A_{W/Z}.C_{W/Z}.L_{int}} \,. \tag{1}$$

Here N is the number of candidate events measured in data, B the number of background events, determined using data and simulation and L_{int} the integrated luminosity corresponding to the run selections and trigger employed. $BR(W/Z \to \ell\nu/\ell\ell)$ stands for branching ratio. The correction by the efficiency factor $C_{W/Z}$, measured partly with data, determines the integrated cross sections σ_{fid} within the fiducial regions of the measurement, while the acceptance factor $A_{W/Z}$, estimated from Monte-Carlo, is introduced to extrapolate the measurement of σ_{fid} to the full kinematic region which determines the total cross section, σ_{tot}. The details of the analysis can be found in Reference [3]. As shown in Figure 1, the measured $W^{\pm}$ and Z/γ^* cross sections

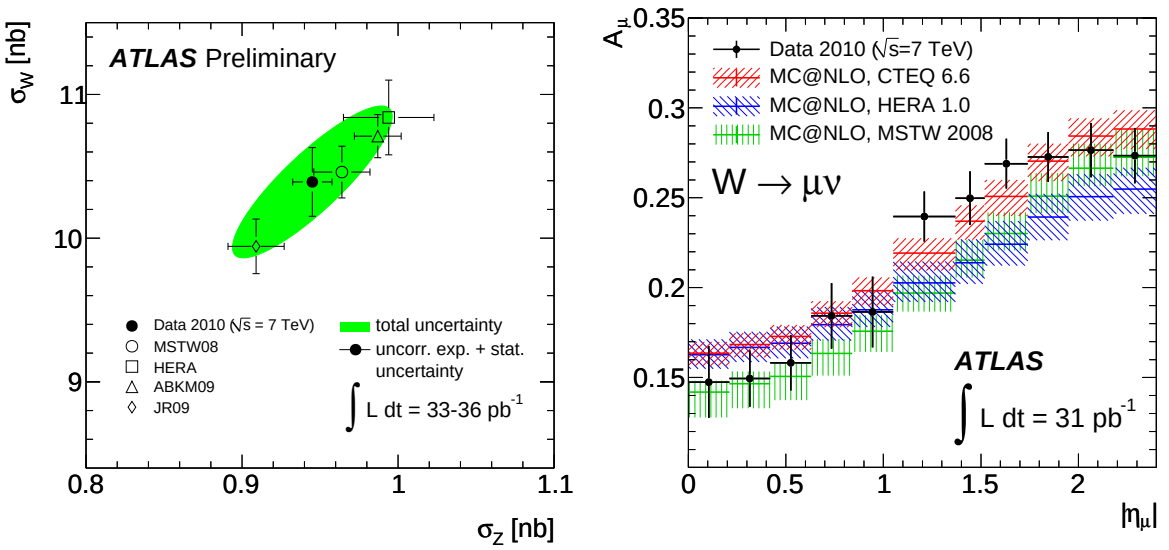

Figure 1: To the left, measured and predicted cross sections times leptonic branching ratios: $(\sigma_{W^+} + \sigma_{W^-})$ vs σ_{Z/γ^*}. The projections of the ellipse to the axes correspond to one standard deviation uncertainty of the cross sections. To the right, the muon charge asymmetry from W-boson decays in bins of absolute pseudorapidity. The data points (shown with error bars including the statistical and systematic uncertainties) are compared to MC@NLO predictions with different PDF sets.

are found to be described by Next-to-Next-to-Leading Order (NNLO) QCD calculations based on a number of different PDF sets.

In pp collisions the overall production rate of W^+ bosons is significantly larger than the corresponding W^- rate, since the proton contains two u and one d valence quarks. The measurement of the lepton charge asymmetry:

$$A_l = \frac{d\sigma_{\mathrm{Wl^+}}/d\eta_l - d\sigma_{\mathrm{Wl^-}}/d\eta_l}{d\sigma_{\mathrm{Wl^+}}/d\eta_l + d\sigma_{\mathrm{Wl^-}}/d\eta_l}\,, \tag{2}$$

can contribute significantly to the understanding of PDFs in the parton momentum fraction range $10^{-3} < x < 10^{-1}$. Systematic effects on the W-production cross-section measurements are typically the same for positive and negative muons, mostly canceling in the asymmetry. Measurements in the muon channel are presented in Figure 1 together with predictions obtained with MC@NLO [4] and different PDF sets. More details can be found in Reference [5]. The data are roughly compatible with all the predictions with different PDF sets, though some are slightly preferred to others. The data presented here are expected to contribute to the determination of the next generation of PDF sets, helping to reduce their uncertainties, particularly the shapes of the valence quark distributions in the low-x region.

3 Measurement of the production cross section for Z/γ^* in association with jets

Production of jets of particles in association with a Z/γ^* boson in the final state was measured. Jets are defined using the anti$-\mathrm{k_T}$ algorithm with $R = 0.4$ and the measurements are performed for jets in the region $p_T^{jet} > 30$ GeV and $|\eta^{\mathrm{jet}}| < 2.8$. The full analysis is described in Reference [6] and the measured cross section as a function of the inclusive jet multiplicity for the electron channel and as a function of p_T^{jet} for the muon channel are presented in Figure 2. The measured cross sections are well described by Next-to-Leading Order (NLO) pQCD predictions obtained by MCFM [7] and including non-perturbative corrections, as well as by the predictions from LO matrix elements supplemented by parton showers, as implemented in the ALPGEN [8] and

SHERPA [9] MC generators but not by PYTHIA [10] which underestimates the measured cross sections.

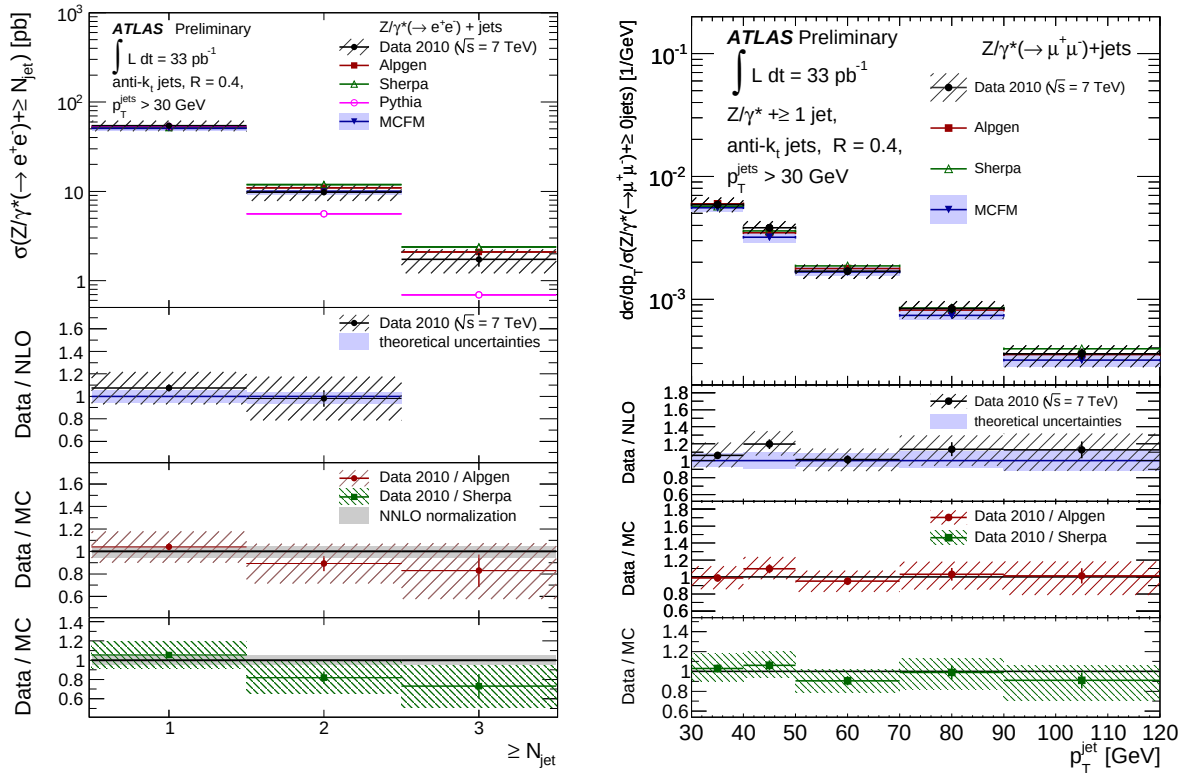

Figure 2: To the left (resp. right), measured cross section (black dots) in $Z/\gamma^*(\rightarrow e^+e^-)$+jets (resp. $Z/\gamma^*(\rightarrow \mu^+\mu^-)$+jets) production as a function of the inclusive jet multiplicity (resp. p_T^{jet}), for events with at least one jet with $p_T^{jet} > 30$ GeV and $|\eta^{\rm jet}| < 2.8$ in the final state. The error bars indicate the statistical uncertainty and the dashed areas the statistical and systematic uncertainties added in quadrature. The measurements are compared to NLO pQCD predictions from MCFM (only available up to 2 jets), as well as the predictions from ALPGEN, SHERPA, and PYTHIA. The shadowed areas around the ALPGEN and SHERPA predictions denote a 5% uncertainty on the absolute normalization.

4 Measurement of diboson production ($W\gamma$,$Z\gamma$,W^+W^-)

ATLAS has also performed the measurement of diboson production of high energy photons in association with either a W or Z boson. Such measurements allow to test pQCD. Moreover, the $W\gamma$ process includes a diagram sensitive to Triple Gauge boson Coupling (TGC) of the electroweak sector. Events with W and Z bosons decaying into high-p_T electrons and muons are required in addition to have a photon with $E_T > 15$ GeV located outside a cone of radius 0.7 in η - ϕ space centered on the lepton(s) from the boson decay. To further reduce the background due to photons from π^0 and η decays, an isolation requirement of $E_T^{iso} < 5$ GeV is applied. E_T^{iso} is the total transverse energy recorded in the calorimeter in a cone of radius 0.4 around the photon direction (excluding a small window which contains the photon energy). E_T^{iso} is corrected for the leakage of the photon energy into the isolation cone and the contributions from the underlying and pile-up activities in the event. A total of 95 (97) $pp \rightarrow e\nu\gamma + \mathrm{X}$ ($pp \rightarrow \mu\nu\gamma + \mathrm{X}$) and 25 (23) $pp \rightarrow e^+e^-\gamma + \mathrm{X}$ ($pp \rightarrow \mu^+\mu^-\gamma + \mathrm{X}$) event candidates are selected [11]. The measured production cross sections, together with the kinematic distributions of the leptons and photons in data signal candidate events, are found to agree with the $O(\alpha\alpha_s)$ Standard Model predictions (see Table 1).

	Experimental measurement $\sigma^{total}[pb]$(measured)	SM model prediction $\sigma^{total}[pb]$(predicted)
$pp \to e\nu\gamma$	$73.9 \pm 10.5(stat) \pm 14.6(syst) \pm 8.1(lumi)$	69.0 ± 4.6(syst)
$pp \to \mu\nu\gamma$	$58.6 \pm 8.2(stat) \pm 11.3(syst) \pm 6.4(lumi)$	69.0 ± 4.6(syst)
$pp \to e^+e^-\gamma$	$16.4 \pm 4.5(stat) \pm 4.3(syst) \pm 1.8(lumi)$	13.8 ± 0.9(syst)
$pp \to \mu^+\mu^-\gamma$	$10.6 \pm 2.6(stat) \pm 2.5(syst) \pm 1.2(lumi)$	13.8 ± 0.9(syst)

Table 1: Total cross sections of the $pp \to l\nu\gamma + X$ and $pp \to ll\gamma + X$ process at $\sqrt{s} = 7\ TeV$. Both, experimental measurement and SM model NLO prediction are given. The total cross sections are measured with $p_T(\gamma) > 10\ GeV$, $\Delta R(l,\gamma) > 0.5$ and $\epsilon_h^p < 0.5$ where ϵ_h^p is defined at particle level as the ratio between sum of the energies carried by final state particles in the cone $\Delta R < 0.4$ around the photon and the energy carried by the photon.

The WW production cross section in pp collisions was also measured using three leptonic decay channels: electron-electron, muon-muon and muon-electron channels. Such processes are also sensitive to TGC as predicted by the Standard Model. The decay products from both top-pair ($t\bar{t} \to WbWb$) and single top ($tW \to WbW$) processes contain also WW in the final states. The top events are characterized by hadronic jet activity in the final state. Using a jet-veto cut the majority of the top background can be removed from the WW event selection. A total of eight candidates are selected with an estimated background of 1.7 ± 0.6 events. The probability for the estimated background to fluctuate up to at least the observed eight events is $1.4{\times}10^{-3}$, corresponding to a signal significance of 3.0 standard deviations. The measured cross section is 40^{+20}_{-16}(stat)$\pm$7(syst) pb, consistent with the SM NLO prediction of 46 ± 3 pb.

5 Summary

First measurements involving W and Z boson production in pp collisions at $\sqrt{s}$=7 TeV with an integrated luminosity of $\sim$35 pb^{-1} recorded by the ATLAS detector at the Large Hadron Collider were presented. Theoretical predictions are in good agreement with all measurements within statistical and systematic uncertainties. The increase of integrated luminosity with 2011 data will permit more stringent test of perturbative QCD and tighter constraints on parton distribution functions.

References

1. G. Aad *et al.* [ATLAS Collaboration], Eur. Phys. J. C **71** (2011) 1577.
2. G. Aad *et al.* [ATLAS Collaboration], Phys. Lett. B **701** (2011) 186.
3. ATLAS Collaboration, ATLAS-CONF-2011-041, `https://atlas.web.cern.ch/Atlas/GROUPS/PHYSICS/CONFNOTES/ATLAS-CONF-2011-041`.
4. S. Frixione and B. R. Webber, JHEP **0206** (2002) 029.
5. G. Aad *et al.* [ATLAS Collaboration], Phys. Lett. B **701** (2011) 31.
6. ATLAS Collaboration, ATLAS-CONF-2011-042, `https://atlas.web.cern.ch/Atlas/GROUPS/PHYSICS/CONFNOTES/ATLAS-CONF-2011-042`.
7. J. M. Campbell and R. K. Ellis. Phys. Rev. D **65** (2002) 113007.
8. M. L. Mangano *et al.* JHEP **0307** (2003) 001.
9. T. Gleisberg *et al.* JHEP **0902** (2009) 007.
10. T. Sjostrand, S. Mrenna and P. Z. Skands, JHEP **0605** (2006) 026.
11. ATLAS Collaboration, ATLAS-CONF-2011-013, `https://atlas.web.cern.ch/Atlas/GROUPS/PHYSICS/CONFNOTES/ATLAS-CONF-2011-013`.
12. ATLAS Collaboration, ATLAS-CONF-2011-015, `https://atlas.web.cern.ch/Atlas/GROUPS/PHYSICS/CONFNOTES/ATLAS-CONF-2011-041`.

W/Z + Jets results from CMS

V. CIULLI on behalf of CMS Collaboration
Dipartimento di Fisica, Università di Firenze, via G. Sansone 1, 50025 Pontedera (PI) Italy

We present an overview of the studies of W and Z boson production with jets in pp collisions at a centre-of-mass energy of 7 TeV using 36 pb^{-1} of data collected in the CMS experiment. We report the measurement of the jet rates as well as the first measurement of the polarization of W bosons with large transverse momentum, and the observation of Z bosons in association with a b-quark jet.

1 Introduction

The study of the production of W and Z vector boson with jets provides a stringent and important test of perturbative QCD calculations. Furthermore, events with vector bosons and jets are the main background to searches for physics beyond the Standard Model. A precise measurement of the cross section and of the jet and boson kinematics is therefore essential. This paper presents the measurement of the jet rates [1], the first observation of W polarization [2], and of a Z boson and a b-quark jet [3], obtained with the full data sample recorded with the CMS experiment [4] during 2010, which amounts to an integrated luminosity of 36 ± 4 pb^{-1}.

2 Event selection and jet rates

The selection of W boson candidates requires one electron (muon), with $p_T > 20\,\text{GeV}$ in $|\eta| < 2.4\,(2.1)$. Misidentified leptons, as well as non prompt leptons arising from decays of heavy-flavor hadrons or decays of light mesons within jets, are suppressed by requiring the lepton to be isolated, i.e. by limiting the additional hadronic activity surrounding the lepton candidate. The transverse mass M_T of the W candidate is calculated from the missing transverse energy (MET) in the event, measured using the particle flow algorithm, and W candidates with $M_T < 20$ GeV are rejected. If a second electron (muon) with $p_T > 10$ GeV in $|\eta| < 2.4$ is found, then the event is considered for a Z candidate. Only Z candidates with a di-lepton mass between 60 and 120 GeV are retained for the following analysis.

Jets are reconstructed from the particle collection created with the particle flow algorithm and are formed with the anti-k_T clustering algorithm [5] with a size parameter of $R = 0.5$. Jet energy corrections are applied to improve the accuracy of the jet transverse energy (E_T) measurement and to flatten the jet energy response as a function of η and E_T [7]. We require $|\eta| < 2.4$, so that the jets fall within the tracker acceptance, and $E_\text{T} > 30$ GeV. The observed, uncorrected distribution of the number of reconstructed jets in the $\text{W} \to \mu\nu$ is shown in Figs. 1. The distribution from simulation, including background processes, is also shown. Overall, a good agreement is found up to $n = 6$ jets. The agreement between data and simulation is

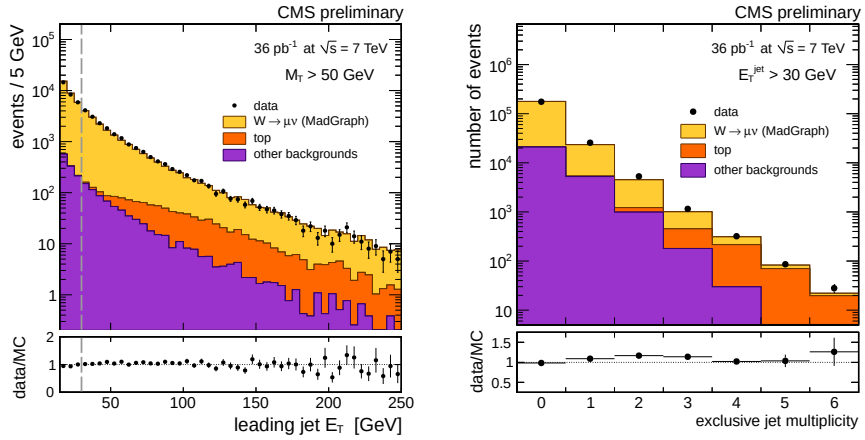

Figure 1: Distributions of the E_{T} for the leading jet (left) and number of reconstructed jets (right) in events $\mathrm{W} \to \mu\nu$. The ratio between the data and the simulation is also shown.

remarkable also for the leading jet E_{T}, which is shown for events with $M_T > 50$ GeV in order to further suppress the background. For each jet multiplicity, the number of signal events in the W channels is determined with an unbinned extended maximum likelihood fit to the transverse mass and the number of b-tagged jets in the event, in order to measure the top background. The measured rates are corrected for the selection efficiency and unfolded for detector smearing using matrix inversion with singular value decomposition. The final results are given for jet counting at particle level in the lepton and jet acceptance to ease the comparison with theory. As shown in Figure 2 for W signal, the results are found in agreement with the predictions from MadGraph [8], a multi-jet matrix element Monte Carlo matched with pythia [9] parton shower, while the pythia parton shower alone underestimates the higher jet rates.

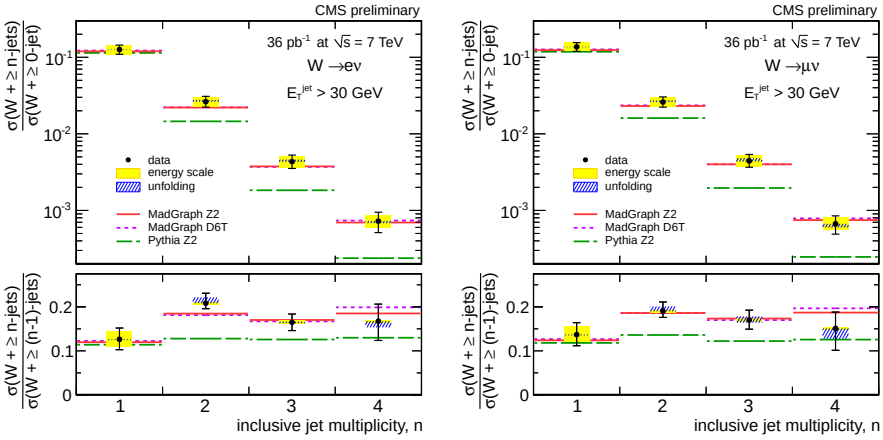

Figure 2: The ratio $\sigma(\mathrm{W} + n \text{ jets})/\sigma(\mathrm{W})$ and $\sigma(\mathrm{W} + n \text{ jets})/\sigma(\mathrm{W} + (n-1) \text{ jets})$ in the electron (left) and muon (right) channel compared to expectations from simulations. The systematic uncertainty due to the jet energy scale and the unfolding are shown, together with the total uncertainty.

3 W polarization

In pp collisions at the LHC the W's recoiling against energetic jets are expected to exhibit a sizable left-handed polarization, because of the dominance of quark-gluon initial states, along with the $V-A$ nature of the coupling of the W boson to fermions [6]. We measure the polarization

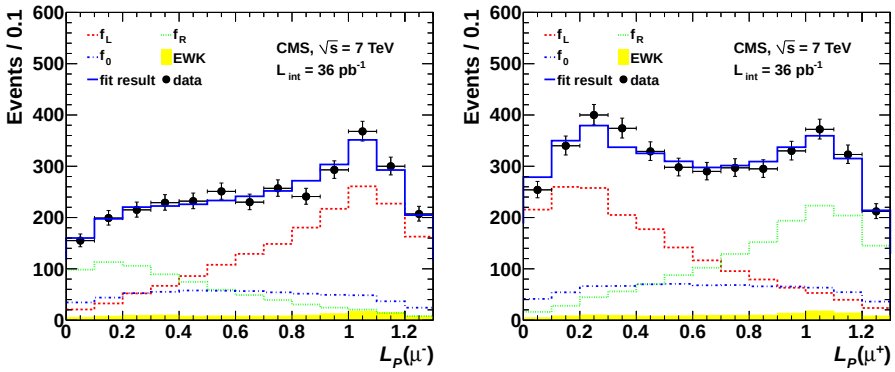

Figure 3: Fit results for the $L_P(\mu^-)$ (left) and $L_P(\mu^+)$ (right) distributions. The left-handed, right-handed and longitudinal W components, with normalization as determined by the fit, are represented by the dashed, dotted, and dash-dotted lines respectively. The shaded distribution shows the backgrounds. The solid line represents the sum of all individual components, and can be directly compared with the data distribution (circles).

of the W boson in the helicity frame, where the polar angle (θ^*) of the charged lepton from the decay in the W rest frame is measured with respect to the boson flight direction in the laboratory frame. However, the inability to determine the momentum of the neutrino along the beam axis introduces a two-fold ambiguity in the determination of the momentum of the W boson. To overcome this ambiguity the lepton projection variable, $L_P = \vec{p}_T(\ell) \cdot \vec{p}_T(\mathrm{W})/|\vec{p}_T(\mathrm{W})|^2$, which exhibits a strong correlation with $\cos\theta^*$, is used. The fractions of left-handed, right-handed, and longitudinal W bosons (f_L, f_R and f_0, respectively) are measured using a binned maximum likelihood fit to the L_P variable, separately for W^+ and W^- bosons in the electron and muon final states. The L_P distribution for each of the three polarization states of the W boson is extracted from Monte Carlo samples which are reweighted to the angular distributions expected from each polarization state in the W boson center-of-mass frame. The L_P distributions for muons are shown in Figs. 3. Also shown are the results of the fit to the individual components corresponding to the three W polarization states, and to the background. The results from $\mathrm{W} \to \mathrm{e}\nu$ and $\mathrm{W} \to \mu\nu$ are consistent. The muon fit result yields the most precise measurement, $(f_L - f_R)^- = 0.240 \pm 0.036\,(\mathrm{stat.}) \pm 0.031\,(\mathrm{syst.})$ and $f_0^- = 0.183 \pm 0.087\,(\mathrm{stat.}) \pm 0.123\,(\mathrm{syst.})$ for negatively charged W bosons, and $(f_L - f_R)^+ = 0.310 \pm 0.036\,(\mathrm{stat.}) \pm 0.017\,(\mathrm{syst.})$ and $f_0^+ = 0.171 \pm 0.085\,(\mathrm{stat.}) \pm 0.099\,(\mathrm{syst.})$ for positively charged W bosons. This measurement establishes a difference between the left-handed and right-handed polarization parameters with a significance of 7.8 standard deviations for W^+ bosons and 5.1 standard deviations for W^- bosons.

4 Observation of Z +b

This final state is important at the LHC, both as a benchmark channel to the production of the Higgs boson in association with b-quarks, and as a Standard Model background to Higgs and new physics searches in final states with leptons and b-jets. In this analysis both electrons (muons) of the Z candidate are required to have $\mathrm{p}_T > 25\,(20)$ GeV. Jets with $p_T > 25$ GeV are searched for the presence of a secondary vertex and a b-tagging discriminant variable is built from the three-dimensional flight distance from the primary vertex to the chosen secondary vertex. We used both an high-efficiency (HE) and an high-purity (HP) selection, where at least two (three) tracks are required to be attached to the secondary vertex, respectively. To extract the purity $\mathcal{P}$ in b-jets, the b-tagging discriminant variable and the mass of the secondary vertex are fitted using a binned likelihood method. The purity in b-jets is found to be $55 \pm 9\,\%$ ($88 \pm 11\,\%$) for the HE (HP) selection, in good agreement with the MC estimate of $57 \pm 3\,\%$ ($82 \pm 4\,\%$). Figure 4 shows the di-lepton mass and secondary vertex mass of events surviving

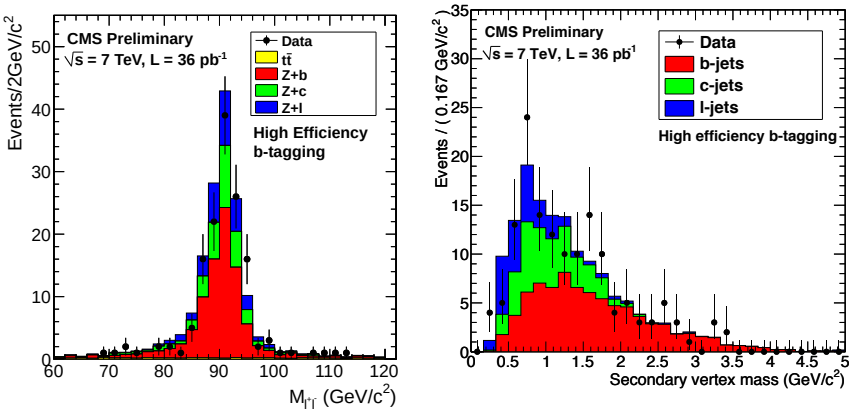

Figure 4: Di-lepton mass (left) and secondary vertex mass (right) of events passing the HE selection compared to the simulation.

the HE selection. Results are summarised in Table 1 for the high-efficiency and high-purity selections. Values expected from simulation and theory are also given.

Table 1: Ratio $\mathcal{R} = \frac{\sigma(pp \to Z+b+X)}{\sigma(pp \to Z+j+X)}$ from data and from MadGraph samples, and expected value from NLO theory.

Sample	$\mathcal{R}(Z \to ee)$ (%), $p_T^e > 25$ GeV, $\lvert\eta^e\rvert < 2.5$	$\mathcal{R}(Z \to \mu\mu)$ (%), $p_T^\mu > 20$ GeV, $\lvert\eta^\mu\rvert < 2.1$
Data HE	$4.3 \pm 0.6(stat) \pm 1.1(syst)$	$5.1 \pm 0.6(stat) \pm 1.3(syst)$
Data HP	$5.4 \pm 1.0(stat) \pm 1.2(syst)$	$4.6 \pm 0.8(stat) \pm 1.1(syst)$
MadGraph	$5.1 \pm 0.2(stat) \pm 0.2(syst) \pm 0.6(theory)$	$5.3 \pm 0.1(stat) \pm 0.2(syst) \pm 0.6(theory)$
MCFM [10]	$4.3 \pm 0.5(theory)$	$4.7 \pm 0.5(theory)$

5 Conclusions

Several studies of the production of jets in association with W and Z bosons in pp collisions at a centre-of-mass energy of 7 TeV using 36 pb^{-1} of collected data have been presented. All measurements, including the jet rates, the polarization of W and the production of b-quarks with Z bosons, are in agreement with Standard Model expectations. The precision reached in these analyses involving lepton, jet and MET reconstruction, and b-tagging, clearly establishes the readiness of the CMS experiment for searches beyond the Standard Model.

References

1. CMS Collaboration, CMS PAS **EWK-10-012**
2. CMS Collaboration, arXiv:1104.3829v1 [hep-ex]
3. CMS Collaboration, CMS PAS **EWK-10-015**
4. CMS Collaboration, JINST 3:S08004 (2008).
5. M. Cacciari, G. P. Salam, and G. Soyez, JHEP 0804:063 (2008).
6. Z. Berg *et al.*, arXiv:1103.5445v2 [hep-ph]
7. CMS Collaboration, CMS PAS **JME-10-010**
8. J. Alwall *et al.*, JHEP **09**, 028 (2007)
9. T. Sjöstrand, S. Mrenna, and P. Skands, JHEP **05**, 026 (2006)
10. J. M. Campbell and R. K. Ellis, PRD **62**, 114012 (2000)

TEVATRON RESULTS ON MULTI-PARTON INERACTIONS

N.B. SKACHKOV
Joint Institute for Nuclear Research, Joliot-Curie 6, Dubna, Russia

The D0 experiment used a sample of $\gamma + 3$ jets events (collected in RunII with an integrated luminosity L about 1fb^{-1}) to determine the fraction of events with double parton (DP) scattering in a single $p\bar{p}$ collision at $\sqrt{s} = 1.96$ TeV. The DP fraction ($f_{\rm DP}$) and effective cross section ($\sigma_{\rm eff}$), a process-independent scale parameter related to the parton density inside the nucleon, are measured in three intervals of the second (ordered in p_T) jet transverse momentum p_T^{jet2} within the range $15 \leq p_T^{jet2} \leq 30$ GeV. In this range, $f_{\rm DP}$ varies between $0.23 \leq f_{\rm DP} \leq 0.47$, while $\sigma_{\rm eff}$ has the average value $\sigma_{\rm eff}^{\rm ave} = 16.4 \pm 0.3({\rm stat}) \pm 2.3({\rm syst})$ mb. The samples of inclusive $\gamma + 2$ jet and $\gamma + 3$ jet events are also used to measure cross sections as a function of the azimuthal angle between the transverse momentum (p_T) of the γ+leading jet system and p_T of the other jet for $\gamma + 2$ jet, or p_T sum of the two other jets for $\gamma + 3$ jet events. The results are compared to different models of multiple parton interactions (MPI) in the PYTHIA and SHERPA Monte Carlo (MC) generators. The data strongly indicate a contribution from events with double parton interactions and are in good agreement with predictions provided by the new PYTHIA MPI models with p_T-ordered showers and by SHERPA with the default MPI model. The $\gamma + 2$ jet data are also used to determine the fraction of events with DP interactions as a function of the azimuthal angle binned in the second jet p_T.

It is commonly assumed that high energy inelastic scattering of nucleons occurs through a single parton-parton interaction and the contribution from double (A and B) parton collisions (see its schematic view in Fig.1 **a)**) is a negligible one. The DP cross section can be defined as:

$$\sigma_{DP} \equiv \frac{\sigma^A \sigma^B}{\sigma_{\rm eff}} \tag{1}$$

Here $\sigma_{\rm A}$ and $\sigma_{\rm B}$ are the cross sections of two independent partonic scatterings A and B. The normalization factor $\sigma_{\rm eff}$ (it has the units of cross section) is a process-independent parameter that can be related to the parton spatial density (see [1,2,3,4,5,6] and the references to basic theoretical papers presented there).

Two years ago there were only four published dedicated measurements of double parton scattering in hadron collisions: the AFS experiment in pp collisions at $\sqrt{s} = 63$ GeV [1], UA2 in $p\bar{p}$ collisions at $\sqrt{s} = 630$ GeV [2] and by CDF in $p\bar{p}$ collisions at $\sqrt{s} = 1.8$ TeV [3], [4]. The four-jet final state has been used in the first three measurements while the last, the most precise one CDF measurement [4], have used $\gamma/\pi^0 + 3$ jets events (accumulated with L =16 pb^{-1}) having the p_T of the second jet (ordered in p_T) within the interval $5 < p_T^{\rm jet2} < 7$ GeV and $p_T^{\gamma} > 16$ GeV. The substitution of one jet by photon leads to an order of magnitude improvement in the ratio of the signal to background over the earlier CDF study [4]. A new technique for extracting $\sigma_{\rm eff}$ was proposed in [4]. It uses only quantities determined from data analysis and minimizes the impact of theoretical assumptions used in previous three measurements with a 4-jet final state [1,2,3].

The results of two new measurements of inclusive $\gamma + 3$ jetand $\gamma + 2$ jet events (see Fig.1 **b)** and **c)**) were presented by D0 during last two years [5,6]. They are based on new methods proposed by CDF for studing the DP processes [4]. High integrated luminosity L =1.02 $\pm$ 0.06 fb^{-1} collected in RunII allowed to extend the mentioned above $p_T^{\rm jet2}$ interval of 2 GeV width, used in [4], up to the range $15 \leq p_T^{jet2} \leq 30$ GeV and to select thee(two) jets $\gamma + 3(2)$ jet $+ X$ events with high photon transverse momentum, $60 < p_T^{\gamma} < 80$ GeV (vs. $p_T^{\gamma} > 16$ GeV in CDF, where "photon" was taken to mean either a single direct photon or multiple photons from neutral meson decay in jet fragmentation [4]) with a large photon purity which is well known from previous D0 RunII measurements [8]. The high p_T^{γ} scale (i.e. the scale of the first parton interaction) allows a better separation of the first and second parton interactions in momentum space.

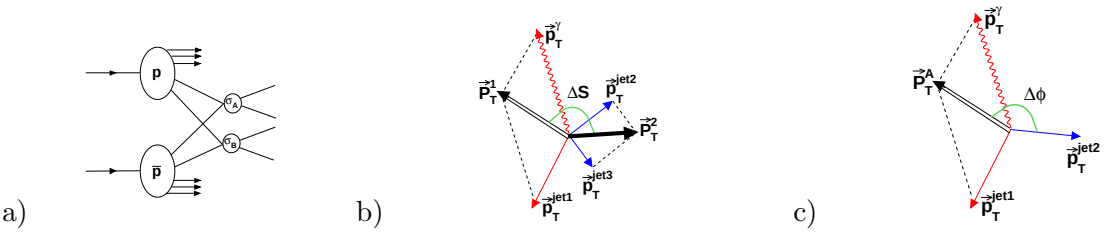

Figure 1: **a)** Schematical diagram of a double parton scattering event; **b)** Diagram showing the two possible sum vectors of the $\gamma + 1$ jet and dijet systems in $\gamma + 3$ jet events; **c)** Diagram showing the two possible sum vector of the $\gamma + 1$ jet system and $\vec{p}_T^{\,\rm jet2}$ in $\gamma + 2$ jet event.

Three DP signal diagrams (DP Type I, DP Type II, DP Type III), which give the most conribution to the cross section, are shown in plot **a)** of Fig.2 together with the diagram of a background single parton-parton (SP) collision with hard gluon bremsstrahlung $qg \to q\gamma gg$, $q\bar{q} \to g\gamma gg$ that has the same $\gamma+$ 3jets signature. In plot **a)** the light and bold lines correspond to two separate parton interactions. The dotted line represents unreconstructed jet. The SP events together with double interaction (DI) events (i.e. events produced in two distinct hard interactions occurring in two separate $p\bar{p}$ collisions in the same beam crossing) provide an essential background.

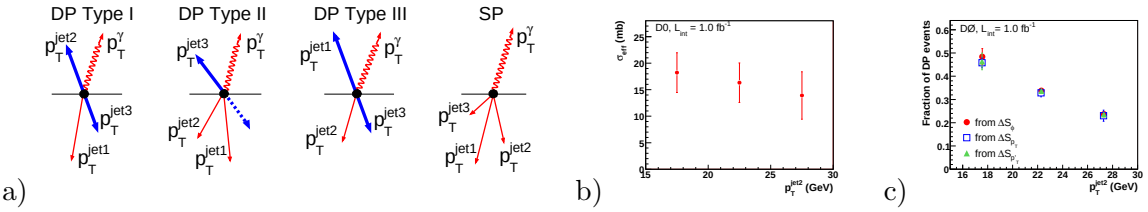

Figure 2: **a)** Diagrams of DP Types I, II, III and SP events. For DP events, the light and bold lines correspond to two separate parton interactions. The dotted line represents unreconstructed jet; **b)** $\sigma_{\rm eff}$ values in the three "p_T^{jet2}" intervals; **c)** Fractions of DP events in the three "p_T^{jet2}" intervals.

D0 experiments[5,6] collected γ+3 jets and γ+2 jets events which were selected with leading (in p_T) jet $p_T > 25$ GeV, while the next-to-leading (second) and third jets must have $p_T > 15$ GeV. Each event must contain at least one γ in the rapidity region $|y| < 1.0$ or $1.5 < |y| < 2.5$ and at least three jets with $|y| < 3.0$. The events used for the analysis should first pass triggers based on the identification of high p_T clusters in the EM calorimeter with loose shower shape requirements for photons. These triggers are 100% efficient for $p_T^{\gamma} > 35$ GeV. Jets are reconstructed using the

iterative midpoint cone algorithm with a cone size of $R_{\eta,\phi} = 0.7$. Jets must satisfy quality criteria which suppress background from leptons, photons, and detector noise effects. The measured jet energy is corrected (different to[4]) for the energy response of the calorimeter, energy showering in and out the jet cone, and additional energy from event pile-up and multiple proton interactions.

The plot **b)** of Fig. 2 shows the values of $\sigma_{\rm eff}$ which were extracted in three intervals of the second jet transverse momentum: $15 < p_T^{jet2} < 20$ GeV, $20 < p_T^{jet2} < 25$ GeV and $25 < p_T^{jet2} < 30$ GeV[5] by comparing the number of the observed DP $\gamma+$ 3 jets events occurring in one $p\bar{p}$ collision to the number of DI $\gamma+$ 3 jets. The knowledge of cross section of inelastic non-diffractive (hard) $p\bar{p}$ interactions σ_{hard} was needed also. It was found by extrapolation of the values σ_{hard}, measured by CDF and D0, up to $\sqrt{s} = 1.96$ TeV.

The fraction of DP events is determined by using a set of ΔS_ϕ , ΔS_{p_T} , and $\Delta S_{p'_T}$ variables sensitive to the kinematic configurations of the two independent scatterings of parton pairs, specifically to the difference between the p_T imbalance of the two object pairs in DP and SP $\gamma+$ 3jets events. The $\Delta S_{p_T}, \Delta S_{p'_T}$ variables are used in [2,4], while the ΔS_ϕ is first proposed in [5] measurement. The extracted values of DP fraction are shown in Fig.2, **c)**. It is seen that the DP fraction, measured by [5] in three (of equal width) intervals of the second (ordered in p_T) jet transverse momentum p_T^{jet2}, gives an essential contribution to total cross section (from about 47% down to 24%) within the $15 < p_T^{jet2} < 30$ GeV range.

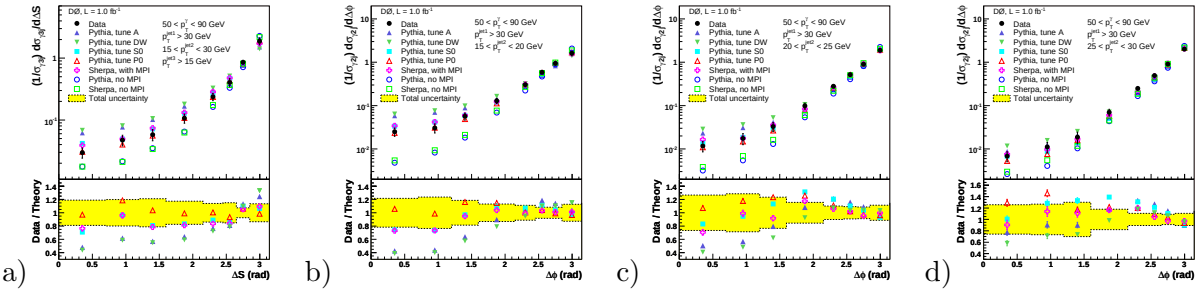

Figure 3: **a)** The $(1/\sigma_{\gamma 3j})d\sigma_{\gamma 3j}/d\Delta S$ cross sections in data and MC models and Data/Theory (only models including MPI) ratios for the bin $15 < p_T^{\rm jet2} < 30$ GeV; **b)** The $(1/\sigma_{\gamma 2j})d\sigma_{\gamma 2j}/d\Delta\phi$ cross sections in data and MC models and Data/Theory (only models including MPI) ratios for the bin $15 < p_T^{\rm jet2} < 20$ GeV; **c)** Same as in **b)**, but for the bin $20 < p_T^{\rm jet2} < 25$ GeV; **d)** Same as in **b)**, but for the bin $25 < p_T^{\rm jet2} < 30$ GeV.

Plots **a)** - **c)** in Fig.3 present the four D0 measurements of differential cross sections (with respect to ΔS- and $\Delta\phi$- angle variables, shown correspondingly in the plots **b)** and **c)** of Fig.2) $(1/\sigma_{\gamma 3j})d\sigma_{\gamma 3j}/d\Delta S$ in a single $p_T^{\rm jet2}$ bin (15−30 GeV) for γ+3 jet events and $(1/\sigma_{\gamma 2j})d\sigma_{\gamma 2j}/d\Delta\phi$ in three $p_T^{\rm jet2}$ bins ($15-20$, $20-25$, and $25-30$ GeV) for $\gamma + 2$ jet events. The differential distributions decrease by two order of magnitude when moving from ΔS $(\Delta\phi) \approx \pi$ to 0 and have a total uncertainty ($\delta_{\rm tot}$) between 7 and 30%, which is dominated by systematics ($\delta_{\rm syst}$). They are compared to predictions from a few multipal parton interactions (MPI) models implemented in PYTHIA and SHERPA. For completeness, predictions from SP models in PYTHIA and SHERPA (SHERPA-1 model) are also shown here. From these plots in Fig.3 one can see that the considered variables, ΔS and $\Delta\phi$, are very sensitive to the models, with predictions varying significantly and differing from each other by up to a factor 2.5 at the small ΔS and $\Delta\phi$ angles, i.e. right in the place where the relative DP contribution is expected to be the highest. It is seen also that that (a) the predictions derived from SP models differ significantly from the measurements; (b) the data favor mostly the predictions done with new PYTHIA MPI models, S0 and Perugia and also SHERPA with its MPI model; while (c) the predictions from old MPI models, tune A and DW, are much less favored. Among the considered new MPI models, agreement with data is a little worse for the S0 and P-soft models [6].

The measurement of the differential cross section with respect to $\Delta\phi$ and predictions for the SP contributions to this cross sections in different models was used to determine the fraction of $\gamma + 2$ jet events which originate from DP interactions as a function of the second parton interaction scale ($p_T^{\rm jet2}$) and of the $\Delta\phi$ angle [6]. Using the uniform distribution for the DP model template and SHERPA-1 as the SP model template, the fit of the $\Delta\phi$ distributions measured in data was done to obtain the fraction of DP events with a maximum likelihood fit. The distributions in data, SP, and DP models, as well as a sum of the SP and DP distributions, weighted with their respective fractions, are shown in plots **a) - c)** of Fig.4 for the three $p_T^{\rm jet2}$ intervals. One can see that the sum of the SP and DP predictions reproduces the data very well.

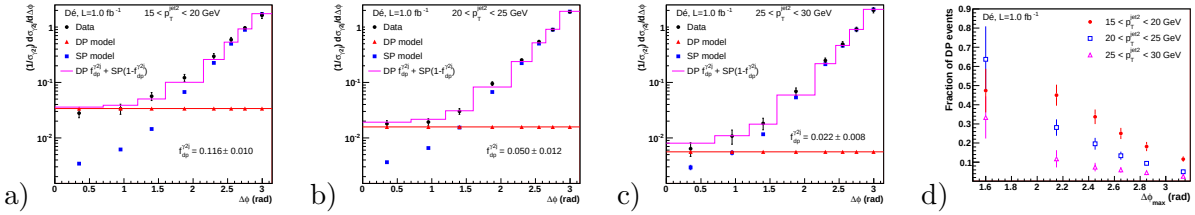

Figure 4: **a)** $\Delta\phi$ distribution in data, SP, and DP models, and the sum of the SP and DP contributions weighted with their fractions in the bin $15 < p_T^{\rm jet2} < 20$ GeV; **b)** Same as in **a)**, but for the bin $20 < p_T^{\rm jet2} < 25$ GeV; **c)** Same as in **a)**, but for the bin $25 < p_T^{\rm jet2} < 30$ GeV; **d)** Fractions of DP events (%) with total uncertainties for $0 \leq \Delta\phi \leq \pi$ in the three $p_T^{\rm jet2}$ bins.

From the same plots in Fig.4 one can see that the fraction of DP events is expected to be higher at smaller $\Delta\phi$ angles. To determine the fractions as a function of the $\Delta\phi$ angle, a simple fit was done in the different $\Delta\phi$ regions by excluding the bins at high $\Delta\phi$ values; for example, by considering the $\Delta\phi$ regions $0 - 2.85, 0 - 2.65, 0 - 2.45, 0 - 2.15$, and $0 - 1.60$. The DP fractions with total uncertainties as functions of the upper limit on $\Delta\phi$ ($\Delta\phi_{\rm max}$) for all three $p_T^{\rm jet2}$ bins are shown in plot **d)**. As expected, they grow significantly for the smaller angles and are higher for smaller $p_T^{\rm jet2}$ bins.

The found sizable DP contribution can provide an important background for searches of deviations from Standard Model at Tevatron and it indicates the importance of performing the analogous measurements of double parton interactions at LHC for searches of Higgs boson and New Physics signals.

References

1. AFS Collaboration, T. Akesson *et al.*, Z.Phys. C **34**, 163 (1987).
2. UA2 Collaboration, J. Alitti *et al.*, Phys. Lett. B **268**, 145 (1991).
3. CDF Collaboration, F. Abe *et al.*, Phys. Rev. D **47**, 4857 (1993).
4. CDF Collaboration, F. Abe *et al.*, Phys. Rev. D **56**, 3811 (1997).
5. D0 Collaboration, V.M. Abazov *et al.*, Phys. Rev. D **81**, 052012 (2010).
6. D0 Collaboration, V.M. Abazov *et al.*, Phys. Rev. D **83**, 052008 (2011)
7. CDF Collaboration, F. Abe *et al.*, Phys. Rev. D **57**, 67 (1998).
8. D0 Collaboration, V.M. Abazov *et al.*, Phys. Lett. B **666**, 435 (2008); Phys. Rev. Lett. B **102** , 192002, (2009).

INVESTIGATIONS OF DOUBLE PARTON SCATTERING EXAMPLE OF $pp \to b\ \bar{b}$ jet jet X

EDMOND L. BERGER
High Energy Physics Division, Argonne National Laboratory, Argonne, IL 60439, U.S.A

Signature kinematic variables and characteristic concentrations in phase space of double parton scattering are discussed. These properties should allow the double-parton contribution to $pp \to b\ \bar{b}$ jet jet X at Large Hadron Collider energies to be distinguished from the usual single parton scattering contribution. A methodology is suggested to measure the size of the double-parton cross section.

1 Introduction

Double parton scattering (DPS) means that two short-distance hard-scattering subprocesses occur in a given hadronic interaction, with two initial partons being active from each of the incident protons in a collision at the Large Hadron Collider (LHC). The concept is shown for illustrative purposes in the left diagram of Fig. 1. It may be contrasted with conventional single parton scattering (SPS) in the right diagram, in which one short-distance subprocess occurs, with one parton active from each initial hadron. Both contribute to the same 4 parton final state. Processes such as sketched in the left diagram of Fig. 1 are included in descriptions of the underlying event in some Monte Carlo codes. Our interest is to investigate whether this second hard process can be shown to be present in LHC data, as a perturbatively calculable hard part of the underlying event.

Studies of double parton scattering have a long history theoretically, with many references to prior work listed in our paper [1], and there is evidence in data [2]. A greater role for double-parton processes may be expected at the LHC where higher luminosities are anticipated along with the higher collision energies. A large contribution from double parton scattering could result in a larger than otherwise predicted rate for multi-jet production, and produce relevant backgrounds in searches for signals of new phenomena. The high energy of the LHC also provides an increased dynamic range of available phase space for detailed investigations of DPS.

Our aims [1] are to address whether double parton scattering can be shown to exist as a discernible contribution in well defined and accessible final states, and to establish the characteristic features that allow its measurement. We show that double parton scattering produces an enhancement of events in regions of phase space in which the contribution from single parton scattering is relatively small. If such enhancements are observed experimentally, with the kinematic dependence we predict, then we will have a direct empirical means to measure the size of the double parton contribution. In addition to its role in general LHC phenomenology, this measurement will have an impact on the development of partonic models of hadrons, since the effective cross section for double parton scattering measures the size in impact parameter space of the incident hadron's partonic hard core.

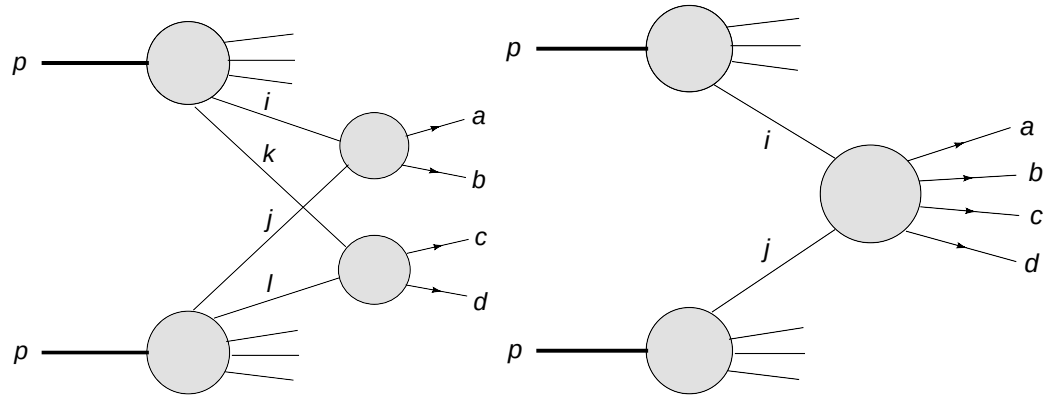

Figure 1: (diagram on the left) Sketch of a double-parton process in which the active partons are i and k from one proton and j and l from the second proton. The two hard scattering subprocess are $A(i\ j \to a\ b)$ and $B(k\ l \to c\ d)$. (diagram on the right) Sketch of a single-parton process in which the active partons are i from one proton and j from the second proton. The hard scattering subprocess is $A(i\ j \to a\ b\ c\ d)$.

From the perspective of sensible rates and experimental tagging, a good process to examine should be the 4 parton final state in which there are 2 hadronic jets plus a b quark and a $\bar{b}$ antiquark, *viz.* $b\ \bar{b}\ j_1\ j_2$. If the final state arises from double parton scattering, then it is plausible that one subprocess produces the $b\ \bar{b}$ system and another subprocess produces the two jets. There are, of course, many single parton scattering (2 to 4 parton) subprocesses that can result in the $b\ \bar{b}\ j_1\ j_2$ final state, and we identify kinematic distributions that show notable separations of the two contributions.

The state-of-the-art of calculations of single parton scattering is well developed whereas the phenomenology of double parton scattering is less advanced. For $pp \to b\bar{b}j_1j_2X$, assuming that the two subprocesses $A(i\ j \to b\ \bar{b})$ and $B(k\ l \to j_1\ j_2)$ in Fig. 1 are weakly correlated, and that kinematic and dynamic correlations between the two partons from each hadron may be safely neglected, we employ the common heuristic expression for the DPS differential cross section

$$d\sigma^{DPS}(pp \to b\bar{b}j_1j_2X) = \frac{d\sigma^{SPS}(pp \to b\bar{b}X)d\sigma^{SPS}(pp \to j_1j_2X)}{\sigma_{\rm eff}}. \qquad (1)$$

The numerator is a product of single parton scattering cross sections. In the denominator, there is a term $\sigma_{\rm eff}$ with the dimensions of a cross section. Given that one hard scatter has taken place, $\sigma_{\rm eff}$ measures the effective probability for a second hard scatter. Collider data [2] yield values in the range $\sigma_{\rm eff} \sim 12$ mb. We use this value for the estimates we make, but we emphasize that the goal should be determine its value in experiments at LHC energies.

The details of our calculation of the double parton and the single parton contributions to $p\ p \to b\ \bar{b}\ j_1\ j_2\ X$ are found in our paper [1]. We perform full event simulations at the parton level and apply a series of cuts to emulate experimental analyses. We also treat the double parton and the single parton contributions to 4 jet production, again finding that good separation is possible despite the combinatorial uncertainty in the pairing of jets [1].

2 Distinguishing variables

Correlations in the final state are predicted to be quite different between the double parton and the single parton contributions. For example, we examine the distribution of events as function of the angle Φ between the planes defined by the $b\bar{b}$ system and by the jj system. If the two scattering processes $ij \to b\bar{b}$ and $kl \to jj$ which produce the DPS final state are truly independent, one would expect to see a flat distribution in the angle Φ. By contrast,

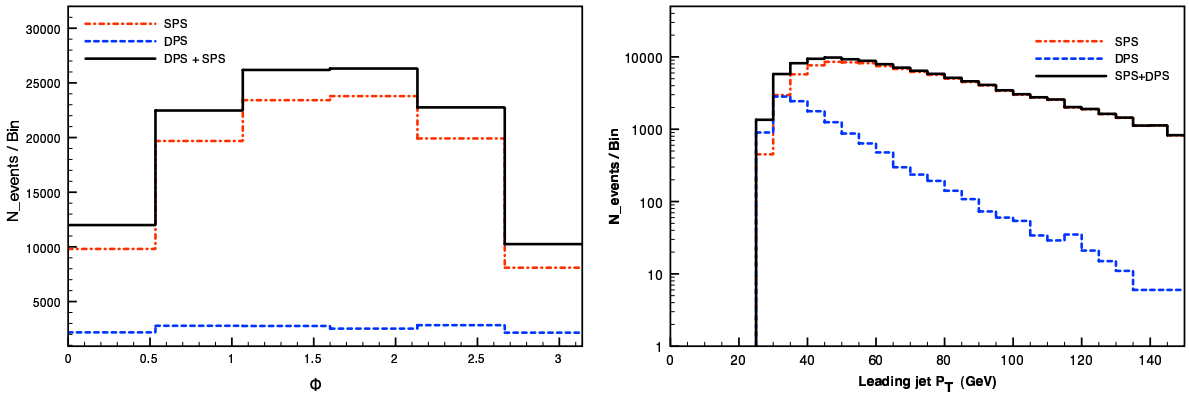

Figure 2: (left panel) Event rate as a function of the angle between the two planes defined by the $b\bar{b}$ and jj systems. In SPS events, there is a correlation among the planes which is absent for DPS events. (right panel) The transverse momentum p_T distribution of the leading jet in $jjb\bar{b}$, either a b jet or a light jet j.

many diagrams, including some with non-trivial spin correlations, contribute to the 2 parton to 4 parton final state in SPS $ij \to b\bar{b}$jetjet, and one would expect some correlation between the two planes. In the left panel of Fig. 2, we display the number of events as a function of the angle between the two planes. There is an evident correlation between the two planes in SPS, while the distribution is flat in DPS, consistent with the expectation that the two planes are uncorrelated.

Another dynamic difference between DPS and SPS is the behavior of event rates as a function of transverse momentum. As an example of this, in the right panel of Fig. 2, we show the transverse momentum distribution for the leading jet (either a b or light j) for both DPS and SPS. SPS produces a relatively hard spectrum, associated with the presence of several propagators in the hard-scattering matrix element. On the other hand, DPS produces a much softer spectrum which (up to issues of normalization in the form of $\sigma_{\rm eff}$) can dominate at small values of transverse momentum. For the value of $\sigma_{\rm eff}$ and the cuts that we use, SPS tends to dominate over the full range of transverse momentum considered. The cross-over between the two contributions to the total event rate is ~ 30 GeV for the acceptance cuts considered. A smaller (larger) value of $\sigma_{\rm eff}$ would move the cross-over to a larger (smaller) value of the transverse momentum of the leading jet.

Although interesting, the two distributions in Fig. 2 would not allow the two components, DPS and SPS, to be separated. We turn next to the search for variables that could allow a clear separation of the contributions. At lowest order for a $2 \to 2$ process, the vector sum of the transverse momenta of the final state pair vanishes, although in reality, radiation and momentum mismeasurement smear the expected peak near zero. Nevertheless, the DPS events are expected to show a reasonably well-balanced distribution in the transverse momenta of the jet pairs. To encapsulate this expectation for both light jet pairs and b-tagged pairs, we use the variable [2]:

$$S'_{p_T} = \frac{1}{\sqrt{2}} \sqrt{\left(\frac{|p_T(b_1, b_2)|}{|p_T(b_1)| + |p_T(b_2)|} \right)^2 + \left(\frac{|p_T(j_1, j_2)|}{|p_T(j_1)| + |p_T(j_2)|} \right)^2}. \qquad (2)$$

Here $p_T(b_1, b_2)$ is the vector sum of the transverse momenta of the two final state b jets, and $p_T(j_1, j_2)$ is the vector sum of the transverse momenta of the two (non b) jets. We expect $p_T \sim 0$ for both of these vector sums.

The distribution in S'_{p_T} is shown in Fig. 3(a). As expected, the DPS events are peaked near $S'_{p_T} \sim 0$ and are well-separated from the total sample. The SPS events, on the other hand, tend to be broadly distributed and show a peak near $S'_{p_T} \sim 1$. The peak near 1 is related to the fact

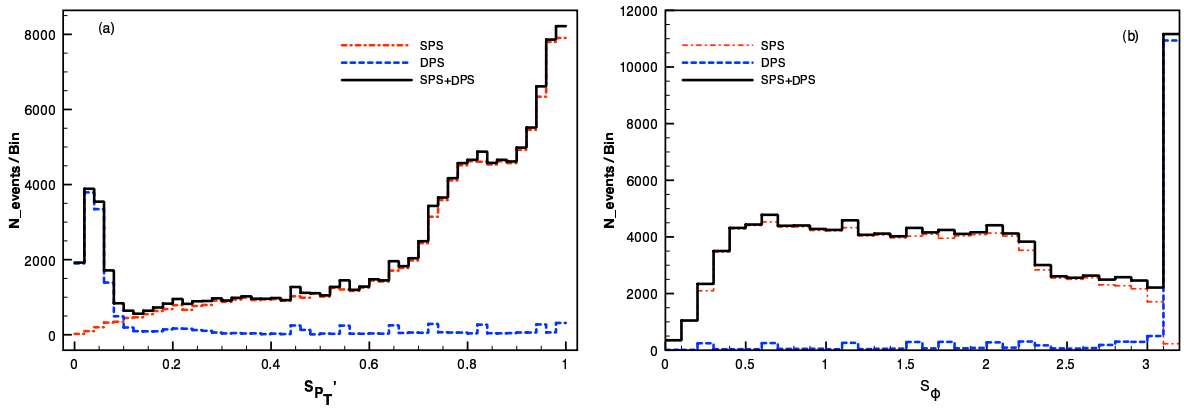

Figure 3: (a) Distribution of events in S'_{p_T} for the DPS and SPS samples. Due to the back-to-back nature of the $2 \to 2$ events in DPS scattering, the transverse momenta of the jet pair and of the b-tagged jet pair are small, resulting in a small value of S'_{p_T}. (b) The variable S_ϕ for DPS and SPS+DPS events provides a stronger separation of the underlying DPS events from the total sample when compared to $\Delta\phi$ for any pair.

that a significant number of the SPS $b\bar{b}$ or jj pairs arise from gluon splitting which yields a large p_T imbalance and, thus, larger values of S'_{p_T}.

The azimuthal angle between pairs of jets is another variable that can represent the roughly back-to-back hard-scattering topology of the DPS events. We expect the azimuthal angle between the pairs of jets corresponding to each hard scattering event to be strongly peaked near $\Delta\phi_{jj} \sim \Delta\phi_{bb} \sim \pi$. Real radiation of an additional jet, where the extra jet is missed because it fails the threshold or acceptance cuts, allows smaller values of $\Delta\phi_{jj}$. There is a clear peak near $\Delta\phi_{jj} = \pi$ for DPS events, while the events are more broadly distributed in SPS events [1]. A secondary peak near small $\Delta\phi_{jj}$ arises from gluon splitting which typically produces nearly collinear jets. As in the case of the S'_{p_T} variable, the separation of DPS events from SPS events becomes more pronounced if information is used from both the $b\bar{b}$ and jj systems. One distribution built from a combination of the azimuthal angle separations of both jj and $b\bar{b}$ pairs is [2]:

$$S_\phi = \frac{1}{\sqrt{2}}\sqrt{\Delta\phi(b_1, b_2)^2 + \Delta\phi(j_1, j_2)^2}. \tag{3}$$

The SPS events are broadly distributed across the allowed range of S_ϕ, shown in Fig. 3(b). However, the combined information from both the $b\bar{b}$ and jj systems shows that the DPS events produce a sharp and substantial peak near $S_\phi \simeq \pi$ which is well-separated from the total sample. The narrow peaks near $\Delta\phi_{jj} = \pi$ and near $S_\phi = 1$ are smeared somewhat once soft QCD radiation and other higher-order terms are included in the calculation.

In our simulations, the variable S'_{p_T} appears to be a more effective discriminator than S_ϕ. However, given the leading order nature of our calculation and the absence of smearing associated with initial state soft radiation, this picture is subject to change, and a variable such as S_ϕ (or some other variable) may offer a clearer signal of DPS at the LHC. Realistically, it would be valuable to study both distributions, once LHC data are available, in order to determine which is more instructive.

The evidence in one-dimensional distributions for distinct regions of DPS dominance prompts the search for greater discrimination in a two dimensional distribution of one variable against another. One scatter plot with interesting features is displayed in Fig. 4. The DPS events are seen to be clustered near $S'_{p_T} = 0$ and are uniformly distributed in Φ. The SPS events peak toward $S'_{p_T} = 1$ and show a roughly $\sin\Phi$ character. While already evident in one-dimensional projections, these two features are more apparent in the scatter plot Fig. 4. Moreover, the scatter plot shows a valley of relatively low density between $S'_{p_T} \sim 0.1$ and ~ 0.4. In an experimental

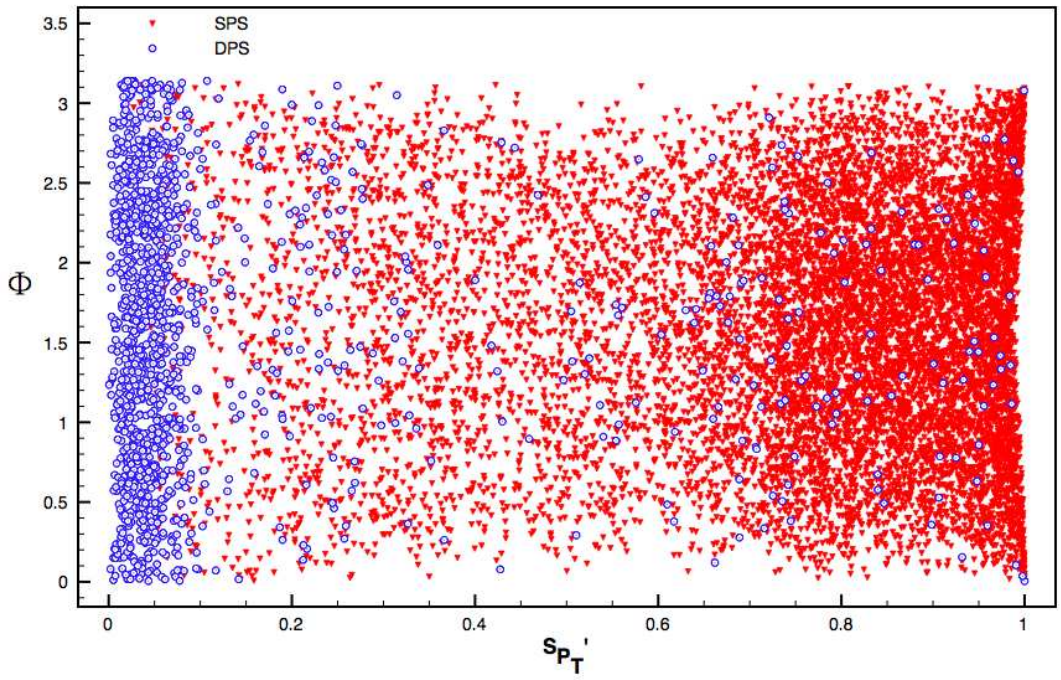

Figure 4: Two-dimensional distribution of events in the inter-plane angle Φ and the scaled transverse momentum variable S'_{p_T} for the DPS and SPS samples.

one-dimensional Φ distribution, one would see the sum of the DPS and SPS contributions. If structure is seen in data similar to that shown in the scatter plot Fig. 4, one could make a cut at $S'_{p_T} < 0.1$ or 0.2 and verify whether the experimental distribution in Φ is flat as expected for DPS events.

3 Strategy and Further Work

The clear separation of DPS from SPS events in Fig. 4 suggests a methodology for the study of DPS. One can begin with a clean process such as $pp \to b\bar{b}j_1j_2X$ and examine the distribution of events in the plane defined by S'_{p_T} and Φ. We expect to see a concentration of events near $S'_{p_T} = 0$ that is uniformly distributed in Φ. These are the DPS events. Assuming that a valley of low density is observed between $S'_{p_T} \sim 0.1$ and ~ 0.4, one can make a cut there that produces an enhanced DPS sample. Relative to the overall sample, this enhanced sample should show a more rapid decrease of the cross section as a function of the transverse momentum of the leading jet, and the DPS enhanced sample can be used to measure $\sigma_{\rm eff}$. A similar examination of other final states, such as 4 jet production, will answer whether the extracted values of $\sigma_{\rm eff}$ are roughly the same. Theoretical and experimental studies of other processes can follow, such as $b\bar{b}t\bar{t}$, Wjj, and Hjj.

On the phenomenological front, next-to-leading order (NLO) expressions should be included for both the SPS and DPS contributions. The NLO effects are expected to change normalizations and, more importantly, the distributions in phase space. The sharp peaks near $S_\phi \simeq \pi$ in Fig. 3(b) and $S'_{p_T} = 0$ in Fig. 3(a) will be broader and likely displaced somewhat. The weak correlation between subprocesses assumed in Eq. (1) cannot be strictly true [3]. With a large enough data sample at the LHC one could investigate the extent to which correlations play a significant role.

Finally, it would be good to examine the theoretical underpinnings of Eq. (1) and, in the

process, gain better insight into the significance of $\sigma_{\rm eff}$. A firm basis is desirable for Eq. (1) starting from the formal expression for the differential cross section in terms of the absolute square of the full matrix element integrated over phase space:

$$d\sigma(pp \to b\bar{b}j_1j_2X) = \frac{1}{2s}|M(pp \to b\bar{b}j_1j_2X)|^2 dPS_{b\bar{b}j_1j_2X}. \tag{4}$$

The amplitude $M(pp \to b\bar{b}j_1j_2X)$ should include a sum of amplitudes for 2-parton collisions (one active from each incident hadron, i.e., $2 \to 4$); 3-parton collisions (two active from one hadron and one active from the other); and 4-parton collisions (two active from each hadron or three from one and one from the other), and so forth that all yield the same 4 parton final state. There will be contributions to the final state from the squares of individual amplitudes as well as interference terms. Specializing to $4 \to 4$, the DPS case, one would start from a 4-parton $\to$ 4-parton hard part. Not evident at this time is how the four-parton matrix element can be reduced to a product of two matrix elements for the single parton scatterings, needed for Eq. (1). The demonstration of clear DPS signals in LHC data would be an important stimulus for further theoretical studies.

Acknowledgments

This work was done in collaboration with Chris Jackson and Gabe Shaughnessy and supported financially by the U. S. Department of Energy under Contract No. DE-AC02-06CH11357. I acknowledge valuable discussions with Tom LeCompte and Jianwei Qiu.

References

1. E. L. Berger, C. B. Jackson and G. Shaughnessy, Phys. Rev. D **81**, 014014 (2010) [arXiv:0911.5348 [hep-ph]] and numerous references therein.
2. V. M. Abazov *et al.* [D0 Collaboration], Phys. Rev. D **81**, 052012 (2010) [arXiv:0912.5104 [hep-ex]] and earlier experimental references cited therein.
3. J. R. Gaunt and W. J. Stirling, JHEP **1003** (2010) 005 [arXiv:0910.4347 [hep-ph]].

SOFT QCD RESULTS FROM ATLAS AND CMS

CLAUDIA-ELISABETH WULZ, for the ATLAS and CMS Collaborations
Institute of High Energy Physics of the Austrian Academy of Sciences,
Nikolsdorfergasse 18, 1050 Vienna, Austria

The ATLAS and CMS Collaborations have measured properties of minimum bias events and have determined characteristics of the underlying event in proton-proton collisions at three LHC centre-of-mass energies. Comparisons to common phenomenological models and partially to other experiments have been made. The production of the strange particles K^0_S, Λ and Ξ is discussed. Particle correlation studies, in particular Bose-Einstein as well as long- and short-range angular correlations in proton-proton and lead ion events are explained.

1 Properties of minimum bias events

Ideally minimum bias events are those recorded with a totally inclusive trigger. The exact definition depends on the experiment. Usually minimum bias only refers to non-single-diffractive (NSD) events. In ATLAS [1] and CMS [2] similar minimum bias trigger detectors are used. ATLAS has two stations of Minimum Bias Trigger Scintillators (MBTS) located upstream and downstream at $z = \pm 3.56$ m from the nominal collision vertex in the pseudorapidity intervals $2.09 < |\eta| < 2.82$ and $2.82 < |\eta| < 3.84$. CMS has Beam Scintillator Counters (BSC) at $z = \pm 10.86$ m within $3.23 < |\eta| < 4.65$. Both experiments also use signals from a beam pick-up based timing system (BPTX) at $z = \pm 175$ m with a time resolution of 200 ps in their minimum bias trigger.

Transverse momentum spectra of charged particles have been measured in a large range of p_T. Fig. 1 shows results from the CMS experiment and comparisons to CDF data [3]. Calorimeter-based transverse energy triggers have been used in the high-p_T-region instead of the normal minimum bias trigger. The data are fully corrected. The inclusive invariant cross-section expressed as a function of the scaling variable $x_T = 2p_T/\sqrt{s}$ is given by Eq. 1.

$$E\frac{d^3\sigma}{dp^3} = F(x_T)/p_T^{n(x_T,\sqrt{s})} = F'(x_T)/\sqrt{s}^{n(x_T,\sqrt{s})} \quad (1)$$

Minimum bias pseudorapidity and multiplicity distributions as measured by ATLAS [4] are depicted in Fig. 2. The rapidity plateau extends to $|\eta| \approx 1$ for both centre-of-mass energies of 0.9 and 7 TeV, however, there is an increase of almost a factor of two in its height. No Monte Carlo tune describes the multiplicity distribution shown in Fig. 2c well.

2 Underlying event studies

The underlying event (UE) comprises all particles except those from a given hard interaction of interest. It has components from multiple semi-hard parton scattering processes and soft

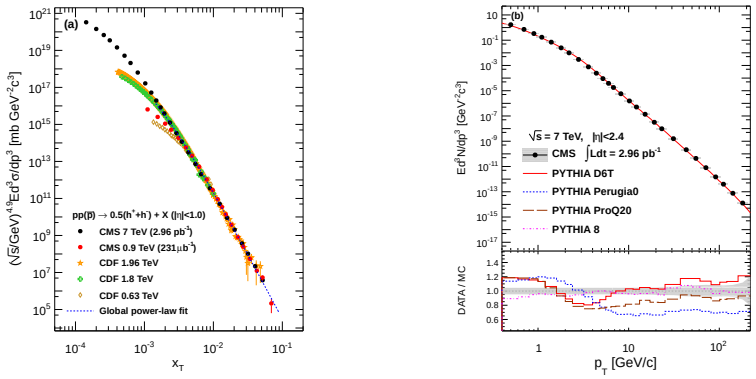

Figure 1: x_T scaling curves (a), inclusive invariant cross-section (b)

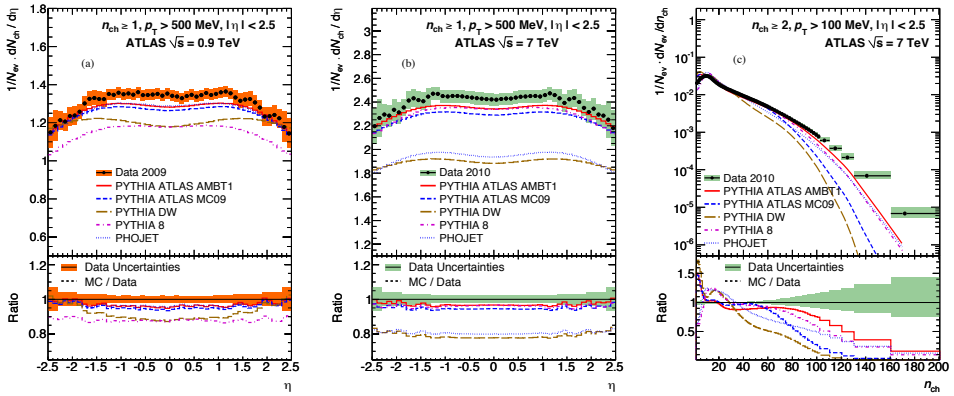

Figure 2: Minimum bias pseudorapidity distributions at $\sqrt{s} = 0.9$ TeV (a) and 7 TeV (b), multiplicity distribution at $\sqrt{s} = 7$ TeV (c)

components from beam-beam remnants. The dominant momentum flow defines three regions in the plane transverse to the incoming beams. It is given by the direction of the highest-p$_T$ track in ATLAS, whereas in CMS the leading track jet is used instead. The region within an azimuthal angle difference of $|\Delta\phi| < 60^0$ with respect to the leading object is called the toward region, and the one opposite ($|\Delta\phi| > 120^0$) the away region. The area in between, the transverse region, is the one that is most sensitive to the UE.

ATLAS[5] and CMS[6] measured various properties of charged particles in the UE such as multiplicity and transverse momentum distributions. Multiplicity and Σp_T densities as a function of the leading-p_T entity were also studied. There is a strong growth of UE activity with $\sqrt{s}$.

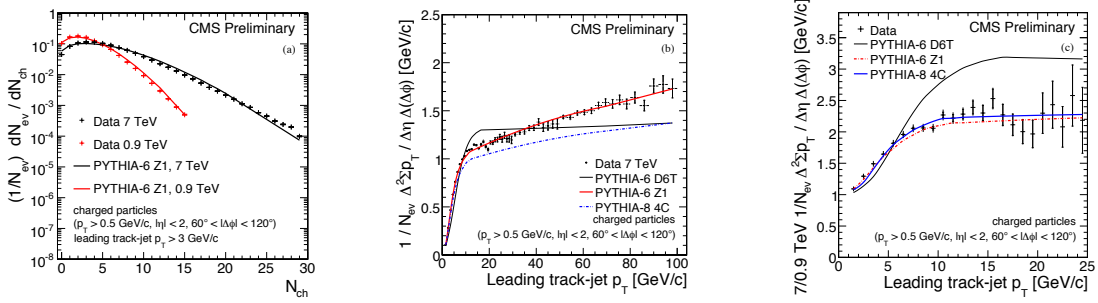

Figure 3: Underlying event multiplicites (a), average scalar momentum sum (b), multiplicity density ratio (c)

Fig. 3a shows the increase of the number of events for centre-of-mass energies from 0.9 to 7 TeV

as a function of multiplicity for the transverse region. The average scalar momentum sum rises sharply till 8 GeV due to the increase of multiple parton interaction activity, followed by a slow increase thereafter (Fig. 3b). The distributions in Fig. 3 are well reproduced by the PYTHIA Z1 Monte Carlo tune [7].

The charged particle multiplicity density in the transverse region is plotted in Fig. 4a. Compared to minimum bias there is about two times more activity in the UE. All Monte Carlo models underestimate the multiplicity. Figs. 4b and 4c show the increase of the UE p_T by about 20% from 0.9 to 7 TeV, well reproduced by a variety of models.

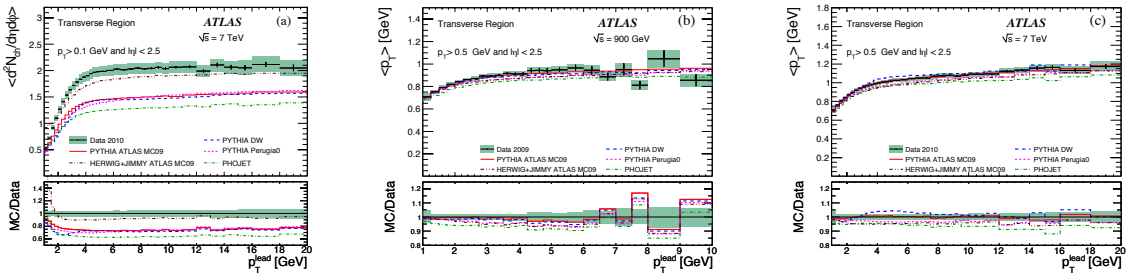

Figure 4: Charged particle multiplicity density (a), average transverse momentum at $\sqrt{s} = 900$ GeV (b) and 7 TeV (c)

3 Strangeness production

The production of the strange hadrons K^0_S, Λ and Ξ has been studied [8]. The mass peaks have been reconstructed, as shown in Fig. 5a for the Ξ^-. Production rates have been measured as functions of rapidity and transverse momentum. The p_T distributions extend from practically zero to 10 GeV for K^0_S (Fig. 5b) and 6 GeV for Ξ^-. The increase in production of strange particles from 0.9 to 7 TeV is approximately consistent with results for charged particles described above, but the rates exceed the predictions by up to a factor of three (Fig. 5c). This deficiency probably originates from parameters regulating the frequency of s-quarks appearing in color strings.

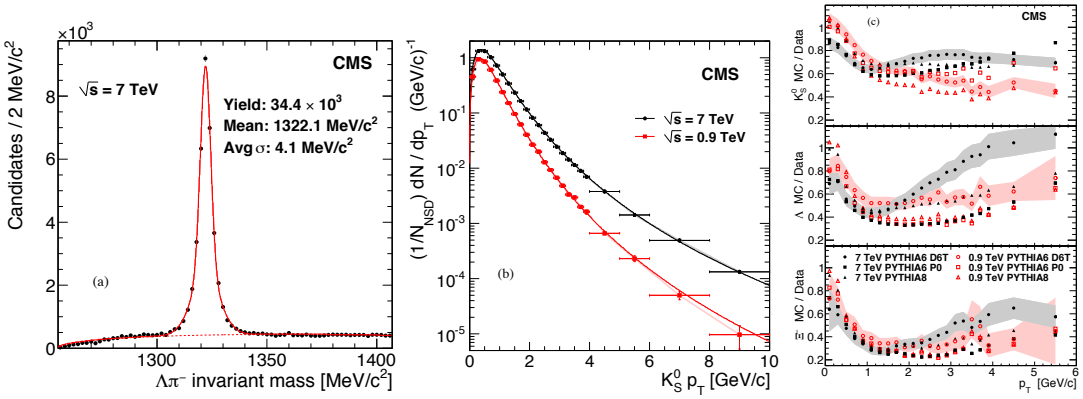

Figure 5: Ξ^- mass peak (a), p_T distribution of K^0_S (b), hyperon p_T yield ratios(c)

4 Particle correlations

Pairs of same-sign charged particles with four-momentum difference Q in the region 0.02 GeV $< Q <$ 2 GeV are analysed to study Bose-Einstein correlations [9]. The radius of the effective

space-time region emitting bosons with overlapping wave functions increases with multiplicity, whereas the correlation strength decreases. Both decrease with increasing momentum difference k_T. Anticorrelations between same-sign charged particles are observed for Q values above the signal region, which can be seen in Fig. 6c showing the double ratio $R(Q)$ [10].

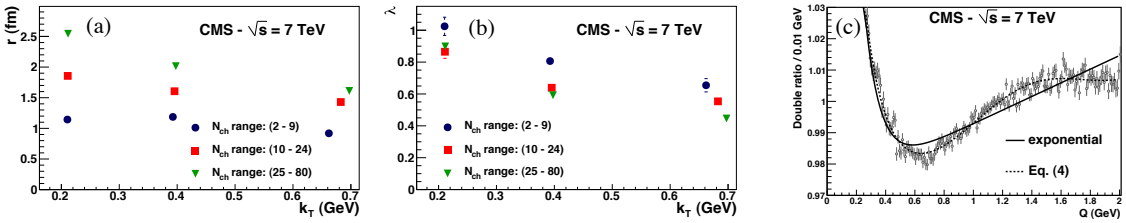

Figure 6: Radius r (a), correlation strength λ (b), double ratio showing anticorrelations (c)

Near-side long-range particle correlations in proton data have first been reported by CMS [11]. A ridge, a pronounced structure in high-multiplicity events for rapidity and azimuth differences of $2.0 < |\Delta\eta| < 4.8$ and $\Delta\phi \approx 0$ has been found. Long- and short-range correlations in ion data have also been studied [12]. The correlation functions of the 0-5% most central collisions show characteristic features not present in minimum bias proton interactions (Fig. 7). The ridge is most evident for p_T's of the trigger particle between 2 and 6 GeV, but disappears at high p_T.

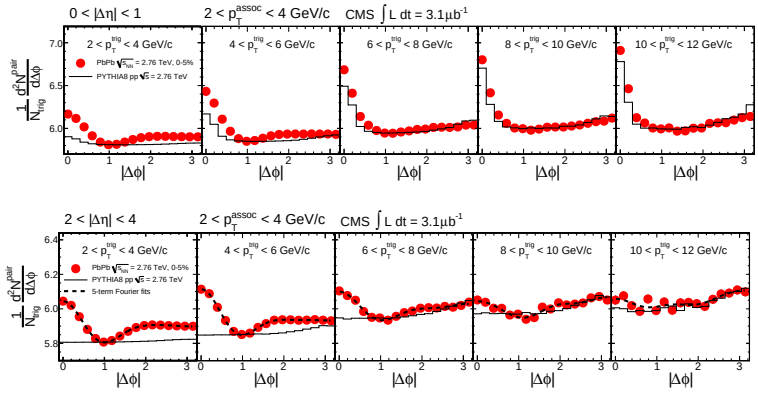

Figure 7: Short-range ($0 < |\Delta\eta| < 1$) and long-range ($2 < |\Delta\eta| < 4$) correlations in lead ion data

References

1. ATLAS Collaboration, *JINST* **3**, S08003 (2008).
2. CMS Collaboration, *JINST* **3**, S08004 (2008).
3. CMS Collaboration, arxiv:1104.3547, submitted to *J. High Energy Phys.*
4. ATLAS Collaboration, arxiv:1012.5104, accepted by *New J. Phys.*
5. ATLAS Collaboration, arxiv:1012.0791, submitted to *Phys. Rev.* D
6. CMS Collaboration, CMS-QCD-10-010.
7. R. Field, arXiv:1010.3558.
8. CMS Collaboration, arxiv:1102.4282, *J. High Energy Phys.* **05**, 064 (2011).
9. CMS Collaboration, arxiv:1101.3518, accepted by *J. High Energy Phys.*
10. T. Csörgő, W. Kittel, W. J. Metzger, T. Novák, *Phys. Lett.* B **663**, 214 (2011).
11. CMS Collaboration, arxiv:1009.4122, *J. High Energy Phys.* **09**, 091 (2010).
12. CMS Collaboration, arxiv:1105.2438, submitted to *J. High Energy Phys.*

Determination of α_S using hadronic event shape distributions of data taken with the OPAL detector

J. Schieck
for the OPAL Collaboration
Ludwig-Maximilians-Universität München , Am Coulombwall 1, 85748 Garching, Germany and Excellence Cluster Universe, Boltzmannstrasse 2, 85748 Garching, Germany

The measurement of the strong coupling α_S using hadronic event shape distributions measured with the OPAL detector at center-of-mass energies between 91 and 209 GeV is summarized. For this measurement hadronic event shape distributions are compared to theoretical predictions based on next-to-next-to-leading-calculations (NNLO) and NNLO combined with resummed next-to-leading-logarithm calculations (NLLA). The combined result using NNLO calculations is $\alpha_S(M_{Z^0}) = 0.1201 \pm 0.0008(\text{stat.}) \pm 0.0013(\text{exp.}) \pm 0.0010(\text{had.}) \pm 0.0024(\text{theo.})$ and the result using NLLO and NLLA calculations is $\alpha_S(M_{Z^0}) = 0.1189 \pm 0.0008(\text{stat.}) \pm 0.0016(\text{exp.}) \pm 0.0010(\text{had.}) \pm 0.0036(\text{theo.})$, with both measurements being in agreement with the world average.

1 Introduction

The annihilation of electron-positron pairs to hadronic final states offers a clean environment to study the theory of the strong interaction, Quantum Chromo Dynamics (QCD). In particular hadronic event shape distributions can be used to measure the strong coupling α_S.

During data-taking of the four LEP-experiments only next-to-leading order calculations (NLO) combined with resummed NLLA predictions were available, leading to a theoretical uncertainty in the α_S measurement dominating the overall uncertainty by far. Only recently new theoretical calculations become available [1,2], which take additional α_S^3 loop corrections into account, so-called NNLO calculations. For this analysis these NNLO predictions are used to determine α_S using data taken with the OPAL detector at LEP. Also the matched NNLO+NLLA calculations are used. This note gives an overview of the analysis performed by the OPAL collaboration. The complete description with all details can be found at [3].

1.1 Data Sample, Monte Carlo Sample and Event Selection

We use data taken with the OPAL detector at LEP at center-of-mass energies between 91 and 209 GeV. Data was taken at 13 different energy points with different event statistics. The largest event statistics of several hundred thousand events is available at 91 GeV, due to the large cross-section at the Z^0-Resonance. At higher energies only few hundred and at most three thousand events are selected. For clarification we group the result in four different energy intervals with mean energies of 91, 133, 177 and 197 GeV.

For correction of acceptance and resolution effects as well as for the simulation of the transition from partons to hadrons a large sample of Monte Carlo events based on the Pythia, Herwig

and Aridane is generated. Pythia is used as the default choice and the other event generators are used to estimate the systematic uncertainty. The validity of the Monte Carlo models is tested with a comparison between the theoretical NNLO calculations and the Monte Carlo predictions at parton level. The difference between the NNLO prediction and the Monte Carlo model is well covered by using the different Monte Carlo as systematic uncertainty.

For the analysis well measured hadronic events are selected. For data taken above the Z^0-resonance events with large initial state radiation are removed. Above the W-pair threshold the expected contribution from this four-fermion processes are removed.

2 Results

2.1 Fit procedure

To measure the strong coupling α_S event shape observables are built from selected hadronic events together with using the theoretical predictions. These observables are constructed in a way that they show a large sensitivity to the strong coupling α_S. The theoretical prediction is then fitted to the data distribution with α_S being the only free parameter. The following event shape observables are used: Thrust, heavy jet mass, the total and the wide jet broadening, the C-parameter and the two-three transition parameter using the Durham jet algorithm. The fit range is determined by requiring the corrections to be small as well as the theoretical predictions to be stable within the fit range. To compare this analysis with the previous analysis the data is also fitted to next-to-leading (NLO) and NLO combined with resummed NLLA calculations. The result from the previous analysis can be reproduced.

To asses the systematic uncertainty the fit is repeated in slightly different ways. Besides the uncertainty due to the correction for hadronization effects, as described in 1.1, uncertainties due to the experimental technique and uncertainties due to the incomplete power series of the theoretical prediction are evaluated. The overall uncertainty is completed by the statistical uncertainty originating from the finite statistics used in the analysis. The main motivation for the re-analysis of the data is the availability of improved theoretical calculations. In the past this uncertainty related to the theoretical prediction dominated the overall uncertainty. However, even with the new improved theoretical predictions the overall uncertainty is still dominated by the theoretical uncertainty. The statistical uncertainty, the experimental uncertainty and the hadronization uncertainty are similar, while the theoretical uncertainty is at least twice as large.

2.2 Combination of results

A single value of the strong coupling α_S is measured for each event shape observable and for each energy interval separately. In order to obtain a single value for each event shape observable or at each energy interval the values of α_S are combined. The correlation between the different event shape observables and the different energy intervals are taken into account.

The combined result for each event shape observable is shown in Fig. 1. It can be clearly seen that the scatter of the α_S-values obtained with different event shape observables using NNLO predictions is smaller compared to the measurement using NLO predictions only. In addition it can be observed, that the overall uncertainty is reduced with including higher order predictions in the measurement. The increase of the uncertainty between NNLO and matched NNLO+NLLA calculations can be explained by the fact that the NNLO renormalization scale variation is compensated in two loops, while the NLLA renormalization scale variation compensation is only in one loop.

The final result combining all event shape observables at all energy intervals is $\alpha_S(M_{Z^0}) = 0.1201 \pm 0.0008(\text{stat.}) \pm 0.0013(\text{exp.}) \pm 0.0010(\text{had.}) \pm 0.0024(\text{theo.})$ using NNLO calculations

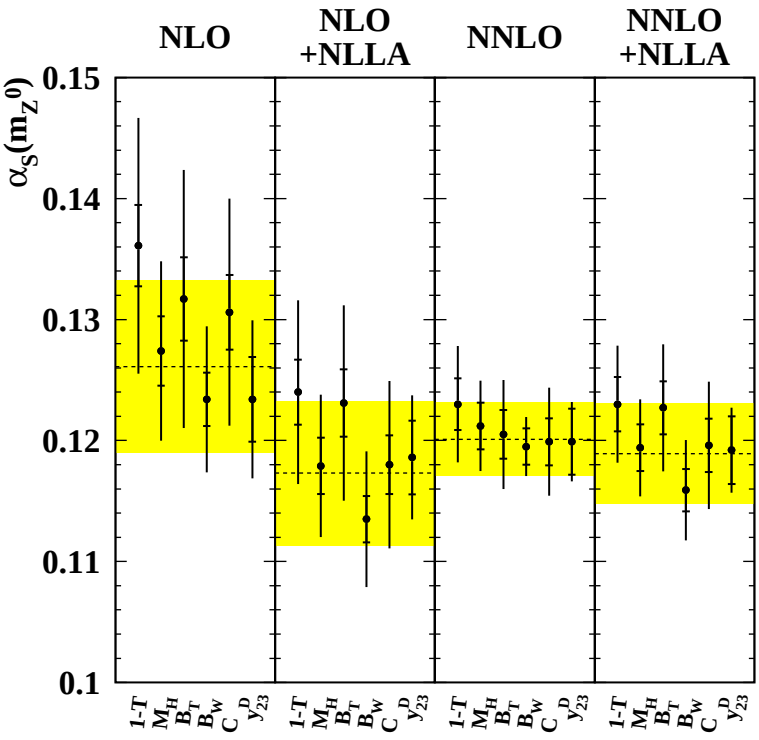

Figure 1: The measured value of α_S for the different event shape observables combined over the complete center-of-mass energy range. The inner uncertainty bar corresponds to the statistical uncertainty the outer one to the total uncertainty. The yellow band represents the combined α_S-value an its uncertainty for all event shape observables using NLO, NLO+NLLA, NNLO and NNLO+NLLA calculations.

only and $\alpha_S(M_{Z^0}) = 0.1189 \pm 0.0008(\text{stat.}) \pm 0.0016(\text{exp.}) \pm 0.0010(\text{had.}) \pm 0.0036(\text{theo.})$ using combined NNLO+NLLA predictions.

2.3 Renormalization scale dependence and running of α_S

The dependence of the result on the choice of the renormalization scale is studied. The fixed-order predictions return for the fit the smallest χ^2-values at a very small renormalization scales, while using the matched NNLO+NLLA predictions smaller χ^2-values for larger renormalization scales are returned.

Together with the re-analyzed JADE result [4] this analysis confirms the running of the strong coupling α_S with center-of-mass energy, as predicted by QCD.

3 Summary

The availability of NNLO predictions for the annihilation of an electron-positron-pair into a pair of quarks lead to a re-analysis of data taken with the OPAL detector. The combined value obtained for the strong coupling using NNLO+NLLA calculations results to $\alpha_S(M_{Z^0}) = 0.1189 \pm 0.0008(\text{stat.}) \pm 0.0016(\text{exp.}) \pm 0.0010(\text{had.}) \pm 0.0036(\text{theo.})$, with the overall uncertainty being dominated by missing higher order terms in the theoretical prediction. The result is consistent with the world average [8]. The result obtained can be compared to similar analyses using NNLO- and NNLO-calculations matched with NLLA [4 5 6 7]. A summary of these results is shown in Fig. 2. As seen in this analysis the results obtained using NNLO+NLLA predictions lead to smaller α_S-value compared to a pure NNLO fit. The smallest overall uncertainty is obtained with a fit to the three-jet rate. Several ways to measure the strong coupling α_S using

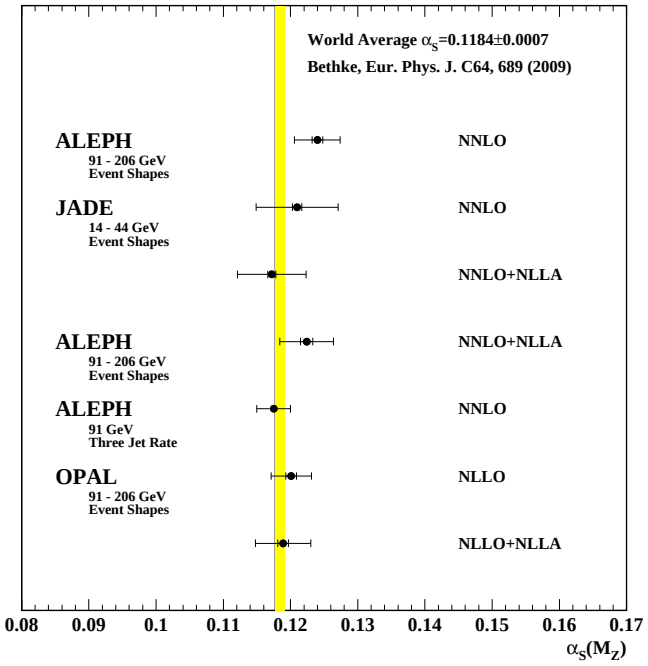

Figure 2: The combined value of the strong coupling α_S compared to similar measurements also using NLLO and matched NLLO+NLLA calculations. The yellow band indicates the world average of the strong coupling α_S.

e^+e^--data do exist. The value obtained using τ-decays or applying a fit to electroweak precision observables result in a smaller overall uncertainty compared to this measurement [8]. Besides a precise determination of a fundamental parameter of the Standard Model this measurement can be seen as a consistency check of the theory of strong interactions, Quantum Chromo Dynamics.

Acknowledgments

This research was supported by the DFG cluster of excellence 'Origin and Structure of the Universe'.

References

1. A. Gehrmann-De Ridder, T. Gehrmann, E.W.N. Glover, G. Heinrich, *JHEP* **12**, 094 (2007).
2. S. Weinzierl, *Phys. Rev. Lett.* **101**, 162001 (2008).
3. The OPAL Collaboration, hep-ex 1101.147v1, submitted to Eur. Phys. J. C.
4. S. Bethke *et al.*, *Eur. Phys. Jour.* C **64**, 351 (2009).
5. G. Dissertori it et al., *JHEP* **02**, 040 (2008).
6. G. Dissertori it et al., *JHEP* **08**, 036 (2009).
7. G. Dissertori it et al., *Phys. Rev. Lett.* **104**, 072002 (2010).
8. S. Bethke, *Eur. Phys. Jour.* C **64**, 689 (2009).

Reaching beyond NLO in processes with giant K-factors

S. SAPETA
LPTHE, UPMC Univ. Paris 6 and CNRS UMR 7589
Paris, France

We present a method, called LoopSim, which allows one to obtain approximate higher order perturbative predictions for observables which exhibit large, kinematically induced NLO corrections. The approach makes use of combining NLO results for different multiplicities. We validate the method against known NNLO results for Drell-Yan lepton p_t spectra and then we use it to compute approximate NNLO results for Z+jet observables. We also study dijet events and show that LoopSim can provide useful information even in cases without giant K-factors.

1 Introduction

Next-to-leading order accuracy of QCD predictions has become a standard for processes calculated for the LHC. Most results show good convergence at NLO with corrections of the order of 10-20%. There are however cases of distributions which show very large K-factors from LO to NLO.

One such example is inclusive Z+j production. At LO, the distributions of the transverse momentum of the Z-boson, $p_{t,Z}$, the transverse momentum of the hardest jet, $p_{t,j1}$, and the scalar sum of transverse momenta of all jets $H_{T,\text{jets}}$ are identical. This is because, as shown in the left diagram of Fig. 1, there are only two particles in the final state: the Z-boson and the parton and therefore their transverse momenta balance each other. At NLO, however, each of these distributions looks very different. While $p_{t,Z}$ spectrum is only slightly higher than at LO, the hadronic observables, $p_{t,j1}$ and $H_{T,\text{jets}}$, receive very large corrections that grow with p_t and correspond to K-factors of $4-6$ and $50-100$, respectively. The reason is that most of the correction to $p_{t,Z}$ spectra at high values of transverse momenta comes from the NLO diagram which preserves LO topology, i.e. the Z-boson the leading jet are back-to-back as depicted in the middle diagram of Fig. 1. For hadronic observables, however, it is not important whether the Z-boson is hard or soft and the dominant topology turns out to be that of dijet type (right diagram of Fig. 1). Integration over soft and collinear emissions of the Z-boson leads to double logarithmic enhancement, which produces the large K-factors for $p_{t,j1}$ and $H_{T,\text{jets}}$ distributions. For the $H_{T,\text{jets}}$ observable the enhancement is even bigger because the dijet topology leads to $H_{T,\text{jets}} \sim 2p_{t,j1}$ instead of $H_{T,\text{jets}} = p_{t,j1}$ at LO.

Hence, even though the $p_{t,j1}$ and $H_{T,\text{jets}}$ distributions for Z+j are formally NLO they are, in some sense, leading contributions. This may raise some doubts about the accuracy of those predictions. Ideally, one would like to calculate the full NNLO corrections for Z+j to see if the convergence is restored. This result is however not yet available, the main difficulty being a proper combination of the tree and the 1-loop diagrams (i.e. Z+2j at NLO) with the 2-loop

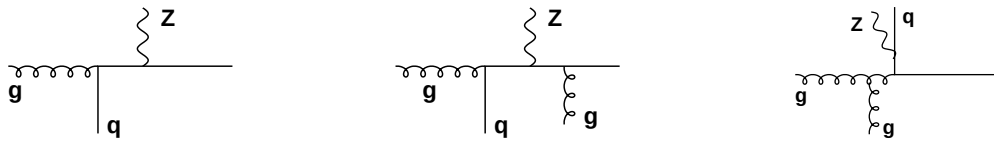

(LO) (NLO) "LO type topology" (NLO) "dijet type topology"

Figure 1: Diagrams contributing to Z+jet production at LO (left) and NLO (middle and right).

contributions. The latter is essential to cancel infra-red and collinear divergences arising from certain configurations of Z+2j NLO result. The 2-loop contribution has however the topology of Z+j at LO and that, as we discussed above, is strongly subleading for the observables exhibiting giant K-factor. Therefore, even an approximate 2-loop contribution would be sufficient to get reliable approximation of NNLO, provided that one could combine it with the tree and the 1-loop diagrams to get finite result for Z+j at the order $\mathcal{O}\big(\alpha_{\rm EW}\alpha_s^3\big)$.

In this proceedings, we present a method, called LoopSim [1], which by the use of unitarity, estimates the missing loop contributions and allows one to obtain approximate higher order QCD corrections for a number of processes.

2 The LoopSim method

Unitarity guarantees that soft and collinear singularities of real diagrams cancel, after phase space integration, with singularities of loop diagrams at any order of the perturbative expansion. That can happen since the pole structure of real and virtual contributions is the same. One could, therefore, use a diagram with n real partons and deduce from it, for instance, the singular terms of the corresponding diagram with $n-1$ real partons and 1 loop. This is the main idea that LoopSim [1] is based on. More precisely, the LoopSim procedure takes as an input an event with n final state particles and returns as an output all events with $n-k$ final state particles (equivalently all k-loop events). The method is capable of taking as an input both tree-level and loop diagrams. This allows one to obtain the highest possible accuracy by approximating only those contributions that are missing (e.g. 2-loop diagrams for Z+j). To distinguish between exact and approximate loops we denote our results as $\bar{n}^p\mathrm{N}^r\mathrm{LO}$ which corresponds to diagrams with exact contributions up to r loops and approximate constitutions for loops from $r+1$ to p. So for example, Z+j at $\bar{n}$NLO corresponds to exact 1-loop and approximate 2-loop diagrams.

In more detail, the procedure consists of the following steps. First, an input ("original") event is clustered with the Cambridge/Aachen algorithm with radius $R_{\rm LS}$ and an emission sequence of particles is attributed to the event. This is done by reinterpreting clustering of particles i and j into k as splitting $k \to ij$. In the next step one identifies which particles reflect the underlying hard structure of an event. We call those particles "Born" and their number, n_B, for a given process is just the number of outgoing particles at leading order (e.g. for Z+j, $n_B = 2$). The particles marked as Born will be those that participate in the n_B hardest branchings, where hardness is measured using the k_t algorithm distance. Finally, a set of loop diagrams is produced from the original event by "virtualizing" in all possible ways the non-Born final state particles. The "virtualization" means a given particle disappears from the list of final state particles and a special procedure [1] is used to redistribute its 4-momentum among remaining particles. Each l-loop event from LoopSim has the weight $w_{n-l} = (-1)^l w_n$, where w_n is the weight of the original event with n particles in the final state.

The input events can have exact loop contributions. To properly merge tree and loop events the procedure is designed such that it avoids double counting. For instance, to obtain $\bar{n}$NLO prediction, LoopSim first generates all diagrams from tree level event with n final state particles

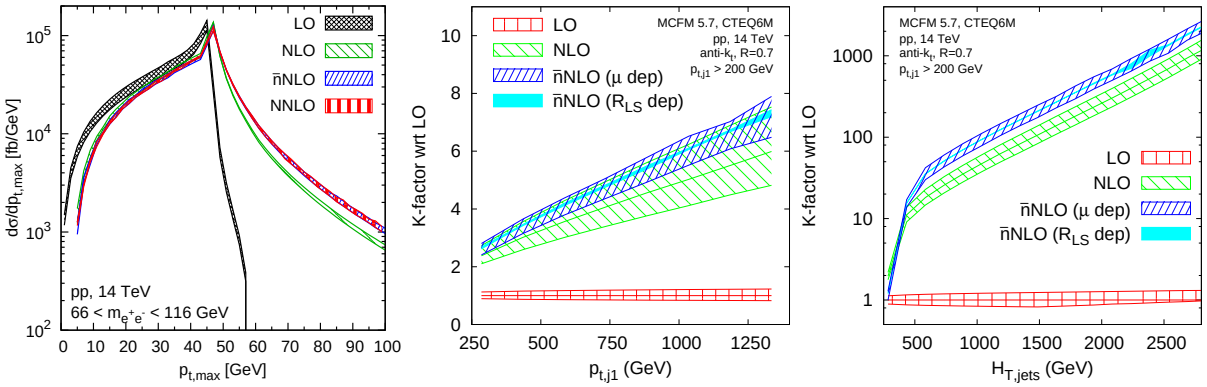

Figure 2: Left: Comparison of spectra of the harder lepton in the Drell-Yan process between $\bar{n}$NLO results from LoopSim+MCFM and full NNLO results from DYNNLO. Middle and Right: Comparison of $\bar{n}$NLO/LO and NLO/LO K-factors from MCFM+LoopSim for $p_{t,j1}$ and $H_{T,\text{jets}}$ observables in the Z+jet process.

and 0-loops. Then, it generates all diagrams from 1-loop event with $n-1$ particles in the final state. Finally, it sorts out double counting by removing all approximate contributions obtained from tree events that have exact counterparts generated from events with exactly 1-loop.

3 Results

We start by showing our predictions for the case of Drell-Yan process for which we can compare to the existing exact NNLO result.[3] The process is suitable to study with LoopSim since above a certain value of transverse momentum, one finds large NLO corrections to the lepton p_t-spectra. This gives an opportunity to use this process for validation of the method.

As shown in the left panel of Fig. 2 the spectrum of the harder lepton falls rapidly above certain value of p_t at LO. At NLO, however, it gets huge correction in this region since the initial-state radiation can give a boost to the Z-boson, causing one of the leptons to shift to higher p_t. As seen from the figure, we find near perfect agreement between the $\bar{n}$NLO and NNLO results. This was expected in the intermediate and high p_t region but not guaranteed a priori below the peak, where the NLO/LO K factor was not large. The uncertainty bands in Fig. 2 come from varying the factorization and renormalization scales by factors 1/2 and 2 around the central value, which was taken to be the mass of the Z-boson. For the LoopSim radius we used $R_{\text{LS}} = 1$.

We turn now to the Z+j process. Here, we provide $\bar{n}$NLO predictions from LoopSim+MCFM[2] for the p_t of the hardest jet and $H_{T,\text{jets}}$. As we see in the middle plot of Fig. 2, the correction from LO to NLO is large. The scale uncertainty is obtained again by variation of a factor of 2 around $\mu_0 = \sqrt{p_{t,j1}^2 + m_Z^2}$. We notice that the $\bar{n}$NLO correction for this observable really makes a difference. The scale uncertainties get significantly smaller and there is a substantial overlap between NLO and $\bar{n}$NLO bands, suggesting convergence of this prediction. We also show the uncertainty corresponding to varying $R_{\text{LS}} = 1 \pm 0.5$.

In the right plot of Fig. 2 we show the $\bar{n}$NLO correction for $H_{T,\text{jets}}$ distribution. Here the situation is different from the case of $p_{t,j1}$, since the NLO and $\bar{n}$NLO bands do not overlap. We have checked by studying dijet events that the K-factor of 2 from NLO to $\bar{n}$NLO is genuine and it comes from additional initial-state radiation, which appears at $\bar{n}$NLO. This radiation can form a third jet, which shifts the $H_{T,\text{jets}}$ distribution to slightly larger values, and because the distribution falls very steeply, one gets a non-negligible correction.

It is also interesting to see what the LoopSim method predicts for dijets events. We have used LoopSim+NLOjet++[4] to study the distribution of the effective mass observables $H_{T,n}$, which are

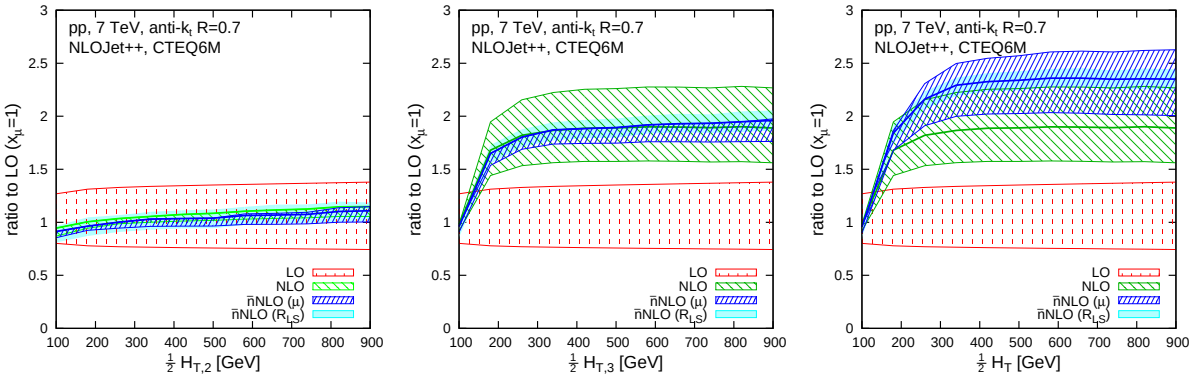

Figure 3: The $\bar{n}$NLO and NLO K-factors for the effective mass observables in dijet events.

just scalar sums of transverse momenta of the n hardest jets above the threshold $p_{t,\min} = 40$ GeV. We also denote $H_T \equiv H_{T,\infty}$. The results are shown in Fig. 3. The uncertainties due to scales and $R_{\rm LS}$ where obtained as in the processes discussed previously. The central value of the scale was taken at $\mu_0 = p_{t,j1}$. Each of the three plots in Fig. 3 carries interesting information. $H_{T,2}$ does not get any at correction at $\bar{n}$NLO. This distribution, which is sensitive only to the two hardest jets, converges already at NLO and extra jets from initial state radiation that appears at higher orders do not affect it. $H_{T,3}$ gets a substantial correction at NLO and here the LoopSim result shows that this observable comes under control at $\bar{n}$NLO. This is because $H_{T,3}$, is insensitive to the fourth jet appearing at $\bar{n}$NLO. However, the H_T distribution at $\bar{n}$NLO still receives substantial enhancement since that observable sums up all jets in the event.

4 Conclusions

We have presented the LoopSim method for computing approximate higher order corrections by making use of unitarity and merging NLO results with different multiplicities. The method is supposed to work best for processes with large K-factors from LO to NLO. We have shown that for the case of Drell-Yan process, whose distributions are known at NNLO, the predictions obtained with LoopSim are in excellent agreement with the exact result. We have also given approximate predictions for NNLO corrections to Z+j and dijets for a range of observables, finding either indication of convergence or further non-negligible corrections, the latter probably being due to additional initial state radiation appearing at higher orders.

Acknowledgments

The original results presented here were obtained with Gavin Salam and Mathieu Rubin. The work was supported by the French ANR under contract ANR-09-BLAN-0060 and by the Groupement d'Intérêt Scientifique "Consortium Physique des 2 Infinis" (P2I).

References

1. M. Rubin, G. P. Salam and S. Sapeta, JHEP **1009**, 084 (2010).
2. J. M. Campbell and R. K. Ellis, *Phys. Rev.* D **60**, 113006 (1999), `http://mcfm.fnal.gov`
3. S. Catani, L. Cieri, G. Ferrera, D. de Florian and M. Grazzini, *Phys. Rev. Lett.* **103**, 082001 (2009); M. Grazzini, `http://theory.fi.infn.it/grazzini/dy.html`
4. Z. Nagy, *Phys. Rev. Lett.* **88**, 122003 (2002); Z. Nagy, *Phys. Rev.* D **68**, 094002 (2003); `http://www.desy.de/~znagy/Site/NLOJet++.html`

Nonlocal Condensate Model for QCD Sum Rules

Ron-Chou Hsieh
Institute of Physics, Academia Sinica, Taipei 11529, Taiwan

We include effects of nonlocal quark condensates into QCD sum rules (QSR) via the Källén-Lehmann (KL) representation for a dressed fermion propagator. Applying our formalism to the pion form factor as an example, QSR results are in good agreement with data for momentum transfer squared up to $Q^2 \approx 10$ GeV^2.

1 Introduction

It is known that the unique feature of the asymptotic freedom and the crucial concepts of infrared safety and factorization make the perturbative quantum chromodynamics (PQCD) method powerful for studying QCD processes. Despite of the remarkable success on high energy hard processes, its applicability at moderate energies is limited. Hence, one needs to seek the aid of non-perturbative approaches, which include lattice QCD, QCD sum rules (QSR) and instanton gas model, etc. The basic idea of QSR is to construct a correlator which relates a quantity we are interested in to an operator-product expansion under the assumption of the quark-hadron duality.

2 Pion decay constant

The quark-hadron duality is implemented via a dispersion relation, in which an unknown parameter s_0 is introduced. The Borel transformation is then applied to determine the value of s_0. We first calculate the pion decay constant as an example, which is defined as

$$\langle \Omega | \eta_\sigma(y) | \pi(p) \rangle = i f_\pi p_\sigma e^{-ip\cdot y}, \quad \eta_\sigma(y) = \bar{u}(y)\gamma_\sigma\gamma_5 d(y), \tag{1}$$

with $|\Omega\rangle$ representing the exact QCD vacuum. The quark-hadron duality leads to the dispersion relation

$$(2\pi) f_\pi^2 \delta(P^2 - m_\pi^2) = \frac{1}{2\pi i} \int_{4m_q^2}^{s_0} ds \frac{\mathrm{Im}\Pi_2(P^2)}{s - P^2}. \tag{2}$$

with

$$\begin{aligned} \Pi_2(P^2) &= \frac{1}{3P^4}\left[4P^\mu P^\nu \Pi_{\mu\nu}(P^2) - P^2 g^{\mu\nu}\Pi_{\mu\nu}(P^2)\right], \\ \Pi_{\mu\nu}(P^2) &= \int d^4x e^{-iP\cdot x} \langle \Omega | \mathtt{T}\left[\eta_\mu(x)\eta_\nu^\dagger(0)\right] | \Omega \rangle. \end{aligned} \tag{3}$$

We then apply the Borel transformation [1] [a]

$$\hat{B}(P^2 \to M^2)F(P^2) = \frac{1}{2\pi i}\int_C \frac{dP^2}{M^2} e^{-P^2/M^2} F(P^2), \tag{4}$$

where C denotes any contour that encloses the branch cuts in the P^2 plane from zero to infinity. Under the above transformation, Eq. (2) becomes

$$f_\pi^2 = -\frac{M^2 e^{m_\pi^2/M^2}}{2\pi}\int_{4m_q^2}^{s_0} ds \hat{B}(P^2 \to M^2)\left[\frac{\mathrm{Im}\Pi_2(P^2)}{s-P^2}\right]. \tag{5}$$

The duality interval s_0 is determined by the requirement that f_π is least sensitive to the Borel mass M in the $f_\pi - M$ plot. In Fig.1(a) we present the M dependence of f_π for three different s_0 inputs. It indicates that for $s_0 = 0.69$ GeV^2, we obtain an almost M-independent behavior for about $M > 2$ GeV, which implies the value of $f_\pi \simeq 0.132$ GeV.

3 Nonlocal condensate model

With the Wick contraction, we express the following matrix element as

$$\begin{aligned}
\langle\Omega|\mathtt{T}\left[\eta_\mu(x)\eta_\nu^\dagger(0)\right]|\Omega\rangle &= -\langle[iS_F^u(0-x)]\gamma_\mu\gamma_5[iS_F^d(x-0)]\gamma_\nu\gamma_5\rangle \\
&+ \langle:\bar{u}(x)\gamma_\mu\gamma_5[iS_F^d(x-0)]\gamma_\nu\gamma_5 u(0):\rangle \\
&+ \langle:\bar{d}(0)\gamma_\nu\gamma_5[iS_F^u(0-x)]\gamma_\mu\gamma_5 d(x):\rangle \\
&+ \langle:\bar{u}(x)\gamma_\mu\gamma_5 d(x)\bar{d}(0)\gamma_\nu\gamma_5 u(0):\rangle.
\end{aligned} \tag{6}$$

where the normal ordering terms, representing non-perturbative effects, are usually dropped for trivial vacuum. We assume that these effects can be absorbed into a dressed fermion propagator,

$$\langle\Omega|\mathtt{T}\left[\eta_\mu(x)\eta_\nu^\dagger(0)\right]|\Omega\rangle = -\langle[iS^u(0-x)]\gamma_\mu\gamma_5[iS^d(x-0)]\gamma_\nu\gamma_5\rangle. \tag{7}$$

The KL representation for a dressed propagator of the quark q is written as [3],

$$\begin{aligned}
\langle\Omega|\mathrm{T}[q(z)\overline{q}(0)]|\Omega\rangle &= i\int\frac{d^4k}{(2\pi)^4}e^{-ik\cdot z}\int_0^\infty d\mu^2\frac{\not{k}\rho_1^q(\mu^2)+\rho_2^q(\mu^2)}{k^2-\mu^2+i\epsilon} \\
&= \frac{1}{16\pi^2}\int_0^\infty ds\exp\left(\frac{z^2}{4}s\right)\int_0^\infty d\mu^2\exp\left(-\frac{\mu^2}{s}\right)\left[\frac{i\not{z}}{2}s\rho_1^q(\mu^2)+\rho_2^q(\mu^2)\right],
\end{aligned} \tag{8}$$

where the spectral density functions $\rho_{1,2}^q(\mu^2)$ describe the glutinous medium effect, and μ is an effective mass. The KL representation can be deemed as a superposition of free quark propagators for all mass eigenstates with the weights $\rho_{1,2}^q(\mu^2)$. We then decompose the above matrix element into the perturbative and non-perturbative pieces

$$\langle\Omega|\mathrm{T}[q(z)\overline{q}(0)]|\Omega\rangle \equiv iZS_F(z,m_q) + \langle\Omega|:q(z)\overline{q}(0):|\Omega\rangle, \tag{9}$$

respectively, with Z being a renormalization constant, $S_F(z,m_q)$ being the quark propagator in perturbation theory, m_q being the quark mass. The non-perturbative piece collects the contribution from large μ^2,

$$\langle\Omega|:q(z)\overline{q}(0):|\Omega\rangle = \frac{1}{16\pi^2}\int_0^\infty ds\exp\left(\frac{z^2}{4}s\right)\int_{\mu_c^2}^\infty d\mu^2\exp\left(-\frac{\mu^2}{s}\right)\left[\frac{i\not{z}}{2}s\rho_1^q(\mu^2)+\rho_2^q(\mu^2)\right]. \tag{10}$$

[a] The Borel transformation can be defined in different ways [2]. In this work we adopt the integral representation.

The lower bound for the integration variable μ^2 is usually set to the multi-particle threshold m_γ^2 in the KL representation. In this work we have modified it into [4]

$$\mu_c^2 = \begin{cases} cs, & s > m_\gamma^2 \\ \\ m_\gamma^2, & s \le m_\gamma^2 \end{cases}, \tag{11}$$

where the free parameter c of order unity will be fixed later. This modification respects the multi-particle threshold, and at the same time guarantees a finite integral in Eq. (10).

We obtain the dressed propagator

$$\begin{aligned} S^q(p) &= \frac{\not p + m_q}{p^2 - m_q^2} - \frac{1}{2} i \frac{(\gamma^\alpha \not p \gamma^\beta G_{\alpha\beta} - m_q \gamma_\alpha G^{\alpha\beta} \gamma_\beta)}{(p^2 - m_q^2)^2} \\ &- \frac{\pi \alpha_s \langle G_{\alpha\beta}^2 \rangle m_q \not p (m_q + \not p)}{(p^2 - m_q^2)^4} + \left[\not p \hat{I}_1^q + \hat{I}_2^q \right] \frac{\exp[c(p^2 - \mu^2)/\mu^2]}{p^2 - \mu^2}, \end{aligned} \tag{12}$$

with the definitions

$$\hat{I}_{1,2}^q f(\mu) \equiv \int_{m_\gamma^2}^\infty d\mu^2 \rho_{1,2}^q(\mu^2) f(\mu). \tag{13}$$

The second and third terms on the right hand side of Eq. (12) arise from the background gluon field [5,6], and the forth term comes from the nonlocal quark condensates with the integrations over μ^2 and s being exchanged in Eq. (10). We define the distribution functions

$$f_s(s) = \frac{-3}{4\pi^2 \langle \bar{q} q \rangle} \int_{\mu_c^2}^\infty d\mu^2 e^{-\mu^2/s} \rho_2^q(\mu^2), \tag{14}$$

$$f_v(s) = \frac{3}{2\pi^2 \langle \bar{q} q \rangle} \int_{\mu_c^2}^\infty d\mu^2 e^{-\mu^2/s} s \rho_1^q(\mu^2), \tag{15}$$

and parameterize the spectral density functions as

$$\rho_1^q(\mu^2) = N_1 \exp(-a\mu^2)/\mu, \quad \rho_2^q(\mu^2) = N_2 \exp(-a\mu^2). \tag{16}$$

The choice of μ_c^2 in Eq. (11) then renders the integral in Eq. (14)

$$f_s(s) \propto \frac{s}{1 + as} \exp(-\mu_c^2/s - a\mu_c^2), \tag{17}$$

exhibit the limiting behaviors $\exp(-m_\gamma^2/s)$ at small s and $\exp(-acs)$ at large s, consistent with $\exp(-m_\gamma^2/s)$ and the exponential ansatz $\exp(-\sigma_q s)$ postulated in the literature [7,8], respectively. The threshold mass m_γ is expected to take a value of order of the constituent quark mass [9], and set to $m_\gamma \sim 0.36$ GeV below.

Comparing the Taylor expansion of the nonlocal quark condensates [2,8] with Eq. (10), we have the constraints

$$\int_0^\infty f_s(s) ds = 1, \quad \int_0^\infty s f_s(s) ds = \frac{1}{2}(\lambda_q^2 - m_q^2), \quad \int_0^\infty f_v(s) ds = m_q, \tag{18}$$

which determine the free parameters a, N_1 and N_2 in Eq. (16), given values of λ_q and m_q. The average virtuality λ_q and the lower bound c in Eq. (11), being not known with certainty, are fixed by fits to the data of the pion decay constant $f_\pi = 0.1307$. In Fig. 1(b) we display the allowed values of c and λ_q as a curve in the c-λ_q plane. We adopt $\lambda_q = 0.75$ GeV and $c = 0.3$, and choose the light quark masses $m_u = 4.2$ MeV and $m_d = 7.5$ MeV. We then solve for the free parameters a, N_1 and N_2 from the constraints in Eq. (18), whose results are listed in Table 1. The opposite signs of N_1 and N_2 imply the violation of positivity, which can be interpreted as a manifestation of confinement [10]. The fixed parameters are then employed to calculate the pion form factor, and the results are shown in Fig. 1(c). It is obvious that our results are consistent with the experimental data for $Q^2 > 1\text{GeV}^2$, the region where QSR are applicable.

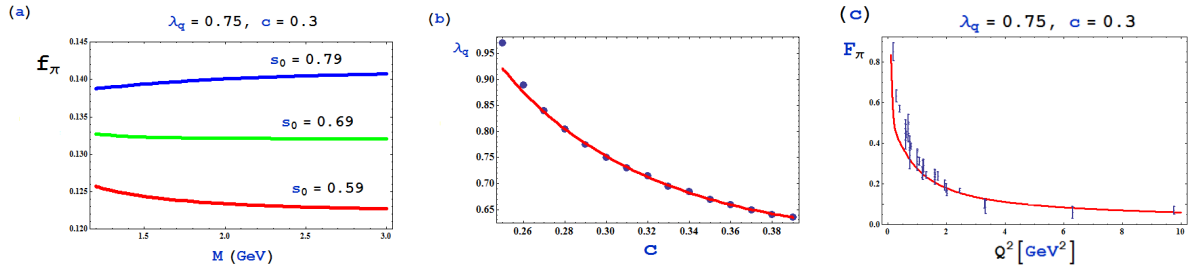

Figure 1: (a) M dependence of f_π for different s_0 with $\lambda_q = 0.75$ GeV and $c = 0.3$. (b) Curve for the allowed values of c and λ_q that produce the pion decay constant $f_\pi = 0.1307$. (c) Q^2 dependence of the pion form factor.

	λ_q (GeV)	m_q (MeV)	a (GeV^{-2})	$N_1/\langle\bar{q}q\rangle$ (GeV^{-4})	$N_2/\langle\bar{q}q\rangle$ (GeV^{-4})
u quark	0.75	4.2	22.7	20.54	-7784.54
d quark	0.75	7.5	22.7	36.70	-7789.33

Table 1: Parameters associated with the quarks u and d in our formalism.

4 Summary

We have included the nonlocal quark condensates into QSR via the KL parametrization for a dressed fermion propagator, which is decomposed into the perturbative and non-perturbative pieces. The negative spectral density function implies that the contribution from higher effective quark masses is non-perturbative. The parametrization of the spectral density functions leads to the known exponential ansatz for the nonlocal condensate model in our formalism. We have analyzed the pion form factor as an example, and the results are in good agreement with the data for Q^2 between 1-10 GeV^2.

Acknowledgments

This work was supported by the National Center for Theoretical Sciences and National Science Council of R.O.C. under Grant No. NSC-98-2112-M-001-015-MY3.

References

1. C. Corianò, A. Radyushkin and G. Sterman, *Nucl. Phys.* B **405**, 481 (1993)
2. A.V. Radyushkin, arXiv:hep-ph/0101227.
3. G. Källén, *Helv. Phys. Acta* **25**, 417 (1952); H. Lehmann, *Nuovo Cimento* **11**, 342 (1954).
4. R.C. Hsieh and H-n. Li, *Phys. Lett.* B **698**, 140 (2011).
5. S. Mallik, *Nucl. Phys.* B **234**, 45 (1984).
6. C. Corianò, *Nucl. Phys.* B **410**, 90 (1993).
7. A.V. Radyushkin, arXiv:hep-ph/9406237.
8. A.P. Bakulev and S.V. Mikhailov, *Z. Phys.* C **68**, 451 (1995); *Mod. Phys. Lett.* A **11**, 1611 (1996); *Phys. Rev.* D **65**, 114511 (2002).
9. A. V. Radyushkin, *Phys. Lett.* B **271**, 218 (1991).
10. R. Alkofer and L.V. Smekal, *Phys. Rept.* **353**, 281 (2001).

AN ALTERNATIVE SUBTRACTION SCHEME FOR NLO CALCULATIONS

T. ROBENS
School of Physics and Astronomy, University of Glasgow, Glasgow, G12 8QQ, Scotland, UK

C.H. CHUNG and M. KRÄMER
Institute for Theoretical Particle Physics and Cosmology, RWTH Aachen, 52056 Aachen, Germany

We present a new subtraction scheme for next-to-leading order QCD calculations, where the momentum mapping and the splitting functions have been derived in the context of an improved parton shower formulation. A main advantage of our scheme is the significantly reduced number of momentum mappings in the subtraction terms compared to standard schemes. We present the major features of our scheme and discuss the process $e\,q \to e\,q\,(g)$ in more detail.

1 Introduction

Both the further validation of the Standard Model (SM) as well as searches for new physics beyond the SM require an exact knowledge of the SM signals at at least Next-to-leading order (NLO). For precise differential predictions, these NLO corrections need to be included in Monte Carlo Event Generators. However, an increase of final state particle multiplicity in the LO process in such codes directly translates to an increase of the computational runtime. This is partially caused by the treatment of infrared (IR) singularities: For standard subtraction schemes, the number of momentum mappings and Born matrix reevaluations rapidly increases with the number of final state particles. We here present a new scheme which significantly reduces the number of the momentum mappings in the real emission subtraction terms.

2 Subtraction schemes

We consider a generic jet cross-section σ with

$$\sigma \;=\; \sigma^{\mathrm{LO}} + \sigma^{\mathrm{NLO}} \;=\; \int_m d\sigma^B + \int_m d\sigma^V + \int_{m+1} d\sigma^R\,, \tag{1}$$

where σ^{B}, σ^{V}, and σ^{R} denote the LO, virtual and real-emission contributions, and with m (m+1) partons in the final state in the LO (real emission) phase space. The IR poles, which are inherent in both $d\sigma^V$ and $d\sigma^R$, cancel in the sum of these two terms; however, the individual pieces are divergent and can thus not be integrated numerically. Subtraction schemes resolve this issue by introducing local counterterms, which match the behaviour of the real-emission matrix element in each singular region. Subtracting the counterterms from the real-emission matrix elements and adding back the corresponding one-particle integrated counterparts to the virtual contribution

then results in overall finite integrands

$$\sigma^{\rm NLO} = \underbrace{\int_m d\sigma^V + \int_{m+1} d\sigma^A}_{\text{finite}} + \underbrace{\int_{m+1} \left[d\sigma^R - d\sigma^A\right]}_{\text{finite}}. \tag{2}$$

The construction of the local counterterms, collectively denoted by $d\sigma^A$ in Eq. (2), relies on the factorisation of the real-emission matrix element in the singular (*i.e.* soft and collinear) limits: $\mathcal{M}_{m+1}(\{\hat{p}\}_{m+1}) \longrightarrow \sum_\ell v_\ell(\{\hat{p}\}_{m+1}) \otimes \mathcal{M}_m(\{p\}_m)$, where $\mathcal{M}_m$ ($\mathcal{M}_{m+1}$) and $\mathcal{M}_m$ denote $m\,(m+1)$ matrix elements and the v_ℓ are generalised splitting functions containing the complete singularity structure. As $\mathcal{M}_{m+1}$ and $\mathcal{M}_m$ live in different phase spaces, a mapping $\{\hat{p}\}_{m+1} \to \{p\}_m$ needs to be introduced, which conserves four-momentum and guarantees onshellness for all external particles in both phase spaces. Squaring and averaging over the splitting functions then leads to subtraction terms of the form

$$W_{\ell\,k} \;=\; v_\ell(\{\hat{p},\hat{f}\}_{m+1}, \hat{s}_j, \hat{s}_\ell, s_\ell)\, v_k(\{\hat{p},\hat{f}\}_{m+1}, \hat{s}_j, \hat{s}_k, s_k)^*\, \delta_{\hat{s}_\ell,s_\ell}\, \delta_{\hat{s}_k,s_k}\,, \tag{3}$$

where our notation follows $p_\ell \to \hat{p}_\ell\, \hat{p}_j$ for parton splitting, and f denotes the parton flavour. We now distinguish two different kinds of subtraction terms: 1) direct squares where $k = \ell$, which contain both collinear and soft singularities; 2) soft interference terms, where $k \neq \ell$. The latter contain only soft singularities and vanish if $f_j \neq g$; here, v is replaced by the eikonal approximation of the splitting function $v^{\rm eik}$. These terms explicitly depend on the spectator four momentum $\hat{p}_k$. In the following, we symbolically write $\mathcal{D}_\ell$ for terms of the form $W_{\ell,\ell}$ and $W_{\ell,k}$. We then have $d\sigma^A = \sum_\ell \mathcal{D}_\ell \otimes d\sigma^B$, with $\otimes$ representing phase-space, spin and colour convolutions. Integrating the subtraction term $d\sigma^A$ over the one-parton unresolved phase space, $d\xi_p$, yields an infrared- and collinear-singular contribution $\mathcal{V}_\ell = \int d\xi_p \mathcal{D}_\ell$ which needs to be combined with the virtual cross section to yield a finite NLO cross section

$$\sigma^{\rm NLO} = \int_m \left[d\sigma^V + \sum_\ell \mathcal{V}_\ell \otimes d\sigma^B\right] + \int_{m+1} \left[d\sigma^R - \sum_\ell \mathcal{D}_\ell \otimes d\sigma^B\right]. \tag{4}$$

In this form, the NLO cross section can be integrated numerically over phase space using Monte Carlo methods. The jet cross-section σ has to be defined in a infrared-safe way by the inclusion of a jet-function F_J, which satisfies $F_J^{(m+1)} \to F_J^{(m)}$ in the collinear and infrared limits.

2.1 Major features of new subtraction scheme

Our scheme[1] uses the splitting functions of an improved parton shower[2] as the basis for the local subtraction terms. The main advantage[a] of our scheme is a novel momentum mapping for final state emitters: for $\hat{p}_\ell + \hat{p}_j \to p_\ell$, we redistribute the momenta according to the global mapping[b]

$$p_\ell \;=\; \frac{1}{\lambda}\,(\hat{p}_\ell + \hat{p}_j) - \frac{1-\lambda+y}{2\,\lambda\,a_\ell}\,Q, \quad p_n^\mu \;=\; \Lambda(K,\hat{K})^\mu{}_\nu\, \hat{p}_n^\nu, \quad n \notin \{\ell,a,b\}\,, \tag{5}$$

where n labels all partons in the m particle phase space which do not participate in the inverse splitting. We here consider the resulting implications on a purely gluonic process with only $g(p_\ell) \to g(\hat{p}_\ell)\, g(\hat{p}_j)$ splittings. For final state emitters, the real emission subtraction terms are

$$d\sigma_{ab}^{A,p_\ell}(\hat{p}_a,\hat{p}_b) \;\;=\;\; \frac{N_{m+1}}{\Phi_{m+1}} \sum_{i=j} \mathcal{D}_{ggg}(\hat{p}_i)\, |\mathcal{M}_{\rm Born,g}|^2(p_a,p_b;p_\ell,p_n), \tag{6}$$

[a] An additional advantage stems from the use of common splitting functions in the shower and the subtraction scheme which facilitates the matching of shower and parton level NLO calculation.

[b] The parameter definitions are $y = \frac{P_\ell^2}{2\,P_\ell\cdot Q - P_\ell^2}$, $a_\ell = \frac{Q^2}{2\,P_\ell\cdot Q - P_\ell^2}$, $\lambda = \sqrt{(1+y)^2 - 4\,a_\ell\,y}$, $P_\ell = \hat{p}_\ell + \hat{p}_j$, $Q = \hat{p}_a + \hat{p}_b = \sum_{n=1}^{m+1} \hat{p}_n$. The Lorentztransformation $\Lambda(K,\hat{K})^\mu{}_\nu$ is a function of $K = Q - p_\ell$, $\hat{K} = Q - P_\ell$.

where $\mathcal{M}_{\mathrm{Born},g}$ is the underlying Born matrix element for the process $p_a + p_b \to \sum_n p_n + p_\ell$, Φ, N are flux and combinatoric factors, and the sum $i = j$ goes over all i final state gluons. $\mathcal{D}_{ggg}$ contains both collinear and soft interference terms:

$$\mathcal{D}_{ggg}(\hat{p}_i) \,=\, \mathcal{D}^{\mathrm{coll}}_{ggg}(\hat{p}_i) \,+\, \sum_{k=a,b} \mathcal{D}^{\mathrm{if}}(\hat{p}_i, \hat{p}_k) \,+\, \sum_{k \neq i} \mathcal{D}^{\mathrm{if}}(\hat{p}_i, \hat{p}_k). \tag{7}$$

While the collinear subtraction terms only depend on the four-momenta $\hat{p}_j$, $\hat{p}_\ell$, the soft interference terms have an additional dependence on the four-momentum of the spectator $\hat{p}_k$ (cf Eq. (3)). The sums over (a, b) and $(k \neq i)$ then run over all possible spectators in soft interference terms; however, *there is a unique mapping per combination* $(\hat{\ell}, \hat{i})$ *in Eq. (6) which is independent of the spectator momenta* $\hat{p}_k$ *in the soft interference terms.* Therefore, the underlying matrix element $|\mathcal{M}_{\mathrm{Born},g}|^2(p_a, p_b; p_\ell, p_n)$ only needs to be evaluated once for all possible spectators. *This is indeed the main feature of our scheme*, which, for N parton final states, leads to a scaling behaviour $\sim N^2/2$ for the number of momentum mappings and LO matrix element reevaluations in the real emission subtraction terms.

3 Results for $e\,q \,\to\, e\,q\,(g)$

The improved scaling behaviour of the scheme leads to more complicated integrated subtraction terms, which partially need to be evaluated numerically. As an example, we discuss the integrated subtraction terms and the resulting integrand in the two particle phase space for the DIS sub-process $e(p_i) + q(p_1) \to e(p_o)q(p_4)$ $(g(p_3))$ on parton level. The effective two particle phase space contribution is given by

$$\begin{aligned}
&|\mathcal{M}|^2_{\mathrm{Born}}(2\,p_i \cdot p_1) \,+\, 2\,\mathrm{Re}\,(\mathcal{M}_{\mathrm{Born}}\,\mathcal{M}^*_{\mathrm{virt}})\,(2\,p_i \cdot p_1) \,+\, \sum_\ell \int d\xi_p \mathcal{D}_\ell\, |\mathcal{M}|^2_{\mathrm{Born}}(2p_i \,\cdot x p_1) = \\
&\quad \int_0^1 dx \left\{ \frac{\alpha_s}{2\,\pi}\, C_F\, \delta(1-x) \left[-9 \,+\, \frac{1}{3}\pi^2 \,-\, \frac{1}{2}\mathrm{Li}_2[(1-\tilde{z}_0)^2] \,+2\,\ln\,2\,\ln\tilde{z}_0 \,+\, 3\,\ln\tilde{z}_0 \,+\, 3\,\mathrm{Li}_2(1-\tilde{z}_0) \right.\right. \\
&\quad \left.\left. + I^{\mathrm{tot},0}_{\mathrm{fin}}(\tilde{z}_0) \,+\, I^1_{\mathrm{fin}}(\tilde{a}) \right] \,+\, K^{\mathrm{tot}}_{\mathrm{fin}}(x;\tilde{z}) \,+\, P^{\mathrm{tot}}_{\mathrm{fin}}(x;\mu_F^2) \right\} |\mathcal{M}|^2_{\mathrm{Born}}(2p_i \cdot x\, p_1),
\end{aligned}$$

where

$$K^{\mathrm{tot}}_{\mathrm{fin}}(x;\tilde{z}) \;\;=\;\; \frac{\alpha_s}{2\,\pi}\, C_F \left\{ \frac{1}{x} \left[2\,(1-x)\,\ln\,(1-x) \,-\, \left(\frac{1+x^2}{1-x} \right)_+ \ln\,x \;+4\,x\, \left(\frac{\ln(1-x)}{1-x} \right)_+ \right] \,+\, I^1_{\mathrm{fin}}(\tilde{z},x) \right\}$$

The integrals $I^{\mathrm{tot},0}_{\mathrm{fin}}(\tilde{z}_0)$, $I^1_{\mathrm{fin}}(\tilde{a}), I^1_{\mathrm{fin}}(\tilde{z},x)$ all need to be integrated numerically; as an example we give

$$I^1_{\mathrm{fin}}(\tilde{z},x) \,=\, \frac{2}{(1-x)_+}\, \frac{1}{\pi} \int_0^1 \frac{dy'}{y'} \left[\int_0^1 \frac{dv}{\sqrt{v\,(1-v)}}\, \frac{\tilde{z}}{N(x,y',\tilde{z},v)} - 1 \right] \tag{8}$$

which explicitly depends on the real emission four vectors $\hat{p}_3$, $\hat{p}_4$ through the variables $N, \tilde{z}$ [c]. Note that $\hat{p}_3$ needs to be reconstructed in the two particle phase space; $\hat{p}_4$ can be obtained from the inverse of Eq. (5). We perform the numerical evaluation of all integrals in parallel to the phase space integration; however, the integrals are process-independent expressions with a functional dependence on maximally two input parameters and can therefore be evaluated generically such that no additional numerical evaluation is necessary in future implementations of our scheme. We have compared the results for the parton level process $q\,e \,\to\, q\,e\,(g)$ numerically with an implementation of the Catani-Seymour dipole subtraction[3]. Fig. 1 shows the behaviour of the

[c] Exact definitions are $N \,=\, \frac{\hat{p}_3 \cdot \hat{p}_4}{\hat{p}_4 \cdot \hat{Q}}\, \frac{1}{1-x} \,+\, y', \tilde{z} \,=\, \frac{1}{x}\, \frac{p_1 \cdot \hat{p}_4}{\hat{p}_4 \cdot \hat{Q}}$, $\tilde{z}_0 \;\overset{y' \to 0}{=}\; \tilde{z}$.

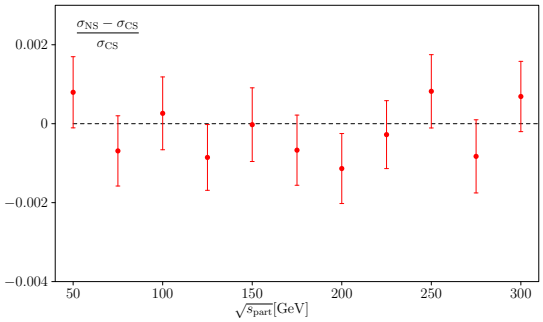

Figure 1: Partonic cross sections for DIS subprocess $eq \to eq(g)$, as a function of parton level (HERA-like) cm energies, with angular cuts $\cos\theta_{ee} < 0.8$. Relative difference between NLO contributions using Nagy-Soper (NS) and Catani Seymour (CS) subtraction terms. Errors are integration errors; results agree at the permil-level.

differences between the application of the two schemes at parton level for varying (HERA-like) center-of-mass energies, where we applied an appropriate jet function to guarantee IR safety of $d\sigma^{\rm B}$. The results agree on the per-mil level, therefore validating our subtraction prescription. We equally observed that this cancellation is non-trivial as the contributions from different phase space integrations vary widely in magnitude for the two schemes.

4 Conclusions and Outlook

Our current results present a first step in the establishment of a new subtraction scheme. The scheme we propose reduces the number of momentum mappings and therefore of reevaluation calls of the underlying LO matrix element. We have derived the splitting functions and validated our scheme by reproducing the literature results for various $1 \to 2$ and $2 \to 2$ processes[1]. The application to processes with more than two particles in the final state is nearly finished[4]; similarly, an implementation of the scheme within the Helac framework is underway [5]. An additional advantage of the scheme comes from the use of splitting functions which are derived from an improved parton shower; this approach promises advantages for the combination of NLO parton level calculations and parton showers.

Acknowledgements

TR wants to especially thank Zoltan Nagy, Dave Soper, and Zoltan Trocsanyi for input and many valuable discussions, as well as the organizers of the Moriond 2011 QCD session for financial support and perfect weather during the midday breaks. This research was partially supported by the DFG SFB/TR9, the DFG Graduiertenkolleg "Elementary Particle Physics at the TeV Scale", the Helmholtz Alliance "Physics at the Terascale", the BMBF, the STFC and the EU Network MRTN-CT-2006-035505.

References

1. T. Robens and C. H. Chung. Alternative subtraction scheme using Nagy Soper dipoles. *PoS*, RADCOR2009:072, 2010.; Cheng-Han Chung, Michael Kramer, and Tania Robens. An alternative subtraction scheme for next-to-leading order QCD calculations. 2010.; C.H.Chung. *An alternative subtraction scheme using Nagy Soper dipoles*. PhD thesis, RWTH Aachen University, Aachen, Germany, 2011.
2. Zoltan Nagy and Davison E. Soper. Parton showers with quantum interference. *JHEP*, 09:114, 2007.; Zoltan Nagy and Davison E. Soper. Parton showers with quantum interference: leading color, spin averaged. *JHEP*, 03:030, 2008.; Zoltan Nagy and Davison E. Soper. Parton showers with quantum interference: leading color, with spin. *JHEP*, 07:025, 2008.
3. S. Catani and M. H. Seymour. A general algorithm for calculating jet cross sections in NLO QCD. *Nucl. Phys.*, B485:291–419, 1997.
4. Cheng Han Chung, Michael Krämer, and Tania Robens. Work in progress.
5. Giuseppe Bevilacqua, Michal Czakon, Michael Krämer, and Michael Kubocz. Work in progress.

THE NNPDF2.1 PARTON SET

F. CERUTTI
Universitat de Barcelona,
Departament d'Estructura i Constituents de la Matèria, Av. Diagonal 647,
Barcelona 08028, España

We discuss the main features of the recent NNPDF2.1 NLO set, a determination of parton distributions from a global set of hard scattering data using the NNPDF methodology including heavy quark mass effects. We present the implications for LHC observables of this new PDF set. Then we briefly review recent NNPDF progress towards NNLO sets, and in particular the impact of the treatment of fixed target NMC data on NNLO Higgs cross sections.

The NNPDF2.1 parton set The NNPDF2.1 set [1] is a NLO determination of parton distributions from a global set of hard scattering data using the NNPDF methodology including heavy quark mass effects. In comparison to the previous parton fit, NNPDF2.0 [2], mass effects have been included using the FONLL-A General–Mass VFN scheme [3] and the dataset enlarged with the ZEUS and H1 charm structure function F_2^c data. The kinematical coverage of the datasets included in the NNPDF2.1 analysis is summarized in Fig. 1. As in NNPDF2.0, we use the FastKernel framework for fast computation of Drell-Yan observables to include these data exactly at NLO accuracy in all stages of the PDF determination, without the need to resort to any K–factor approximation.

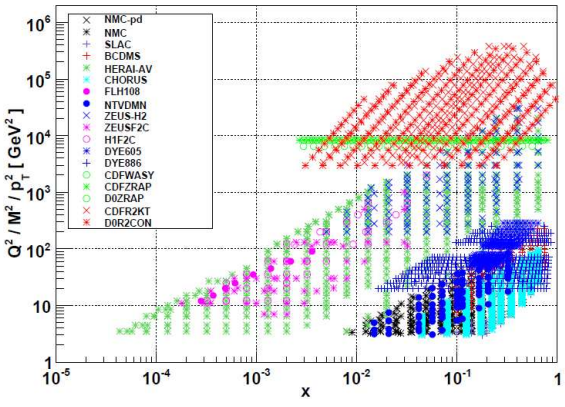

Figure 1: Experimental data sets which enter the NNPDF2.1 analysis.

The NNPDF2.1 PDFs are compared to the other two NLO global PDF sets CT10 [4] and MSTW08 [5] in Fig. 2. One finds generally good agreement of the three gluon distributions, except in the region $x \lesssim 0.1$ where the agreement is marginal, with implications for important processes like Higgs production. There are also differences from the singlet PDF, part of which

can be traced back to the different treatment of strangeness in each set.

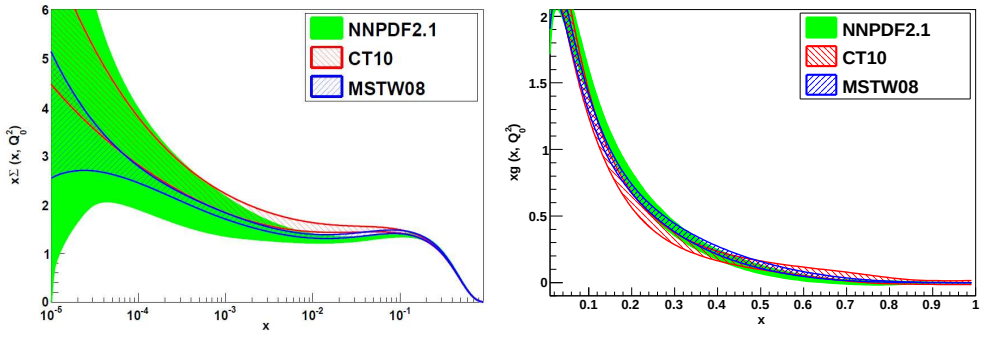

Figure 2: The singlet and gluon NNPDF2.1 PDFs, compared with the CT10 and MSTW08 PDFs. The results for NNPDF2.1 have been obtained with $N_{\rm rep} = 1000$ replicas. All PDF errors are given as one-σ uncertainties.

LHC phenomenology The assessment of the theoretical uncertainties on LHC standard candles is especially important now that the first 7 TeV LHC results on inclusive cross-sections are appearing. In Ref. [1] we presented results at $\sqrt{s}$ =7 TeV and $\sqrt{s}$ =14 TeV for $W^{\pm}$, Z_0, $t\bar{t}$ and Higgs production in gluon fusion. All observables were computed at NLO QCD using MCFM. We compared the predictions for these cross-sections obtained using the NNPDF2.1, NNPDF2.0, CT10 and MSTW08 sets. In the case of the last two sets, results were computed both using the respective default value of $\alpha_s(M_Z)$ and at the common value of $\alpha_s(M_Z) = 0.119$. A subset of these results, the NLO cross sections for W^+ and $t\bar{t}$ production at LHC 7 TeV, is shown in Fig. 3.

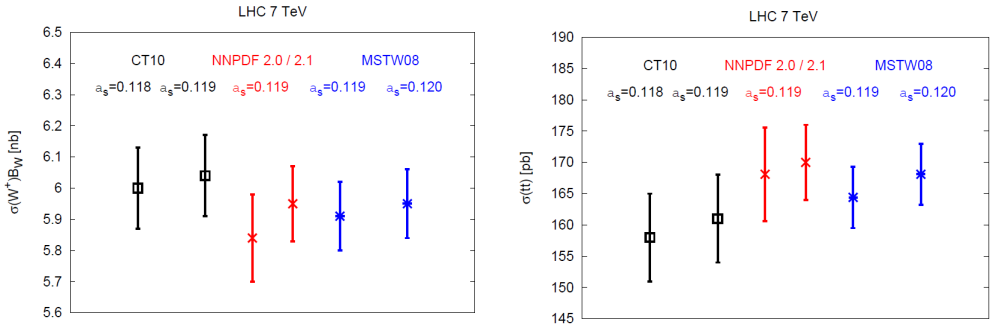

Figure 3: LHC standard candles: W^+ and $t\bar{t}$ production.

The differences between NNPDF2.0 and NNPDF2.1 are at most at the one-σ level for W and Z production, while predictions for the $t\bar{t}$ and Higgs are essentially unchanged: these observables are only minimally affected by the heavy quark treatment. NNPDF2.1 predictions are in rather good agreement with MSTW08 for all observables, though differences with CT10 are somewhat larger, especially for observables which are most sensitive to the gluon distribution, like Higgs and $t\bar{t}$ production. The use of a common value for the strong coupling α_s leads to better agreement between predictions, especially for processes which depend on α_s already at leading order such as Higgs production in gluon fusion.

Dependence on heavy quark masses The dependence of PDFs on the heavy quark masses has been studied by repeating the NNPDF2.1 fit with different mass values. In particular, we have repeated the reference fit for charm quark masses m_c of 1.5, 1.6 and 1.7 GeV as well as for

bottom masses m_b of 4.25, 4.5, 5.0 and 5.25 GeV. It is important to observe that at the order at which we are working, the perturbative definition of the heavy quark mass is immaterial: indeed different definitions (such as, for example, the pole and MS mass definitions) differ by terms of $\mathcal{O}(\alpha_s^2)$ only.

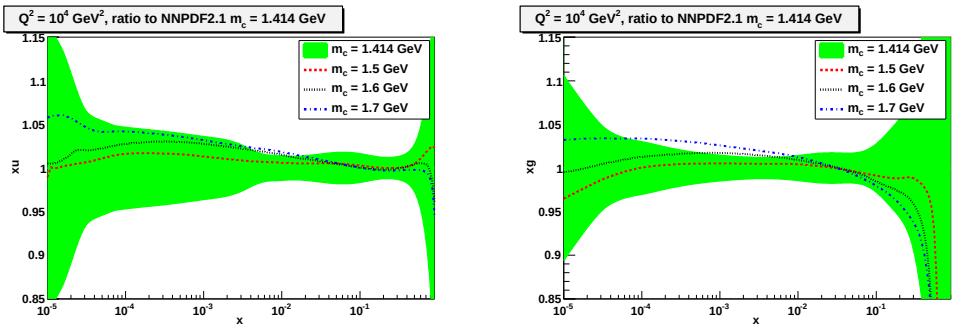

Figure 4: Ratio of NNPDF2.1 PDFs obtained for different values of the charm quark mass to the reference NNPDF2.1 set at $Q^2 = 10^4$ GeV^2. Left: up PDF ratio; right: gluon PDF ratio.

Selected results are shown in Fig. 4 where the ratio of PDFs for different values of m_c to the reference NNPDF2.1 fit are plotted as a function of x for $Q^2 = 10^4$ GeV^2. The dependence of the heavy quark PDFs on the value of the mass can be understood: heavy quark PDFs are generated radiatively, and assumed to vanish at a scale equal to their mass. Therefore, a lower mass value corresponds to a longer evolution length and thus to a larger heavy quark PDF, and conversely. Because of the momentum sum rule, if the charm PDF becomes larger, other PDFs are accordingly smaller (and conversely).

The variation of the W and Z cross section is at the percent level for charm mass variations of order of 10%, as can be seen in Fig. 5. It is also interesting to observe that the variations seen when modifying sub-leading charm mass terms is of the same order of magnitude and in fact somewhat larger. This suggests that even though PDF uncertainties on standard candles are still dominant at present, theoretical uncertainties related to the treatment of charm will become relevant and possibly dominant as soon as PDF uncertainties are reduced by a factor of two or three.

NMC data and NNLO Higgs production at colliders Recently, there have been claims [6] that differences in the treatment of fixed–target NMC data in global PDF analysis has a large impact for predictions of Higgs production at hadron colliders. More precisely, Ref. [6] claims that replacing NMC structure functions (as used by CT, MSTW and NNPDF) with reduced cross sections lowers by a sizable amount the predictions for Higgs cross section in gluon fusion at the Tevatron and the LHC, with important implications for the definition of exclusion limits in Higgs searches.

In Ref. [7] we addressed this issue using the NNPDF2.1 NLO set and found that nor using cross–section data instead of structure functions for NMC neither removing NMC altogether from the global fit leads to any appreciable modification of the NLO predictions for Higgs production at the Tevatron and the LHC. However, Ref. [6] finds that this effect is much more important at NNLO than at NLO. Using the preliminary NNPDF2.1 NNLO set, we have performed a similar analysis than the one performed at NLO. Although a more detailed description of the result will be presented elsewhere, here we present the main conclusions of this new study.

We have produced a NNPDF2.1 NNLO set based on structure functions for NMC proton data instead of the default choice of reduced cross sections. In Fig. 6 we compare the NNLO gluon for the two fits: it is clear that they are statistically equivalent. We have also computed the NNLO Higgs production in gluon fusion cross section in the two cases. Again from Fig. 6

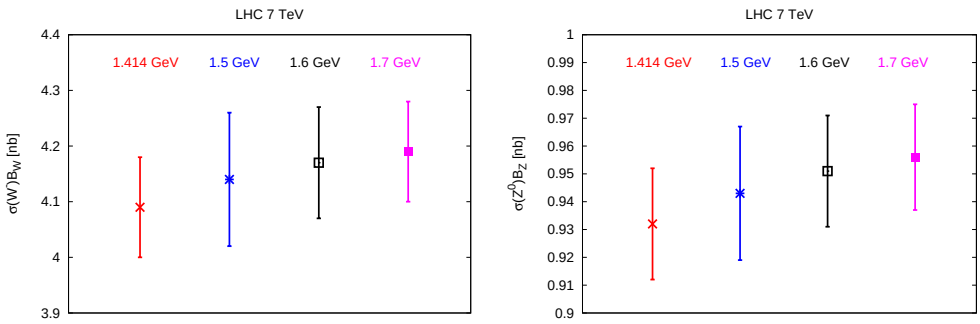

Figure 5: The total NLO W^- and Z^0 cross sections computed with the NNPDF2.1 set with varying charm quark mass m_c.

it is clear that also at NNLO the details of the treatment of NMC data are irrelevant for the predictions of Higgs production cross sections at hadron colliders.

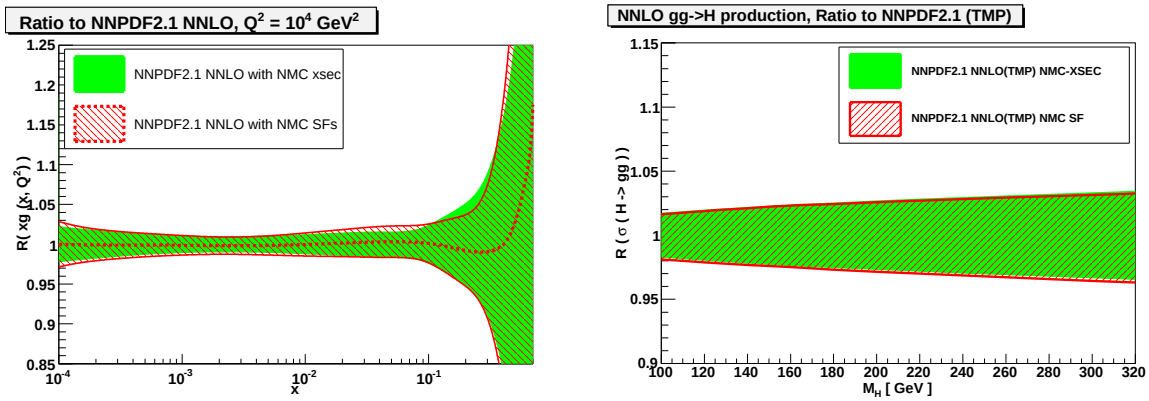

Figure 6: Left plot: Comparison of the ratio of the NNPDF2.1 NNLO gluon for the fits with the different treatment of NMC data. Right plot: The total NNLO Higgs cross section in gluon fusion from the preliminary NNLO NNPDF2.1 sets, comparing the fits in which NMC data is treated at the level of structure functions and at the level of reduced cross sections.

Therefore we have shown that the treatment of NMC data does not induce appreciable modifications for Higgs production at hadron colliders. Note however that in Ref. [6] the strong coupling was also fitted, and its best fit value was found to strongly depend on the treatment of NMC data. Our results show that if α_s is kept fixed, the impact of the treatment of NMC data is negligible.

References

1. NNPDF Collaboration, R. D. Ball, et al., *Nucl. Phys.* B **849**, 296-363 (2011), arXiv:1101.1300
2. NNPDF Collaboration, R. D. Ball, et al., *Nucl. Phys.* B **838**, 136 (2010), arXiv:1002.4407.
3. S. Forte et al., *Nucl. Phys.* B **834**, 116 (2010), arXiv:1001.2312.
4. H. L. Lai et al., Phys. Rev. D **82**, 074024 (2010), arXiv:1007.2241.
5. A. D. Martin, W. J. Stirling, R. S. Thorne and G. Watt, Eur. Phys. J. C **63** (2009) 189, arXiv:0901.0002.
6. S. Alekhin, J. Blumlein and S. Moch, arXiv:1101.5261.
7. NNPDF Collaboration, R. D. Ball, et al., arXiv:1102.3182.

HOLOGRAPHIC DESCRIPTION OF HADRONS FROM STRING THEORY [a]

Shigeki SUGIMOTO
Institute for the Physics and Mathematics of the Universe (IPMU), the University of Tokyo, 5-1-5 Kashiwanoha, Kashiwa City, Chiba 277-8583, Japan

We give a very brief summary of the basic idea and some of the interesting results in holographic QCD. Using the gauge/string duality, we obtain a low energy e ective theory of hadrons based on string theory. Mesons and baryons are obtained as open strings and D-branes, respectively, and a lot of properties of hadrons can be extracted using this new description.

1 Claim

The main claim in this talk is that string theory can be a theory of hadrons. Here, I am not claiming that QCD is wrong. Our claim is that QCD can have a dual description based on string theory, in which the string scale is around 1 GeV. This duality is one of the examples of gauge/string duality which has been discussed extensively since the discovery of the AdS/CFT correspondence.

The gauge/string duality is a duality between gauge theory and string theory. Although this is still a conjecture, there are good reasons to believe that this kind of duality really exists. The basic idea is as follows. It is well-known that the low energy e ective theory of open strings attached on D-branes is a gauge theory. On the other hand, in some parameter region, the D-branes are better described as the corresponding curved background, which is analogous to the fact that a heavy point-like object in general relativity is described by Schwarzschild background. Therefore, there are two descriptions of the D-branes. One of them is a gauge theory and the other one is string theory in a curved background. Since they are describing the same object, they should be equivalent. The typical example of the gauge/string duality is the duality between 4 dimensional $\mathcal{N} = 4$ super Yang-Mills theory and type IIB string theory in $\mathrm{AdS}_5 \times S^5$ background. Though the direct proof of the equivalence between these two descriptions is still an open problem, there are a lot of evidence supporting this duality and it is widely believed that they are physically equivalent. Our aim is to apply this idea to more realistic gauge theory (QCD) and see what we can learn from string theory.

2 Holographic QCD

To realize QCD in string theory, we consider N_c D4-branes and N_f D8-$\overline{\mathrm{D8}}$ pairs. The D4-branes are extended along $x^{0\sim4}$ directions and D8-$\overline{\mathrm{D8}}$ pairs are extended along $x^{0\sim3}$ and $x^{5\sim9}$ directions. To realize a non-supersymmetric 4 dimensional gauge theory on the D4-branes, the x^4 direction

[a] Main part of this talk is based on the works done in collaboration with T. Sakai, H. Hata, S. Yamato, K. Hashimoto and T. Imoto. [1,2,3,4,5]

is compacti ed to S^1 with an anti-periodic boundary condition for fermions. It is possible to show that the low energy e ective theory of the open strings in this system is $U(N_c)$ QCD with N_f massless quarks. There are two parameters in the system. One of them is the radius of the S^1, denoted as $M_{\rm KK}^{-1}$, and the other parameter is the 't Hooft coupling $\lambda = g_{\rm YM}^2 N_c$. Note that there are KK modes of mass of order $M_{\rm KK}$, which cannot be interpreted as particles in QCD. Therefore, $M_{\rm KK}$ can be though of as a cut-o scale below which the theory becomes QCD.

To obtain a holographic description, we replace the D4-branes with the corresponding curved background found in [6]. Then, the radius of the S^1 becomes r dependent, where r is the radial coordinate of the $x^{5\sim9}$ plane, and we obtain a cigar-like geometry as depicted in Figure 1. The

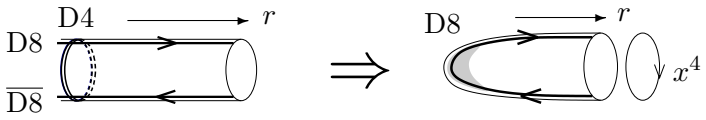

Figure 1: Replacing D4-brane with the corresponding curved background.

topology of the space-time is $\mathbf{R}^{1,3} \times \mathbf{R}^2 \times S^4$, where $\mathbf{R}^{1,3}$ and $\mathbf{R}^2$ factors are parametrized by $x^{0\sim3}$ and (r, x^4), respectively, and S^4 corresponds to the angular directions of the $x^{5\sim9}$ plane. The D8-branes are treated as probe branes. The D8-$\overline{\rm D8}$ pairs are now smoothly connected as in Figure 1. In this description, it can be shown that the string coupling is proportional to $1/N_c$ and the string length is proportional to $\lambda^{-1/2}$. Therefore, this description can be trusted when N_c and λ are large enough. The latter condition ($\lambda \gg 1$) implies that this description works better at low energy.

3 Surprise

Using the holographic description explained in the previous section, a lot of properties of hadrons can be extracted. Here, we just show some of the interesting results without trying to explain the details. The readers should keep in mind that the approximations we made are not very accurate. We have only estimated the leading terms in the $1/N_c$ and $1/\lambda$ expansions, and we have not checked whether or not the corrections are small enough. In our quantitative results, we set $M_{\rm KK}$ to be around 1 GeV, which is not high enough to justify the decoupling of unwanted KK modes. In addition, we have neglected the e ect of the quark masses. Therefore, we should not expect too much. But, don't be too pessimistic. It turns out that the results are much better than what one would naively expect.

First of all, hadrons are nicely realized in our framework. As depicted in Figure 2, glueballs, mesons, and baryons in QCD are realized as closed strings, open strings attached on the D8-branes, and D4-branes wrapped on the S^4, respectively. The e ective theory of mesons can

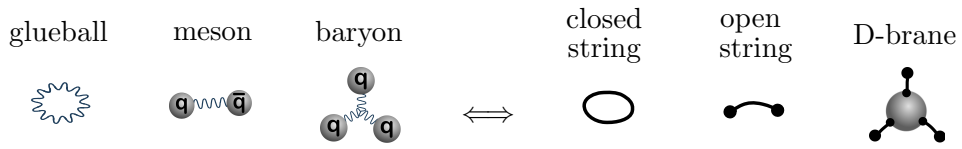

Figure 2: Hadrons in the model

be obtained from the e ective theory of open strings attached on the D8-branes. Using the standard D8-brane e ective action, and integrating over the S^4 direction, we obtain the following 5 dimensional $U(N_f)$ Yang-Mills-Chern-Simons theory:

$$S_{\rm 5dim} \simeq S_{\rm YM} + S_{\rm CS}$$

$$S_{\rm YM} = \kappa \int d^4x dz {\rm Tr} \left(\frac{1}{2} h(z) F_{\mu\nu}^2 + k(z) F_{\mu z}^2 \right) \ , \quad S_{\rm CS} = \frac{N_c}{24\pi^2} \int_{\rm 5dim} \omega_5(A) \ , \tag{1}$$

where $h(z) = (1+z^2)^{-1/3}$ and $k(z) = 1+z^2$. Here $\mu, \nu = 0 \quad 3$ correspond to the coordinates of our 4 dimensional world, and $\infty < z < \infty$ is the coordinate parametrizing the D8-brane world-volume in the right side of Figure 1. The coe cient κ in $S_{\rm YM}$ is a constant proportional to λN_c and $\omega_5(A)$ in $S_{\rm CS}$ is the Chern-Simons 5 form. The 5 dimensional gauge eld can be decomposed as

$$A_\mu(x^\mu, z) = \sum_{n \geq 1} B_\mu^{(n)}(x^\mu) \psi_n(z) \ , \quad A_z(x^\mu, z) = \sum_{n \geq 0} \varphi^{(n)}(x^\mu) \phi_n(z) \ , \tag{2}$$

using complete sets $\{\psi_n\}_{n\geq 1}$ and $\{\phi_n\}_{n \geq 0}$ of functions of z. We can show that $B_\mu^{(n)}$ with odd (even) n correspond to vector (axial-vector) elds, and $\varphi^{(0)}$ is a massless pseudo scalar eld. $\varphi^{(n)}$ $(n \geq 1)$ are absorbed by $B_\mu^{(n)}$ to make them massive. Now, we interpret $B_\mu^{(1)}$, $B_\mu^{(2)}$, $B_\mu^{(3)}$, etc., as the -meson, a_1-meson, $'$-meson, etc., and $\varphi^{(0)}$ as the pion.

Inserting these expansions into the 5 dimensional action (1) and integrating over z, we obtain a traditional 4 dimensional e ective action of the mesons π, , a_1, etc.:

$$S_{\rm 5dim}(A) = S_{\rm 4dim}(\pi, \ , a_1, \ ', a_1', \quad) \ . \tag{3}$$

Remarkably, the meson e ective theory obtained in this way reproduces a lot of old phenomenological models of hadrons, such as Skyrme model, vector meson dominance model, Gell-Mann - Sharp - Wagner model, hidden local symmetry model, etc., without making any phenomenological assumptions. Furthermore, masses and couplings calculated in (3) roughly agree with the experimental data. (See Table 1.)

Table 1: Masses and couplings calculated in our model. Here, $M_{\rm KK}$ and λ are xed by tting the ρ meson mass and the pion decay constant f_π.

mass	our model	experiment
ρ	[776 MeV]	776 MeV
a_1	1189 MeV	1230 MeV
ρ'	1607 MeV	1465 MeV

coupling	our model	experiment
f_π	[92.4 MeV]	92.4 MeV
L_1	0.58×10^{-3}	$(0.1 \sim 0.7) \times 10^{-3}$
L_2	1.2×10^{-3}	$(1.1 \sim 1.7) \times 10^{-3}$
L_3	-3.5×10^{-3}	$-(2.4 \sim 4.6) \times 10^{-3}$
L_9	8.7×10^{-3}	$(6.2 \sim 7.6) \times 10^{-3}$
L_{10}	-8.7×10^{-3}	$-(4.8 \sim 6.3) \times 10^{-3}$
$g_{\rho\pi\pi}$	4.8	6.0
g_ρ	0.16 GeV^2	0.12 GeV^2
$g_{a_1\rho\pi}$	4.6 GeV	$2.8 \sim 4.2$ GeV

Other mesons, including higher spin mesons, are obtained as excited string states. For example, $a_2(1320)$, $b_1(1235)$, $\pi(1300)$, $a_0(1450)$, etc., are interpreted as the rst excited open string states. $_3(1690)$ and $\pi_2(1670)$, are interpreted as the second excited states. The lightest spin J mesons with $J \geq 1$ are $(J \quad 1)$-th excited open string states. See [5] for more details.

As mentioned above, baryons are obtained as D4-branes wrapped on S^4. It is known that a D4-brane embedded in D8-brane world-volume is equivalent to a soliton in the gauge theory realized on the D8-brane. In our 5 dimensional gauge theory (1), baryons are described as a soliton carrying non-trivial instanton number

$$\frac{1}{8\pi^2} \int_{\mathbf{R}^4} {\rm Tr}(F \wedge F) = N_B \ , \tag{4}$$

where $\mathbf{R}^4$ is a four dimensional space $(x^{1\sim 3}, z)$ and N_B is an integer interpreted as the baryon number. This is analogous to the description of baryons as solitons in Skyrme model. Applying

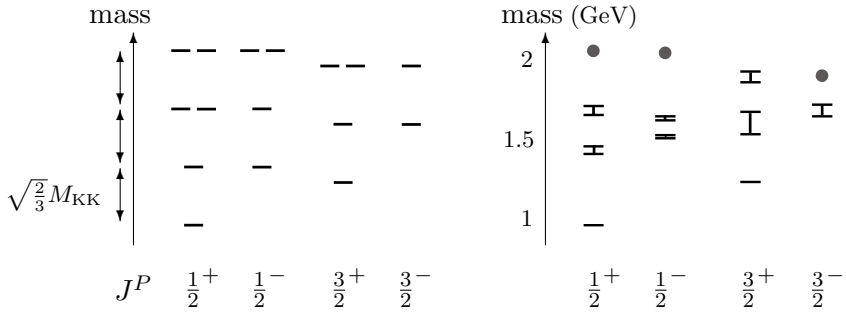

Figure 3: Left side is the baryon spectrum obtained in the model, while the right side is the spectrum of the baryons with $I = J$ taken from particle listings by Particle Data Group. Here I and J are the isospin and spin, respectively, and and P is the parity.

the techniques developed in the Skyrme model to our system, we can analyze various properties of baryons. The spectrum of the baryon is obtained as in Figure 3. It is interesting to note that our result suggests that second lightest baryon with $J^P = \frac{1}{2}^+$ and the lightest one with $J^P = \frac{1}{2}^-$ are degenerate. This feature is found in the experiment and has been a mystery in hadron physics for a long time. The results for the charge radii and magnetic moments for nucleons are listed in Table 2.

Table 2: $\langle r^2 \rangle_{I=0}$, $\langle r^2 \rangle_{I=1}$ and $\langle r^2 \rangle_A$ are isoscalar, isovector and axial mean square radii, respectively. $g_{I=0}$ and $g_{I=1}$ are isoscalar and isovector g-factors. g_A is the axial coupling.

	our model	experiment
$\langle r^2 \rangle_{I=0}$	$(0.74\text{ fm})^2$	$(0.81\text{ fm})^2$
$\langle r^2 \rangle_{I=1}$	$(0.74\text{ fm})^2$	$(0.94\text{ fm})^2$
$\langle r^2 \rangle_A$	$(0.54\text{ fm})^2$	$(0.67\text{ fm})^2$
$g_{I=0}$	1.7	1.8
$g_{I=1}$	7.0	9.4
g_A	0.73	1.3

Acknowledgments

We would like to thank the organizers of the Moriond workshop for kind invitation and hospitality. We are also grateful to K. Hashimoto, H. Hata, T. Imoto, T. Sakai, and S. Yamato for pleasant collaborations. This work is supported in part by the Grant-in-Aid for Young Scientists (B), Ministry of Education, Culture, Sports, Science and Technology (MEXT), Japan, JSPS Grant-in-Aid for Creative Scienti c Research No. 19GS0219 and also by World Premier International Research Center Initiative (WPI Initiative), MEXT, Japan.

References [b]

1. T. Sakai, S. Sugimoto, Prog. Theor. Phys. **113**, 843-882 (2005).
2. T. Sakai, S. Sugimoto, Prog. Theor. Phys. **114**, 1083-1118 (2005).
3. H. Hata, T. Sakai, S. Sugimoto, S. Yamato, Prog. Theor. Phys. **117**, 1157 (2007).
4. K. Hashimoto, T. Sakai, S. Sugimoto, Prog. Theor. Phys. **120**, 1093-1137 (2008).
5. T. Imoto, T. Sakai, S. Sugimoto, Prog. Theor. Phys. **124**, 263-284 (2010).
6. E. Witten, Adv. Theor. Math. Phys. **2**, 505 (1998)

[b] We apologize for not being able to cite all the relevant references. See the references in our papers.[1,2,3,4,5]

Nuclear matter and chiral phase transition at large-N_c

Francesco Giacosa
Institute of theoretical Physics, Johann Wolfgang Goethe University
Max-von-Laue Str. 1, D-60438, Frankfurt am Main, Germany

Two aspects of the QCD phase diagrams are studied in the limit of a large number of colors: at zero temperature and nonzero density the (non)existence of nuclear matter, and at zero density and nonzero temperature the chiral phase transition.

1 Introduction and Summary

The limit in which the number of colors N_c is sent to infinity (large-N_c limit) represents a systematic approach [1] to study properties of QCD. The world for $N_c \gg 3$ is simpler because planar diagrams dominate. However, the basic ingredients 'survive' in the large-N_c limit: quark-antiquark mesons exist and become weakly interacting, baryons also exist but are formed of N_c quarks. Recently, a lot of effort has been spent to study the properties of the phase diagram of QCD when N_c is varied [2].

Along the line of zero temperature and nonzero chemical potential, a natural question [3] is if nuclear matter binds for $N_c > 3$. We shall find that this is not the case: in view of the peculiar nature of the scalar attraction between nuclei we obtain that nuclear matter ceases to form as soon as $N_c > 3$ is considered. Namely, the scaling behavior of the scalar attraction depends on the nature of the exchanged field with a mass of about 0.6 GeV. Present knowledge in low-energy QCD spectroscopy [4] shows that this light scalar field is (predominately) not a quark-antiquark field, the alternative possibilities being tetraquark, pion-pion interpolating field, molecular state, etc. In all these interpretations the scalar attraction diminishes in comparison with the vector repulsion, mediated by the well-known vector meson ω, when N_c is increased. As a result, nuclear matter does not take place [3]: the investigation leading to this result is achieved though a simple effective model of the Walecka type.

When moving along the finite temperature axis while keeping the density to zero, it is interesting to study how different chiral effective models behave at large-N_c. It is quite remarkable that two very well-known models, the quark-based Nambu Jona-Lasinio (NJL) model [5,6] and the hadron-based σ-model [7,8], deliver different result for the critical temperature for chiral restoration T_c. While in the NJL model T_c scales as N_c^0 and is thus, just as the deconfinement phase transition, large-N_c independent, in the σ-model one obtains that $T_c \propto \sqrt{N_c}$. This mismatch can be solved by including in the σ-model one (or more) T-dependent parameter(s): a rather simple modification of the mass term is enough to reobtain the expected scaling $T_c \propto N_c^0$.

The paper [a] is organized as follows: in Sec. 2 and Sec. 3 we study nuclear matter and the

[a] Based on the presentation given at 'Rencontres de Moriond, QCD and High Energy Interactions', March 20-27 2011, La Thuile (Italy).

chiral phase transition for $N_c > 3$, respectively. In Sec. 4 we briefly present our conclusions.

2 Nuclear matter at large-N_c

Nuclear matter at large-N_c is studied by means of an effective Walecka-Lagrangian [9]

$$\mathcal{L} = \bar{\psi}[\gamma^\mu(i\partial_\mu - g_\omega\omega_\mu) - (m_N - g_S S)]\psi + \frac{1}{2}\partial^\mu S\partial_\mu S - \frac{1}{2}m_S^2 S^2 + \frac{m_\omega^2}{2}\omega_\mu\omega^\mu + ... \qquad (1)$$

where S represents a scalar field with a mass of about 0.6 GeV and ω the isoscalar vector meson. The large-N_c scaling properties of the latter are well known: $m_\omega \propto N_c^0$, $g_\omega \propto \sqrt{N_c}$. We now examine the possibilities [3] for the scalar state S:

• S as quark-antiquark field: $m_S \propto N_c^0$ and $g_S \propto \sqrt{N_c}$. This is the only case in which nuclear matter exists in the large-N_c limit. The binding energy increases with N_c. However, this scenario is –as previously anticipated– unfavored [4].

• S as tetraquark field [10]: $m_S \propto N_c$ and $g_S \propto N_c^0$. Nuclear matter does not bind for $N_c > 3$. On the contrary, for $N_c = 2$ an increased binding is found. This scenario represents a viable possibility in agreement with phenomenology. It might also play an important role at nonzero temperature and density [11].

• S as an effective two-pion-exchange effect [12]: $m_S \sim 2m_\pi \propto N_c^0$, $g_S \propto \sqrt{N_c}$. Although the scaling laws are the same as in the quark-antiquark case, no binding is obtained in view of numerical details.

• S as a low-mass scalar glueball [13]: $m_S \propto N_c^0$ and $g_S \propto N_c^0$. No binding for $N_c > 3$ is obtained. Note, this scenario is unfavored by present lattice data which place the glueball at about 1.6 GeV [14].

The result that no nuclear matter exists for large-N_c is stable and does not depend on numerical details. In the framework of the so-called strong anthropic principle it is then natural that we live in a world in which N_c is not large.

3 Chiral phase transition at large-N_c

The σ-model has been widely used to study the thermodynamics of QCD [15]. In one of its simplest forms it reads (as function of N_c):

$$\mathcal{L}_\sigma(N_c) = \frac{1}{2}(\partial_\mu\Phi)^2 + \frac{1}{2}\mu^2\Phi^2 - \frac{\lambda}{4}\frac{3}{N_c}\Phi^4 \ , \qquad (2)$$

where $\Phi^t = (\sigma, \vec{\pi})$ describes the scalar field σ and the pseudoscalar pion triplet $\vec{\pi}$. The quark-antiquark field σ represents the chiral partner of the pion: as mentioned in the previous section, it does not correspond to the resonance $f_0(600)$ with a mass of about 0.6 GeV but to the resonance $f_0(1370)$ with a mass of about 1.3 GeV [4,8]. The scaling law $\lambda \to 3\lambda/N_c$ takes into account that the meson-meson scattering amplitude scales as N_c^{-1}. On the contrary, μ^2 contains no dependence on N_c: in this way the quark-antiquark meson masses scales –as desired– as N_c^0.

The critical temperature T_c for the chiral phase restoration is calculated by using the so-called CJT formalism [16] , which is a self-consistent resummation scheme for field theoretical calculations at nonzero temperature. In the Hartree and in the double-bubble approximation T_c is given by the expression

$$T_c(N_c) = f_\pi\sqrt{2\frac{N_c}{3}} \propto \sqrt{N_c} \ , \qquad (3)$$

where $f_\pi = 92.4$ MeV is the pion decay constant. The scaling of T_c is thus in disagreement with the NJL model [6] where $T_c \propto N_c^0$ and with basic expectations [2]. This result is due to the

fact that for $N_c \gg 3$ a gas of free mesons is realized and thus no transition takes place. In fact, the mechanism responsible for the restoration of chiral symmetry in hadronic models is given by mesonic loops, whose effect vanishes for $N_c \gg 3$. On the contrary, in the NJL model the restoration of chiral symmetry is generated by the quark loops, which do not vanish in the large-N_c limit.

The inconsistency between the NJL model and the σ-model can be easily solved by replacing

$$\mu^2 \to \mu(T)^2 = \mu^2 \left(1 - \frac{T^2}{T_0^2}\right) \tag{4}$$

(i.e., making it T-dependent) where the parameter $T_0 \simeq \Lambda_{QCD} \propto N_c^0$ introduces a new temperature scale. This is in line with the fact that the σ-model can be obtained by hadronization of the NJL model. In this scheme the parameters of the σ-model turn out to be temperature-dependent. Note also that the here considered T^2-behavior –although naive at the first sight– has been also obtained in Ref. [17]. In this way the critical temperature is modified to

$$T_c(N_c) = T_0 \left(1 + \frac{1}{2}\frac{T_0^2}{f_\pi^2}\frac{3}{N_c}\right)^{-1/2} \propto N_c^0 \ , \tag{5}$$

which is now large-N_c independent, just as in the NJL case. For $N_c = 3$, using $T_0 = \Lambda_{QCD} \simeq 225$ MeV, the critical temperature T_c is lowered to $T_c \simeq 113$ MeV. Interestingly, in the framework of σ-models with (axial-)vector mesons [8], one has to make the replacement $f_\pi \to Z f_\pi$ with $Z = 1.67 \pm 0.2$. In this way the critical temperature reads $T_c \simeq 157$ MeV, which is remarkably close to the lattice results [18].

Beyond the phenomenologically motivated modification presented here, one can go further and couple the present σ-model (and generalizations thereof) to the Polyakov loop [19]. Also in this case [20] the critical temperature turns out to be, as desired, independent on N_c. The reason for this behavior can be traced back to the fact that the transition of the Polyakov loop (which describes the confinement-deconfinemet phase transition) triggers also the restoration of chiral symmetry.

4 Conclusions

In this work we have investigated the properties of nuclear matter and chiral phase transition in the large-N_c limit.

We have found that present knowledge on the spectroscopy of scalar mesons indicates that nuclear matter does not bind for $N_c > 3$. Namely, the nucleon-nucleon attraction in the scalar-isoscalar channel turns out not to be strong enough to bind nuclei when N_c is increased. Therefore, nuclear matter seems to be a peculiar property of our $N_c = 3$ world.

For what concerns the chiral phase transition at nonzero temperature and zero density, we have found that care is needed when using effective hadronic models of the σ-type. The critical temperature T_c does not scale as expected in the large-N_c limit. It is however possible to introduce simple modifications of chiral hadronic models in such a way that the expected result $T_c \propto N_c^0$ is recovered.

Acknowledgments

The author thanks L. Bonanno, A. Heinz, and D. H. Rischke for cooperation [3,20] and S. Lottini, G. Torrieri, G. Pagliara and H. Warringa for discussions.

1. E. Witten, Nucl. Phys. B **160** (1979) 57. G. 't Hooft, Nucl. Phys. B **72** (1974) 461.

2. L. McLerran and R. D. Pisarski, Nucl. Phys. A **796** (2007) 83. G. Torrieri and I. Mishustin, Phys. Rev. C **82** (2010) 055202. S. Lottini and G. Torrieri, arXiv:1103.4824 [nucl-th]. T. Kojo, Y. Hidaka, L. McLerran and R. D. Pisarski, Nucl. Phys. A **843** (2010) 37. C. Sasaki and I. Mishustin, Phys. Rev. C **82** (2010) 035204.
3. L. Bonanno and F. Giacosa, arXiv:1102.3367 [hep-ph].
4. C. Amsler and N. A. Tornqvist, Phys. Rept. **389**, 61 (2004). E. Klempt and A. Zaitsev, Phys. Rept. **454** (2007) 1. F. Giacosa, Phys. Rev. D **80** (2009) 074028.
5. Y. Nambu, G. Jona-Lasinio, Phys. Rev. **122**, 345-358 (1961); Y. Nambu, G. Jona-Lasinio, Phys. Rev. **124**, 246-254 (1961).
6. S. P. Klevansky, Rev. Mod. Phys. **64** (1992) 649.
7. M. Gell-Mann, M. Levy, Nuovo Cimento, **16**, 705 (1960). S. Gasiorowicz, D. A. Geffen, Rev. Mod. Phys. **41**, 531-573 (1969).
8. D. Parganlija, F. Giacosa, D. H. Rischke, Phys. Rev. **D82**, 054024 (2010). S. Gallas, F. Giacosa, D. H. Rischke, Phys. Rev. **D82** (2010) 014004. S. Janowski, D. Parganlija, F. Giacosa and D. H. Rischke, arXiv:1103.3238 [hep-ph].
9. J. D. Walecka, Annals Phys. **83**, 491 (1974). B. D. Serot and J. D. Walecka, Adv. Nucl. Phys. **16**, 1 (1986). B. D. Serot and J. D. Walecka, Int. J. Mod. Phys. E **6**, 515 (1997).
10. R. L. Jaffe, Phys. Rev. D **15** (1977) 267. L. Maiani, F. Piccinini, A. D. Polosa and V. Riquer, Phys. Rev. Lett. **93** (2004) 212002 [arXiv:hep-ph/0407017]. F. Giacosa, Phys. Rev. D **74** (2006) 014028. F. Giacosa, Phys. Rev. D **75** (2007) 054007. A. H. Fariborz, R. Jora and J. Schechter, Phys. Rev. D **72** (2005) 034001.
11. A. Heinz, S. Struber, F. Giacosa and D. H. Rischke, Phys. Rev. D **79** (2009) 037502. S. Gallas, F. Giacosa and G. Pagliara, arXiv:1105.5003 [hep-ph].
12. N. Kaiser, R. Brockmann and W. Weise, Nucl. Phys. A **625** (1997) 758. A. Calle Cordon and E. Ruiz Arriola, Phys. Rev. C **81** (2010) 044002.
13. C. Amsler and F. E. Close, Phys. Rev. D **53** (1996) 295. W. J. Lee and D. Weingarten, Phys. Rev. D **61**, 014015 (2000). F. E. Close and A. Kirk, Eur. Phys. J. C **21**, 531 (2001). F. Giacosa, T. Gutsche, V. E. Lyubovitskij and A. Faessler, Phys. Rev. D **72**, 094006 (2005); Phys. Lett. B **622**, 277 (2005). H. Y. Cheng, C. K. Chua and K. F. Liu, Phys. Rev. D **74** (2006) 094005. L. Bonanno and A. Drago, Phys. Rev. C **79**, 045801 (2009). V. Mathieu, N. Kochelev and V. Vento, Int. J. Mod. Phys. E **18** (2009) 1.
14. Y. Chen *et al.*, Phys. Rev. D **73** (2006) 014516.
15. D. H. Rischke, Prog. Part. Nucl. Phys. **52** (2004) 197. E. Megias, E. Ruiz Arriola, L. L. Salcedo, Phys. Rev. **D74**, 065005 (2006).
16. J. M. Cornwall, R. Jackiw, E. Tomboulis, Phys. Rev. **D10**, 2428-2445 (1974).
17. J. Gasser, H. Leutwyler, Phys. Lett. **B184**, 83 (1987).
18. M. Cheng, N. H. Christ, S. Datta, J. van der Heide, C. Jung, F. Karsch, O. Kaczmarek, E. Laermann *et al.*, Phys. Rev. **D74** (2006) 054507.
19. A. Dumitru, R. D. Pisarski, Phys. Lett. **B504** (2001) 282-290.
20. A. Heinz, F. Giacosa, and D. H. Rischke, in preparation.

Recent Results on Light Hadron Spectroscopy at BESIII

Zhi Wu (for BESIII collaboration)

19B YuquanLu, Shijingshan District BeijingChina, 100049

Using about $226 \times 10^6 J/\psi$ events and $106 \times 10^6 \psi'$ events accumulated with BESIII detector operating at BEPCII e^+e^- collider, the existence of $p\bar{p}$ mass threshold enhancement and $X(1835)$ is confirmed. Two resonances, $X(2120)$ and $X(2370)$ are first observed in $J/\psi \to \gamma\eta'\pi^+\pi^-$. In the study of $J/\psi \to \omega\eta\pi^+\pi^-$, a narrow structure denoted as $X(1870)$ is seen with a significance of 7.1σ. In addition, a direct measurement of $f_0(980) \to a_0^0(980)$ and $a_0^0(980) \to f_0(980)$ mixing transitions is presented to probe the nature of the two scalar states.

1 BESIII and BEPCII

BEPCII/BESIII[1] is a major upgrade of the BEPC accelerator and BESII detector. The primary physics purposes are aimed at the study of hadron spectroscopy and τ-charm physics. The analysis reported here are based on the data samples of $226 \times 10^6 J/\psi$ and $106 \times 10^6 \psi'$ events.

2 Confirmation of $p\bar{p}$ Mass Threshold Enhancement

An anomalously strong $p\bar{p}$ mass threshold enhancement was first observed by BESII experiment in the radiative decay of $J/\psi \to \gamma p\bar{p}$ [2] in 2003. A fit with an S-wave Breit-Wigner resonance function indicates that the peak mass is at $M = 1859^{+3}_{-10}(stat.)^{+5}_{-25}(sys.)$ MeV/c^2, and the total width is $\Gamma < 30$MeV/c^2(at the 90% C.L.). One intriguing feature of this enhancement structure is that the corresponding structures are absent in the relative channels, including B-meson decays[3], radiative decays of ψ'[4] and Υ[5], and the decay of $J/\psi \to \omega p\bar{p}$[6]. These negative observations disfavor the interpretation of pure final state interaction(FSI).

Fig. 1 shows the fitting results of $p\bar{p}$ mass spectrum in $\psi' \to \pi^+\pi^- J/\psi(\gamma p\bar{p})$ and the threshold enhancement structure can be observed. The mass of fitted resonant parameters are $M = 1861^{+6}_{-13}(stat.)^{+7}_{-26}(sys.)$ MeV/c^2, and the total width is $\Gamma < 38$MeV/c^2 at the 90% C.L..

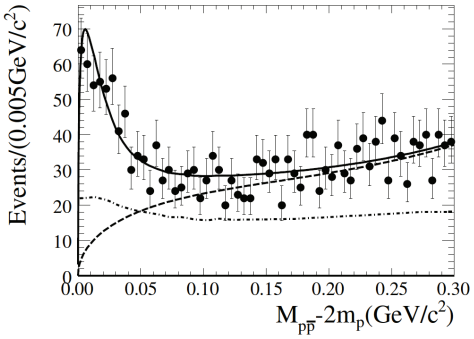

Figure 1: The $p\bar{p}$ mass spectrum for the $\psi' \to \pi^+\pi^- J/\psi(\gamma p\bar{p})$ after final event selection. The solid curve is the fit result; the dashed curve shows the fitted background function, and the dash-dotted curve indicates how the acceptance varies with $p\bar{p}$ invariant mass.

3 Observation of $X(1835)$ and Two New Resonances in $J/\psi \to \gamma\eta'\pi^+\pi^-$

$X(1835)$ is first observed in the study of $J/\psi \to \gamma\eta'\pi^+\pi^-$ at BESII with a statistical significance of 7.7σ [7]. Extensive theoretical interpretations have been raised to settle the nature of this resonance, such as the $p\bar{p}$ bound state [8], glueball [9], radial excitation of η' [10] and so on.

At BESIII, two decay modes of η', $\eta' \to \gamma\rho$ and $\eta' \to \eta\pi^+\pi^-$ are utilized to study the channel of $J/\psi \to \gamma\eta'\pi^+\pi^-$. Fig. 2(a) and Fig. 2(b) show the mass spectrum of $\eta'\pi^+\pi^-$ in both decay modes of η'. In addition to the clear $X(1835)$ peak, two structures located at around 2.1 and 2.3 GeV/c^2 are also first observed.

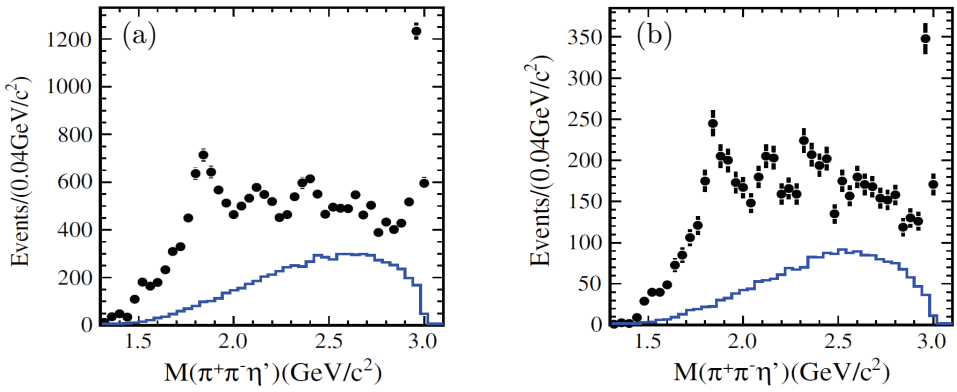

Figure 2: (a) is the mass spectrum of $\eta'\pi^+\pi^-$ with $\eta' \to \gamma\rho$; (b) is the mass spectrum of $\eta'\pi^+\pi^-$ with $\eta' \to \eta\pi^+\pi^-$. The dots with error bars shows the data, and the blue histogram in (a) and (b) stands for the distribution of arbitrarily normalized phase space Monte Carlo sample.

Fig. 3 shows the fitting result of the $\eta'\pi^+\pi^-$ mass spectrum with the contribution of two decay modes of η' combined together. The existence of $X(1835)$ is confirmed with a significance of larger than 20σ. The statistical significance of $X(2120)$ and $X(2370)$ are determined to be 7.2σ and 6.4σ respectively.

4 Observation of $X(1870)$ in $J/\psi \to \omega\eta\pi^+\pi^-$

$X(1835)$ is reported in the analysis of $J/\psi \to \gamma\eta'\pi^+\pi^-$ as covered in the last section. The study of the decay patterns of the resonance, i.e. to search for similar structures in relative channels and with other side particles is very important to clarify its nature. In this sense, the analysis of $J/\psi \to \omega\eta\pi^+\pi^-$ will shed light on the properties of the resonance.

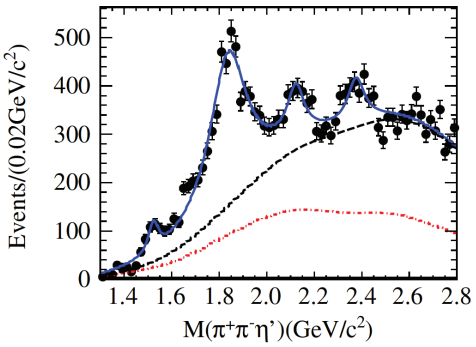

Figure 3: Mass spectrum fitting with four resonances. The dash-dotted red curve is the contribution from non-η' events and $J/\psi \to \pi^0\eta'\pi^+\pi^-$ events, and the dashed black curve represents the total background.

Fig. 4 shows the fitting result of $\eta\pi^+\pi^-$ mass spectrum within the $a_0^0(980)$ signal region in $M(\eta\pi^\pm)$. The signal peaks of $f_1(1285)$, $\eta(1405)$ and $X(1870)$ are parameterized with efficiency-corrected Breit-Wigner function convoluted with Gaussian resolution function, and the background curve is described by a floating polynomial. The mass and width of $f_1(1285)$ and $\eta(1405)$ agree quite well with their PDG values [11]. The fit yields the mass and width of $X(1870)$ to be $M = 1877.3 \pm 6.3$ MeV/c^2, and $\Gamma = 57 \pm 12$MeV/c^2. The statistical significance of $X(1870)$ is conservatively estimated as 7.1σ. Whether the $X(1870)$, $X(1860)$ and $X(1835)$ are the same particle need further study.

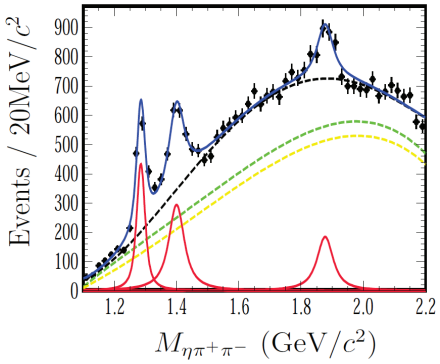

Figure 4: Mass spectrum fitting results with either $\eta\pi^+$ or $\eta\pi^-$ located in the 100 MeV/$c2$ mass window of $a_0(980)$. The yellow dashed curve shows the contribution of non-ω and/or non-$a_0(980)$ background, green dashed line in addition includes the contribution of $J/\psi \to b_1(1235)a_0(980)$, the black dashed curve stands for the total background with the non-resonant $J/\psi \to \omega a_0^\pm(980)\pi^\mp$ included.

5 Study of $a_0^0(980) - f_0(980)$ Mixing

The nature of the scalar mesons $a_0^0(980)$ and $f_0(980)$ has been a hot topic in light hadron physics for many years. The possibility of mixing between $a_0^0(980)$ and $f_0(980)$ was suggested long ago, and its measurement will shed light on the nature of these two resonances [12]. There has been various theoretical predications with various models, yet no firm experimental evidence is available. The most significant signature of this isospin-violating mixing process is a very narrow peak of about 8 MeV/$c2$ in the mass spectrum of $a_0^0(980)/f_0(980)$ [13]. At BESIII, we perform a direct measurement of $a_0^0(980) \leftrightarrow f_0(980)$ mixing intensity via the process of $J/\psi \to \phi f_0(980) \to \phi a_0^0(980) \to \phi\eta\pi^0$ and $\chi_{c1} \to \pi^0 a_0^0(980) \to \pi^0 f_0(980) \to \pi^0\pi^+\pi^-$.

For the decay of $J/\psi \to \phi f_0(980) \to \phi a_0^0(980) \to \phi\eta\pi^0$, a simultaneous fit is performed to

the $\eta\pi^0$ mass spectrum recoiling against the ϕ mass signal and the ϕ mass side band, as shown in Fig. 5(a). The upper limit of the mixing branching ratio is set to be $Br(J/\psi \to \phi f_0(980) \to \phi a_0^0(980) \to \phi\eta\pi^0) < 5.4 \times 10^{-6}$ at the 90% C.L.. The upper limit (90% C.L.) of the mixing intensity for the $f_0(980) \to a_0^0(980)$ transition is defined and calculated to be [14]:

$$\xi_{fa} = \frac{Br(J/\psi \to \phi f_0(980) \to \phi a_0^0(980) \to \phi\eta\pi^0)}{Br(J/\psi \to \phi f_0(980) \to \phi\pi\pi} < 1.1\% \quad (1)$$

For the decay of $\chi_{c1} \to \pi^0 a_0^0(980) \to \pi^0 f_0(980) \to \pi^0\pi^+\pi^-$, a simultaneous fit is performed to the $\pi^+\pi^-$ mass spectrum in the χ_{c1} signal region and the χ_{c1} mass side band, as shown in Fig. 5(b). The upper limit of the mixing branching ratio is set to be $Br(\chi_{c1} \to \pi^0 a_0^0(980) \to \pi^0 f_0(980) \to \pi^0\pi^+\pi^-) < 6.0 \times 10^{-7}$ at the 90% C.L.. The upper limit (90% C.L.) of the mixing intensity for the $a_0^0(980) \to f_0(980)$ transition is defined and calculated to be [11]:

$$\xi_{af} = \frac{\chi_{c1} \to \pi^0 a_0^0(980) \to \pi^0 f_0(980) \to \pi^0\pi^+\pi^-}{\chi_{c1} \to \pi^0 a_0^0(980) \to \pi^0\pi^0\eta} < 1.0\% \quad (2)$$

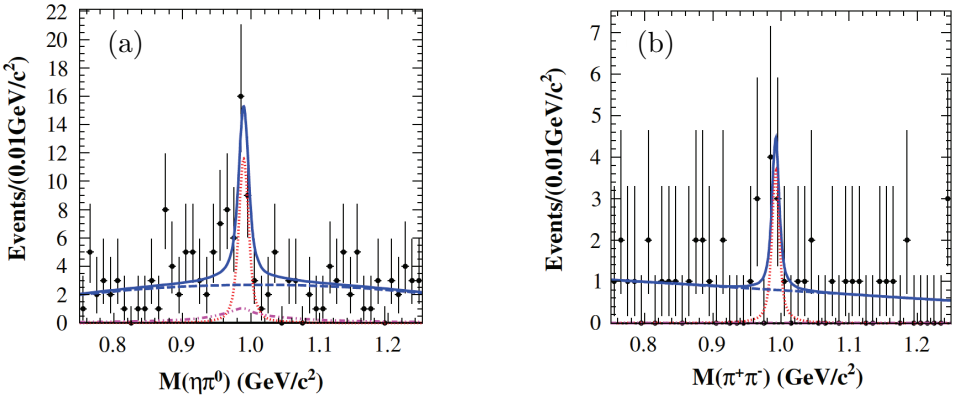

Figure 5: (a) is the fitting result of $\eta\pi^0$ mass spectrum recoiling against ϕ signal; (b) is the fitting result of $\pi^+\pi^-$ mass spectrum in the signal region of χ_{c1}. The red dotted line stands for the mixing signal, the green dash-dotted line shows the $a_0^0(980)/f_0(980)$ contribution from other processes, and the blue dashed line is the background polynomial.

References

1. M. Ablikim et al. (BES Collaboration), *Nucl. Instrum. Meth. A* **614**, 345 (2010).
2. J. Z. Bai et al. (BES Collaboration), *Phys. Rev. Lett.* **91**, 022001 (2003)
3. M. A. Wang et al., *Phys. Rev. Lett.* **92**, 131801 (2004)
4. M. Ablikim et al. (BES Collaboration), *Phys. Rev. Lett.* **99**, 011802 (2007)
5. S. B. Athar et al. (CLEO Collaboration), *Phys. Rev.* D **73**, 032001 (2006)
6. M. Ablikim et al. (BES Collaboration), *Eur. Phys. J. C* **53**, 15 (2008)
7. M. Ablikim et al. (BES Collaboration), *Phys. Rev. Lett.* **95**, 262001 (2005)
8. A. Datta and P. J. ODonnel, *Phys. Lett.* B **567**, 273 (2003)
9. N. Kochelev and D. P. Min, *Phys. Lett.* B **633**, 283-288 (2006)
10. T. Huang and S. L. Zhu, *Phys. Rev.* D **73**, 014023 (2006)
11. C. Amsler et al. (Particle Data Group), *Phys. Lett.* B **667**, 1 (2008)
12. N.N. Ashasov, S. A. Devyanin, G. N. Shestokov, *Phys. Lett.* B **88**, 367 (1979)
13. J. J. Wu, Q. Zhao and B. S. Zou, *Phys. Rev.* D **78**, 074017 (2008)
14. M. Ablikim et al. (BES Collaboration), *Phys. Lett.* B **607**, 243 (2005)

MEASUREMENT OF THE J/ψ INCLUSIVE PRODUCTION CROSS-SECTION IN PP COLLISIONS AT $\sqrt{s}$=7 TeV WITH ALICE AT THE LHC

J. WIECHULA for the ALICE COLLABORATION
Physikalisches Institut der Universität Tübingen, Auf der Morgenstelle 14, 72076 Tübingen, Germany

ALICE measures the J/ψ production at mid-rapidity ($|y| < 0.9$) in the di-electron decay channel as well as at forward rapidity ($2.5 < y < 4.0$) in the di-muon decay channel. In both channels the acceptance goes down to zero transverse momentum. We present the rapidity dependence of the inclusive J/ψ production cross-section and transverse momentum spectra.

1 Introduction

The measurement of the J/ψ production cross-section in pp collisions is crucial for testing QCD models of quarkonium production in the new energy regime provided by the LHC. Several theoretical models [1,2] have been proposed to describe the J/ψ production. However none of them consistently describes the production cross-section, the transverse momentum and rapidity dependences and the polarisation. Measurements of these variables are therefore essential to help understanding the underlying production mechanisms.

The main focus of ALICE [3] is to study the deconfined hot and dense QCD phase which is expected to be formed in heavy-ion collisions. The J/ψ is an essential observable for this state of matter and the cross-section measurement in pp collisions is important as a reference.

ALICE measures the J/ψ production in two rapidity windows: at mid-rapidity ($|y| < 0.9$) as well as at forward rapidity ($2.5 < y < 4$). We present first results of the J/ψ production cross-section as well as its p_T and rapidity dependence in pp collisions at $\sqrt{s} = 7\,\text{TeV}$ [4]. The data were not corrected for feed-down contributions from other charmonium states (χ_c, ψ') or B-hadron decays (inclusive production).

2 J/ψ measurement with ALICE

ALICE is a general purpose heavy-ion experiment. It consists of a central part with a pseudo rapidity coverage of $|\eta| < 0.9$ and full acceptance in ϕ and a muon spectrometer placed at forward rapidity ($-4 < \eta < -2.5$). J/ψ production is measured in both rapidity regions, at mid-rapidity in the di-electron and at forward rapidity in the di-muon decay channel

The main detectors used for the analysis at mid-rapidity are the Inner Tracking System [3,5] (ITS) and the Time Projection Chamber [6] (TPC). The ITS, placed at radii between 3.9 cm and 43 cm, consists of six cylindrical layers of silicon detectors, equipped with silicon pixel, silicon drift and silicon strip technology, two layers each. The main purpose of the ITS is to provide the reconstruction of the primary collision vertex as well as secondary vertices from decays. In addition it improves the momentum resolution of the TPC. The main tracking device in ALICE

is a cylindrical TPC. It has a length of 5 m and reaches from 85 cm to 247 cm in radial direction. The TPC provides particle identification (PID) via the measurement of the specific energy loss ($\mathrm{d}E/\mathrm{d}x$) of particles in the detector gas. Due to the excellent $\mathrm{d}E/\mathrm{d}x$ resolution of $\sim 5.5\,\%$ PID could be performed for electrons with $1 \lessapprox p \lessapprox 6\,\mathrm{GeV}/c$ using TPC information only.

The muon spectrometer consists of a $3\,\mathrm{T{\cdot}m}$ dipole magnet, 5 tracking stations made of two planes of Cathode Pad Chambers each, a set of muon filters and a trigger system. Particles emerging from the collision in the forward direction have to traverse a front absorber with $10\,\lambda_I$, removing most hadrons and electrons. The remaining particles are reconstructed in the tracking system with an intrinsic position resolution of about $70\,\mu\mathrm{m}$ in the bending direction. An iron wall ($7.2\,\lambda_I$) is placed between the last tracking station and the muon trigger system. The front absorber combined with the muon filter stop muons with momenta less than 4 GeV/c. The trigger consists of 2 stations with 2 planes of Resistive Plate Chambers achieving a time resolution of $\sim 2\,\mathrm{ns}$. An additional absorber, placed around the beam pipe over the full length of the muon arm, protects the detector from secondaries produced in the beam pipe.

Data were collected using a minimum bias (MB) trigger condition, defined as the logical OR of at least one fired chip in the pixel detector and a signal in one out of two scintillator arrays which are placed in forward direction on either side of the interaction region. A muon trigger is required additionally in case of the di-muon analysis (μ-MB condition).

For the analysis in the di-electron channel a total of $2.4 \cdot 10^8$ MB events were analysed, corresponding to an integrated luminosity of $L_{int} = 3.9\,\mathrm{nb}^{-1}$. Events are required to have a reconstructed vertex with a z position within $|z_{vtx}| < 10\,\mathrm{cm}$ from the nominal interaction point. Several cuts are applied on the level of the single track. Tracks are required to be in the detector acceptance ($|\eta| < 0.9$) and have a transverse momentum larger than $1\,\mathrm{GeV}/c$. In addition the tracks have to fulfil certain reconstruction quality criteria. They need to be well defined in the ITS and TPC, the χ^2 per cluster needs to be less than 4, at least 70 out of 159 clusters need to be attached in the TPC and a hit in at least one of the first two layers of the ITS is required. The latter helps to reject electrons from photon conversions. Finally electrons are identified by cutting on the $\mathrm{d}E/\mathrm{d}x$ signal of the TPC in terms of number of sigma, where σ is the width of the gaussian response of the TPC ($\mathrm{d}E/\mathrm{d}x$-resolution). The requirements are to be within $\pm 3\sigma$ from the electron expectation and more than 3σ (3.5σ) away from the proton (pion) expectation.

The obtained invariant mass spectrum of the opposite-sign (OS) di-electron pairs is shown in Fig. 1 (left, top panel, red points). The remaining background is described by combining like-sign (LS) di-electron pairs as $N^{++} + N^{--}$ and scaling the LS spectrum to match the integral of the OS spectrum in the invariant mass range of $3.2 - 5\,\mathrm{GeV}/c^2$ (Fig. 1, left, top panel, blue points). The arithmetic mean was preferred over the geometric mean in order to remove the bias that would occur in the scaling due to bins with zero entries in the LS spectrum. After background subtraction the number of J/ψ candidates is extracted by bin counting in the invariant mass range $2.92 - 3.16\,\mathrm{GeV}/c^2$. This yields $\mathrm{N}_{J/\psi} = 249 \pm 27$ (stat.) $\pm$ 20 (syst.). The systematic uncertainties are described below.

The analysis in the di-muon channel was performed on a data sample of $1.9 \cdot 10^8$ μ-MB events ($L_{\mathrm{int}} = 15.6\,\mathrm{nb}^{-1}$). For further analysis only events were selected for which at least one muon candidate has a match in the muon trigger chambers. This significantly reduces the background of hadrons which are produced in the absorber. Further selection criteria are a reconstructed vertex in the ITS, the rejection of muons emitted under very small angles, which cross a significant fraction of the beam pipe and requiring the di-muon pair to be in the detector acceptance ($2.5 < y < 4$) in order to minimise edge effects.

Applying all selection criteria $1.75 \cdot 10^5$ OS muon pairs are found. Figure 1 (right) shows the invariant mass spectrum of OS di-muon pairs of a subset of data. The signal is extracted by simultaneously fitting a Crystal Ball function to describe the signal shape and two exponentials for the background. By integrating the Crystal Ball function over the full mass range, the

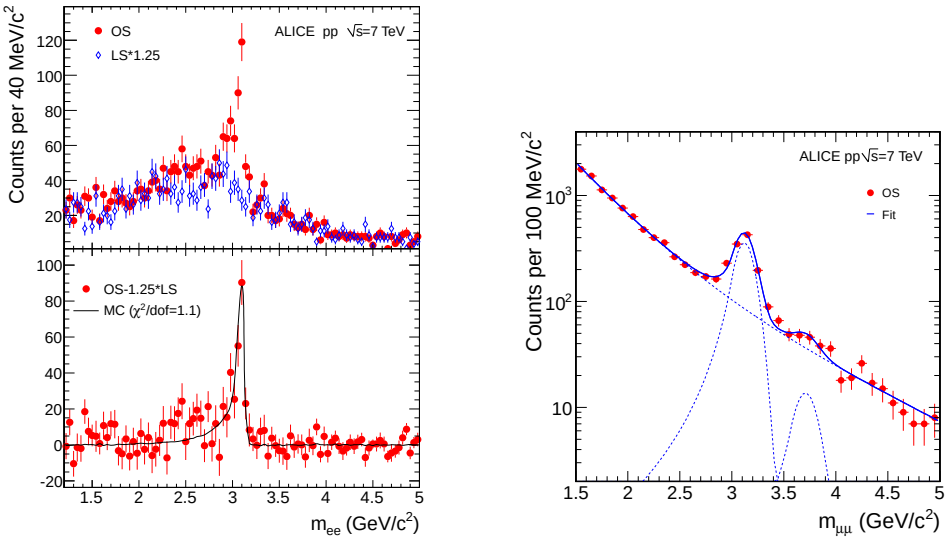

Figure 1: Invariant mass spectra for the di-electron (left) and di-muon (right) decay channel [4].

extracted J/ψ yield of the complete analysed statistics is $N_{J/\psi} = 1924 \pm 77(\text{stat.}) \pm 144(\text{syst.})$.

The systematic uncertainties were obtained considering various sources: signal extraction, acceptance effects due to the p_T and rapidity distributions used as input for the MC studies, muon trigger efficiency, reconstruction efficiency, error on the luminosity measurement and the uncertainty of the branching ratio. The total uncertainty is 12.6 % in the di-muon and 16.1 % in the di-electron channel. However, the largest uncertainty results from the unknown polarisation of the J/ψ due to its influence on the acceptance corrections. To quantify the effect, the impact of fully transverse ($\lambda = 1$) and fully longitudinal ($\lambda = -1$) polarisation for the case of the helicity (HE) as well as the Collins-Soper (CS) reference frame was investigated. Maximum variations between -15 % and +32 % were estimated and will be quoted separately. For details see [4].

3 Results

The production cross-section is determined by normalising the efficiency and acceptance corrected signal ($N^{corr}_{J/\psi} = N_{J/\psi}/(A \times \epsilon)$) to the integrated luminosity or the cross-section of a reference process. For this analysis the minimum-bias cross-section itself was chosen as a reference. Thus the J/ψ cross-section is given by

$$\sigma_{J/\psi} = \frac{N^{corr}_{J/\psi}}{BR(J/\psi \to l^+l^-)} \times \frac{\sigma_{MB}}{N_{MB}},$$

where $BR(J/\psi \to l^+l^-) = (5.94 \pm 0.06)\%$ is the branching ratio of J/ψ to di-leptons, N_{MB} is the number of analysed minimum bias events and $\sigma_{MB} = 62.3 \pm 0.4$ (stat.) ± 4.3 (syst.) mb is the minimum bias cross-section, which was derived from a Van-der-Meer scan [7]. The acceptance times efficiency value ($A \times \epsilon$) is 10.0 % for the di-electron, 32.9 % for the di-muon decay channel.

The measured integrated cross-sections for the two rapidity ranges are:
$\sigma_{J/\psi}(|y| < 0.9) = 10.7 \pm 1.2$ (stat.) ± 1.7 (syst.) + 1.6 ($\lambda_{HE} = 1$) - 2.3 ($\lambda_{HE} = -1$) μb and
$\sigma_{J/\psi}(2.5 < y < 4) = 6.31 \pm 0.25$ (stat.) ± 0.80 (syst.) $+0.95(\lambda_{CS} = 1) - 1.96(\lambda_{CS} = -1)$ μb.

In addition for both rapidity ranges the differential cross-sections $\mathrm{d}^2\sigma_{J/\psi}/\mathrm{d}p_T\mathrm{d}y$ and $\mathrm{d}\sigma_{J/\psi}/\mathrm{d}y$ ($p_T > 0$) were determined. The spectra are presented in Fig. 2 and compared with results from ATLAS [8] ($p_T > 7\,\mathrm{GeV}/c$, $|y| < 0.75$), CMS [9] ($p_T > 6.5\,\mathrm{GeV}/c$, $|y| < 1.2$) and LHCb [10] ($p_T > 0$, $2.5 < y < 4$). All results are compatible. The ALICE measurement at mid-rapidity extends down to $p_T = 0$ an thus is complementary to those of ATLAS and CMS.

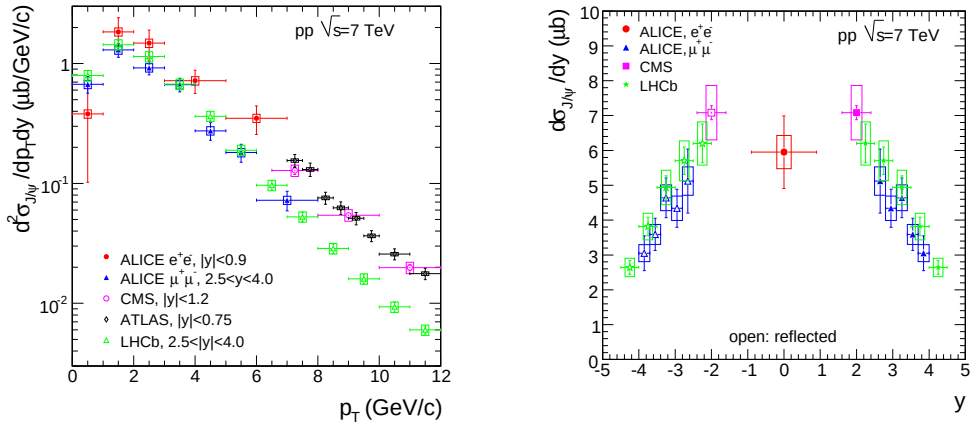

Figure 2: Differential J/ψ production cross-sections as a function of p_T (left) and rapidity (right) [4].

4 Summary and Outlook

We have presented first results on the J/ψ inclusive production cross-section measured with the ALICE detector system. In addition the p_T-differential cross-section and the rapidity dependence were shown and compared to the other LHC experiments. ALICE is the only experiment at LHC measuring J/ψ at mid-rapidity down to zero transverse momentum.

With increased statistics and a different PID strategy, the large statistical as well as systematic uncertainty of the measurement at mid-rapidity will be reduced significantly. To provide a better electron identification other detectors will be used in addition to the TPC. Under investigation are the Time Of Flight detector, to extend the electron identification towards lower momenta ($p \lessapprox 1\,\mathrm{GeV}/c$) as well as the Transition Radiation Detector to allow a better electron to pion separation at higher momenta ($p \gtrapprox 2\,\mathrm{GeV}/c$).

Ongoing analyses in both decay channels are the measurement of the feed-down from B-hadron decays, the analysis of pp data at $\sqrt{s} = 2.76\,\mathrm{TeV}$ and the multiplicity dependence of the J/ψ production in pp collisions. In addition the measurement of the polarisation will help to put limits on the largest contribution to the systematic uncertainty.

In parallel to the analysis of pp collision, the data from the Pb–Pb run at $\sqrt{s_{NN}} = 2.76\,\mathrm{TeV}$ of November/December 2010 are being analysed. First results were presented at the Quark Matter 2011 conference [11].

References

1. N. Brambilla et al.(Quarkonium Working Group), Eur. Phys. J. **C71**, 1534 (2011)
2. J.P. Lansberg, Eur. Phys. J. **C61**, 693 (2009)
3. K. Aamodt et al. (ALICE Collaboration), JINST **3**, S08002 (2008)
4. K. Aamodt et al. (ALICE Collaboration), arXiv:1105.0380, submitted to Phys. Lett. B.
5. K. Aamodt et al. (ALICE Collaboration), JINST **5**, P03003 (2010).
6. J. Alme et al. (ALICE Collaboration), *Nucl. Instrum. Methods* **A622**, 316 (2010)
7. K. Oyama et al. (ALICE Collaboration), proc. of the Workshop "LHC Lumi Days", to be published.
8. G. Aad et al. (ATLAS Collaboration), arXiv:1104.3038, submitted to Nucl. Phys. B.
9. V. Khachatryan et al. (CMS Collaboration), Eur. Phys. J. **C71**, 1575 (2011)
10. R. Aaij et al.(LHCb Collaboration), Eur. Phys. J. **C71**, 1645 (2011)
11. Quark Matter 2011 conference, 23-28 May 2011, http://qm2011.in2p3.fr

STUDY OF K_{e4} DECAYS IN THE NA48/2 EXPERIMENT AT CERN

B. BLOCH-DEVAUX
Department of Physics, Università degli Studi di Torino,
via P.Giuria 1, 10125 Torino, Italy

Large samples of kaon decays have been collected in $2003-2004$ by the NA48/2 collaboration in the charged ($K^{\pm} \to \pi^+\pi^-e^{\pm}\nu$) and neutral ($K^{\pm} \to \pi^0\pi^0e^{\pm}\nu$) K_{e4} modes. In the charged mode, form factors have been extensively studied from a sample of more than one million decays and a preliminary branching ratio measurement is reported here. In the neutral mode, a sample of 44 000 decays has been analyzed and provides a new branching ratio value with $1-2\%$ precision, a factor of ten improvement with respect to the current knowledge. Both modes contribute to the study of low energy QCD and are powerful tests of Chiral Perturbation Theory predictions.

1 Introduction

Kaon decays have been identified as a perfect laboratory to study low energy strong interaction. Semileptonic four-body decays are of particular interest because of the small number of hadrons in the final state which are related to the study of $\pi\pi$ interaction. The development of chiral perturbation theory (ChPT) [1] over more than 30 years has reached a competitive precision level in its predictions of both $\pi\pi$ scattering lengths values and form factors appearing in the weak hadronic current of the K_{e4} decay matrix element. The global analysis of $\pi\pi, \pi K$ and K_{e4} data allows the determination of the Low Energy Constants (LEC) of ChPT at Leading and Next to Leading Orders (LO,NLO,NNLO) [2,3] and subsequent predictions of form factors and decay rates. Current experimental measurements [4] and NA48/2 improved sensitivity are shown in Table 1. The possibility to study high statistics samples collected concurrently by NA48/2 in several modes will bring improved inputs and will allow stronger tests of ChPT predictions.

Table 1: Number of analyzed K_{e4} events, measured decay rates and NA48/2 improvements for the two reported modes. Relative errors are given within parentheses.

Decay mode	PDG 2010		This measurement	
$K^+ \to \pi^+\pi^-e^+\nu_e$	418 000	3304 ± 81 (2.4%)	$1.11\ 10^6$	28 (0.8%)
$K^+ \to \pi^0\pi^0e^+\nu_e$	37	1777 ± 323 (18.2%)	44 000	34 (1.6%)

2 Kinematics

The K_{e4} decay is fully described by the five kinematic Cabibbo-Maksymowicz variables [7]: two invariant masses $S_\pi = M^2_{\pi\pi}$ and $S_e = M^2_{e\nu}$ and three angles θ_π, θ_e and ϕ. Form factors can be developed in a partial wave expansion [8]. Limiting the expansion to S- and P- wave and considering

a unique phase δ_p for all P-wave form factors, two complex axial (F,G) and one complex vector (H) form factors contribute to the transition amplitude: $F = F_s\ e^{i\delta_s} + F_p\ e^{i\delta_p} cos\theta_\pi$, $G = G_p\ e^{i\delta_p}$, $H = H_p\ e^{i\delta_p}$. Four real form factors (F_s, F_p, G_p and H_p) and a single phase ($\delta = \delta_s - \delta_p$) have to be measured, including their energy variation. In the neutral mode, the variables θ_π and ϕ are irrelevant and the form factors reduce to the single F_s value due to Bose statistics. In addition if $\Delta I = \frac{1}{2}$ holds, F_s values should be equal in the charged and neutral K_{e4} modes.

3 Experimental setup

Two simultaneous $K^\pm$ beams were produced by 400 GeV protons from the CERN/SPS impinging on a beryllium target. Opposite charge particles with a central momentum of 60 GeV/c and a momentum band of $\pm 3.8\%$ were selected and focused $\sim$ 200 m downstream at the first spectrometer chamber. A schematic view of the beam line can be found in [5] and a detailed description of the NA48/2 detector in [6]. The magnetic spectrometer consists of a dipole magnet surrounded by two sets of drift chambers (DCH). The momentum of charged decay products is measured with a relative precision of $\sim 1\%$ for 10 GeV/c tracks. It is followed by a scintillator hodoscope consisting of two planes segmented into horizontal and vertical strips achieving a very good $\sim$ 150 ps time resolution. A liquid krypton calorimeter (LKr), 27 radiation length thick, is used to measure electromagnetic deposits and identify electrons through their E/p ratio (the energy and position resolutions are $\sim 1\%$ and $\sim$ 1.5 mm (resp.) for 10 GeV showers). A two-level trigger logic selects and flags event with a high efficiency for both K_{e4} topologies.

4 Branching ratio measurements

The K_{e4} branching ratio (BR) is measured relative to a normalization mode (n) as :

$$\mathrm{BR}(K_{e4}) = \frac{N_s - N_b}{N_n} \cdot \frac{A_n\ \varepsilon_n}{A_s\ \varepsilon_s} \cdot \mathrm{BR}(n) \tag{1}$$

where N_s, N_b, N_n are the numbers of signal, background and normalization candidates, A_s and ε_s are the geometrical acceptance and trigger efficiency for the signal sample, A_n and ε_n the geometrical acceptance and trigger efficiency for the normalization sample.

4.1 The charged ($K^\pm \to \pi^+\pi^- e^\pm \nu$) K_{e4} analysis

The charged K_{e4} BR is measured relative to the abundant $K^\pm \to \pi^+\pi^-\pi^\pm$ mode ($\mathrm{BR}(n) = (5.59 \pm 0.04)\%$) which has a similar topology in terms of number of charged particles and is recorded concurrently by the same trigger logic. A very large sample of 1.13 million charged K_{e4} decays has been analyzed [5] to measure $\pi\pi$ scattering lengths with a few percent precision. Form factors values, and their energy dependence, have been obtained relative to a single overall factor f_s which can be determined from the BR value. The energy dependence is described using a series expansion of the dimensionless invariants $q^2 = (S_\pi/4m^2_{\pi^+}) - 1$ and $S_e/4m^2_{\pi^+}$ (three terms for F_s, two terms for G_p and one term for F_p, H_p). It is recalled below:

$$\begin{array}{llllll}
f'_s/f_s = & 0.152 & \pm 0.007_{\mathrm{stat}} & \pm 0.005_{\mathrm{syst}} & g_p/f_s = & 0.868 \quad \pm 0.010_{\mathrm{stat}} \quad \pm 0.010_{\mathrm{syst}} \\
f''_s/f_s = & -0.073 & \pm 0.007_{\mathrm{stat}} & \pm 0.006_{\mathrm{syst}} & g'_p/f_s = & 0.089 \quad \pm 0.017_{\mathrm{stat}} \quad \pm 0.013_{\mathrm{syst}} \\
f'_e/f_s = & 0.068 & \pm 0.006_{\mathrm{stat}} & \pm 0.007_{\mathrm{syst}} & & \\
f_p/f_s = & -0.048 & \pm 0.003_{\mathrm{stat}} & \pm 0.004_{\mathrm{syst}} & h_p/f_s = & -0.398 \quad \pm 0.015_{\mathrm{stat}} \quad \pm 0.008_{\mathrm{syst}}
\end{array}$$

In the BR measurement, several requirements were loosened or removed from the event selection of the form factor analysis. Extra accidental track activity and possible accompanying

photons were accepted while particle identification requirements were loosened. Many stability checks were performed ensuring the robustness of the procedure and defining systematic uncertainties. Out of $\sim 2.3\ 10^{10}$ total recorded triggers, $1.11\ 10^6$ K_{e4} candidates were selected, 10545 background events and $1.9\ 10^9$ normalization candidates. The geometrical acceptances (based on a GEANT3 simulation) have large and similar values of 18.22%(K_{e4}) and 24.18%($K_{3\pi}$). They make use of our best knowledge of the signal and normalization matrix elements [5,9]. Trigger efficiencies are measured using minimum bias control triggers [a]. They have high similar values of 98.3%(K_{e4}) and 97.5%($K_{3\pi}$). The analysis has been performed for each kaon charge (K^-_{e4} mode has never been measured) and the results statistically combined. The details of the common systematic uncertainties are given in Table 2. The preliminary values (including radiative K_{e4} decays) are found to be:

$$\mathrm{BR}(K^+_{e4}) = (4.277 \pm 0.009_{stat+trig})10^{-5} \text{ and } \mathrm{BR}(K^-_{e4}) = (4.283 \pm 0.012_{stat+trig})10^{-5} \quad (2)$$

$$\text{combined into } \mathrm{BR}(K_{e4}) = (4.279 \pm 0.006_{stat+trig} \pm 0.015_{\mathrm{syst}} \pm 0.031_{ext})10^{-5} \quad (3)$$

The total error $\pm 0.035\ 10^{-5}$ (0.8% relative) is dominated by the external error (0.7% relative). This measurement brings a factor of three improvement with respect to the world average [4] $(4.09 \pm 0.10)10^{-5}$ and a factor of more than five on the relative decay rate to $K_{3\pi}$: $\Gamma(K_{e4})/\Gamma(K_{3\pi}) = (7.654 \pm 0.030_{exp})10^{-4}$ while the world average is $(7.31 \pm 0.16)10^{-4}$.

Table 2: Summary of the uncertainties δBR $\times 10^5$ on BR(K_{e4}) measurements.

$K^\pm \to \pi^+\pi^- e^\pm \nu$		$K^\pm \to \pi^0\pi^0 e^\pm \nu$	
Acceptance and beam geometry	0.0077	Beam geometry	0.0026
Muon vetoing	0.0068	Simulation statistic	0.0031
Accidental activity	0.0064	Form factor dependence	0.0052
Background control	0.0060	Background control	0.0091
Particle identification	0.0038	Electron identification	0.0026
Radiative effects	0.0034	Radiative effects	0.0060
Trigger efficiency	0.0051	Trigger efficiency	0.0208
Statistical error	0.0038	Statistical error	0.0120
External error	0.0308	External error	0.0324
Total	0.0346	Total	0.0424

4.2 The neutral ($K^\pm \to \pi^0\pi^0 e^\pm \nu$) K_{e4} analysis

The neutral K_{e4} BR is measured relative to the more abundant mode $K^\pm \to \pi^0\pi^0\pi^\pm$ (BR(n) = (1.761±0.022)%). Both modes have a similar topology in term of final state: one charged particle and two π^0 detected as four decay photons in the LKr. They are recorded concurrently by the same trigger logic. The event selection and reconstruction follow very closely those developed for the detailed analysis of the normalization mode [10]. Normalization events are required to cluster at low transverse momentum relative to the beam line (p_t) and reconstruct the $\pi\pi^0\pi^0$ mass close to the kaon mass when m_{π^+} is assigned to the charged particle while signal events are required to reconstruct the $\pi\pi^0\pi^0$ mass away from the kaon mass together with a sizable p_t with respect to the beam line (Figure 1a). Additional requirements on the LKr energy associated to the charged track (E/p close to 1 and shower properties) ensure electron identification. The dominant background comes from $K_{3\pi}$ events with misidentification of the charged pion as an electron. Its contribution can be measured from control regions in the two modes. The background from $K_{3\pi}$

[a] because of downscaling, control samples have limited statistics

events with a subsequent $\pi^{\pm} \to e^{\pm}\nu$ decay has been studied from simulation and contributes one order of magnitude lower. The total background is estimated to be $\sim 1.3\%$ relative to the signal. Geometrical acceptances have been computed using GEANT3-based simulations, including our best knowledge of the normalization mode [11] which describes accurately the observed cusp effect and using the charged K_{e4} measured F_s value [5] for the signal simulation. They amount to 4.11% and 1.77% (resp.) [b]. The analysis selected $\sim 71\ 10^6$ normalization events, 44909 K_{e4} candidates and 598 background events. Trigger efficiencies have been measured from minimum bias control triggers. They vary with data taking conditions between 92 and 98% but the ratio $\varepsilon_n/\varepsilon_s$ is stable and close to unity. Preliminary systematic uncertainties have been quoted conservatively and are displayed in Table 2. Trigger efficiency related uncertainties will be reduced by a statistical treatment of sub-samples recorded in stable trigger conditions. A preliminary branching ratio value (including radiative K_{e4} decays) for the combined $K^{\pm}$ mode is obtained as:

$$\mathrm{BR}(K_{e4}) = (2.595 \pm 0.012_{\mathrm{stat}} \pm 0.024_{\mathrm{syst}} \pm 0.032_{ext})10^{-5} \quad (4)$$

The total error $\pm 0.042\ 10^{-5}$ (1.6% relative) is dominated by the external error (1.25% relative). This measurement brings a factor of ten improvement on the total error with respect to the world average $(2.2 \pm 0.4)10^{-5}$. The agreement between data and simulation over the whole range of the $M^2_{\pi^0\pi^0}$ variable is shown in Figure 1b. The final form factor analysis will include a correction for small negative interference of the charged K_{e4} mode with final state charge exchange scattering $(\pi^+\pi^- \to \pi^0\pi^0)$ below $(2m_{\pi^+})^2$ threshold.

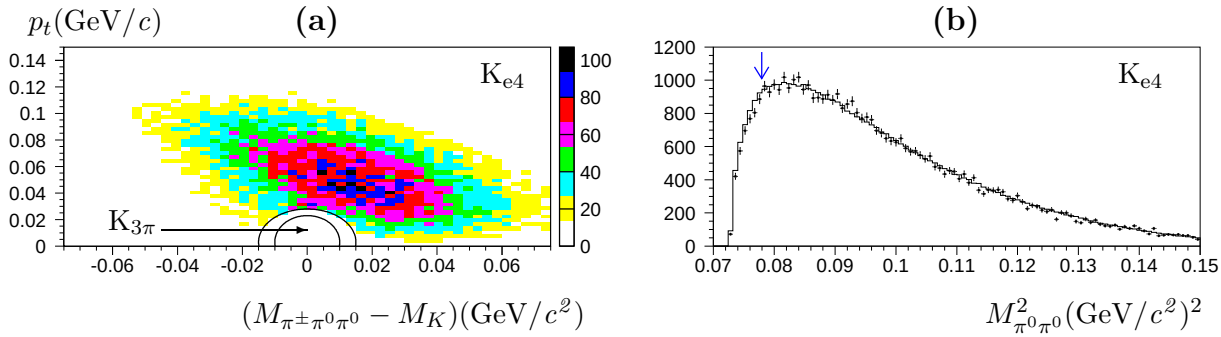

Figure 1: **(a)** Distribution of selected K_{e4} events in the plane $(M_{\pi^\pm\pi^0\pi^0} - M_K, p_t)$. $K_{3\pi}$ normalization events (not displayed) cluster inside the tight cut contour. **(b)** Distribution of $M^2_{\pi^0\pi^0}$ for data (dots) and simulation (histogram) . The arrow indicates the $(2m_{\pi^+})^2$ threshold.

References

1. S. Weinberg, *Physica* A **96**, 327 (1979).
2. J. Bijnens, G. Colangelo, J. Gasser, *Nucl. Phys.* B **427**, 427 (1994).
3. J. Bijnens and I. Jemos, arXiv:1103.5945 [hep-ph].
4. K. Nakamura *et al* (Particle Data Group), *J. Phys.* G **37**, 075021 (2010).
5. J. Batley *et al*, *Eur. Phys. J.* C **70**, 635 (2010).
6. V. Fanti *et al*, *Nucl. Instrum. Methods* A **574**, 433 (2007).
7. N. Cabibbo and A. Maksymowicz, *Phys. Rev.* **B438**, 137 (1965).
8. A. Pais and S. Treiman, *Phys. Rev.* **168**, 1858 (1968).
9. J. Batley *et al*, *Phys. Lett.* B **649**, 349 (2007).
10. J. Batley *et al*, *Eur. Phys. J.* C **64**, 589 (2009).
11. J. Batley *et al*, *Phys. Lett.* B **686**, 101 (2010).

[b] because of the light mass of the electron, about 45% of the signal events are discarded at trigger level by the anti $K^{\pm} \to \pi^{\pm}\pi^0$ cut while the $K_{3\pi}$ events are unaffected

6.
Structure Functions
Diffraction

HADRONIC FINAL STATES AND DIFFRACTION AT HERA

I.A. RUBINSKIY (ON BEHALF OF THE H1 AND ZEUS COLLABORATIONS)
DESY, Notkestrasse 85,
Hamburg, Germany

Recent results from the *ep* (electron-proton) collider HERA are presented. Jet production and diffraction type reactions allow tests of predictions of Quantum Chromodynamics (QCD). Jet measurements are used to improve the combined H1-ZEUS parton density fits by adding an additional constraint on the gluon distribution in the proton and, at the same time, providing information on α_s. Measurements of inclusive diffraction and diffractive dijet data are discussed in the context of factorisation in diffraction. Diffractive $\Upsilon(1S)$ production was studied to extract the t-slope of the process, which was found to be consistent with the other exclusive vector meson data and can be interpreted in terms of the gluonic radius of the proton.

1 Introduction

At the *ep* collider HERA, electrons of 27.6 GeV were collided with 920 (820) GeV protons. HERA effectively provided photon-proton collisions at a centre-of-mass energy W, up to its maximum value, set by the centre-of-mass energy of the electron-proton system $\sqrt{s} = 310$ GeV. The photon virtuality Q^2 ranged up to several thousand GeV^2. The reaction phase space can be divided into photoproduction (γp), $Q^2 \approx 0$ GeV^2, and deep-inelastic scattering (DIS), where $Q^2 > 1$ GeV^2. From the first DIS experiments on the proton it is known that the proton has a structure, which can not be calculated from the first principles of QCD. The inclusive double differential DIS cross section can be expressed in terms of the proton structure functions $F_2(x, Q^2)$ and $F_L(x, Q^2)$, where x in lowest order corresponds to the fraction of proton momentum carried by the struck parton. The structure functions are strongly related to the parton density functions (PDF). The Q^2 dependence of the PDFs is described by evolution equations [1]. At low values of x ($x < 10^{-2}$) the gluon PDFs significantly exceed the quark contribution.

At certain conditions the struck parton in its hadronization process can form a jet, a highly collimated group of particles. Both the DIS and γp jet production can be used to constrain the proton and photon PDFs and measure the strong coupling constant, α_s.

Diffractive reactions, when the scattered proton stays intact, at HERA constitute about 10% of the total cross section. The corresponding diffractive PDFs can be defined and, due to their unversality, applied to predict diffractive processes cross section at the Tevatron or LHC experiments. Exclusive diffractive vector meson production provides a tool for estimating the transverse distribution of gluons in the proton.

In this contribution, recent results from the H1 and ZEUS collaborations on jet production and diffractive reactions are presented and their impact on proton PDFs and α_s measurements are discussed.

2 Hadronic Final States and Diffraction at HERA

2.1 Jets, α_s and PDFs

Cross section predictions can be factorised into a perturbatively calculable QCD part (pQCD), where a "hard" scale for a series expansion in α_s can be defined, and a "soft" part, which consists of the proton PDFs and hadronization scheme of the partons produced in the reaction. Perturbative calculations lead to partonic final states which are not directly accessible to the measurement. The observed hadrons or dense groups of hadrons, called jets, are the results of the fragmentation of coloured partons. Typical "hard" scales in jet production are the Q^2 or a the jet transverse energy, E_T.

Several algorithms are used to identify jets at hadron level, like k_T, or newly developed, like anti-k_T and SIScone. Since the details of each jet algorithm are different (e.d. radius, combination scheme), the hadronization corrections are different for different algorithms. Benchmarking of the jet algorithms has been performed by ZEUS both for γp [2], and DIS [3] jet production. The recently developed infrared- and collinear-safe jet algorithms, anti-kt [4] and SIScone [5], have been shown to be compatible with the previously widely used k_T algorithm. Theoretical uncertainties on PDFs and α_s are very similar for all three algorithms, corrections for the terms beyond the next-to-leading order (NLO) and hadronization are very similar for k_T and anti-k_T, but larger for SIScone (Fig. 1a).

The jet production cross sections have the potential to constrain the proton and photon PDFs [6]. It has been demonstrated in the combined H1-ZEUS HERAPDF 1.6 fit [7] that by adding jet data to the inclusive DIS cross sections the fit procedure does not depend on external information on the strong coupling constant α_s and can provide an independent α_s measurement (Fig. 1b,c).

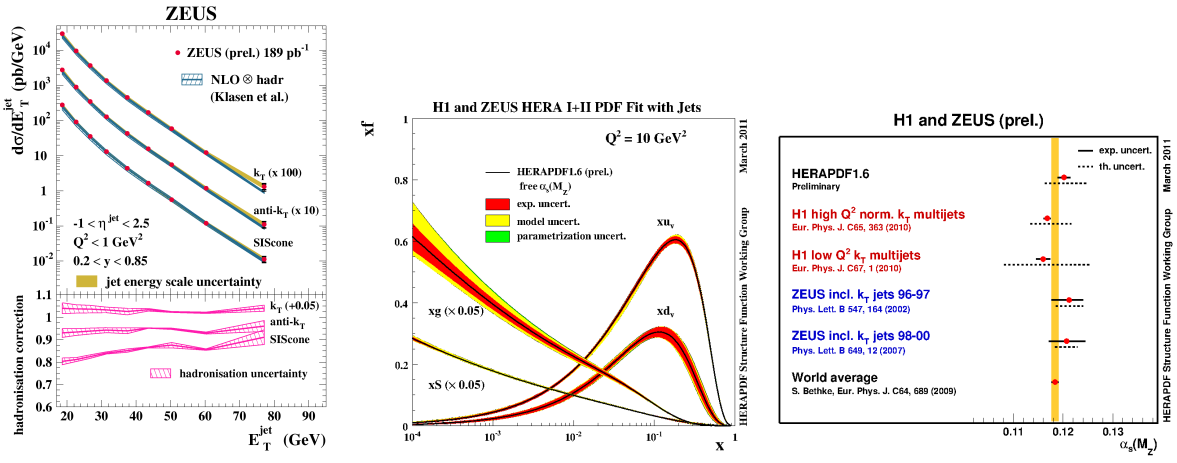

(a) (b) (c)

Figure 1: a) comparison of three jet clustering algorithms, b) HERAPDF 1.6 proton PDFs (with the jet data) and the c) HERAPDF 1.6 fit α_s measurement (the data subsets used in the fit and their α_s measurements are shown).

2.2 Diffraction, F_2^D, F_L^D, dijets, $\Upsilon(1S)$

About 10% of all electron-proton collisions at HERA are diffractive. Diffractive reactions are characterized by the exchange of a colorless object with the quantum numbers of the vacuum (often called Pomeron). Experimentally diffractive reactions can be selected by a large rapidity

gap (LRG) between the reaction products or by explicit tagging of the proton with a proton spectrometer system. Due to the factorisation theorem for diffractive DIS [8] it is possible to define diffractive PDFs of the proton. The diffractive inclusive double differential DIS cross section can be written as:

$$\frac{d^4\sigma_D^{ep}(x_{IP},\beta,t,Q^2,)}{dx_{IP}d\beta dtdQ^2} = \frac{4\pi\alpha_{em}^2}{xQ^4}Y_+[F_2^D(x_{IP},\beta,t,Q^2) - \frac{y^2}{Y_+}F_L^D(x_{IP},\beta,t,Q^2)], \quad (1)$$

with a so called reduced cross section:

$$\sigma^{D(4)}(x_{IP},\beta,t,Q^2) = F_2^D(x_{IP},\beta,t,Q^2) - \frac{y^2}{Y_+}F_L^D(x_{IP},\beta,t,Q^2), \quad (2)$$

where x_{IP} is the IPomeron momentum fraction, β - the momentum fraction of the hard scattered parton, and t - the squared 4-momentum transfer at the proton interaction vertex.

The H1 proton spectrometers, the FPS (Forward Proton Spectrometer) and the VFPS (Very Forward Proton Spectrometer), were used for proton tagging and measurement of the $F_2^D(4)$ [9]. Since the LRG method does not provide the t measurement one can use only the $\sigma^{D(3)}$ for comparison with proton spectrometer method measurements. The two different methods cover a vast region in the phase space and agree well in the acceptance overlap [10,11,12] (Fig. 2a).

The longitudinal structure function F_L^D contribution becomes non-negligible only at high y. It has direct sensitivity to the gluon density function. The measurement [13] is consistent with the gluon density determined from the scaling violations of the F_2^D structure function and from diffractive jet production.

The diffractive PDFs (DPDF), if known, allow cross section calculations for other DDIS observables. The calculations for DDIS at HERA have been performed with very good agreement for the jet [14] and heavy quark production measurements [15]. However, DPDF-based predictions for hard diffractive processes such as dijet production in $p\bar{p}$ scattering fail by around an order of magnitude to describe the data [16,17]. The issues of DPDFs applicability and possible "rapidity gap survival probability" were studied at HERA in diffractive dijet photoproduction [21,22]. In leading order the virtual photon with zero virtuality, $Q^2 \approx 0$, can be viewed as either "direct" or "resolved". In direct photon processes the photon enters the hard interaction directly, while in resolved processes it enters the hard interaction via its partonic structure and has a point-like and a hadron-like components. There are both theoretical and experimental arguments that the "resolved"-photon contribution can be suppressed by a significant gap suppression factor. For the hadron-like component the "gap suppression" factor has been estimated to be ~ 0.34 [18,19], and the point-like component suppressed by a factor 0.7-0.8 depending on the jet E_T^{jet} [19,20]. It has been shown that the introduction of the "resolved" component suppression factors improves the data to theory agreement [21](Fig. 2b) at low x_γ where resolved processes are expected to dominate.

Exclusive vector meson (VM) production at HERA can be studied in terms of the color dipole model. The photon-proton collision can be treated as a $q\bar{q}$ - proton interaction. The t-dependence of the exclusive vector meson production can be related to the transverse size of the interaction region, which is set by the gluon distribution. At higher values of the VM mass, M_V, or of Q^2, the $q\bar{q}$ pair transverse size vanishes, so the proton gluonic transverse size can be determined. As it is seen in Fig. 2c the t-dependence slope flattens already after $M_V^2 + Q^2 > 10$ GeV^2 at $b \approx 5$ GeV^{-2}. This value can be roughly translated into $r_{gluons} \approx 0.5\ fm$ which is smaller then the electromagnetic radius of the proton, $r_{em} \approx 0.8\ fm$. A new measurement of the $\Upsilon(1S)$ diffractive production [23] extends the $M_V^2 + Q^2$ tested range by a factor 2 and agrees well with the other VM measurements.

3 Summary

A brief overview of recent results from the HERA collider published by the H1 and ZEUS collaborations is given. The measurements provide information on the parton structure of the proton and precise measurement of the strong coupling constant α_s. High energy diffraction keeps being a very interesting field for QCD studies. Further understanding of rapidity gap suppression mechanism is required for the ongoing and future collider experiment programs.

References

1. Yu. L. Dokshitzer. Sov.Phys. JETP, 46:641 (1977); V.N. Gribov, L,N. Lipatov. Sov.J.Nucl.Phys. 15:438 (1972); G. Altarelli and G. Parisi. Nucl. Phys. B126:298 (1977).
2. Inclusive-jet cross sections in photoproduction, ZEUS-prel-10-003; Inclusive-jet cross sections in photoproduction at HERA and a comparison of the kt, anti-kt and SIScone jet algorithms, ZEUS-prel-10-015.
3. Inclusive-jet production in NC DIS with HERA II, ZEUS-prel-10-002.
4. M. Cacciari, G. P. Salam and G. Soyez, "The anti-kt jet clustering algorithm", JHEP 0804 (2008) 063 [arXiv:0802.1189].
5. G. P. Salam and G. Soyez, JHEP 0705 (2007) 086 [arXiv:0704.0292]
6. Dijets in γp and constraints on p and gamma PDFs, ZEUS-prel-10-014
7. HERAPDF 1.6, H1prelim-11-034, ZEUS-prel-11-001
8. J.Collins, PR D57 (1998) 3051.
9. Measurement of the Diffractive Deep-Inelastic Scattering Cross Section with a Leading Proton at HERA, Eur.Phys.J.C71:1578,2011, (arXiv:1010.1476v1)
10. Diffractive structure function $F_2^{D(3)}$ measurement with LRG, H1prelim-10-011.
11. Diffractive structure function $F_2^{D(3)}$ measurement with VFPS, H1prelim-10-014.
12. Measurement of the Diffractive Deep-Inelastic Scattering Cross Section with a Leading Proton at HERA
13. Measurement of the longitudinal diffractive structure function F_L^D at low Q2 at HERA, H1prelim-10-017, H1prelim-09-011.
14. C. Adloff et al. [H1 Collaboration], Eur. Phys. J. C 20 (2001) 29 [hep-ex/0012051]; S. Chekanov et al. [ZEUS Collaboration], Eur. Phys. J. C 52 (2007) 813 [arXiv:0708.1415].
15. A. Aktas et al. [H1 Collaboration], Eur. Phys. J. C 50 (2007) 1 [hep-ex/0610076]; S. Chekanov et al. [ZEUS Collaboration], Nucl. Phys. B 672 (2003) 3 [hep-ex/0307068].
16. A. Affolder et al. [CDF Collaboration], Phys. Rev. Lett. 84 (2000) 5043.
17. M. Klasen and G. Kramer, Phys. Rev. D 80 (2009) 074006 [arXiv:0908.2531].
18. A. Kaidalov, V. Khoze, A. Martin and M. Ryskin, Phys. Lett. B 567 (2003) 61 [hep-ph/0306134].
19. A. Kaidalov, V. Khoze, A. Martin and M. Ryskin, Eur. Phys. J. C 66 (2010) 373 [arXiv:0911.3716].
20. M. Klasen and G. Kramer, Eur. Phys. J. C 38 (2004) 93 [hep-ph/0408203].
21. Diffractive Dijet Photoproduction in ep Collisions at HERA, Eur.Phys.J.C70:15-37,2010 [arXiv:1006.0946]
22. Diffractive Jet Production in Deep-Inelastic Scattering with a Leading proton at HERA-2, H1prelim-10-013
23. Diffractive $\Upsilon(1S)$ photoproduction t-slope measurement, ZEUS-prel-10-020.

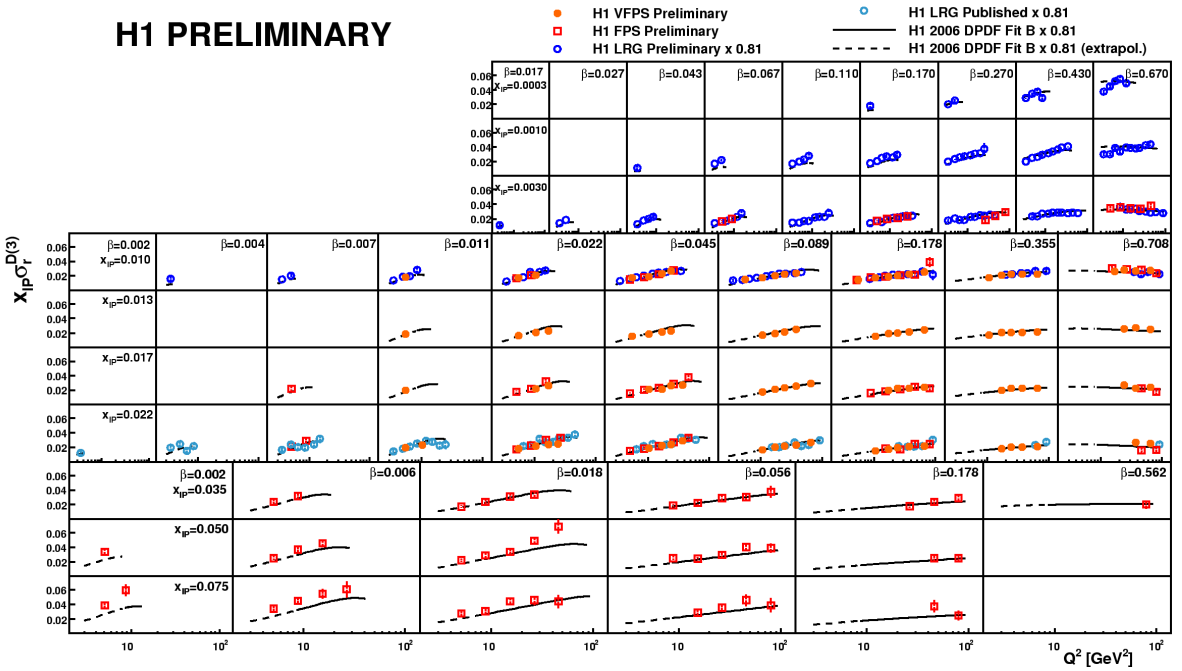

(a)

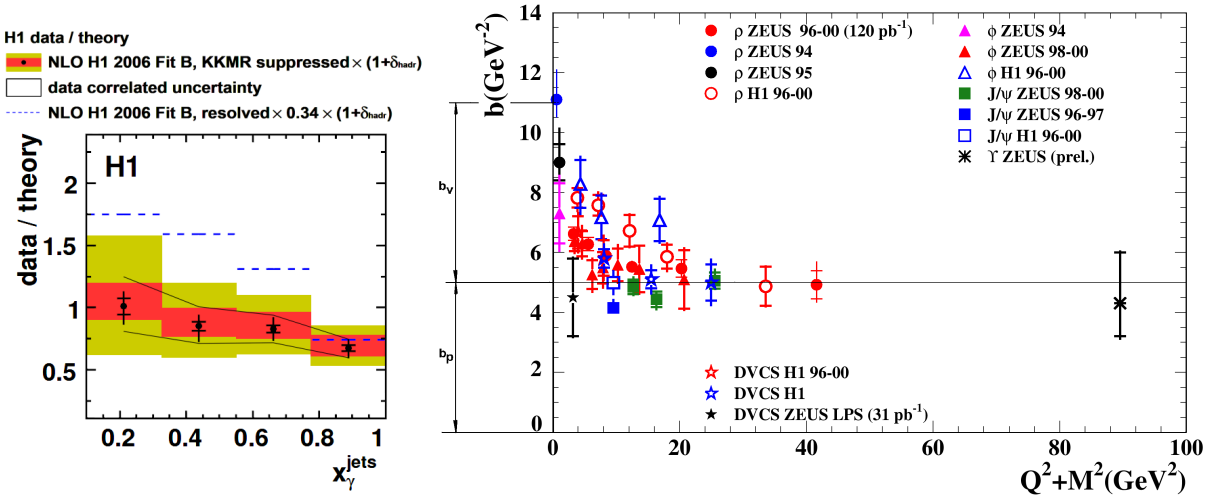

(b) (c)

Figure 2: a) Reduced cross section measured by proton spectrometers, FPS and VFPS, and LRG method. b) The ratio of the measured to the predicted diffractive dijet cross sections as function of the photon momentum fraction x_γ after the "gap suppression" correction implementation. The NLO QCD predicted cross section was done based on the FR framework and the H1 2006 Fit B DPDF set, corrected for hadronisation effects. The FR theoretical prediction for resolved photons is modified by applying the scale factors from the KKMR model for point-like interactions (KKMR suppressed)[18] or for hadron-like interactions (resolved 0.34)[19]. c) Diffractive process t-slope, b, for light and heavy vector mesons measured at different Q^2 values. The value b is expected to be a sum of two components coming from the vector meson, b_V, and the proton, b_p.

Using HERA Data to Determine the Infrared Behaviour of the BFKL Amplitude

H. Kowalski [1], L.N. Lipatov [2,3], D.A. Ross [4], and G. Watt [5]
[1] *Deutsches Elektronen-Synchrotron DESY, D-22607 Hamburg, Germany*
[2] *Petersburg Nuclear Physics Institute, Gatchina 188300, St. Petersburg, Russia*
[3] *II. Institut für Theoretische Physik, Universität Hamburg, D-22761 Hamburg, Germany*
[4] *School of Physics and Astronomy, University of Southampton, Highfield, Southampton SO17 1BJ, UK*
[5] *Theory Group, Physics Department, CERN, CH-1211 Geneva 23, Switzerland*

We determine the infrared behaviour of the BFKL forward amplitude for gluon–gluon scattering. Our approach, based on the discrete pomeron solution, leads to an excellent description of the new combined inclusive HERA data at low values of x (< 0.01) and at the same time determines the unintegrated gluon density inside the proton, for squared transverse momenta of the gluon less than 100 GeV^2. The phases of this amplitude are sensitive to the non-perturbative gluonic dynamics and could be sensitive to the presence of Beyond-the-Standard-Model particles at very high energies.

1 Introduction

One of the major results from HERA (see [1], and references therein) is that the inclusive cross-section for the scattering of virtual photons against protons at low x (i.e. high energy), is dominated by the gluon density inside the proton. This allows one to study the behaviour of the gluon density as a function of gluon momenta, i.e. the fraction of the proton's longitudinal momentum x and the transverse momentum $\mathbf{k}$. The study of the dynamics of the gluon density is usually motivated by its importance to other physics reactions, like dijet or Higgs production at the LHC. In addition to this merely "utilitarian" aspect the dynamics are very interesting because the gluon density is a fundamental quantity, comparable to black-body radiation in QED, and because gluon–gluon interactions are the source of the forces which keep matter together.

The dynamics of the gluon distribution at sufficiently low x is best determined by the amplitude for the scattering of a gluon on a gluon, described by the BFKL analysis. In this analysis the pomeron is considered as a composite state of two so-called reggeized gluons [2]. One of the salient features of the purely-perturbative BFKL analysis is the prediction of a cut-singularity with a branch-point λ leading to a low-x behaviour for the gluon density of the form

$$xg(x) \sim x^{-\lambda}, \tag{1}$$

with only logarithmic corrections in x. In leading order, λ is given by

$$\lambda = \frac{12 \ln 2}{\pi} \alpha_s. \tag{2}$$

The branch-point λ only depends on Q^2 through the running coupling α_s. Experimentally, this branch point is given by the rate of rise of F_2 with diminishing x, $F_2 \sim x^{-\lambda}$. Thus, for many years, it was claimed that BFKL analysis was not applicable to HERA data, firstly because the value of λ obtained from (2) was much larger than the observed value, and secondly because HERA found substantial variation of λ with Q^2.

The first of these difficulties was ameliorated by the NLO contribution to λ [3], once the very large corrections were resummed using the collinear resummation technique [4]. On the other hand, we have shown that the second difficulty, the strong Q^2 dependence of λ, can be solved using a modification of the BFKL formalism, which leads to discrete solutions, i.e. Regge poles rather than a cut.

2 BFKL analysis

The fundamental ingredient of the BFKL analysis is the amplitude for the scattering of a gluon with transverse momentum $\mathbf{k}$ off another gluon with transverse momentum $\mathbf{k}'$ at centre-of-mass energy $\sqrt{s}$ which is much larger than the momentum transfer and much larger than the magnitudes of the gluon transverse momenta. In the forward case (zero momentum transfer) this amplitude, $\mathcal{A}(s, \mathbf{k}, \mathbf{k}')$, is found to obey an evolution equation in s given by

$$\frac{\partial}{\partial \ln s}\mathcal{A}(s, \mathbf{k}, \mathbf{k}') \;=\; \delta(k^2 - k'^2)\,\delta\left(\ln\frac{s}{kk'}\right) + \int dq^2 \mathcal{K}(\mathbf{k}, \mathbf{q})\mathcal{A}(s, \mathbf{q}, \mathbf{k}'), \tag{3}$$

where $\mathcal{K}(\mathbf{k}, \mathbf{k}')$ is the BFKL kernel, currently calculated to order α_s^2 [3]. The kernel is obtained by summing all graphs which contribute to this process, but keeping only leading (and sub-leading) terms in $\ln s$. Such graphs can be drawn in terms of an effective "gluon ladder". The Green function evolution equation (3) can be solved in terms of the eigenfunctions of the kernel

$$\int dk'^2 \mathcal{K}(\mathbf{k}, \mathbf{k}') f_\omega(\mathbf{k}') \;=\; \omega f_\omega(\mathbf{k}). \tag{4}$$

In leading order and with fixed strong coupling α_s the eigenfunctions are parameterized by a "frequency" ν and are of the form

$$f_\omega(\mathbf{k}) \;=\; \left(k^2\right)^{i\nu - 1/2}, \tag{5}$$

with an eigenvalue, ω, given by

$$\omega \;=\; \alpha_s \chi_0(\nu), \tag{6}$$

where $\chi_0(\nu)$ is the leading order characteristic function. The maximum value of ω, at $\nu = 0$, is equal to the branch-point, λ.

In the modified BFKL approach, which was proposed by one of us [5], the strong coupling constant α_s is running as one moves away from the top or bottom of the gluon ladder. This allows the transverse momenta of the gluons $\mathbf{k}$, which dominate the amplitude, to have a large range as one moves away from the ends of the ladder and results in a solution to the eigenvalue equation, (4), in which the frequencies of oscillation ν are themselves $\mathbf{k}$ dependent. The solution is obtained in terms of discrete eigenfunctions f_{ω_n}, which depend on the phase η determined at the boundary between the perturbative and non-perturbative region.

3 Summary and conclusions

We have shown that NLLA solutions of the BFKL equation with the running coupling describe all properties of HERA F_2 data very well, for $Q^2 > 4$ GeV^2 and $x < 10^{-2}$, provided we allow

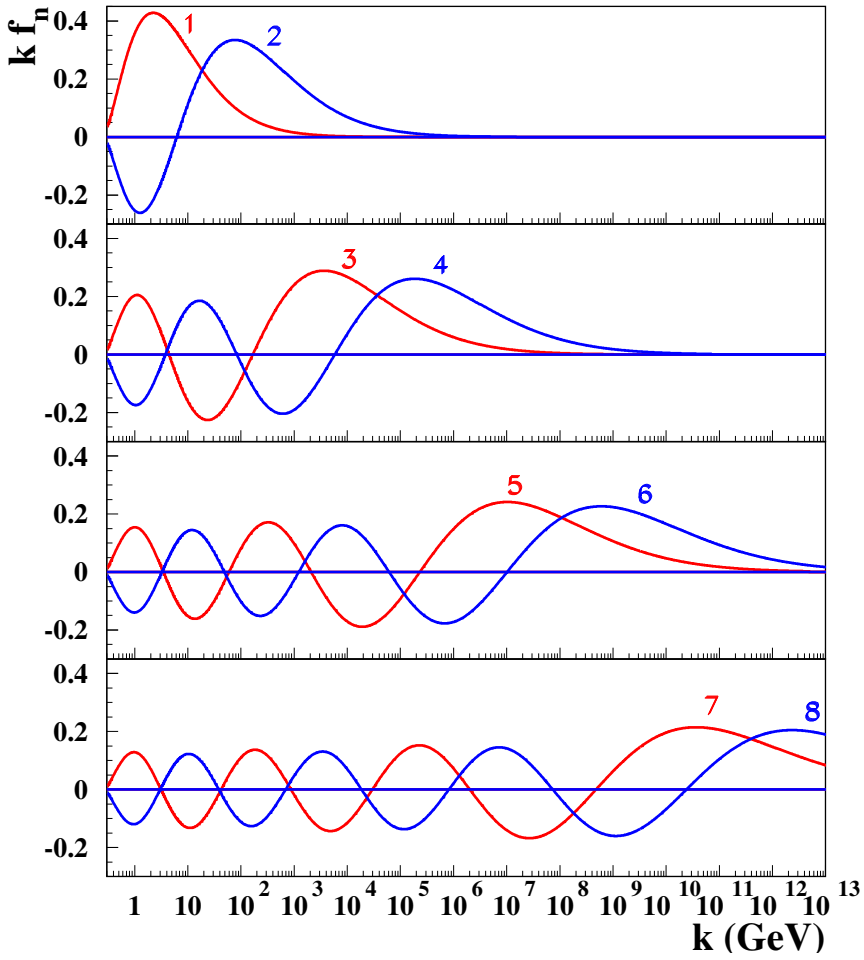

Figure 1: The first eight eigenfunctions f_{ω_n}, $n = 1 \ldots 8$ determined at $\eta = 0$.

the infrared phase, η, to vary with the eigenvalues ω_n. The solutions of this equation have oscillatory form, in which the frequencies $\nu(k^2)$ are varying due to the running of $\alpha_s(k^2)$. We solve the equation near the point $\nu = 0$ which singles out a specific value of $k = k_{\rm crit}$, where $\nu(k^2_{\rm crit}) = 0$. We show that the solutions of the BFKL equation obtained here can be considered as a quantized version of the solutions of the DGLAP equation. The matching of the BFKL solutions in the region $k \sim k_{\rm crit}$ leads to a unique set of discrete eigenfunctions which cannot be obtained from the DGLAP equation alone.

The description of data is obtained by convoluting the Green function with the photon and the proton impact factors. The photon impact factor is known, while the shape of the proton impact factor was assumed to follow a simple exponential form. The comparison with data shows that a particular functional form of the proton impact factor is not very important as long as it is positive and concentrated at the values of $k < \mathcal{O}(1)$ GeV. The limited support of the proton impact factor requires, however, a convolution with a large number of the eigenfunctions, subjected to a specific phase condition which was determined from the fit to data.

The fitting procedure, especially the finding of the proper infrared phase condition, was only possible because of recently published combined H1 and ZEUS F_2 data from HERA. The increased precision of this data requires a large number of eigenfunctions, up to 120, to obtain a

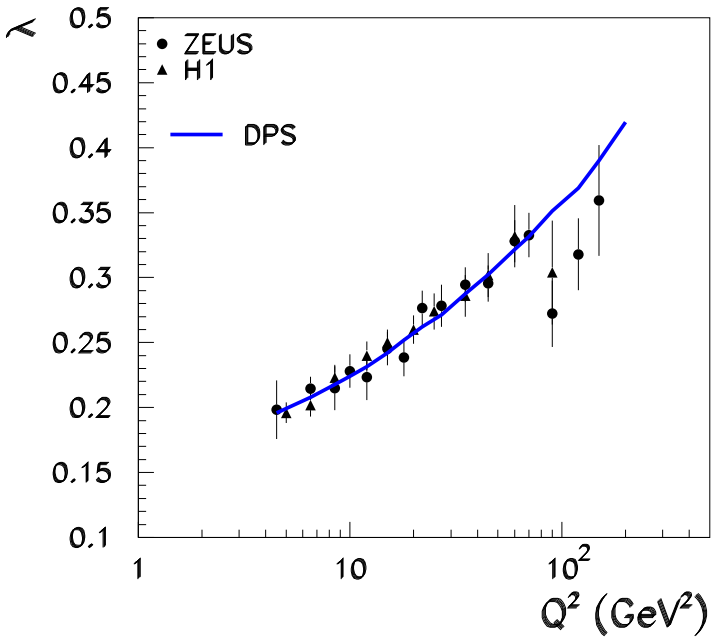

Figure 2: The rate of rise λ, defined by $F_2 \propto (1/x)^{\lambda}$ at fixed Q^2, as determined in the DPS fit and in the direct phenomenological fit to the data [6].

good fit. The resulting fit permits a very good description of the F_2 data and the Q^2 dependence of the exponent, λ, of $1/x$, for small-x. The resulting gluon density is positive, in the range of HERA energies.

At higher energies the resulting gluon density is sensitive to the number of eigenfunctions used in the fit. Since the higher eigenfunctions have eigenvalues which become closer together, the inclusion of such eigenfunctions effectively simulates a continuum on top of the first few discrete (clearly separated) ones. This could indicate that we are approaching a continuum limit which could be better described by the DGLAP evolution alone. So the BFKL solution could determine the gluon density up to k^2 of the order of $\mathcal{O}(100)$ GeV^2, and from then on the DGLAP solution could be used. This could provide a method to overcome the problem of negative gluon densities at low x and small scales pertinent to the standard DGLAP fits. For example, in Ref. [7], in contrast to the standard DGLAP result, the input gluon at $Q_0^2 = 1$ GeV^2 obtained from a global fit including small-x resummation was positive and slightly increasing as $x \to 0$.

The solutions of the BFKL equation together with HERA data determine the relation between the eigenvalue ω and the phase η which consists of a polynomial term and a singular term in ω. The polynomial term contains information about the non-perturbative gluonic dynamics inside the pomeron because we show that the BFKL equation can be considered to be analogous to the Schrödinger equation for the wavefunction of the (interacting) two-gluon system. The BFKL kernel corresponds to the Hamiltonian with the eigenvalues ω_n. The analogy with the Schrödinger equation suggests that perturbative wavefunctions can be smoothly extended to very low virtuality values, k^2, i.e. into the non-perturbative region. In this region an as-yet-unknown dynamics determines the values of the phase of wavefunctions which in turn determine the boundary conditions η_Λ.

The singular term, on the other hand, is presumably generated by the perturbative effects which were not fully taken into account in our evaluation. This term is sensitive to the high virtuality behaviour of the gluon–gluon amplitude, much beyond the virtualities which are actually tested in the experiment. This remarkable property is due to the fact that in the evolution scheme developed here, the BFKL equation is solved near the critical point, $k_{\rm crit}$, and the value of $k_{\rm crit}$ grows quickly with the increase of the eigenfunction number, rapidly crossing proposed thresholds for new physics and even the Planck scale. Since we found that the proper description of data requires a large number of eigenfunctions we obtain an apparent sensitivity to the BSM effects. We recall that in our approach the eigenfunctions with large n correspond to Regge poles which are similar to hadrons with a very small size, because $k_{\rm crit}$ is very large. Their masses (i.e. ω_n) are small but can depend on the BSM physics. The sheer potential existence of BSM particles, although never produced in the interactions relevant to the fitted data, modify the running of the coupling and the (NLO) characteristic function of the BFKL equation below the critical momenta and, in turn, modify the frequency, amplitude and phase of the eigenfunctions at low-energy. We have shown that these states have a soft hadronic tail (i.e. a part of the eigenfunctions around $k \sim \Lambda_{\rm QCD}$) by which they interact with proton and photon and give an essential contribution to the structure functions.

However, only a full NLLA evaluation which takes into account all possible BSM states can show whether this apparent sensitivity turns out to be real. If it turns out to be sufficient to act as a signal for BSM physics this would provide a new method of "telescoping the Planck scale" [8].

1. F. D. Aaron *et al.* [H1 and ZEUS Collaborations], JHEP **1001** (2010) 109.
2. I. I. Balitsky and L. N. Lipatov, Sov. J. Nucl. Phys. **28** (1978) 822;
   E. A. Kuraev, L. N. Lipatov and V. S. Fadin, Sov. Phys. JETP **44** (1976) 443;
   V. S. Fadin, E. A. Kuraev and L. N. Lipatov, Phys. Lett. B **60** (1975) 50.
3. V. S. Fadin and L. N. Lipatov, Phys. Lett. B **429** (1998) 127;
   M. Ciafaloni and G. Camici, Phys. Lett. B **430** (1998) 349.
4. G. P. Salam, JHEP **9807** (1998) 019.
5. L. N. Lipatov, Sov. Phys. JETP **63** (1986) 904.
6. C. Adloff *et al.* [H1 Collaboration], Eur. Phys. J. C **21** (2001) 33;
   S. Chekanov *et al.* [ZEUS Collaboration], Eur. Phys. J. C **21** (2001) 443.
7. C. D. White and R. S. Thorne, Phys. Rev. D **75** (2007) 034005.
8. P. Zerwas, "High-energy physics: Telescoping the Planck scale", Farewell Colloquium for Rolf-Dieter Heuer, 5 December 2008, `http://heuer-colloquium.desy.de/e9/`.

The AdS Graviton/Pomeron Description of Deep Inelastic Scattering at Small x

Richard C. Brower [a]
Department of Physics, Boston University, Boston MA 02215

Marko Djurić
Centro de Física do Porto, Universidade do Porto, 4169-007 Porto, Portugal

Ina Sarčević
Physics Department, University of Arizona, Tucson AZ 85721, Department of Astronomy and Steward Observatory, University of Arizona, Tucson, AZ 85721

Chung-I Tan
Physics Department, Brown University, Providence RI 02912

In the holographic or AdS/CFT dual to QCD, the Pomeron is identified with a Reggeized Graviton in AdS_5 [1,2,3]. We emphasize the importance of confinement, which in this context corresponds to a deformation of AdS_5 geometry in the IR. The holographic Pomeron provides a very good fit [4] to the combined data from HERA for Deep Inelastic Scattering at small x, lending new confidence to this AdS dual approach to high energy diffractive scattering.

Pomeron-Graviton Duality: Traditionally, Deep Inelastic Scattering (DIS) at small-x, at least for Q^2 large, has been modeled using perturbative QCD. At small to moderate Q^2, confinement should be taken into account but it is often ignored, or incorporated in an ad hoc fashion. Here we use a formulation based on the AdS/CFT correspondence at strong coupling, which has the advantage of a unified soft and hard diffractive mechanism. We show, in particular, that the Q^2 dependence for the "effective Pomeron intercept", $\alpha_{eff} = 1 + \epsilon_{eff}(Q^2)$, observed at HERA, can be understood in terms of diffusion in AdS_3 in the holographic approach. In this analysis, the bare BPST Pomeron intercept is taken to be $j_0 = 1.22$.

In lowest order in weak 't Hooft coupling for QCD, a bare Pomeron was first identified by Low and Nussinov as a two gluon exchange corresponding to a Regge cut in the J-plane at $j_0 = 1$. Going beyond the leading order, Balitsky, Fadin, Kuraev and Lipatov (BFKL) summed all the diagrams for two gluon exchange to first order in $\lambda = g^2 N_c$ and *all* orders in $(g^2 N_c \log s)^n$, thus giving rise to the so-called BFKL Pomeron. The position of this J-plane cut is at $j_0 = 1 + \log(2) g^2 N_c/\pi^2$, recovering the Low-Nussinov result in the $\lambda \to 0$ limit. In a holographic approach to diffractive scattering [1,2,3,5], the weak coupling Pomeron is replaced by the "Regge graviton" in AdS space, as formulated by Brower, Polchinski, Strassler and Tan (BPST) [1,3] which has both hard components due to near conformality in the UV and soft Regge behavior in the IR. Corrections to the strong coupling lower the intercept from $j = 2$ to

$$j_0 = 2 - 2/\sqrt{g^2 N_c}\,. \tag{1}$$

[a] speaker

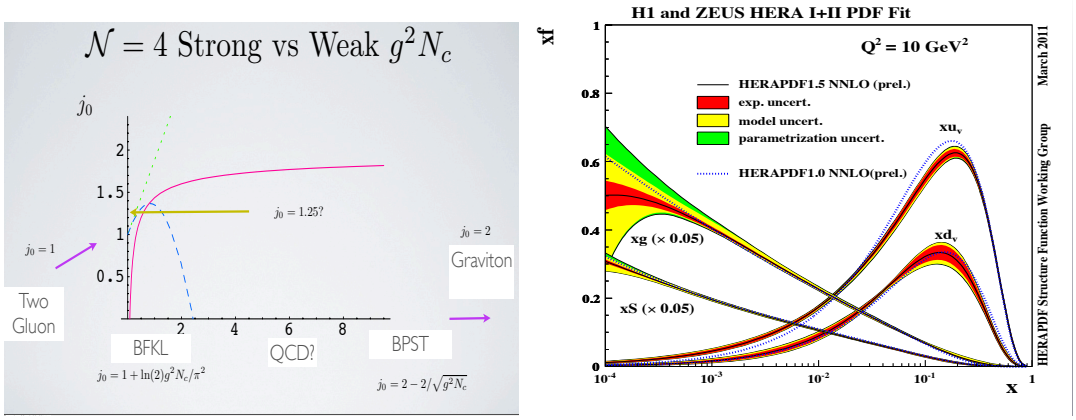

Figure 1: On the left, intercept j_0 in $\mathcal{N}=4$ YM shown as a function of 't Hooft coupling λ for the BPST Pomeron (solid red) and for BFKL (dotted and dashed to first and second order in λ respectively). On the right, a typical partonic fit to HERA DIS data demonstrating the dominance for gluon dynamics at small x.

In Fig. 1, we compare this with the weak coupling BFKL intercept to second order. A typical phenomenological estimates for this parameter for QCD is about $j_0 \simeq 1.25$, which suggests that the physics of diffractive scattering is in the cross over region between strong and weak coupling. A corresponding treatment for Odderons has also been carried out [6]. We also show in Fig. 1 the dominance of gluons, in a conventional partonic approach, thus further justifying the large N_c approximation, where quark constituents are suppressed.

Holographic Treatment to Deep Inelastic Scattering: We make use of the fact that the DIS cross section can be related to the Pomeron exchange amplitude via the optical theorem, $\sigma = s^{-1}\mathrm{Im}A(s,t=0)$. In the holographic approach, the impact parameter space $(b_\perp, z)$ is 3 dimensional, where $z \geq 0$ is the warped radial 5th dimension. Conformal dilatations ($\log z \to \log z + \text{const}$) take one from the UV boundary at $z=0$ deep into the IR $z=$ large. The near forward elastic amplitude takes the eikonal form,

$$A(s,t) = 2is \int d^2b\, e^{i\vec{q}\cdot\vec{b}} \int dz dz'\; P_{13}(z) P_{24}(z') \{1 - e^{i\chi(s,b,z,z')}\}\;. \tag{2}$$

where $t=-q_\perp^2$ and the eikonal function, χ, is related to a BPST Pomeron kernel in a transverse AdS_3 representation, $\mathcal{K}(s,b,z,z')$, by $\chi(s,b,z,z') = \frac{g_0^2}{2s}(\frac{R^2}{zz'})^2 \mathcal{K}(s,b,z,z')$. AdS/CFT correspondence gives expressions for all structure functions F_i; we focus here on $F_2(x,Q^2) = \frac{Q^2}{\pi^2\alpha_{em}}(\sigma_T(\gamma^* p) + \sigma_L(\gamma^* p))$. An important unifying features for the holographic map is factorization in the AdS space. For hadron-hadron scattering, $P_{ij}(z) = \sqrt{-g(z)}(z/R)^2 \phi_i(z)\phi_j(z)$ involves a product of two external normalizable wave functions for the projectile and the target respectively. For DIS, states 1 and 3 are replaced by currents, and we can simply replace P_{13} by product of the appropriate unnormalized wave-functions. In the conformal limit, P_{13} was calculated in [8] in terms of Bessel functions, so that, to obtain F_2, we simply replace in (2),

$$P_{13}(z) \to P_{13}(z,Q^2) = \frac{1}{z}(Qz)^2(K_0^2(Qz) + K_1^2(Qz)) \tag{3}$$

When expanded to first order in χ, Eq. (2) provides the contribution from exchanging a single Pomeron. In the conformal limit, a simple expression can be found. Confinement can next be introduced, eg., via a hardwall model $z > z_{cut-off}$. The effect of saturation can next be included via the full transverse AdS_3 eikonal representation (2).

Pomeron Kernel: The leading order BFKL Pomeron has remarkable properties. It enters into the first term in the large N_c expansion with zero beta function. Thus it is in effect the weak coupling cylinder graph for the Pomeron for a large N_c conformal theory, the same approximations used in the AdS/CFT approach albeit at strong coupling. Remarkable BFKL integrability properties allows one to treat the BFKL kernel as the solution to an $SL(2,\mathcal{C})$ conformal spin chain. Going to strong coupling, the two gluon exchange evolves into a close string of infinitely many tightly bound gluons but the same underlying symmetry persists, referred to as Möbius invariance in string theory or the isometries of the transverse AdS_3 impact parameter geometry. The position of the j-plane cut moves from $j_0 = 1 + \log(2) g^2 N_c/\pi^2$ up to $j_0 = 2 - 2/\sqrt{g^2 N_c}$ and the kernel obeys a Schrödinger equation on AdS_3 space for the Lorentz boost operators M_{+-} ,

$$\left[(-\partial_u^2 - te^{-2u})/2 + \sqrt{\lambda}(j - j_0)\right] G_j(t, z, z') = \delta(u - u'), \tag{4}$$

with $z = e^{-u}$. In the conformal limit, $G_j(t, z, z') = \int dq\ q\ J_{\tilde{\Delta}(j)}(zq) J_{\tilde{\Delta}(j)}(qz')/(q^2 - t)$, $\tilde{\Delta}(j)^2 = 2\lambda(j - j_0)$, and the Pomeron kernel is obtained via an inverse Mellin transform. At $t = 0$ the solution for the imaginary part of the Pomeron kernel exhibits diffusion

$$\text{Im}\ \mathcal{K}(s, t = 0, z, z') \sim \frac{s^{j_0}}{\sqrt{\pi \mathcal{D} \log s}}\ e^{-(\log z - \log z')^2/\mathcal{D} \log s}, \tag{5}$$

in the "size" parameter $\log z$ for the exchanged closed string, analogous to the BFKL kernel at weak coupling, with diffusing taking place in $\log(k_\perp)$, the virtuality of the off shell gluon dipole. The diffusion constant takes on $\mathcal{D} = 2/\sqrt{g^2 N_c}$ at strong coupling compared to $\mathcal{D} = 7\zeta(3) g^2 N_c/2\pi^2$ in weak coupling. The close analogy between the weak and strong coupling Pomeron suggests the development of a hybrid phenomenology leveraging plausible interpolations between the two extremes.

Fit to HERA Data Both of these integrals, z and z' in (2), remain sharply peaked, the first around $z \sim 1/Q$ and the second around the inverse proton mass, $z' \equiv 1/Q' \sim 1/m_p$. We approximate both of them by delta functions. Under such an "ultra-local" approximation, all structure functions take on very simple form, e.g,

$$F_2(x, Q^2) = \frac{g_0^2}{8\pi^2 \lambda} \frac{Q}{Q'} \frac{e^{(j_0 - 1)\ \tau}}{\sqrt{\pi \mathcal{D} \tau}}\ e^{-(\log Q - \log Q')^2/\mathcal{D}\tau} + \text{Confining Images}. \tag{6}$$

with diffusion time given more precisely as $\tau = \log(s/QQ'\sqrt{\lambda}) = \log(1/x) - \log(\sqrt{\lambda} Q'/Q)$. Here the first term is conformal and, for hardwall, the confining effect can be expressed in terms of image charges [4]. It is important to note that taking the $s \to \infty$ limit, the amplitude corresponding to (6) grows asymptotically as $(1/x)^{j_0} \sim s^{j_0}$, thus violating the Froissart unitarity bound at very high energies. The eikonal approximation in AdS space [2,5,7] plays the role of implementing "saturation" to restore unitary via multi-Pomeron shadowing.

We have shown various comparisons of our results [4] to the data from the combined H1 and ZEUS experiments at HERALD [9] in Fig. 2. Both the conformal, the hard-wall model as well as the eikonalized hard-wall model can fit the data reasonably well. This can best be seen in the left figure which exhibits the Q^2 dependence of an effective Pomeron intercept. This can be understood as a consequence of diffusion. However, it is important to observe that the hard-wall model provides a much better fit than the conformal result for Q^2 less than $2 \sim 3\ GeV^2$. The best fit to data is obtained using the hard-wall eikonal model, with a $\chi^2 = 1.04$. This is clearly shown by the figure to the right, where we present a comparison of the relative importance of confinement versus eikonal at the current energies. We observe that the transition scale $Q_c^2(x)$ from conformal to confinement increases with $1/x$, and it comes before saturation effect becomes important. For more details, see Ref. [4]

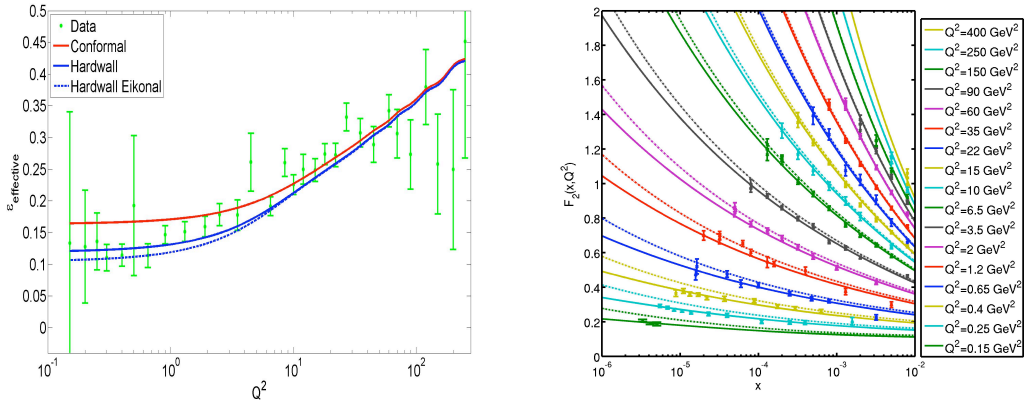

Figure 2: In the left, with the BPST Pomeron intercept at 1.22, Q^2 dependence for "effective intercept" is shown for conformal, hardwall and hardwall eikonal model. In the right, a more detailed fit is presented contrasting the fits to HERA data at small x by a single hardwall Pomeron vs hardwall eikonal respectively.

Conclusions: We have presented the phenomenological application of the AdS/CFT correspondence to the study of high energy diffractive scattering for QCD. Fits to the HERA DIS data at small x demonstrates that the strong coupling BPST Graviton/Pomerons [1] does allow for a very good description of diffractive DIS with few phenomenological parameters, the principle one being the intercept to the bare Pomeron fit to be $j_0 \simeq 1.22$. Encouraged by this, we plan to undertake a fuller study of several closely related diffractive process: total and elastic cross sections, DIS, virtual photon production and double diffraction production of heavy quarks. The goal is that by over constraining the basic AdS building blocks of diffractive scattering, this framework will give a compelling phenomenology prediction for the double diffractive production of the Higgs in the standard model to aid in the analysis of LHC data.

Acknowledgments: The work of RCB was supported by the Department of Energy under contract DE-FG02-91ER40676, that of IS by the Department of Energy under contracts DEFG02- 04ER41319 and DE-FG02-04ER41298 that of CIT by the Department of Energy under contract DE-FG02-91ER40688, Task-A, and that of MD by FCT project CERN/FP/116358/2010.

References:

1. R. C. Brower, J. Polchinski, M. J. Strassler, C-I Tan, JHEP **0712**, 005 (2007).
2. R. C. Brower, M. J. Strassler and C-I Tan, JHEP **0903**, 050 (2009).
3. R. C. Brower, M. J. Strassler and C-I Tan, JHEP **0903**, 092 (2009).
4. R. C. Brower, M. Djurić, I. Sarcevic, C-I Tan, JHEP **1011**, 051 (2010).
5. L. Cornalba, M. S. Costa, J. Penedones, R. Schiappa, Nucl. Phys. **B767**, 327-351 (2007); L. Cornalba, M. S. Costa, J. Penedones, JHEP **0806**, 048 (2008); JHEP **0709**, 037 (2007); Phys. Rev. Lett. **105**, 072003 (2010).
6. R. C. Brower, M. Djuric and C-I Tan, JHEP **0907**, 063 (2009).
7. Y. Hatta, E. Iancu and A. H. Mueller, JHEP **0801**, 026 (2008) J. L. Albacete, Y. V. Kovchegov, A. Taliotis, JHEP **0807**, 074 (2008); Y. V. Kovchegov, Z. Lu, A. H. Rezaeian, Phys. Rev. **D80**, 074023 (2009). E. Levin, I. Potashnikova, JHEP **1008**, 112 (2010).
8. J. Polchinski, M. J. Strassler, JHEP **0305**, 012 (2003).
9. F. D. Aaron *et al.* [H1 and ZEUS Collaboration], JHEP **1001**, 109 (2010).
10. R. C. Brower, M. Djurić, C-I Tan, in preparation.

DIFFRACTION, SATURATION AND *pp* CROSS SECTIONS AT THE LHC

K. GOULIANOS
The Rockefeller University, 1230 York Avenue, New York, NY 10065-6399, USA

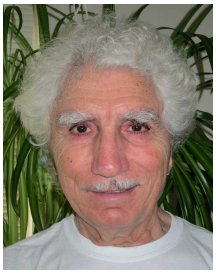

Results from the large hadron collider (LHC) show that no available Monte Carlo simulation incorporates our pre-LHC knowledge of soft and hard diffraction in a way that could be reliably extrapolated to LHC energies. As a simulation is needed to establish triggers, perform underlying event corrections and calculate acceptances, the lack of a robust simulation affects all measurements at the LHC. Particularly affected are the measurements of processes with large diffractive rapidity gaps, which constitute about one quarter of the inelastic cross section. In this paper, a previously described phenomenological model based on a saturation effect observed in single diffraction dissociation in pre-LHC data, validated by its successful application to several diffractive processes, is used to predict the total and total-inelastic *pp* cross sections at the LHC. The prediction for the total-inelastic cross section at $\sqrt{s} = 7$ TeV is compared with recent results from ATLAS and CMS.

1 Introduction

The Froissart bound for the total *pp* cross section, $\sigma_t^{s\to\infty} < C \cdot (\ln \frac{s}{s_o})^2$ (where s is the *pp* collision energy squared, C is a constant and s_o a scale parameter), which was published fifty years ago [1] created a keen interest among the physics community as well as a controversy, which continue to this date. Among the reasons for the continuing interest, as an example, is the possibility of using the optical theorem that relates σ_t to the imaginary part of the forward elastic scattering amplitude, $\mathrm{Im}f_{el}|_{t=0}$, where t is the 4-momentum transfer squared, and dispersion relations that relate the imaginary to the real part, $\mathrm{Re}f_{el}|_{t=0}$, coupled with a measurement of $\rho = \mathrm{Re}f_{el}|_{t=0}/\mathrm{Im}f_{el}|_{t=0}$, to look for violations as signs for new physics [2]. On the other hand, the controversy stems from the coefficient C, which was set to $C = \pi/m_\pi^2$ in 1966 [3], using $s_o = 1$ (GeV/c)^2, and updated to $C = \frac{1}{4}\pi/m_\pi^2$ in 2009 [4]. With such large values of C, the bound is more than 100 times higher than the σ_t measured at Tevatron energies and in cosmic ray experiments at higher energies, rendering the form of $\sigma_t(s)$ and extrapolations to LHC subject to phenomenological modeling feeding the controversy.

Measuring cross sections at the LHC involve Monte Carlo (MC) simulations to establish triggers, perform underlying event (UE) corrections and calculate detector acceptances. In

anticipation of LHC measurements, MC tuning was intensified and is presently continuing with no "light at the end of the tunnel" seen in the search for a MC model that could reliably accommodate all diffractive processes. The present paper is based on a QCD inspired model (RENORM) that addresses all diffractive processes and final states.

RENORM predictions have been previously presented in Ref. [5] (June 2009) and updated in Ref. [6] (May 2010). The 2010 paper [6] represents a concise summary of the talk delivered at the present conference, and the reader is referred to that paper for details and for the proposed MC strategy for the LHC. In the present paper, we will focus on an update of our model to include a prediction of the total-inelastic cross section, σ_{inel}.

This update was motivated by the preliminary results for σ_{inel} at $\sqrt{s} = 7$ TeV at the LHC released by ATLAS in February 2011 [7]. As the measurement of σ_{inel} involves an extrapolation from a "visible" to the total-inelastic cross section using MC simulations, and due to the interest in using σ_{inel} to measure/monitor the machine luminosity, the simulation of diffractive processes has gained popularity among particle and machine physicists alike. This interest was spread out into the entire particle physics community due to the need to understand the contributions of the diffractive processes to the UE, which affects all measurements at the LHC.

Below, in Sec. 2, we discuss our predictions for σ_t, σ_{el} and σ_{inel} for various values of $\sqrt{s}$ at the LHC, and in Sec. 3 we conclude.

2 The total, elastic and total-inelastic cross sections

The elastic, total and single-diffractive (SD) pp cross sections are usually described by Regge theory (see, e.g., Ref. [8]). At high energies, they are dominated by Pomeron ($I\!P$) exchange, and for a Pomeron intercept $\alpha(0) = 1 + \epsilon$ the s-dependence has a power law behavior,

$$(d\sigma_{el}/dt)_{t=0} \sim (s/s_o)^{2\epsilon}\,, \quad \sigma_t = \beta^2_{I\!Ppp}(0) \cdot (s/s_o)^{\epsilon}\,, \quad \text{and } \sigma_{sd} \sim \left(s'/s_o\right)^{2\epsilon}\,, \tag{1}$$

where $s' = M^2 = s\xi$, M is the mass of the diffractive system and ξ is the forward momentum loss of the proton. As s increases, this would lead to unitarity violations when the elastic and/or single SD cross section would exceed σ_t. In the case of SD, CDF measurements at $\sqrt{s} = 540$ GeV [1800 GeV] showed that a violation of unitarity is avoided by a suppression of $\sigma_{sd}(s)$ by a factor of $\mathcal{O}(5)$ [factor of $\mathcal{O}(10)$] relative to Regge expectations (see Ref. [9]).

Theoretical models predicting cross sections at the LHC must satisfy necessary unitarity constraints. Unitarization procedures employed by different authors differ in concept and in the number of parameters used that need to be tuned to available accelerator and cosmic ray data. While a rise of the total cross section from Tevatron to LHC is generally obtained, the predictions for LHC are spread out over a wide range. For example, in Ref. [5], authors predict a σ_t at $\sqrt{s} = 14$ TeV ranging from 90 to 250 mb. The inherently unitarized RENORM model is based on a saturated Froissart bound and is only subject to uncertainties propagated from the uncertainties in two experimentally determined parameters: a scale parameter s_o, and a saturation s-value s_F above which the Froissart bound is reached.

The model has been justified in a recent paper [10], where it was introduced as a special phenomenological interpretation of the parton model for the Pomeron in QCD discussed in Ref. [11]. This model is based on wee-parton cascades and yields formulae similar in form to those of Regge theory. Interpreting the term which is equivalent to the Pomeron flux in this model as a gap formation probability, naturally leads to the concept of renormalization as a procedure that eliminates overlapping rapidity gaps in an event, which otherwise would be counted as additional events. The overlapping rapidity gaps are precisely those responsible for the $s^{2\epsilon}$ factor in SD and elastic scattering in the Regge picture, and would lead to a unitarity violation in the absence of any unitarization.

In Ref. [6], the saturated Froissart bound above $s = s_F$ leads to a cross section of the form:

$$\sigma_t(s > s_F) = \sigma_t(s_F) + (\pi/s_o) \cdot \ln^2(s/s_F). \quad (2)$$

The parameter s_F is determined from the position of a *knee* observed in the energy dependence of σ_{sd} at $\sqrt{s} = \sqrt{s}_{\rm knee}$ (see Fig. 1 in Ref. [6]). The knee is attributed to a saturation in multiple wee-parton exchanges, manifesting as the scaling parameter s_o of the sub-energy-squared of the diffractive system, $s' \equiv M^2$ (see Eq. 1), which identifies s_o as a mass-squared, $s_o \equiv M_o^2$. Thus, M_o is reasonably interpreted as the mass of a saturated partonic glueball-like exchange, whimsically named *superball* in Ref. [5]. Inserting s_o into Eq. (2) in place of m_π^2 yields an analytic expression for the total cross section for $s > s_F$.

Predicting the total cross section at the LHC using Eq. (2) requires knowledge of $\sigma_t(s_F)$. The cross section at $\sqrt{s_F} = 22$ GeV, however, has substantial Reggeon-exchange contributions, and also contributions from the interference between the nuclear and Coulomb amplitudes. A complete description must take into consideration all these contributions, using Regge or parton-model amplitudes to describe Reggeon exchanges, and dispersion relations to obtain the real part of the amplitude from measured total cross sections up to Tevatron energies. In the RENORM model, we follow a strategy that bypasses all these hurdles. For completeness, we outline below all the steps in the cross section evaluation process:

(i) Use the Froissart formula as a *saturated* bound;
(ii) Eq. (2) should then describe the cross section above the *knee* in σ_{sd} vs $\sqrt{s}$, which occurs at $\sqrt{s_F} = 22$ GeV, and therefore should be valid at the Tevatron at $\sqrt{s} = 1800$ GeV;
(iii) replace m_π^2 by $m^2_{superball} = s_o/(\hbar c)^2 \approx (3.7 \pm 1.5)/0.389$ GeV^2 in the coefficient $C = \pi/m_\pi^2$;
(iv) note that Reggeon-exchange contributions at $\sqrt{s} = 1800$ GeV are negligible (see Ref. [12]);
(v) obtain the total cross section at the LHC as:

$$\sigma_t^{\rm LHC} = \sigma_t^{\rm CDF} + \frac{\pi}{s_o}\left[\left(\ln\frac{s^{\rm LHC}}{s_F}\right)^2 - \left(\ln\frac{s^{\rm CDF}}{s_F}\right)^2\right]. \quad (3)$$

Using the CDF $\sigma_t^{\rm CDF} = 80.03 \pm 2.24$ mb at $\sqrt{s} = 1.8$ TeV, this formula predicts the cross sections shown in Table 1. The values for σ_{el} and σ_{inel} are also shown, obtained using the ratios of $R_{el/t} \equiv \sigma_{el}/\sigma_t$ of the global fit of Ref. [12]. The result for σ_t at $\sqrt{s} = 14$ TeV falls within the

Table 1: Predicted σ_t, σ_{el} and σ_{inel} pp cross sections [mb] at LHC; uncertainties are dominated by that in s_o.

$\sqrt{s}$	σ_t	σ_{el}	σ_{inel}
7 TeV	98 ± 8	27 ± 2	71 ± 6
8 TeV	100 ± 8	28 ± 2	72 ± 6
14 TeV	109 ± 12	32 ± 4	76 ± 8

range of cross sections predicted by the various authors in Ref. [5], and is in good agreement with the value of 114 ± 5 mb of the global fit of Ref. [12], where the uncertainty was propagated from the $\pm\delta\epsilon$ value reported in the paper using the correlation between σ_t and ϵ through $\sigma_t \sim s^\epsilon$.

The February 2011 (pre-Moriond) ATLAS result for $\sqrt{s} = 7$ TeV was [7]:

$$\sigma_{inel}(\xi > 10^{-5}) = 57.2 \pm 0.1({\rm stat.}) \pm 0.4({\rm syst.}) \pm 6.3({\rm Lumi})\ {\rm mb} \quad (4)$$

Based on a PYTHIA (PHOJET) extrapolation, a $\sigma_{inel} = 63.3 \pm 7.0$ mb (60.1 ± 6.6 mb) was obtained. These results/predictions provided the motivation for updating the RENORM prediction and presenting the result in Moriond-2011.

After Moriond-2011, ATLAS reported the following results from an updated analysis [13]:

$$\sigma_{inel}(\xi > 10^{-6}) = 60.33 \pm 2.10(\text{exp.}) \pm 0.4 \text{ mb} \quad (5)$$

$$\sigma_{inel}(\xi > m_p^2/s) = 69.4 \pm 2.4(\text{exp.}) \pm 6.9(\text{extr.}) \text{ mb} \quad (6)$$

Also after Moriond-2011, CMS reported a measurement [14] of σ_{vtx}^{inel} based on events with 3 or more particles with $p_T > 200$ MeV/c in $|\eta| < 2.4$, $\sigma_{vtx}^{inel} = 59.7 \pm 0.1(\text{stat.}) \pm 1.1(\text{syst.}) \pm 2.4(\text{Lumi})$ mb, and using MC models to extrapolate to σ_t^{inel} obtained:

$$66.8 \leq \sigma_t^{inel} \leq 74.8 \text{ mb}. \quad (7)$$

Both the ATLAS and CMS results are in good agreement with the RENORM prediction.

3 Conclusion

The total pp cross section at the LHC is predicted in a phenomenological approach that obeys all unitarity constraints. The approach is based on a saturated Froissart bound above a pp collision energy-squared $s = s_F$, leading to an analytic $\ln^2(s/s_F)$-dependence, $\sigma_t = (\pi/s_o) \cdot \ln^2(s/s_F)$. The scale parameters s_F and s_o are experimentally determined from pre-LHC SD results. Using the ratio $R_{el/t} \equiv \sigma_{el}/\sigma_t$ from a global fit to cross sections [12] to extract σ_{el} from σ_t, a $\sigma_{inel}^{model} = 71 \pm 6$ mb at $\sqrt{s} = 7$ TeV is obtained, which is in agreement with the ATLAS $\sigma_{inel}(\xi > m_p^2/s) = 69.4 \pm 2.4(\text{exp.}) \pm 6.9(\text{extr.})$ mb and the CMS $66.8 \leq \sigma_t^{inel} \leq 74.8$ mb results.

Acknowledgments

Warm thanks to The Rockefeller University and the U.S. Department of Energy Office of Science for financial support, and to my colleagues at Rockefeller, CDF and CMS for many discussions.

References

1. M. Froissart, Phys. Rev **3**, 123 (1961).
2. Bourrely, C., Khuri, N.N., Martin, A., Soffer, J., Wu, T.T.; http://en.scientificcommons.org/16731756.
3. A. Martin, Nuovo Cimento **42**, 930 (1966).
4. A. Martin, Phys. Rev. D **80**, 065013 (2009).
5. K. Goulianos, EDS-2009, arXiv:1002.3527: "Diffractive and total pp cross sections at LHC," pp. 6-11; "Factorization breaking in diffraction," pp. 121-127.
6. K. Goulianos, "Diffractive cross sections and event final states at the LHC," Forward Physics at LHC Workshop - La Biodola, Elba, Italy 27-29/05/2010; arXiv:1009.5413 v2[hep-ph].
7. ATLAS Collaboration, "Measurement of the inelastic proton-proton cross section at $\sqrt{s} =$ 7 TeV using the ATLAS detector," ATLAS-CONF-2011-002, February 6, 2011.
8. K. Goulianos, Phys. Rept. **101**, 169 (1983).
9. K. Goulianos, Phys. Lett. B **358**, 379 (1995); Erratum-*ib.* **363**, 268 (1995).
10. K. Goulianos, Phys. Rev. D 80, 111901(R) (2009).
11. E. Levin, Report No. DESY 98-120; arXiv:hep-ph/9808486v1.
12. R. J. M. Covolan, J. Montanha and K. Goulianos, "A New determination of the soft pomeron intercept," Phys. Lett. B **389**, 176 (1996).
13. ATLAS Collaboration, arXiv:1104.0326v1 [hep-ex] 2 Apr 2011 (reference added in proof).
14. CMS Collaboration, "Measurement of the pp inelastic cross section using pile-up events," DIS-2011, Newport News, Va, USA (reference added in proof).

Transverse Energy Flow with Forward and Central Jets at the LHC [a]

M. Deak[1], F. Hautmann[2], H. Jung[3] and K. Kutak[4]
[1] *IFT-UAM/CSIC, Universidad Autónoma de Madrid, E-28049 Madrid*
[2] *Theoretical Physics Department, University of Oxford, Oxford OX1 3NP*
[3] *Deutsches Elektronen Synchrotron, D-22603 Hamburg*
[4] *Institute of Nuclear Physics IFJ-PAN, PL 31342 Cracow*

We observe that at the LHC, using forward + central detectors, it becomes possible for the first time to carry out measurements of the transverse energy flow due to "minijets" accompanying production of two jets separated by a large rapidity interval. We present parton-shower calculations of energy flow observables in a high-energy factorized Monte Carlo framework, and discuss the role of these observables to analyze high parton multiplicity effects.

The production of final states created with high momentum transfers and boosted to forward rapidities is a new feature of the Large Hadron Collider compared to previous collider experiments, subject of intense experimental and theoretical activity [1]. Forward high-$p_\perp$ production enters the LHC physics program in both new particle discovery processes (e.g., jet studies in decays of boosted massive states [2]) and new aspects of standard model physics (e.g., QCD at small x and its interplay with cosmic ray physics [3]).

Investigating such final states poses new challenges to both experiment and theory. On one hand, measurements of jet observables in the forward region call for new experimental tools and analysis techniques [1,4,5]. On the other hand, the evaluation of QCD theoretical predictions is made complex by the forward kinematics forcing high-$p_\perp$ production into a region characterized by multiple hard scales, possibly widely disparate from each other. This raises the issue of whether potentially large corrections arise beyond finite-order perturbation theory which call for perturbative QCD resummations [6,7,8] and/or contributions beyond single parton interaction [9,10,11,12,13]. It is thus relevant to ask to what extent current Monte Carlo generators can provide realistic event simulations of forward particle production, and how LHC experimental measurements can help improve our understanding of QCD effects in the forward region.

To this end, Refs. [8,14] have proposed measuring correlations of a forward and a central jet, and performed a numerical analysis of the effects of noncollinear, high-energy corrections to initial-state QCD showers. First experimental studies have since appeared in preliminary form in [15]. Ref. [16] has further pointed out that the capabilities of forward + central detectors at the LHC allow one to perform detailed investigations of the event structure by measuring the associated transverse energy flow as a function of rapidity, both in the interjet region and in the region away from the trigger jets (Fig. 1). Such energy flow measurements have not been made before at hadron-hadron colliders. Measurements of this kind were made in lepton-proton collisions at HERA, where one had roughly an average transverse energy flow of 2 GeV per unit rapidity [17]. This increases by a factor of five at the LHC to about 10 GeV or more per unit rapidity out to forward rapidity, as a result of the large phase space opening up for high-$p_\perp$ production. Then it becomes possible to carry out measurements of the flow resulting from "mini-jets" with transverse energy above a few GeV, thus suppressing the sensitivity of the observable to soft particle production. Ref. [16] suggests this minijet energy flow as a way to investigate the detailed structure of events with forward and central jets.

These measurements could be viewed as complementary to measurements performed by the CMS Collaboration [18] on the energy flow in the forward direction in minimum bias events and in events containing a central dijet system. The studies [18] are designed to investigate properties of the soft underlying event; in particular, they illustrate that the energy flow observed in the

[a] Contributed at the XLVI Rencontres de Moriond, March 2011.

forward region is not well described by tunes of the PYTHIA Monte Carlo generator [11,12] based on charged particle spectra in the central region, especially for the minimum bias sample. The energy flow observables discussed in [16], on the other hand, can serve to investigate features of events that depend on (semi)hard color radiation. For proposed studies of forward event shapes and correlations to investigate minimum bias, see [19].

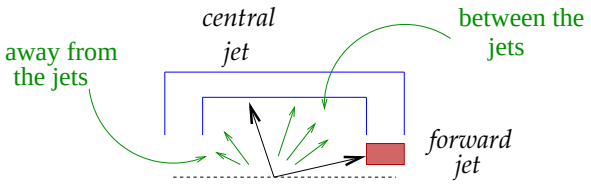

Figure 1: *Production of forward and central jets: energy flow in the inter-jet and outside regions.*

In Ref. [16] we consider different experimental definitions for selecting forward and central jets. In what follows we focus on the case of selection cuts

$$1 < \eta_c < 2 \ , \qquad -4 < \eta_f < -5 \ , \tag{1}$$

where η_c and η_f are the central and forward jet pseudorapidities, and consider the associated transverse energy flow as a function of pseudorapidity

$$\frac{dE_\perp}{d\eta} = \frac{1}{\sigma} \int dq_\perp \ q_\perp \ \frac{d\sigma}{dq_\perp \ d\eta} \ . \tag{2}$$

The energy flow is sensitive to color radiation associated with the trigger specified in Eq. (1). We observe that the transverse factor $q_\perp$ in the integrand on the right hand side in Eq. (2) enhances the sensitivity to the high momentum transfer end of the QCD parton cascades compared to the inclusive jet cross sections. On one hand, it makes the transverse momentum ordering approximation less physically justified in the long-time evolution of the parton cascade. On the other hand, it increases the importance of corrections due to extra hard-parton emission in the jet production subprocess at the shortest time scales.

The energy flow can be analyzed by employing the approach suggested in [14], in which one couples the short distance forward-jet matrix elements[8], which contain extra hard-gluon emission via high-energy factorization [7], to the transverse-momentum dependent parton showers [20,21], which go beyond the collinear ordering approximation by implementing CCFM evolution in the CASCADE Monte Carlo. (See [22] for a study of phenomenological implications of this dynamics on multi-jet final states.) In addition to radiative corrections from multiple emission in a single parton chain, the evaluation of $dE_\perp/d\eta$ is sensitive to possible contributions of multiple parton chains. See [16] for discussion of this.

Fig. 2 shows the transverse energy flow in the interjet region for the cases of particle flow and of minijet flow. Besides the calculation above given by the curves labelled CASCADE, we report results obtained from PYTHIA [12] and POWHEG [23] Monte Carlo event generators. The particle energy flow plot shows the jet profile picture, and indicates an enhancement of the energy flow in the inter-jet region with respect to the PYTHIA result from the next-to-leading radiation in POWHEG and from higher order emissions in CASCADE. The minijet energy flow plot indicates the same effect, with reduced sensitivity to infrared radiation. These results are of interest for the QCD tuning of Monte Carlo generators, especially in connection with the estimation of QCD backgrounds in search channels involving two jets far apart in rapidity such as Higgs boson searches from vector boson fusion [24,25]. As mentioned earlier, multiple parton interactions can likely contribute extra radiation in the inter-jet region, and the energy flow measurements proposed in [16] can be used to investigate this quantitatively.

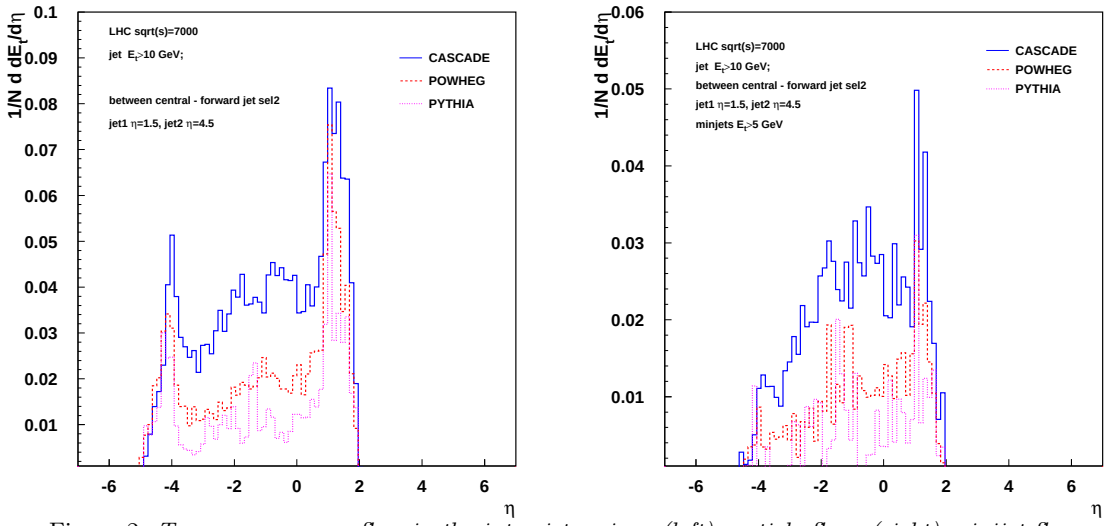

Figure 2: *Transverse energy flow in the inter-jet region: (left) particle flow; (right) minijet flow.*

It will also be of interest to measure the energy flow in the outside region corresponding to rapidities opposite to the forward jet, far in the backward region. In this region, one may expect a suppression of the transverse flow due to phase space from single-shower calculations. As noted in [14], in this region one is probing rather large values of longitudinal momentum fraction x, and the effects of corrections to collinear ordering, taken into account by the CASCADE result, are not large. On the other hand, contributions from multiple showers could be significant, due to gluon radiation shifting to larger values of x in each of the sequential parton chains, as the total energy available to the collision is shared between the different chains.

Note that the analysis discussed in [14,16] can be extended to the case of forward-backward jets. Here one can look for Mueller-Navelet effects [1,4,6]. Investigating QCD radiation associated with forward-backward jets will serve to analyze backgrounds in Higgs searches from vector boson fusion channels [25] and studies based on a central jet veto [26] to extract information on Higgs couplings [24]. In this case too the underlying jet activity accompanying the Higgs may receive comparable contributions [27] from finite-angle radiative contributions to single-chain showers, extending across the whole rapidity range, and from multiple-parton interactions.

Our focus in this article has been on initial state radiation effects in energy flow observables, relevant to studies of initial-state distributions that generalize ordinary parton distributions [28,29] to more exclusive descriptions of event structure. It will be relevant to also investigate final-state effects such as those in [30,31,32], associated with emission of color in restricted phase space regions and depending on the algorithms used to reconstruct the jets.

Acknowledgments

We thank the Moriond organizers and staff for the invitation and for the nice atmosphere at the meeting.

References

1. Z. Ajaltouni et al., arXiv:0903.3861 [hep-ph].
2. A. Abdessalam et al., arXiv:1012.5412 [hep-ph].
3. M. Grothe, F. Hautmann and S. Ostapchenko, arXiv:1103.6008 [hep-ph].
4. D. d'Enterria, arXiv:0911.1273 [hep-ex].
5. S. Abdullin et al., Eur. Phys. J. C **53** (2008) 139.
6. A.H. Mueller and H. Navelet, Nucl. Phys. B**282** (1987) 727; C. Ewerz, L.H. Orr, W.J. Stirling and B.R. Webber, J. Phys. G**26** (2000) 696.

7. S. Catani, M. Ciafaloni and F. Hautmann, Phys. Lett. B**242** (1990) 97; Nucl. Phys. B**366** (1991) 135; Phys. Lett. B**307** (1993) 147; S. Catani and F. Hautmann, Phys. Lett. B**315** (1993) 157; Nucl. Phys. B**427** (1994) 475.
8. M. Deak, F. Hautmann, H. Jung and K. Kutak, JHEP **0909** (2009) 121; arXiv:0908.1870.
9. T. Sjöstrand and M. van Zijl, Phys. Rev. D**36** (1987) 2019; Phys. Lett. B**188** (1987) 149.
10. P. Bartalini and L. Fanò (eds.), arXiv:1003.4220, Proceedings 1st MPI Workshop (Perugia, 2008), DESY-PROC-2009-06.
11. T. Sjöstrand, S. Mrenna, and P. Skands, JHEP **0605** (2006) 026.
12. P. Skands, Phys. Rev. D**82** (2010) 074018.
13. J.R. Gaunt and W.J. Stirling, arXiv:1103.1888 [hep-ph]; JHEP **1003** (2010) 005; B. Blok, Yu. Dokshitzer, L. Frankfurt and M. Strikman, arXiv:1009.2714 [hep-ph]; M. Strikman and W. Vogelsang, Phys. Rev. D**83** (2011) 034029; T.C. Rogers and M. Strikman, Phys. Rev. D**81** (2010) 016013; G. Calucci and D. Treleani, Phys. Rev. D**83** (2011) 016012; Phys. Rev. D**80** (2009) 054025; Phys. Rev. D**79** (2009) 074013; F.A. Ceccopieri, Phys. Lett. B**697** (2011) 482; M. Diehl and A. Schäfer, arXiv:1102.3081 [hep-ph]; S. Domdey, H.-J. Pirner and U.A. Wiedemann, Eur. Phys. J. C **65** (2010) 153; M.G. Ryskin and A.M. Snigirev, arXiv:1103.3495 [hep-ph]; E. Maina, JHEP **1101** (2011) 061; JHEP **0909** (2009) 081; JHEP **0904** (2009) 098; E.L. Berger, C.B. Jackson and G. Shaughnessy, Phys. Rev. D**81** (2010) 014014.
14. M. Deak, F. Hautmann, H. Jung and K. Kutak, arXiv:1012.6037 [hep-ph].
15. CMS Coll., CMS-PAS-FWD-10-006 (2011); CMS Coll., CMS-PAS-FWD-10-003 (2011).
16. M. Deak, F. Hautmann, H. Jung and K. Kutak, Oxford preprint OUTP-11-38-P (2011).
17. C. Adloff et al. [H1 Coll.], Eur. Phys. J. C **12** (2000) 595.
18. CMS Coll., CMS-PAS-FWD-10-011 (2011).
19. P. Skands and K. Wraight, arXiv:1101.5215 [hep-ph].
20. H. Jung et al., Eur. Phys. J. C **70** (2010) 1237.
21. H. Jung, Comput. Phys. Commun. **143** (2002) 100.
22. F. Hautmann and H. Jung, JHEP **0810** (2008) 113; arXiv:0804.1746 [hep-ph].
23. S. Alioli et al., arXiv:1012.3380 [hep-ph].
24. B.E. Cox, J.R. Forshaw and A.D. Pilkington, Phys. Lett. B**696** (2011) 87.
25. K.J.C. Leney [on behalf of the ATLAS Coll.], arXiv:0810.3144 [hep-ex]; M. Vazquez Acosta [on behalf of the CMS Coll.], arXiv:0901.3098 [hep-ex].
26. J.M. Butterworth, B.E. Cox and J.R. Forshaw, Phys. Rev. D**65** (2002) 096014.
27. M. Deak et al., arXiv:1006.5401 [hep-ph]; F. Hautmann, H. Jung and V. Pandis, arXiv:1011.6157 [hep-ph]; F. Hautmann, arXiv:0909.1240; Phys. Lett. B **535** (2002) 159.
28. F. Hautmann, Acta Phys. Polon. B **40** (2009) 2139; F. Hautmann and H. Jung, Nucl. Phys. Proc. Suppl. **184** (2008) 64 [arXiv:0712.0568 [hep-ph]]; arXiv:0808.0873 [hep-ph].
29. S. Mert Aybat and T.C. Rogers, arXiv:1101.5057 [hep-ph]; P.J. Mulders and T.C. Rogers, Phys. Rev. D**81** (2010) 094006; S. Mantry and F. Petriello, arXiv:1011.0757 [hep-ph]; arXiv:1007.3773 [hep-ph]; T. Becher and M. Neubert, arXiv:1007.4005 [hep-ph]; I.W. Stewart, F.J. Tackmann and W.J. Waalewijn, JHEP **1009** (2010) 005; A. Idilbi and I. Scimemi, Phys. Lett. B**695** (2011) 463; arXiv:1012.4419 [hep-ph]; M. Garcia-Echevarria, A. Idilbi and I. Scimemi, arXiv:1104.0686 [hep-ph]; I. Cherednikov and N. Stefanis, arXiv:1104.0168 [hep-ph]; Phys. Rev. D**80** (2009) 054008; Mod. Phys. Lett. A **24** (2009) 2913; F. Hautmann, Phys. Lett. B**655** (2007) 26; arXiv:0708.1319; J.C. Collins and F. Hautmann, JHEP **0103** (2001) 016; Phys. Lett. B**472** (2000) 129.
30. A. Banfi, M. Dasgupta, K. Khelifa-Kerfa and S. Marzani, JHEP **1008** (2010) 064.
31. C.F. Berger, T. Kucs and G. Sterman, Phys. Rev. D**68** (2003) 014012.
32. I. Sung, Phys. Rev. D**80** (2009) 094020; Y. Hatta and T. Ueda, Phys. Rev. D**80** (2009) 074018; A. Papaefstathiou, J.M. Smillie and B.R. Webber, JHEP **1004** (2010) 084.

7.
Heavy Ions

FIRST MEASUREMENTS IN PB–PB COLLISIONS AT $\sqrt{s_{\rm NN}}$=2.76 TeV WITH ALICE AT THE LHC

M. NICASSIO FOR THE ALICE COLLABORATION
Dipartimento Interateneo di Fisica 'M. Merlin' and Sezione INFN,
Via Orabona 4, 70126 Bari, Italy

With the first Pb–Pb data collected at the Large Hadron Collider at the end of 2010, the ALICE Collaboration has measured bulk properties such as the multiplicity of charged particles, space-time properties and collective effects of the system created. In the following, after a brief introduction on the event and centrality selections, these studies as a function of centrality will be summarized and compared to RHIC results and model predictions.

1 Introduction

At the end of 2010, the LHC produced its first Pb–Pb collisions. The ALICE experiment [1] is specifically designed to study heavy-ion physics at the LHC and investigate the properties of the hot and dense deconfined matter, the Quark-Gluon Plasma, whose formation is predicted by Quantum-Chromodynamics at high energy density. To characterize the collisions, the ALICE Collaboration measured fundamental observables which are sensitive to the properties of this matter. For the analyses described here, the relevant data come from the following detectors: the Inner Tracking System (ITS), the Time Projection Chamber (TPC), the V0 scintillators at forward rapidity, placed on either side (A and C) of the interaction point and the Zero Degree Calorimeters (ZDC).

1.1 Trigger and event selection

The detectors used for triggering are V0 scintillators and the first two layers of the ITS, namely the Silicon Pixel Detector (SPD). Minimum bias events have been triggered requiring two out of three of the following signals: two chips fired in the SPD outer layer, a signal in the V0 on the A side and a signal in the V0 on the C side. The trigger condition has been tightened during the run period requiring a signal in both the V0s, which is more efficient in rejecting electromagnetic interactions.

In order to remove background, events are further selected offline requiring a minimal energy deposit in the each of the neutron ZDC to reduce electromagnetic processes and the V0 timing information together with the correlation between TPC tracks and SPD hits is used to remove beam–gas interactions.

1.2 Centrality determination

For the centrality determination the main ingredients are a Glauber calculation to model inelastic A–A interactions and a two component model for particle production with sources distributed

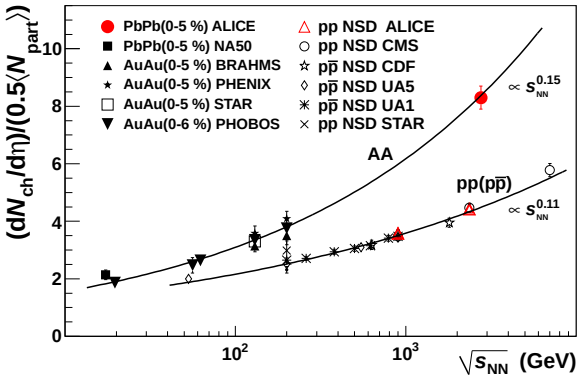

Figure 1: $\mathrm{d}N_{\mathrm{ch}}/\mathrm{d}\eta$ at central pseudorapidity ($|\eta| < 0.5$) per participant pair as a function of the centre-of-mass energy for the 5% most central A–A collisions and for pp collisions. The data have been fitted using a power law (curves).

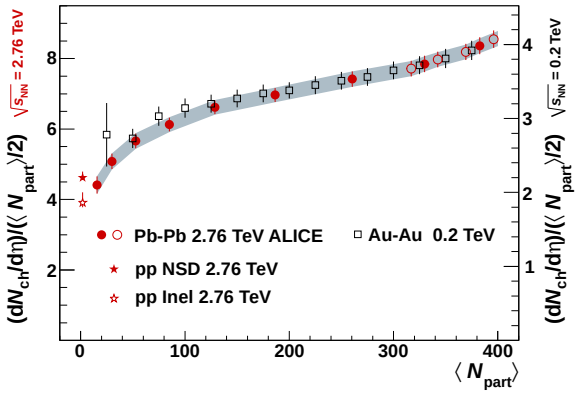

Figure 2: $\mathrm{d}N_{\mathrm{ch}}/\mathrm{d}\eta$ per participant pair as a function of the number of participants in Pb–Pb collisions at $\sqrt{s_{\mathrm{NN}}}$=2.76 TeV and in Au–Au collisions at $\sqrt{s_{\mathrm{NN}}}$=0.2 TeV. The latter are scaled by a factor 2.1 (scale on the right). The grey band shows the correlated uncertainties and the error bars the uncorrelated ones. pp data have been obtained interpolating data at 2.36 and 7 TeV.

as $N_{\mathrm{coll}} + f \times N_{\mathrm{part}}$, where each source emits particles distributed according to a Negative Binomial Distribution. The experimental distribution of the summed amplitudes in the V0 detector is fitted using the Glauber model above an anchor point where the trigger efficiency is 100% and the background contamination from electromagnetic processes is negligible. This point corresponds to 88% of the inelastic cross section. To determine centrality classes the data are sliced in percentile bins and the number of participant N_{part} is determined geometrically from the Glauber model.

2 Multiplicity density of primary charged particles

The pseudorapidity density measure is based on tracklets reconstructed in the SPD, correcting for acceptance and efficiency and subtracting the combinatorial background [2]. In Fig. 1 the pseudorapidity density at mid-rapidity scaled by the number of participating nucleons measured in the 5% most central collision is shown for A–A collisions and compared to pp data. Both are fitted with a power law: the growth with $\sqrt{s_{\mathrm{NN}}}$ is faster in A–A than in pp collisions. The multiplicity density is a factor 1.9 higher compared to pp at similar energies and a factor 2.1 compared to RHIC. Most of the model calculations underpredict the measurement.

The evolution of the multiplicity with centrality has also been measured [3]. Compared to RHIC data, the multiplicity is a factor two higher and increases also by a factor two going from peripheral to central events (Fig. 2). The centrality dependence is similar to that found at RHIC.

Comparing measurements with model predictions, in particular two-component models and saturation models, those incorporating a moderation of the multiplicity with centrality provide a better description of the data.

3 Elliptic flow of primary charged particles

The first anisotropic flow studies[4] with tracks reconstructed in the TPC and ITS are summarized in this section. The elliptic flow coefficient v_2, the second moment of the azimuthal distribution

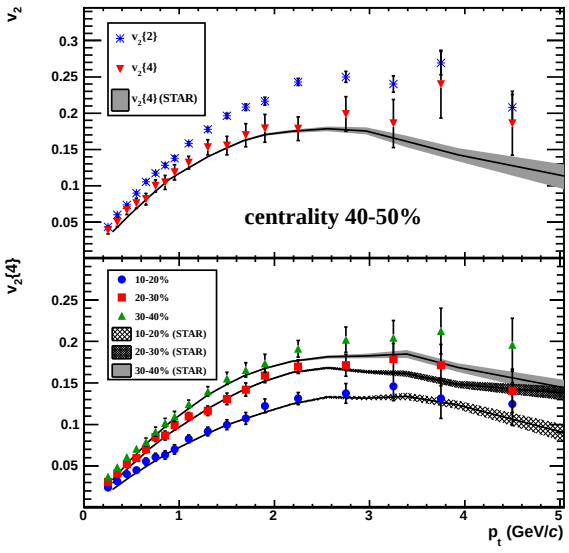

Figure 3: $v_2(p_\mathrm{t})$ for the centrality class 40-50% obtained with the 2- and 4-particle cumulant methods (top panel) and $v_2\,\{4\}(p_\mathrm{t})$ for several centrality classes compared to STAR data (lower panel).

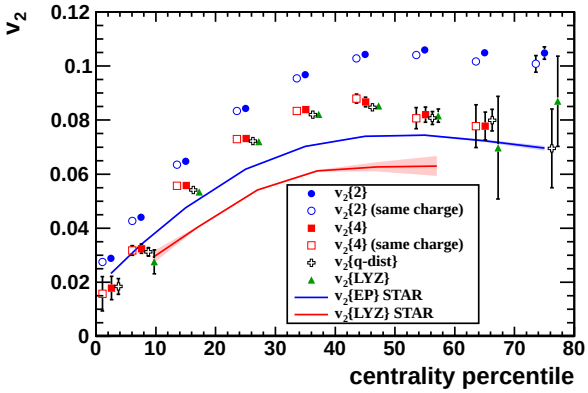

Figure 4: Elliptic flow coefficient v_2 obtained with several methods as a function of centrality compared to RHIC measurements in Au–Au collisions at $\sqrt{s_\mathrm{NN}}$=0.2 TeV.

of hadrons in the final state, has been measured using several analysis techniques which have different sensitivity to non-flow effects and flow fluctuations. The differential flow is shown in Fig. 3 (left plot) for one centrality class and two methods: the values are the same as those found at RHIC within the uncertainties and the difference between the two methods is due to non-flow effects, which are negligible for the 4-particle cumulant method, and to fluctuations which have opposite sign. In the same figure (right plot) v_2 is shown in several centrality classes compared to RHIC data for the 4-particle cumulant method: the dependence on p_t does not change with centrality.

In Fig. 4 the centrality dependence of v_2 is shown for several methods, for example the 2- and 4-particle cumulant methods by correlating particles of the same charge (for which correlations due to non-flow effects are weaker). The integrated elliptic flow is larger at the LHC than at RHIC because the mean p_t is higher. The increase is about 30% for more peripheral centralities and is reproduced by hydrodynamic predictions with low viscous corrections and some hybrid models, while ideal hydrodynamic models predict a lower increase.

4 Two-pion Bose–Einstein correlations in central collisions

The space-time properties of the particle-emitting system created in central collisions have been measured using the Bose–Einstein enhancement of identical pion pairs close in phase-space (HBT analysis) [5]. The two-pion correlation functions have been studied in transverse momentum bins using tracks reconstructed in the TPC. The pion source radii define the homogeneity volume (the region from which particle pairs with a certain momentum are most likely emitted). The radii have been measured to be up to 35% larger than those measured at RHIC in central Au–Au collisions at $\sqrt{s_\mathrm{NN}}$=0.2 TeV and, as observed at lower energies, show a decreasing trend with increasing transverse momentum, characteristic feature of expanding particle sources. In Fig. 5 (left plot) the quantity $R_\mathrm{out}R_\mathrm{side}R_\mathrm{long}$, related to the volume of the homogeneity region and therefore representing only a fraction of the whole particle-emitting source, is compared

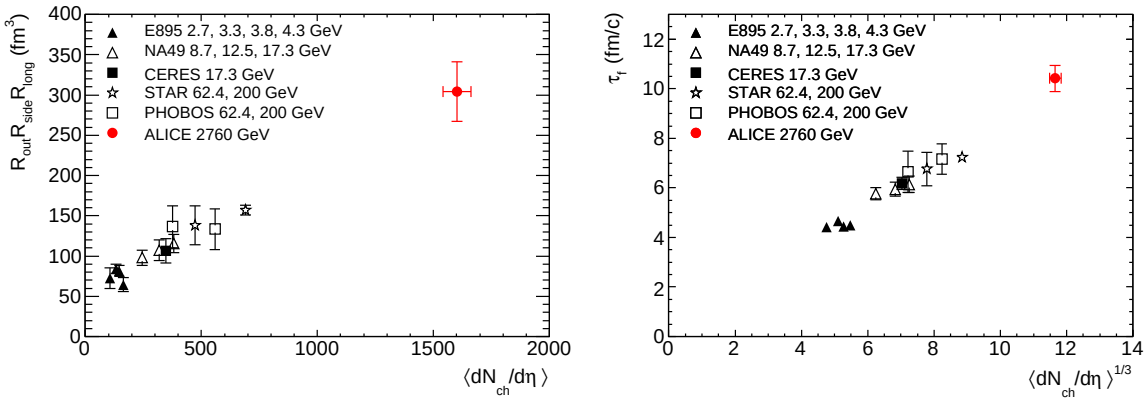

Figure 5: Product of the HBT radii at k_{T}=0.3 GeV/c (left panel) and decoupling time extracted from $R_{\mathrm{long}}(k_{\mathrm{T}})$ (right panel) as a function of the mean $\mathrm{d}N_{\mathrm{ch}}/\mathrm{d}\eta$. ALICE results are compared to lower energy data at the AGS, SPS and RHIC.

with measurements at lower energies. It is found to be twice the value measured in the most central collisions at RHIC. The decoupling time, i.e. the time of hadron chemical freeze-out, has been measured from R_{long}, which is proportional to the total duration of the longitudinal expansion. It is about 30% larger than the one measured at RHIC (Fig. 5 on the right) and a linear scaling with $<\mathrm{d}N_{\mathrm{ch}}/\mathrm{d}\eta>^{1/3}$ is observed. The expansion of the fireball created in Pb–Pb collisions at $\sqrt{s}$=2.76 TeV is modeled using the relativistic viscous hydrodynamics and models tuned to reproduce RHIC data still hold at the LHC and reproduce the observed growth with energy.

5 Conclusions

After few weeks from the first Pb–Pb collisions, the ALICE Collaboration has extracted the main properties of the matter produced. The first measurements with Pb–Pb collisions show an increase in the multiplicity of charged particles compared to RHIC (about factor 2) but with the same centrality dependence. The increase is higher than expected. The elliptic flow is found to be stronger than at RHIC and the system created behaves as a very low viscosity fluid. As for two-pion Bose–Einstein correlations, the pion source radii and the decoupling time exceed significantly those measured at RHIC and follow the trend observed at lower energies.

References

1. ALICE Collaboration K. Aamodt *et al*, *JINST* **3**, S08002 (2008).
2. ALICE Collaboration K. Aamodt *et al*, *Phys. Rev. Lett.* **105**, 252301 (2010).
3. ALICE Collaboration K. Aamodt *et al*, *Phys. Rev. Lett.* **106**, 032301 (2011).
4. ALICE Collaboration K. Aamodt *et al*, *Phys. Rev. Lett.* **105**, 252302 (2010).
5. ALICE Collaboration K. Aamodt *et al*, *Phys. Lett.* B **696**, 328-337 (2011).

TWO-, THREE-, AND JET-HADRON CORRELATIONS AT STAR

Kolja Kauder for the STAR Collaboration
University of Illinois at Chicago, Dept. of Physics, 845 W Taylor Street M/C 273, Chicago IL 60607, USA

Selected results of jet-medium interaction studies via hadron correlation techniques are presented. Jet modifications are studied using a p_T-dependent autocorrelation analysis and a two-dimensional fit model, which allow connection between the observed near-side correlation structures and theory. Analysis of both sides of a di-jet-like event with the 2+1 technique provides indications of a tangential emission bias in these types of events. Jet-hadron correlations on the away-side find softening and broadening of the recoil jet in the medium.

1 Multi-Hadron Correlation Analyses

The discovery of the jet-quenching effect was an early piece of evidence that a strongly-interacting medium had been created at RHIC. The nuclear modification factor (R_{AA}) shows an inclusive yield suppression in central Au+Au collisions at 200 GeV by a factor of five compared to binary scaled pp in the fragmentation region above $p_T = 4$ GeV/c. Such a suppression can not be seen in the cold nuclear matter created for example in d+Au collisions[1,2]. STAR's di-hadron correlation measurement revealed a more differential insight into the mechanism of this energy loss[3]: surviving jets triggering a 4-6 GeV/c threshold appear similar or identical to those in pp or d+Au at small relative angles, whereas the away-side around $\Delta\phi = \pi$ is severely suppressed when considering associates in the intermediate $p_T > 2$ GeV/c range. This correlation measurement, together with R_{AA} results, is indicative of strong energy loss in the medium that hadronic models could not successfully reproduce. To further explore the mechanisms of energy loss in the medium, a multitude of differential correlation measurements to study jets in heavy ion collisions have been developed. Here we present three selected STAR results from the past year. The main detector components relevant for this discussion are STAR's Time Projection Chamber (TPC) for tracking of charged particles, and the Barrel Electromagnetic Calorimeter (BEMC) for triggering on high energy particles and full jet reconstruction. Both have full azimuthal coverage with nearly uniform rapidity acceptance of $|\eta| < 1$. For the results presented below, 18M central triggered and 14M minimum bias Au+Au events from year 2004 as well as 1.1M high-energy (BEMC) triggered and 74M minimum bias Au+Au events from 2007 were used. d+Au reference data comes from 5.5M events from year 2003 as well as 46M (minimum bias) and 6M (high energy) events from 2008. 150k pp high-energy events from 2006 were also used.

2 Autocorrelation

The correlation of tracks in the TPC is explored by recording relative angles. Cuts on the transverse momentum of the involved particles serve to select specific kinematic regions. The

correlation density is computed as a function of the relative azimuth $\Delta\phi$ and relative pseudorapidity $\Delta\eta$ between all possible pairs of tracks that pass typical quality cuts. To account for the combinatorial background, the result is normalized by a reference correlation of tracks from different (mixed) events which is free of physical correlation structures besides acceptance effects. At low p_T, HBT-effects and photon conversions are expected to dominate small-angle correlation while at higher p_T jets should become the main source of structures at small angles. In ref. [4], the p_T threshold was gradually increased to study the evolution of the prominent features. The focus of this study is on the near-side with $|\Delta\phi| < \frac{\pi}{2}$ where jet remnants are expected to appear. Figure 1 shows two developments: The narrow elongation along the pseudorapidity dimension often called the "soft ridge" flattens out into a plateau with no more apparent dependence on $\Delta\eta$ as p_T goes beyond 2 GeV/c . At the same time, a jet-like peak emerges and the soft contributions no longer dominate the pair density correlation. Whether the jet peak is unmodified compared to vacuum fragmentation is an ongoing study.

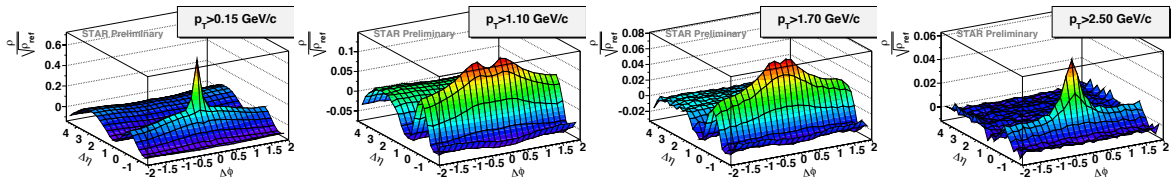

Figure 1: Two-dimensional autocorrelations with a p_T threshold progressing from left to right as indicated.

Above 2 GeV/c, the correlation becomes quite similar to the "hard ridge" found in triggered correlations [5]. At higher momentum, a significant fraction of hadrons is related to jet fragmentation. The gradual evolution suggests that the same mechanism may be responsible for both the soft and the hard ridge. In order to assess possible models, quantifiable observables were extracted from this plot using a two-dimensional fit model. A two-dimensional Gaussian models the ridge in this picture, other ingredients describe the jet cone, flow terms, and other terms detailed in [4]. A comparison to one model that tries to connect both ridges is shown in figure 2. The original model described the soft ridge with breaking flux tubes in a color glass condensate, boosted by radial flow. At low p_T, jet contributions are negligible, and the plotted predictions for the amplitude and width in $\Delta\phi$ agree very well with the values obtained from the fit to data. The centrality evolution is also captured well. Around 1 GeV/c both amplitude and width begin to deviate from the predicted value. The authors addressed this with a hybrid model that adds combinations of jet and bulk particles, shown in [6]. The resulting combined amplitude provides a better attempt to describe the measured values. Yet the hybrid model does not quite capture an overall trend of width evolution for the ridge. Jet-jet correlations were not taken into account in the model yet, and it will be interesting to see whether this additional amendment will then converge to a description of the ridge in both regimes.

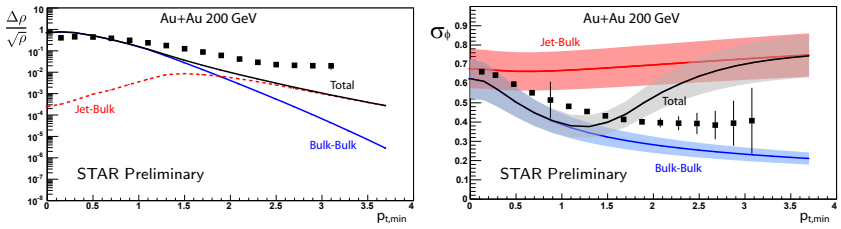

Figure 2: Left panel: Amplitude of the same-side elongated gaussian in black symbols. Right panel: $\Delta\phi$-width of the same-side gaussian. Two model calculations in red and blue lines are shown. The red Jet-Bulk curve is a correction term to the original calculation, the combined prediction is shown in black.

3 Di-Jets through Correlations

To enhance the jet sample, one can choose a high-p_T trigger particle which is done in a number of di-hadron correlation analyses[3,5,7]. Adding a second, azimuthally correlated trigger allows to explore di-jets more directly. For that we use a three-particle correlation where we require a second high-p_T trigger back-to-back with the primary trigger and consider the particle distribution with respect to such a trigger pair. This is known as "2+1" technique with two triggers and softer associated particles[8]. For similar trigger thresholds, the away-side in central Au+Au was found no longer suppressed and appearing of similar width and correlation strength as the same-side correlation. Both same- and away-side are found identical to the d+Au reference. Furthermore, apparent absence of medium-induced modifications is confirmed by the spectra of associated hadrons, showing no evidence of softening or suppression. Tangential emission of the selected di-jet could provide a natural explanation for this observation, with all surviving di-jets coming from the surface.

To vary the di-jet path length in the medium, it has been suggested to impose a large(r) energy difference between the two correlated triggers[9]. For this measurement the electromagnetic calorimeter was used to select primary triggers with transverse energy greater than 10 GeV, the rest of the analysis was carried out as before. Figure 3 shows that the away-side has higher yield, as one would expect to make up for the energy difference. But the same is happening in the d+Au reference, with very similar yields and shapes. The medium seems all but opaque to the trigger particles selected. These findings are not consistent with theory expectations of significant energy deposition in the medium for back-to-back di-jet triggers[10]. Further theoretical input is necessary to explain this result.

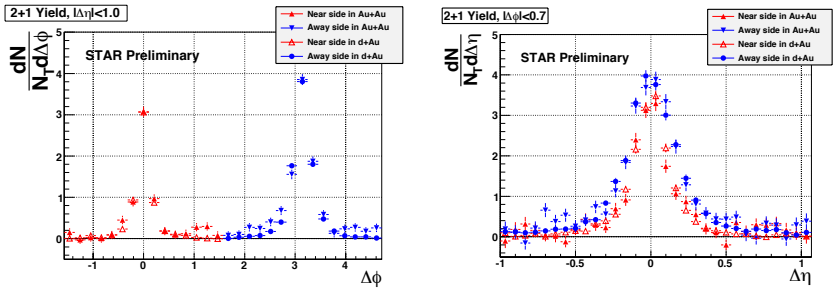

Figure 3: $\Delta\phi$ and $\Delta\eta$ projection of 2+1 correlations for for $E_T^{trig1} > 10$ GeV, $p_T^{trig2} > 4$ GeV/c and $p_T^{assc} > 1.5$ GeV/c.

4 Jet-hadron correlations

More direct information about the jet energy and direction can be obtained from full jet reconstruction. We use the anti-k_T jetfinder to reconstruct jets from clusters in the BEMC and charged tracks in the TPC[11]. Jets are required to have a 5.4 GeV cluster. Jet reconstruction in a high-multiplicity heavy ion collision environment is complicated, but it has the potential to increase the kinematic reach compared to dihadron correlations. One common issue is the smearing of the jet spectrum due to particles from the underlying event. This is corrected with a data-driven unfolding technique[12]. The techniques have matured to where Jet-hadron correlations have become a valuable tool to assess energy loss in the hot medium[13].

Figure 4 shows p_T evolution and integrated away-side associated hadron yield per trigger relative to the pp reference (I_{AA}) for different jet energies. One can observe strong away-side suppression above 2 GeV/c in this plot. This suppression at high p_T is balanced by an enhancement in the soft region. In a similar region below 2-3 GeV/c, a significant broadening of the

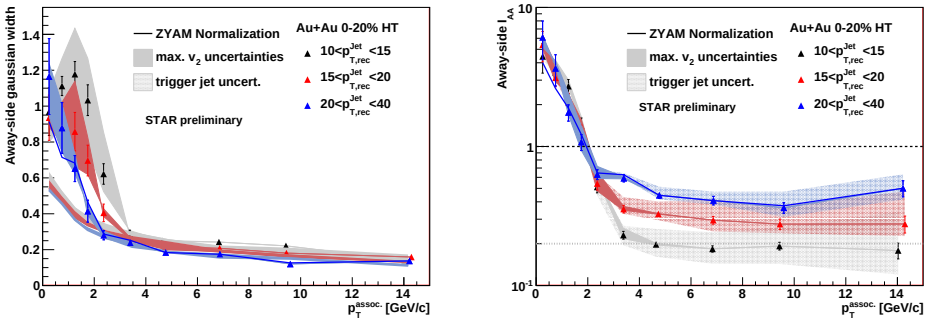

Figure 4: Left panel: Gaussian width of the away-side jet-like peak for three different jet energies. The corresponding widths in the *pp* reference are shown as shaded error bands only. Right panel: Away-side associated yield suppression compared to *pp*.

away-side peak becomes visible. Both effects get stronger with lower jet energies, corresponding to more heavily modified jets. Jets traversing the medium get softened and broadened.

5 Summary

Correlation techniques allow a unique differential view into the mechanisms of jet energy loss. The results presented in this work address the modification of jet properties by the hot and dense QCD medium. On the near-side, a p_T-dependent autocorrelation analysis illustrated a gradual evolution of the long-range pseudo-rapidity correlation of soft hadrons into the correlation similar to so-called ridge associated with high-p_T triggers in the triggered di-hadron correlations. Model attempts to bridge that gap theoretically allowed first connection to the measured data and are awaiting further progress. A jet-like peak emerged at higher p_T, and if and how it is modified is being studied. The 2+1 analysis allowed to trigger on di-jets and view both sides on equal footing. Little to no modification was found, regardless whether the trigger energy difference was small or large, suggesting strong surface bias of surviving di-jets. Di-Jet production and interaction with the medium still challenges the theoretical understanding. Finally, the analysis of the away-side in jet-hadron correlations showed how it softened and broadened as the recoil jet traverses the medium, illustrating and quantifying the action of jet quenching.

References

1. I. Arsene *et al.*, *Phys. Rev. Lett.* **91**, 072305 (2003).
2. S. S. Adler *et al.*, *Phys. Rev. Lett.* **91**, 072303 (2003).
3. J. Adams *et al.*, *Phys. Rev. Lett.* **91**, 072304 (2003).
4. C. L. DeSilva, RBRC Workshop on *Initial State Fluctuations and Final-State Particle Correlations* (2011).
5. B. I. Abelev *et al.*, *Phys. Rev.* C **80**, 064912 (2009).
6. G. Moschelli and S. Gavin, *Nucl. Phys.* A **836**, 43-58 (2010).
7. J. Adams *et al.*, *Phys. Rev. Lett.* **97**, 162301 (2006).
8. H. Agakishiev *et al.*, arXiv:1102.2669, to appear in *Phys. Rev.* C, Rapid Communications.
9. H. Pei, 27th Winter Workshop on Nuclear Dynamics (2011).
10. T. Renk, *Phys. Rev.* C **78**, 014903 (2008).
11. M. Cacciari and G. Salam, *Phys. Lett.* B **641**, 57 (2006).
12. J. Putschke *et al.*, *Nucl. Phys.* A **855**, 83-91 (2011).
13. A. Ohlson, 27th Winter Workshop on Nuclear Dynamics (2011).

Forward Physics in d+Au Collisions: Cold Nuclear Matter Probed with J/ψ Production and Pion Correlations

Richard K. Seto for the PHENIX Collaboration
Department of Physics and Astronomy, University of California at Riverside, Riverside, California, USA

Large nuclei which provide the initial condition in high energy heavy ion collisions have turned out to be more complex and interesting than that of a simple superposition of protons and neutrons. One notable explanation of this phenomenon is the Color-Glass Condensate model of gluon saturation. The production of particles in d+Au collisions, particularly at forward rapidity, is sensitive to these effects. This talk covers two measurements made by the PHENIX collaboration: a) the production of J/ψ's at forward rapidity, and b) the correlations of pions at forward rapidity with pions at either mid or forward rapidity. A comparison to models and their implications is discussed.

1 Introduction

A major task in relativistic heavy ion physics is to explain how the strongly interacting Quark Gluon Plasma (sQGP) created at RHIC and the LHC is formed. The initial state is that of a cold nucleus which naively might be described as a superposition of nucleons, the structure of which is well known in terms of the parton distribution functions. However the production and scattering of particles behave as if the parton distribution functions in a nucleus are altered. In particular, gluons with $x_{BJ} < 0.01$ appear to be suppressed. Such gluons are of particular interest, since they produce the majority of particles making up the sQGP. A variety of phenomena have been invoked to explain this modification of low-x gluons. These include shadowing, the modification of the parton distribution functions, coherence models, higher twist effects, and initial state energy loss. [9,10,11]

One of the most intriguing explanation is the Color Glass Condensate (CGC),a model of gluon saturation. [5] The Heisenberg Uncertainty principle requires that the transverse size of low-x gluons in the nucleus be large. At low enough x, the gluons begin to overlap and recombine leading to a suppression. This effect is amplified in a relativistically contracted nucleus since the thickness contributes to the number of gluons which overlap in some transverse area. Scattering is no longer described by the PQCD quark-gluon diagram, but rather as the scattering of a quark with a large number of overlapping gluons i.e. a color glass condensate. This description is valid in the region of forward rapidity (low x). At backward-rapidity (moderate x) pQCD inspired calculations are more appropriate.

In order to study this effect, the PHENIX experiment has measured the production of J/ψ's and back to back π^0 pairs in d+Au collisions at $\sqrt{s}$=200 GeV per nucleon. Of particular interest is the forward region, where sensitivity to the low-x partons is the greatest.

We will compare the predictions of the CGC to a model of modified parton (primarily gluon) distribution functions in nuclei. The latest such distribution functions are due to Eskola,

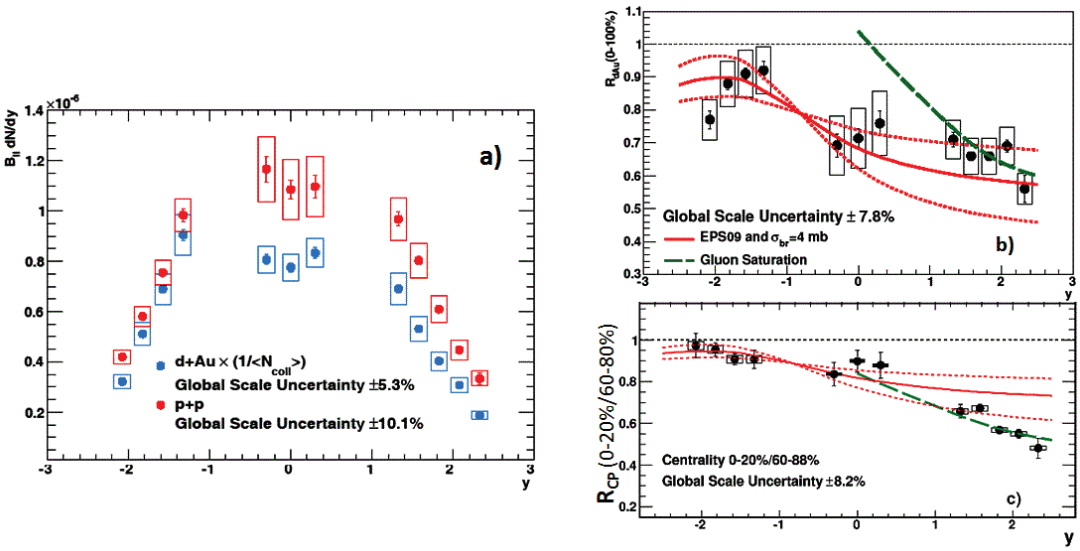

Figure 1: (a) J/ψ rapidity distribution in p+p and d+Au collisions. The d+Au yields are divided by $\langle N_{\rm coll}\rangle$=7.6. (b) $R_{d\rm Au}$ for minimum bias collisions. (c) $R_{\rm CP}$.

Paukkunen and Salgado (EPS09),[4] where they have fit the available data on nuclear collisions, primarily from lepton scattering and Drell-Yan experiments. At low Q^2, there are large uncertainties for x< 0.01. These uncertainties will be reflected in the comparisons to the data. We add two additional assumptions. First, to obtain an impact parameter (centrality) dependence, we assume a linear relationship to the density-weighted nuclear thickness. Second, in the case of J/ψ production, we assume a cross section σ_{br} to account for a possible breakup of the $c\bar{c}$ pair when traversing the nucleus. The value of σ_{br}=4mb is chosen to match the unbiased backward rapidity $R_{d\rm Au}$ data.[6]

2 J/ψ production

The scattering of two gluons is the primary mechanism for production of the J/ψ at RHIC energies. The PHENIX experiment[1] has large rapidity coverage for the detection of the J/ψ into di-leptons. The two central arms cover -0.35< η <0.35 and measure the J/ψ to di-electrons. Two forward arms cover 1.2< $|\eta|$ <2.4 and measure the J/ψ to di-muons. The p_T integrated yields are shown in figure 1a as a function of rapidity for p+p and minimum bias d+Au collisions. The yield in d+Au collisions has been divided by $\langle N_{\rm coll}\rangle$=7.6., the average number of nucleon-nucleon collisions as determined by a Glauber model. The suppression at forward and mid-rapidity is clearly visible. We then divide the two distributions to form

$$R_{d\rm Au} = \frac{\frac{dN^{d+\rm Au}}{dy}}{\langle \rm N_{coll}\rangle \frac{dN^{p+p}}{dy}} \qquad (1)$$

for minimum bias events and compare with the two models (Fig. 1b). The EPS09 nPDF with σ_{br}=4mb is in reasonable agreement with the data at all rapidities. We are however, most interested in the low-x region at forward rapidity - the region of validity for the CGC models. In this region the gluon saturation model[7] is also in agreement with the data. An enhancement, predicted at midrapidity due to double-gluon exchange is not seen.

To further discriminate between the models, we divide the data into centrality bins and take

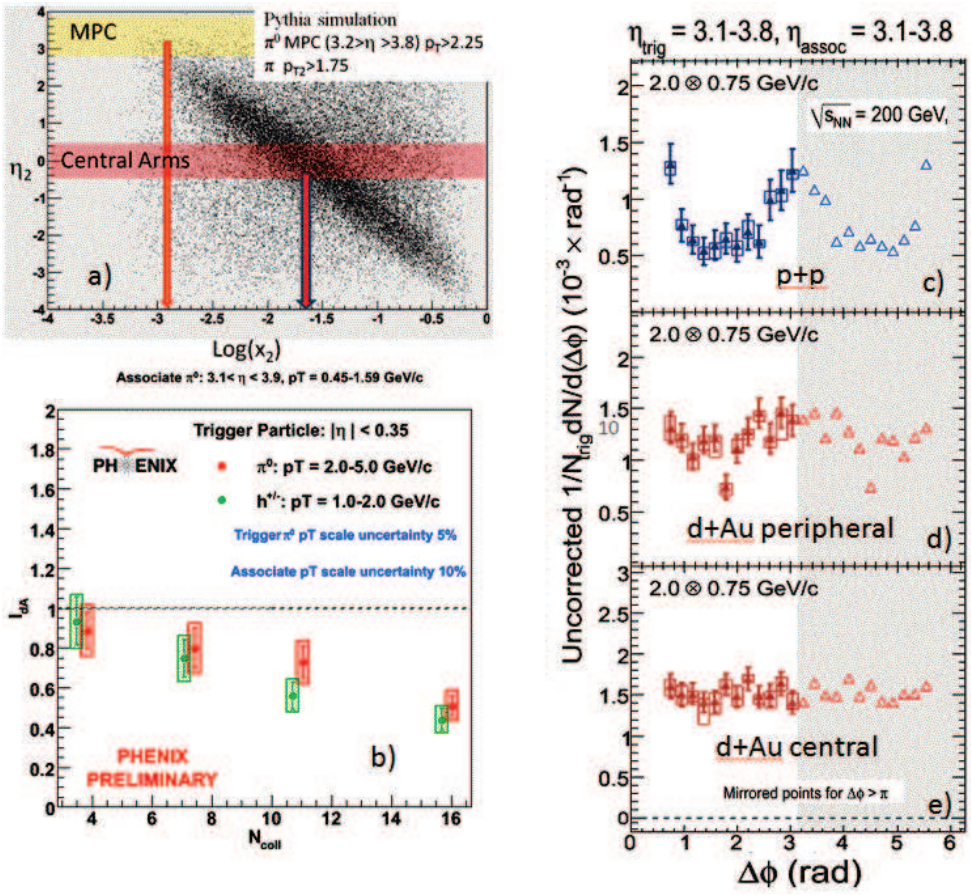

Figure 2: (a) Rapidity of a second π^0 (η_2) vs. log(x_2) where we require the first pion to be in the acceptance of the MPC, as described in the text. For this example we require $p_{T\pi 1} > 2.25$ GeV/c and $p_{T\pi 2} > 1.75$ GeV/c. (b) I_{dAu} vs N_{coll}. (c) The raw correlation function for p+p, (d) d+Au peripheral, and (e) d+Au central collisions.

the ratio between the most central (0-20%) and most peripheral (60-88%) bins to form

$$R_{\rm CP} = \frac{\frac{dN^{d+\rm Au}(0-20\%)}{dy} / \langle N_{\rm coll}(0-20\%)\rangle}{\frac{dN^{d+\rm Au}(60-88\%)}{dy} / \langle N_{\rm coll}(60-88\%)\rangle}. \quad (2)$$

At forward rapidity the data clearly favors the gluon saturation model, whereas the EPS09 nPDF under-predicts the suppression (Fig. 1c). [a]

3 Pion Correlations

In an attempt further examine the predictions of the CGC we turn to dihadron ($2\pi^0$) correlations. PHENIX has acceptance for π^0s in the central arms (-0.35< η <0.35) and at forward rapidity (3.1< $|\eta|$ <3.8) in the muon-piston calorimeters (MPC). If one requires the first pion of the di-pion pair to be in the acceptance of the MPC, one can see a strong correlation between the rapidity of a second pion on the opposite side in azimuth to x_{gluon} (x_2)(Fig. 2a). In particular, if one requires that the second π^0 to be in the central arms we are probing the nucleus at x$\sim$ 0.02, while if we require it to be in the MPC we are probing the nucleus at x$\sim 10^{-3}$. As one moves to

[a] One might well ask the question whether a modified nPDF such as EPS09 together with a J/ψ breakup cross section can describe the data. If one makes a general assumption about the dependence of the suppression on the density weighted pathlength, one finds that standard cold nuclear matter effects (nPDF's with a σ_{br}) cannot be reconciled with the data. [2]

lower x, or forward rapidity one expects a suppression of the two-particle correlation function. To quantify the effect, we define first the correlated yield $CY = (N_{pair}/\epsilon_{assoc})/N_{trig}$ corrected for efficiency. We can then make a comparison between the correlated yields in d+Au collisions and p+p collisions by defining $I_{dAu} = CY|_{dAu}/CY|_{pp}$. Fig. 2b shows I_{dAu} as a function of N_{coll}, i.e. the centrality. In this case the forward π^0 is required to have a p_T of between 0.45 and 1.6 GeV/c, and the particle in the central arm can either be a π^0 with p_T =2-5 GeV/c or a charged hadron with p_T =1-2 GeV/c. [b] As expected, one sees a increasing suppression as one goes to more central collisions. We can require both hadrons (π^0s) to be in the MPC, where we reach the lowest value of x. In the CGC picture, the scattering occurs coherently off of many gluons and the correlation should completely disappear. [8c] Fig. 2 c,d,e shows the acceptance corrected correlation function

$$CF = \frac{1}{acc}\frac{dN(\Delta\phi)}{d(\Delta\phi)} \tag{3}$$

for p+p, peripheral d+Au, and central Au+Au events. In p+p the CF shows the away side peak at $\Delta\phi = \pi$ from the scattered gluon. As one goes from p+p to peripheral d+Au to central Au+Au, the away side peak disappears, presumably since the momentum is being absorbed by a "condensate" of gluons.

4 Conclusions

Both the J/ψ and the pion correlation results from PHENIX are consistent with a CGC picture, however, other pictures may explain all or some of the data. Further work will be forthcoming, making more complete comparisons with models, in particular for the pion correlation data [3]. There are also many other channels in which the various models can be tested, for example heavy quark production, direct photon production, and the correlations of fully reconstructed jets. It is important that we find a unified, single picture of the cold nucleus at low-x which can explain the variety of phenomena, both in hadron-nucleus and nucleus-nucleus collisions. The sQGP is a low p_T phenomena, whose initial state is from low-x gluons. To a large extent pQCD inspired techniques will probably not work in the relevant region. We will need non-perturbative models such as the CGC, and and other methods not mentioned here (e.g. AdS/CFT based calculations) to make a major headway in our understanding.

References

1. K. Adcox *et al.* [PHENIX Collaboration], Nucl. Instrum. Meth. A **499**, 469 (2003).
2. A. Adare *et al.*, arXiv:1010.1246.
3. PHENIX collaboration, in preparation.
4. K. J. Eskola, H. Paukkunen and C. A. Salgado, JHEP **0904**, 065 (2009)
5. L. McLerran, Nucl. Phys. A **752**, 355 (2005).
6. R. Vogt, Phys. Rev. C **71**, 054902 (2005).
7. D. Kharzeev and K. Tuchin, Nucl. Phys. A **770**, 40 (2006).
8. J. L. Albacete and C. Marquet, Phys. Rev. Lett. **105**, 162301 (2010).
9. L. Frankfurt, V. Guzey and M. Strikman, Phys. Rev. D **71**, 054001 (2005).
10. J. W. Qiu, J. P. Vary and X. F. Zhang, Phys. Rev. Lett. **88**, 232301 (2002).
11. B. Z. Kopeliovich, et al, Phys. Rev. C **83**, 014912 (2011).

[b] We show the case where the trigger particle is in the central arm and the associated particle is in the MPC which is strictly speaking different than the case where the trigger particle is in the MPC. However in practice they are equivalent since the suppression factor for hadrons in the central arm is essentially unity in d+Au collisions.

[c] This is reminiscent of the Mössbauer effect in crystals.

Measurement of jet quenching with I_{CP} and $I_{AA,Pythia}$ in Pb-Pb collisions at $\sqrt{s_{NN}} = 2.76\,\mathrm{TeV}$ with ALICE

Jan Fiete Grosse-Oetringhaus for the ALICE collaboration
CERN, 1211 Geneva 23

This paper discusses the measurement of I_{CP} and $I_{AA,Pythia}$ with ALICE (A Large Ion Collider Experiment). An away-side suppression is found expected from in-medium energy loss. Further, and unexpected, a near-side enhancement is seen which has not been reported by previous experiments at lower energies.

The objective of the study of ultra-relativistic heavy ion-collisions is the characterization of the quark–gluon plasma, the deconfined state of quarks and gluons. Recent measurements by ALICE indicate that in central Pb-Pb collisions at the LHC unprecedented color charge densities are reached. For example, the suppression of charged hadrons in central Pb-Pb collisions at $\sqrt{s_{NN}} = 2.76\,\mathrm{TeV}$ expressed as the nuclear modification factor R_{AA} as a function of transverse momentum (p_T) reaches a value as low as 0.14.[1]

Di-hadron correlations allow for the further study of in-medium energy because for most pairs of partons scattered in opposite directions, one will have a longer path through the medium than the other. Thus, two-particle correlations can be used to study medium effects without the need of jet reconstruction. In such studies the near-side (particles found close to each other in azimuthal angle) and the away-side (particles found at azimuthal angles different by about π) yields are compared between central and peripheral events (I_{CP}) or studied with respect to a pp reference (I_{AA}). Previous measurements at RHIC have shown a significant suppression of the away-side yield consistent with a strongly interacting medium.[2,3] On the near-side no significant modifications have been observed at high p_T. Such analysis usually require the subtraction of non-jet correlations, e.g. flow, which are present in A+A collisions but not in pp collisions and therefore have influence on the extracted yields. This analysis chooses a p_T-region where the jet peak is the dominant correlated signal and thus the influence of non-jet correlations is small.

1 Detector and Data Sample

The ALICE detector is described in detail elsewhere.[4] For the present analysis the Inner Tracking System (ITS) and the Time Projection Chamber (TPC) are used for vertex finding and tracking. The TPC has a uniform acceptance in azimuthal angle and a pseudorapidity coverage of $|\eta| < 0.9$. The uniform acceptance results in only small required acceptance corrections. Forward scintillators (V0) are used to determine the centrality of the collisions.

About 12 million minimum-bias events recorded in fall 2010 have been used in the analysis. Good-quality tracks are selected by requiring at least 70 (out of 159) associated clusters in the TPC, and a χ^2 per space point of the momentum fit smaller than 4. In addition, tracks are required to originate from within $2 - 3\,\mathrm{cm}$ of the primary vertex.

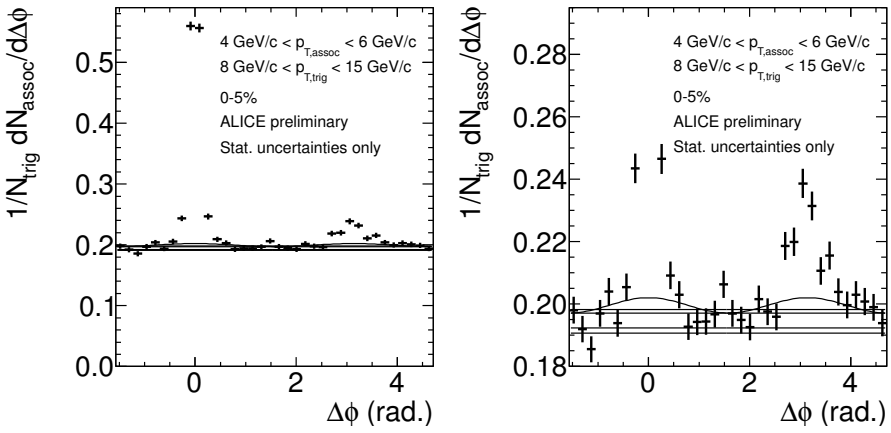

Figure 1: Per-trigger yield in an example bin: the right panel shows a zoom of the left panel. Indicated are the determined pedestal values (horizontal lines) and the v_2 component ($\cos 2\Delta\phi$ term). For details see text.

2 Analysis

The quantity which is obtained in this analysis is the associated per-trigger yield as function of the azimuthal angle difference:

$$\frac{dN}{d\Delta\phi}(\Delta\phi) = \frac{1}{N_{\rm trig}} \frac{dN_{\rm assoc}}{d\Delta\phi} \tag{1}$$

where $N_{\rm trig}$ is the number of trigger particles to which $N_{\rm assoc}$ particles are associated at $\Delta\phi = \phi_{\rm trig} - \phi_{\rm assoc}$. We measure this quantity for all pairs of particles where $p_{T,\rm assoc} < p_{T,\rm trig}$ within $|\eta| < 0.8$ and normalize by $\Delta\eta = 1.6$. Due to the flat acceptance in ϕ no mixed-event correction is needed. The per-trigger yield is extracted in bins of $p_{T,\rm trig}$ and $p_{T,\rm assoc}$.

Pedestal Subtraction To remove uncorrelated background from the associated yield, the pedestal value needs to be determined. This is done by fitting the region close to the minimum of the $\Delta\phi$ distribution ($\Delta\phi \approx \pm\frac{\pi}{2}$) with a constant and using this value as pedestal (zero yield at minimum – ZYAM). One cannot exclude a correlated contribution in this region (e.g. from 3-jet events), and we do not claim that we only remove uncorrelated background. Instead we measure a yield with the prescription given here. To estimate the uncertainty on the pedestal determination, we use four different approaches (different fit regions as well as averaging over a number of bins with the smallest content). Fig. 1 shows the per-trigger yield for an example bin. The horizontal lines indicate the determined pedestal values; their spread gives an idea of the uncertainty. Also indicated is a background shape considering v_2. The v_2 values are taken from an independent measurement (a measurement of v_2 at high p_T similar to [5]. For the centrality class $60-90\%$ no v_2 measurement was available, therefore, as an upper limit, v_2 is taken from the $40-50\%$ centrality class as it is expected to reduce towards peripheral collisions). For a given bin the v_2 background is $2\langle v_{2,\rm trig}\rangle\langle v_{2,\rm assoc}\rangle \cos 2\Delta\phi$ where the $\langle ...\rangle$ is calculated taking into account the p_T distribution of the trigger and associated particles. The yields are then calculated with and without removing the v_2 component. Subsequently to the pedestal (and optionally v_2) subtraction, the near and away side yields are integrated within $\Delta\phi$ of ± 0.7 and $\pi \pm 0.7$, respectively.

Systematic Uncertainties The influence of the following effects has been studied and considered for the systematic uncertainty on the extracted yields: detector efficiency and two-track effects, uncertainties in the centrality determination, p_T resolution, the size of the integration window for the near and away-side yield as well as uncertainties in the pedestal determination.

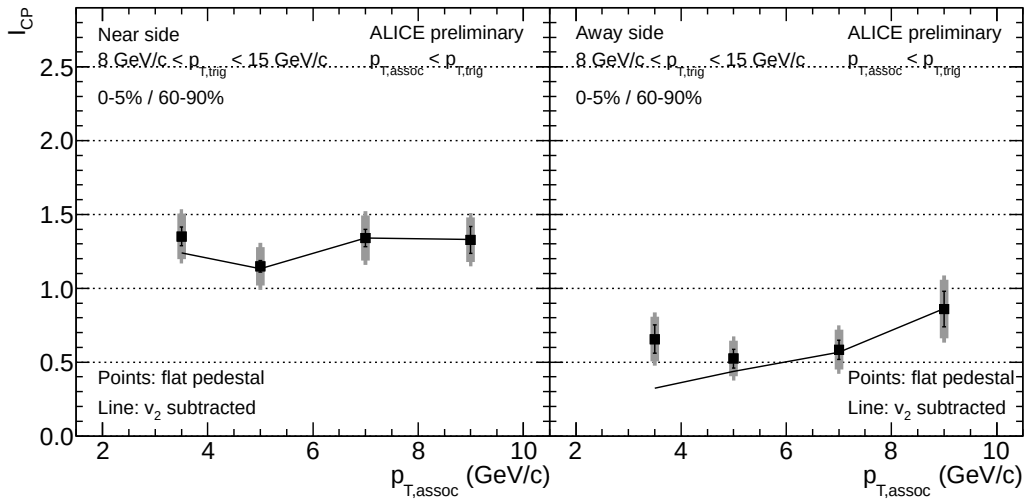

Figure 2: I_{CP}: the data points are calculated with a flat pedestal; the line is based on v_2 subtracted yields.

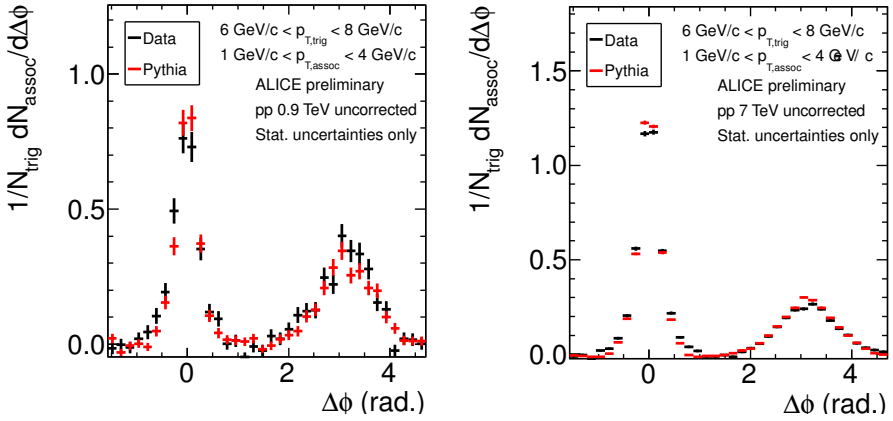

Figure 3: Uncorrected pedestal-subtracted per-trigger yields from pp collisions at 0.9 (left) and 7 TeV (right) are compared to a scaled MC (Pythia 6.4 with the tune Perugia-0).

The last mentioned item has the largest contribution (7-20%) to the systematic uncertainties on I_{CP} and $I_{AA,Pythia}$.

Results To quantify the effect of the in-medium energy loss, ratios of central to peripheral yields are calculated $I_{CP} = Y_{\text{central}}/Y_{\text{peripheral}}$ where Y_{central} ($Y_{\text{peripheral}}$) is the yield in central (peripheral) collisions, respectively. Fig. 2 shows I_{CP} using the flat pedestal (data points) and v_2 subtracted yields (lines). That the only significant difference is in the lowest bin of $p_{T,\text{assoc}}$ confirms the small influence of flow in this p_T region. It should be noted that we only consider v_2 here, although the v_3 contribution might be of the same order, particularly for central events. The away-side suppression from in-medium energy loss is seen, as expected. Moreover, there is an unexpected enhancement above unity on the near-side.

To study this further, and in particular if the enhancement is due to using peripheral events in the denominator, it is interesting to calculate $I_{AA} = Y_{\text{Pb-Pb}}/Y_{\text{pp}}$ where $Y_{\text{Pb-Pb}}$ (Y_{pp}) is the yield in Pb-Pb (pp) collisions, respectively. No pp collisions at the same center-of-mass energy than the recorded Pb-Pb collisions had been produced yet at the time of this analysis. Therefore the option of using a MC as reference has been investigated. Fig. 3 compares uncorrected pedestal-subtracted per-trigger yields of pp collisions taken with ALICE to Pythia[6] 6.4 with the tune Perugia-0[7] at $\sqrt{s} = 0.9$ and 7 TeV. The MC has been scaled such that the yields on the near side agree with each other. The required scaling factor is $0.8 - 1$ depending on p_T. One can see

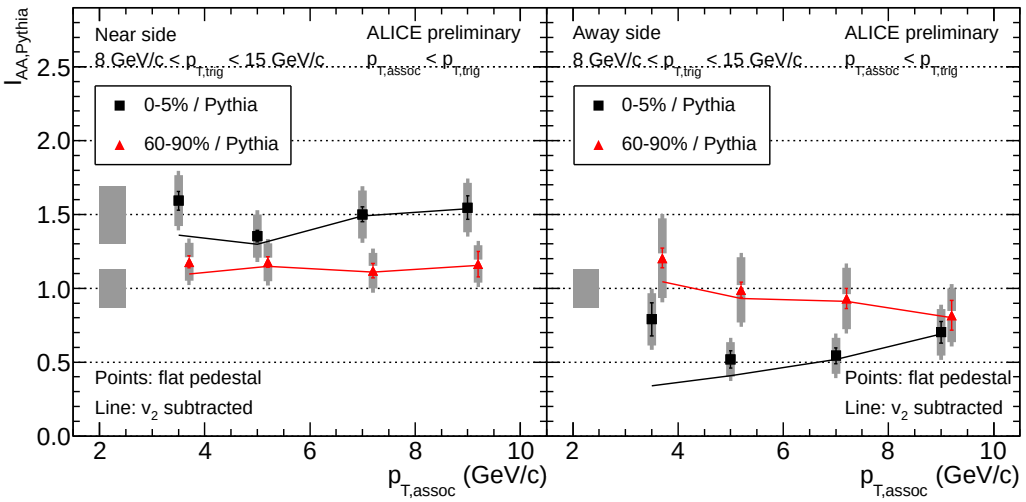

Figure 4: $I_{AA,Pythia}$: the data points are calculated with a flat pedestal; the line is based on v_2 subtracted yields.

that the away side is described well without applying an additional scaling. The scaling factor interpolated to the Pb-Pb energy of 2.76 TeV is then found to be $0.93 \pm 13\%$.

Yields extracted from Pythia 6.4 Perugia-0 with the mentioned scaling factor are used to measure $I_{AA,Pythia}$, shown in Fig. 4. As before the data points use the flat pedestal subtraction and the lines use the v_2 subtraction. The difference is rather small and only in the smallest $p_{T,\mathrm{assoc}}$ bins. $I_{AA,Pythia}$ in peripheral events is consistent with unity, but the near side is slightly higher than the away side. This could indicate a slightly different description of the near and away side in the MC. The qualitative behavior of $I_{AA,Pythia}$ in central events is consistent with I_{CP}. The away side is suppressed and the near side significantly enhanced. Such an enhancement has not been reported at lower energies. E.g. STAR measured a near-side I_{AA} consistent with unity[3].

Near-Side Enhancement A near-side enhancement at LHC was predicted albeit for larger $p_{T,\mathrm{trig}}$: an enhancement of $10-20\%$ is reported and attributed to the enhanced relative abundance of quarks w.r.t. gluons escaping the medium.[8] Gluons couple stronger to the medium due to their different color charge and their abundance is reduced. The quarks fragment harder and thus produce an enhanced associated yield. Furthermore, a near-side enhancement can be understood if one assumes that the near-side parton is also quenched. Then trigger particles with similar p_T stem from partons with higher p_T in Pb-Pb collisions than in pp collisions. Consequently, more energy is available for particle production on near and away side.

It should be stressed that a MC was used as a reference for $I_{AA,Pythia}$ and it will be interesting to study if I_{AA} using pp collisions shows the same behavior. Such a study is ongoing using newly taken data of pp collisions provided by the LHC in the week after this conference.

References

1. K. Aamodt *et al.* [ALICE Collaboration], Phys. Lett. **B696** (2011) 30-39.
2. A. Adare *et al.* [PHENIX Collaboration], Phys. Rev. Lett. **104** (2010) 252301.
3. J. Adams *et al.* [STAR Collaboration], Phys. Rev. Lett. **97** (2006) 162301.
4. K. Aamodt *et al.* [ALICE Collaboration], JINST **3** (2008) S08002.
5. K. Aamodt *et al.* [ALICE Collaboration], Phys. Rev. Lett. 105, 252302 (2010).
6. T. Sjöstrand, Comput. Phys. Commun. **82**, 74 (1994)
7. P.Z. Skands, arXiv:0905.3418[hep-ph] (2009).
8. T. Renk and K. J. Eskola, Phys. Rev. C **77** (2008) 044905.

Jet Reconstruction and Jet Quenching in Heavy Ion Collisions at ATLAS

Martin Spousta*
on behalf of the ATLAS Collaboration
* *Charles University in Prague, Institute of Particle and Nuclear Physics, V Holesovickach 2, 180 00 Prague 8, Czech republic*

We present a measurement of dijet asymmetry and dijet azimuthal correlations in Pb+Pb collisions at $\sqrt{s_{NN}} = 2.76$ TeV using the ATLAS detector. This measurement provides the first evidence of a strong jet quenching in relativistic heavy ion collisions at TeV energies. The jet reconstruction procedure is discussed as well as studies which have been performed to check that the observed asymmetry is not produced by detector effects and underlying event backgrounds.

1 Introduction

Ultra-relativistic heavy ion collisions are expected to produce hot and dense QCD matter. One of the main tools to study the production of such matter and its properties is a measurement of jets. Fast quarks or gluons produced in hard processes are expected to lose energy and/or have their parton shower modified in the medium of high color-charge density [1]. This may lead to a modification of jet yields and/or the structure of jets. Such an effect is called "jet quenching". The first indirect evidence for jet quenching has been observed by experiments at the Relativistic Heavy Ion Collider (RHIC) by measuring the spectra of fast hadrons or di-hadron azimuthal correlation [2,3]. Even if there are many phenomenological models aiming to describe the effect of the jet quenching, there is no unique understanding of mechanisms responsible for the in-medium jet modifications. LHC energies provide an opportunity to study fully reconstructed jets and their properties. In these proceedings we present a first observation of a possible jet modification measured using the ATLAS detector [4].

For this study, jets are defined using the anti-k_{T} clustering algorithm with the distance parameter $R = 0.4$. The inputs to this algorithm are "towers" of calorimeter cells of size $\Delta\eta \times \Delta\phi = 0.1 \times 0.1$ with the cell energies weighted using energy-density-dependent factors to correct for calorimeter non-compensation and other energy losses. Jet four-momenta are constructed by the vectorial addition of cell four-vectors which are assumed to be massless. The average contribution from the underlying event (UE) to the jet energy is subtracted from each jet candidate. The estimate of UE contribution is calculated independently for each event as a function of longitudinal calorimeter layer in bins of width $\Delta\eta = 0.1$ by averaging the transverse energy over the azimuth outside of jet regions of interest. Jet regions of interest are selected using a ratio of maximum tower energy to mean tower energy inside a jet which is required to be greater than 5. The value of this discriminant cut is based on simulation studies, and the results have been tested to be stable against variations in this parameter. The efficiency of the jet reconstruction algorithm, and other event properties, have been studied using PYTHIA [5] jet

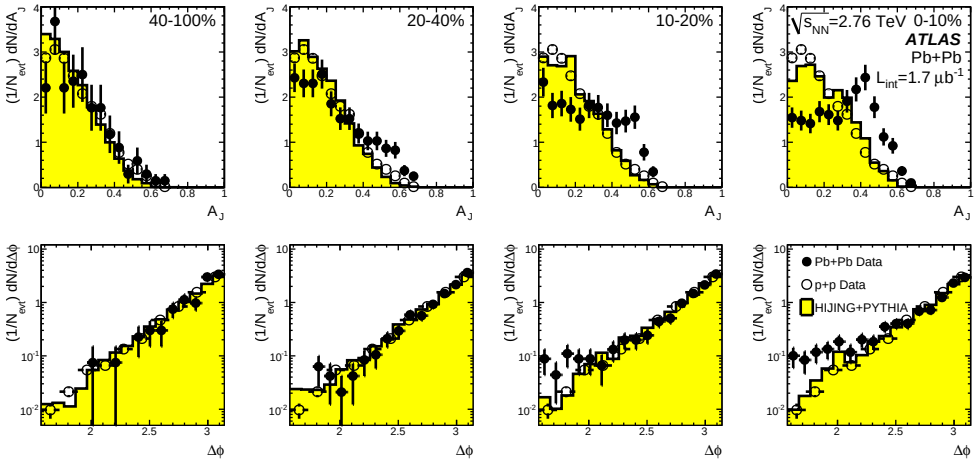

Figure 1: (top) Dijet asymmetry distributions for data (points) and unquenched HIJING with superimposed PYTHIA dijets (solid yellow histograms), as a function of collision centrality (left to right from peripheral to central events). Proton-proton data from $\sqrt{s} = 7$ TeV, analyzed with the same jet selection, is shown as open circles. (bottom) Distribution of $\Delta\phi$, the azimuthal angle between the two jets, for data and HIJING+PYTHIA, also as a function of centrality.

events superimposed on HIJING events [6].

2 Di-jet asymmetry and azimuthal correlation

The cross-section of dijet production is a dominant contribution to the total jet production cross-section. Jets are therefore most often produced in pairs well balanced in azimuth and transverse energy. Jet quenching may lead to an imbalance in the transverse energy since each jet, or initial parton, traverses a different path length in the QCD medium. Such an imbalance can be quantified using the asymmetry defined as $A_J = (E_{T,1} - E_{T,2})/(E_{T,1} + E_{T,2})$, where $E_{T,1} > E_{T,2}$ are transverse energies of jets in a dijet system. We focus on the balance between the highest transverse energy pair of jets in events. These jets are required to have an azimuthal angle separation, $\Delta\phi = |\phi_1 - \phi_2| > \pi/2$ to reduce contributions from multi-jet final states. Furthermore the first jet is required to have $E_{T,1} > 100$ GeV, and the second jet $E_{T,2} > 25$ GeV. The jet selection is chosen such that the first (leading) jet has high reconstruction efficiency and the second (sub-leading) jet is above the distribution of background fluctuations and soft jets associated with the collision. The jet selection criteria yield a sample of 1693 events from the 2010 Pb+Pb data corresponding to an integrated luminosity of approximately 1.7 μb^{-1}. The dijets are expected to have the asymmetry with a maximum near zero and rapidly decreasing towards the kinematic limit determined by the selected cuts which lies near the asymmetry of 0.7.

Figure 1 shows the result of the measurement, upper plots show the dijet asymmetry, lower plots show the dijet azimuthal correlations. The measurement is evaluated in four bins of collision centrality going from the most central (0-10%) to the most peripheral (40-100%). The centrality is defined using the total sum of transverse energy (ΣE_T) deposited in the forward calorimeters (FCal). The asymmetry distribution for dijets measured in p+p collisions at $\sqrt{s} = 7$ TeV is shown in open symbols in the upper plots of Fig. 1. The yellow distributions show the Monte Carlo (MC) reference which consists of fully reconstructed PYTHIA dijets embedded into the underlying event simulated by the HIJING MC generator. The presence of dijets with large asymmetries both in the reference samples and p+p data reflects the contribution from events with a topology of three or more jets, and the detector effects. Compared to the reference, the asymmetry measured in central heavy ion collisions exhibits the absence of the global maximum

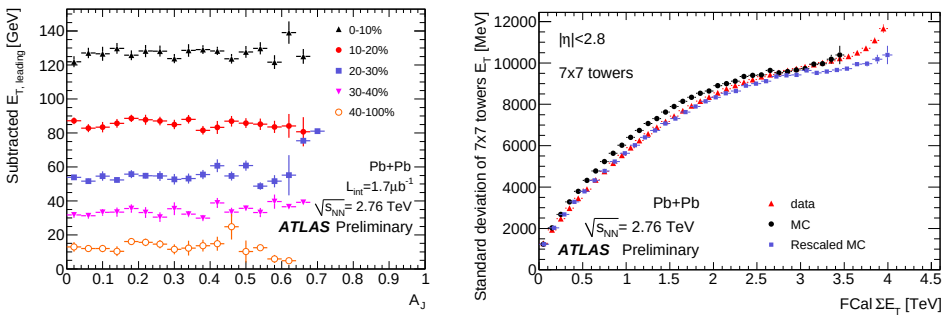

Figure 2: (left) Mean value of the UE E_T subtracted form the leading jet as a function of dijet asymmetry. (right) Mean standard deviation of transverse energy at electromagnetic scale in 0.7×0.7 windows (7×7 calorimeter towers) as a function centrality quantified using the FCal ΣE_T. The data (red) are compared to MC with (blue) and without (black) rescaling of the endpoint of the FCal ΣE_T MC distribution to the endpoint measured in data. The rescaling allows a direct comparison with the data which extend to larger FCal ΣE_T than the MC.

near zero and a rather flat plateau for asymmetries below ≈ 0.4. With decreasing centrality the asymmetry is getting smaller and it returns back to a good agreement with the reference p+p data and MC simulations. Simultaneously with the dijet asymmetry we measure the dijet azimuthal correlations which are presented in the lower plots of Fig. 1, again for different centrality bins. The measurement of dijet azimuthal correlations ensures that the effect clearly seen in central collisions does not come from correlated background fluctuations or detector effects. The back-to-back configuration of dijets persists even in the most central collisions.

Numerous studies have been performed to verify that the events with large asymmetry are not produced by backgrounds or detector effects. In the following section we will briefly discuss some of the studies performed to ensure the correctness of the obtained result.

3 Further cross-checks and measurement of the energy flow

One of the possible biases might come from the subtraction of the underlying event during the jet reconstruction. To check that the underlying event subtraction does not influence the measured asymmetry distribution we evaluate the amount of subtracted energy as a function of the dijet asymmetry. The result for the leading jet is shown in the left plot of Fig. 2. The size of the background subtraction does not change for jets with large asymmetry, neither for the leading nor for the sub-leading jet. To further test the reliability of the comparison of data with HIJING we compare the magnitude of the calorimeter fluctuations in the Minimum Bias reconstructed HIJING events with those in Pb+Pb events. The calorimeter fluctuations are quantified by the mean standard deviation of the non-calibrated transverse energy of towers grouped in "windows" of 7×7 towers. The 7×7 window approaches the size of an average jet defined using the anti-k_T algorithm with $R = 0.4$. The standard deviation is calculated event by event and the mean is evaluated in fine bins of centrality. The right plot of Fig. 2 shows the comparison of the mean standard deviation as a function of centrality for MC and data. As before, the centrality is defined using the total sum of transverse energy deposited in forward calorimeters. The 0-10% central events correspond to FCal ΣE_T greater than approximately 2.4 TeV. One can see a very good correspondence between the data and MC suggesting a good modeling of UE fluctuations and therefore appropriate modeling of the jet energy resolution.

One step further in understanding of the origin of the large dijet asymmetry is a measurement of the energy flow or momentum flow in the event. In this measurement, the transverse energy is summed over strips of size $\Delta\eta \times \Delta\phi = 0.8 \times 0.1$, centered at the pseudorapidity position of the leading jet or sub-leading jet. The dependence of the energy on the azimuthal angle

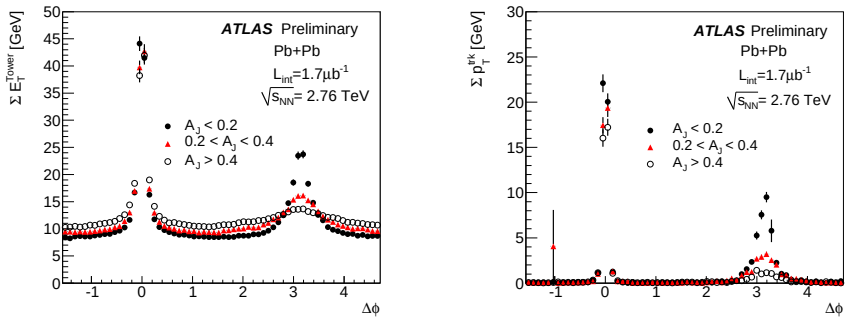

Figure 3: Energy flow measured using non-calibrated non-subtracted calorimeter towers (left) and tracks with $p_T > 4$ GeV (right). The transverse energy of towers or transverse momentum of tracks is summed over strips of size, $\Delta\eta \times \Delta\phi = 0.8 \times 0.1$, centered at the pseudorapidity position of the leading jet or sub-leading jet.

measured with respect to the leading jet strip provides a method for evaluating the jet characteristics without requiring per-event background subtraction. The transverse energy sum is also independent of the jet calibration which provides a further cross-check that the measurement is not an artifact of a bad calibration. The left plot of Fig. 3 shows the sum of the transverse energy for three bins in the measured jet asymmetry. The asymmetry is clearly visible even at the level of non-calibrated, non-subtracted towers. One can also see the overall offset of the distribution due to the UE event which is not subtracted. The offset of the distribution is larger for jets with larger asymmetries, since these occur in more central collisions. The similar measurement of the energy flow is performed using the charged particles measured in the Inner Detector as shown in the right plot of Fig 3. The threshold on minimum p_T of charged particles was selected to be 4 GeV in order to suppress tracks coming from UE. The result for charged particles is similar to that obtained from calorimeter towers. The offset due to the UE is not visible since the 4 GeV cut effectively suppresses the particles coming from the underlying event.

4 Conclusions

We observe a large dijet asymmetry in a sample of events with a reconstructed jet with transverse energy of 100 GeV or more. The asymmetry that is observed between the transverse energies of the leading and sub-leading jets increases with the centrality of the collisions. The measured dijets remain well correlated in azimuth. The result has been tested to exclude possible biases such as detector effects, jet energy scale and resolution, and background subtraction. The natural interpretation of the observation is a strong jet quenching present in central heavy ion collisions.

References

1. U. A. Wiedemann, arXiv:0908.2306
2. PHENIX Collaboration, K. Adcox et al., *Phys. Rev. Lett.* **88**, 022301 (2002)
3. STAR Collaboration, C. Adler et al., *Phys. Rev. Lett.* **90**, 082302 (2003)
4. ATLAS Collaboration, *Phys. Rev. Lett.* **105**, 252303 (2010)
5. T. Sjostrand, S. Mrenna, P. Z. Skands *JHEP* **0605**, 026 (2006)
6. X.-N. Wang, M. Gyulassy, *Phys. Rev.* D **44**, 3501 (1991)

Studies of Jet Quenching in HI Collisions at CMS

Frank Ma for the CMS Collaboration
Massachusetts Institute of Technology
Cambridge, Massachusetts 20139, USA

Jet production in PbPb collisions at a nucleon-nucleon center-of-mass energy of 2.76 TeV was studied using the CMS detector at the LHC, using a data sample corresponding to an integrated luminosity of 6.7 inverse microbarn. Dijets were reconstructed using the CMS calorimeters, and a significant energy imbalance was observed between the leading jet and the away-side jet with increasing centrality. Correlation studies of jets and tracks reveal that the energy of the away-side jet is redistributed to lower pt and wider angle outside of the jet cone.

1 Introduction

Heavy ion collisions at the Large Hadron Collider (LHC) allow one to study the thermodynamic properties of the fundamental theory of the strong interaction — Quantum Chromodynamics (QCD). Studying the modification of jets that are created from within the medium has long been proposed as a particularly useful tool for probing the QCD medium properties [1,2]. In the presence of a QCD medium, the partons may lose energy to the medium via elastic processes (collisional parton energy loss) or inelastic processes (radiative parton energy loss). The study of medium-induced modifications of dijet properties can therefore shed light on the transport properties of collective QCD matter created by heavy ion collisions.

2 Experimental Methods

This analysis was performed using the data collected in 2010 from PbPb collisions at a nucleon-nucleon center-of-mass energy of $\sqrt{s_{NN}} = 2.76$ TeV at the Compact Muon Solenoid (CMS) detector [3]. Jets were reconstructed with background subtraction based on their energy deposits in the CMS calorimeters [4], and the events were selected from a jet-triggered dataset [5].

Because heavy ions are extended objects, the impact parameter is an important characterization of the events. The amount of overlap between the two colliding nuclei is what we mean by "centrality" of the collision. In this analysis, centrality was determined from minimum events based on the total energy from both forward hadronic calorimeters [5]. Simulations can be used to correlate centrality, as quantified using the fraction of the total interaction cross section, with physically meaningful quantities such as the total number of nucleons in the two lead (^{208}Pb) nuclei which experienced at least one inelastic collision (N_{part}).

3 Results

3.1 Dijet Properties in pp and PbPb data

To obtain a clean dijet selection, we select events with a leading jet having corrected $p_{\mathrm{T},1} > 120$ GeV/c, a subleading jet with $p_{\mathrm{T},2} > 50$ GeV/c, and a minimum azimuthal angle between them ($\Delta\phi_{12} > 2\pi/3$). Only jets within $|\eta| < 2$ were considered. Given this selection, we observe a sharp $\Delta\phi_{12}$ correlation between leading and subleading jets [5] , indicating true dijet pairs.

In-medium induced parton energy loss can significantly alter the detector level jet energy (and hence dijet energy balance) by either transporting energy outside of the jet cone or shifting the energy towards low momentum particles that will not be detected in the calorimeter. To characterize the dijet momentum balance quantitatively, we use the asymmetry ratio,

$$A_J = \frac{p_{\mathrm{T},1} - p_{\mathrm{T},2}}{p_{\mathrm{T},1} + p_{\mathrm{T},2}} \ , \tag{1}$$

where p_T is the corrected p_T of the reconstructed calorimeter jet. The subscript 1 always refers to the leading jet, so that A_J is positive by construction.

In Fig. 1 (a), the A_J dijet asymmetry observable calculated by PYTHIA is compared to pp data at $\sqrt{s} = 7$ TeV. We see that data and event generator are found to be in excellent agreement, demonstrating that PYTHIA (at $\sqrt{s} = 2.76$ TeV) can serve as a good reference for the dijet imbalance analysis in PbPb collisions. Figs. 1 (b)-(f) show the centrality dependence of A_J for PbPb collisions. To separate effects due to the medium itself from effects simply due to reconstructing jets in the complicated environment of the underlying PbPb event, the reference PYTHIA dijet events were embedded into a minimum bias selection of PbPb events at the raw data level [5]. In contrast to PYTHIA+DATA, we see that data shows a dramatic decrease of balanced dijets with increasing centrality.

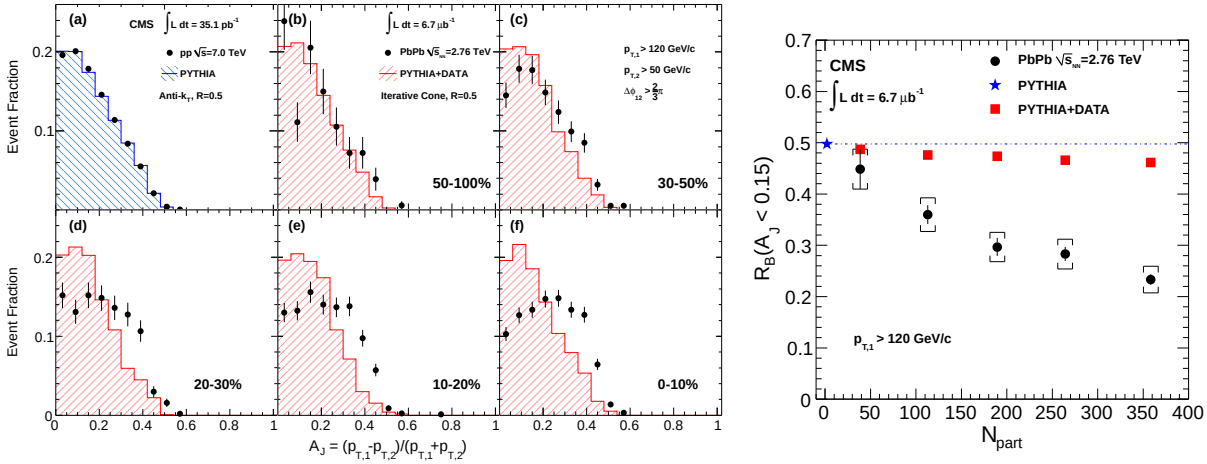

Figure 1: Left 6 panels show dijet asymmetry distribution, A_J, of selected dijets for 7 TeV pp collisions (a) and 2.76 TeV PbPb collisions in several centrality bins: (b) 50–100%, (c) 30–50%, (d) 20–30%, (e) 10–20% and (f) 0–10%. Data are shown as black points, while the histograms show (a) PYTHIA events and (b)-(f) PYTHIA events embedded into PbPb data. Right panel shows fraction of selected dijets with $A_J < 0.15$ out of all events with a leading jet with $p_{\mathrm{T},1} > 120$ GeV/c as a function of N_{part}. The result for reconstructed PYTHIA dijet events (blue filled star) is plotted at $N_{\mathrm{part}} = 2$. The other points (from left to right) correspond to centrality bins shown in (b)-(f) in the left 6 panels. The red squares are for reconstruction of PYTHIA+DATA events and the filled circles are for the PbPb data. For the data points, vertical bars and brackets represent the statistical and systematic uncertainties, respectively.

The centrality evolution of the dijet momentum balance can be explored more quantitatively by studying the fraction of balanced jets in the PbPb events. The balanced fraction, $R_B(A_J <$

0.15), is plotted as a function of collision centrality (in terms of $N_{\rm part}$) in the right panel of Fig. 1. It is defined as the fraction of all events with a leading jet having $p_{\rm T,1} > 120$ GeV/c for which a subleading partner with $A_J < 0.15$ and $\Delta\phi_{12} > 2\pi/3$ is found. The A_J threshold of 0.15 was chosen because it is the median of the A_J distribution for selected dijets in pure PYTHIA events. In contrast to PYTHIA+DATA dijets, the PbPb data show a rapid decrease in the fraction of balanced jets with collision centrality. The effect is much larger than the combined systematic uncertainties. These results imply a degradation of the parton energy, or jet quenching, in the medium produced in central PbPb collisions. The final systematic uncertainties, stemming mainly from uncertainties in the jet energy scale, are described in [5].

3.2 Overall Momentum balance of Dijet Events

We next turn to the question of where and how the medium energy loss occurs by exploiting additional information from the entire CMS tracker. We measure overall transverse momentum balance in the dijet events using the projection of missing p_T of reconstructed charged tracks onto the leading jet axis, defined as,

$$\not{p}_{\rm T}^{\parallel} = -\sum_{\rm i} p_{\rm T}^{\rm i} \cos\left(\phi_{\rm i} - \phi_{\text{Leading Jet}}\right), \tag{2}$$

where the sum is over all tracks with $p_T > 0.5$ GeV/c and $|\eta| < 2.4$. For this study, the leading and subleading jets are required to have a slightly smaller η range ($|\eta| < 1.6$) to allow the jets to remain fully inside the CMS tracker acceptance. No background subtraction in the track distribution is needed since the underlying PbPb tracks cancel in the $\not{p}_{\rm T}^{\parallel}$ sum.

In Fig. 2, $\langle \not{p}_{\rm T}^{\parallel} \rangle$ is shown as a function of A_J in the 0–30% centrality bin, where we expect the medium effects to be the strongest. Here A_J is the same calorimeter jet A_J as described in Sec. 3.1. The left column shows $\langle \not{p}_{\rm T}^{\parallel} \rangle$ using all selected tracks. One sees that in both data and simulation, the overall momentum balance of the events (shown as solid circles) is recovered within uncertainties even for dijets with large energy asymmetry. This cross-checks the soundness of the detector, since regardless of medium effects, net transverse momentum is conserved. The figure also shows the contributions to $\langle \not{p}_{\rm T}^{\parallel} \rangle$ for five transverse momentum ranges from 0.5–1 GeV/c to $p_T > 8$ GeV/c, shown as stacked histograms.

Important insights into the dijet asymmetry emerge when we look at the $\langle \not{p}_{\rm T}^{\parallel} \rangle$ differential in radial distance from the jets. The middle and right columns of Fig. 2 show $\langle \not{p}_{\rm T}^{\parallel} \rangle$ separately for tracks inside cones of size $\Delta R = 0.8$ around the leading and subleading jet axes, and for tracks outside of these cones. We see that for both data and MC an in-cone imbalance of $\langle \not{p}_{\rm T}^{\parallel} \rangle \approx -20$ GeV/c is found for the $A_J > 0.33$ selection. This shows that track momentum sums within the leading and subleading jet cones confirm the calorimeter dijet asymmetry results showed earlier in Sec. 3.1. In addition, both data and simulation show similar large negative contribution to $\langle \not{p}_{\rm T}^{\parallel} \rangle$ (i.e., in the direction of the leading jet) in the $p_T > 8$ GeV/c range. This cross-checks that the dijet energy asymmetry in data is not caused by fake jets from background fluctuation, because only genuine high p_T jets give rise to high p_T tracks. Looking now at the right column, we see that in both data and MC the in-cone energy difference is balanced by a corresponding out-of-cone imbalance of $\langle \not{p}_{\rm T}^{\parallel} \rangle \approx 20$ GeV/c. However, in the PbPb data the out-of-cone contribution is carried almost entirely by tracks with $0.5 < p_T < 4$ GeV/c whereas in MC more than 50% of the balance is carried by tracks with $p_T > 4$ GeV/c, with a negligible contribution from $p_T < 1$ GeV/c. The PYTHIA+HYDJET results are indicative of semi-hard initial or final-state radiation as the underlying cause for large A_J events in the MC study. This is in contrast to the results for large-A_J PbPb data, which show that a large part of the momentum balance is carried by soft particles ($p_T < 2$ GeV/c) and radiated at large angles to the jet axes ($\Delta R > 0.8$).

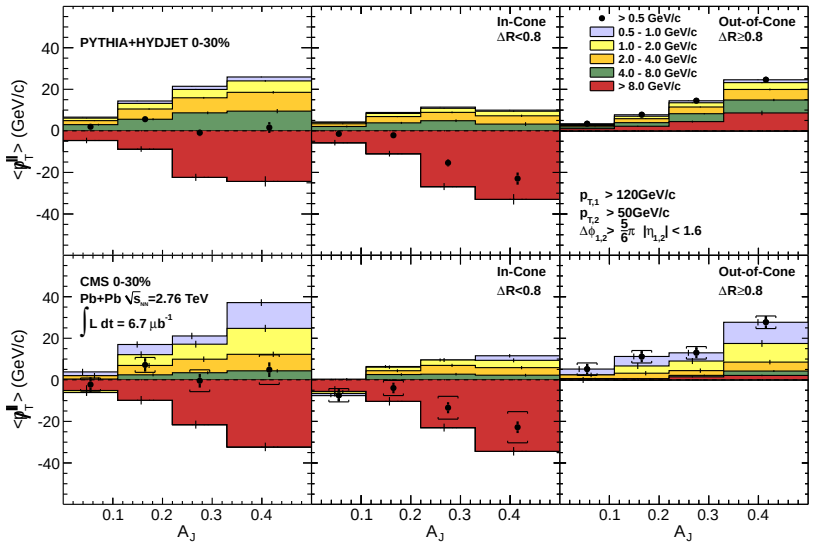

Figure 2: Average missing transverse momentum, $\langle \not{p}_{\mathrm{T}}^{\parallel} \rangle$, for tracks with $p_T > 0.5$ GeV/c, projected onto the leading jet axis (solid circles). The $\langle \not{p}_{\mathrm{T}}^{\parallel} \rangle$ values are shown as a function of dijet asymmetry A_J in 0–30% central events, for the full event (left), inside ($\Delta R < 0.8$) one of the leading or subleading jet cones (middle) and outside ($\Delta R > 0.8$) the leading and subleading jet cones (right). For the solid circles, vertical bars and brackets represent the statistical and systematic uncertainties, respectively. Colored bands show the contribution to $\langle \not{p}_{\mathrm{T}}^{\parallel} \rangle$ for five ranges of track p_T. The top and bottom rows show results for PYTHIA+HYDJET and PbPb data, respectively. For the individual p_T ranges, the statistical uncertainties are shown as vertical bars. Note that as the underlying PbPb event in both data and MC is not ϕ-symmetric on an event-by-event basis, the back-to-back requirement was tightened to $\Delta\phi_{12} > 5\pi/6$.

4 Summary and Conclusion

A strong increase in the fraction of highly unbalanced jets has been seen in central PbPb collisions compared with peripheral collisions and model calculations, consistent with a high degree of parton energy loss in the produced QCD medium. A large fraction of the momentum balance of these unbalanced jets is carried by low-$p_T$particles at large radial distance, in contrast to PYTHIA simulations embedded into heavy ion events. The results provide qualitative constraints on the nature of the jet modification in PbPb collisions and quantitative input to models of the transport properties of the medium created in these collisions.

References

1. D. A. Appel, "Jets as a probe of quark-gluon plasmas", *Phys. Rev.* **D33** (1986) 717. doi:10.1103/PhysRevD.33.717.
2. J. P. Blaizot and L. D. McLerran, "Jets in Expanding Quark - Gluon Plasmas", *Phys. Rev.* **D34** (1986) 2739. doi:10.1103/PhysRevD.34.2739.
3. CMS Collaboration, "The CMS experiment at the CERN LHC", *JINST* **3** (2008) S08004. doi:10.1088/1748-0221/3/08/S08004.
4. O. Kodolova, I. Vardanian, A. Nikitenko et al., "The performance of the jet identification and reconstruction in heavy ions collisions with CMS detector", *Eur. Phys. J.* **C50** (2007) 117. doi:10.1140/epjc/s10052-007-0223-9.
5. CMS Collaboration, "Observation and studies of jet quenching in PbPb collisions at nucleon-nucleon center-of-mass energy = 2.76 TeV", arXiv:1102.1957.

JET QUENCHING FROM RHIC TO LHC

B.G. ZAKHAROV
L.D. Landau Institute for Theoretical Physics, GSP-1, 117940,
Kosygina Str. 2, 117334 Moscow, Russia

We perform a joint analysis of the data from PHENIX at RHIC and ALICE at LHC on the nuclear modification factor R_{AA}. The computations are performed within the light-cone path integral approach to induced gluon emission. Our results show that slow variation of R_{AA} from RHIC to LHC energies indicates that the QCD coupling constant is suppressed in the quark-gluon plasma produced at LHC.

1. One of the most striking results of experiments at RHIC is strong suppression of high-p_T hadrons in AA-collisions [1] (called "jet quenching"). Recently, a similar effect has been observed in the ALICE experiment at LHC [2] for $Pb+Pb$ collisions at $\sqrt{s}=2.76$ TeV. The most natural reason for this phenomenon is parton energy loss (radiative and collisional) in the hot quark-gluon plasma (QGP) produced in the initial stage of AA-collisions. It is of great interest to perform a joint analysis of the RHIC and LHC data. It is interesting since variation of the nuclear modification factor R_{AA} from RHIC to LHC energies should not be very sensitive to the systematic theoretical uncertainties that are rather large. These uncertainties come mostly from multiple induced gluon emission. The available theoretical approaches to radiative induced gluon emission [3,4,5,6,7,8] are restricted to one gluon emission, and the multiple gluon emission is usually evaluated in the approximation of independent gluon radiation [9].

In this talk, I will present results of an analysis of the data on R_{AA} for $Au+Au$ collisions at $\sqrt{s}=200$ GeV from PHENIX [10] and for $Pb+Pb$ collisions at $\sqrt{s}=2.76$ TeV from ALICE [2]. The analysis is based on the light-cone path integral (LCPI) approach [4]. We evaluate the nuclear modification factor using the method developed in [11]. A major purpose of this analysis is to decide whether the variation of R_{AA} from RHIC to LHC indicates that the QCD coupling constant becomes smaller in the plasma produced at LHC, which is hotter than that at RHIC.

2. The nuclear modification factor R_{AA} for a given impact parameter b can be written as

$$R_{AA}(b)=\frac{dN(A+A\to h+X)/d\mathbf{p}_T dy}{T_{AA}(b)d\sigma(N+N\to h+X)/d\mathbf{p}_T dy}\,. \tag{1}$$

Here $\mathbf{p}_T$ is the hadron transverse momentum, y is rapidity (we consider the central region $y=0$), $T_{AA}(b)=\int d\boldsymbol{\rho}T_A(\boldsymbol{\rho})T_A(\boldsymbol{\rho}-\mathbf{b})$, T_A is the nucleus profile function. The differential yield for high-p_T hadron production in AA-collision can be written in the form

$$\frac{dN(A+A\to h+X)}{d\mathbf{p}_T dy}=\int d\boldsymbol{\rho}T_A(\boldsymbol{\rho})T_A(\boldsymbol{\rho}-\mathbf{b})\frac{d\sigma_m(N+N\to h+X)}{d\mathbf{p}_T dy}\,, \tag{2}$$

where $d\sigma_m(N+N\to h+X)/d\mathbf{p}_T dy$ is the medium-modified cross section for the $N+N\to h+X$ process. Similarly to the ordinary pQCD formula, we write it as

$$\frac{d\sigma_m(N+N\to h+X)}{d\mathbf{p}_T dy}=\sum_i\int_0^1\frac{dz}{z^2}D^m_{h/i}(z,Q)\frac{d\sigma(N+N\to i+X)}{d\mathbf{p}^i_T dy}\,. \tag{3}$$

Here $\mathbf{p}^i_T=\mathbf{p}_T/z$ is the parton transverse momentum, $d\sigma(N+N\to i+X)/d\mathbf{p}^i_T dy$ is the hard cross section, $D^m_{h/i}$ is the medium-modified fragmentation function (FF) for transition of a parton i into the observed hadron h. For the parton virtuality scale Q we take the parton transverse momentum p^i_T. We assume that hadronization occurs outside of the QGP. For jets with $E\lesssim 100$ GeV the hadronization scale, μ_h, is relatively small. Indeed, one can easily show that the L dependence of the parton virtuality reads $Q^2(L)\sim\max(Q/L,Q_0^2)$, where $Q_0\sim 1-2$ GeV is some minimal nonperturbative scale. For RHIC and LHC, when $\tau_{QGP}\sim R_A$ (τ_{QGP} is the typical lifetime/size of the QGP, R_A is the nucleus radius), it gives $\mu_h\sim Q_0$ (for $E\lesssim 100$ GeV). Then we can write

$$D^m_{h/i}(z,Q)\approx\int_z^1\frac{dz'}{z'}D_{h/j}(z/z',Q_0)D^m_{j/i}(z',Q_0,Q)\,, \tag{4}$$

where $D_{h/j}(z,Q_0)$ is the vacuum FF, and $D^m_{j/i}(z',Q_0,Q)$ is the medium-modified FF for transition of the initial parton i with virtuality Q to a parton j with virtuality Q_0. For partons with $E\lesssim 100$ GeV the typical length scale dominating the energy loss in the DGLAP stage is relatively small $\sim 0.3-1$ fm [11]. This length is of the order of the formation time of the QGP $\tau_0\sim 0.5$ fm. Since the induced radiation stage occurs at larger length scale $l\sim\tau_0\div\tau_{QGP}$, to the first approximation one can ignore the overlap of the DGLAP and induced radiation stages at all [11]. Then we can write

$$D^m_{j/i}(z,Q_0,Q)=\int_z^1\frac{dz'}{z'}D^{ind}_{j/l}(z/z',E_l)D^{DGLAP}_{l/i}(z',Q_0,Q)\,, \tag{5}$$

where $E_l=Qz'$, $D^{ind}_{j/l}$ is the induced radiation FF (it depends on the parton energy E, but not virtuality), and $D^{DGLAP}_{l/i}$ is the vacuum DGLAP FF.

We have computed the DGLAP FFs with the help of the PYTHIA event generator [12]. One gluon induced emission has been computed within the LCPI formalism [4] using the method elaborated in [13]. As in [13,11] we take $m_q=300$ and $m_g=400$ MeV for the quark and gluon quasiparticle masses. Our method of calculation of the in-medium FF via the one gluon probability distribution is described in detail in [11], and need not to be repeated here. We just enumerate its basic aspects. The multiple gluon emission is accounted for employing Landau's method as in [9]. For quarks the leakage of the probability to the unphysical region of $\Delta E>E$ is accounted for by renormalizing the FF. We also take into account the $q\to g$ FF. Its normalization is fixed from the momentum conservation for $q\to q$ and $q\to g$ transitions. The normalization of the $g\to g$ FF is also fixed from the momentum sum rule. The collisional energy loss, which is small [14], is taken into account by renormalizing the temperature of the QGP for the radiative FFs using the condition: $\Delta E_{rad}(T_0^{'})=\Delta E_{rad}(T_0)+\Delta E_{col}(T_0)$, where $\Delta E_{rad/col}$ is the radiative/collisional energy loss, T_0 is the real initial temperature of the QGP, and $T_0^{'}$ is the renormalized temperature.

We calculate the hard cross sections using the LO pQCD formula. To simulate the higher order K-factor we take for the virtuality scale in α_s the value cQ with $c=0.265$ as in the PYTHIA event generator [12]. We account for the nuclear modification of the parton densities (which leads to some small deviation of R_{AA} from unity even without parton energy loss) with the help of the EKS98 correction [15]. For the vacuum FFs we use the KKP parametrization [16].

As in [11], we evaluate the induced gluon emission and the collisional energy loss for the running α_s frozen at some value α_s^{fr} at low momenta. For vacuum a reasonable choice is $\alpha_s^{fr}\approx 0.7$.

This value was previously obtained by fitting the low-x proton structure function F_2 within the dipole BFKL equation [17]. To study the role of the in-medium suppression of α_s we perform the computations for several smaller values of α_s^{fr}.

3. We describe the QGP in the Bjorken model [18] which gives $T_0^3\tau_0 = T^3\tau$. We take $\tau_0 = 0.5$ fm. To simplify numerical computations for each impact parameter b we neglect variation of the initial temperature T_0 in the transverse directions. We evaluate its value using the entropy/multiplicity ratio $dS/dy\Big/dN_{ch}/d\eta \approx 7.67$ obtained in [19]. For the central $Au + Au$ collisions at $\sqrt{s} = 200$ GeV $T_0 \approx 300$ MeV and for $Pb+Pb$ collisions at $\sqrt{s} = 2.76$ TeV $T_0 \approx 400$ MeV. For the nuclear density we use the Woods-Saxon nucleus density with parameters as in [2]. The fast parton path length in the QGP, L, in the medium has been calculated according to the position of the hard reaction in the impact parameter plane. To take into account the fact that at times about $1-2$ units of R_A the transverse expansion should lead to fast cooling of the hot QCD matter [18] we also impose the condition $L < L_{max}$. We performed the computations for $L_{max} = 8$ and 10 fm. The difference between these two versions is small.

4. In Fig. 1 the theoretical R_{AA} obtained for $\alpha_s^{fr} = 0.7$, 0.6, and 0.5 for the chemically equilibrium and purely gluonic plasmas is compared to the PHENIX data [10] on π^0 production in the 0-5% central $Au+Au$ collisions at $\sqrt{s} = 200$ GeV. The results are presented for radiative energy

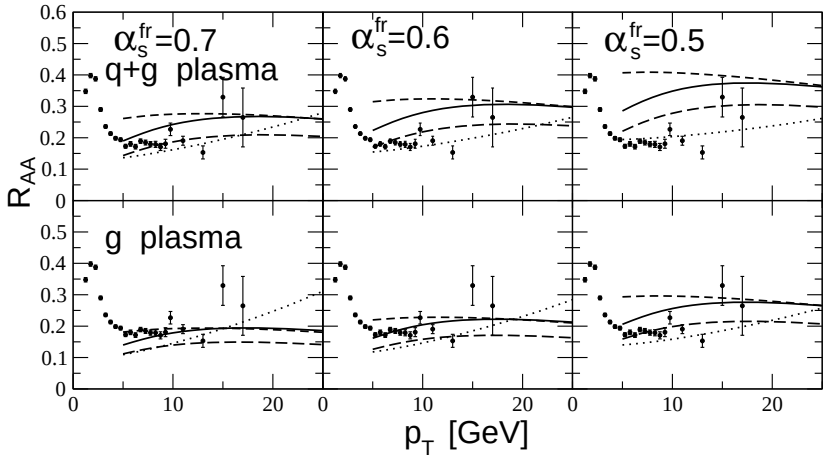

Figure 1: The factor R_{AA} for π^0 production in the 0-5% central $Au+Au$ collisions at $\sqrt{s} = 200$ GeV for $\alpha_s^{fr} = 0.7$, 0.6, and 0.5. The upper panels are for the chemically equilibrium plasma, and the lower ones for purely gluonic plasma. Solid line: the total radiative part (quarks plus gluons); dashed line: the radiative quark part; dotted line: the radiative gluon part; long-dash line: the radiative (quarks and gluons) plus collisional, and plus energy gain due to gluon absorption. The theoretical curves obtained for $L_{max} = 8$ fm. The experimental points are the PHENIX data [10].

loss and with inclusion of collisional energy loss and radiative energy gain. The effect of the radiative energy gain on R_{AA} is practically negligible and can be safely neglected. The growth of R_{AA} for gluons in Fig. 1 is due to the $q \to g$ transition which is usually neglected. However, it does not affect strongly the total R_{AA} since for $\sqrt{s} = 200$ GeV the gluon contribution to the hard cross section is small at $p_T \gtrsim 15$ GeV. In Fig. 2 we compare our results for $\alpha_s^{fr} = 0.7$, 0.5, and 0.4 with the ALICE data [2] for charged hadrons in $Pb + Pb$ collisions at $\sqrt{s} = 2.76$ TeV.

As can be seen from Figs. 1, 2, the collisional energy loss suppresses R_{AA} only by about 15-25%. For the equilibrium plasma the data for $\sqrt{s} = 200$ GeV can be described with $\alpha_s^{fr} \approx 0.6 \div 0.7$. The data for $\sqrt{s} = 2.76$ TeV agree better with $\alpha_s^{fr} \approx 0.4 \div 0.5$. It provides evidence for the thermal suppression of α_s at LHC due to higher temperature of the QGP.

5. In summary, we have analyzed the data on R_{AA} obtained in the PHENIX experiment on $Au + Au$ collisions at $\sqrt{s} = 200$ GeV [10] at RHIC and in the ALICE experiment on $Pb + Pb$

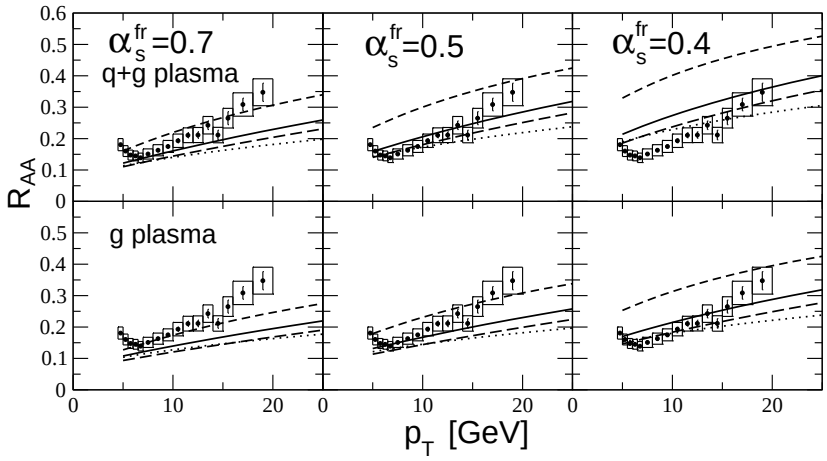

Figure 2: The same as in Fig. 1 for the charged hadrons in $Pb+Pb$ collisions at $\sqrt{s}=2.76$ TeV for $\alpha_s^{fr}=0.7$, 0.5 and 0.4. The experimental points are the ALICE data [2], as in [2] the boxes contain the systematic errors.

collisions at $\sqrt{s}=2.76$ TeV [2] at LHC. Our results show that slow variation of R_{AA} from RHIC to LHC supports that the QCD coupling constant becomes smaller in the hotter QGP at LHC.

Acknowledgments

I am grateful to the organizers for such an enjoyable and stimulating meeting and for financial support of my participation.

References

1. P.M. Jacobs, M. van Leeuwen, Nucl. Phys. A**774**, 237 (2006) and references therein.
2. K. Aamodt *et al.* [ALICE Collaboration], Phys. Lett. B**696**, 30 (2011).
3. R. Baier, Y.L. Dokshitzer, A.H. Mueller, S. Peigné, and D. Schiff, Nucl. Phys. B**483**, 291 (1997); *ibid.* B**484**, 265 (1997); R. Baier, Y.L. Dokshitzer, A.H. Mueller, and D. Schiff, Nucl. Phys. B**531**, 403 (1998).
4. B.G. Zakharov, JETP Lett. **63**, 952 (1996); *ibid* **65**, 615 (1997); **70**, 176 (1999); Phys. Atom. Nucl. **61**, 838 (1998).
5. R. Baier, D. Schiff, and B.G. Zakharov, Ann. Rev. Nucl. Part. **50**, 37 (2000).
6. U.A. Wiedemann, Nucl. Phys. A**690**, 731 (2001).
7. M. Gyulassy, P. Lévai, and I. Vitev, Nucl. Phys. B**594**, 371 (2001).
8. P. Arnold, G.D. Moore, and L.G. Yaffe, JHEP **0206**, 030 (2002).
9. R. Baier, Yu.L. Dokshitzer, A.H. Mueller, and D. Schiff, JHEP **0109**, 033 (2001).
10. A. Adare *et al.* [PHENIX Collaboration], Phys. Rev. Lett. **101**, 232301 (2008).
11. B.G. Zakharov, JETP Lett. **88**, 781 (2008) [arXiv:0811.0445 [hep-ph]].
12. T. Sjostrand, L. Lonnblad, S. Mrenna, and P. Skands, arXiv:hep-ph/0308153.
13. B.G. Zakharov, JETP Lett. **80**, 617 (2004) [arXiv:hep-ph/0410321].
14. B.G. Zakharov, JETP Lett. **86**, 444 (2007) [arXiv:0708.0816 [hep-ph]].
15. K.J. Eskola, V.J. Kolhinen, and C.A. Salgado, Eur. Phys. J. C**9**, 61 (1999).
16. B. A. Kniehl, G. Kramer, and B. Potter, Nucl. Phys. B**582**, 514 (2000).
17. N.N. Nikolaev and B.G. Zakharov, Phys. Lett. B**327**, 149 (1994).
18. J.D. Bjorken, Phys. Rev. D**27**, 140 (1983).
19. B. Müller and K. Rajagopal, Eur. Phys. J. C**43**, 15 (2005).

ELECTRICAL CONDUCTIVITY OF QUARK MATTER IN MAGNETIC FIELD

B. KERBIKOV
ITEP, Moscow, Russia

M. ANDREICHIKOV
MIPT–NBIC, Moscow, Russia

Fermion currents in dense quark matter embedded into magnetic field are under intense discussions motivated by Chiral Magnetic Effect. We argue that conductivity of quark matter may be independent of the magnetic field direction and not proportional to the magnetic field strength.

Magnetic field created by heavy ion currents at RHIC and LHC at the collision moment is huge, $|eB| \geq m_\pi^2 \sim 10^{18}$ G [1]. An intriguing effect observed by STAR collaboration and first reported at the XLIV-th Recontres de Moriond QCD [2] in the electric current induced in the direction of the magnetic field — Chiral Magnetic Effect [3]. The relaxation time of the magnetic field crucially depends on the quark matter electric conductivity [4]. It is clear that the problem of quark matter conductivity in magnetic field is an important albeit a complicated one. The approach to the problem which we briefly present below patterns on the method developed in condensed matter physics [5]. Kubo formula relates the conductivity to a two–point correlator of the current:

$$\sigma_{lm}(i\omega_k, \mathbf{q}) = \frac{e^2 T}{\omega_k} \mathrm{Tr} \sum_{\mathcal{E}, \mathbf{p}} G^M(\mathbf{p}, \tilde{\mathcal{E}}_n) \gamma^l G^M(\mathbf{p}+\mathbf{q}, \tilde{\mathcal{E}}_n + \omega_k) \gamma^m, \tag{1}$$

where Tr is taken over Dirac indices, color and flavour indices are omitted, G^M is the relativistic Matsubara propagator, $\tilde{\mathcal{E}}_n = \mathcal{E}_n + \frac{1}{2\tau} sgn(\mathcal{E}_n)$, $\mathcal{E}_n = \pi T(2n+1)$, τ is the momentum relaxation time. In the disordered system quark acquires the self–energy proportional to the inverse relaxation time τ on chaotically distributed scatterers. Depending on the averaging procedure of the correlator (1) over the disorder one obtains two different sets of diagrams giving two contributions to the conductivity, namely the Drude (Boltzmann) one σ_{cl} and the so–called quantum correction σ_q. Relation between the two is given by $\sigma_q \simeq (p_f l)^{-1} \sigma_{cl}$, where p_F is the Fermi momentum and l is the quark mean free path. The values of these parameters depend upon the location of the system on the QCD phase diagram in the (T, μ) coordinates. As an example, we take the quark chemical potential $\mu \simeq 0.4$ GeV, consider chiral quarks $p_F \simeq \mu$, and $l \simeq 0.5 \div 1$ fm. Then $\sigma_q \geq 0.5 \sigma_{cl}$ and the term "correction" used in condensed matter physics is no more meaningful. Omitting the derivation we present the resulting expression for the frequency dependent conductivity:

$$\sigma(\omega) = \sigma_{cl} + \sigma_q = \frac{ne^2}{m} \frac{\tau}{1+\omega\tau} - \frac{2\mathcal{D}e^2}{\pi} \int \frac{\mathrm{d}^3\mathbf{q}}{(2\pi)^3} \frac{1}{-i\omega + \mathcal{D}\mathbf{q}^2} \tag{2}$$

Here $\mathcal{D}$ is the diffusion coefficient and the appearance of the slow diffusion mode is an important feature of the quantum conductivity. The first term is the Drude conductivity. Similar structure of the conductivity emerges in the hydrodynamic approach to strongly coupled CFT [6]. Our interest here is σ_q. The negative sign reflects the fact that due to quantum interference the probability of quark returns increases, at $(p_F l) > 1$ the system undergoes Anderson transition and becomes an insulator [7]. One may view quantum conductivity as being originated by the presence of a fictitious spin–zero particle with a charge $2e$ and a mass $1/2\mathcal{D}$. The simplest model of this particle would be a fluctuating Cooper pair. The fact that the effective charge carrier is a scalar particle is at the core of the unusual behaviour of quantum conductivity in magnetic field. To introduce the magnetic field we choose the gauge $A_x = 0$, $A_y = Bx$, $A_z = 0$, so that $\mathbf{B}$ is directed along the z–axis. There are three characteristic length scales in the problem: the mean free path l, the magnetic length $l_B = (eB)^{-1/2}$, and the phase–randomizing length $l_\varphi = (2\mathcal{D}\tau_\varphi)^{1/2}$, where τ_φ is the phase–breaking time due to inelastic processes. We assume that $l_\varphi \gg l$ which is a questionable supposition for the quark matter. Returning to (2), we may say that the characteristic momentum scale for σ_{cl} is $p > 1/l$, while for σ_q it is $p < 1/l$. In magnetic field and with phase–breaking interaction the denominator $(-i\omega + \mathcal{D}\mathbf{q}^2)$ in (2) is substituted by $\left[-i\omega + \mathcal{D}q_z^2 + \Omega(n + \frac{1}{2}) + \tau_\varphi^{-1}\right]$, with $\Omega = 4eB\mathcal{D}$, n numerates Landau levels. Integration over p_y, making use of the completeness of the Landau wave functions and integrating over $|p_z| < 1/l$, we obtain:

$$\sigma_q = -\frac{e^2}{\pi^3 l_B} \sum_{n=0}^{n_{\max}} \frac{1}{\sqrt{n + \frac{1}{2} + \delta}} \arctan\left(\frac{l_B}{2l\sqrt{n + \frac{1}{2} + \delta}}\right), \tag{3}$$

where $n_{\max} = l_B^2/l^2$, $\delta = l_B^2/l_\varphi^2$. Truncation of the sum over the Landau levels at $n_{\max}$ corresponds to the condition $p < 1/l$ formulated above. When $n_{\max} \gg 1$ (weak field) we may substitute summation by integration and obtain:

$$\sigma_q = -\frac{e^2}{\pi^2}\left(\frac{1}{l} - \frac{1}{l_\varphi}\right). \tag{4}$$

This means that for $l_B \gg l_\varphi \gg l$ quantum conductivity does not feel the magnetic field. For $l \simeq 1$ fm, $\tau_\varphi \sim 4\tau$ this corresponds to $|eB| \ll 1 \cdot 10^4$ MeV^2, i.e. magnetic field at RHIC $|eB| \sim m_\pi^2 \sim 2 \cdot 10^4$ MeV^2 is not to strong in the above sense.

Let us denote σ_q in this "weak" field limit by $\sigma_q^<$ and for stronger field by $\sigma_q^>$. It may be shown that $|\sigma_q^>| < |\sigma_q^<|$ and

$$\sigma_q^> - \sigma_q^< \sim l_B^{-1} \sim \sqrt{eB}. \tag{5}$$

Summarizing we may say that:

(i) quantum contribution is an important part of quark matter conductivity;

(ii) it makes the total conductivity smaller;

(iii) it only weakly depends on the magnetic field and does not depend on the field direction.

Our final remark is that due to Lorentz contraction ultra–relativistic ions are effectively two–dimensional objects. In two–dimensional systems σ_q logarithmically diverges at $\omega \to 0$.

Acknowledgments

One of the authors (B.K.) gratefully aknowledges support from the RFBR grants 10-0209311–NTSNIL-a, 11-02-08030-z and from the organizers of the Recontres de Moriond. This work was partly done during INT workshop "Fermions from Cold Atoms to Neutron Stars".

References

1. D.E. Kharzeev, L.D. McLellan and H.J. Waringa, *Nucl. Phys.* A **803**, 227 (2008); V. Skokov, A. Illarionov and V. Toneev, *Int. J. Mod. Phys.* A **24**, 5925 (2009).
2. H. Caines, in *Proceedings of the XLIV-th Recontres de Moriond QCD*, p. 375 (ed. E. Auge, J. Dumarchez, B. Pietrzyk and Jean TranThanh, Van, The Gioi Publihers, 2009).
3. D.E. Kharzeev, L.D. McLellan and H.J. Warringa, *Nucl. Phys.* A **803**, 227 (2008); D.E. Kharzeev and H.J. Warringa, *Phys. Rev.* D **80**, 034028 (2009).
4. K. Tuchin, *Phys. Rev.* C **82**, 034904 (2010).
5. L.P. Gorkov, A.I. Larkin and D.E. Khmelnitskii, *JETP Letters* **30**, 228 (1979).
6. Subir Sachdev, *Condensed matter and AdS/CFT*, arXiv:1002.2947.
7. B. Kerbikov and E.V. Lushevskaya, *Phys. Atom. Nucl.* **71**, 364 (2008).

The effect of triangular flow in jet-medium interaction

Chin-Hao Chen for the PHENIX Collaboration
Department of Physics and Astronomy, Stony Brook University,, Stony Brook, New York, United States, 11790-3800

When jets pass through the hot dense QCD medium created in heavy ion collisions, some exotic structures are observed. There is enhancement of jet-associated particle yields in the η direction along trigger jets, known as 'the ridge'. A double peak structure referred to as 'the shoulder'. One possible explanation for the ridge and shoulder is triangular flow or v_3. We present the two particle $\Delta\eta$-$\Delta\phi$ correlations at PHENIX. By analyzing the Fourier spectra of the correlation function, we find significant enhancement in the third moment in central Au+Au collisions. We also measured v_3 directly, which enables us to study how v_3 affects unfolding the jet signal from the background.

When two heavy ions collide relativistically, a hot dense QCD matter is created in the colliding area, which is known as the quark-gluon plasma (QGP). This new type of matter has several interesting properties. A significant energy loss has been observed for fast partons traversing the QCD medium [1]. This matter also has strong collective motion, which is quantified as v_2 [2].

When two nuclei collide, the colliding area has an almond-like shape. We can extract the anisotropy, v_n, by measuring the azimuthal distribution of particles with respect to the event plane, ψ_n, as Eq. 1

$$\frac{dN}{d\phi} \propto (1 + \Sigma 2 v_n \cos n(\phi - \psi_n)), \tag{1}$$

where v_n is the nth order Fourier coefficient, and ψ_n is the nth order event plane. If the two nuclei are perfectly spherical, then all the v_{odd} term will be zero due to the azimuthal symmetry. In reality, the Au nuclear is not a perfect sphere, therefore the colliding area is no longer a perfect almond. In this case, since the azimuthal symmetry is broken, there should be non-zero v_{odd} [3].

If there is a non-zero v_3 in heavy ion collisions, one of the immediate possible applications is in two-particle azimuthal correlations. The two particle azimuthal correlations measure the relative azimuthal angle distribution between the trigger and associated particles. Previously, in order to study the jet shape, the underlying v_2 modulated background has been subtracted from correlation functions. This background, FL($\Delta\phi$), is described by Eq. 2, where b_0 is the level of the underlying event, and v_2^{trig} and v_2^{assoc} are the v_2 of the trigger and associated particles respectively.

$$FL(\Delta\phi) = b_0(1 + 2 v_2^{trig} v_2^{assoc} \cos 2\Delta\phi) \tag{2}$$

In p+p collisions, in which there is no medium, we see a back to back di-jet structure which peaks at $\Delta\phi \approx 0$ (same side) and π (away-side). In Au+Au collisions, after the underlying event described by Eq. 2 has been subtracted, the shape of the jet is significantly modified. In the away-side there is a double-peak structure where there are two peaks sitting at $\Delta\phi \approx \pi \pm 1$. At $\Delta\phi \approx \pi$, there is a local minimum instead of a peak. This double-peak structure is known as 'shoulder' [5,6,7]. In the near-side, the peak at $\Delta\phi = 0$ remains, but with an enhancement along the $\Delta\eta$ direction known as the 'ridge'[8,9]. Since v_3, which is the coefficient of $\cos 3\Delta\phi$, peaks at 0, $\pi/3$ and $2\pi/3$, it is a natural candidate to explain the ridge and shoulder structure.

In order to answer if v_3 can fully explain these structures, we need to have direct measurement of v_3. The PHENIX experiment at Relativistic Heavy Ion Collider in Brookhaven National Laboratory has measured the v_2, v_3 and v_4 with two different methods, the event plane method and the two-particle correlation method. For the event plane method, PHENIX uses several forward detectors such as the Reaction Plane Detector (RXN, $1.0 < |\eta| < 2.8$), Muon Piston Calorimeter (MPC, $3.1 < |\eta| < 3.7$) and Beam Beam Counter (BBC, $3.1 < |\eta| < 3.9$) to reconstruct the nth event plane, ψ_n. We then measured the particle distribution along with ψ_n, and extract v_n according to Eq. 1. The v_2, v_3 and v_4 are measured as a function of particle p_T and centrality and are shown in Fig. 1. Fig. 1 shows that there is a non-zero v_3 which exists in all centralities. v_3 increases with p_T but does not have a strong centrality dependence. In previous PHENIX meausrements [2], we published the results of v_4 measured with respect to ψ_2. The v_4 shown here is measured with respect to ψ_4, which should maximize the v_4 value. The value here ($v_4\{\psi_4\}$) is significantly large than ($v_4\{\psi_2\}$) [2].

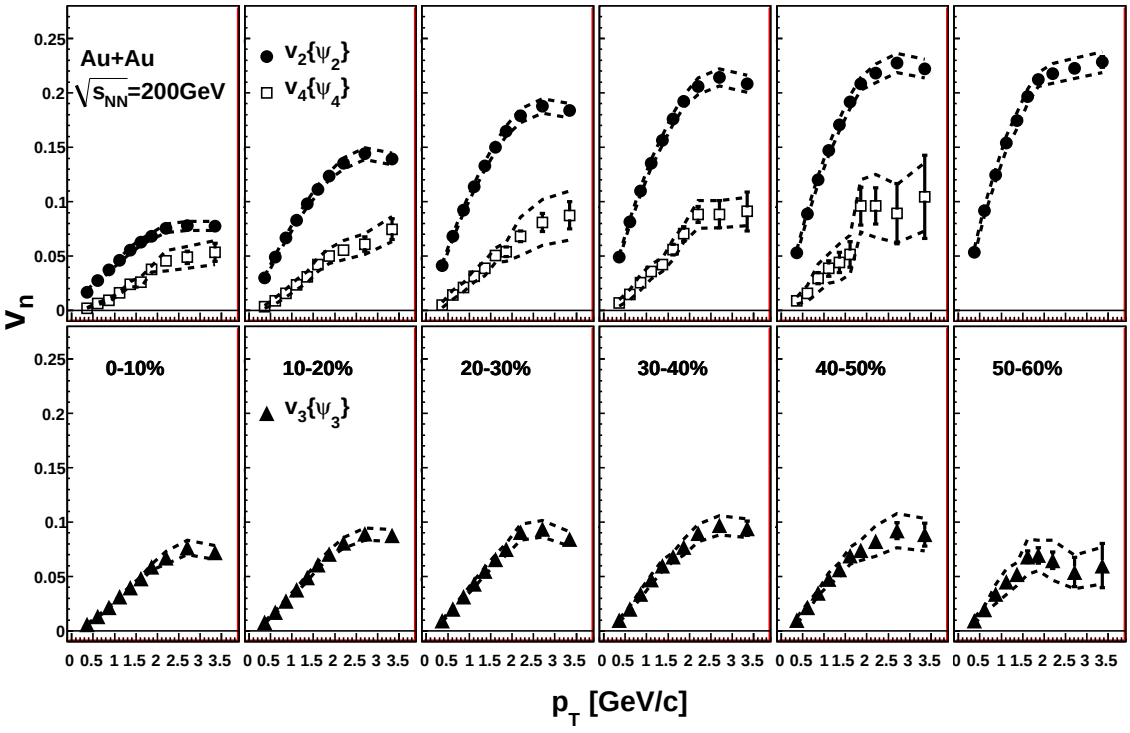

Figure 1: v_n measured with event plane method in various centralities.

The second method we used to measure v_n is via the two particle correlations. The two particle azimuthal correlation can be expanded as a Fourier series as Eq. 3, where $c_n = v_n^{trig}(p_T^{trig})v_n^{assoc}(p_T^{assoc})$

$$CF(\Delta\phi) \propto (1 + \Sigma 2c_n \cos n(\Delta\phi)) \tag{3}$$

When both trigger and associated particles are in the same p_T bin, $v_n = \sqrt{c_n}$. In PHENIX, we use both trigger and partner particles detected by the central arm ($|\eta| < 0.35$). In order to reduce the jet contribution while still keeping enough signal, we require the η difference between the two particles to be $0.3 < |\Delta\eta| < 0.7$. The result, $v_3\{2P\}$, is compared with the event plane method and is shown in Fig. 2. The v_3 from both methods agrees very well. But $v_3\{2P\}$ is generally larger than $v_3\{\psi_3\}$.This difference is likely due to some residual jet contribution in the two particle correlation method, which makes the measured v_3 larger than the event plane method.

We also compared these results with hydrodynamical predictions with Glauber initial state distribution and $\eta/s = 0.08$ [10]. The prediction agrees well with the data, which indicates that v_3, just like v_2, can be well described by viscous hydrodynamical calculations.

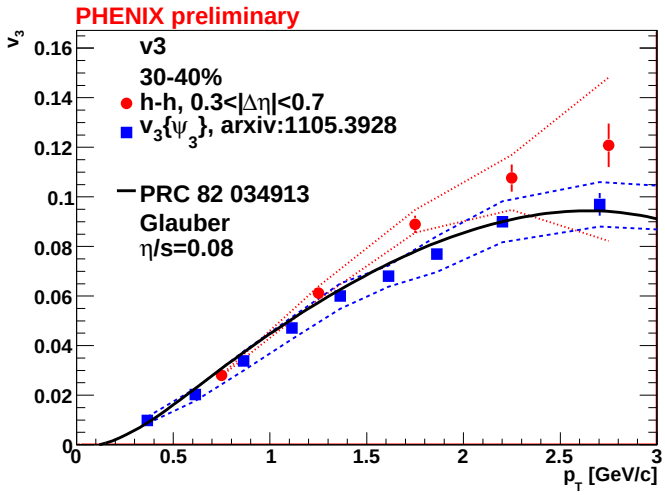

Figure 2: v_3 measured in event plane method and two particle correlation methods comparing with predictions.

One of the most important questions in two particle correlations is whether the ridge and shoulder can be described by v_3. In order to study this, we study the jet function from Au+Au with the underlying event shape described by Eq. 2 removed. With the v_2 only background removed, the jet function shows a clear ridge and shoulder structure. We expand the jet function into a Fourier series via Eq. 4

$$JF(\Delta\phi) = \Sigma C_n \cos n(\Delta\phi) \tag{4}$$

In order to compare with Au+Au jet functions, we use two p+p baseline jet functions. First we consider the case of an unmodified jet, which is simply the p+p jet itself. Second we consider the extreme case of a fully quenched away-side jet, which can be represented by manually setting the away-side p+p jet to zero. If the Fourier spectra of Au+Au is beyond these two baseline, then it indicates there is some possible jet-medium interaction happening.

Fig. 3 shows the Fourier spectra of the jet function from Au+Au in 4 different centralities. The result is compared with the two baseline p+p references. If we look at the two p+p baselines only, we see that for the n=0 term, which is equivalent to the total yield summed over $\Delta\phi$ from 0 to 2π, the unmodified p+p case is higher than the fully quenched p+p case. When looking at the n=3 term, we see, even without the existence of the medium, simply quenching the away-side jet increases the contribution of the third harmonic.

For the most central Au+Au case, 0-20%, the C_0 term in Au+Au is significantly larger than p+p, which is due to the existence of the ridge and shoulder. For the C_1 and C_2 term, the Au+Au point is roughly between the two p+p references. For the C_3 term, we see that Au+Au

is significantly larger than both p+p cases, which is not surprising due to the clear ridge and shoulder structure. This enhancement is much larger than simply quenching the away-side jet can provide, which means there must be some other source which contributes to this strong enhancement. At the current stage, we do not know what the main sources for this enhancement is. Also notable is that the C_4 term seems to have some excess compared to p+p.

In conclusion, PHENIX has measured the higher harmonics, v_2, v_3 and v_4 in various centrality and p_T combinations with two different methods. The measured v_3 is described well by hydrodynamical calculations. When studying the Fourier spectra of the jet functions (with v_2 shape background subtracted) in Au+Au compared to p+p, we see that the third harmonic, C_3, is significantly larger in Au+Au, which indicates some source other than the jet contributes to this anomalous enhancement.

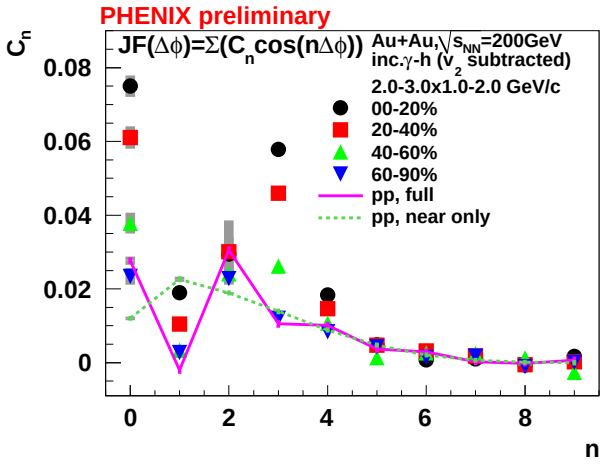

Figure 3: Fourier spectra of Au+Au jet functions in different centralities and compare with p+p.

References

1. A. Adare *et al*, *Phys. Rev. Lett.* **101**, 232301 (2008).
2. A. Adare *et al*, *Phys. Rev. Lett.* **105**, 062301 (2010).
3. B. Alver and G. Roland, *Phys. Rev.* C **81**, 054905 (2010).
4. A. Adare *et al*, arXiv:1105.3928.
5. S. S. Adler *et al*, *Phys. Rev. Lett.* **97**, 052301 (2006).
6. A. Adare *et al*, *Phys. Rev. Lett.* **98**, 232302 (2007).
7. A. Adare *et al*, *Phys. Rev.* C **78**, 014901 (2008).
8. B. I. Abelev *et al*, *Phys. Rev.* C **80**, 064912 (2010).
9. B. I. Abelev *et al*, *Phys. Rev. Lett.* **104**, 062301 (2010).
10. B. Alver *et al*, *Phys. Rev.* C **82**, 034913 (2010).

The first Z boson measurement in the dimuon channel in PbPb collisions at $\sqrt{s} = 2.76$ TeV at CMS

Lamia Benhabib

On behalf of CMS collaboration

We present the first measurement of Z bosons in the di-muon channel in Pb-Pb collisions at $\sqrt{s_{NN}} = 2.76$ TeV made by the CMS experiment at the LHC, establishing that no modification is observed with respect to next-to-leading order pQCD calculations, scaled by the number of binary collisions. Using a $7.2\mu\text{b}^{-1}$ data sample, we report on the 39 Z candidates counted in the di-muon 60-120 GeV/c^2 invariant mass window, and we detail the Z yield as a function of rapidity (y), transverse momentum (p_T) and centrality. The results are compared to and agree with theoretical predictions within statistical and systematic uncertainties.

1 Introduction

The W and Z bosons were first observed by the UA1 and UA2 experiments at CERN nearly thirty years ago in proton-antiproton collisions at $\sqrt{s} = 540$ GeV [1]. Since then, their properties have been characterized in detail by a succession of collider experiments. Today their known properties such as their mass and their width (as well as their inclusive and differential cross sections) have been well–measured at different center-of-mass energies. The LHC offers the opportunity to study W and Z boson production in nucleus-nucleus collisions, due to the large center-of-mass energy and the expansive capabilities of the multipurpose LHC detectors, *i.e.* CMS and ATLAS. We now embark on a program of probing the hot dense medium known as the quark gluon plasma, (QGP) created in heavy ion collisions, via the di-leptons decay of the weakly–interacting gauge bosons, Z and W. In this paper, we will focus on measurements of the Z boson through its decay to dimuons – a channel of particular interest since the charged leptons pass freely through the medium being probed, regardless of its nature (be it partonic or hadronic) or its properties. Therefore, dileptons from Z bosons can serve as a reference to the processes expected to be heavily modified in the QGP, such as quarkonia production, or the production of an opposite-side jet in Z+jet processes [2]. However, in AA collisions, Z boson production can be affected by various initial-state effects. This modification is expected to be about 3% for the isospin effect [3], and for energy loss and multiple scattering of the initial partons [4]. In addition, shadowing is expected to modify the Z boson yield by less than 20% [3]. Those estimations are predicted by theory and are compared to our measurement performed with a 55 million minimum bias (MB) event sample registered from PbPb collisions at $\sqrt{s} =$ 2.76 TeV, corresponding to an integrated luminosity of 7.2 mb^{-1}.

2 CMS and data taking

CMS [5] is a general purpose apparatus with a silicon tracker detector, a lead tungstate crystal electromagnetic calorimeter (ECAL) and a brass scintillator hadron calorimeter (HCAL) enclosed in a 3.8 T solenoidal magnetic field. The magnet is surrounded by an instrumented iron return yoke which uses gaseous detectors made of three technologies: Drift Tubes (DT), Cathode Strip Chambers (CSC), and Resistive Plate Chambers (RPC). In addition, CMS has forward calorimeters which cover the pseudo–rapidity range $2.9 < |\eta| < 5.2$ and allows for triggering on PbPb collisions. The expected cross section for hadronic inelastic collisions is 7.65 barns, while ultraperipheral collisions (UPC) with large impact parameters lead to the breakup of one, or both, Pb nuclei with a much larger probability. Collisions in which the Pb nuclei interact hadronically and can produce anywhere from just a few up to about 1600 particles per unit pseudorapidity, depending on the impact parameter. As a result, more than 97% of these collisions produce double-sided (coincident) trigger signals in the BSC (Beam Scintillator Counters), and in the hadronic forward (HF) calorimeters. About 55 million minimum bias events have been recorded, and a dedicated muon trigger has been used in this analysis. At the hardware level (L1), two muon candidates in the muon spectrometer are required; at the software-based higher-level (HLT), two reconstructed tracks in the muon detectors are required with p_T of at least 3 GeV/c each. In order to study the dimuon trigger efficiency, events are also collected with a single-muon trigger, requiring $p_T > 20$ GeV/c.

3 Signal extraction

The muon reconstruction in PbPb collisions with CMS is similar to the one used in *pp* collisions described in [6]. We can distinguish two types of reconstructed muons: Stand Alone muons (STA), reconstructed using information only from muon stations, and Global muons, reconstructed by matching heavy-ion reconstructed tracks to muon station tracks. The latter are measured with high resolution, (1-2% for p_T up to 100 GeV/c) even in the high–multiplicity environment of heavy ion collisions. In this analysis, the muon is required to be found with both algorithms – a good consistency between tracker and muon detector measurements is essential to reduce the contamination from muons produced by decays–in–flight of hadrons, from punch–through pions and accidental matches due to noise, or due to background tracks or segments. The muons used to construct the Z bosons are restricted to the pseudo-rapidity range $\eta \in [-2.4, 2.4]$ and with the requirement $p_T > 10$ GeV/c, this removes only about 1% of the generated Z bosons, and renders insignificant any trigger turn–on effects. In addition to those kinematic cuts, the global muon must have at least one valid hit in the muon chamber and greater than 10 hits in the inner tracker. In order to select good quality muons with high efficiency and reduce fake-rates, the following selection cuts have been chosen:

- χ^2/ ndf <10 for the global fit (to remove fake tracks from real data)
- cut on the longitudinal impact parameter of the inner track with respect to the primary vertex $|dz_{prim\ vtx}| < 1.5$ mm
- χ^2 / ndf < 4.0 for the inner tracker

The resulting spectrum for the invariant mass of the two muons is shown in figure 1 (right), superimposed to the corresponding distribution measured in *pp* collisions at 7 TeV. In figure 1 (left) an event display of one of the first Z $\rightarrow \mu^+ \mu^-$ observed by the CMS experiment.

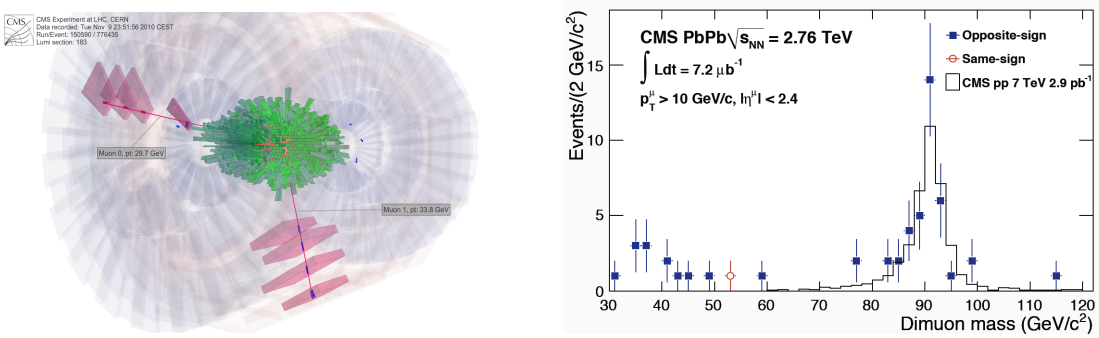

Figure 1: Dimuon invariant mass spectra. Full squares are opposite-sign dimuons, while the empty circle shows a unique like-sign dimuon candidate. The histogram shows the corresponding distribution measured in pp collisions at 7 TeV within 60-120 GeV/c^2, scaled to the 39 PbPb candidates.

4 Correction factors

In order to estimate the Z corrected spectrum, one can typically divide the measured one by the acceptance x efficiency, the latter being the product of trigger, identification and reconstruction efficiency. The corrections are computed directly from PYTHIA [7]-simulation by generating Z distribution in p_T and y embedded in real data. We estimated separately those various contributions : the acceptance (78%), the trigger efficiency (94%) , the reconstruction efficiency (72%) and the identification efficiency (98%). For those efficiencies, we compare different techniques systematically. The final corrections are based on peak counting from Z signal embedded in data. This overall method is in the same spirit of the one used for the p+p [8], in which there was twice the statistics. The most significant systematic uncertainty is estimated to be 9.8% and is driven by the tracking efficiency, followed by the uncertainty on dimuon trigger efficiency (4.5%) and then by the un-subtracted background (4%). The uncertainty associated with the selection criteria is considered to be equal to the 2.6% loss of events. The MB trigger efficiency as well as the uncertainties coming from the acceptance correction are around 3%. Other contributions for systematic uncertainties are estimated to sum to less than 1.5%. By summing in quadrature those contributions, we obtain a total systematic uncertainties of 13%.

5 Results

We then calculate the yield of $Z \to \mu^+ \mu^-$ per minimum bias event,

$$\frac{dN}{dy} = \frac{N}{\alpha \, \epsilon \, N_{MB} \, \Delta y} \tag{1}$$

where $N = 39$ is the number of measured Z candidates counted in a mass window of $60 - 120$ GeV/c^2, $N_{MB} = 55 \times 10^6$ is the number of corresponding minimum bias events, α and ϵ are the acceptance and the overall efficiency corrections mentioned above, and $\Delta y = 4.0$ is the rapidity bin width. We find a yield per event of $dN/dy(|y| < 2.0) = (33.8 \pm 5.5 \pm 3.4) \times 10^{-8}$, where the first uncertainty is statistical and the second is systematic. Given the small number of observed Z candidates, we choose to separate the data into three kinematic bins in y, p_T, and centrality [a]. The full data sample is divided into the following centrality bins: 30-100% (most peripheral), 10-30% (intermediate) and 0-10% (most central); these are ordered from the lowest to highest fractional HF energy deposition. In figure (a) the differential dN/dy yield

[a] Centrality is defined as the fraction of energy deposited in the HF calorimeter.

divided by the expected nuclear overlap function T_{AB} [b] is shown as a function of the number of participant nucleons (N_{part}). This is compared to curves from Paukkunen and Salgado, where the unmodified CT10 and modified nuclear EPS09 [9] parton densities are utilized. It is also compared to curves from Neufeld and Vitev [10, 11] using the MSTW08 PDF set and modeling energy loss, and to POWHEG [12] interfaced with the PYTHIA parton-shower generator. In figure (b) and (c), the yields dN/dy and $d^2N/dydp_T$ are represented, respectively, as functions of p_T and rapidity and are compared to the same predictions as figure (a) when available. In all cases, the PbPb data agrees within uncertainties with a pp POWHEG simulation scaled by the nuclear geometry – none of the subtler initial state effects can be discerned. There is apparently no significant centrality dependence of the Z boson yield. These data confirm that Z boson production is unmodified by the presence of the dense QGP produced in central collisions. The nuclear modification factor ($R_{AA} = dN/T_{AB} \times d\sigma_{pp}$, where $d\sigma_{pp}$ is given by POWHEG) is also computed and found to be consistent with 1 within statistical and systematic uncertainties [13].

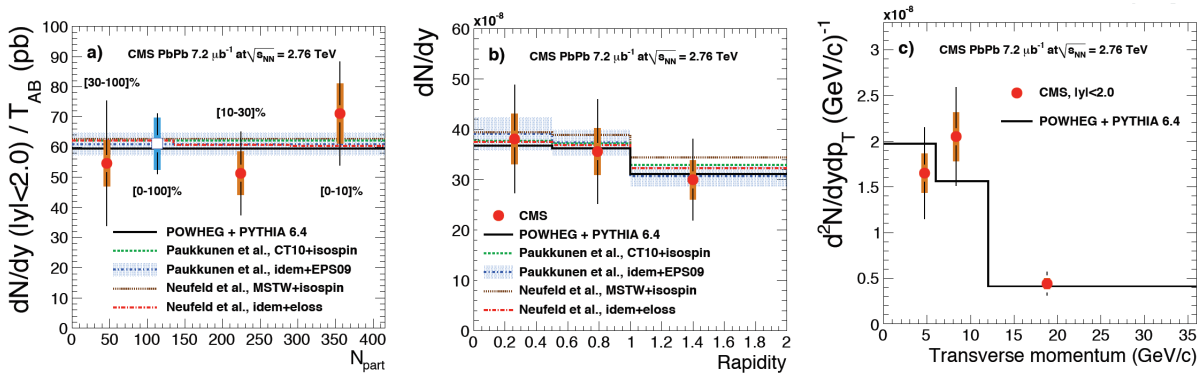

Figure 2: The yields of $Z \to \mu^+\mu^-$ per event: (a) dN/dy divided by the expected nuclear overlap function T_{AB} and as a function of event centrality parametrized as the number of participating nucleons N_{part} (b) dN/dy versus the Z boson y (c) $d^2N/dydp_T$ versus the Z boson p_T. Data points are located horizontally at average values measured within a given bin. Vertical lines (bands) correspond to statistical (systematic) uncertainties. Theoretical predictions are computed within the same bins as the data, and are described in the text.

6 Conclusion

The Z boson yield has been measured for the first time in the dimuon channel in heavy-ion collisions. Within uncertainties, (19% in the integrated case, summing the systematic and statistical uncertainties quadratically) no modification was observed with respect to theoretical NLO pQCD proton-proton cross sections scaled by elementary nucleon-nucleon collisions. This measurement establishes the feasibility of carrying out detailed Z-physics studies in heavy-ion collisions with the CMS detector. With upcoming PbPb collisions at higher luminosity and energy, the Z boson promises to be a powerful reference tool for initial state (nuclear PDFs) and final state (Z+jet) processes in nucleus-nucleus collisions at the LHC.

References

1. P. Bagnaia *et al.* [UA2 Collaboration], "Evidence for $Z^0 \to e^+e^-$ at the CERN $\bar{p}p$ Collider," Phys. Lett. B **129**, 130 (1983).

[b] The nuclear overlap function is equal to the number of elementary nucleon-nucleon binary collisions divided by the elementary NN cross section and can be interpreted as NN equivalent integrated luminosity per AA collision at a given centrality.

2. V. Kartvelishvili, R. Kvatadze and R. Shanidze, "On Z and Z+jet production in heavy ion collisions," Phys. Lett. B **356**, 589 (1995) [arXiv:hep-ph/9505418].
3. H. Paukkunen and C. A. Salgado, "Constraints for the nuclear parton distributions from Z and W production at the LHC," JHEP **1103**, 071 (2011) arXiv:1010.5392 [hep-ph].
4. R. B. Neufeld, I. Vitev and B. W. Zhang, "Toward a determination of the shortest radiation length in nature," arXiv:1010.3708 [hep-ph].
5. R. Adolphi *et al.* [CMS Collaboration], "The CMS experiment at the CERN LHC," JINST **3**, S08004 (2008).
6. M. Mulders *et al.*, "Performance of CMS muon measurements in pp collisions at $\sqrt{s}$ = 7 TeV," CMS Analysis Note 2010/211 (2010).
7. T. Sjostrand, S. Mrenna, and P. Skands, "PYTHIA 6.4 physics and manual", JHEP 05 (2006) 026, arXiv:hep-ph/0603175.
8. V. Khachatryan *et al.* [CMS Collaboration], "Measurements of Inclusive W and Z Cross Sections in pp Collisions at $\sqrt{s} = 7$ TeV," JHEP **1101**, 080 (2011) arXiv:1012.2466 [hep-ex].
9. K. J. Eskola, H. Paukkunen, and C. A. Salgado, EPS09 - a New Generation of NLO and LO Nuclear Parton Distribution Functions, JHEP 04 (2009) 065, arXiv:0902.4154.
10. R. B. Neufeld, I. Vitev, and B. W. Zhang, Toward a determination of the shortest radiation length in nature, arXiv:1010.3708.
11. R. B. Neufeld, I. Vitev, and B. W. Zhang, The physics of $Z^0/*\gamma$-tagged jets at the LHC, arXiv:1006.2389.
12. S. Alioli, P. Nason, C. Oleari et al., NLO vector-boson production matched with shower in POWHEG, JHEP 07 (2008) 060, arXiv:0805.4802.
13. S. Chatrchyan *et al.* [CMS Collaboration], "Study of Z Boson Production in PbPb Collisions at $\sqrt{s_{NN}} = 2.76$ TeV" Phys. Rev. Lett. **106**, 212301 (2011) arXiv:1102.5435 [nucl-ex].

Heavy-flavour production in pp and Pb–Pb collisions at ALICE

André Mischke [a] for the ALICE Collaboration
ERC-Research Group QGP-ALICE*, Institute for Subatomic Physics,*
Utrecht University, Princetonplein 5, 3584 CC Utrecht, the Netherlands

In this contribution, recent ALICE measurements of the production cross section of single electrons, single muons and open charmed mesons in proton-proton collisions at $\sqrt{s} = 7$ TeV are reported. The data are compared to next-to-leading-order perturbative QCD calculations. First open charm signals in Pb–Pb collisions at $\sqrt{s_{\rm NN}} = 2.76$ TeV are shown.

1 Introduction

Heavy quarks (charm and beauty) are sensitive penetrating probes to study the properties of the hot quark matter state that is formed in collisions of heavy atomic nuclei at high energy densities. Due to their large mass, they are believed to be predominantly produced in the early stage of the collision by gluon-fusion processes, so that they explore the entire evolution of the produced matter. The Large Hadron Collider (LHC) at CERN allows to create and carefully study such matter in heavy-ion collisions at an unprecedented energy. ALICE collected a rich pp data sample at a collision energy of 7 TeV. These measurements are important to test predictions from pQCD (such as the D meson production cross sections) in the new energy domain and provide an essential baseline for the comprehensive studies in heavy-ion collisions.

2 ALICE detector, trigger and data set

ALICE, A Large Ion Collider Experiment, is the dedicated detector for measurements in heavy-ion collisions [? ?], demonstrated in the first LHC Pb–Pb run [?]. Its characteristic features are the very low momentum cut-off (100 MeV/c), the low material budget and the excellent particle identification and vertexing capabilities in a high multiplicity environment. Tracking and particle identification through the measurement of the specific energy loss ($\mathrm{d}E/\mathrm{d}x$) is performed using the large volume Time Projection Chamber (TPC) located inside the large L3 solenoidal magnet with a field of $B = 0.5$ T. The TPC has a coverage of -0.9 to 0.9 in pseudo-rapidity and 2π in azimuth. The particle identification at about $p_{\rm T} > 2$ GeV/c is performed with the Time Of Flight (TOF) detector. The Inner Tracking System consists of six concentric cylindrical layers of silicon detectors and provides excellent reconstruction of displaced vertices with a transverse impact parameter resolution better than 75 μm for $p_{\rm T} > 1$ GeV/c (cf. Fig. **??** (left panel)). The minimum bias event selection is based on a signal in either of the VZERO scintillator counters or at least one hit in one of the two innermost silicon layers. The results presented in this paper correspond to 100M and 180M minimum-bias pp events at $\sqrt{s} = 7$ TeV for the D meson

[a] Email: a.mischke@uu.nl

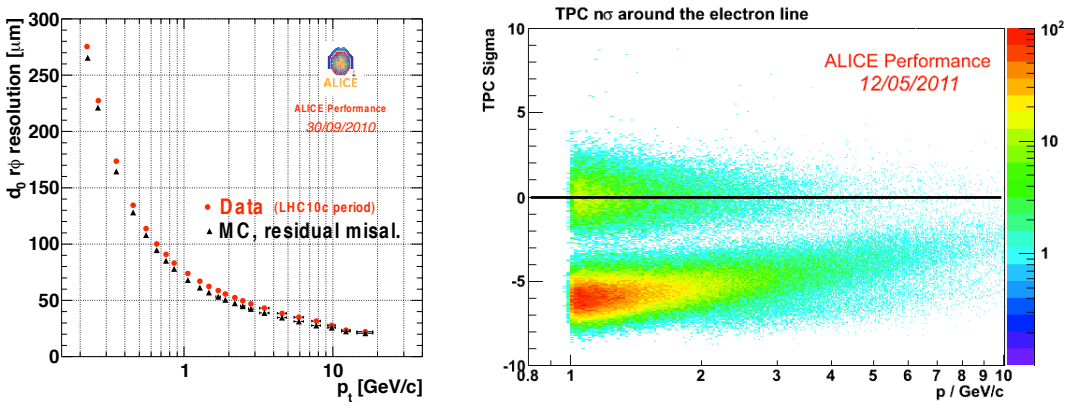

Figure 1: Left: p_{T} dependence of the track impact parameter resolution in the transverse plane (r direction) for data and Monte-Carlo simulations. Right: Electron identification using the normalized TPC $\mathrm{d}E/\mathrm{d}x$ distribution. The upper band are electrons and the lower ones charged pions.

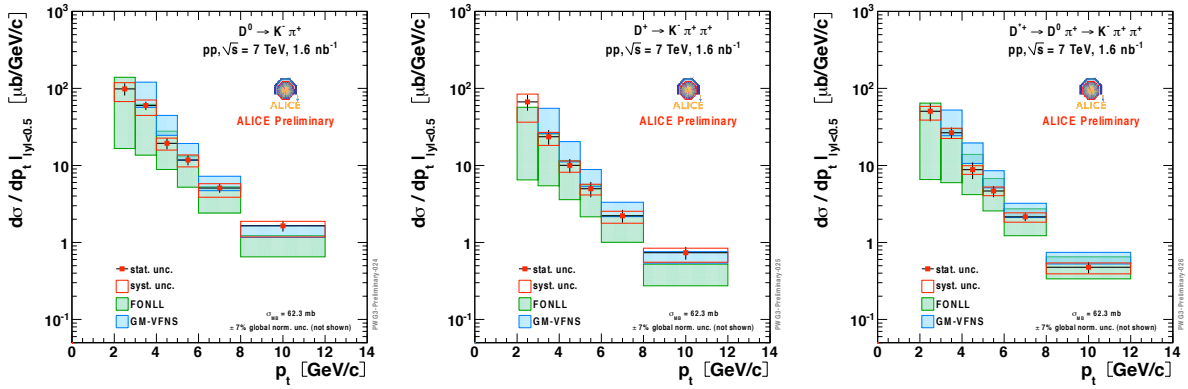

Figure 2: p_{T} differential cross section for D^0, D^+ and D^{*+} mesons in pp collisions at $\sqrt{s} = 7$ TeV, compared to next-to-leading-order perturbative QCD predictions from FONLL and GM-VFNS calculations.

(integrated luminosity: 1.6 nb^{-1}) and single electron analyses (2.6 nb^{-1}), respectively, and 2M muon triggered events (3.49 nb^{-1}).

3 D mesons

The reconstruction of D mesons is based on their decay topology and the invariant mass technique. Details of the analysis can be found in [?]. The kaon and pion identification using TPC and TOF helps to reduce background at low p_{T}. Figure **??** shows the p_{T} differential cross section for prompt D^0, D^+ and D^{*+} mesons using 20% of the 2010 statistics. The feed-down from beauty decays is calculated from theory and gives a contribution of 10-15%. A data driven method will be used with the full 2010 statistics. The data are well described by pQCD calculations at Fixed-Order plus Next-to-Leading Logarithm (FONLL) level [?] and GM-VFNS predictions [?]. The open charm signals in the first Pb–Pb collisions at $\sqrt{s_{\mathrm{NN}}} = 2.76$ TeV (cf. Fig. **??**) indicate that a detailed study of the modification of the D meson production in hot quark matter will be possible with the 2010 data sample.

4 Single electrons

The open heavy-flavour production cross section at mid-rapidity has also be studied through the measurement of single electrons. Those electrons are identified on a statistical basis by subtract-

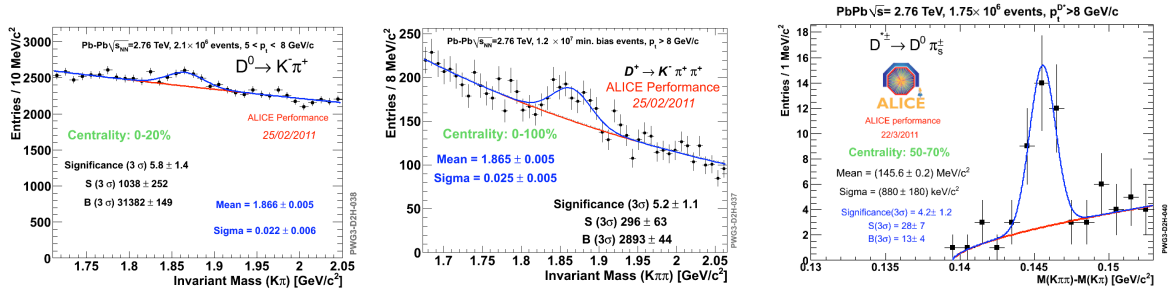

Figure 3: Invariant mass distribution for $K^-\pi^+$ (left panel), $K^-\pi^+\pi^+$ pairs (middle panel) and $M(K\pi\pi)-M(K\pi)$ (right panel) in lead-lead collisions at 2.76 TeV per nucleon-nucleon pair.

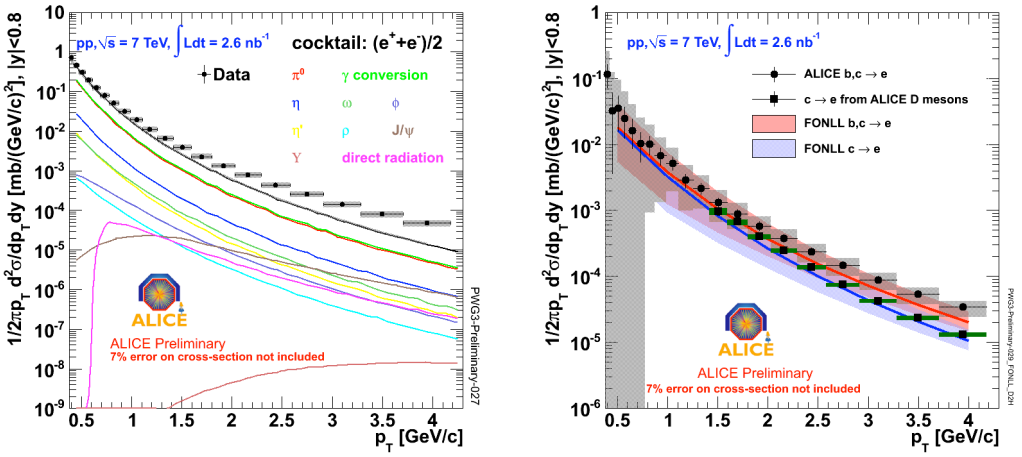

Figure 4: Invariant inclusive electron cross section, compared to the cocktail of background electrons (left panel) and invariant single electron cross section, compared to FONLL calculations and to expectations from D meson decay electrons (right panel).

ing a cocktail of background electrons from the inclusive electron spectrum. This background arises mainly from electrons from γ conversion in the detector material and π^0 Dalitz decays. For $p_{\rm T}$ up to a few GeV/c this cocktail can be determined precisely by means of the measured π^0 cross section. Figure **??** (right panel) depicts the momentum dependence of the normalized TPC dE/dx distribution after applying a cut on the TOF signal, which rejects kaons ($<$ 1.5 GeV/c) and protons ($<$ 3 GeV/c). A dE/dx cut clearly separates electrons from charged pions up to about 10 GeV/c with a residual pion contamination of less than 15%. The corrected inclusive electron spectrum is shown in Fig. **??** (left panel) together with the cocktail of background electrons. Figure **??** (right panel) illustrates the single electron cross section, which has a total systematic uncertainty of 16-20% ($p_{\rm T}$ dependent) plus 7% for the normalization. The data are well described by FONLL calculations [?] within errors. Moreover, the low $p_{\rm T}$ single electron spectrum agrees with expectations from D meson decay electrons. The $p_{\rm T}$ range will be extended with the TRD and EMCAL detectors in the near future. Electrons from beauty decays will be identified through displaced vertices.

5 Single muons

Heavy-flavour production at forward rapidities can be studied in ALICE with single muons using the muon spectrometer, which covers an η-range from -4 to -2.5. The extraction of the heavy-flavour contribution of the single muon spectra requires the subtraction of three main background sources: a) muons from the decay-in-flight of light hadrons (decay muons); b)

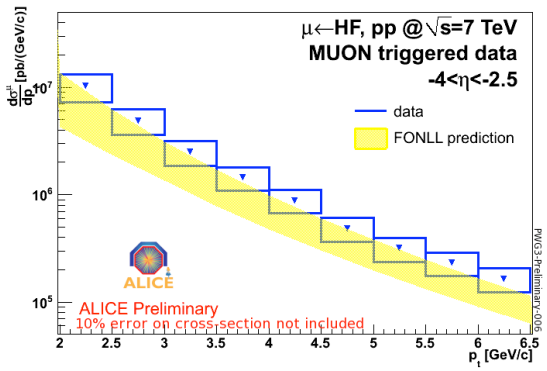

Figure 5: Differential transverse momentum cross section for single muons in $-4 < \eta < -2.5$. The statistical error is smaller than the markers. The systematic errors (open boxes) do not include an additional 10% error on the minimum-bias pp cross section. The yellow band indicates the FONLL prediction.

muons from the decay of hadrons produced in the interaction with the front absorber (secondary muons); c) punch-through hadrons. The last contribution can be efficiently rejected by requiring the matching of the reconstructed tracks with the tracks in the trigger system. Due to the lower mass of the parent particles, the background muons have a softer $p_{\rm T}$ distribution than the heavy-flavour muons, and dominate the low-$p_{\rm T}$ region. Therefore, the analysis is restricted to the $p_{\rm T}$ range 2-6.5 GeV/c, where the upper limit is being determined by the current $p_{\rm T}$ resolution of spectrometer with partial alignment. Simulation studies indicate that, in this $p_{\rm T}$ range, the contribution of secondary muons is small (about 3%). The main source of background in this region consists of decay muons (about 25%), which have been subtracted using Monte Carlo simulations. Figure **??** illustrates the single muon $p_{\rm T}$ cross section after corrections. The systematic uncertainties are 20-25%. The FONLL calculation [?] agrees with the data within uncertainties.

6 Summary

Recent ALICE results on open charmed mesons and single leptons in pp collisions at 7 TeV are presented. The production cross-section of single electrons, single muons and D mesons are measured up to $p_{\rm T}$ = 4, 6.5 and 12 GeV/c, respectively, and show good agreement with NLO pQCD calculations. First D meson signals are shown for Pb–Pb collisions at $\sqrt{s_{\rm NN}}$ = 2.76 TeV.

Acknowledgments

The European Research Council has provided financial support under the European Community's Seventh Framework Programme (FP7/2007-2013) / ERC grant agreement no 210223. This work was supported in part by a Vidi grant from the Netherlands Organisation for Scientific Research (project number 680-47-232).

References

1. P. Cortese *et al.* [ALICE Collaboration], J. Phys. G: Nucl. Part. Phys. **32**, 1295 (2006).
2. K. Aamodt *et al.* [ALICE Collaboration], J. Instrum. **3**, S08002 (2008).
3. K. Aamodt *et al.* [ALICE Collaboration], Phys. Rev. Lett. **105**, 252301 (2010).
4. K. Aamodt *et al.* [ALICE Collaboration], J. Instrum. **5**, P03003 (2010).
5. A. Grelli for the ALICE Collaboration, PoS (ICHEP 2010) 191.
6. M. Cacciari *et al.*, private communication.
7. B.A. Kniehl *et al.*, private communication.

Direct Photons and Photon-Hadron Correlations at PHENIX

B. Sahlmueller[a]
Department of Physics and Astronomy, Stony Brook University,
Stony Brook, NY 11790, USA

Direct photons are a powerful tool to study the hot and dense matter created in heavy-ion collisions at RHIC, since they are created in the different stages of the collision. Since they do not interact via the strong force, they can travel through the hot and dense matter mostly unaffected. The PHENIX experiment has measured direct photons using different methods, over a broad range of transverse momentum (p_T), in different collision systems, and at different energies. These measurements help interpreting the measurement of hadrons as well as understanding the temperature of the created quark-gluon plasma (QGP). The azimuthal anisotropy of direct photons may shed light on the thermalization time of the medium. Using direct photons to tag jets is a crucial tool to understand the energy loss of scattered partons in the medium.

The experimental program at the Relativistic Heavy-Ion Collider has found evidence for the creation of a quark-gluon plasma in collisions of Au nuclei at center-of-mass energies of 200 GeV per nucleon. [1] One of the crucial signatures are direct photons that are produced in such collisions and can traverse the created QGP mostly unaffected.

Direct photons are defined as photons that are not from decays of hadrons, such as π^0 or η. These photons are produced in different stages of a heavy-ion collision over a broad range of transverse momentum. At large and intermediate transverse momentum (p_T) they are produced mainly from initial hard scattering processes of the colliding quarks or gluons such as $q + g \rightarrow q + \gamma$ or $q + \bar{q} \rightarrow g + \gamma$, as bremsstrahlung emitted by a scattered parton, from the fragmentation of such quarks and gluons, or from the interaction of a scattered parton with the strongly interacting medium created in such collisions [2]. In the hard scattering processes, a parton is emitted opposite to the photon, that will subsequently fragment into a hadronic jet. Hence, the energy of the jet is balanced with the energy of the direct photon on the opposite side. At low p_T, the medium can emit thermal direct photons directly. Their p_T distribution depends on the average temperature of the medium. [3] To account for nuclear effects, the direct photon yield in Au+Au collisions is compared to the cross section in $p + p$ collisions with the help of the nuclear modification factor which is defined as

$$R_{AA} = \frac{d^2N/dp_T dy|_{AuAu}}{\langle T_{AA} \rangle \, d^2\sigma^{pp}/dp_T dy} \ , \tag{1}$$

where $\langle T_{AA} \rangle$ is the nuclear overlap function.

The azimuthal anisotropy of direct photons is sensitive to the different production processes, it is measured in terms of the anisotropy parameter v_2 which is the second harmonic of the Fourier

[a] for the PHENIX collaboration

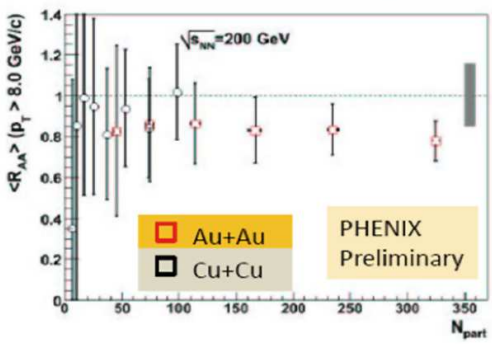

Figure 1: Average nuclear modification factor $< R_{AA} >$ for direct photons in Au+Au and Cu+Cu collisions at 200 GeV, plotted versus N_{part}.

expansion of the azimuthal distribution. The elliptic flow of thermal direct photons is sensitive to the thermalization time τ_0 of the QGP, small τ_0 would lead to small v_2.[4]

Direct photons can be measured using different subsystems of the central arm of the PHENIX detector, with different methods of measurement. The PHENIX detector is described elsewhere.[5] Photons can be measured directly using the Electromagnetic Calorimeters, the decay photons from π^0 and other mesons are subtracted statistically from the measured inclusive photon sample, charged hadrons and electrons are rejected with the help of the central arm tracking detectors. This method is described in more detail in earlier publications [6]. It is most feasible at high p_T, at low p_T the signal to background ratio gets too small to make a significant measurement. Therefore, two other methods have been developed, using the electron ID capabilities of the PHENIX detector and measuring direct photons indirectly through conversions.

The so-called internal conversion method uses the idea that virtual direct photons are produced in conjunction with real direct photons, and convert into low mass e^+e^- pairs, in a process similar to the π^0 Dalitz decay. The method benefits from the limited phase space of such pairs from the π^0 Dalitz decay, hence the signal to background ratio is improved compared to the direct calorimeter measurement at low p_T. The method is based on the measurement of e^+e^- pairs, the background is removed using like-sign pairs, the resulting distribution is compared to a cocktail of dilepton pairs that includes all expected hadronic sources. An excess over that cocktail at low invariant mass is then interpreted as a virtual direct photon signal. A more detailed description of this method is given in [7].

A new method has been developed to measure direct photons through external conversions in the detector material. The back plane of the PHENIX Hadron-Blind Detector (HBD), which was installed during the 2007 RHIC run for commissioning, offers a well-defined conversion point for photons, about 60 cm away from the interaction point, with a radiation length of about $4\%X_0$. To account for the wrongly reconstructed opening angle of such conversion pairs, that leads to an apparent invariant mass, an alternate track model was developed that assumes the origin of the pairs at the HBD back plane. Using this model moves the peak of the invariant mass from about 12 MeV/c^2 to 0, it also helps separating the conversion pair from pairs from Dalitz decays. Using this method, the misidentification rate of conversion photons is found to be less than 3%. This method is described in more detail in [8].

The nuclear modification factor R_{AA} has been measured in 200 GeV Au+Au collisions and was found to be consistent with unity for most p_T.[9] This result is a confirmation that $\langle T_{AA} \rangle$ scaling works, since at a first approximation, photons are not affected by the QGP. However, there appears to be a possible suppression of photons at $p_T > 15$ GeV/c, which is not fully understood. Such a suppression could be an initial state effect, for example an effect of the different isospin composition of the proton and of the gold nuclei, and would thus be visible in

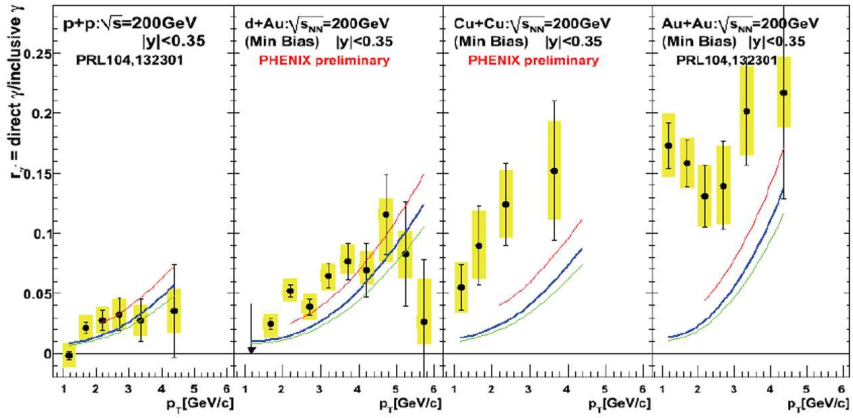

Figure 2: Fraction of direct photons over inclusive photons, for different collision systems, at center-of-mass energy of 200 GeV: $p+p$, d+Au. Cu+Cu, Au+Au (from left to right).

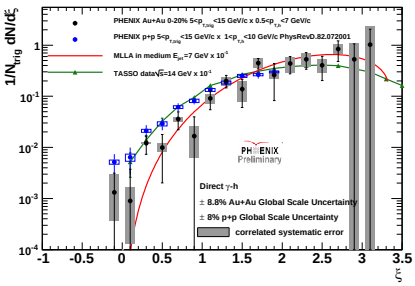

Figure 3: ξ distribution for PHENIX Au+Au (black circles) and $p+p$ (open blue circles), compared to a MLLA prediction (red line) and TASSO data (green triangles).

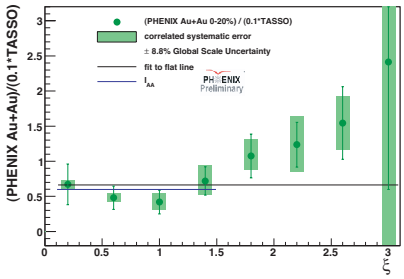

Figure 4: Ratio of Au+Au to TASSO data scaled by a factor of 10. The black line is a fit to the ratio, the blue line is a fit to the I_{AA} using PHENIX $p+p$ as reference.

d+Au collisions at the same energy. The isospin effect would also be visible in Au+Au collisions at 62.4 GeV, at lower p_T, since it scales with $x_T = 2p_T/\sqrt{s_{NN}}$. PHENIX has done both measurements, with the 2003 and 2004 datasets, respectively, and they are both statistically too limited to draw any conclusion. Direct photons have also been measured in Cu+Cu collisions at 200 GeV, the averaged nuclear modification factor is compared with Au+Au collisions in Fig. 1 and found to be consistent for similar numbers of participants.

The virtual direct photon measurement has been done for four different collision systems at 200 GeV collision energies, a $p+p$ measurement works as a baseline to understand the other measurements, a d+Au measurement is used to look for effects of cold nuclear matter, and the measurements in Au+Au and Cu+Cu are used to study properties of the QGP, also with respect to different system sizes. The ratio of direct photons and inclusive photons is shown in Fig. 2 for all four collision systems. While the $p+p$ measurement shows that pQCD agrees well with the data, there is a clear excess in the Au+Au data. The excess is smaller in Cu+Cu and does not appear in the d+Au measurement, which gives evidence that it is indeed a final state effect. When fitting the excess over scaled pQCD of direct photon yield in Au+Au with an exponential, the average temperature of the medium can be extracted as the inverse slope of the function. It is found to be $221 \pm 19(stat) \pm 19(sys)$ MeV.

The external conversion measurement is still on its way, its final goal is to measure the elliptical flow of thermal photons. The method has been found to produce reliable results for the inclusive photon v_2, this measurement agrees well with an earlier measurement using the EMCal. [8]

Another way of using direct photons to study the QGP is using direct photons as trigger to tag jets, for photons from hard scattering processes balance the energy from jets on the opposite side. To measure the modification of the jet, PHENIX uses correlations of direct photons and hadrons. Since direct photons cannot be measured on an event-by-event basis, first the yield per trigger (Y_{inc}) of inclusive photons and hadrons is measured as well as the yield per trigger of the π^0 and hadrons. The yield per trigger for decay photons (Y_{dec}) is calculated based on the π^0-hadron correlation, and finally, using the ratio of inclusive and decay photons, R_γ, the yield per event for direct photons is calculated as

$$Y_{dir} = \frac{R_\gamma Y_{inc} - Ydec}{R_\gamma - 1} \ . \tag{2}$$

A much more detailed description of this analysis is given in another publication [10].

The integrated yield on the away side is calculated for both $p+p$ and Au+Au data, it is plotted as a function of the fragmentation variable $z = p_T^h / p_T^{trigger}$ to show the fragmentation function. An alternative way of plotting is showing the distribution as a function of $\xi = -\ln(x_E)$, where $x_E = p_T^h \cos(\Delta\phi)/p_T^{trigger}$, this plot is shown in Fig. 3 for both $p+p$ and Au+Au, including also e^+e^- data from TASSO [11] and a theoretical prediction from the Modified Leading Logarithmic Approximation (MLLA) in the medium [12], the latter two curves are scaled down arbitrarily by a factor of 10 to account for the limited PHENIX acceptance.
Dividing the yield in Au+Au by the yield in $p+p$, I_{AA} can be calculated, a variable to quantify effects of the medium in Au+Au. Since the scaled TASSO agrees with the PHENIX $p+p$ data, and since it extends to higher ξ, it can be used as a baseline instead of the $p+p$. The I_{AA} like ratio calculated with the TASSO data is shown in Fig. 4. The shape is consistent with a flat line and a suppression of the Au+Au yield below $\xi = 1.8$, but the points above indicate a change in shape and suggest an enhancement at highest ξ values, which can be interpreted as the response of the medium to the lost energy.

In summary, direct photons are a powerful tool to study the QGP created in ultrarelativistic heavy-ion collisions. The measurement of direct photons shows that binary scaling works when comparing heavy-ion collisions to baseline $p+p$ or d+Au collisions. Photons are also emitted from the medium directly or through interaction of partons with the medium. An excess of direct photons at low p_T can be interpreted as a thermal signal from the QGP, and an average medium temperature of $221 \pm 19(stat) \pm 19(sys)$ MeV could be extracted. The measurement of flow of direct photons could further disentangle different photon production mechanisms. Direct photons are also crucial for probing the matter with direct photon-hadron correlations where the photon balances the jet energy. This measurement showed suppression of the away side and a shape suppression of the fragmentation function at high ξ which can be related to the medium response to energy loss.

1. K. Adcox et al., *Nucl. Phys.* A **757**, 184 (2005)
2. C. Gale, arXiv:0904.2184 (hep-ph) (2009)
3. P. Stankus, Ann.Rev.Nucl.Part.Sci. **55**, 517 (2005)
4. R. Chatterjee, D. Srivastava, *Phys. Rev.* C **79**, 021901 (2009)
5. K. Adcox et al., *Nucl. Instrum. Methods* A **499**, 469 (2003)
6. S. S. Adler et al., *Phys. Rev. Lett.* **94**, 232301 (2005)
7. A. Adare et al., *Phys. Rev. Lett.* **104**, 132301 (2010)
8. R. Petti, conference proceedings, WWND 2011, to be published (2011)
9. T. Isobe, J.Phys.G **34**, 1015 (2007)
10. M. Connors, *Nucl. Phys.* A **855**, 335 (2011)
11. W. Braunschweig et al., Z.Phys.C **47**, 187 (1990)
12. N. Borghini and A. Wiedemann, arXiv:hep-ph-0506218 (2005)

Probing nuclear parton densities and parton energy loss processes through photon + heavy-quark jet production

François Arleo[1], Ingo Schienbein[2] and Tzvetalina Stavreva[2]
[1] *Laboratoire de Physique Subatomique et de Cosmologie, UJF, CNRS/IN2P3, INPG, 53 avenue des Martyrs, 38026 Grenoble, France*

[2] *Laboratoire d'Annecy-le-Vieux de Physique Théorique (LAPTH), UMR5108, Université de Savoie, CNRS, BP 110, 74941 Annecy-le-Vieux cedex, France*

We present a detailed phenomenological study of the associated production of a prompt photon and a heavy-quark jet (charm or bottom) in proton-nucleus (p-A) and nucleus-nucleus (A-A) collisions. The dominant contribution to the cross-section comes from the gluon–heavy-quark (gQ) initiated subprocess, making this process very sensitive to the gluon and the heavy quark nuclear parton densities. We show that the future p-A data to be collected at the LHC should allow one to disentangle the various nPDF sets currently available. In heavy-ion collisions, the photon transverse momentum can be used to gauge the initial energy of the massive parton which is expected to propagate through the dense QCD medium produced in those collisions. The two-particle final state provides a range of observables (jet asymmetry, photon-jet pair momentum, among others), through the use of which a better understanding of parton energy loss processes in the massive quark sector can be achieved, as shown by the present phenomenological analysis carried out in Pb-Pb collisions at the LHC.

1 Introduction

The production of a prompt photon in association with a heavy-quark jet provides us with the opportunity to study the structure of the proton and the nucleus as well as the mechanisms of heavy quark energy loss. The information obtained depends on the collision type:

- For $p - \bar{p}$ collisions (at the Tevatron) it was shown in Ref. [1] that this process is sensitive to the charm/bottom PDF, and therefore can provide information and constraints on the presence of intrinsic charm/bottom (IC/IB) in the proton [2].

- In $p - A$ collisions (at RHIC and the LHC) $\gamma + Q$ production can be used to constrain the gluon nuclear PDF (nPDF), [3], which presently carries a large error to it, as will be shown in more detail in Section 2. One should underline that knowing the precise nPDFs is necessary for obtaining reliable predictions in $A - A$ collisions.

- In $A - A$ collisions the study of prompt photons and heavy quarks provides an ideal tool for investigating the energy lost by heavy partons in the hot medium (Section 3). As an electromagnetic probe the photon is expected to traverse the medium unaffected and thus gauge the quenching of the energy of the heavy jet. Furthermore, the comparison between $\gamma + c$ and $\gamma + b$ production provides access to the mass hierarchy of parton energy loss.

2 Constraining the gluon nPDF through $\gamma + Q$ production

Unlike the PDF for a gluon inside a free proton, the nuclear gluon PDF is largely unconstrained due to the dearth of available data. Currently, only the NMC structure function data ($F_2^D(x, Q^2)$ and $F_2^{Sn}/F_2^C(x, Q^2)$) impose weak constraints on the gluon nPDF in the x-range $0.02 \lesssim x \lesssim 0.2$ (also note that the EPS09 fit also includes data on π^0 production at RHIC), so that a precise determination is not possible. This large uncertainty in $g^A(x, Q^2)$ is presented by the nuclear modification factor to the gluon nPDF, $R_g^{Pb}(x, Q) = g^{p/Pb}(x, Q)/g^p(x, Q)$, in Fig. 1a) where a comparison between the different nuclear PDF sets currently available (nCTEQ [4,5,6], HKN07

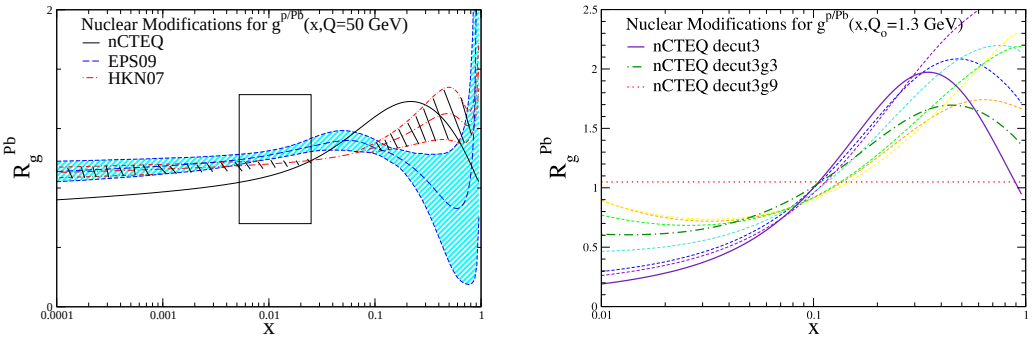

Figure 1: a) $R_g^{Pb}(x, Q = x\sqrt{S}/2 \sim p_T)$ for nCTEQ decut3, decut3g3, decut3g9, EPS09 + error band, HKN07 + error band b) $R_g^{Pb}(x, Q = x\sqrt{S}/2 \sim p_T)$ for different nCTEQ decut3, decut3g1-decut3g9.

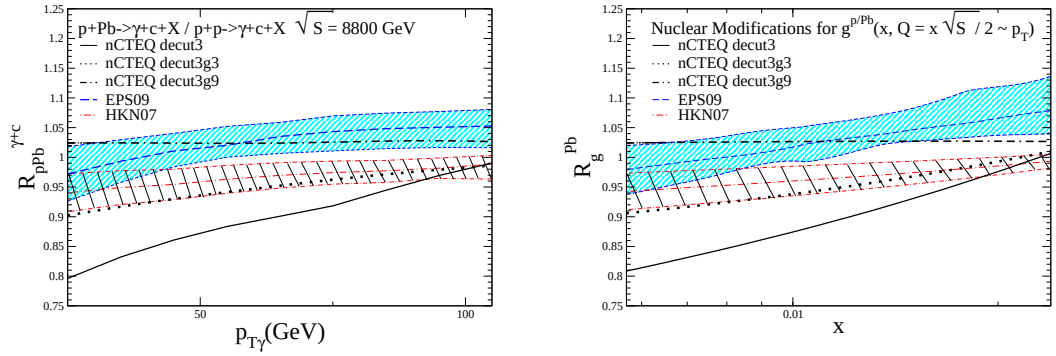

Figure 2: a) $R_{pPb}^{\gamma+c}$ at LHC within ALICE PHOS acceptances, using nCTEQ decut3, decut3g3, decut3g9, EPS09 + error band, HKN07 + error band. b) $R_g^{Pb}(x, Q = x\sqrt{S}/2 \sim p_T)$ in the x region probed at the LHC.

[7], EPS09 [8]) is shown. Fig. 1b) furthermore shows different fits with equally good χ^2, whose spread represents a lower limit on the uncertainty associated with the nCTEQ set[a]. The need for measurements of processes sensitive to the gluon nPDF is evident. Here we point out that $\gamma + Q$ production is an excellent probe of $g^A(x, Q^2)$, and can serve as one such process, as evidenced by Fig. 9 and Fig. 10 in Ref. [3]. Fig. 9 shows the differential cross-section for both $\gamma + c$ and $\gamma + b$ at $\sqrt{s_{\rm NN}} = 8.8$ TeV for $p - Pb$ collisions at ALICE EMCal acceptances. The anticipated event rate (before experimental efficiencies) is sufficiently large for a measurement ($N_{\gamma+c}^{pPb} = 11900$, $N_{\gamma+b}^{pPb} = 2270$). In Fig. 10 the subprocess contributions to $d\sigma_{\gamma+c}^{pPb}/dp_{T\gamma}$ are presented, with $g - Q$ and $g - g$ being the dominant ones; for more details see Ref. [3]. The sensitivity to the gluon nPDF further shows up in the nuclear modification factor to the cross-section, $R_{pPb}^{\gamma+c} = \frac{1}{208}\frac{d\sigma/dp_{T\gamma}(p\mathrm{Pb}\to\gamma+c+X)}{d\sigma/dp_{T\gamma}(pp\to\gamma+c+X)}$ in Fig. 2a), when compared to $R_g^{Pb}(x, Q)$ in Fig. 2b). It can clearly be seen by juxtaposing Fig. 2a) and Fig. 2b) that $R_{pPb}^{\gamma+c}$ follows closely R_g^{Pb} in the region of x probed at the LHC for each nPDF set. Therefore we can conclude that this process is an excellent candidate for constraining the gluon nuclear distribution as a measurement of the prompt photon + heavy jet process with appropriately small error bars will be able to distinguish between the three different nPDF sets. This process is thus particularly complementary to the measurement of single inclusive photons in order to constrain parton distributions in nuclei [9].

[a] These fits are available at http://projects.hepforge.org/ncteq/ .

3 Heavy Quark Energy Loss in $\gamma + Q$ Production

The study of two-particle final states in heavy-ion collisions provides a much more versatile access to quantifying the energy loss in the Quark Gluon Plasma (QGP), as compared to the study of a single inclusive process. This is further the case if one of the final-state particles is medium insensitive, in particular the study of γ+jet [10] or γ+hadron [11] correlations helps to evaluate the amount of quenching experienced by jets as they traverse the medium while the photon's energy serves as a gauge of the initial parton energy. Here, the focus on the associated production of γ+*heavy jet* can help clarify the energy loss in the heavy quark sector. Currently, due to the dead cone effect a definite hierarchy of the energy loss is expected, $\epsilon_q > \epsilon_c > \epsilon_b$, with the heavier quarks losing less energy [12]. This hierarchy remains to be clarified experimentally, and prompt photon + heavy-quark jet production is a natural and promising process for this verification.

In Fig. 3a) we show the effects of the medium on the leading order (LO) differential cross-section versus $p_{T\gamma}$ and p_{TQ}. The energy loss of the heavy quark, ϵ_Q, is computed on an event by event basis, with the use of the quenching weight obtained perturbatively [13]. These effects show up in the difference between $\frac{d\sigma^{\gamma+c;med}}{dp_{TQ}}$ and $\frac{d\sigma^{\gamma+c;vac}}{dp_{TQ}}$. The small difference between $\frac{d\sigma^{med}}{p_{T\gamma}}$ and $\frac{d\sigma^{vac}}{p_{T\gamma}}$ at low p_T is due to experimental cuts. However, we need not limit ourselves to only one-particle observables as the information obtained by investigating the correlations of the two final state particles (e.g. photon-jet energy asymmetry, momentum imbalance, photon-jet pair momentum [11]) provides a much better handle on the amount of energy loss. In Fig. 3b) we focus in more detail on the differential cross-section as a function of the photon-jet pair momentum, $q_\perp = |\vec{p}_{T\gamma} + \vec{p}_{TQ}|$. At LO accuracy, for the direct contribution one has $q_\perp \simeq \epsilon_Q$, whereas for the fragmentation contribution the shift between the q_T spectrum in vacuum versus the one in medium is given by $< \epsilon_Q >$. Unfortunately when one investigates two-particle observables for this process at LO, only the fragmentation contributions in medium and in vacuum can be compared, as due to the kinematic constraints the direct component in vacuum is non-zero only when $q_T = 0$. In Fig. 4 the fragmentation contributions in medium to $\gamma+c$ and $\gamma+b$ normalized to the $p-p$ case are shown. Clearly $\Delta E_c > \Delta E_b$ at small q_T, while as q_T grows the difference disappears, as the quenching weight depends on m/E, which becomes similar for charm and bottom quarks at large q_T. However, definite conclusions can only be drawn after a study at NLO accuracy [14].

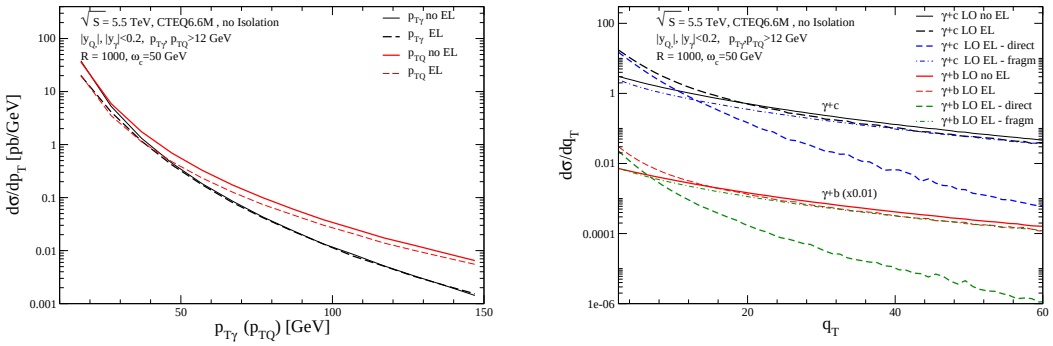

Figure 3: a) The LO $\gamma + c$ differential cross-section versus: $p_{T\gamma}$ in vacuum (solid black line), in medium (dashed black line); p_{TQ} in vacuum (solid red line), in medium (dashed red line). b) The LO differential cross-section versus $q_\perp$ for $\gamma + c$ and $\gamma + b$, showing the fragmenation and direct contributions in vacuum and in medium.

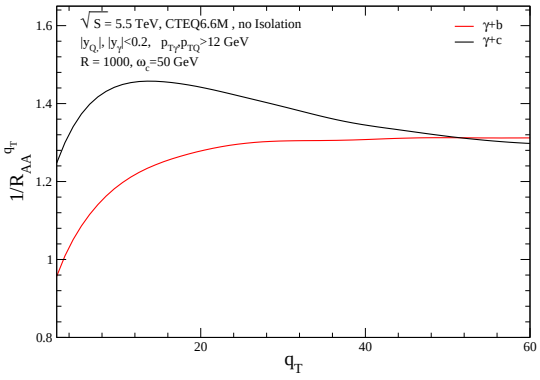

Figure 4: a) The ratio of the LO vacuum fragmentation contribution to the medium fragmentation contribution for $\gamma + c$ (black line) and $\gamma + b$ (red line) production.

4 Conclusion

Prompt photon + heavy-quark jet production has proven to be an extremely useful and versatile process. It can can be employed to constrain the heavy quark PDFs in hadron-hadron collisions, while measurements in $p - A$ collisions can help constrain the gluon nPDF.

In heavy-ion collisions it can help estimate the quenching experienced by a heavy jet, while also providing access to the mass hierarchy of parton energy loss.

References

1. T. Stavreva and J. Owens, Phys.Rev. **D79** (2009) 054017 [0901.3791].
2. **D0** Collaboration, V. M. Abazov *et al.*, Phys. Rev. Lett. **102** (2009) 192002 [0901.0739].
3. T. Stavreva *et al.*, JHEP **01** (2011) 152 [1012.1178].
4. I. Schienbein *et al.*, Phys. Rev. **D77** (2008) 054013 [0710.4897].
5. I. Schienbein *et al.*, Phys. Rev. **D80** (2009) 094004 [0907.2357].
6. K. Kovarik, I. Schienbein, F. Olness, J. Yu, C. Keppel *et al.*, Phys.Rev.Lett. **106** (2011) 122301 [1012.0286].
7. M. Hirai, S. Kumano and T. H. Nagai, Phys. Rev. **C76** (2007) 065207 [0709.3038].
8. K. J. Eskola, H. Paukkunen and C. A. Salgado, JHEP **04** (2009) 065 [0902.4154].
9. F. Arleo, K. J. Eskola, H. Paukkunen and C. A. Salgado, JHEP **04** (2011) 055 [1103.1471].
10. X.-N. Wang, Z. Huang and I. Sarcevic, Phys. Rev. Lett. **77** (1996) 231 [hep-ph/9605213].
11. F. Arleo, P. Aurenche, Z. Belghobsi and J.-P. Guillet, JHEP **11** (2004) 009 [hep-ph/0410088].
12. Y. L. Dokshitzer and D. E. Kharzeev, Phys. Lett. **B519** (2001) 199–206 [hep-ph/0106202].
13. N. Armesto, A. Dainese, C. A. Salgado and U. A. Wiedemann, Phys. Rev. **D71** (2005) 054027 [hep-ph/0501225].
14. F. Arleo, I. Schienbein and T. Stavreva, Work in Progress.

MEASUREMENTS OF X_{max} AND TESTS OF HADRONIC INTERACTIONS WITH THE PIERRE AUGER OBSERVATORY

C. Bleve* for the Pierre Auger Collaboration†
*Bergische Universität Wuppertal, FB C Physik, Gaußstr. 20, D-42097 Wuppertal, Germany
†Observatorio Pierre Auger, Av. San Martin Norte 304, 5613 Malargüe, Argentina
full author list at http://www.auger.org/archive/authors_2011_3.html

The Pierre Auger Observatory is designed to detect the particle showers produced in the atmosphere by the most energetic cosmic rays, particles with individual energies up to E$\simeq$ 10^{20} eV. The challenge is to measure their spectrum, arrival directions and mass composition. The depth of the maximum of the longitudinal shower developement ($X_{\rm max}$) is an indicator of the elemental composition. We present the measurement of the first two moments of the $X_{\rm max}$ distribution for $E > 10^{18}$ eV. The interpretation in terms of primary masses can only be done by comparison with predictions of hadronic interaction models. The description of hadronic interactions can be tested by determining the muon content of air shower data. Our results at E $\sim$ 10^{19} eV are compared with the predictions of the QGSjetII model for both proton and iron primaries, showing an observed excess of muons with respect to the model.

1 Introduction

Cosmic rays (CR) are a natural beam of ionized atomic nuclei with a rapidly falling energy spectrum that extends up to E $\sim$ 10^{20} eV. To understand the sources and propagation of CRs, the measurement of their flux, elemental composition and distribution of arrival directions is needed. In the highest energy range of the CR spectrum, fluxes are too low for direct observation with satellites or balloon-borne instruments: ground based detectors are used. They observe the particle showers initiated by CRs when interacting with the terrestrial atmosphere. From the point of view of particle physics, the detection of CRs at extreme energies can be regarded as a fixed target collider experiment. The first interactions between primary CRs and atmospheric nuclei reach energies equivalent to p-p collisions at $\sqrt{s} \simeq 400$ TeV, about one order of magnitude above those accessible with the LHC.

2 The Pierre Auger Observatory

The Pierre Auger Observatory operates in the Ultra High Energy (UHE) range (E>10^{18}eV). Its Southern Site is located in the Mendoza province, in Argentina. The Auger Observatory is a hybrid experiment combining two complementary detection techniques. A 3,000 km^2 surface detector (SD) samples the shower particles reaching ground level with 1660 water-Cherenkov detectors. The SD is overlooked by a fluorescence detector[1] (FD): 27 telescopes at 4 sites detect the fluorescence light emitted along the longitudinal path of the shower. The SD has $\sim$100% duty cycle, and detection efficiency $> 97\%$ above 3 EeV for zenith angles $< 60^\circ$.[2] The signal in each water-Cherenkov detector is recorded as FADC traces from 3 photomultipliers. The FD,

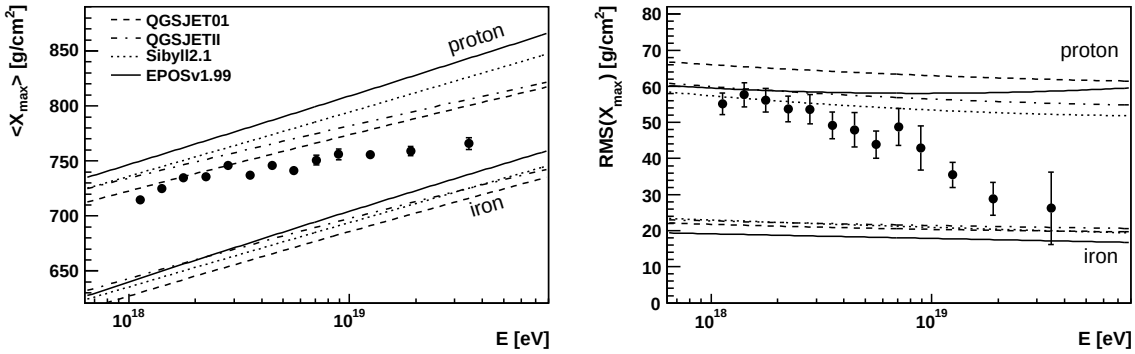

Figure 1: The measured $X_{\rm max}$ and RMS($X_{\rm max}$) as a function of the primary energy are compared with air shower simulations using different primary particles and hadronic interaction models. The RMS($X_{\rm max}$) distribution is obtained after subtracting in quadrature the detector resolution.[6]

which operates in clear moonless nights (duty cycle $\tilde{1}5\%$), can detect CRs down to an energy of $\sim 10^{18}$ eV and is able to observe, within its field of view, the longitudinal profile of the shower. The coexistence of the two detectors combines the high exposure of the SD, yelding high statistics, and the almost calorimetric measurement of the energy of air showers provided by the FD. A subset of high quality hybrid events (golden hybrids), detected and reconstructed independently by the SD and FD, are used to calibrate the SD energy scale on the FD one.[3] The estimate of the total systematic uncertainty on the energy scale is 22%.[4]

3 Measurements of X_{max}

The depth at which the longitudinal developement of the shower reaches its maximum contains information about the mass of the primary CR initiating the shower and about the properties of hadronic interactions. It can be measured with high accuracy by the FD. The average value $\langle X_{\rm max}\rangle$ depends on the primary energy E and on the number of nucleons A:

$$\langle X_{\rm max}\rangle = \alpha\,(\ln E - \langle \ln A\rangle) + \beta, \tag{1}$$

with α and β depending on the the details of hadronic interactions. Their values are very sensitive to changes in cross-section, multiplicity and elasticity.[5] Eq. 1 is derived from a simple generalization of the Heitler model to showers induced by hadronic primaries, but it provides a good description of the $X_{\rm max}$ evolution predicted by hadronic models currently in use. In the energy range of interest for the Auger Observatory, α and β can be considered independent of E. Another mass sensitive quantity is RMS($X_{\rm max}$), expressing quantitatively the shower-to-shower fluctuations of $X_{\rm max}$. It is expected to decrease with the number of nucleons A. The measurement of $X_{\rm max}$ and RMS($X_{\rm max}$) presented in Fig. 1 is based on the analysis of hybrid data collected between December 2004 and March 2009[6]. Hybrids are defined as events observed by the FD and at least one SD station. After quality cuts, 3754 hybrid events are used. The number of events per energy bin is shown in Fig. 2, left. A comparison with four widely used high-energy hadronic interaction models [7,8,9,10] suggests a gradual transition to heavier composition with increasing primary energy (Fig. 1, left). In the simple hypothesis of two mass components, however, the RMS($X_{\rm max}$) results from the RMS of individual species and from the separation of their $\langle X_{\rm max}\rangle$: a gradual transition form p to Fe primaries should lead to an increase of RMS($X_{\rm max}$) above the value predicted for protons.[11] This effect is not observed in the Auger measurements (Fig. 1, right).

The elongation rate, defined as the variation of $X_{\rm max}$ per decade of energy, is sensitive to changes in composition with energy. A constant elongation rate cannot describe the measured evolution of $\langle X_{\rm max}\rangle$ with energy. A broken line is used in Fig. 2 (left) to fit the distribution: a change of

82^{+25}_{-21} g/cm^2/decade in the elongation rate occurs at $\log_{10}$(E/eV)=18.24 $\pm$ 0.05. This is close to the energy of the spectral ankle[3] at $\log_{10}(E_{ankle}/eV)=18.65 \pm 0.09(stat)^{+0.10}_{-011}(sys)$, which is usually interpreted in terms of transition from galactic to extragalactic CRs. This interpretation is supported by the observed change in the elongation rate, under the assumption that hadronic interactions are not significantly changing with energy.

4 Muon content of air showers

The sensitivity of the Auger Observatory to both the electromagnetic and muonic components of air showers, allows us to test predictions of their relative contributions given by hadronic interaction models. The detector cannot, at present, measure separately the muon content of air showers, but several methods have been developed for an indirect estimate of the contribution:

(a) the **universality method**[12], based on the hypothesis that the electromagnetic and muonic signals measured at the ground for a fixed energy and a given distance from the shower axis have a universal dependence on the difference in grammage between the observation level and the shower maximum. The relative normalization of the muonic component can then be determined by requiring the total signal to match the experimental observations;

(b) the **jump method**[13] correlates the signal differences between consecutive bins of the SD FADC traces and the muon fraction of the total signal;

(c) the **smoothing method**[14] finds muon-induced peaks in the FADC traces of the SD stations through an iterative smoothing procedure;

(d) the **golden hybrid analysis**[14] selects, in a set of simulations with the same energy and geometry of a given event, the longitudinal profile that matches most closely the measured one. The simulated SD response is then compared with the SD measurement.

Events selected in the energy range $\log_{10}(E/eV) = 19 \pm 0.2$ ($\sqrt{s} \simeq 140$ TeV for proton primaries) and zenith $\theta < 50°$ have been analysed to obtain the muonic content at 1000 m from the shower axis.[14] The number of muons N_μ^{rel} relative to the prediction of QGSjetII[9] for protons is shown in Fig. 2 (right). The results obtained with the different methods are compatible with each other.

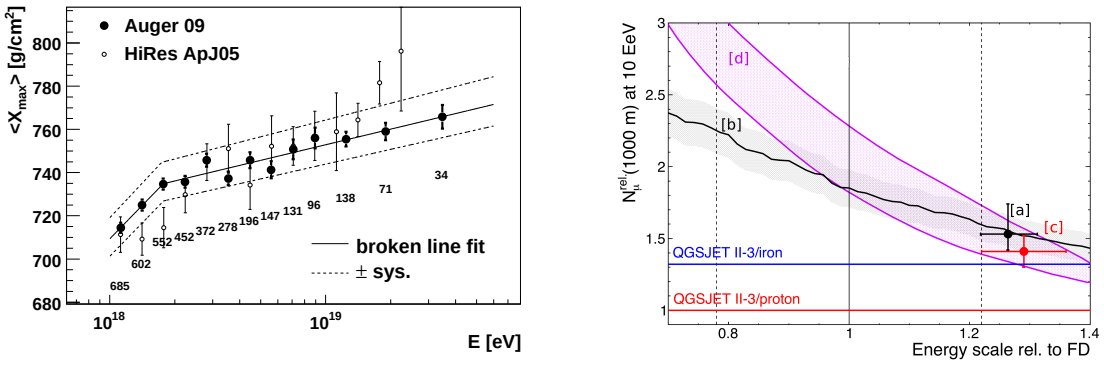

Figure 2: Left: A broken line is used to fit the evolution of $\langle X_{max} \rangle$ with the logarithm of the primary energy. The change of slope (elongation rate) supports a change in the mass composition of cosmic rays at the ankle. The measurements of X_{max} published by the HiRes collaboration[15] are shown for comparison. Right: The muon content of E=$10^{19\pm0.2}$ eV air showers is determined at 1000 m from the shower axis with different indirect methods (a-d, see text and references therein) and expressed as a number relative to the prediction of the QGSjetII model for protons primaries. That number is shown as a function of the shift in energy scale with respect to the FD one.

Methods (a) and (c) constrain the energy scale to values higher than the FD scale but compatible with its systematic uncertainty. If the energy is fixed at this new scale, the muon content in the data exceeds the QGSjetII prediction for protons by 30% to 70%. The model prediction for iron primaries ($N_\mu^{rel} = 1.32$, blue horizontal line) is marginally compatible with the results of the methods within their systematic uncertainties. The measurement of $X_{\max}$ at the same energy, hovever, is not compatible with QGSjetII predictions for a pure iron composition (Sec. 3).
The AMIGA[16] extension of the Auger Observatory (in R&D) will employ scintillation counters buried 2.3 m underground to avoid the detection of the electromagnetic component of air showers. AMIGA will provide, on a fraction of the SD area, a direct measurement of the muonic component that can be used to test and calibrate the indirect methods used so far.

5 Conclusions

The Pierre Auger Observatory is the largest detector currently in operation for the detection of cosmic rays in the UHE range. Its main scientific goal, from the point of view of astrophysics, is to find clues about the sources, acceleration and propagation of cosmic rays. From the point of view of particle physics, it observes, through air showers, collisions up to $\sqrt{s} \simeq$400 TeV, where the properties of particle interactions have large uncertainties and are extrapolated from collider measurements using hadronic interaction models. On the one hand reliable models are required for a precise interpretation of data, in particular for determining the mass composition of CRs, on the other hand the data collected with the Auger Observatory provide a unique test bed for constraining model predictions at extreme energies. The depth of the shower maximum, its fluctuations and the muon content of showers at ground level are important observables related to the elemental composition and are model dependent. The measurement of $X_{\max}$ suggests a transition toward increasingly heavier primaries with increasing energies, although the measured RMS($X_{\max}$) is smaller than models would predict. The QGSjetII model was tested against data: at $\sim 10^{19}$ eV it fails to describe consistently both $X_{\max}$ and muon content at 1000 m from the axis. A deficit of muons is found in the predictions of the QGSjetII model.

References

1. The Pierre Auger Coll., *Nucl. Instrum. Methods* A **620**, 227 (2010).
2. The Pierre Auger Coll., *Nucl. Instrum. Methods* A **613**, 29 (2010).
3. The Pierre Auger Coll., *Phys. Lett.* B **685**, 239 (2010).
4. C. Di Giulio [Pierre Auger Coll.], Proc. of 31st ICRC (2009) arXiv:0906.2189.
5. R. Ulrich, *Phys. Rev.* D **83**, 054026 (2011).
6. The Pierre Auger Coll., *Phys. Rev. Lett.* **104**, 091101 (2010).
7. E. -J. Ahn *et al.*, *Phys. Rev.* D **80**, 094003 (2009).
8. N.N. Kalmykov and S.S. Ostapchenko, Phys. Atom. Nucl. **56**, 346 (1993).
9. S.S. Ostapchenko, Nucl. Phys. Proc. Suppl. **151**, 143 (2006).
10. T. Pierog and K. Werner, Phys. Rev. Lett. **101**, 171101 (2008).
11. M. Unger [Pierre Auger Coll.], Proc. of UHECR2010 (2010) arXiv:1103.5857.
12. F. Schmidt *et al.*, *Astropart. Phys.* **29**, 355 (2008).
13. M. Healy [Pierre Auger Coll.], Proc. of 30th ICRC (2007) vol. 4, p. 377.
14. A. Castellina [Pierre Auger Coll.], Proc. of 31st ICRC (2009), arXiv:0906.2319.
15. The HiRes Coll., *Phys. Rev. Lett.* **100**, 101101 (2008).
16. M. Platino [Pierre Auger Coll.], Proc. of 31st ICRC (2009) arXiv:0906.2354.

8.
Conference Summary

EXPERIMENTAL SUMMARY: ENTERING THE LHC ERA

C. VALLEE
Centre de Physique des Particules de Marseille
163 Avenue de Luminy, Case 902, 13288 Marseille cedex 09, France

The Moriond QCD 2011 Conference takes place in the transition period when the LHC is taking over from the previous generation of colliders (LEP, HERA, Tevatron, RHIC, B factories) for investigations at the high energy frontier, study of high density matter and low energy precision measurements. This reflects in the high proportion of experimental talks (~ 40%) devoted to LHC results, a qualitatively new feature compared to previous Moriond editions. This experimental summary attempts to present the new results from LHC in comparison with those of other colliders, outlining the achieved precision and short term prospects.

1 Introduction

Most of the LHC results presented at Moriond QCD 2011 are based on the full data set collected by the experiments in 2010, their first full year of operation. The useful luminosity (~35 pb^{-1}) collected by ATLAS and CMS in pp collisions at a centre of mass energy of 7 TeV, though much lower than that analysed at TEVATRON (~6 fb^{-1}), already provides a higher sensitivity to the highest energy phenomena thanks to the higher centre of mass energy. The pp data collected by LHCb also provide B meson precisions measurements competitive with TEVATRON and B factories. In addition, the one month dedicated Heavy Ion Pb-Pb run performed at the end of 2010 at a nucleon-nucleon centre of mass energy of 2.76 TeV allows the LHC experiments to extend the probe of high density matter in new domains compared to RHIC. The following summarizes the results obtained in each of these three fields.

2 High Energy Frontier

The centre of mass energy presently available at LHC provides a 3.5 higher resolution than at TEVATRON for probing the fundamental constituents of matter. It also makes measurements at the EW scale more sensitive to low-x parton densities, which therefore need to be controlled with a higher precision. New combined measurements of H1 and ZEUS performed with the full HERA I+II data sets (figure 1) improve the control of the initial state at LHC not only in the low x domain,

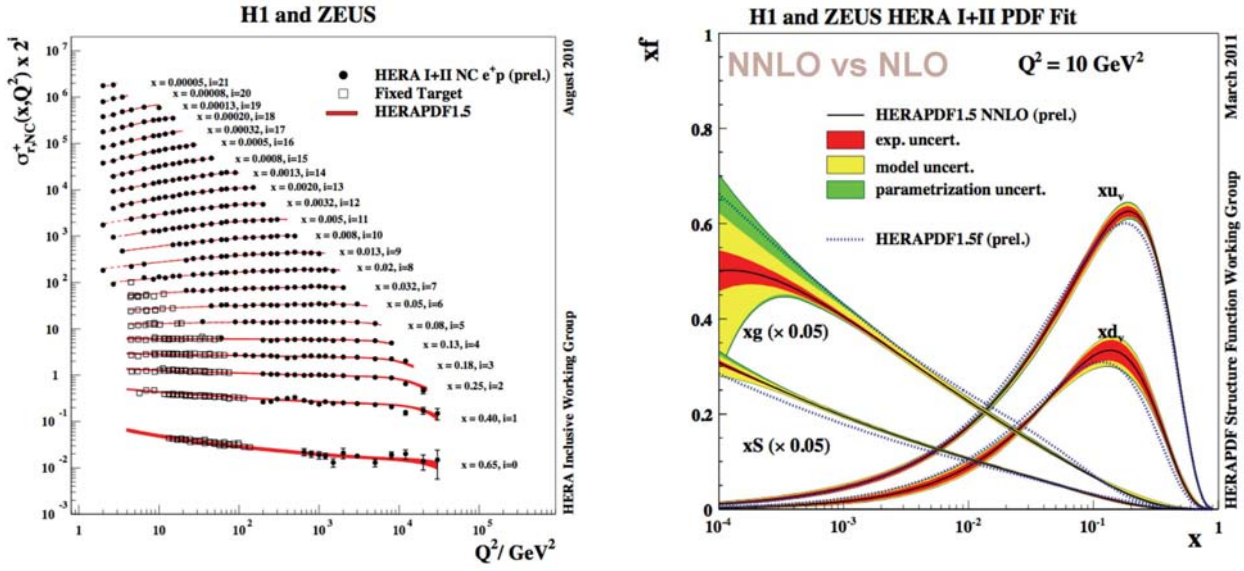

Figure 1:
Combined inclusive Neutral Current cross-section at HERA (left) and associated PDF QCD fits (right)

but also for valence quarks involved in the highest energy interactions. Global Parton Distribution Function (PDF) fits are currently in progress at HERA, involving exclusive jets and charm cross sections in addition to inclusive structure functions. The LHC experiments have also started to contribute to the control of PDF's through cross-section measurements of weak boson production, with LHCb extending the range of measurements to lower x than at HERA.

The phenomena of primary interest for search of new physics at LHC involve inclusive signatures like dijets (figure 2), di-leptons (figure 3) and lepton+missing P_T (figure 4).

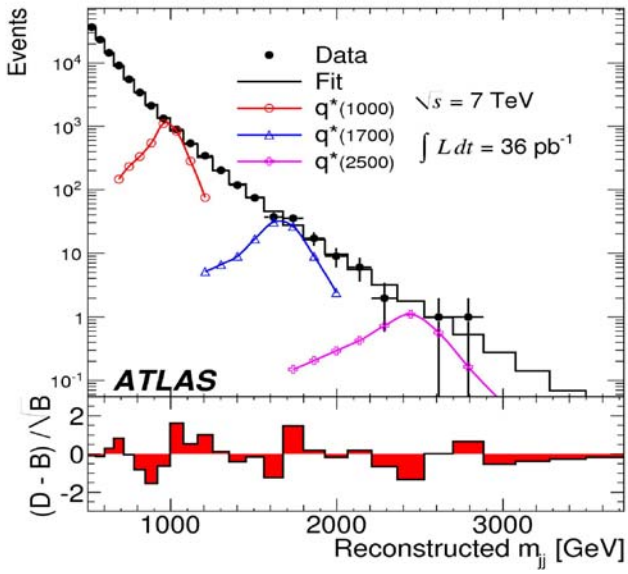

Figure 2:
Inclusive dijet mass distribution measured by ATLAS, compared to possible excited quark signals.

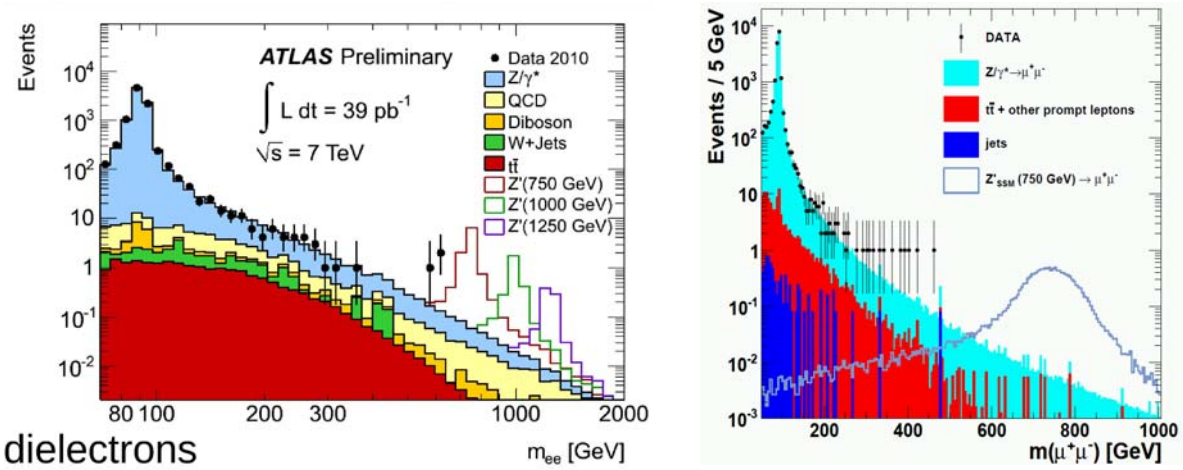

Figure 3: Dielectron (left) and dimuon (right) mass spectra measured by ATLAS and CMS respectively, compared to possible Z' signals.

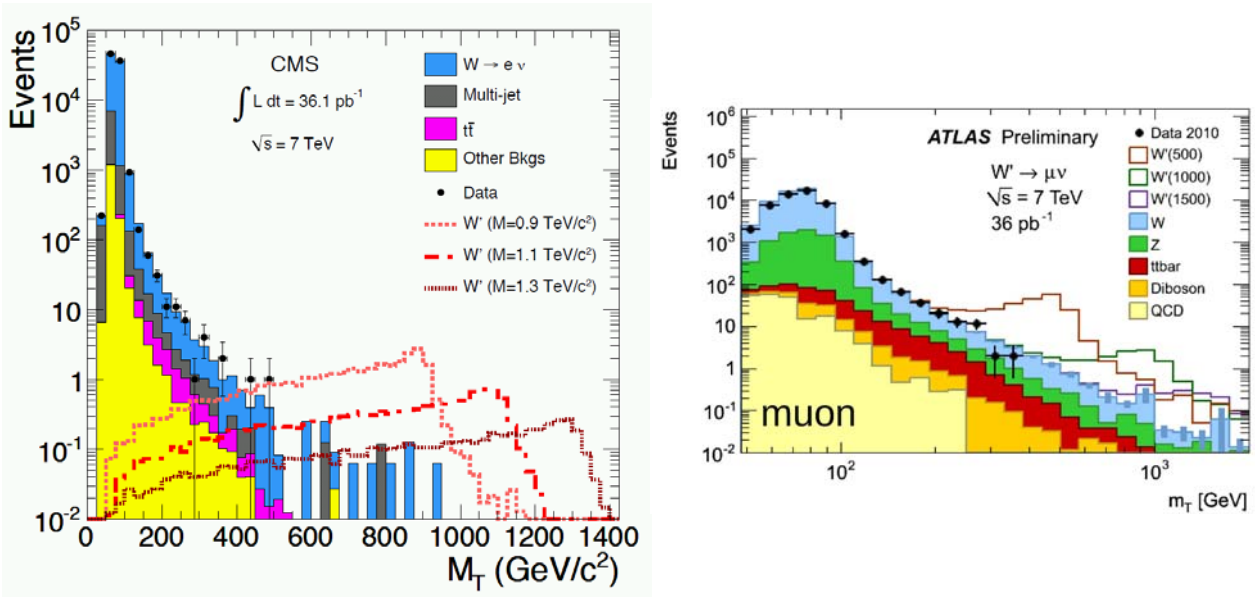

Figure 4: Inclusive electron (left) and muon (right) + missing P_T transverse mass spectra measured by CMS and ATLAS respectively, compared to possible W' signals.

No deviation from the Standard Model (SM) is presently seen. The corresponding lower mass limits released for new heavy particles are in the range of ~2.1 TeV (excited quarks), ~1.1 TeV (Z') and 1.5 TeV (W'), extending the exclusion from TEVATRON. Semi inclusive searches also show no deviation from the SM and allow to extend the exclusion of Minimal Super Symmetry Models in a larger parameter space domain as at TEVATRON (figure 5).

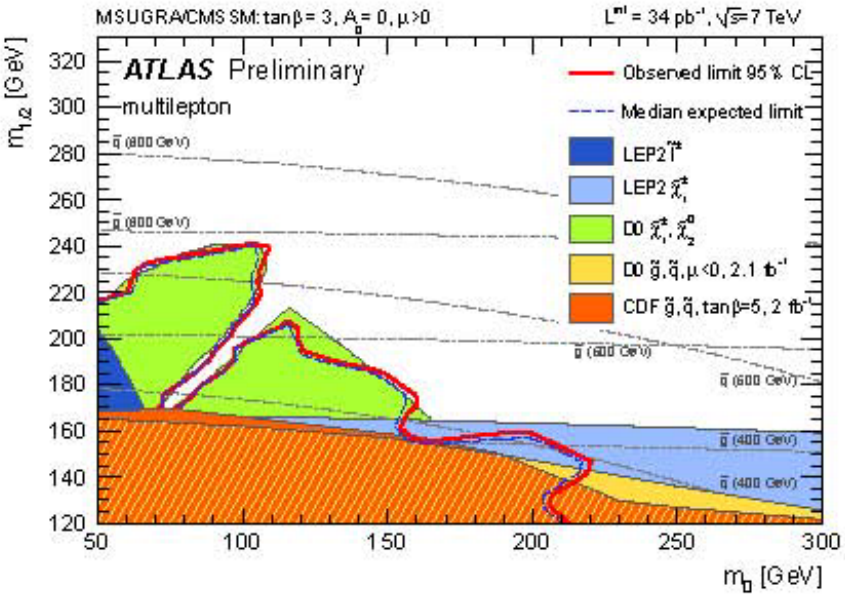

Figure 5:
mSUGRA parameter space excluded by ATLAS using semi-inclusive 3 leptons+jet signature.

The sensitivity to Standard Model Higgs production is still dominated by the TEVATRON experiments, which have released a new combined limit in the high mass domain dominated by the H → WW decay channel (figure 6).

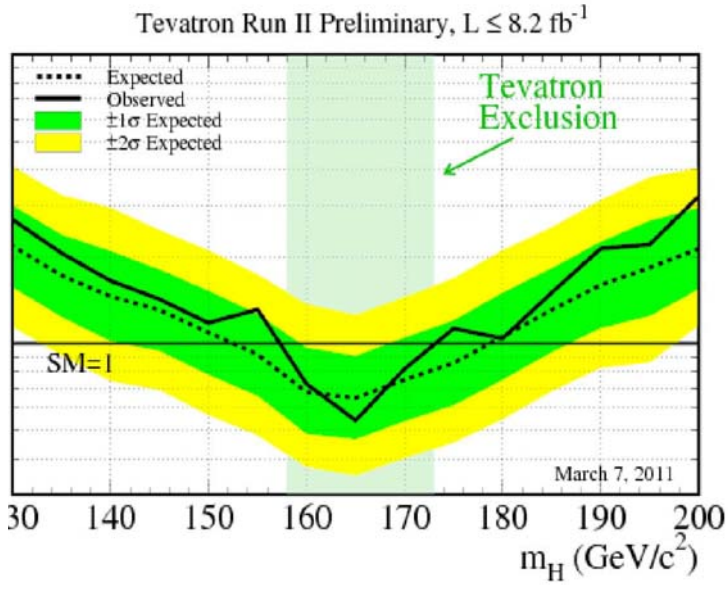

Figure 6:
New SM Higgs combined exclusion limit from the Tevatron experiments.

The ATLAS and CMS experiments have also started to provide SM Higgs limits and will become competitive with Tevatron when an integrated luminosity of ~1 fb^{-1} has been accumulated. Both Tevatron and LHC experiments control Higgs decay processes from measurements of very low cross-section di-boson production. Figure 7 shows that these processes are already seen and measured in agreement with the SM at LHC.

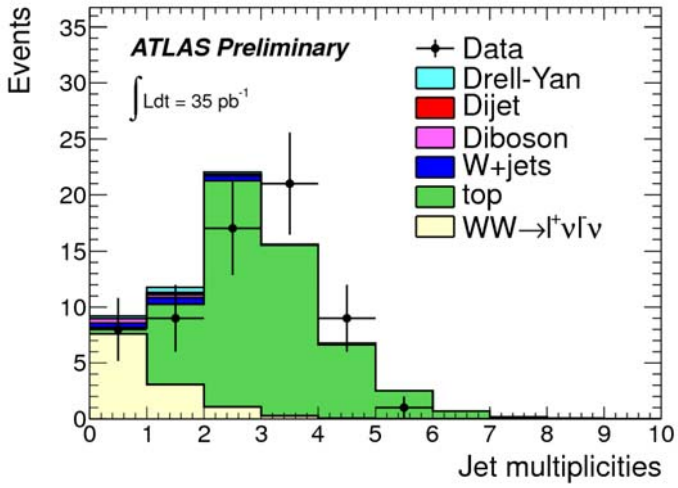

Figure 7: WW production measured by ATLAS compared to expectations.

Another domain where Tevatron is still leading the way is top physics. The Tevatron experiments have now in hands samples of several thousand top-antitop pairs and are constantly updating the investigation of all decay channels to improve the measurements of top properties (figure 8).

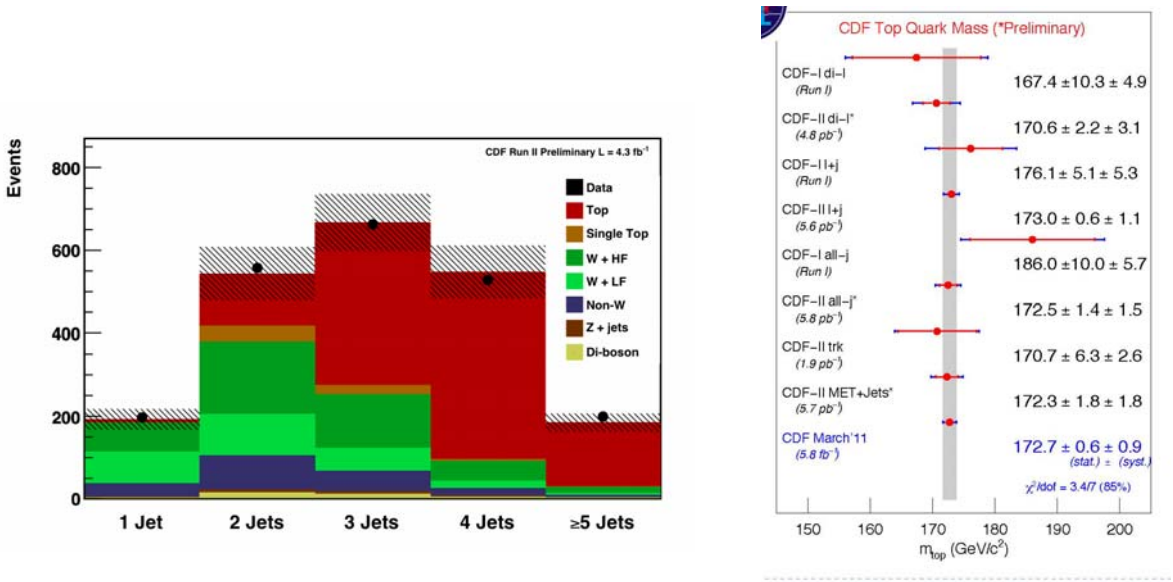

Figure 8: Recent CDF top measurement in the hadronic decay channel (left) and compilation of top mass determination (right).

One intriguing observation is the indication of a forward-backward asymmetry between the 2 tops of the top pair system, observed by both Tevatron experiments (figure 9) in contrast with the small asymmetry expected in the SM. There is however no visible deviation from SM in the measured top pair mass spectrum (figure 10).

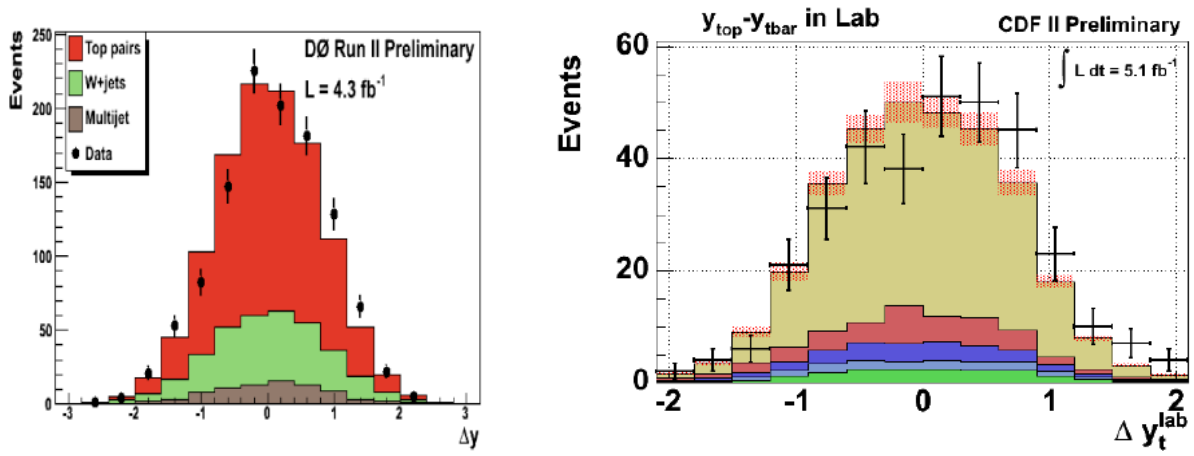

Figure 9:
Forward-backward asymmetry measured by D0 (left) and CDF (right) in top pair production.

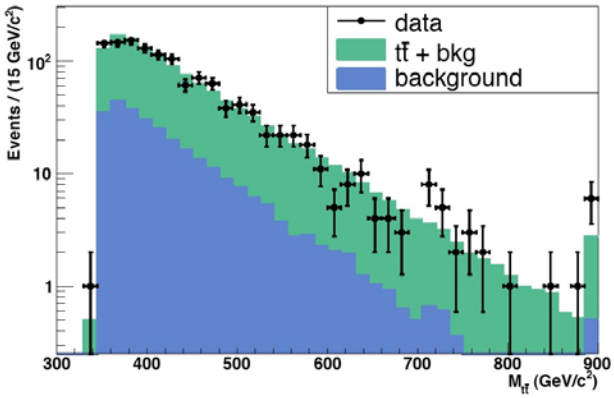

Figure 10: Top pair mass spectrum measured by CDF

The LHC experiments have also started to measure both top pair and single top cross sections (figure 11). The results are in agreement with the SM expectation.

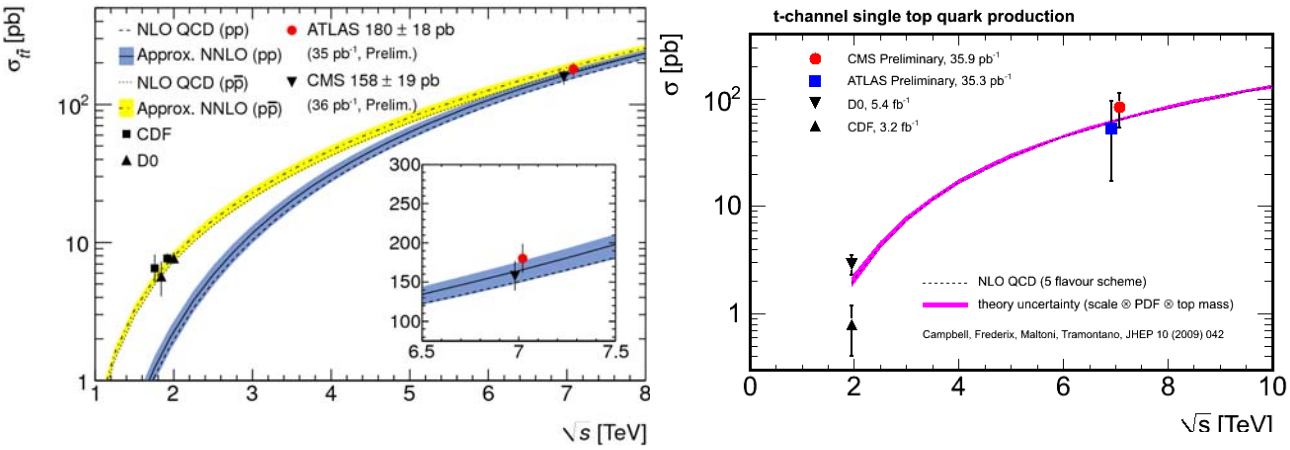

Figure 11:
Top pair (left) and single top (right) cross-sections measured at LHC in comparison with Tevatron .

The investigations of low cross-section Higgs and top processes rely on a good understanding of the SM background originating from high cross-section processes with hadronic jets and/or electroweak bosons. The LHC experiments have shown that their measurements of QCD processes are in good agreement with the SM within the present statistical and systematic errors.

3 High Density Matter

The one-month dedicated Lead-Lead run performed at LHC end of 2010 at a nucleon-nucleon centre of mass energy of 2.76 TeV has opened a new era in the study of the deconfined Quark Gluon Plasma (QGP). LHC investigates the QCD phase transition in the same domain of the temperature - baryonic potential phase plane as RHIC, but the higher centre of mass energy of the initial state probes the deconfined medium further away from the phase transition, and dramatically enhances the yield of hard probes like heavy quarks and electroweak bosons.

Electroweak bosons have been observed for the first time by ATLAS and CMS in Heavy Ion collisions (figure 12) and their yield, as expected, shows no indication of dependence with the centrality of the collision. This opens the way to a direct control of nuclear PDF's and possible saturation effects at low x.

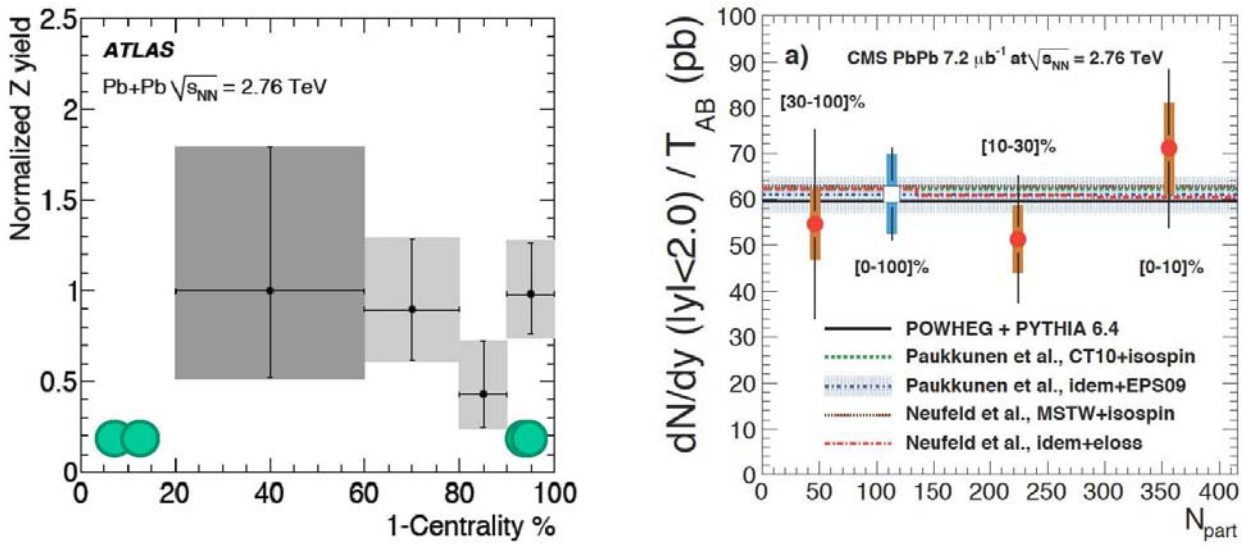

Figure 12: Z yields measured in Pb-Pb collisions by ATLAS (left) and CMS (right) as a function of the collision centrality.

The QGP global properties, as measured by ALICE (figure 13) from particle densities, elliptic flow or Bose-Einstein correlations, are in agreement with the predictions of the standard QGP thermodynamical model adjusted on RHIC data, with some additional viscous corrections. The particle flow measured in Heavy Ion collisions however shows unexpected long range rapidity correlations ("the ridge"). Further investigations of this effect at RHIC shows apparition of a jet-like structure as the particle transverse momenta increase (figure 14). The "ridge" is confirmed by ALICE in Pb-Pb collisions and also visible in high multiplicity pp collisions at the LHC energy.

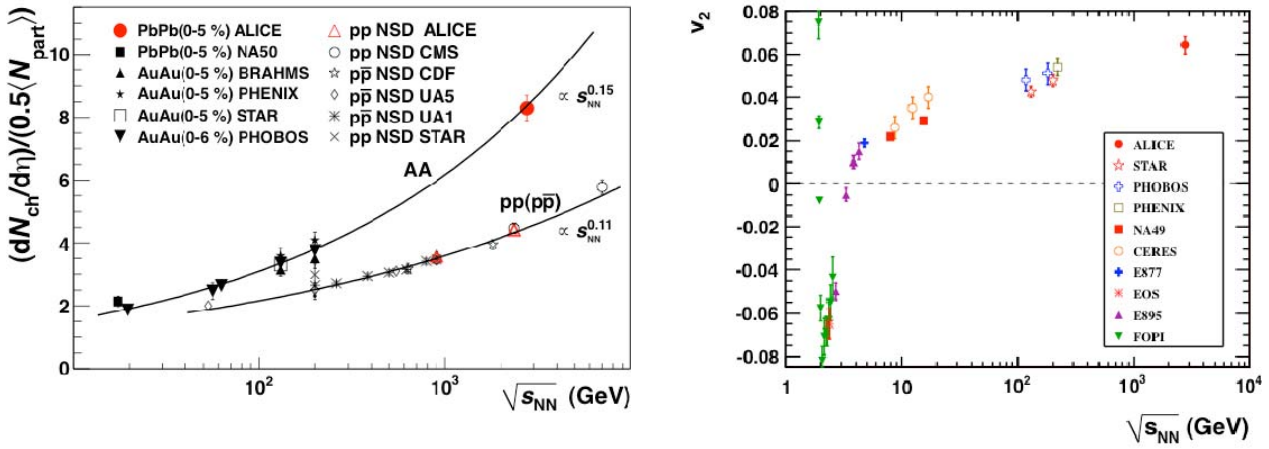

Figure 13: Particle densities (left) and ellipticity (right) measured by ALICE in comparison with lower energy experiments.

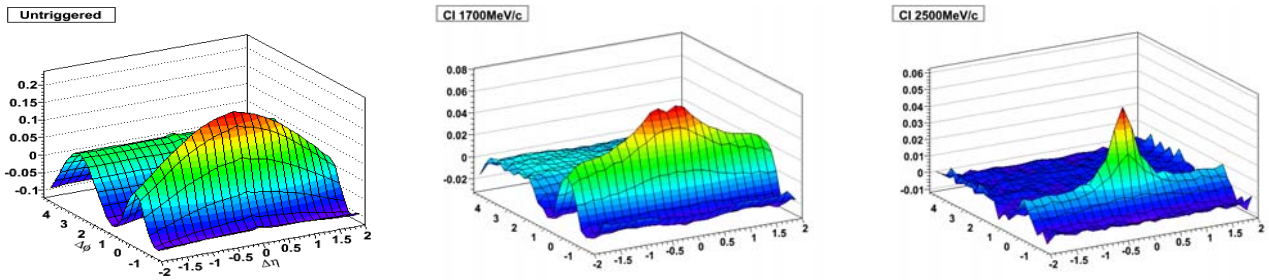

Figure 14: η-φ correlations between particles measured at RHIC by the STAR experiment in domains of increasing P_T: P_T > 0.15 GeV (left), 1.7 GeV (middle) and 2.5 GeV (right).

A domain of particular interest is the influence of the QGP medium on parton flow, studied from the yields of individual high-P_T hadrons or hadronic jets as function of centrality. In central collisions, ALICE measures a stronger quenching of high-P_T hadrons as at RHIC (figure 15). As regards hadronic jets, a qualitatively new measurement, made possible by the high centre of mass energy and the 4π calorimetric coverage of the detectors, is the observation by ATLAS and CMS of direct jet quenching, visible from event by event dijet asymmetries increasing with centrality. The study of the azymuthal energy flow as function of this dijet asymmetry shows that the quenched energy is released in softer particles emitted away from the direction of the initial high-P_T parton (figure 16). This feature is not described by conventional PYTHIA radiation.

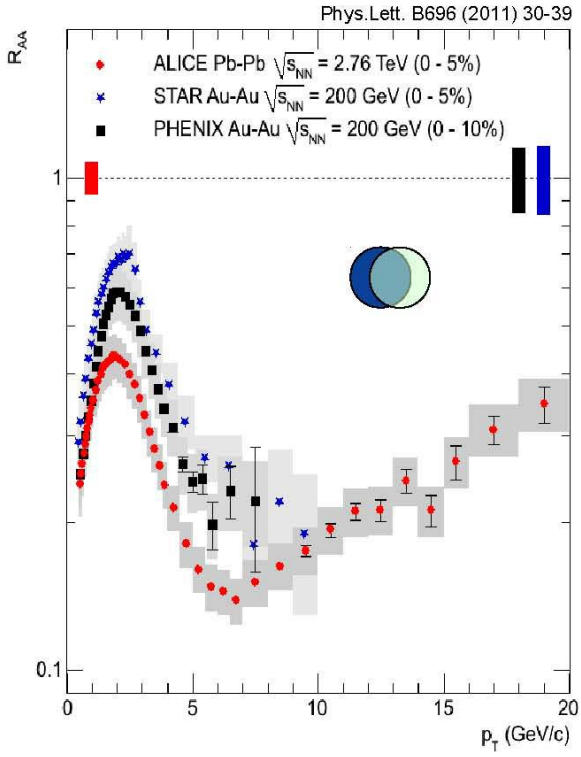

Figure 15: Yield of high-P_T hadrons normalized to pp collisions, measured in central Heavy Ion collisions as function of the hadron transverse momentum.

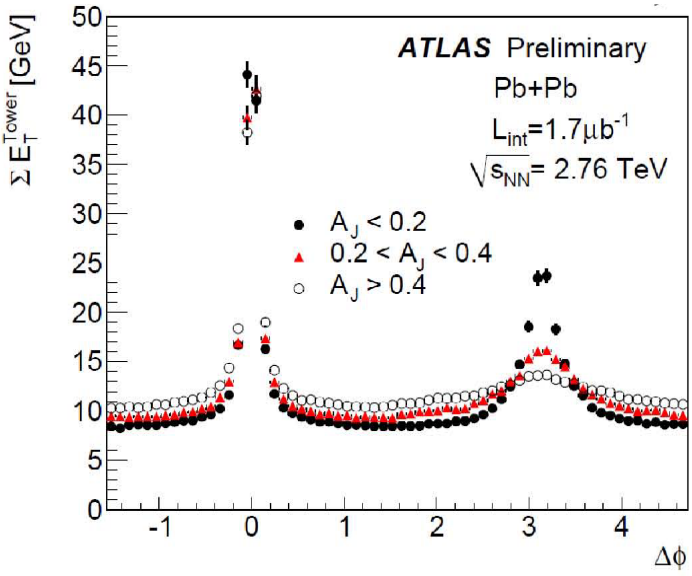

Figure 16: Transverse energy flow in dijet events measured by ATLAS in Pb-Pb collisions for 3 domains of dijet asymmetry.

4 Low energy precision

Spectroscopy of the whole spectrum of heavy flavors is still a very active field. K factories like NA48 are measuring K decays with very low branching ratios, constraining chiral perturbative QCD computations of mesons form factors. The BES III charm factory is now fully operational and provides a harvest of high precision results including several unexpected effects which could be related to glueball production. At B factories BABAR and BELLE are completing their measurements of rare D decays and D meson masses, providing results in reasonable agreement with QCD expectations (figure 17).

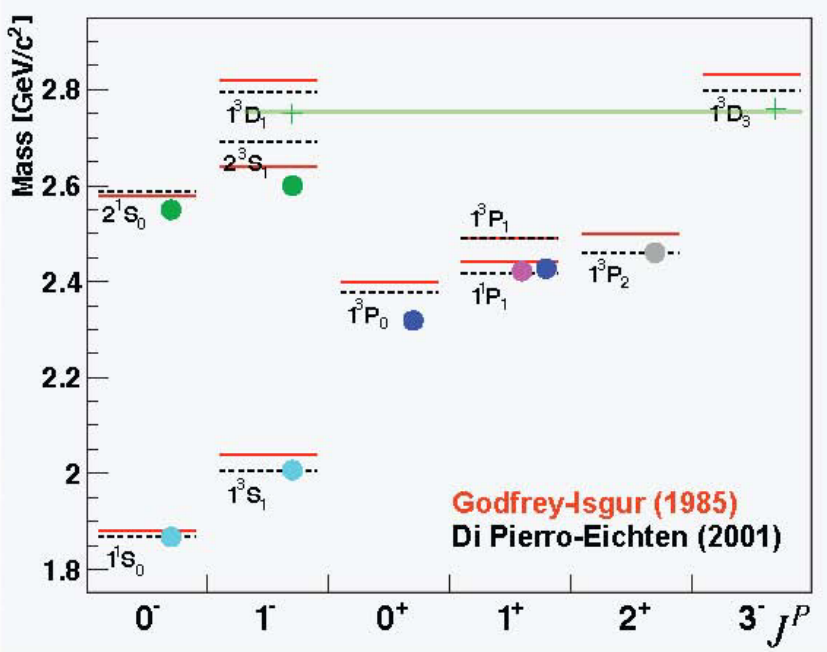

Figure 17: Latest measurements of the masses of D mesons states (top) by BABAR and BELLE, compared to QCD computations.

The highlight of the 2011 Moriond QCD edition however comes from the B physics results from the Tevatron experiments and the LHCb Collaboration. Compared to B factories, hadron colliders benefit from much higher production cross sections of B mesons, with an extra large enhancement at LHCb compared to Tevatron due to the forward configuration of the experiment. There is currently a strong focus on the B_s^o meson, which cannot be precisely studied at B factories due to its production threshold, and whose oscillation pattern gives access to the V_{ts} term of the CKM matrix, as well as to possible non-SM extra terms. The oscillation of the B_s^o system is characterized by 3 parameters: Δm_s, the mass difference of the 2 mass eigenstates, which controls the frequency of the oscillation, $\Delta\Gamma_s$, the life time difference of the 2 mass eigenstates, and $\Phi_s = -2\beta_s$, the phase

difference related to the amplitude of the oscillation. LHCb already measures Δm_s (figure 18) with a precision competitive with Tevatron, including a slightly higher statistical error but a significantly smaller systematic error, which validates the B_s flavor tagging method used in the measurement.

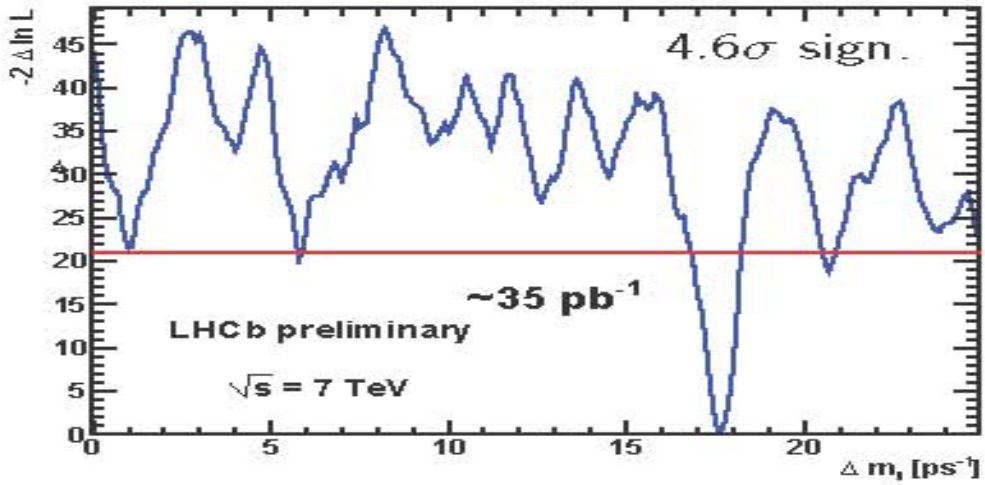

Figure 18: Δm_s measurement from LHCb.

The $\Delta\Gamma_s$ and Φ_s terms can be measured together from the interference between oscillation and decay in the $B_s^o \rightarrow J/\psi\ \varphi$ channel. The CDF and D0 results agree with the SM within one standard deviation (figure 19). LHCb has started to investigate this channel but, at the time of Moriond QCD 2011, still needs to add flavor tagging as well as more statistics to compete with Tevatron.

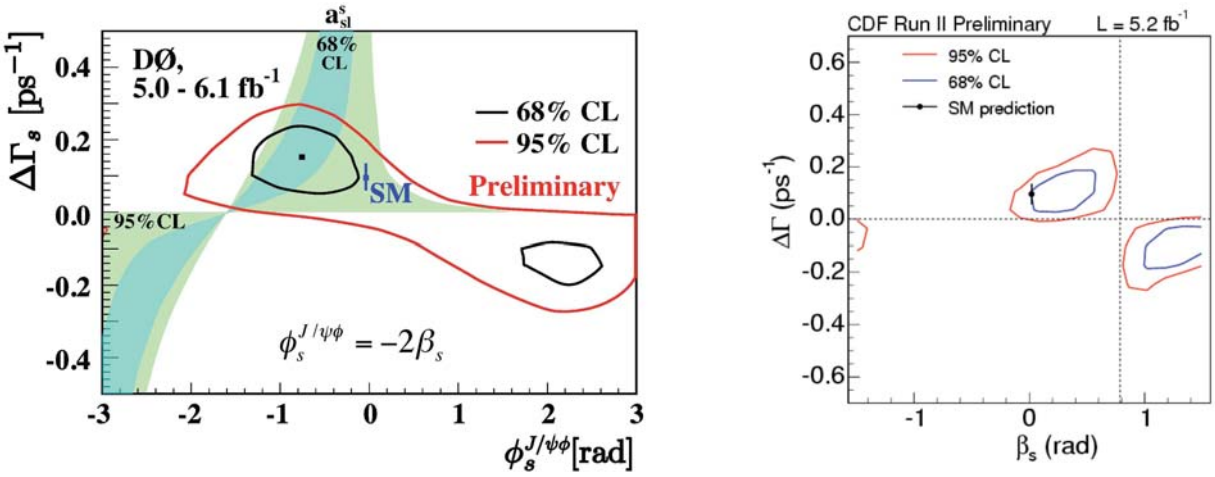

Figure 19: Measurement of ($\Delta\Gamma_s$,Φ_s) by D0 (left) and CDF (right) in the $B_s^o \rightarrow J/\psi\ \varphi$ channel.

Sensitivity to Φ_s and anomalous CP violation is also provided by the charge asymmetry measured in inclusive semi-leptonic B decays. At Tevatron, this asymmetry is related to the sum of the a^d and a^s

asymmetries associated to B_d and B_s mesons respectively. The measurement from D0 shows a deviation from the SM by 3.2 standard deviations (figure 20). CDF is also investigating this asymmetry but with an expected larger uncertainty due to their impossibility to revert the magnetic field to control systematic effects. At LHC similar measurements will give sensitivity to the difference a^d - a^s (figure 20) due to the different initial state.

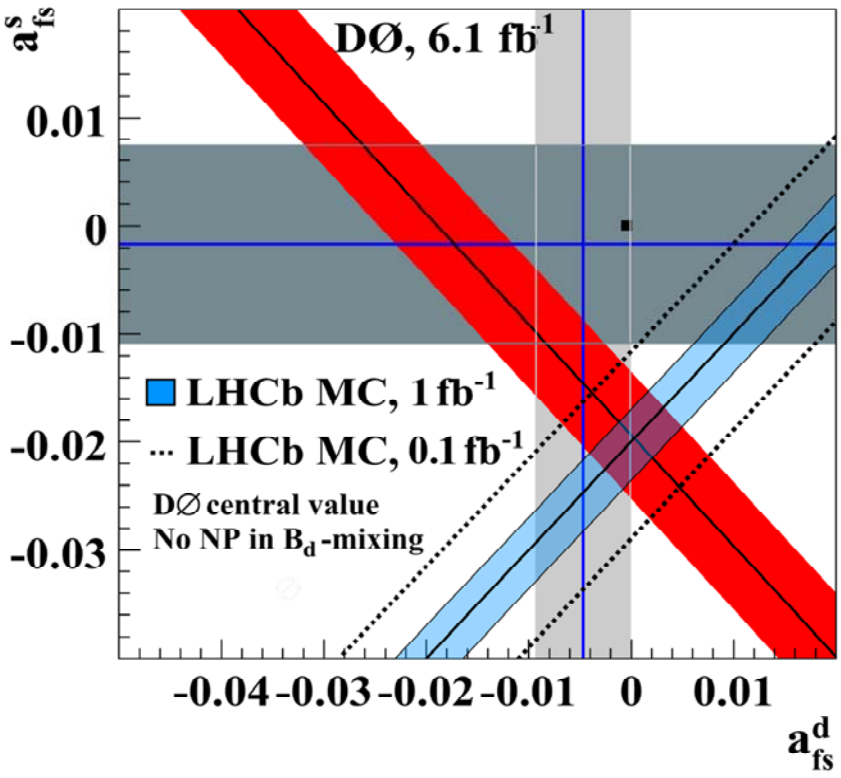

Figure 20: Charge asymmetry in inclusive semi-leptonic B decays measured by D0 (red band) compared to the SM prediction (black square) and the LHCb prospects (blue band).

Ultra-rare B decays, e.g. $B_s \rightarrow \mu^+\mu^-$ whose branching ratio is below 10^{-9} in the SM, are also a promising field to detect new physics at hadron colliders. The upper limit obtained by LHCb on this channel is already competitive with Tevatron, though still a factor 10 above the SM prediction.

5 Outlook

In 2011 more than 1 fb^{-1} of pp collisions are expected to be collected by the LHC experiments, whereas the Tevatron is scheduled to stop data taking at the end of the year. On the short term a lively competition between the two colliders is expected for Higgs hunting and searches for anomalous top and B physics.

List of Participants

XLVIth Rencontres de Moriond

QCD and High Energy Interactions

List of Participants

Family name	First name	Institution	Country	Email address
Amerio	Silvia	INFN	Italy	silvia.amerio@pd.infn.it
Aref'eva	Irina	Steklov Mathematical Institute	Russia	arefeva@mi.ras.ru
Arleo	Francois	LAPTH	France	arleo@lapp.in2p3.fr
Arnaud	Nicolas	LAL	France	narnaud@lal.in2p3.fr
Augé	Etienne	CNRS/IN2P3	France	eauge@admin.in2p3.fr
Barlow	Nick	University of Cambridge	UK	nbarlow@hep.phy.cam.ac.uk
Bartos	Pavol	Comenius University	Slovakia	bartos.palik@gmail.com
Bazterra	Victor	University of Illinois	USA	baites@fnal.gov
Becher	Thomas	University of Bern	Switzerland	becher@itp.unibe.ch
Behari	Satyajit	Johns Hopkins University	USA	behari@fnal.gov
Ben-Haim	Eli	LPNHE	France	benhaim@in2p3.fr
Benhabib	Lamia	LLR - École Polytechnique	France	lamia.benhabib@gmail.com
Berger	Edmond	Argonne National Laboratory	USA	berger@anl.gov
Bernardi	Gregorio	LPNHE	France	gregorio@fnal.gov
Bettler	Marc-Olivier	INFN	Italy	marc-olivier.bettler@cern.ch
Bleve	Carla	Bergische Universitaet Wuppertal	Germany	bleve@physik.uni-wuppertal.de
Bloch-Devaux	Brigitte	University of Torino	Italy	brigitte.bloch@cern.ch
Bopp	FritzWilhelm	University of Siegen	Germany	bopp@physik.uni-siegen.de
Brandt	Oleg	University of Goettingen II	Germany	obrandt@fnal.gov
Brower	Richard	Boston University	USA	brower@bu.edu
Bu	Xuebing	Fermilab	USA	xbbu@fnal.gov
Camarda	Stefano	IFAE - Barcelona	Spain	camarda@ifae.es
Castro	Nuno	LIP - Minho	Portugal	nuno.castro@cern.ch
Cenci	Riccardo	University of Maryland	USA	cenci@slac.stanford.edu
Cerutti	Francesco	Universidad de Barcelona	Spain	francesco.cerutti@gmail.com
Chen	Chin-Hao	Stony Brook University	USA	chinchen@ic.sunysb.edu
Chiorboli	Massimiliano	Universitá di Catania	Italy	massimiliano.chiorboli@cern.ch
Cho	DooKee	Brown University	USA	dkcho@fnal.gov
Choudhary	Brajesh	University of Delhi	India	brajesh@fnal.gov
Ciulli	Vitaliano	Universitá di Firenze	Italy	vitaliano.ciulli@cern.ch
Cooke	Michael	Fermilab	USA	mpc@fnal.gov
Costa	Miguel	Universidade do Porto	Portugal	miguelc@fc.up.pt
Cristinziani	Markus	Physikalisches Institut	Germany	cristinz@uni-bonn.de
Del Duca	Vittorio	INFN	Italia	delduca@lnf.infn.it
Dell'Acqua	Andrea	CERN	Switzerland	dellacqu@mail.cern.ch
Dixon	Lance	SLAC	USA	lance@slac.stanford.edu
Djouady	Abdelhak	LPT Orsay	France	abdelhak.djouadi@cern.ch
Djuric	Marko	Universidade do Porto	Portugal	marko.djuric@fc.up.pt
Dolezal	Zdenek	Charles University	Czech Republic	dolezal@ipnp.troja.mff.cuni.cz
Dremin	Igor	Lebedev Physical Institute	Russia	dremin@lpi.ru
Federic	Pavol	Comenius University	Slovakia	pavol.federic@cern.ch
Fleischer	Robert	Nikhef	The Netherlands	Robert.Fleischer@nikhef.nl
Garmash	Alexey	Budker Institute of Nuclear Physics	Russia	garmash@inp.nsk.su
Giacosa	Francesco	Institute of Theoretical Physics	Germany	giacosa@th.physik.uni-frankfurt.de
Giammanco	Andrea	UCL	Belgium	andrea.giammanco@cern.ch
Gonzalez Suarez	Rebeca	Vrije Universiteit Brussel	Belgium	regonzal@vub.ac.be
Goulianos	Konstantin	The Rockefeller University	USA	dino@rockefeller.edu
Gris	Philippe	Laboratoire de Physique Corpusculaire	France	gris@clermont.in2p3.fr
Grohsjean	Alexander	CEA Saclay IRFU/SPP	France	agrohsje@fnal.gov
Grosse-Oetringhaus	Jan Fiete	CERN	Switzerland	jgrosseo@mail.cern.ch
Gruschke	Jasmin	KIT - Institut für Experimentelle Kernphysik	Germany	jasmin.gruschke@kit.edu
Hamilton	Keith	INFN - Universitá di Milano-Bicocca	Italy	keith.hamilton@mib.infn.it
Harel	Amnon	University of Rochester	USA	Amnon.Harel@cern.ch
Harland-Lang	Lucian	HEP Group	UK	lh367@cam.ac.uk
Hautmann	Francesco	University of Oxford	UK	francesco.hautmann@cern.ch
Hays	Jonathan	HEP Imperial College	UK	jonathan.hays@imperial.ac.uk
Heintz	Ulrich	Brown University	USA	Ulrich_Heintz@brown.edu
Hoeppner	Christian	TU Muenchen	Germany	christian.hoeppner@cern.ch
Hsieh	Ron-Chou	Academia Sinica	Taiwan	hsiehrc@phys.sinica.edu.tw
Hughes	Emlyn	Columbia University	USA	ewh42@columbia.edu
Kauder	Kolja	University of Illinois	USA	kkaude2@uic.edu
Kerbikov	Boris	ITEP	Russia	borisk@itep.ru

Family name	First name	Institution	Country	Email address
Klima	Boaz	Fermilab	USA	klima@fnal.gov
Koshelkin	Andrey	Moscow Institute for Physics and Engineering	Russia	A_Kosh@internets.ru
Kowalski	Henri	DESY	Germany	henri.kowalski@desy.de
Lambert	Rob	CERN	Switzerland	Rob.Lambert@cern.ch
Lamont	Mike	CERN	Switzerland	Mike.Lamont@cern.ch
Landsberg	Greg	Brown University	USA	landsberg@hep.brown.edu
Langenbruch	Christoph	Physikalisches Institut Heidelberg	Germany	clangenb@physi.uni-heidelberg.de
LI	Shi-Yuan	Shandong University	China	lishy@sdu.edu.cn
Liventsev	Dmitri	ITEP	Russia	livent@itep.ru
Lu	Cai-Dian	IHEP - Institute of High Energy Physics	China	lucd@ihep.ac.cn
Lysak	Roman	Academy of Sciences of the Czech Republic	Czech Republic	lysak@fzu.cz
Ma	Frank	MIT	USA	frankma@mit.edu
Maggiora	Marco	University of Turin	Italy	marco.maggiora@to.infn.it
Makovec	Nikola	LAL	France	makovec@lal.in2p3.fr
Mangiafave	Nicola	Cavendish Laboratory	UK	nicola.mangiafave@gmail.com
Mannel	Thomas	Siegen University	Germany	mannel@tp1.physik.uni-siegen.de
Melia	Tom	Rudolf Peierls Centre for Th. Physics	UK	t.melia1@physics.ox.ac.uk
Mesropian	Christina	The Rockefeller University	USA	christina.mesropian@rockefeller.edu
Mischke	Andre	ERC-Starting Independent Research Group	The Netherlands	a.mischke@uu.nl
Narain	Meenakshi	Brown University	USA	narain@hep.brown.edu
Nicassio	Maria	INFN	Italy	maria.nicassio@ba.infn.it
Onofre	Antonio	LIP / University of Minho	Portugal	antonio.onofre@cern.ch
Pachucki	Krzysztof	University of Warsaw	Poland	krp@fuw.edu.pl
Pandolfi	Francesco	Universitá di Roma "Sapienza"	Italy	francesco.pandolfi@cern.ch
Paz	Gil	The University of Chicago	USA	gilpaz@uchicago.edu
Pierog	Tanguy	Karlsruher Institut fuer Technologie	Germany	tanguy.pierog@kit.edu
Pietrzyk	Bolek	LAPP	France	pietrzyk@lapp.in2p3.fr
Pohl	Randolf	Max-Planck-Institut für Quantenoptik	Germany	randolf.pohl@mpq.mpg.de
Pospelov	Gennady	Max-Planck-Institut für Physik	Germany	pospelov@mppmu.mpg.de
Qiao	Congfeng	Graduate Univ.f Chinese Academy of Scieces	China	qiaocf@gucas.ac.cn
Quayle	William	University of Wisconsin	USA	wbquayle@gmail.com
Radescu	Voica	DESY	Germany	voica@mail.desy.de
Richter-Was	Elzbieta	Jagiellonian University	Poland	elzbieta.richter-was@uj.edu.pl
Rimoldi	Adele	Universitá di Pavia / INFN	italy	adele.rimoldi@cern.ch
Robens	Tania	School of Physics and Astronomy	UK	trobens@physics.gla.ac.uk
Rubinskiy	Igor	DESY	Germany	rubinsky@mail.desy.de
Sahlmueller	Baldo	Stony Brook University	USA	baldo@bnl.gov
Salvachúa	Belen	Argonne National Laboratory	USA	Belen.Salvachua@cern.ch
Sapeta	Sebastian	LPTHE	France	sapeta@lpthe.jussieu.fr
Schieck	Jochen	Ludwig-Maximilians-Universität	Germany	Jochen.Schieck@lmu.de
Schoeffel	Laurent	CEA Saclay	France	laurent.schoeffel@cea.fr
Seto	Richard	University of California	USA	richard.seto@ucr.edu
Skachkov	Nikolay	Joint Institute for Nuclear Research	Russia	nikskach@gmail.com
Spousta	Martin	Charles University - IPNP	Czech Republic	spousta@ipnp.troja.mff.cuni.cz
Spradlin	Patrick	University of Glasgow	UK	Patrick.Spradlin@cern.ch
Starovoitov	Pavel	CERN	Switzerland	Pavel.Starovoitov@cern.ch
StDenis	Richard	University of Glasgow	UK	r.stdenis@physics.gla.ac.uk
Strologas	John	University of New Mexico	USA	strolog@fnal.gov
Sugimoto	Shigeki	IPMU - University of Tokyo	Japan	shigeki.sugimoto@ipmu.jp
Tan	Chung-I	Brown University	USA	tan@het.brown.edu
Tang	Aihong	Brookhaven National Laboratory	USA	aihong@bnl.gov
Taylor	Tomasz	Northeastern University	USA	taylor@neu.edu
Thäder	Jochen	GSI Research Division / EMMI	Germany	jochen@thaeder.de
Thompson	Emily	University of Massachusetts	USA	emily.thompson@gmail.com
Todorova	Sharka	Tufts University	USA	sarka.todorova@cern.ch
Tokar	Stano	Comenius University	Slovakia	Stanislav.Tokar@cern.ch
Ulmer	Keith	University of Colorado	USA	keith.ulmer@colorado.edu
Valencia	German	Iowa State University	USA	valencia@iastate.edu
Vallee	Claude	CPPM	France	vallee@cppm.in2p3.fr
Wang	Jianxiong	IHEP - Institute of High Energy Physics	China	jxwang@ihep.ac.cn
Was	Zbigniew	Institute of Nuclear Physics / IFJ-PAN	Poland	zbigniew.was@cern.ch
White	Christopher	School of Physics and Astronomy,	UK	c.white@physics.gla.ac.uk
Wiechula	Jens	Eberhard Karls Universität Tübingen	Germany	Jens.Wiechula@cern.ch
Wosiek	Barbara	Institute of Nuclear Physics PAS	Poland	barbara.wosiek@ifj.edu.pl
Wu	Zhi	IHEP - Institute of High Energy Physics	China	wuz@ihep.ac.cn
Wulz	Claudia-Elisabeth	Institute of High Energy Physics	Austria	claudia.wulz@cern.ch
Ye	Zhenyu	Fermilab	USA	yezhenyu@fnal.gov
Zakharov	Bronislav	L.D. Landau Institute for Theoretical Physics	Russia	bgz@itp.ac.ru